DOC.20080108.0003

QA: QA

MDL-NBS-HS-000006 REV 03

August 2007

UZ Flow Models and Submodels

THIS DOCUMENT CONTAINS THE FOLLOWING, LOCATED AT THE BACK OF THE DOCUMENT:
1) ADDENDUM 001, DATED 12/21/2007

Prepared for:
U.S. Department of Energy
Office of Civilian Radioactive Waste Management
Office of Repository Development
1551 Hillshire Drive
Las Vegas, Nevada 89134-6321

Prepared by:
Sandia National Laboratories
OCRWM Lead Laboratory for Repository Systems
1180 Town Center Drive
Las Vegas, Nevada 89144

Under Contract Number
DE-AC04-94AL85000

DISCLAIMER

This report was prepared as an account of work sponsored by an agency of the United States Government. Neither the United States Government nor any agency thereof, nor any of their employees, nor any of their contractors, subcontractors or their employees, makes any warranty, express or implied, or assumes any legal liability or responsibility for the accuracy, completeness, or any third party's use or the results of such use of any information, apparatus, product, or process disclosed, or represents that its use would not infringe privately owned rights. Reference herein to any specific commercial product, process, or service by trade name, trademark, manufacturer, or otherwise, does not necessarily constitute or imply its endorsement, recommendation, or favoring by the United States Government or any agency thereof or its contractors or subcontractors. The views and opinions of authors expressed herein do not necessarily state or reflect those of the United States Government or any agency thereof.

UZ Flow Models and Submodels

MDL-NBS-HS-000006 REV 03

August 2007

ACKNOWLEDGEMENTS

Additional contributors to this report are G. Lu; K. Zhang; Y. Zhang; L. Pan; E.L. Sonnenthal; G. Zhang; H.H. Liu; J.E. Houseworth; T. Xu; C.K. Ho; and E. Hardin.

INTENTIONALLY LEFT BLANK

Model Signature Page/Change History

Complete only applicable items.

1. Total Pages: 390

2. Type of Mathematical Model

☒ Process Model ☐ Abstraction Model ☐ System Model

Describe Intended Use of Model

The purpose of this report is to document the unsaturated zone (UZ) fluid flow and solute transport models and submodels as well as the flow fields generated utilizing the UZ flow model of Yucca Mountain (UZ Model), Nevada

3. Title

UZ Flow Models and Submodels

4. DI (including Revision No. and Addendum No.):

MDL-NBS-HS-000006 REV03

	Printed Name	Signature	Date
5. Originator	Yu-Shu Wu	Yu-Shu Wu	8/24/07
6. Independent Technical Reviewer	Ming Zhu / Susan Altman	Ming Zhu for Susan Altman	8/24/07
7. Checker	Charles Haukwa	Charles Haukwa	8/24/07
8. QCS/Lead Lab QA Reviewer	John Devers	John K Devers	08/25/07
9. Responsible Manager/Lead	Cliff Ho	Clifford K. Ho	8/25/07
10. Responsible Manager	Stephanie Kuzio	Stephanie Kuzio	8/30/07

11. Remarks

Change History

12. Revision No. and Addendum No.	13. Description of Change
REV 00 / ICN 01	This ICN updates data tracking number (DTN) status and usage and makes minor editorial changes. "To-be-verified" (TBV) designations were removed, and verified and qualified DTNs were identified that contain the same data. No input or output values to this technical product were affected by this activity. TBV-4755 was addressed by replacing unqualified DTN: GS000399991221.004 with qualified and verified DTN: MO0109HYMXPROP.001. TBV-3608 was addressed by deleting Section 6.4.4.3 associated with unqualified DTN: GS010908315214.003. TBV-0536 was addressed by replacing unqualified DTN: GS960208312261.001 with qualified, superseding DTN GS981008312313.003 with qualified and verified DTN GS980508312313.001. TBV-3999, formerly identified with LBNL software code infil2grid V. 1.6, was removed because the associated software is now qualified. The input status of DTNs: GS960908312231.004, GS980408312232.001, and GS980908312242.036 was corrected to N/A - Corroborative Information to reflect actual use of data in the report.

	Reference to input transmittals MOL.19991027.0149, MOL.19991014.0102, MOL.20000118.0092, and MOL.19991213.0041 was removed and replaced with citations for DTNs: MO0109HYMXPROP.001, GS000399991221.003, GS950308312231.002, and GS960808312231.004, respectively. Table 3-1 was changed to identify the correct operational systems used in preparing the report. Section 6.4.3.3 was determined to be unnecessary and was deleted along with the associated Figure 6-32. Seven DTNs: (LB991121233129.001 to LB991121233129.007) were removed from Table 4-1 and Section 8.3 and inserted into Section 8.4 because they are actually technical product outputs of this report. Incomplete reference citations in Section 8.1, 8.3, and 8.4 were updated. A printout of the Document Input Reference System (DIRS) sheets for this report, formerly presented in Attachment I, has been replaced with a reference to the YMP electronic DIRS database. Attachment III of this technical product contains documentation of single use software routines that were qualified under procedure AP-SI.1Q, *Software Management*, prior to the release of Rev. 3 of said procedure. As the scope of the ICN did not involve a change to the routine codes, and they have not been used to develop additional quality affecting information in this technical product, these single use software routines will remain documented herein, in accordance with AP-SI.1Q prior to release of Rev. 3. These changes made in this ICN are identified by change bars. This ICN affects Sections 1, 2, 3, 4, 6, 8, and Attachment I. Only the footer was changed in Attachment II and a footer with page numbers was added to Attachment III. This ICN affects pages 17, 19, 21, 24 to 27, 41, 45, 53, 54 to 55, 68, 73, 75, 77, 81, 83, 85, 88, 90, 102, 104 to 405, 125, 128 to 129, 142 to 144, 149, 152, 159, 160 to 164, 166 to 170, and I-1.
REV 01	The entire model documentation was revised. Side bars are not used because the changes were too extensive to use Step 5.9d)1) per AP-SIII.10Q, Rev. 1/ICN 2.
REV 01 ERRATA 001	Response to CR-1357.
REV 02	Increased transparency in response to the regulatory-focused evaluation performed by the Regulatory Integration Team. Entire model documentation was revised. Side bars are not used because the changes were too extensive to use Step 5.8f)1) per AP-SIII.10Q, REV 02, ICN 07.
REV03	The entire document was revised and updated, including (1) incorporation of updated infiltration maps for present-day and future climates; (2) incorporation of newly calibrated model properties; (3) updated model calibrations and sensitivity studies; (4) estimates of UZ flow weighting factors, and (5) updated model validation efforts. Changes are too extensive to be indicated by sidebars. This revision addresses CRs 7174, 7225, 7453, 8009, 9213, 9227, and 9957.

CONTENTS

Page

CONTENTS (Continued)

Page

CONTENTS (Continued)

Page

CONTENTS (Continued)

Page

CONTENTS (Continued)

Page

INTENTIONALLY LEFT BLANK

FIGURES

Page

FIGURES (Continued)

Page

FIGURES (Continued)

Page

FIGURES (Continued)

Page

FIGURES (Continued)

Page

FIGURES (Continued)

Page

FIGURES (Continued)

Page

FIGURES (Continued)

Page

TABLES

Page

TABLES (Continued)

TABLES (Continued)

INTENTIONALLY LEFT BLANK

ACRONYMS AND ABBREVIATIONS

AFM	active fracture model
BSC	Bechtel SAIC Company, LLC
CHn	Calico Hills nonwelded hydrogeologic unit
DOE	U.S. Department of Energy
ECRB	Enhanced Characterization of Repository Block
ESF	Exploratory Studies Facility
FEP	feature, event, or process
FEHM	finite element heat and mass
LA	license application
MINC	multiple interacting continua
NRC	U.S. Nuclear Regulatory Commission
PTn	Paintbrush nonwelded hydrogeologic unit
QA	quality assurance
QARD	Quality Assurance Requirements and Description
SNL	Sandia National Laboratory
SR	site recommendation
SZ	saturated zone
TCw	Tiva Canyon welded hydrogeologic unit
TDMS	Technical Data Management System
TSPA	total system performance assessment
TSw	Topopah Spring welded hydrogeologic unit
TWP	technical work plan
USGS	United States Geological Survey
UZ	unsaturated zone
UZ model	unsaturated zone flow models and submodels
YMP	Yucca Mountain Project
YMRP	*Yucca Mountain Review Plan, Final Report*

INTENTIONALLY LEFT BLANK

1. PURPOSE

The purpose of this report is to document the unsaturated zone (UZ) flow models and submodels, as well as the flow fields that have been generated using the UZ Flow model(s) of Yucca Mountain, Nevada. In this report, the term *UZ Model* refers to the UZ flow model and the several submodels, which include tracer transport, temperature or ambient geothermal, pneumatic, or gas flow, and geochemistry (chloride, and strontium) submodels. The term *UZ Flow Model* refers to the three-dimensional site-scale UZ flow models used for calibration and simulation of UZ flow fields. This work was planned in *Technical Work Plan for: Unsaturated Zone Flow, Drift Seepage and Unsaturated Zone Transport Modeling* (BSC 2006 [DIRS 177465]) with BSC Level I validation efforts, equivalent to Lead Laboratory procedures, according to SCI-PRO-002, *Planning for Science Activities*.

The unsaturated zone model presented in this report is a revision of that documented in *UZ Flow Models and Submodels* (BSC 2004 [DIRS 169861]). This revision incorporates the new infiltration model results (SNL 2007 [DIRS 174294]) and recalibration of hydrologic properties (SNL 2007 [DIRS 179545]), and implements changes to repository design (SNL 2007 [DIRS 179466]). In this revision, the UZ model results are also used with the infiltration model results to estimate probabilities for flow-field uncertainty associated with infiltration uncertainty. The flow fields provide fracture–fracture, matrix–matrix, and fracture–matrix liquid flow rates, their spatial distributions, and moisture conditions in the unsaturated zone system. These three-dimensional UZ flow fields are used directly by Total System Performance Assessment (TSPA). The UZ model evaluates important hydrogeologic processes in the unsaturated zone as well as geochemical and geothermal conditions. These models provide the necessary framework to test hypotheses of flow and transport at different scales, and predict flow and transport behavior under a variety of climatic conditions. The limitations of the UZ model are discussed in Section 8.11.

This model report relies on many direct inputs, as listed in Section 4, and other data sources. The required information and data sources are taken primarily from following reports: a conceptual model from *Conceptual Model and Numerical Approaches for Unsaturated Zone Flow and Transport* (BSC 2004 [DIRS 170035]); numerical grids from *Development of Numerical Grids for UZ Flow and Transport Modeling* (BSC 2004 [DIRS 169855]); fracture and matrix rock property data as described in *Analysis of Hydrologic Properties Data* (BSC 2004 [DIRS 170038]) and in *Calibrated Unsaturated Zone Properties* (SNL 2007 [DIRS 179545]); geological and mineralogical models from *Geologic Framework Model (GFM2000)* (BSC 2004 [DIRS 170029]) and *Mineralogic Model (MM3.0) Report* (BSC 2004 [DIRS 170031]), and infiltration rates from *Simulation of Net Infiltration for Present-Day and Potential Future Climates* (SNL 2007 [DIRS 174294]).

The three-dimensional flow fields corresponding to 10-, 30-, 50-, and 90-percentile infiltration maps are generated using the UZ flow model in this report. The flow fields are developed for twelve spatially varying maps representing these infiltration uncertainty scenarios for the present-day climate and two projected future climates during the first 10,000 years, monsoon, and glacial transition. For the post-10k-yr period, an additional four uncertainty cases are developed, based on the prescribed percolation flux distribution through the repository footprint, as given in the proposed rule (10 CFR 63). This results in a total of 16 base-case flow fields. These flow fields have been submitted to the Technical Data Management System (TDMS) for

TSPA activities. This report, as well as the studies and results of the previous UZ flow model, has also supported activities and investigations in a number of other model reports, including:

- *Ventilation Model and Analysis Report*
- *Multiscale Thermohydrologic Model*
- *EBS Radionuclide Transport Abstraction*
- *Seepage Model for PA Including Drift Collapse*
- *Seepage Calibration Model and Seepage Testing Data*
- *Mountain-Scale Coupled Processes (TH/THC/THM)*
- *Radionuclide Transport Models Under Ambient Conditions*
- *Drift-Scale Coupled Processes (DST and TH Seepage) Models*
- *Drift Scale THM Model*
- *Abstraction of Drift Seepage*
- *Particle Tracking Model and Abstraction of Transport Process*
- *Total System Performance Assessment (TSPA) Model/Analysis for the License Application.*

The UZ flow model results are limited to mountain-scale flow phenomena under natural, ambient conditions. This model does not account for perturbations to the natural system as a result of the presence of repository drifts, repository engineered materials, or repository waste heat. These aspects of the repository system, potentially important for flow phenomena near waste emplacement drifts, have been determined to have a negligible effect on mountain-scale flow behavior. Similarly, the effects of seismic and volcanic disruptive events have been evaluated to have a negligible effect on mountain-scale UZ flow in *FY 2007 LA FEP List and Screening* (MO0706SPAFEPLA.001 [DIRS 181613]) and therefore are not incorporated into this model. The numerical discretization of the model limits the results to larger-scale flow phenomena on the order of hundreds of meters horizontally and tens of meters vertically. Repository emplacement and access drifts are not explicitly represented in the model. Therefore, details of flow behavior near these excavations under subgridblock scale are not considered in this model. The model uses a steady-state flow approximation determined to be suitable for flow behavior below the Paintbrush nonwelded hydrogeologic unit (PTn) because the hydrologic characteristics of the PTn curtail flow transients (Section 6.1.2). In contrast, the Tiva Canyon welded hydrogeologic unit (TCw), which lies above the PTn, is susceptible to infiltration changes at the ground surface.

The UZ flow models and submodels documented in this report include the UZ flow model(s), ambient thermal submodel, pneumatic submodel, chloride submodel, calcite submodel, and strontium submodel. The UZ flow model is used for generating three-dimensional UZ flow fields, estimating current and future unsaturated zone conditions, and studying tracer-transport behavior. The ambient thermal or temperature submodel characterizes ambient geothermal conditions with temperature data for use in the UZ model, and provides the boundary and initial condition for the mountain-scale coupled processes thermal-hydrologic (TH) model. Pneumatic data are used for additional calibration of the three-dimensional UZ flow model using the pneumatic submodel. The chloride submodel examines the spatial and temporal variations in chloride chemistry, and the results are compared with pore-water concentrations measured in samples from boreholes, the Exploratory Studies Facility (ESF), and the Enhanced Characterization of Repository Block (ECRB) Cross Drift. Modeling calcite deposition can be

used to constrain hydrological parameters such as the infiltration-percolation flux. The calcite modeling also provides additional evidence for validation of the UZ model. Moreover, the strontium submodel incorporates the effects of rate-limited dissolution and precipitation on the concentration of a solute, in addition to dispersion, radioactive decay, and linear equilibrium adsorption. Also, the temperature submodel and chloride submodel are used for flow field weighting (Section 6.8). The primary objectives of developing the UZ flow model and its submodels are to:

- Integrate all available field data and conceptual knowledge of the unsaturated zone system into a single, comprehensive, and calibrated three-dimensional model for simulating ambient hydrological, thermal, and geochemical conditions, and for predicting system responses to future climate conditions.

- Quantify the flow of moisture, dissolved solutes, heat, and gas through the unsaturated zone under present-day and predicted future climate scenarios.

- Perform detailed studies of perched water, percolation through the PTn, flow patterns through Calico Hills nonwelded (CHn) zeolitic units, and pore-water chemical and calcite analyses.

- Predict the migration of potential radionuclide releases in the unsaturated zone after waste emplacement

- Contribute model parameters and boundary conditions for drift seepage and other modeling studies

- Provide TSPA and Repository Design with a scientifically defensible and credible model of relevant unsaturated zone flow processes.

Calibrated Unsaturated Zone Properties (SNL 2007 [DIRS 179545]) deviates from the TWP (BSC 2006 [DIRS 177465]), which states the calibrated property sets are to be documented as an appendix to this document. The deviation is that this analysis is documented as a separate analysis report. Additional deviations to the TWP (BSC 2006 [DIRS 177465]) are identified in Sections 6.8.1 and 7 of this report.

This model report addresses the condition reports (CR) associated with previous versions as follows:

- CR 7453 identified use as input, in REV 02, of an output from a cancelled document without adequate justification. The present revision does not use any inputs that are outputs from cancelled documents.

- CR 9213 concerns a differing professional opinion. The derivation of weighting factors for flow fields, as documented in Section 6.8, implements the agreed-upon resolution of this differing professional opinion.

- CR 9227 identified misinterpretation of some data in the infiltration map that was output from *Simulation of Net Infiltration for Present-Day and Potential Future Climates*

(BSC 2004 [DIRS 170007]). That infiltration map is not used as input in the present report.

- CR 9957 identified incorrect reference to analysis of ^{14}C data used for calibration of the active fracture parameter. The correct reference is cited in Section 7.5 of the present report.

- CR 7225 concerns different definitions of the repository cells in the previous version of this report (BSC 2004 [DIRS 169861]) and in *Particle Tracking Model and Abstraction of Transport Processes* (BSC 2004 [DIRS 170041]). In the current analyses, the two representations of the repository used the same definition of the outer boundary of the repository, but because of different intended uses of the repository region, the node lists for the two reports are still slightly different. This is acceptable because the purpose of of defining repository nodes within the "repository footprint" is to assess the mean percolation flux and groundwater travel times with tracers released fron nodes within the footprint (Section 7). These are different requirements, and the slight differences in the repository node lists that are still present reflect these different requirements. Therefore, this CR has been addressed.

- CR 8009 identifies a software problem with TOUGHREACT V3.0. TOUGHREACT V3.0 is used in this report but no errors have resulted because the problem is only manifest at temperatures near boiling; the present report contains only flow simulations under ambient-temperature condition.

- CR 7174 concerns several issues that were identified in REV 01 of this report. They have been addressed in the present revision as follows: (i) fractures are included in model of vitric units (Section 6.1.1); (ii) The active-fracture parameter has been recalibrated, increasing the fracture-matrix interaction (Table B-1); and discussions of lateral flow in the PTn in Sections 6.6.2.1 and 6.6.2.2, and temporal damping of episodic infiltration in Section 6.9; discussion of heterogeneity in Section 6.10.1. Other issues identified in CR 7174 either were resolved in REV 02 of this report, or no action was needed.

In this report, Section 1 outlines the purpose of the document and Section 2 summarizes the QA procedure on which this report is based. Section 3 lists the software, its usage, and reasons for use. Section 4 provides Data Tracking Numbers (DTNs) for direct input data sources for model calibration, verification, and development. The main assumptions used in model development are summarized in Section 5. Section 6 presents the main contents of model description, calibration, development, results, and analyses of the current UZ flow model and its submodels. In addition, Section 6.7 discusses tracer transport from the repository horizon to the water table, Section 6.8 provides the methodology and results for UZ flow weighting factors, Section 6.9 investigates the effect of temporal damping on episodic infiltration pulses in the unsaturated zone, and Section 6.10 analyzes uncertainties in parameters and models. Section 7 documents model validation efforts and Section 8 provides conclusions and summaries of this report.

Among the appendices, Appendix A provides the main mathematical equations used in the modeling studies, and Appendix B provides the lists of three-dimensional calibrated parameter sets used for UZ model calibrations and simulation. Appendix C gives locations and coordinates

of selected boreholes used for model calibration or validation. Appendix D shows more results from simulated saturation and water potentials and calculations of chloride flux. Appendix E discusses how to calculate percolation flux and fracture-matrix flow components. Appendix F presents additional percolation fluxes at repository and water table horizons. Appendix G provides supporting files in determining unsaturated zone flow weighting factors, and Appendix H evaluates the impact of the new infiltration model on downstream products. Finally, Appendix I presents data qualification efforts to qualify water table temperature data.

INTENTIONALLY LEFT BLANK

2. QUALITY ASSURANCE

Development of this report and the supporting modeling activities have been determined to be subject to the YMP Quality Assurance (QA) Program, as indicated in *Technical Work Plan for: Unsaturated Zone Flow, Drift Seepage and Unsaturated Zone Transport Modeling* (BSC 2006 [DIRS 177465], Section 8.1). The TWP was developed under Bechtel SAIC Company, LLC (BSC) procedures effective at the time; the work since the Lead Laboratory transition has been conducted under equivalent Lead Laboratory procedures. Approved QA procedures identified in the TWP (BSC 2006 [DIRS 177465], Section 4) have been used to conduct and document the activities described in this report. Since this activity was transitioned to the Lead Laboratory QA program, the corresponding lead lab procedures were used. The methods used to control the electronic management of data (BSC 2006 [DIRS 177465], Section 8.4) during the analysis and documentation activities are described in IM-PRO-002, *Control of the Electronic Management of Information*. The model activities and associated calculations herein were conducted and documented following SCI-PRO-006, *Models*.

INTENTIONALLY LEFT BLANK

3. USE OF SOFTWARE

The software and routines used in the modeling study of this report are listed in Table 3-1. These codes are appropriate for the intended application and were used strictly within the range of validation. These codes were obtained from Software Configuration Management in accordance with IM-PRO-003, *Software Management*.

Table 3-1. Qualified Software Used in This Report

Software Name, Codes	Version	Software Tracking Number (STN)	DIRS Reference Number	Operating Environment (Platform/Operating System)
T2R3D	1.4	10006-1.4-00	[DIRS 146654]	Dec Alpha/UNIX
TOUGHREACT	3.0	10396-3.0-00	[DIRS 161256]	Dec Alpha/OSF1 V5.1
TOUGH2	1.6	10007-1.6-01	[DIRS 161491]	Dec Alpha/OSF1 V5.1, PC-DOS Window98
infil2grid	1.7	10077-1.7-00	[DIRS 154793]	Dec Alpha/OSF1 V4.0
2kgrid8.for	1.0	10503-1.0-00	[DIRS 154787]	Dec Alpha/OSF1 V4.0, PC-DOS Window95
bot_sum.f	1.0	10349-1.0-00	[DIRS 153471]	UNIX/OSF1 V4.0
WINGRIDDER	2.0	10024-2.0-00	[DIRS 154785]	PC/Windows NT 4.0
TOPTEMP_V0.f	1.0	10224-1.0-00	[DIRS 147030]	Dec Alpha/OSF1 V4.0
GET_TEMP_V0.f	1.0	10222-1.0-00	[DIRS 147027]	Dec Alpha/OSF1 V4.0
Tbgas3D	2.0	10882-2.0-00	[DIRS 160107]	SUN/SUN O. S. 5.5.1
T2FEHM	4.0	10997-4.0-00	[DIRS 163161]	Dec Alpha/OSF1 V5.1
WTRISE	2.0	10537-2.0-00	[DIRS 163453]	Dec Alpha/OSF1 V5.1
Bkread.f	1.0	10894-1.0-00	[DIRS 162143]	SUN/SUN O. S. 5.5.1
Smesh.f	1.0	10896-1.0-00	[DIRS 162142]	SUN/SUN O. S. 5.5.1
iTOUGH2	4.0	10003-4.0-00	[DIRS 139918]	SUN/SUN O. S. 5.5.1/ OS V4.0

DIRS = Document Input Reference System.

The use of the codes listed in Table 3-1 is documented in Section 6. These codes and routines have been qualified and meet IM-PRO-003 requirements. TOUGH2 V1.6 (STN: 10007-1.6-01 [DIRS 161491]) is used to generate flow fields (Section 6) and to conduct model calibrations (Sections 6.2, 6.3, 6.4, and 6.6). T2R3D V1.4 (STN: 10006-1.4-00 [DIRS 146654]) is used for tracer transport simulations, tracer transport travel-time estimates (Section 6.7), and modeling pore-water chemistry (Sections 6.5, 7.5, and 7.6). TOUGHREACT V3.0 (STN: 10396-3.0-00 [DIRS 161256]) is used for conducting calcite studies (Section 7.7). WINGRIDDER V2.0 (STN: 10024-2.0-00 [DIRS 154785]) is used to generate a three-dimensional thermal model grid (Section 6.3). The infil2grid V1.7 (STN: 10077-1.7-00 [DIRS 154793]) code is used to apply infiltration maps onto the grids used for simulating flow and transport (Section 6). It is also used (Section 6.1) to map infiltration maps into GENER files of TOUGH2 input data. For the same reason, 2kgrid8.for V1.0 (STN: 10503-1.0-00 [DIRS 154787]) is used to generate dual-permeability grids (Section 6.1). The bot_sum.f (STN: 10349-1.0-00 [DIRS 153471]) code is used for calculation of water mass flux at the water table boundary conditions (Section 6.2.5). TOPTEMP_V0.f (STN: 10224-1.0-00 [DIRS 147030] and GET_TEMP_V0.f (STN: 10222-1.0-00 [DIRS 147027] are used for estimating initial and boundary temperature

conditions (Section 6.3). Tbgas3D V2.0 (STN: 10882-2.0-00 [DIRS 160107] is used for generating surface gas pressure boundary conditions (Section 6.4).

Standard spreadsheets (Microsoft Excel 97 and Microsoft Excel 2002) and plotting programs (Tecplot V9.0) are used and documented according to SCI-PRO-006. Details and procedures for calculations using Excel and its standard functions in postprocessing and flow-field extraction are provided in Appendix C. The output flow-field files of TOUGH2 V1.6 are then used as input files to the routine T2FEHM V4.0 (STN: 10997-4.0-00 [DIRS 163161]), which converts TOUGH2 output files with the format of *flow9.dat* into files readable by FEHM. WTRISE V2.0 (STN: 10537-2.0-00 [DIRS 163453]) is used in Section 6.6.3 to adjust the FEHM-readable files for a higher future water table.

These software, in particular the TOUGH2 family of codes (TOUGH2, T2R3D, and TOUGHREACT), are selected for use in this model report because of their generalized capability for handling UZ flow and transport in fractured rock. There are no limitations in outputs to these software within the range of use for modeling unsaturated flow and transport through fractured, porous rock.

4. INPUTS

This section provides documentation for data (Table 4.1-1) used as direct inputs to this report. The quality assurance (Q)-status of all input and a description of the data are shown in the Document Input Reference System database. The inputs to the modeling activities described in this report are obtained from the TDMS and include:

- Stratigraphy data from borehole logs
- Infiltration maps
- Calibrated fracture and matrix properties
- Geochemistry data from the ESF, the ECRB, and boreholes
- UZ model grids
- Temperature data for boreholes
- Pneumatic-pressure data
- Locations and elevations of perched water in boreholes
- Uncalibrated fracture properties
- Water-potential data
- Matrix liquid-saturation data
- Residual and satiated saturations.

4.1 DIRECT INPUT

The key input data used in the UZ flow model and its submodel development include the following (see Table 4.1-1):

- Fracture properties (frequency, permeability, van Genuchten α and m parameters, porosity, and interface area per unit volume rock) for each UZ model layer

- Matrix properties (porosity, permeability, and the van Genuchten α and m parameters) for each UZ model layer

- Thermal and transport properties (grain density, wet and dry thermal conductivity, grain specific heat, and tortuosity coefficients) for each UZ model layer

- Fault properties (fracture parameters) for each major hydrogeologic unit as defined by Table 6.1-1. Matrix properties in faults are the same as the adjacent matrix blocks of nonfault zones.

The calibrated parameter sets also include an estimate for each model layer of the active-fracture parameter, γ, that accounts for the reduction in interaction between matrix and fracture flow resulting from flow fingering and channelization (Liu et al. 1998 [DIRS 105729]). Uncertainty in the input data and parameters are addressed in Section 6.10. Specific input data sets and associated data tracking numbers (DTNs) are listed in Table 4.1-1.

Table 4.1-1. Input Data Source and Data Tracking Numbers

Current DTN	Location in this Report			Description/Remarks
	Section(s)	Figure(s)	Table(s)	
LB03023DKMGRID.001 [DIRS 162354]	6.1.1	6.1-1		Three-dimensional UZ flow model grid
LB03013DSSCP3I.001 [DIRS 162379][a]	6.2		B-1, B-2, B-3, B-4	Calibrated three-dimensional properties
SN0609T0502206.028 [DIRS 178753]	6.1.4, 6.4-2, 6.5, 6.5.1.2, 6.8.4, 6.10.2, 7.2, D.2.1	6.1-2	6.1-2	Net infiltration maps for present-day climate
SN0609T0502206.024 [DIRS 179063]	6.1.4, 6.10.2	6.1-3	6.1-2, 6.2-6	Net infiltration maps for monsoon climate
SN0609T0502206.029 [DIRS 178862]	6.1.4, 6.1.3, 6.10.2	6.1-4	6.1-2, 6.2-6, 6.7-2	Net infiltration maps for glacial transition climate
LB0611MTSCHP10.001 [DIRS 178586] LB0611MTSCHP30.001 [DIRS 180293] LB0612MTSCHP50.001 [DIRS 180294] LB0612MTSCHP90.001 [DIRS 180295]	6.1.5, 6.2, 6.2.3			One-dimensional site scale calibrated properties
LB0612MTSCHPFT.001 [DIRS 180296]	6.1.5, 6.2, 6.4.1, 6.4.2	6.4-1 to 6.4-4		Two-dimensional site scale calibrated fault properties and gas pressure data
LB0205REVUZPRP.001 [DIRS 159525]	6.2.3			Fracture properties
LB0207REVUZPRP.002 [DIRS 159672]	6.7.1			Matrix properties
GS950208312232.003 [DIRS 105572]	6.3.2, 6.3.3, 6.8.6.1, G			Surface temperature for Boreholes NRG-6 and NRG-7a
GS031208312232.005 [DIRS 179284], GS031208312232.004 [DIRS 182187]	6.3	6.2-4, 6.3-2 to 6.3-6		Temperature data in Boreholes NRG-7a, SD-12 UZ#4, UZ#5, and UZ-7a
GS031208312232.003 [DIRS 171287]	6.2, 6.3	6.2-4, 6.3-2 to 6.3-6, D.1-5	6.2-1	In situ water potential measurement and temperature data in Boreholes NRG-6, NRG-7a, SD-12 UZ#4, UZ#5, and UZ-7a
LB0210THRMLPRP.001 [DIRS 160799]	6.3.4, 6.7.1			Thermal properties
LB0302AMRU0035.001 [DIRS 162378]	6.4.1			Measured atmospheric barometric pressure
GS031208312232.007 [DIRS 178751] GS031208312232.006 [DIRS 182186]	6.3	6.3-2 to 6.3-6		Temperature data in Boreholes NRG-6, NRG-7a, SD-12 UZ#4, UZ#5, and UZ-7a
LB991091233129.001 [DIRS 125868][b]	6.4.1			Pneumatic pressure data used for calibration

Table 4.1-1. Input Data Source and Data Tracking Numbers (Continued)

Current DTN	Location in this Report			Description/Remarks
	Section(s)	Figure(s)	Table(s)	
MO9906GPS98410.000 [DIRS 109059]	Appendix I			Borehole locations
MO0109HYMXPROP.001 [DIRS 155989] GS980808312242.014 [DIRS 106748] LB0208UZDSCPMI.001 [DIRS 161285] SNT02110894001.002 [DIRS 105067] GS040108312312.001 [DIRS 181234] GS980708312242.010 [DIRS 106752] GS980508312313.001 [DIRS 109746]	6.2, 7.3	6.2-2, 6.2-3, 7.3-1 D.1-1, D.1-3 to D.1-7	6.2-1	Matrix saturation, water potential, or perched water elevation data used for calibration
LB0303GASFLW3D.001 [DIRS 180351]	6.4.1			Gas pressure data at boundaries
LB0303THERMESH.001 [DIRS 165168]	6.3.1, 6.3.4	6.3-1, 6.3-4	6.3-1	Three-dimensional grid for thermal modeling
LB0303THERMSIM.001 [DIRS 165167]	6.3.2, 6.3.3	6.3-7, 6.3-8		Calibrated three-dimensional thermal model results

[a] DTN: LB03013DSSCP3I.001 [DIRS 162379] from previous technical product outputs are suitable for their intended use within this report because (1) these data were originated from a reliable source, (2) these data were generated by a qualified organization, Lawrence Berkeley National Laboratory, and (3) these data have been used in previous analyses of UZ flow and transport (i.e., they are pertinent to the properties of interest).

[b] DTN: LB991091233129.001 [DIRS 125868] from historic technical product outputs is suitable for its intended use in this report because: (1) the measured pressure data of this DTN were measurements originated from a reliable source and have not been changed, and (2) the data set has been used in previous model calibration of UZ flow analyses.

DTN = data tracking number; LA = license application; PTn = Paintbrush nonwelded hydrogeologic unit; TSPA = total system performance assessment.

This report documents the UZ flow models and submodels. It utilizes properties from two related unsaturated zone parameter reports in *Calibrated Unsaturated Zone Properties* (SNL 2007 [DIRS 179545]) and *Analysis of Hydrologic Properties Data* (BSC 2004 [DIRS 170038]). The input and output files for the model runs presented in this report are listed in Tables 6.2-6 and 6.7-2, and some of the model input fracture and matrix parameters are given in Appendix B. The data used as direct input for the UZ flow model and UZ flow fields are all qualified in accordance with *Quality Assurance Requirements Description* (QARD) (DOE 2006 [DIRS 177092]) requirements. The model input data are available, qualified data (Section 7.6). The qualified data are appropriate for this study because they represent fracture and matrix properties calibrated for the unsaturated zone at Yucca Mountain. The appropriateness of the data is also discussed in Sections 6 and 7, where they are used for modeling and validation calculations.

4.2 CRITERIA

Technical requirements to be satisfied by performance assessment (PA) are based on 10 CFR 63.114 [DIRS 173273] (*Requirements for Performance Assessment*) and 10 CFR 63.115 [DIRS 173273] (*Requirements for Multiple Barriers*). The acceptance criteria that will be used by the U.S. Nuclear Regulatory Commission to determine whether the technical requirements have been met are identified in *Yucca Mountain Review Plan, Final Report* (YMRP) (NRC 2003 [DIRS 163274]).

The pertinent requirements and acceptance criteria for this report are from *Flow Paths in the Unsaturated Zone* (NRC 2003 [DIRS 163274], Section 2.2.1.3.6). The acceptance criteria identified in Section 2.2.1.3.6 of the YMRP (NRC 2003 [DIRS 163274]) are included below. In cases where subsidiary criteria are listed in the YMRP (NRC 2003 [DIRS 163274]) for a given criterion, only the subsidiary criteria addressed by this model report are listed below. Where a subcriterion includes several components, only some of those components may be addressed. How these components are addressed is summarized in Section 8.12.

Acceptance Criteria from Section 2.2.1.3.6, *Flow Paths in the Unsaturated Zone*

Acceptance Criterion 1, *System Description and Model Integration Are Adequate*:

(1) The total system performance assessment (TSPA) adequately incorporates, or bounds, important design features, physical phenomena, and couplings, and uses consistent and appropriate assumptions throughout the flow paths in the unsaturated zone abstraction process. Couplings include thermal-hydrologic-mechanical-chemical effects, as appropriate.

(2) The aspects of geology, hydrology, geochemistry, physical phenomena, and couplings that may affect flow paths in the unsaturated zone are adequately considered. Conditions and assumptions in the abstraction of flow paths in the unsaturated zone are readily identified and consistent with the body of data presented in the description.

(3) The abstraction of flow paths in the unsaturated zone uses assumptions, technical bases, data, and models that are appropriate and consistent with other related U.S. Department of Energy abstractions. For example, the assumptions used for flow paths in the unsaturated zone are consistent with the abstractions of quantity and chemistry of water contacting waste packages and waste forms, climate and infiltration, and flow paths in the saturated zone (NRC 2003 [DIRS 163274], Sections 2.2.1.3.3, 2.2.1.3.5, and 2.2.1.3.8, respectively). The descriptions and technical bases are transparent and traceable to site and design data.

(4) The bases and justification for modeling assumptions and approximations of radionuclide transport in the unsaturated zone are consistent with those used in model abstractions for flow paths in the unsaturated zone and thermal-hydrologic-mechanical-chemical effects.

(5) Sufficient data and technical bases to assess the degree to which features, events, and processes have been included in this abstraction are provided.

(6) Adequate spatial and temporal variability of model parameters and boundary conditions are employed in process-level models to estimate flow paths in the unsaturated zone, percolation flux, and seepage flux.

(7) Average parameter estimates used in process-level models are representative of the temporal and spatial discretizations considered in the model.

(8) Reduction in unsaturated zone transport distances, after a climate-induced water table rise, is considered.

(9) Guidance in NUREG–1297 and NUREG–1298 (Altman et al. 1988 [DIRS 103597], [DIRS 103750]), or other acceptable approaches for peer review and data qualification, is followed.

Acceptance Criterion 2, *Data Are Sufficient for Model Justification*:

(1) Hydrological and thermal-hydrological-mechanical-chemical values used in the license application are adequately justified. Adequate descriptions of how the data were used, interpreted, and appropriately synthesized into the parameters are provided.

(2) Data on the geology, hydrology, and geochemistry of the unsaturated zone, are collected using acceptable techniques.

(3) Estimates of deep-percolation flux rates constitute an upper bound, or are based on a technically defensible unsaturated zone flow model that reasonably represents the physical system. The flow model is calibrated using site-specific hydrologic, geologic, and geochemical data. Deep-percolation flux is estimated using the appropriate spatial and temporal variability of model parameters, and boundary conditions that consider climate-induced change in soil depths and vegetation.

(5) Sensitivity or uncertainty analyses are performed to assess data sufficiency, and verify the possible need for additional data.

(6) Accepted and well-documented procedures are used to construct and calibrate numerical models.

(7) Reasonably complete process-level conceptual and mathematical models are used in the analyses. In particular: (1) mathematical models are provided that are consistent with conceptual models and site characteristics; and (2) the robustness of results from different mathematical models is compared.

Acceptance Criterion 3, *Data Uncertainty Is Characterized and Propagated through the Model Abstraction*:

(1) Models use parameter values, assumed ranges, probability distributions, and bounding assumptions that are technically defensible, reasonably account for uncertainties and variabilities, and do not result in an under-representation of the risk estimate.

(2) The technical bases for the parameter values used in this abstraction are provided.

(3) Possible statistical correlations are established between parameters in this abstraction. An adequate technical basis or bounding argument is provided for neglected correlations.

(4) The initial conditions, boundary conditions, and computational domain used in sensitivity analyses and/or similar analyses are consistent with available data. Parameter values are consistent with the initial and boundary conditions and the assumptions of the conceptual models for the Yucca Mountain site.

(6) Uncertainties in the characteristics of the natural system and engineered materials are considered.

Acceptance Criterion 4, *Model Uncertainty Is Characterized and Propagated through the Model Abstraction*:

(1) Alternative modeling approaches for features, events, and processes, consistent with available data and current scientific understanding, are investigated. The results and limitations are appropriately considered in the abstraction.

(2) The bounds of uncertainty created by the process-level models are considered in this abstraction.

(3) Consideration of conceptual model uncertainty is consistent with available site characterization data, laboratory experiments, field measurements, natural analogue information and process-level modeling studies; and the treatment of conceptual model uncertainty does not result in an under-representation of the risk estimate.

Acceptance Criterion 5, *Model Abstraction Output Is Supported by Objective Comparisons*:

(1) The models implemented in this TSPA abstraction provide results consistent with output from detailed process-level models and/or empirical observations (laboratory and field testing and/or natural analogues).

(2) Abstractions of process-level models conservatively bound process-level predictions.

(3) Comparisons are provided between the output of abstracted models for flow paths in the unsaturated zone and the outputs of sensitivity studies, detailed process-level models, natural analogues, and empirical observations, as appropriate.

4.3 CODES, STANDARDS, AND REGULATIONS

Here the term "code" refers to a law, not software as used in Section 3. The post-10k-yr flow fields developed in this report follow the proposed rule change to 10 CFR 63.342(c), which stipulates the probability distribution for average percolation flux through the repository footprint. No other codes, standards, or regulations are used in this report.

5. ASSUMPTIONS

Assumptions are listed in this section only if they are necessitated by lack of data in the development of the UZ flow model and its submodels. Several approximations and idealizations are used for model development, such as selection of hydrogeological conceptual models, use of numerical modeling approaches, and specification of model boundary conditions. These are discussed and justified as appropriate in Section 6. In particular, modeling idealizations and approximations used for specific modeling studies are appropriately discussed in Section 6.

This section presents the rationale and justification for assumptions, discusses whether further confirmation is needed, and references the sections in the report where these assumptions are used. The assumptions used in developing the UZ flow models and submodels are as follows:

1. In the UZ flow model, faults are assumed to be vertical or inclined 30 m wide zones, crossing the entire unsaturated zone thickness from the surface to the water table. This assumption is used for the three-dimensional UZ flow model (Sections 6.1, 6.2, 6.5, 6.6, and 6.7) and three-dimensional ambient thermal model (Sections 6.3 and 6.4).

   Basis: This assumption is consistent with the assumptions and approximations used in designing the three-dimensional UZ model grid (BSC 2004 [DIRS 169855]). Considering the large-scale averaging performed by the three-dimensional mountain-scale UZ model, in which horizontal grid spacings are typically on the order of 100 m, a 30 m width is compatible with a spatial discretization of 100 m lateral spacing in the adjacent, nonfault gridblocks. The impact of fault widths or cross-sectional areas on results of steady-state flow simulation in the unsaturated zone is equivalent to that of variation in fault permeability. The sensitivity modeling analysis (BSC 2005 [DIRS 174191]) showed that three-orders-of-magnitude variations in fault transmissivity had very small impact on UZ flow and tracer transport from the repository to the water table. Therefore, this assumption is considered adequate and requires no further confirmation.

2. In describing the top temperature boundary condition, the ambient thermal model (Section 6.3) assumes that the average surface temperature is a linear function of surface elevation. Therefore, the entire temperature ranges along the top model boundary can be determined using a linear equation whose coefficients are estimated using average annual temperature data measured from two boreholes.

   Basis: The surface temperature is controlled by the local atmosphere conditions, while variations in the mean atmospheric temperature are dependent primarily on elevation, which are handled as linear functions of elevation. Therefore, this assumption is considered reasonable and adequate, and requires no further confirmation.

3. In describing infiltration, the uncertainty distribution for the past Modern Interglacial Climate is fully correlated with the uncertainty distribution for the future Monsoon Climate and the future Glacial Transition Climate.

Basis: Perfect correlation of the uncertainty scenarios across climate states for the flux boundary condition at the upper boundary of the UZ flow model is used, for three reasons. First, the correlation of the uncertainty scenarios across climate states cannot be quantified with the available data. The assumption of a totally uncorrelated sequence across climate states would lead to a tendency to remove the highest flux extremes from the simulations as compared with using perfect correlation. Second, the computational burden for an uncorrelated case is more than three times larger than that using perfect correlation, because more computational runs are required for statistically meaningful correlation. The uncorrelated climate requires more sets of properties for the UZ flow models to correlate with future climate scenarios, resulting in an increase of computational burden. For the correlated case, each future climate uncertainty scenario involves just one unsaturated zone parameter set, (e.g., the monsoon 10th percentile case uses the parameter set developed for the present-day 10th percentile case). For the uncorrelated case, each future climate uncertainty scenario involves all four unsaturated zone parameter sets (e.g., the monsoon 10th percentile case will need to be computed using each of the four parameter sets developed to present-day climate). The reason for this is that the parameters appropriate to present-day conditions do not change with climate. For example, present-day is represented by the 50th percentile scenario and moves (for the uncorrelated case) into the monsoon 10th percentile scenario. This monsoon flow field needs to be computed using the 50th percentile property set. Therefore, the uncorrelated case results in an additional 36 flow fields to be computed (three additional flow fields for each of the 12 future climate scenarios), for a total of 52 flow fields, as compared with the 16 required for the correlated case. This additional computational burden for the uncorrelated case. This burden is not only reflected in the generation of more UZ flow fields, but also in other TSPA submodels (e.g., the thermohydrologic submodel), making the uncorrelated approach computationally infeasible. Third, uncorrelated uncertainty would result in some realizations that would have lower infiltration and percolation flux for the monsoon and glacial-transition climate than they would the present-day—an undesirable outcome that would be, by definition, wrong, since these future climates are unanimously expected to be wetter.

6. MODEL DISCUSSION

As outlined in Section 1, this report documents the development and results of the updated UZ flow model and the temperature and geochemistry submodels. This section consists of the following:

- Model description (Section 6.1)
- Three-dimensional UZ flow model calibrations (Section 6.2)
- Ambient geothermal model (Section 6.3)
- Gas flow analysis and pneumatic calibration (Section 6.4)
- Geochemical submodel for chloride (Section 6.5)
- Flow patterns and analysis of three-dimensional flow fields (Section 6.6)
- Groundwater travel times and tracer transport (Section 6.7)
- UZ flow weighting factors (Section 6.8)
- Analysis of episodic infiltration pulses (Section 6.9)
- Model uncertainties and alternative models (Section 6.10)
- Representation of the unsaturated zone flow fields with an evaluated water table (Section 6.11).

The UZ flow model, temperature model, and geochemistry submodels have all been developed to simulate past, present, and future hydrological, geothermal, and geochemical conditions in the unsaturated zone at Yucca Mountain. Field data collected at Yucca Mountain have been used to help develop conceptual and numerical models for investigating the hydrological, geothermal, and geochemical conditions of the site. These models simulate ambient, steady-state UZ flow conditions and perform predictive studies of changes in the mountain caused by climatic, thermal, and geochemical perturbations. The comprehensive model that integrates pertinent data from the UZ at Yucca Mountain is the three-dimensional site-scale UZ model, developed over the past decade, as documented, for example, in "Overview of Scientific Investigations at Yucca Mountain—The Potential Repository for High-Level Nuclear Waste," *Journal of Contaminant Hydrology* by Bodvarsson et al. (1999 [DIRS 120055]); Wu et al. (1999 [DIRS 117161]; 2002 [DIRS 160195]); 2004 [DIRS 173953]). Model development described in this report results from the continuing modeling investigations and field studies of flow and transport behavior in the unsaturated zone system of Yucca Mountain (BSC 2004 [DIRS 169861])

The UZ model is a process model developed according to *Technical Work Plan for Unsaturated Zone Flow, Drift Seepage and Unsaturated Zone Transport Modeling* (BSC 2006 [DIRS 177465]) and for support of the TSPA-LA. The TSPA-LA will use the UZ flow model results (i.e., three-dimensional UZ flow fields) to perform TSPA analyses and to provide input to other models such as ambient and thermal drift-scale models, the mountain-scale thermal-hydrological model, and the UZ radionuclide transport model. The UZ flow model and its submodels evaluate features and processes that are important to the performance of the repository, all of which contribute to the TSPA-LA, such as:

- The spatially distributed values of the percolation flux at the repository horizon
- The components of fracture, matrix, and fault flow at and below the repository horizon

- The possible flow diversion in the PTn
- The perched water zones and associated flow barriers
- The probable flow paths from the repository to the water table
- Tracer transport times and paths from the repository to the water table, and breakthrough curves and areas of tracers at the water table.

The UZ flow model described here provides a defensible and credible UZ model for evaluation of Yucca Mountain as an underground radioactive waste repository. Major activities accomplished in this revision include incorporation of updated net infiltration maps for present-day, monsoon, glacial transition, and post-10k-yr climates; updated model calibrated property sets; updated model calibration studies of three-dimensional UZ flow; evaluation of the effects of PTn and perched water; updated geochemical and geothermal conditions; updated estimates of tracer and radionuclide transport times; estimates of UZ flow weighting factors; and intensive model validation efforts.

Other activities have involved generating 16 three-dimensional flow fields (Sections 6.2 and 6.7) to evaluate the uncertainties and sensitivity of the UZ model relative to fracture and matrix parameters and infiltration rates of four climates over the mountain by using four sets of model parameters, and sixteen infiltration scenarios. A total of 16 flow fields have been submitted to the TDMS as output DTNs. The sixteen flow fields are provided for use in TSPA calculations of radionuclide transport through the unsaturated zone system, and for other activities such as drift seepage abstraction.

FEPs included through this report are discussed in Section 6.2.6 and in Table 6.2-8.

6.1 MODEL DESCRIPTION

The conceptual and numerical models used for the modeling studies are documented in this report as well as in *Conceptual Model and Numerical Approaches for Unsaturated Zone Flow and Transport* (BSC 2004 [DIRS 170035]). The conceptual and numerical models are presented in this section so that a complete discussion of the models can be made.

6.1.1 Geological Model and Numerical Grids

The geologic framework model (GFM2000) (DTN: MO0012MWDGFM02.002 [DIRS 153777]) is used for incorporating geological features into the UZ flow model and its submodels. The development and features of the three-dimensional model grids are documented in *Development of Numerical Grids for UZ Flow and Transport Modeling* (BSC 2004 [DIRS 169855]). Table 6.1-1 lists the geological units/layers for different hydrogeologic units and the associated UZ model numerical grid-layer information. These geological formations have been organized into layered hydrogeologic units based primarily on the degree of welding (Montazer and Wilson 1984 [DIRS 100161]). These are the Tiva Canyon welded hydrogeologic unit (TCw), the Paintbrush nonwelded hydrogeologic unit (PTn), the Topopah Spring welded unit (TSw), the Calico Hills nonwelded hydrogeologic unit (CHn), and the Crater Flat undifferentiated unit.

Table 6.1-1. GFM2000 Lithostratigraphy, UZ Model Layer, and Hydrogeological Unit Correlation Used in the UZ Flow Model and Submodels

Major Unit[a]	Lithostratigraphic Nomenclature[b]	UZ Model Grid Unit/Layer[c]	Hydrogeological Unit [d]
Tiva Canyon welded (TCw)	Tpcr	tcw11	CCR, CUC
	Tpcp	tcw12	CUL, CW
	TpcLD		
	Tpcpv3	tcw13	CMW
	Tpcpv2		
Paintbrush nonwelded (PTn)	Tpcpv1	ptn21	CNW
	Tpbt4	ptn22	BT4
	Tpy (Yucca)		
		ptn23	TPY
		ptn24	BT3
	Tpbt3		
	Tpp (Pah)	ptn25	TPP
	Tpbt2	ptn26	BT2
	Tptrv3		
	Tptrv2		
Topopah Spring welded (TSw)	Tptrv1	tsw31	TC
	Tptrn		
		tsw32	TR
	Tptrl, Tptf	tsw33	TUL
Topopah Spring welded (TSw)	Tptpul, RHHtop		
	Tptpmn	tsw34	TMN
	Tptpll	tsw35	TLL
	Tptpln	tsw36	TM2 (upper 2/3 of Tptpln)
		tsw37	TM1 (lower 1/3 of Tptpln)
	Tptpv3	tsw38	PV3
	Tptpv2	tsw39 (vit, zeo)	PV2
Calico Hills nonwelded (CHn)	Tptpv1	ch1 (vit, zeo)	BT1 or BT1*a* (altered)
	Tpbt1		
	Tac (Calico)	ch2 (vit, zeo)	CHV (vitric) or CHZ (zeolitic)
		ch3 (vit, zeo)	
		ch4 (vit, zeo)	
		ch5 (vit, zeo)	
	Tacbt (Calicobt)	ch6 (vit, zeo)	BT
	Tcpuv (Prowuv)	pp4	PP4 (zeolitic)
	Tcpuc (Prowuc)	pp3	PP3 (devitrified)
	Tcpmd (Prowmd)	pp2	PP2 (devitrified)

Table 6.1-1. GFM2000 Lithostratigraphy, UZ Model Layer, and Hydrogeological Unit Correlation Used in the UZ Flow Model and Submodels (Continued)

Major Unit[a]	Lithostratigraphic Nomenclature[b]	UZ Model Grid Unit/Layer[c]	Hydrogeological Unit [d]
Calico Hills nonwelded (CHn) (Continued)	Tcplc (Prowlc)		
	Tcplv (Prowlv)	pp1	PP1 (zeolitic)
	Tcpbt (Prowbt)		
	Tcbuv (Bullfroguv)		
Crater Flat undifferentiated (CFu)	Tcbuc (Bullfroguc)	bf3	BF3 (welded)
	Tcbmd (Bullfrogmd)		
	Tcblc (Bullfroglc)		
	Tcblv (Bullfroglv)	bf2	BF2 (nonwelded)
	Tcbbt (Bullfrogbt)		
	Tctuv (Tramuv)		
	Tctuc (Tramuc)	tr3	Not Available
	Tctmd (Trammd)		
	Tctlc (Tramlc)		
	Tctlv (Tramlv)	tr2	Not Available
	Tctbt (Trambt) and below		

Sources: [a]Montazer and Wilson 1984 [DIRS 100161]; [b]BSC 2004 [DIRS 170029]; [c]BSC 2004 [DIRS 169855]; [d]Flint 1998 [DIRS 100033].

NOTES: [c]Defined by the rock material type, represented by the code name, for grid layers or blocks belonging to the same rock unit. [d]Hydrogeologcal units or layers defined for the UZ model exclude alluvial covers. The top model boundary is at the ground surface of the mountain (or the tuff-alluvium contact in areas of significant alluvial covers).

UZ = unsaturated zone.

The three-dimensional UZ model domain, as well as the numerical grid for this study (DTN: LB03023DKMGRID.001 [DIRS 162354]), is shown in plan view in Figure 6.1-1, encompassing approximately 40 km^2 of the area over the mountain. The UZ model grid, shown in Figure 6.1-1, is referred to as the TSPA-LA grid. It is primarily designed for model calibration and simulations of three-dimensional flow fields used in TSPA-LA calculations. As shown in Figure 6.1-1, this three-dimensional model grid uses a refined mesh in the vicinity of the repository, located near the center of the model domain, covering the region from the Solitario Canyon fault to Ghost Dance fault in the west-east direction, and from borehole G-3 in the south to beyond Sever Wash fault in the north (SNL 2007 [DIRS 179466]). Also shown in Figure 6.1-1 are the locations of several boreholes used in model calibrations and analyses. The model domain is selected to focus on the study area of the repository and to investigate the effects of different infiltration scenarios and major faults on moisture flow around and below the repository. In the model grid, faults are represented in the model by vertical or inclined 30 –m wide zones (Section 5). The top model boundary is set at the ground surface or the tuff–alluvium interface; the bottom model boundary is set to the water table. The water table is set to the average water table elevation across the model domain, fully supported by borehole water table measurement data. The water table, which is the bottom boundary of the UZ model, is shown to be a relatively flat, stable surface in most of the model domain, increasing its elevation only in the north (BSC 2004 [DIRS 169855]). This rise has little effect on flow simulation results within

the model domain, because the flow is essentially determined by upstream, or geological layers above, not by downstream (water table) conditions in the unsaturated zone. In the eastern part of the site to the Solitario Canyon fault, the water table elevation of the flat portion is about 730 m above sea level (BSC 2004 [DIRS 169855]).

The three-dimensional numerical model grid, as shown in its plan view in Figure 6.1-1, has 2,042 mesh columns, with some columns having more cells than others, and an average of 59 computational grid layers in the vertical direction. There are two gridblocks, one fracture and one matrix block, per grid location, resulting in a total of 245,506 gridblocks and 982,451 connections in a dual permeability grid.

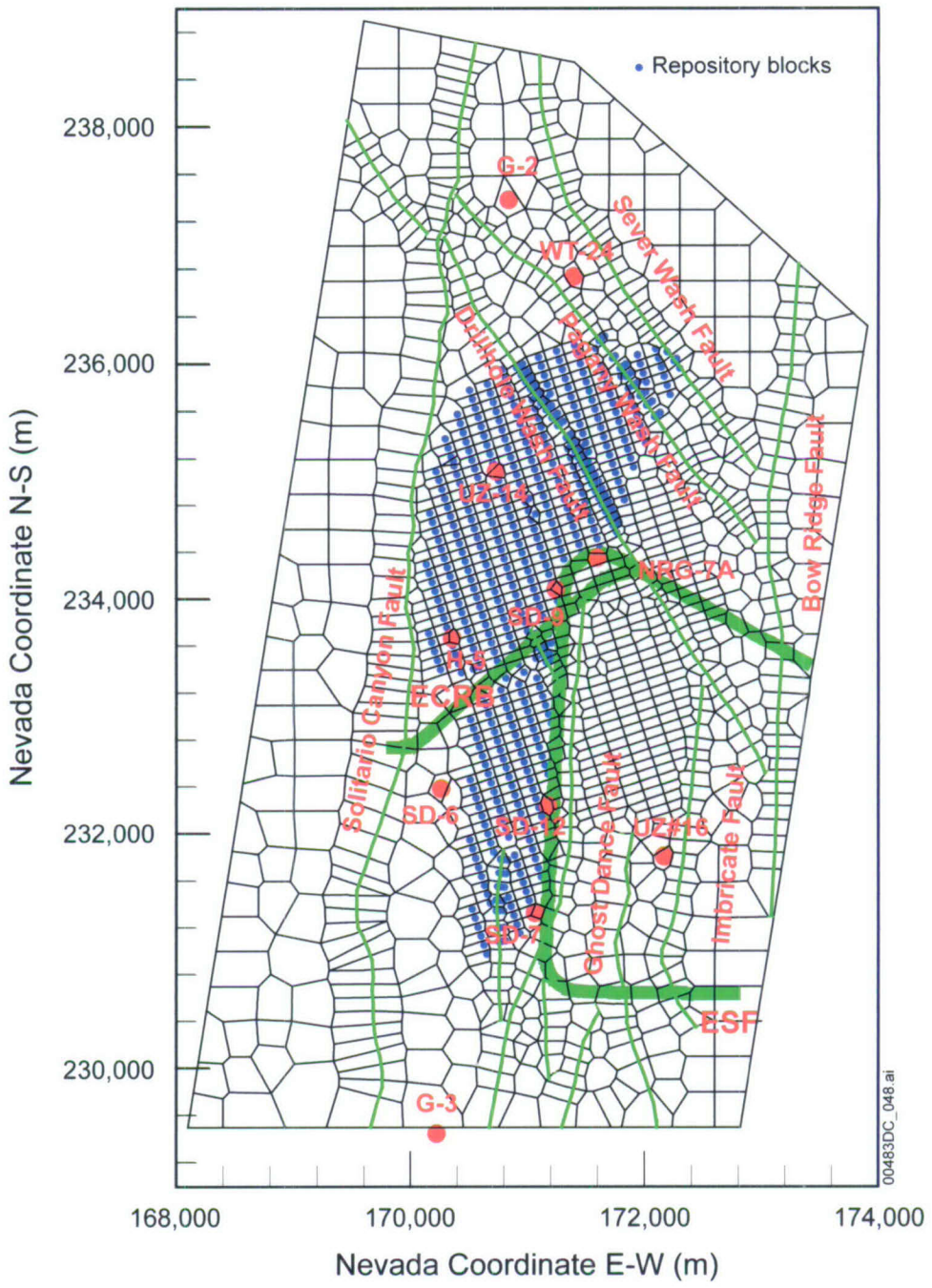

Source DTN: LB03023DKMGRID.001 [DIRS 162354].

Figure 6.1-1. Plan View of the Three-Dimensional Unsaturated Zone TSPA-LA Model Grid

6.1.2 Numerical Codes and Modeling Approach

The model calibration and simulation results presented in this report were carried out mainly using TOUGH2 V1.6 (2003 [DIRS 161491]) and T2R3D V1.4 (1999 [DIRS 146654]), as summarized in Section 3. The single active liquid-phase flow module (EOS9) of the TOUGH2 code was used to calibrate the UZ flow model and several submodels, as well as to generate

three-dimensional TSPA-LA flow fields. For gas flow simulation and ambient temperature calibration, the TOUGH2 V1.6 (2003 [DIRS 161491]) EOS3 module was used. Tracer transport and chloride studies were performed using the decoupled module of T2R3D V1.4 (1999 [DIRS 146654]) with flow fields generated by the EOS9 module. TOUGH2 V1.6 (2003 [DIRS 161491]) and T2R3D V1.4 (1999 [DIRS 146654]) were selected because they have been qualified and baselined for modeling flow and transport in heterogeneous fractured rock (e.g., Wu et al. (2002 [DIRS 160195]). These numerical codes were used for this work because they were qualified and baselined for use in this report, and they have the generalized capability of handling fractured rock with local and global fracture–matrix interaction, which was required for modeling studies of this report.

To model unsaturated flow and transport processes in the unsaturated zone system at Yucca Mountain, mathematical models or governing equations are needed to describe the physical processes quantitatively. The physical processes associated with flow and transport in porous media are governed by the fundamental conservation laws (i.e., conservation of mass, momentum, and energy), which govern the behavior of fluid flow, chemical migration, and heat transfer through unsaturated fractured porous media. The macroscopic continuum approach has been most commonly used in practical applications (Bear 1972 [DIRS 156269]). In this approach, the physical laws governing flow of several fluids, transport of multicomponents, and heat transfer in porous media are represented mathematically on the macroscopic level by a set of partial differential or integral equations. Fluid and heat flow and chemical-transport processes in fracture and matrix systems in the unsaturated zone are described using a macroscopic, dual-permeability continuum approach.

In addition to the conservation or continuity equations of mass and thermal energy in fracture and matrix systems, specific relationships or *mechanisms* are needed that describe how fluid flow, solute/tracer transport, and heat transfer occur in porous and fractured media. The following specific laws and constitutive relationships act as such mechanisms by governing local fluid flow, component transport, and heat-transfer processes in porous and fractured media:

1. The governing equation for describing isothermal, unsaturated liquid flow is the Richards equation (Richards 1931 [DIRS 104252]; Pruess et al. 1999 [DIRS 160778], Equation A-17, p. 146), based on the conservation of mass and Darcy's law (Bear 1972 [DIRS 156269]) with flux driven by gravity and capillary pressure gradient. The unsaturated flux is a product of the unsaturated hydraulic conductivity and the driving gradient. Hydraulic conductivity is proportional to effective permeability and fluid density, and inversely proportional to fluid viscosity. Rock and fluid properties can be treated as constants under isothermal conditions. The effective permeability (relative permeability times absolute permeability or saturated permeability) is related to water content (saturation times porosity) and capillary pressure, as described by the van Genuchten model (1980 [DIRS 100610]). The governing equations for unsaturated flow under isothermal conditions are given in Appendix A. Exceptions to the use of the Richards equation are the ambient temperature the gas flow model, and the calcite model, which use the two-phase (water and air, TOUGH2 EOS3 module) flow equation instead of Richards equation for the isothermal or nonisothermal water and airflow flow.

The UZ flow model and its submodels adopt the dual-continuum approach for modeling flow through fractures and the matrix. The Richards equation is applied to fracture and matrix continuum for unsaturated flow under isothermal conditions. Fluid exchange between fracture continuum and matrix continuum is the fracture–matrix interaction, which is simulated by the dual-permeability concept, and is further modified by an active fracture model (AFM) (Liu et al. 1998 [DIRS 105729]) in the UZ flow model.

The active fracture model (AFM) was developed within the context of the dual-continuum approach (Liu et al. 1998 [DIRS 105729]). It is based on the reasoning that, on account of fingering flow, only a portion of fractures in a connected, unsaturated fracture network contribute to liquid water flow, while other fractures are simply bypassed. The portion of the connected fractures that actively conduct water are called active fractures. Thus, the AFM uses a combination of a continuum approach and a simple filtering concept to model fracture flow. Inactive fractures are filtered out in modeling fracture–matrix interaction and flow in the fracture continuum.

Darcy's law (Appendix A) and the van Genuchten model can be generalized for multiphase flow under nonisothermal conditions. The governing equations for gas and liquid flow and heat flow are based on conservation of mass for fluid phases, and on conservation of energy for conductive and convective heat transfer processes, respectively. The full set of equations for nonisothermal, two-phase flow of gas and water in fractures and matrix are presented in a report by Pruess et al. (1999 [DIRS 160778], Appendix A).

In solving the governing equations (Appendix A), a number of known parameters are given as input to the UZ flow model. Some of those variables are treated as constants—for example, fluid viscosity under isothermal conditions. Others are provided as known parameters measured either in the laboratory or in field tests, and/or further calibrated. Examples of known parameters are rock density, porosity, and absolute permeability. Input parameters are further discussed in Section 6.1.5. In addition, boundary conditions are needed to solve governing equations (Section 6.1.3). The top boundary for the UZ flow model is subject to net infiltration from the land surface (Section 6.1.4). With these input parameters and boundary conditions, the solving of the full set of equations (Pruess et al. 1999 [DIRS 160778]) in the UZ flow model provides outputs for variables such as liquid saturation, phase pressures, capillary pressure, mass or percolation flux, and Darcy's velocity, in addition to temperatures in the thermal model.

2. The migration of dissolved mass components or chemical species within a fluid in the two-phase, fractured porous media system is governed mainly by advective, diffusive, and dispersive processes. However, migration may also be subject to other processes such as radioactive decay, adsorption, mass exchange or partition between phases, and other chemical reactions under local thermodynamic equilibration or kinetic reaction. The generalized Fick's law (Wu and Pruess 2000 [DIRS 153972], Equations 3.1.5 to 3.1.7, p. 705), including hydrodynamic dispersion effects in a multiphase system, is used to evaluate diffusive and dispersive flux of chemical transport.

In research and application, the multiphase extension of Darcy's law (Pruess et al. 1999 [DIRS 160778], Equation A-5, p. 145), the Richards equation (Richards 1931 [DIRS 104252]), and the generalized Fick's law (Wu and Pruess 2000 [DIRS 153972], pp. 704 to 707) have been used as fundamental laws that govern multiphase flow and transport processes within porous media and fractured rocks. These fundamental laws or correlations, based on theory, experiment, and field studies, reflect the current understanding of porous-medium physics. Richards' equation is extended for use in fracture and matrix flow, as well as interflow between fractures and the matrix.

A key issue for simulating fluid and heat flow and chemical transport in the fractured porous rock of Yucca Mountain is how to handle fracture and matrix flow and interaction under multiphase, multicomponent, and isothermal or nonisothermal conditions. The available methods for treating fluid flow in fractures and the rock matrix using a numerical approach include: (1) an explicit discrete-fracture and matrix representation; (2) the dual continuum method, including double- and multiporosity, dual-permeability, or the more general "multiple interacting continua" (MINC) method (Pruess and Narasimhan 1985 [DIRS 101707]); and (3) the generalized effective continuum method. For the work documented in this report, the dual permeability modeling approach is applied to evaluate fluid and heat flow and chemical transport in the fracture and matrix system of the unsaturated zone system of Yucca Mountain, in which the AFM is adopted to modify fracture–matrix interface areas for flow and transport between fracture and matrix systems.

The dual continuum conceptualization provides an appropriate representation of flow and transport processes within the Yucca Mountain unsaturated zone (Doughty 1999 [DIRS 135997]; BSC 2004 [DIRS 170035]). It is much less demanding in computational effort or in data requirements than the discrete-fracture modeling approach. The dual-continuum method has been shown to be able to match different types of data from Yucca Mountain and, therefore, become the main approach used in the modeling studies of the YMP (Wu et al. 1999 [DIRS 117161]; 2002 [DIRS 160195]; 2004 [DIRS 173953]). The dual-permeability methodology for handling fluid flow, tracer transport, and heat transfer through fractured rocks accounts for fracture and rock matrix flow and interaction between the matrix and fracture continua. In this approach, each gridblock of the primary mesh is divided into two gridblocks, one representing fractures and the other matrix, locally connected to each other. Because of the one-block representation of fracture or matrix, the interflow between fractures and matrix has to be handled using a quasi-steady-state flow approximation, and this may limit its application in estimating the gradients of pressures, temperatures, and concentrations within the matrix. The UZ flow model of this report has been developed to simulate steady-state UZ flow conditions at Yucca Mountain. Under steady-state flow conditions, however, such gradients near the matrix

surfaces become minimal, and the one block matrix-fracture representation is expected to produce accurate solutions (Doughty 1999 [DIRS 135997]).

The utility and appropriateness of conceptual and numerical approach of dual-permeability for modeling several flow and transport processes has been discussed by Doughty (1999 [DIRS 135997]) through a one-dimensional column extracted from a three-dimensional UZ site-scale model of the unsaturated zone at Yucca Mountain, NV. Within the dual-continua models, the formulation for fracture–matrix (F–M) interface area can have a major effect on the hydrodynamic response to an infiltration pulse and tracer arrival at various horizons, with fracture responses becoming earlier as F–M interface area decreases. The number of matrix blocks also has a significant effect on response time, with the more accurate multi-matrix-gridblock models yielding slower fracture response times. For steady-state moisture flow, most of the numerical and conceptual models provide similar results for saturation and fracture flow profiles. When advection and diffusion play a significant role in tracer transport, the arrival time of tracer fronts is strongly dependent on the choice of F–M interface area formulation, as this area controls the magnitude of F–M diffusion in addition to F–M fluid flow. In general, as F–M interface area decreases, tracer travel time through the fractures decreases. For the cases studied, considering a uniform, relatively small infiltration rate, tracer front arrival time is somewhat sensitive to the choice of one or more matrix blocks, with dual-permeability models predicting earlier fracture arrival times for cases in which F–M interface area is reduced. For thermal loading, preliminary studies indicate that the dual-permeability model does capture all the significant physical processes, in which rapid fluid and heat flow occurs in the fractures before the matrix has a chance to equilibrate.

As applied in this report, the traditional dual-permeability concept is further modified using an AFM (Liu et al. 1998 [DIRS 105729]) to represent fingering effects of liquid flow through fractures and to limit flow into the matrix system. The active fracture concept has been evaluated in *Conceptual Model and Numerical Approaches for Unsaturated Zone Flow and Transport* (BSC 2004 [DIRS 170035]) and further sensitivity analyses are provided in Section 6.8. The dual-permeability conceptual model is used for describing fracture–matrix interaction with all geological units as well as faults.

As an alternative modeling approach, the discrete-fracture or "weeps" type model have extremely high uncertainties with respect to fracture distribution data within the mountain, as well as an extensive computational burden that cannot be solved currently or in the near future. On the other hand, the effective-continuum approach, although the most computationally efficient, may not capture important, nonequilibrium interaction in flow and transport between fractures and matrix in the unsaturated zone. Therefore, it may also not be appropriate for use in modeling UZ flow and transport at Yucca Mountain.

In model calibration of moisture flow and tracer transport, ambient, variably saturated flow in the unsaturated zone underlying Yucca Mountain is treated as an isothermal, steady-state flow system. This is considered to be a good approximation of the unsaturated zone below the PTn unit, because the relatively unfractured nonwelded PTn unit is expected to damp and homogenize downward-moving transient pulses arising from episodic surface infiltration events (Wu et al. 2000 [DIRS 154918]; Wu et al. 2002 [DIRS 161058]; Flint et al. 2001 [DIRS 164506]; Zhang et al. 2006 [DIRS 180273]). Additional analyses of PTn damping effects using the updated UZ model are presented in Section 6.9, to show the effectiveness of the PTn unit in redistributing

percolation flux for the units below. Therefore, estimated surface net infiltration rates may effectively be described as steady-state water recharge (Section 6.1.4).

In the development of the UZ flow model and its submodels over the past decade, the steady-state nature of the flow fields and the damping of transient pulses were evaluated in different studies. Wu et al. (1999 [DIRS 117161], p. 186) referred to the early work of Wang and Narasimhan (1985 [DIRS 108835]; 1993 [DIRS 106793], Figure 7.4.7), which suggested that effects of infiltration pulses at the surface are damped by the underlying tuff units, especially the PTn. The welded tuff of the repository horizon exhibited only small changes in saturations, pressures, and potentials from steady-state values in response to the transient pulses. Pan et al. (1997 [DIRS 164181]) investigated transient flow behavior for downward water flow through sloping layers in the vadose zone, with up-slope flow developed during heavy rain, likely enhancing the downward flow. Wu et al. (2002 [DIRS 161058], pp. 35-1 to 35-12) analyzed the capillary barrier capacities in unsaturated units and indicated that, on average, it took several thousands years for water to travel through the PTn. Wu et al. (2000 [DIRS 154918], 2002 [DIRS 161058]) and Flint et al. (2003 [DIRS 163967]) analyzed the implications of capillary barrier development in subunits of the PTn for lateral diversion of flow in the PTn. Along sloping layers, strong capillary barriers, if formed, will promote lateral diversions, even though the degree or scale of lateral diversion can be evaluated by: (1) comparative sensitivity studies, (2) detailed analysis of field data including geochemical evidences, and (3) long-term controlled field tests. A more recent study, conducted by Zhang et al. (2006 [DIRS 180273]) using three-dimensional and one-dimensional model results, shows that the PTn can attenuate episodic infiltration pulses significantly, most percolating water is damped by the subunits at the top of the PTn, and a small percentage of percolation flux is diverted into faults.

6.1.3 Model Boundary Conditions

The ground surface of the mountain (or the tuff-alluvium contact in areas of significant alluvial cover) is taken as the top model boundary; the water table is treated as the bottom model boundary. The top and bottom boundaries of the model are treated as Dirichlet-type conditions with specified constant, but spatially varying temperature and gas pressure. For flow simulations using the EOS9 module, only water pressure or saturation values are needed along the top and bottom model boundaries. Surface infiltration, as discussed below in Section 6.1.4, is applied using a source term in the fracture gridblocks within the second grid layer from the top. This method was adopted because the first layer is treated as a Dirichlet-type boundary, with constant pressure, saturation, and temperature to represent average atmospheric conditions at the mountain.

The water table is used as the bottom model boundary, a surface where the water pressure is a single, fixed value. Within the numerical models, only one set of model primary variables for solving Richards' equations is specified for the bottom boundary, equivalent to specifying a constant saturation. For gas and/or heat flow simulations, the bottom model boundary representing the water table is subject to fixed gas pressure, equal to the atmospheric pressure at that elevation (Sections 6.3.3 and 6.4.1). Lateral boundaries, as shown in Figure 6.1-1, are treated as no-flow (closed) boundaries, which allow flow to occur exclusively along the vertical plane. This treatment is reasonable for the eastern boundary, which is along or near the Bow Ridge fault, because high vertical permeability and lower capillary forces are expected within the faults (see fault properties estimated in *Calibrated Unsaturated Zone Properties* (SNL 2007

[DIRS 179545]). For the western and northern lateral boundaries, no-lateral-flow boundaries have little effect on moisture flow within and near the repository areas, because these boundaries are separated from the repository by faults. For the southern lateral boundary, this is also true because it is far from the repository (Figure 6.1-1).

The spatially distributed values of temperatures along the top and bottom boundaries are based on field observation. This treatment is corroborated by data reported by Sass et al. (1988 [DIRS 100644]) and the calibrated temperature distribution along the water table (Section 6.3), and further confirmed by matching qualified temperature profiles from a number of boreholes (as described in Section 6.3).

Pressure conditions at the bottom boundary of the model are based on observed gas-pressure values. The water table, which is the bottom boundary of the UZ model, is shown to be a relatively flat, stable surface over most of the model domain, increasing its elevation only in the north. The rise in the north has little effect on flow simulation results within the model domain, because the flow is essentially determined by upstream, or geological layers above, not by downstream (water table) conditions in the unsaturated zone. In the eastern part of the site (eastward from the Solitario Canyon fault), the water table elevation of the flat portion is about 730 m above sea level. The gas pressures are estimated using a pressure value of 92 kPa at an elevation of 730 m. Surface gas pressures are determined by running the TOUGH2, EOS3 module to steady-state under given temperature, bottom pressure, and surface-infiltration conditions. This is necessary to generate a steady state, equilibrated gas-pressure boundary to avoid artificial airflow or circulation, which may occur if nonequilibrated pressures are imposed on the model top ground surface and bottom water-table boundaries.

6.1.4 Infiltration Scenarios

Water entering the unsaturated zone as net infiltration from precipitation at the land surface has significant impact on overall hydrological and thermal-hydrological conditions within the Yucca Mountain unsaturated zone. Net infiltration is the ultimate source of percolation through the unsaturated zone. Water percolating downward through the unsaturated zone will be the principal means by which radionuclides may be transported from the repository to the water table.

The net infiltration rates are determined for present-day and two future climate scenarios of monsoon and glacial transition (DTNs: SN0609T0502206.028 [DIRS 178753], SN0609T0502206.024 [DIRS 179063], and SN0609T0502206.029 [DIRS 178862] for the present-day, monsoon, and glacial transition climates, respectively). Relevant discussions in generating these infiltration maps are documented in *Simulation of Net Infiltration for Present-Day and Potential Future Climates* (SNL 2007 [DIRS 174294]). Each infiltration rate for the three climatic scenarios consists of 40 equally probable infiltration-rate maps for the climatic scenario. A total of twelve infiltration maps, corresponding to 10th, 30th, 50th, and 90th percentiles from the 120 maps, are implemented with the UZ model and its submodels. Their average values over the UZ model domain are summarized in Table 6.1-2.

The UZ model uses net infiltration rates as water recharge at the top boundary. The upper layer was never saturated, which supports the boundary condition as implemented. The model is concerned primarily with steady-state flow under each climate infiltration scenario, while in the

climate analysis, reference to future climates indicates that climates are expected to change from present-day to monsoon, and then to glacial-transition modes for specific periods. The spatial distribution of infiltration is approximate. Net infiltration represents an average estimate over the entire duration of the climate and does not provide uncertainty estimates for corresponding local values. Inputs with the greatest impact on infiltration uncertainty are assumptions of effective uniform soil depths and effective uniform holding capacities of soil (SNL 2007 [DIRS 174294], Section 6.6.2).

Table 6.1-2. Infiltration Rates and Statistics Averaged for 12 Selected Maps over the UZ Model Domain

Climate	Scenarios	Percentile[4]	Average Infil (mm/yr)
Present-Day[1]	pd_10	10	3.03
	pd_30	30	7.96
	pd_50	50	12.28
	pd_90	90	26.78
Monsoon[2]	mo_10	10	6.74
	mo_30	30	12.89
	mo_50	50	15.37
	mo_90	90	73.26
Glacial Transition[3]	gt_10	10	11.03
	gt_30	30	20.45
	gt_50	50	25.99
	gt_90	90	46.68

[1]Values averaged from DTN: SN0609T0502206.028 [DIRS 178753] and output DTN: LB06123DPDUZFF.001.
[2]Values averaged from DTN: SN0609T0502206.024 [DIRS 179063] and output DTN: LB070123DMOUZFF.001.
[3]Values averaged from DTN: SN0609T0502206.029 [DIRS 178862] and output DTN: LB070123DGTUZFF.001.
[4]Correpsonding percentile infiltration map.

As shown in Table 6.1-2, for example, the average rate over the model domain for the present-day 10th percentile infiltration with the UZ model grid is 3.03 mm/yr. The use of the different percentile infiltration values is intended to cover the uncertainties associated with the infiltration for each climate. The two future climatic scenarios, the monsoon and glacial transition periods, are used to account for possible climate-induced changes in precipitation and net infiltration. The infiltration rates on the top boundary mesh of the UZ model domain were extracted from the infiltration maps. Over the area of a gridblock on the top boundary of the UZ model, its infiltration value was obtained by finding the corresponding average of the infiltration flux on the infiltration map. This mapping of the infiltration maps to the model top boundary meshes as source terms was implemented by the software routine infil2grid V1.7 (2002 [DIRS 154793]). The average values in Table 6.1-2 are estimated using the TSPA-LA grid, shown in Figure 6.1-1 for infiltration maps (DTNs: SN0609T0502206.028 [DIRS 178753], SN0609T0502206.024 [DIRS 179063], and SN0609T0502206.029 [DIRS 178862]).

A plan view of the spatial distribution in the three 10th percentile infiltration maps, as interpolated onto the TSPA-LA grid, is shown in Figures 6.1-2, 6.1-3, and 6.1-4 for the present day, monsoon, and glacial transition 10th percentile infiltration scenarios, respectively. The models uses previously determined values of the calibrated properties from the selected scenarios. Other than differences in the magnitude in the infiltration rates, the figures show similar patterns of flux distributions with the three infiltration rates, with higher infiltration rates in the northern part of the model domain and along the mountain ridge east of the Solitario Canyon fault.

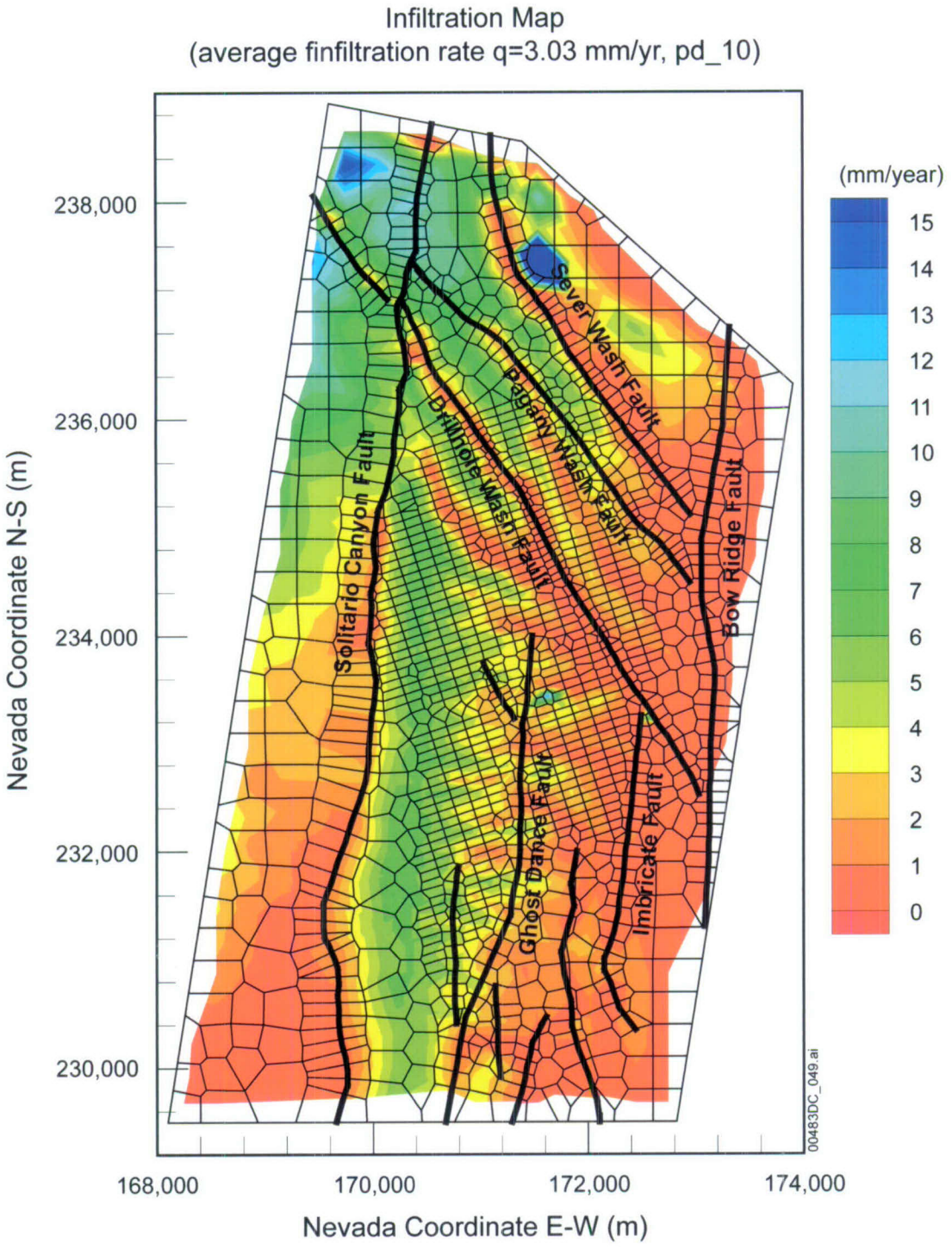

Source: DTN: SN0609T0502206.028 [DIRS 178753].

Output DTN: LB06123DPDUZFF.001.

Figure 6.1-2. Plan View of Net Infiltration Distributed over the Three-Dimensional Unsaturated Zone TSPA-LA Model Grid for the Present-Day 10th Percentile Infiltration Scenario

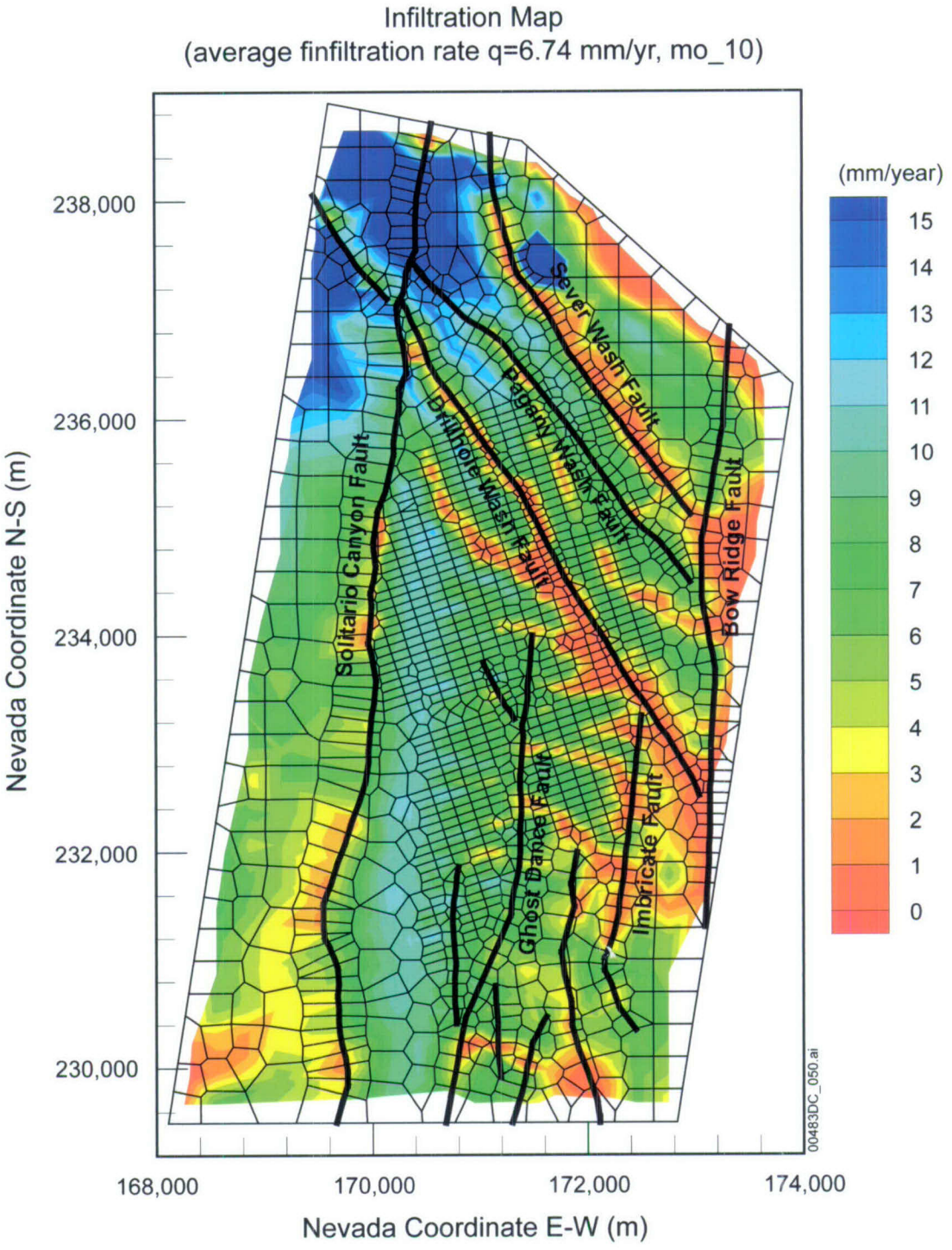

Source: DTN: SN0609T0502206.028 [DIRS 179063].
Output DTN: LB07013DMOUZFF.001.

Figure 6.1-3. Plan View of Net Infiltration Distributed over the Three-Dimensional Unsaturated Zone TSPA-LA Model Grid for the Monsoon 10th Percentile Infiltration Scenario

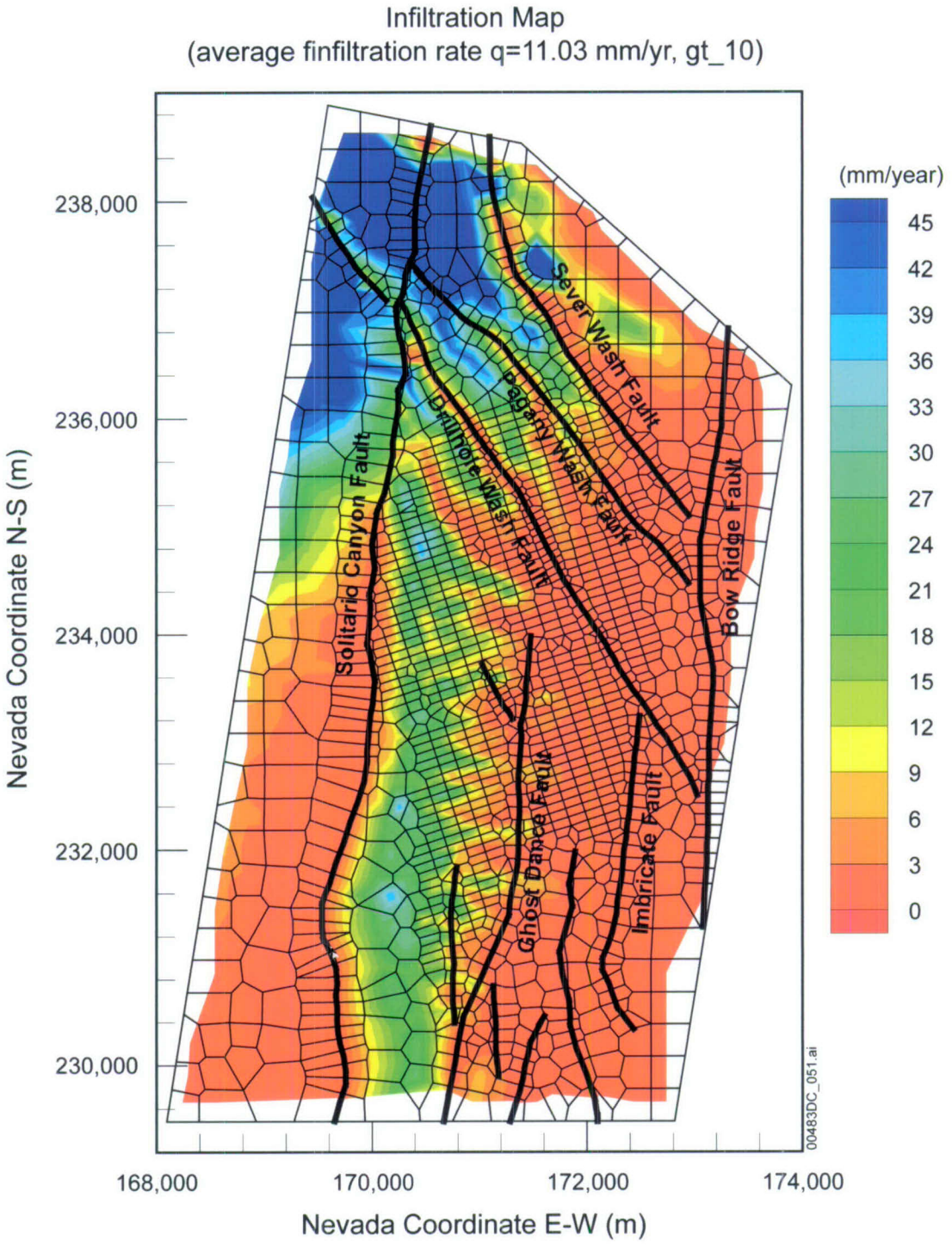

Source: DTN: SN0609T0502206.029 [DIRS 178862].

Output DTN: LB07013DGTUZFF.001.

Figure 6.1-4. Plan View of Net Infiltration Distributed over the Three-Dimensional Unsaturated Zone TSPA-LA Model Grid for the Glacial Transition 10th Percentile Infiltration Scenario

One additional climate scenario for the post-10,000-year period (post-10k-yr) was considered, using the average percolation flux ranges specified by the U.S. Nuclear Regulatory Commission (NRC) (BSC 2006 [DIRS 177465]). The stipulated distribution of average percolation flux to the repository is given as a log-uniform distribution ranging from 13 to 64 mm/yr, according to the NRC-proposed rule ([DIRS 178394], 10 CFR 63.342(c), p. 53,320). The NRC directs the Department of Energy to accordingly consider the dose calculations during the post-10k-yr time period.

Because the UZ flow model specifies flux at the upper boundary, not at an interior surface such as the repository, the appropriate flux is specified in the repository footprint projected up to the ground surface. Computations have shown that the average flux flowing to the repository is within three percent of the average flux specified at the ground surface over the projected repository area. The values for average water flux are taken to be at the same four probabilities used for present day, monsoon, and glacial transition climates. This is discussed in Section 6.8, where the calibrated probabilities for 10th, 30th, 50th, and 90th scenarios are developed. The adjusted probabilities for these cases are found to be (Table 6.8-1) 62%, 16%, 16%, and 6%, respectively. The midpoints of these probability ranges for a cumulative probability distribution are at 31%, 70%, 86%, and 97%, respectively. Using these percentiles and the log-uniform percolation flux distribution gives the values shown in Table 6.1-3, averaged over the repository footprint. An infiltration map must be developed to spatially distribute infiltration for a given average infiltration rate.

For the available 12 infiltration maps implemented for the pre-10k-yr period (10th, 30th, 50th, and 90th scenarios for each of present-day, monsoon, and glacial transition) (Table 6.1-2), the average infiltration rates through the repository footprint were first calculated. The infiltration map with a calculated average infiltration rate that most closely matches the first of the four target values (21.29, 39.52, 51.05, and 61.03 mm/yr in Table 6.1-3) for the post-10k-yr period was selected. This selection process was repeated for maps for the second through the fourth target. Then the infiltration rates for that map were scaled such that the target value for the average infiltration through the repository footprint is obtained to meet the NRC requirement. Specifically, the infiltration rates for the maps of present-day 90th percentile, glacial transition 50th percentile, glacial transition 90th percentile, and monsoon 90th percentile infiltration scenarios were then scaled such that the average infiltration flux through the repository footprint closely matched the target value. This scaled infiltration map was then used as the infiltration boundary condition for the UZ flow model to generate the post-10k-yr flow field. With the infiltration boundary condition specified, computing the post-10k-yr UZ flow fields was the same as computing the pre-10k-yr flow field. The resulting percolation fluxes over the UZ model domain, as well as through the repository footprint for the post-10k-yr climate, are shown in Table 6.1-3. Figure 6.1-5 shows UZ flow model results for the case of the 10th percentile post-10k-yr climate.

Table 6.1-3. Average and Target Infiltration Rates for Four Selected Maps over the UZ Model Domain and within Repository Footprint for Post-10k-year Climate

Scenario	Percentile	Average Infil of Selected Map Over UZ Model Domain		Target Average Infil within Repository Footprint	
		Average (mm/yr)	Scenario	Rate (mm/yr)	Mid-point Cumulative Probability
pkd_q1	10	16.89	present-day 90th percentile	21.29	0.3096
pkd_q2	30	28.99	glacial transition 50th percentile	39.52	0.6975
pkd_q3	50	34.67	glacial transition 90th percentile	51.05	0.8582
pkd_q4	90	48.84	monsoon 90th percentiles	61.03	0.9702

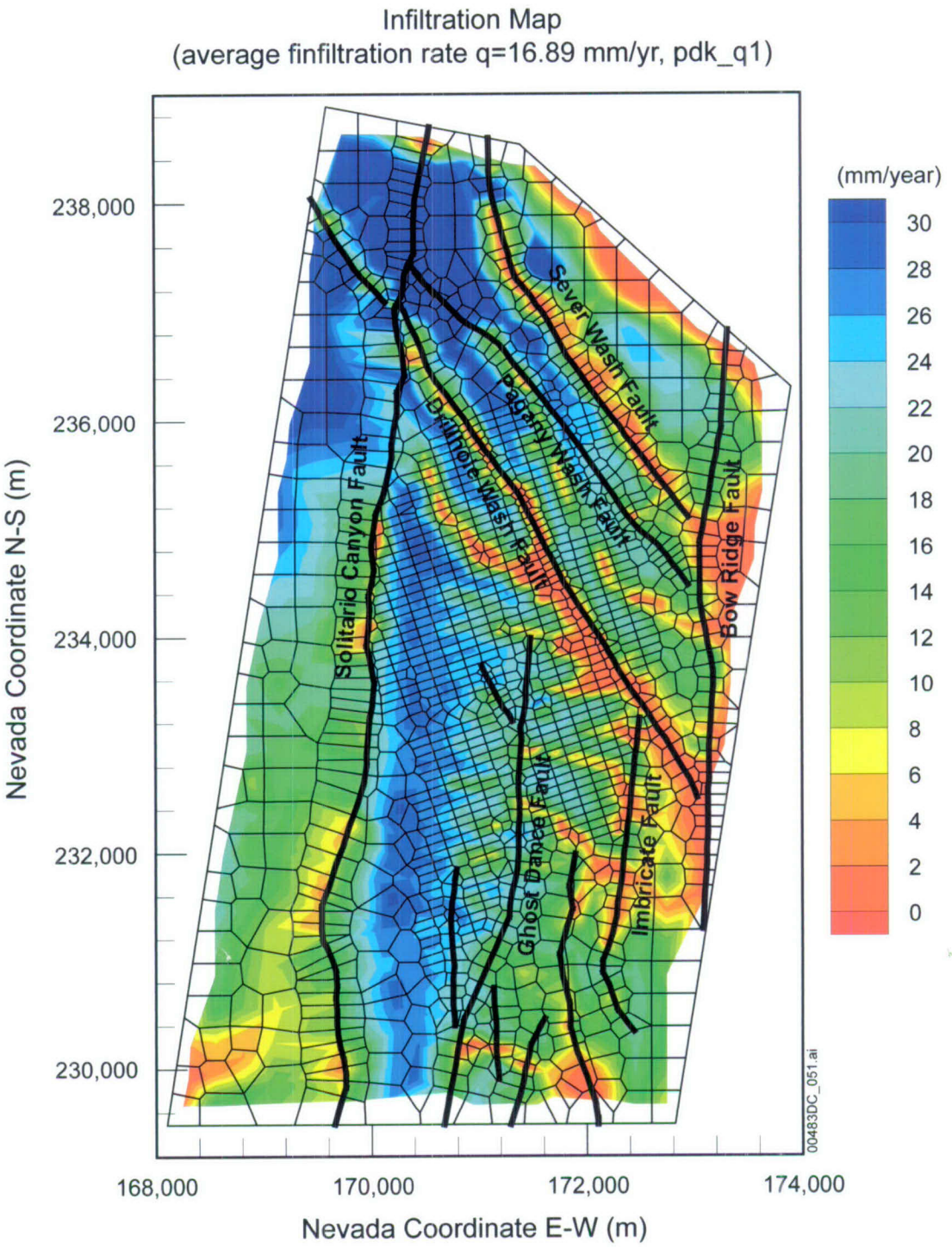

Output DTN: LB0702UZP10KFF.002.

Figure 6.1-5. Plan View of Net Infiltration Distributed over the Three-Dimensional Unsaturated Zone TSPA-LA Model Grid for the Post-10,000-yr Period Climate, 10th Percentile Infiltration Scenario

A comparison of the computed average percolation flux distribution through the repository footprint and the theoretical log-uniform distribution is shown in Figure 6.1-6. The cumulative probability is derived from the GLUE-adjusted average weighting factor in Table 6.8-1. First, a cumulative probability distribution is computed from the average weighting factors. Then the midpoints of each of the cumulative probability ranges are computed and plotted against percolation flux (mm/yr) through the repository footprint in Table 6.1-3.

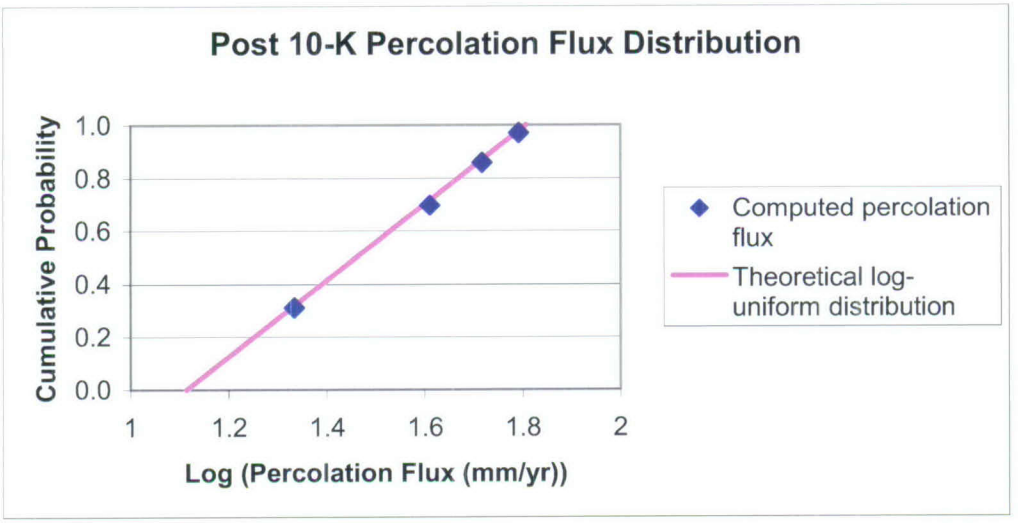

Source: Table 6.1-3.

Figure 6.1-6. Comparison of Computed Percolation Flux with the Log-Uniform Distribution

6.1.5 Model Parameters and Rock Properties

The key input rock and fluid-flow parameters used in UZ model development are summarized in Section 4. They include (1) fracture properties (frequency, permeability, van Genuchten α and m parameters, porosity, fracture–matrix interface area, and residual and satiated saturations) for each UZ model layer; (2) matrix properties (porosity, permeability, the van Genuchten α and m parameters, and residual and satiated saturations) for each UZ model layer; (3) thermal and transport properties (grain density, wet and dry thermal conductivity, grain specific heat, and tortuosity coefficients) for each UZ model layer; and (4) fault properties (DTN: LB0612MTSCHPFT.001 [DIRS 180296]) for each of the major hydrogeologic units (Table 6.1-1). The development and estimation of these parameters are presented in *Calibrated Unsaturated Zone Properties* (SNL 2007 [DIRS 179545]) (DTNs: LB0611MTSCHP10.001 [DIRS 178586], LB0611MTSCHP30.001 [DIRS 180293], LB0612MTSCHP50.001 [DIRS 180294], LB0612MTSCHP90.001 [DIRS 180295]), as well as the calibration results of this report.

The rock-parameter specification in the three-dimensional UZ model and its submodels is, in general, uniform layer-wise (BSC 2004 [DIRS 169855]). However, certain portions of grid layers representing the CHn unit are partly altered from vitric to zeolitic. In these altered layers, different rock properties are specified for vitric or zeolitic zones accordingly. The UZ model treats all of the geological units, including those representing fault zones, as fracture and matrix

systems using a dual-permeability approach. In addition, the van Genuchten relative permeability and capillary pressure functions (van Genuchten 1980 [DIRS 100610]) are used to describe flow in fractures and matrix.

In addition to fracture and matrix properties, lithophysal cavities are found in several hydrogeological layers of upper lithophysal (tsw33) and lower lithophysal (tsw35) units. These cavities, according to their local association with fractures or matrix blocks, mainly contribute storage space to fracture or matrix systems in terms of impact on flow and transport through these tuff layers. Lithophysal cavities can be considered as part of fracture or matrix porosity, but the effect of these cavities on tracer transport from the repository to the water table is expected to be small and are not explicitly incorporated into the UZ flow model. Under steady-state flow conditions, fracture or matrix porosity does not affect UZ flow fields. This is commensurate with the main objective of the UZ flow model—development of three-dimensional steady-state UZ flow fields, which are independent of the values of fracture or matrix porosity used under steady-state flow condition. In addition, porosity has little effect on pneumatic flow, which is largely controlled by fracture properties and only negligibly by matrix porosity. However, porosity has a certain influence on transient transport. The geological layers with cavities are located either higher than or at the repository horizon, and cavities will remain dry. Little water is expected to flow through cavities, owing to the strong capillary barrier effect on seepage into cavities. Therefore, the existence of these lithophysal cavities has virtually no impact on the calibration and simulation results of the UZ flow model (Section 6.10.2).

6.2 THREE-DIMENSIONAL UZ FLOW MODEL CALIBRATION

A critical step in developing the three-dimensional UZ flow model was to use field-measured liquid saturation, water potential, perched water, and pneumatic data to calibrate the three-dimensional model. This calibration is essential for of the important iterative processes of model verification, which increase confidence in model predictions for the site conditions. A detailed model-calibrating investigation is reported in *Calibrated Unsaturated Zone Properties* (SNL 2007 [DIRS 179545]), using one- and two-dimensional models for estimating model parameters with water potential, and saturation. However, these one-dimensional models cannot predict whether lateral flow or perched water occurs in several hydrogeological units of the unsaturated zone below the repository level. This section documents a further model calibration effort, focusing on three-dimensional flow patterns: perched water calibrations using the three-dimensional model grid (Figure 6.1-1).

The three-dimensional flow model calibration is conducted using the four sets of parameters of one-dimensional site-scale calibrated properties (SNL 2007 [DIRS 179545]); DTNs: LB0611MTSCHP10.001 [DIRS 178586], LB0611MTSCHP30.001 [DIRS 180293], LB0612MTSCHP50.001 [DIRS 180294], LB0612MTSCHP90.001 [DIRS 180295]), two-dimensional site-scale calibrated fault properties (DTN: LB0612MTSCHPFT.001 [DIRS 180296]), three present-day infiltration rates (see Table 6.1-2), and the geological model and numerical grid for calibration (BSC 2004 [DIRS 169855]). In addition, previously developed three-dimensional properties for the perched water zone unit (DTN: LB03013DSSCP3I.001 [DIRS 162379]) developed from *Hydrologic Properties Data* (BSC 2004 [DIRS 170038]) and based on information from the previous version of this report (BSC 2004 [DIRS 169861]) are adopted in this report. As shown in Section 6.2.2.2, even with

changes in infiltration rate, the simulated extent and location of perched water is still consistent with observed moisture saturation and water potential. A permeability-barrier water-perching model is developed, as discussed in Section 6.2.2.2. In this model, rock properties are locally adjusted for several grid layers of the lower basal vitrophyre in the TSw unit and upper zeolites in the CHn unit. The objective of perched water calibrations is (1) to match perched water occurrences as observed at the site and (2) to investigate the effects of flow-through and bypassing of perched bodies on tracer transport.

6.2.1 Calibration Data

The field data used in the three-dimensional UZ flow model calibration include matrix liquid saturations, matrix water potentials, and perched water elevations, as observed from boreholes. Table 6.2-1 shows the types of data from boreholes used in the calibration, and Figure 6.1-1 shows the locations of the boreholes and the tunnel at Yucca Mountain. A subset of these boreholes (with the exception of borehole USW G-2) was used in the calibration of properties using a one-dimensional calibration model (SNL 2007 [DIRS 179545]). To accommodate lateral flow and perched waters that can only be appropriately simulated in a three-dimensional flow model, the moisture data from these boreholes are utilized in the model calibration for the UZ flow model.

Table 6.2-1. Sources for Borehole Moisture Data Used for Three-Dimensional Flow Model Calibration

Borehole	Matrix Liquid Saturation (Core)	Matrix Liquid Water Potential[a]	Perched Water Elevation (Meters above Sea Level)
USW NRG-7a	DTN: MO0109HYMXPROP.001 [DIRS 155989]		Rousseau et al. 1997 [DIRS 100178]: Figure 4.2.1-7
USW SD-6	DTN: GS980808312242.014 [DIRS 106748]	DTN: GS980808312242.014 [DIRS 106748]	
USW SD-7	DTN: MO0109HYMXPROP.001 [DIRS 155989]		DTN: SNT02110894001.002 [DIRS 105067], *s98288_001_018.pdf*, *s98288_001_019.pdf*, and *s98288_001_032.pdf*
USW SD-9	DTN: MO0109HYMXPROP.001 [DIRS 155989]		Rousseau et al. 1999 [DIRS 102097], Figure 81 and p. 171
USW SD-12	DTN: MO0109HYMXPROP.001 [DIRS 155989]	DTN: GS031208312232.003 [DIRS 171287] (in situ measurement) (organized in DTNs: LB0208UZDSCPMI.001 [DIRS 161285]	Rousseau et al. 1997 [DIRS 100178], Figure 4.2.1-4
USW UZ-14	DTN: MO0109HYMXPROP.001 [DIRS 155989]		DTN: GS040108312312.001 [DIRS 181234], *Water level measurements.xls*
USW WT-24[b]	DTN: GS980708312242.010 [DIRS 106752]	DTN: GS980708312242.010 [DIRS 106752]	DTN: GS980508312313.001 [DIRS 109746], Table s98171_002

Table 6.2-1. Sources for Borehole Moisture Data Used for Three-Dimensional Flow Model Calibration (Continued)

Borehole	Matrix Liquid Saturation (Core)	Matrix Liquid Water Potential[a]	Perched Water Elevation (Meters above Sea Level)
USW G-2			DTN: GS980508312313.001 [DIRS 109746], Table s98171_001
UZ#16	DTN: MO0109HYMXPROP.001 [DIRS 155989]		

[a] Water potential data DTN: [MO0109HYMXPROP.001 [DIRS 155989] for SD-7, SD-9, SD-12, and UZ-7 are not used because they were not in situ measured water potential data (SNL 2007 [DIRS 179545], Section 4.1.2.2).

[b] WT-24 saturation from 105°C oven calculations. Not used in the current model is saturation set from air dried under relative humidity conditions (60°C and 65% relative humidity)—a measurement seemingly yields low saturation values.

NOTE: Unless otherwise noted, data in this table are used as direct input for model calibration. Data from Rousseau et al. 1997 [DIRS 100178] and Rousseau et al. 1999 [DIRS 102097] are used as indirect input for corroboration of model results.

6.2.2 Conceptual Models of UZ Flow

Subsurface flow and transport processes in the unsaturated zone occur in a heterogeneous system of layered, anisotropic, fractured volcanic rocks. Greater understanding of such processes has been contributed by a continual effort of data collection and analysis as well as modeling studies (Wu et al. 2004 [DIRS 173953]). *Conceptual Model and Numerical Approaches for Unsaturated Zone Flow and Transport* (BSC 2004 [DIRS 170035]) presents a discussion of these conceptual models used in the study of UZ flow processes within this report. Figure 6.2-1 illustrates a typical geological profile along a vertical east-west transect as well as the conceptual model that characterizes potential lateral flow in the PTn unit, and the effects of faults and perched water on the unsaturated zone system (Wu et al. 2004 [DIRS 173953]).

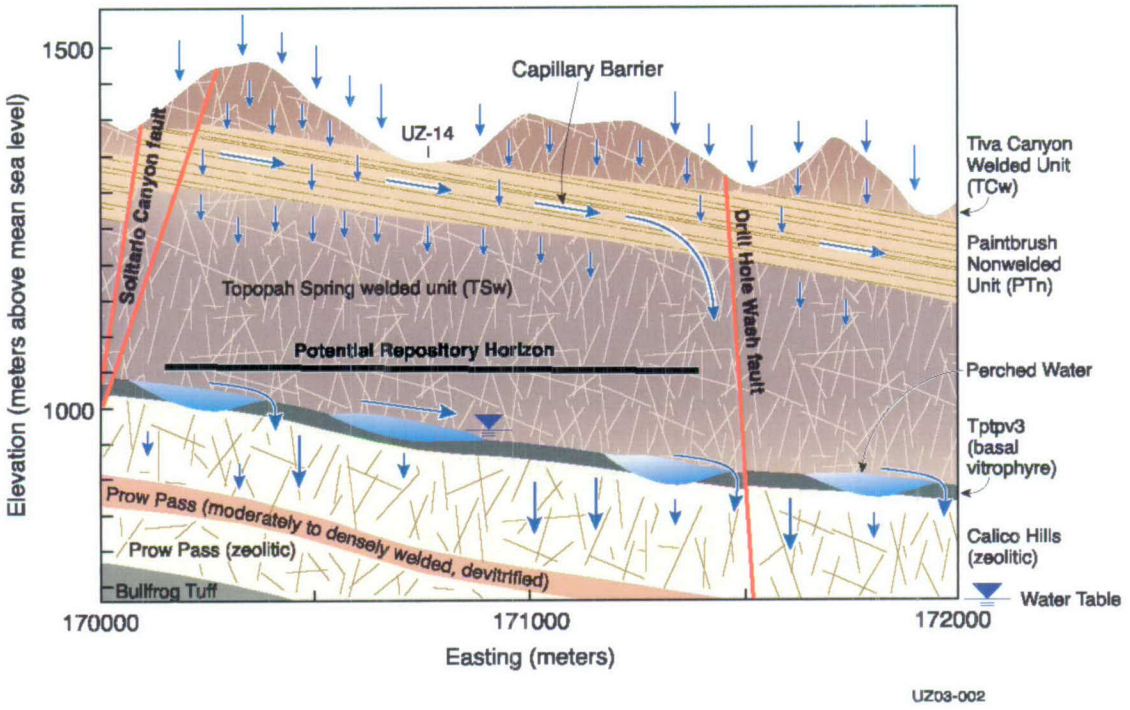

Source: For illustration purposes only.

Figure 6.2-1. Schematic Showing the Conceptualized Flow Processes and Effects of Capillary Barriers, Major Faults, and Perched Water Zones within a Typical Cross Section of the Unsaturated Zone Flow Model Domain in the East-West Direction

The PTn unit, as described by the current geological model, consists primarily of non- to partially welded tuffs. The dip of these layers is generally less than 10° to the east or southeast. The combined thickness of the PTn layers ranges from 150 m in the north of the model area to 30 m or less, even completely disappearing in several areas of the south. However, the PTn unit is present over the entire repository area, where the thickness of the PTn unit ranges from approximately 30 to 60 m, and it is even thicker to the north of the repository. The PTn unit as a whole exhibits very different hydrogeologic properties from the TCw and TSw units that bound it above and below. The TCw and TSw units have low porosity and intense fracturing typical of the densely welded tuffs at Yucca Mountain. In contrast, the PTn has high porosity and low fracture intensity, and its matrix system has a large capacity for storing groundwater. It has been shown to effectively damp spatial and temporal variations in percolation flux (Wu et al. 2000 [DIRS 154918], pp. 30 to 32 and 39 to 41; Zhang et al. 2006 [DIRS 180273]). Therefore, water flow through the unsaturated zone is modeled to occur under steady-state conditions, while the temporal damping effect of episodic flux is studied in Section 6.9.

6.2.2.1 Capillary Barriers

The concept of capillary barriers has been advanced to explain flow behavior within the PTn at Yucca Mountain (Montazer and Wilson 1984 [DIRS 100161], pp 26 to 30). These capillary barriers are due to the large contrast in rock properties across predominantly horizontal interfaces within the PTn unit. The presence of faults and larger fractures prevents development of

extensive lateral flow or laterally extensive or continuous capillary barriers. Field data obtained from tens of boreholes have been used to characterize the distribution of rock properties within the PTn unit. In general, field data indicate that the Yucca Mountain formation is more heterogeneous vertically than horizontally, so that layer-wise representations provide reasonable approximation of the complex geological system. Calibration using this conceptual model matches different types of observation data, as further demonstrated in the following sections. However, characterizing general flow behavior within the unsaturated zone system is complicated by the presence of faults, which interrupt the lateral continuity in the rock matrix properties of sloping layers.

The key conceptualizations made in the UZ flow model concerning lateral flow above the repository horizon are as follows: (1) the hydrogeological units/layers are internally homogeneous, and the material properties of each unit are continuous throughout each layer (Table 6.1-1) unless interrupted by faults; (2) ambient water flow in the system is at a steady-state condition; and (3) faults are represented by vertical or inclined columns of gridblocks having finite or small width. The flow patterns associated with capillary barriers within the PTn are studied in the following sections using this conceptual model.

6.2.2.2 Perched Water

Conceptual models of perched water occurrence are of particular interest in assessing the system performance of the repository and UZ flow patterns below the repository. Waste-isolation strategies and unsaturated zone natural barrier capability depend, in part, on sorption within the zeolitic portions of the CHn and on tracer transport times between the repository horizon and the water table. Several conceptual models have been proposed for the genesis of perched water at Yucca Mountain (e.g., Wu et al. 1999 [DIRS 117167]; Wu et al. 2004 [DIRS 173953]).

Perched water may occur where percolation flux exceeds the capacity of the geological media to transmit vertical flux in the unsaturated zone. Perched water has been encountered in a number of boreholes at Yucca Mountain, including UZ-14, SD-7, SD-9, SD-12, NRG-7a, G-2, and WT-24. These perched water occurrences are found to be associated with low-permeability zeolites in the CHn or the densely welded basal vitrophyre (Tptpv3, Table 6.1-1) of the TSw unit. Some possible mechanisms of water perching in the unsaturated zone of Yucca Mountain may be permeability or capillary barrier effects at faults, or a combination of both.

The permeability-barrier conceptual model for perched water occurrence has been used in UZ flow modeling studies since 1996 (Wu et al. (1999 [DIRS 117167]; Wu et al. 2004 [DIRS 173953]). In this model, perched water bodies in the vicinity of the ESF North Ramp (near Boreholes UZ- 14, SD-9, NRG-7a, G-2, and WT-24) are observed to occur above the base of the TSw, underlain by a zone of low-permeability, zeolitized rock. The perched water bodies in this northern area of the repository may be interconnected. However, the perched water zones at Boreholes SD-7 and SD-12 are considered here as local, isolated bodies. In this conceptual model, vertical and lateral water movement in the vicinity of the perched zones is considered to be controlled mainly by the fracture and matrix permeability distribution in these areas. The major aspects of the permeability-barrier conceptual model are: (1) no large-scale, vertically connected, potentially fluid-conducting fractures transect the underlying low-permeability units; (2) vertical and horizontal permeabilities within and below the perched water zone are small

compared with permeabilities outside perching zones; and (3) sufficient percolation flux (greater than 1 mm/yr) exists locally.

Perched water occurrence caused by permeability barrier effects is consistent with the conceptual model that ambient conditions reflect long-term, steady-state, or transient flow through the unsaturated zone, and that perched water under steady-state flow conditions may only result from a permeability barrier. Previous modeling studies (Wu et al. 1999 [DIRS 117167]; Wu et al. 2004 [DIRS 173953]) and the current modeling investigations (Section 6.2.5) conclude that this conceptual water-perching model is able to match the observed perched water elevations in the Yucca Mountain. In particular, these studies show that modeling results using this conceptual model are consistent with other moisture data, such as water potential and matrix saturation. In the present numerical studies, the occurrence of perched water is assumed to follow the conceptual model of a permeability barrier. In other words, perched water bodies are formed as a result of permeability barrier effects.

6.2.3 Parameter Adjustment

Calibrated Unsaturated Zone Properties (SNL 2007 [DIRS 179545]) provides basic input parameter sets of fractures and matrix rocks for the modeling efforts in this report. However, these properties were estimated through a series of one-dimensional model calibrations, in which lateral flow, perched water, and capillary barrier effects cannot be rigorously simulated. Use of a three-dimensional model allows further parameter adjustment to match field observation data. This section presents calibrated parameters after adjustment through a series of three-dimensional model calibrations. This section describes the approach used to obtain calibrated parameters that incorporate three-dimensional flow processes. The calibration involves adjustment of one-dimensional calibrated parameters to produce observed three-dimensional flow processes (e.g., location and extent of perched water) by performing a series of three-dimensional simulations. The parameters adjusted during the calibration include fracture and matrix properties for the top TSw layer, perched water zones (location and extent of the perched water zones), and fracture permeabilities in the upper TSw layers. Properties of the perched water zone are organized as a rock card in the TOUGH2 input file, and gridblocks belonged to the perched water zone are assigned these property data.

In addition to estimating model parameters, these calibration studies can also be used to examine the adequacy of discretization for the three-dimensional model grid. (Note that *Development of Numerical Grids for UZ Flow and Transport Modeling* (BSC 2004 [DIRS 169855], Section 6.6) examined the adequacy of discretization). The three-dimensional unsaturated zone TSPA-LA grid (Figure 6.1-1 for its plan view) uses finer vertical discretization than those used in the TSPA site recommendation model (BSC 2001 [DIRS 158726]), particularly, for the PTn unit and the potential perched water layers. For example, the PTn unit consists, in general, of six hydrogeological units vertically (namely, ptn21, ptn22, ptn23, ptn24, ptn25, and ptn26; Table 6.1-1), each of which is discretized into one or several vertical grid layers with maximum thickness of 2 or 5 m, respectively. The details of discretization are described in *Development of Numerical Grids for UZ Flow and Transport Modeling* (BSC 2004 [DIRS 169855], Section 6.6).

The three-dimensional model calibration was performed by starting with the sets of calibrated parameters from the one-dimensional calibrations in *Calibrated Unsaturated Zone Properties*

(SNL 2007 [DIRS 179545]) in forward three-dimensional simulations. Then, model results were compared with the field-observed data of matrix liquid saturation, along with water-potential data, perched water elevations, and gas pressures. In general, some model parameters from one-dimensional calibrations are found to need adjustment in order to capture three-dimensional flow behavior or match Yucca Mountain field data. The following modifications made to the one-dimensional rock properties were found necessary: modifying the fracture α of the tsw31 unit, using fracture–matrix properties from the previous three-dimensional calibration, locally adjusting fracture–matrix properties for the model layers associated with perched water occurrence, and adjusting fracture permeability for the TSw units.

When the one-dimensional calibrated fracture–matrix properties from *Calibrated Unsaturated Zone Properties* (SNL 2007 [DIRS 179545]) were used directly without any modifications as input to the three-dimensional model, significant lateral flow was predicted to occur along the top layer of the TSw unit (tsw31) under present-day scenarios. This prediction results from the limitation of a one-dimensional model; there is no evidence to support lateral flow within this layer. The three-dimensional simulation results indicated that a strong capillary barrier is formed between this tsw31 layer and the layer below. Examination of the calibrated fracture parameters for this layer showed that such large lateral flow was artificially created by the small value of fracture α in tsw31, estimated by the one-dimensional calibration. The one-dimensional calibrated fracture $\alpha = 1.82 \times 10^{-5}$ Pa^{-1}, 2.08×10^{-5} Pa^{-1}, 2.00×10^{-5} Pa^{-1}, and 2.00×10^{-5} Pa^{-1} (DTNs: LB0611MTSCHP10.001 [DIRS 178586], LB0611MTSCHP30.001 [DIRS 180293], LB0612MTSCHP50.001 [DIRS 180294], LB0612MTSCHP90.001 [DIRS 180295]), respectively, for the 10th, 30th, 50th, and 90th percentiles of present-day infiltration rates. These one-dimensional calibrated fracture α values at the same layer are similar to or even smaller than the corresponding matrix α values (= 2.80×10^{-5} Pa^{-1}, 2.90×10^{-5} Pa^{-1}, 1.07×10^{-5} Pa^{-1}, and 3.38×10^{-5} Pa^{-1}) for the 10th, 30th, 50th, and 90th percentiles, respectively. This is an artifact of the one-dimensional calibration model. The top layer of the TSw unit is the transition from matrix-dominated flow in the PTn to fracture-dominated flow in the TSw, for which a strong capillary suction is needed within the fractures, leading to large lateral flow. In three dimensions, the presence of many large fractures along the top layer of the TSw unit prevents extensive lateral suction, resulting in larger effective α (DTN: LB0205REVUZPRP.001 [DIRS 159525]). Therefore, a larger, uniform fracture α (= 10^{-4} Pa^{-1}) is used instead, leading to a good match between observed data (as discussed in Section 6.2.5) and three-dimensional models with little lateral flow in the tsw31 layer.

The second modification to the three one-dimensional calibrated property sets is to implement perched water properties. For perched water calibration, calibrated parameters of fracture and matrix permeabilities within perched zones are determined from many modeling studies with three-dimensional simulations. The perched water conceptual model with respect to water-perching scenarios is realized and carried out by modifying the three-dimensional UZ model grid file as follows:

- The grid-layer properties of tsw38 (tswF8/tswM8), tsw39 (tswF9/tswM9), ch1z (ch1Fz/ch1Mz), and ch2z (ch2Fz/ch2Mz) are replaced by (pcF38/pcM38), (pcF39/pcM39), (pcF1z/pcM1z), and (pcF2z/pcM2z), respectively, where the basal vitrophyre of the TSw is underlain by zeolitic units.

- Near borehole SD-7, properties for the gridblocks in grid columns q45, i80, i81, i84, i87, o92, and o95, over grid layers of ch5z (ch5Fz/ch5Mz), ch6z (ch6Fz/ch6Mz) and pp4 (pp4Fz/pp4Mz) are replaced by (pcF5z/pcM5z), (pcF6z/pcM6z), and (pcF4p/pcM4p), respectively.

- Near borehole SD-12, properties for the gridblocks in grid columns q47, b93, b99, k61, k62 and k67, over grid layers of tsw38 (tswF8/tswM8), tsw39 (tswF9/tswM9), and ch1v (ch1Fv/ch1Mv) are replaced by (pcF38/pcM38), (pcF39/pcM39), and (pcF1z/pcM1z), respectively.

Fracture and matrix permeabilities of potential perched layers/zones, as identified above, are calibrated based on the three-dimensional model calibrated values and shown in Tables 6.2-2, 6.2-3, and 6.2-4. All properties except intrinsic permeabilities, van Genuchten's α and m parameters, and residual saturations for matrix blocks within perched zones are identical to parameters estimated from the current one-dimensional calibrations discussed in *Calibrated Unsaturated Zone Properties* (SNL 2007 [DIRS 179545]). The active-fracture parameter, γ, is set to zero for the perched zones, causing the fracture and matrix interface-area factor to be equivalent to liquid saturation (Liu et al. 1998 [DIRS 105729]). Tables 6.2-2, 6.2-3, 6.2-4, and 6.2-5 present the final four sets of calibrated rock properties at zones with perched water, with 10th, 30th, 50th, and 90th present-day infiltration scenarios, respectively. The modified "fracture" properties in the following three tables are close to those of the matrix, so that fractures in water perching layers are effectively removed.

In Tables 6.2-2 to 6.2-5, as well as those in Appendix B, the symbols and notations standing for parameters are defined as follows: k_M and k_F are intrinsic permeability of matrix and fracture systems; α_M and α_F are van Genuchten α parameters of the matrix and fracture systems; m_M and m_F are van Genuchten m parameters of the matrix and fracture systems; and γ is the AFM parameter.

Table 6.2-2. Calibrated Parameters of Perched water Conceptual Model for the Present-Day, 10th Percentile Infiltration Scenario

Model Layer	k_M (m^2)	α_M (1/Pa)	m_M (–)	k_F (m^2)	α_F (1/Pa)	m_F (–)	γ (–)
pcM38/ pcF38	3.000×10^{-19}	1.878×10^{-6}	0.286	3.000×10^{-18}	1.878×10^{-6}	0.286	0.00
pcM39/ pcF39	6.200×10^{-18}	4.610×10^{-6}	0.059	6.200×10^{-17}	4.610×10^{-6}	0.059	0.00
pcM1z/ pcF1z	9.300×10^{-20}	2.120×10^{-7}	0.349	9.300×10^{-19}	2.120×10^{-7}	0.349	0.00
pcM2z/ pcF2z	2.400×10^{-18}	2.250×10^{-6}	0.257	2.400×10^{-17}	2.250×10^{-6}	0.257	0.00
pcM5z/ pcF5z	2.400×10^{-18}	2.250×10^{-6}	0.257	2.400×10^{-18}	2.250×10^{-6}	0.257	0.00
pcM6z/ pcF6z	1.100×10^{-19}	1.560×10^{-7}	0.499	1.100×10^{-19}	1.560×10^{-7}	0.499	0.00
pcM4p/ pcF4p	7.700×10^{-19}	6.310×10^{-6}	0.474	7.700×10^{-19}	6.310×10^{-6}	0.474	0.00

Output DTN: LB07043DCRXPRP.001.

Table 6.2-3. Calibrated Parameters of Perched water Conceptual Model for the Present-Day, 30th Percentile Infiltration Scenario

Model Layer	k_M (m^2)	α_M (1/Pa)	m_M (–)	k_F (m^2)	α_F (1/Pa)	m_F (–)	γ (–)
pcM38/ pcF38	3.000×10^{-19}	3.105×10^{-6}	0.286	3.000×10^{-18}	3.105×10^{-6}	0.286	0.00
pcM39/ pcF39	6.200×10^{-18}	4.610×10^{-6}	0.059	6.200×10^{-17}	4.610×10^{-6}	0.059	0.00
pcM1z/ pcF1z	9.300×10^{-20}	2.120×10^{-7}	0.349	9.300×10^{-19}	2.120×10^{-7}	0.349	0.00
pcM2z/ pcF2z	2.400×10^{-18}	2.250×10^{-6}	0.257	2.400×10^{-17}	2.250×10^{-6}	0.257	0.00
pcM5z/ pcF5z	2.400×10^{-18}	2.250×10^{-6}	0.257	2.400×10^{-18}	2.250×10^{-6}	0.257	0.00
pcM6z/ pcF6z	1.100×10^{-19}	1.560×10^{-7}	0.499	1.100×10^{-19}	1.560×10^{-7}	0.499	0.00
pcM4p/ pcF4p	7.700×10^{-19}	6.310×10^{-7}	0.474	7.700×10^{-19}	6.310×10^{-7}	0.474	0.00

Output DTN: LB07043DCRXPRP.001.

Table 6.2-4. Calibrated Parameters of Perched water Conceptual Model for the Present-Day, 50th Percentile Infiltration Scenario

Model Layer	k_M (m^2)	α_M (1/Pa)	m_M (–)	k_F (m^2)	α_F (1/Pa)	m_F (–)	γ (–)
pcM38/ pcF38	3.000×10^{-19}	3.691×10^{-6}	0.286	3.000×10^{-18}	3.691×10^{-6}	0.286	0.00
pcM39/ pcF39	6.200×10^{-18}	4.610×10^{-6}	0.059	6.200×10^{-17}	4.610×10^{-6}	0.059	0.00
pcM1z/ pcF1z	9.300×10^{-20}	2.120×10^{-7}	0.349	9.300×10^{-19}	2.120×10^{-7}	0.349	0.00
pcM2z/ pcF2z	2.400×10^{-18}	2.250×10^{-6}	0.257	2.400×10^{-17}	2.250×10^{-6}	0.257	0.00
pcM5z/ pcF5z	2.400×10^{-18}	2.250×10^{-6}	0.257	2.400×10^{-18}	2.250×10^{-6}	0.257	0.00
pcM6z/ pcF6z	1.100×10^{-19}	1.560×10^{-7}	0.499	1.100×10^{-19}	1.560×10^{-7}	0.499	0.00
pcM4p/ pcF4p	7.700×10^{-19}	6.545×10^{-6}	0.474	7.700×10^{-19}	6.545×10^{-6}	0.474	0.00

Output DTN: LB07043DCRXPRP.001.

Table 6.2-5. Calibrated Parameters of Perched water Conceptual Model for the Present-Day, 90th Percentile Infiltration Scenario

Model Layer	k_M (m^2)	α_M (1/Pa)	m_M (–)	k_F (m^2)	α_F (1/Pa)	m_F (–)	γ (–)
pcM38/ pcF38	3.000×10^{-19}	4.777×10^{-6}	0.286	3.000×10^{-18}	4.777×10^{-6}	0.286	0.00
pcM39/ pcF39	6.200×10^{-18}	4.610×10^{-6}	0.059	6.200×10^{-17}	4.610×10^{-6}	0.059	0.00
pcM1z/ pcF1z	9.300×10^{-20}	2.120×10^{-7}	0.349	9.300×10^{-19}	2.120×10^{-7}	0.349	0.00
pcM2z/ pcF2z	2.400×10^{-18}	2.250×10^{-6}	0.257	2.400×10^{-17}	2.250×10^{-6}	0.257	0.00
pcM5z/ pcF5z	2.400×10^{-18}	2.250×10^{-6}	0.257	2.400×10^{-18}	2.250×10^{-6}	0.257	0.00
pcM6z/ pcF6z	1.100×10^{-19}	1.560×10^{-7}	0.499	1.100×10^{-19}	1.560×10^{-7}	0.499	0.00
pcM4p/ pcF4p	7.700×10^{-19}	6.310×10^{-6}	0.474	7.700×10^{-19}	6.310×10^{-6}	0.474	0.00

Output DTN: LB07043DCRXPRP.001.

The third and last parameter adjustment is the fracture permeability in the TCw and TSw units under the present-day, 10th and 30th percentile infiltration scenarios (see Section 6.4). The present-day, 10th and 30th percentile infiltration rates are used for gas flow calibration because the pneumatic tests were conducted in a small time scale of days to years at present-day conditions. This calibration, described in Section 6.4, was made from three-dimensional gas

flow analysis, with the calibrated fracture permeability results summarized in Tables 6.4-2 and 6.4-3.

The final results and calibrated parameter sets of the three-dimensional UZ flow modeling studies are given in Tables B-1 to B-4 of Appendix B.

6.2.4 Numerical Treatment and Solution Convergence

Numerical modeling of large-scale three-dimensional flow and transport in the Yucca Mountain unsaturated zone is mathematically challenging. The principal difficulty stems from the highly nonlinear coupling of the flow system. First, the hydrogeological system is distinctly heterogeneous on all model scales, and, for example, there are orders-of-magnitude contrasts in permeabilities across geological layers or between fracture and matrix rock. Secondly, the two-phase flow functions of relative permeability and capillary pressure estimated for Yucca Mountain tuffs are extremely nonlinear for both fractures and matrix systems. The mathematical burden is further increased with the use of the dual-permeability modeling approach for handling fracture–matrix interaction. In this case, flow through fractures and matrix is on very different time scales, with fracture flow being orders-of-magnitude faster than matrix flow. Furthermore, fracture elements have a much smaller storage space than matrix elements. In general, it takes simulation times of thousands to millions of years (performed over hundreds to thousands of computation time steps) for the system to achieve steady-state conditions.

All flow simulations (this section and Section 6.7) were carried out using the EOS9 module. With the EOS9 module, two-phase flow problems are solved with one equation per gridblock instead of solving two or three equations, as required by the EOS3 module. Numerical tests show that for moisture flow and distributions at steady state, the EOS9 solutions are, in general, identical to EOS3 ("true two-phase" flow solutions).

Model calibrations and flow-field simulations are both based on steady-state solutions using the EOS9 module. In each simulation, fracture, fault, and zeolitic element volumes are increased by a factor of 10,000, while keeping other mesh geometric information unchanged, to overcome convergence difficulties associated with the large contrast between the volume of these elements and the volume of the associated matrix elements. This approach does not affect the final solution as long as a "true" steady-state solution is obtained for a given run. The initial condition for a new scenario run is estimated using a default (uniform) initial condition or results of a previous run with a similar modeling condition. Each simulation is usually subdivided into stages. For the first-stage runs, a large convergence tolerance on the order of 10,000 or more is used to keep simulation progressing with a large time step. Evaluation of the steady-state solution using a global mass balance (Table 6.2-7) shows that using large residual tolerance in the first stage has no effect on the final, steady-state solutions, as long as no oscillations or unphysical solutions occur. After running the solution to 10^9 years or more with a large tolerance, the convergence tolerance is reduced to 10^{-2} to 10^{-3}, and the model is run until a steady-state solution is reached. The final steady-state solutions are confirmed using a global mass-balance check, as discussed in Section 6.2.5.

6.2.5 Simulation Scenarios, Results, and Analyses

This section summarizes the three-dimensional flow model calibration scenarios performed for this report, including simulation results and analyses. The model calibrations are performed using (1) the three-dimensional TSPA-LA grid (Figure 6.1-1) and four net infiltration maps of present-day climate, as discussed in Section 6.1.4; (2) the four parameter sets (Tables B-1, B-2, B-3, and B-4); and (3) the UZ flow conceptual models of Section 6.2.2 above. Flow simulation scenarios for three future climates of monsoon, glacial transition, and post-10,000-yr are carried out as forward simulations. Simulation results are called TSPA-LA flow simulations or UZ flow fields in this report.

Simulation Scenarios: Table 6.2-6 summarizes these 16 simulation scenarios, associated parameter sets, and infiltration rates used.

Table 6.2-6. Sixteen UZ Flow Simulation Scenarios: Data Files, Parameter Sets, and Infiltration Maps for the UZ Model Calibrations

Designation/ Simulation/	Parameter Set/Calibration (Output DTN: LB07043DCRXPRP.001)	Infiltration Map
pd_10	Parameter set from Table B-1	Present-day 10th percentile infiltration DTN: SN0609T0502206.028 [DIRS 178753]
pd_30	Parameter set from Table B-2	Present-day day 30th percentile infiltration DTN: SN0609T0502206.028 [DIRS 178753]
pd_50	Parameter set from Table B-3	Present-day 50th percentile infiltration DTN: SN0609T0502206.028 [DIRS 178753]
pd_90	Parameter set from Table B-4	Present-day 90th percentile infiltration DTN: SN0609T0502206.028 [DIRS 178753]
mo_10	Parameter set from Table B-1	Monsoon h 10th percentile infiltration DTN: SN0609T0502206.024 [DIRS 179063]
mo_30	Parameter set from Table B-2	Monsoon 30th percentile infiltration DTN: SN0609T0502206.024 [DIRS 179063]
mo_50	Parameter set from Table B-3	Monsoon 50th percentile infiltration DTN: SN0609T0502206.024 [DIRS 179063]
mo_90	Parameter set from Table B-4	Monsoon 90th percentile infiltration DTN: SN0609T0502206.024 [DIRS 179063]
gt_10	Parameter set from Table B-1	Glacial-transition 10th percentile infiltration DTN: SN0609T0502206.029 [DIRS 178862]
gt_30	Parameter set from Table B-2	Glacial-transition 30th percentile infiltration SN0609T0502206.029 [DIRS 178862]
gt_50	Parameter set from Table B-3	Glacial-transition 50th percentile infiltration DTN: SN0609T0502206.029 [DIRS 178862]
gt_90	Parameter set from Table B-4	Glacial-transition 90th percentile infiltration DTN: SN0609T0502206.029 [DIRS 178862]
pkd_q1	Parameter set from Table B-1	Post-10,000-yr, 10th percentile infiltration DTN: LB0702UZP10KFF.002
pkd_q2	Parameter set from Table B-2	Post-10,000-yr, 30th percentile infiltration DTN: LB0702UZP10KFF.002
pkd_q3	Parameter set from Table B-3	Post-10,000-yr, 50th percentile infiltration DTN: LB0702UZP10KFF.002
pkd_q4	Parameter set from Table B-4	Post-10,000-yr, 90th percentile infiltration DTN: LB0702UZP10KFF.002

Mass Balance and Solution Convergence: Table 6.2-7 shows the mass-balance results for the sixteen simulation scenarios. In Table 6.2-7, "inflow" is the total infiltration rate over the entire model top boundary, representing a net water recharge rate (water mass) into the system for the infiltration scenario simulated. "Outflow" is the cumulative total-flow rate out of the model and into the lower boundary representing the water table. Global mass-balance errors between inflow and outflow from the system, as shown in Table 6.2-7, are less than 0.013% for all 16 simulations, leading to the conclusion that steady-state solutions are obtained for all the simulations.

Table 6.2-7. Mass-Balance Results for Checking Steady State Status of Sixteen Flow Simulation Results

Simulation Scenarios	Inflow from Infiltration (kg/s)	Outflow to Water Table (kg/s)	Relative Error (%)
pd_10	3.821408495	3.8210676	0.0089
pd_30	10.05089517	10.0496168	0.0127
pd_50	15.50822442	15.5082076	0.0001
pd_90	33.81826331	33.8182842	0.0001
mo_10	8.511510348	8.5115148	0.0001
mo_30	16.28484915	16.2848381	0.0001
mo_50	19.41794042	19.4179219	0.0001
mo_90	92.51816511	92.5183180	0.0002
gt_10	13.93611829	13.9360979	0.0001
gt_30	25.82297803	25.8229675	0.0001
gt_50	32.81793890	32.8179286	0.0000
gt_90	58.95021503	58.9500578	0.0003
pkd_q1	21.33438025	21.3344012	0.0001
pkd_q2	36.61220864	36.6123755	0.0005
pkd_q3	43.78254941	43.7827807	0.0005
pkd_q4	61.67639555	61.6727082	0.0060

Output DTNs: LB06123DPDUZFF.001; LB07013DMOUZFF.001; LB07013DGTUZFF.001; LB0702UZP10KFF.002.

Model Calibrations and Results: As listed in Table 6.2-6, there are a total of 16 model scenarios, covering 16 infiltration rate distributions for four (present-day, monsoon, glacial transition, and post-10k-yr) climates. The four present-day cases (10th, 30th, 50th, and 90th percentiles) out of the 16 simulations are for model calibrations, and the other twelve scenarios are forward runs for providing UZ flow fields as well as sensitivity analyses. The four present-day simulations have been calibrated against the field-observed data of perched water. In addition, the observed matrix liquid saturations and water potentials (when available) are also used to examine these modeling results. A perched water body is defined as fully liquid saturated gridblocks with zero capillary pressure for calibration. The data source used in the calibrations are listed in Section 4.1 and in Table 6.2-1. Only in situ measurement of water potentials among the water-potential data are used. In this section, the simulation results of the four present-day simulations are presented and discussed in terms of: (1) comparisons with matrix liquid saturation, water potential, and perched water data; (2) examination of simulated

perched water bodies; and (3) examination of simulated percolation flux and fracture–matrix flow components.

All 12 simulations for the present-day, monsoon, and glacial transition climates are checked against observed saturation, water potential, and perched water data. Only a few of these comparisons are shown here, and boreholes UZ-14 and SD-12 are selected to show the match between observed and modeled vertical-saturation profiles and perched water locations for four present-day climate simulations with perched water occurrence. Table C-1 lists the surface elevations and coordinates of selected boreholes for conversion from depth to elevation. Matches to other borehole data are similar. Most borehole observation data used in this section and the following sections are given relative to depth. In plots of this report, elevations are used to illustrate model results and comparisons. Appendix D provides more comparisons of the saturation and potential profiles of all boreholes evaluated by the model.

Matrix saturation and water potential data are not used in the GLUE analysis in Section 6.8, because, as shown below, simulated distributions for the matrix saturation and water potential are not very sensitive to the percolation flux in the unsaturated zone. Pneumatic pressure data are not considered, either, because the water percolation process does not significantly affect pneumatic signals in the unsaturated zone when fractures are very dry.

Comparisons with Liquid Saturation, Water Potential, and Perched Water Data: Measured matrix liquid saturation, water-saturation data and perched water elevations are compared against three-dimensional model results from the twelve simulations. Matrix liquid saturation, water potential, and perched water data used for comparisons are taken from nine boreholes (NRG-7a, SD-6, SD-7, SD-9, SD-12, UZ-14, UZ#16, WT-24, and G-2). The locations of these boreholes are shown in Figure 6.1-1.

The comparisons of simulated and observed matrix liquid saturations along the vertical column representing boreholes UZ-14 and SD-12 are shown, as examples, in Figures 6.2-2 and 6.2-3, from the UZ flow models with four present-day infiltration scenarios. Plots for other seven boreholes are documented in Appendix D-1. Figure 6.2-4 shows a comparison with water potentials for SD-12. In general, the modeled results from the twelve simulations with the UZ flow conceptual model are in reasonable agreement with the measured saturation and water-potential profiles, as shown in Figures 6.2-2, 6.2-3, and 6.2-4. It should be mentioned that there are some differences between simulated and observed saturation data, as shown in Figures 6.2-2, 6.2-3, and 6.2-4, which are primarily caused by formation heterogeneity and grid coarseness.

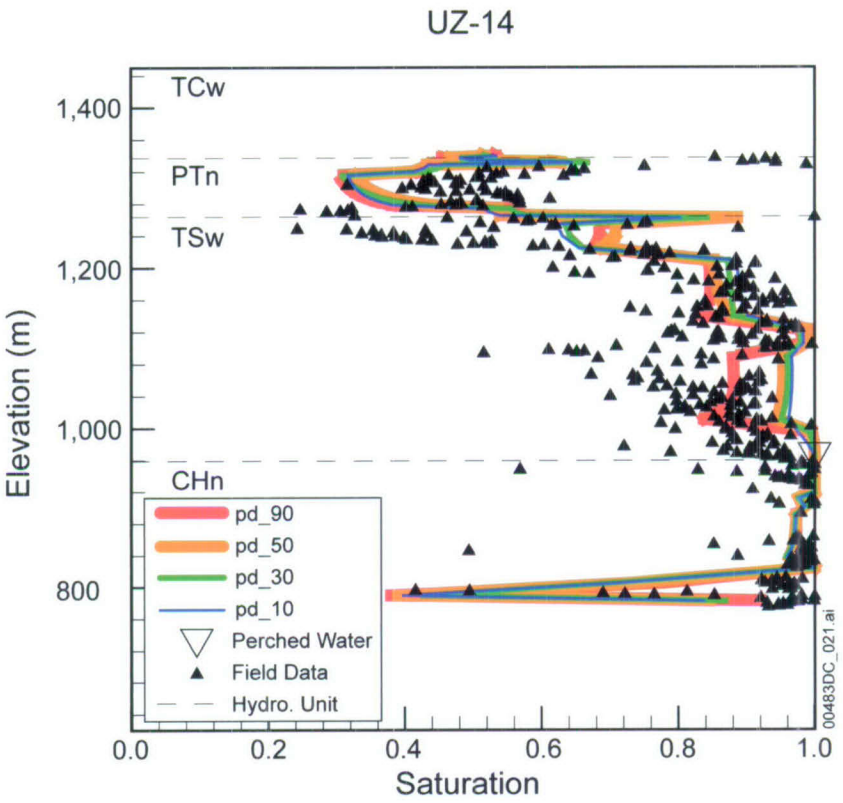

Sources: DTNs: GS040108312312.001 [DIRS 181234]; MO0109HYMXPROP.001 [DIRS 155989]; MO0004QGFMPICK.000 [DIRS 152554].

Output DTN: LB06123DPDUZFF.001.

Figure 6.2-2. Comparison to the Simulated and Observed Matrix Liquid Saturations and Perched Water Elevations for Borehole UZ-14, Using the Results of the Simulations with Four Present-Day (PD) Infiltration Rates

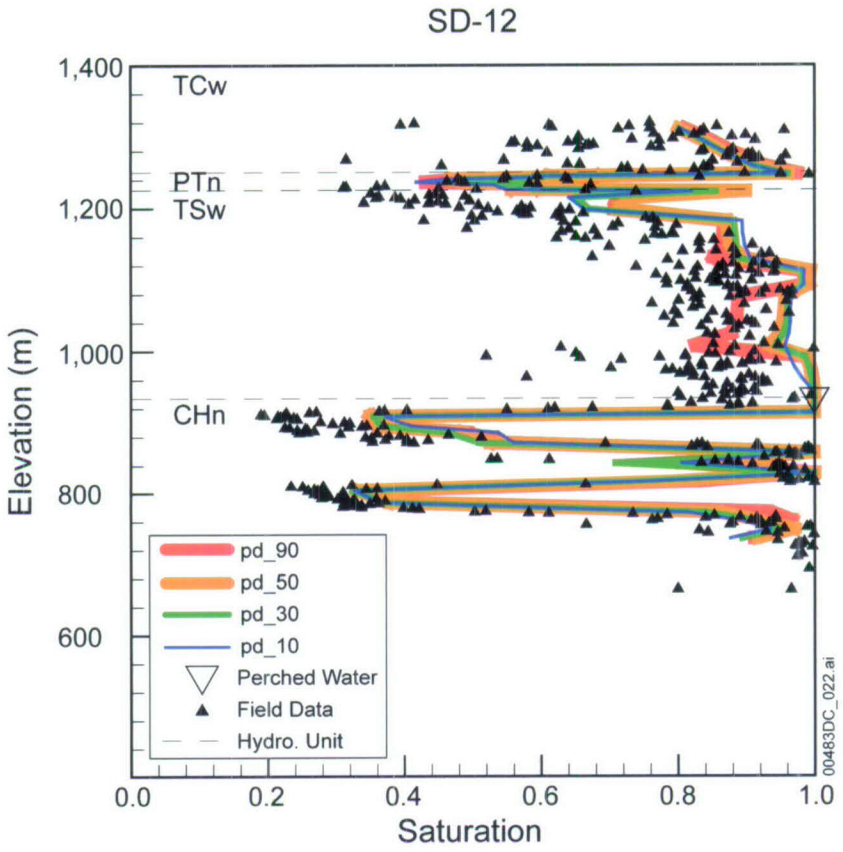

Sources: Rousseau et al. 1997 [DIRS 100178]; DTNs: MO0109HYMXPROP.001 [DIRS 155989]; MO0004QGFMPICK.000 [DIRS 152554].

Output DTN: LB06123DPDUZFF.001.

Figure 6.2-3. Comparison to the Simulated and Observed Matrix Liquid Saturations and Perched Water Elevations for Borehole SD-12, Using the Results of the Simulations with Four Present-Day (PD) Infiltration Rates

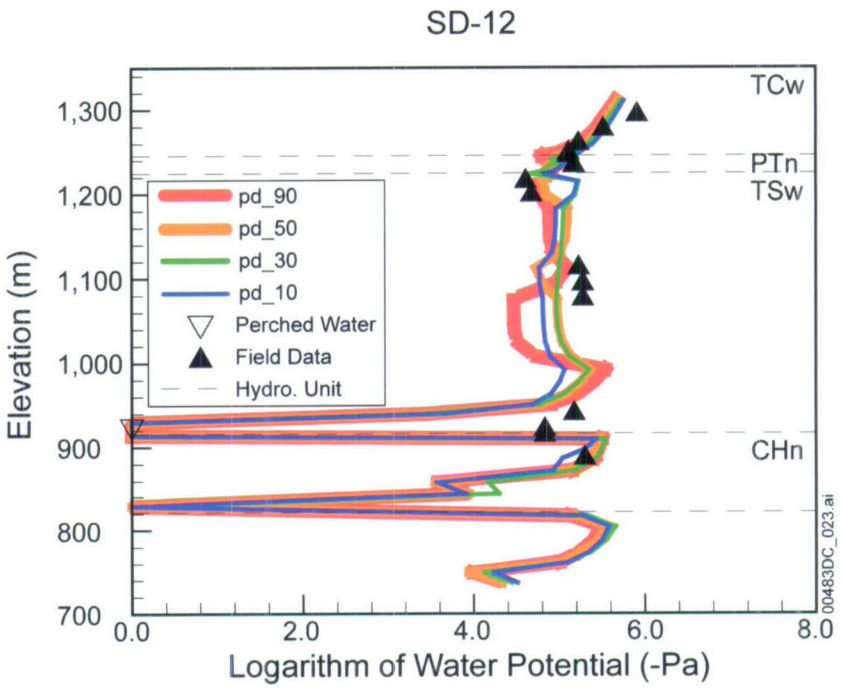

Source: DTNs: MO0004QGFMPICK.000 [DIRS 152554]; Model Results – Output DTN: LB06123DPDUZFF.001.

NOTE: Field data shown in figure are from DTNs: GS031208312232.003 [DIRS 171287], GS031208312232.005 [DIRS 179284].

Figure 6.2-4. Comparison to the Simulated and Averaged Observed Water Potentials and Perched Water Elevations for Borehole SD-12, Using the Results of the Simulations with Four Present-Day (PD) Infiltration Rates

Also shown in Figures 6.2-2, 6.2-3, and 6.2-4 are the perched water elevations at the two boreholes, indicating a good agreement between observed and simulated data. In addition, each of the twelve simulations for present-day monsoon, and glacial transition climates has been compared to perched water data, as observed from the seven perched water boreholes of Table 6.2-1 (see Appendix D for detailed comparisons). The results are as follows:

- For the present-day, 10th, 30th, 50th, and 90th infiltration scenarios (pd_10, pd_30, pd_50, and pd_90, Table 6.2-6), the simulated perched water zones generally match the observations.

- In addition, under the two future climates of monsoon and glacial transition, the UZ model also predict perched water occurrence at these borehole locations.

6.2.6 Features, Events, and Processes

The results from this model report are part of the basis for the treatment of features, events, and processes (FEPs). FEPs that are included in TSPA through output of the UZ Flow model are summarized in Table 6.2-8. These FEPS have been taken from *FY 2007 LA FEP List and Screening* (DTN: MO0706SPAFEPLA.001 [DIRS 181613]).

Table 6.2-8. FEPs Addressed in This Report

FEP Number and FEP Name	FEP Description	Summary of Technical Basis and Approach for FEP Inclusion
1.2.02.01.0A Fractures	Groundwater flow in the Yucca Mountain region and transport of any released radionuclides may take place along fractures. The rate of flow and the extent of transport in fractures are influenced by characteristics such as orientation, aperture, asperity, fracture length, connectivity, and the nature of any linings or infills.	Fractures are included in process models for unsaturated zone flow and transport by using models based on the dual-permeability concept, with fractures represented by a distinct continuum. The fracture continuum models spatially averaged flow through discrete fractures. The fracture continuum interacts with the matrix continuum, which represents matrix blocks separated by the network of fractures. Fracture porosity, fracture spacing, and fracture volume fraction measured in the field and within different stratigraphic units determine geometrical parameters of fractures that are incorporated in the model.
1.2.02.02.0A Faults	Numerous faults of various sizes have been noted in the Yucca Mountain region, and specifically in the repository area. Faults may represent an alteration of the rock permeability and continuity of the rock mass, an alteration or short-circuiting of the flow paths and flow distributions close to the repository, and (or) unexpected pathways through the repository.	Stratigraphic displacement, dip-slip, strike-slip, and detachments due to faulting within the model domain are explicitly discretized in the site-scale unsaturated zone flow and transport models. Specific hydrogeologic properties are assigned to the fault zones, supported by measurements within fault zones or across faults. The net effect on flow is reflected in the unsaturated zone flow fields that include flow through faults.
1.3.01.00.0A Climate change	Climate change may affect the long-term performance of the repository. This includes the effects of long-term change in global climate (e.g., glacial–interglacial cycles) and shorter-term change in regional and local climate. Climate is typically characterized by temporal variations in precipitation and temperature.	Climate change is addressed in TSPA based on the record of climate changes in the past, which are used to predict the expected changes in climate for the future. Climate modeling is incorporated into TSPA through the unsaturated zone flow fields that use different surface water flux boundary condition maps corresponding to three different climates during the first 10,000 years. This is incorporated in TSPA through the unsaturated zone flow model output, which uses the results of the infiltration model to assign the water flux boundary conditions at the model's upper boundary. For the post-10,000-year period, the surface water flux boundary condition for the unsaturated zone flow model is assigned using the percolation flux distribution given in the proposed rule (70 Fed. Reg. 173).
1.3.07.02.0B Water table rise affects unsaturated zone	Climate change could produce increased infiltration, leading to a rise in the regional water table, possibly affecting radionuclide release from the repository by altering flow and transport pathways in the unsaturated zone. A regionally higher water table and change in unsaturated zone flow patterns might flood the repository.	The potential for water table rise caused by climate change is included in TSPA calculations using a water table rise model based on climate data, which allows the water table to change elevation instantaneously upon change in climate.
1.4.01.01.0A Climate modification increases recharge	Climate modification causes an increase in recharge in the Yucca Mountain region. Increased recharge might lead to increased flux through the repository, perched water, or water table rise.	The effects of climate changes on unsaturated zone flux through the repository are incorporated through explicit simulations of unsaturated zone flow fields corresponding to the four uncertainty cases for water flux at the upper boundary of the unsaturated zone flow model and three distinct climate states: present-day, monsoon, and glacial transition as well as the post-10,000-year period.

Table 6.2-8. FEPs Addressed in This Report (Continued)

FEP Number and FEP Name	FEP Description	Summary of Technical Basis and Approach for FEP Inclusion
2.1.08.01.0A Water influx at the repository	An increase in the unsaturated water flux at the repository may affect thermal, hydrologic, chemical, and mechanical behavior of the system. Increases in flux could result from climate change, but the cause of the increase is not an essential part of the FEP.	Changes in unsaturated zone flow in response to climate changes are incorporated in the output flow fields developed for use in the TSPA. The outputs from the site-scale unsaturated zone flow model are also used by other models that are intermediate between the site-scale unsaturated zone flow model and the TSPA model.
2.2.03.01.0A Stratigraphy	Stratigraphic information is necessary information for performance assessment. This information should include identification of the relevant rock units, soils, and alluvium and their thickness, lateral extents, and relationships to each other. Major discontinuities should be identified.	This FEP is included in the unsaturated zone flow and coupled process models by use of grids developed from geologic information in the geologic framework model. The stratigraphic units and layers provide the structural basis for the site-scale unsaturated zone model grids. Because the assignment of hydrologic properties is associated with the grids used for the site-scale unsaturated zone flow and coupled process models, the stratigraphy information is embedded in the TSPA through the outputs from these models.
2.2.03.02.0A Rock properties of host rock and other units	Physical properties, such as porosity and permeability of the relevant rock units, soils, and alluvium, are necessary for the performance assessment. Possible heterogeneities in these properties should be considered. Questions concerning events and processes that may cause these physical properties to change over time are considered in other FEPs.	Rock properties used are defined for each of the stratigraphic units and layers classified in the geologic framework model, which is further developed into a model grid for the site-scale unsaturated zone flow model. Heterogeneity is modeled in terms of the sequence of hydrogeologic units and discrete faults. Therefore, rock properties are embedded in the TSPA through the output flow fields, in which the site-scale layering and faults are taken into account.
2.2.07.02.0A Unsaturated groundwater flow in the geosphere	Groundwater flow occurs in unsaturated rocks in most locations above the water table at Yucca Mountain, including at the location of the repository. See related FEPs for discussions of specific issues related to unsaturated flow.	This FEP is included in the unsaturated zone process model flow models. The ambient flow model uses a three-dimensional steady flow in a heterogeneous dual-permeability system that includes discrete fault zones that allow for a realistic description of flow pathways in the unsaturated zone. The flow fields generated by the site-scale unsaturated zone flow model are used directly by the TSPA and are also included in the TSPA via intermediate models; for example, the models of seepage.
2.2.07.03.0A Capillary rise in the unsaturated zone	Capillary rise involves the drawing up of water, above the water table or above locally saturated zones, in continuous pores of the unsaturated zone until the suction gradient is balanced by the gravitational pull downward.	Capillary forces are included in the site-scale unsaturated zone flow model. These forces affect the distribution of water in the unsaturated zone through capillary effects on water flow, also known as capillary wicking. Parameters used for capillarity modeling are incorporated within the matrix properties and fracture properties. These parameters are used as direct input to the site-scale unsaturated zone flow model and are incorporated into the output flow fields used in the TSPA.

Table 6.2-8.FEPs Addressed in This Report (Continued)

FEP Number and FEP Name	FEP Description	Summary of Technical Basis and Approach for FEP Inclusion
2.2.07.04.0A Focusing of unsaturated flow (fingers, weeps)	Unsaturated flow can differentiate into zones of greater and lower saturation (fingers) that may persist as preferential flow paths. Heterogeneities in rock properties, including fractures and faults, may contribute to focusing. Focused flow may become locally saturated.	The unsaturated zone flow fields represent the redistribution of water flux at the upper boundary of the unsaturated zone flow model through unsaturated zone layers, with faults explicitly taken into account. The flux redistribution is based on tuff layer properties, including fracture–matrix interaction. Faults are included in the site-scale unsaturated zone flow model as discrete features; therefore, flow in faults is also included in the site-scale unsaturated zone flow model. Flow model results indicate that, as flow moves downward through the unsaturated zone, the flow tends to focus into fault zones.
2.2.07.07.0A Perched water develops	Zones of perched water may develop above the water table. If these zones occur above the repository, they may affect unsaturated zone flow between the surface and the waste packages. If they develop below the repository (e.g., at the base of the TSw unit), they may affect flow pathways and radionuclide transport between the waste packages and the saturated zone.	The seepage abstraction model contains a wide range of seepage possibilities, including flow focusing and variability. Therefore, the potential for effects of perched water above the repository are indirectly captured in the seepage abstraction model through cases with high percolation flux. However, above the repository, no perched water bodies were observed and are not included in the fields predicted by the site-scale unsaturated zone flow model. The effects of existing perched-water zones below the repository are included, as are potential changes in these perched-water zones caused by climate. The potential for this effect is captured in the output flow fields developed for use in TSPA.

Table 6.2-8. FEPs Addressed in This Report (Continued)

FEP Number and FEP Name	FEP Description	Summary of Technical Basis and Approach for FEP Inclusion
2.2.07.08.0A Fracture flow in the unsaturated zone	Fractures or other analogous channels may act as conduits for fluids to move into the subsurface to interact with the repository and as conduits for fluids to leave the vicinity of the repository and be conducted to the saturated zone. Water may flow through only a portion of the fracture network, including flow through a restricted portion of a given fracture plane.	The site-scale unsaturated zone flow model is based on the dual-permeability concept, with the fractures represented by a continuum. The fracture continuum represents the spatially averaged flow through discrete fractures. The fracture continuum interacts with the matrix continuum, which represents matrix blocks separated by fractures. Fracture continuum properties, including permeability, porosity, interface area per unit volume, van Genuchten parameters for the saturation-capillary pressure and relative permeability functions, and active fracture parameter, are developed for each unsaturated zone model layer and include effects of channeling in the unsaturated zone (FEP 2.2.07.04.0A). Permeabilities and other properties are further calibrated using inverse modeling based on measured air permeability, matrix saturation, and moisture potential. The fracture-continuum properties are used as inputs to the site-scale unsaturated zone flow model, and their effects are incorporated into the output flow fields developed for use in TSPA.
2.2.07.09.0A Matrix imbibition in the unsaturated zone	Water flowing in fractures or other channels in the unsaturated zone may be imbibed into the surrounding rock matrix. This may occur during steady flow, episodic flow, or into matrix pores that have been dried out during the thermal period.	Matrix imbibition is included in the process model for unsaturated zone flow at the site scale. Matrix imbibition refers to the movement of water into the matrix as a result of capillary forces. This process affects the distribution of flow between fractures and matrix in a dual-permeability flow model for fractured rock. The influence of matrix imbibition on episodic flow imbibition is captured in the site-scale unsaturated zone flow model through capillarity modeling, which uses matrix and fracture properties as model input. Therefore, the effect of imbibition is incorporated in the output flow fields used in the TSPA.
2.2.07.19.0A Lateral flow from Solitario Canyon Fault enters drifts	Water movement down Solitario Canyon Fault could enter waste emplacement drifts through lateral flow mechanisms in the TSw unit. This percolation pathway is more likely to transmit episodic transient flow to waste emplacement locations due to the major fault pathway through the overlying units.	The site-scale unsaturated zone flow model contains potential hydrogeologic connections between the Solitario Canyon Fault and the waste emplacement horizon. The potential connection is captured using a property set of the PTn unit with calibrated fracture–matrix properties that favor lateral flow. Therefore, flow from this fault to waste emplacement locations is addressed. This water may seep into waste emplacement drifts if the flux is sufficient to overcome the capillary barrier represented in the drift seepage model. The lateral flow effect is incorporated in the output flow fields used in the TSPA. Other aspects of flow include focusing in faults (FEP 2.2.07.04.0A) and locally saturated flow (perched water, FEP 2.2.07.07.0A).

Table 6.2-8. FEPs Addressed in This Report (Continued)

FEP Number and FEP Name	FEP Description	Summary of Technical Basis and Approach for FEP Inclusion
2.2.10.03.0B Natural geothermal effects on flow in the unsaturated zone	The existing geothermal gradient and spatial or temporal variability in that gradient may affect groundwater flow in the unsaturated zone.	Natural geothermal effects, observed as the natural temperature profile in the unsaturated zone, are included in the unsaturated zone model calibration. The temperature profile is primarily determined by the ground surface temperature, the water table temperature, water flux through the unsaturated zone, and the thermal conductivity from layer to layer. The influence of water flux on temperature is utilized to calibrate the probabilities for different surface water flux boundary conditions for the unsaturated zone flow model. The calibration is based on the GLUE methodology utilizing temperature observations and model predictions as well as chloride observations and model predictions. The probabilities for surface water flux are applied as flow weighting factors for unsaturated zone flow fields in TSPA, which are used for present-day, monsoon, and glacial-transition climates.
2.3.11.01.0A Precipitation	Precipitation is an important control on the amount of recharge. It transports solutes with it as it flows downward through the subsurface or escapes as runoff. Precipitation influences the agricultural practices of the receptor. The amount of precipitation depends on climate.	Precipitation affects the net infiltration. These effects are captured in the net infiltration map outputs used as inputs for the site-scale unsaturated zone flow model. Flow fields developed for use in TSPA using the site-scale unsaturated zone flow model include the effects of precipitation and changes of precipitation under future climate conditions and associated uncertainty through the water flux boundary condition used at the upper boundary of the unsaturated zone flow model.
2.3.11.02.0A Surface runoff and flooding	Surface runoff and evapotranspiration are components in the water balance, together with precipitation and infiltration. Surface runoff produces erosion and can feed washes, arroyos, and impoundments, where flooding may lead to increased recharge.	Evapotranspiration and surface runoff affect the net infiltration. These effects are captured in the net infiltration map outputs used as inputs for the site-scale unsaturated zone flow model. Flow fields developed for use in TSPA using the site-scale unsaturated zone flow model include the effects of precipitation and changes of precipitation under future climate conditions and associated uncertainty through the water flux boundary condition used at the upper boundary of the unsaturated zone flow model.
2.3.11.03.0A Infiltration and recharge	Infiltration into the subsurface provides a boundary condition for groundwater flow. The amount and location of the infiltration influences the hydraulic gradient and the height of the water table. Different sources of recharge water could change the composition of groundwater passing through the repository. Mixing of these waters with other groundwaters could result in precipitation, dissolution, and altered chemical gradients.	The hydrologic effects of infiltration and recharge are included in the infiltration model (see FEP 1.3.01.00.0A). The infiltration model includes the effects of seasonal and climate variations, climate change, surface-water runoff, and site topology, such as hill slopes and washes. The time dependence of infiltration results is linked to the timing of climate change (FEP 1.3.01.00.0A). This is incorporated into the TSPA through the unsaturated zone flow fields that use the infiltration model results as inputs as the water flux boundary condition used at the upper boundary of the unsaturated zone flow model.

Source: DTN: MO0706SPAFEPLA.001 [DIRS 181613].

6.3 TEMPERATURE CALIBRATION

The percolation and moisture distributions under present-day conditions are used as initial conditions for performing thermal-hydrological studies of the unsaturated zone system, as well as repository performance studies under thermal loading conditions. The ambient geothermal and moisture conditions serve as the initial and boundary conditions of a thermal model (Wu et al. 2006 [DIRS 180274]). This section describes a three-dimensional ambient geothermal submodel of the UZ model developed to evaluate steady-state, ambient thermal, and moisture conditions of the unsaturated zone system with different infiltration rates for use in various scale TH modeling studies. Subsequent temperature calibration then provides an independent examination of percolation fluxes simulated by the UZ flow model. As discussed in Section 6.3.4, percolation flux (or infiltration rate) is one of the factors that control thermal conditions. As discussed in Section 6.3.4, percolation flux (or infiltration rate) is one of the factors that control the ambient temperature distribution within the unsaturated zone (Bodvarsson et al. 2003 [DIRS 162477]). By matching borehole temperature measurements, the ambient TH model helps to constrain infiltration-rate ranges as well as fracture–matrix parameter values. Note that except for this section, the rest of the three-dimensional model development and calibration in this report deal with isothermal conditions. The three-dimensional calibrated isothermal unsaturated zone flow properties developed in Section 6.2 are used in the three-dimensional thermal model.

6.3.1 Three-Dimensional Thermal Model Grid

For thermal calibration as well as the gas flow calibration described in the next section, a three-dimensional grid (Figure 6.3-1), smaller than the TSPA-LA grid (Figure 6.1-1), is used (DTN: LB0303THERMESH.001 [DIRS 165168]). This grid is designed to reduce the computational burden needed in thermal modeling studies using a three-dimensional dual-permeability grid. The thermal model domain is selected to focus on geothermal conditions and thermal loading effects at and near the repository area. The model domain is considered to provide sufficient accuracy for such studies, because of the small thermal impact expected in the lateral directions from repository thermal loading.

This three-dimensional grid, featuring a smaller model domain than that of the UZ flow model (Figure 6.1-1), is referred to as the three-dimensional thermal model grid. As shown in the plan view of Figure 6.3-1, the thermal-model-grid domain covers approximately 20 km^2 of the area. Similar to the TSPA-LA grid of Figure 6.1-1, the thermal model grid (Figure 6.3-1) also uses a refined mesh in the vicinity of the repository and includes the locations of several boreholes used in temperature calibrations and analyses. In particular, the thermal model grid explicitly incorporates every repository drift by taking into account orientations, lengths, elevations, and spacings of the drifts. A grid spacing of 81 m is used in the direction perpendicular to drifts, such that each individual drift segment can be inserted into the three-dimensional thermal grid for thermal loading studies, such as in a previous report (BSC 2005 [DIRS 174101]; Wu et al. 2006 [DIRS 180274]). In the model, faults are also represented by vertical or inclined 30 m wide zones.

The thermal model grid of Figure 6.3-1 consists of 980 mesh columns of fracture and matrix continua, 86,440 gridblocks, and 340,202 connections in a dual-permeability grid. Vertically, the thermal grid has an average of 45 computational grid layers.

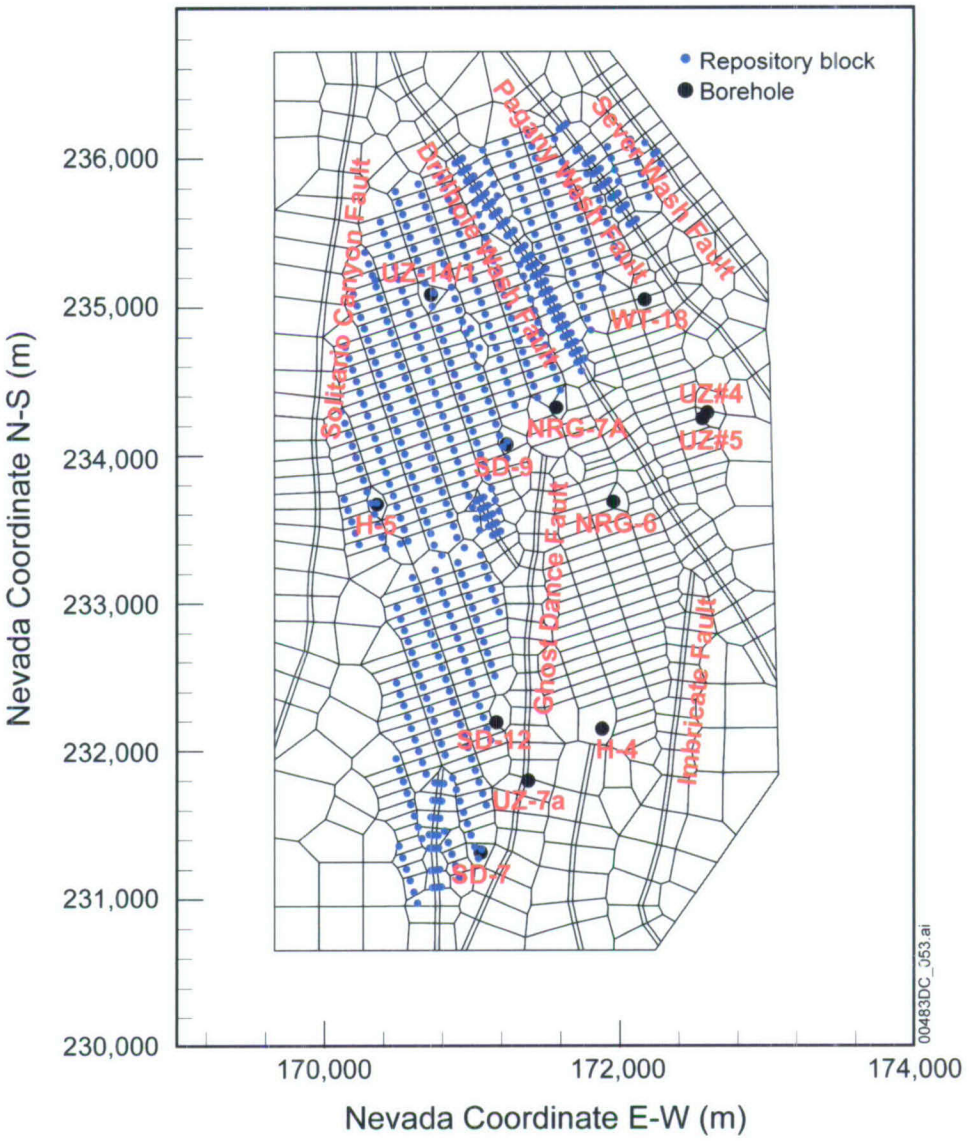

Source: DTN: LB0303THERMESH.001 [DIRS 165168]; Output DTN: LB0701UZMTHCAL.001.

Figure 6.3-1. Plan View of the Three-Dimensional Thermal Model Grid, Showing the Model Domain, Faults Incorporated, Several Borehole Locations, and TH Model Boundaries

6.3.2 Top Boundary Temperature

The input file for initial top boundary conditions is directly obtained from DTN: LB0303THERMSIM.001 [DIRS 165167]. To account for variations in atmospheric temperature with surface elevations in the mountain, measured mean surface temperatures and a linear equation that correlates surface temperature with elevation are used. The annual-average temperature was measured for near-surface sensors in boreholes NRG-6 and NRG-7a

(DTNs: GS031208312232.008 [DIRS 178750], GS951108312232.008 [DIRS 106756], and GS950208312232.003 [DIRS 105572]), with several years of continuous temperature monitoring data. The surface temperatures, T_s, at any elevation, Z, are then computed using the routine toptemp_v0.f V1.0 (LBNL 2000 [DIRS 147030]), and are treated as constants according to the following equation (Wu et al. 1999 [DIRS 117161], Equation 4):

$$T_s = T_{ref} - \lambda[Z - Z_{ref}] \quad \text{(Eq. 6.3-1)}$$

where T_{ref} is mean surface temperature at reference elevation Z_{ref} and λ is the dry adiabatic atmospheric lapse rate in °C/m. A lapse rate of is 0.01°C/m was adopted from Driscoll (1986 [DIRS 116801], p. 50). In this formulation, the surface reference temperature used is 18.23°C at an elevation of 1,231.0 m, averaged using measured data from borehole NRG-6. The averaged temperature measurement of NRG-7a at an elevation of 1,282.2 m is 17.78°C. The calculated mean lapse rate, based on these field measurements, is 0.009°C/m, which is consistent with the value presented by Driscoll (1986 [DIRS 116801], p. 50). Because the lapse rate estimated in this report is based on a limited number of borehole temperature data, Driscoll's value, that may be more reliable, is adopted for the calculations.

Uncertainty in the predicted temperatures is mainly a result of uncertainty in the bottom boundary conditions and the thermal conductivity. The standard deviation for temperature at the ground surface is small (approximately ± 0.1°C). The temperature measurements at about 20 m below the ground surface are stable over time. Using the top boundary conditions from previous calculations should be adequate for the current ambient thermal simulation.

6.3.3 Bottom Boundary Temperature

The bottom temperature boundary condition was first estimated using the software routine of get_temp_v0.f V1.0 (2000 [DIRS 147027]) at a flat surface of an elevation of 730 m. Because the water table is no longer flat with the current UZ and TH models, the actual estimates of the water table or bottom-model-boundary temperatures were interpolated between the values at 730 m elevation and the model surface boundary. Nonqualified measured temperature profiles (Sass et al. 1988 [DIRS 100644]; DTN: GS950408318523.001 [DIRS 107244]) are qualified in Appendix I and used to confirm water table boundary temperature contours in DTN: LB0303THERMSIM.001 [DIRS 165167]. The initially estimated water table temperatures show a good match to the measurements through comparison with the qualified temperature data in boreholes NRG-6, NRG-7a, SD-12 UZ#4, UZ#5, and UZ-7A (DTNs: GS950208312232.003 [DIRS 105572], GS031208312232.005 [DIRS 179284], GS031208312232.004 [DIRS 182187], GS031208312232.007 [DIRS 178751], GS031208312232.006 [DIRS 182186], and GS031208312232.003 [DIRS 171287]).

Uncertainty in temperatures for defining the bottom temperature boundary conditions is relatively small. This is because multiple-year temperature data set (qualified in Appendix I with Output DTN: LB0708WTTEMDAT) was used to derive the temperature distributions at the water table, model bottom temperature boundary. The long-term variation of the measured temperatures is minor, with standard deviation < 0.1°C in 32 out of the 34 boreholes. Somewhat larger deviation over certain measurement periods was found in a couple of boreholes, with borehole NRG-7a having a maximum deviation of 0.24°C/yr, and borehole NRG-6 of 0.58°C/yr

(Appendix I, Table I-1). In addition, the data set also provides comparable temperature values against the 6 qualified boreholes in the ambient thermal model. Specifically, their temperature differences obtained from borehole-location-wise proximity, are within 0.82°C, or less than 3.6% (Appendix I, Table I-3). Using the bottom temperature boundary conditions from these data is adequate for the current ambient thermal simulation.

6.3.4 Calibration of Ambient Temperatures

The temperature profiles or geothermal gradients in the unsaturated zone system are controlled by several factors, such as formation thermal conductivity and net infiltration rates, in addition to the regional weather condition or surface temperatures. Measured thermal conductivities are relatively accurate for the different geological units at the site. Because of the fewer uncertainties involved in measured thermal conductivities related to simulated heat flow, temperature calibration may be conducted using either ambient infiltration, or model boundary temperatures, or both (Wu et al. 2006 [DIRS 180274]).

In this report, four ambient net infiltration rates for the present-day climate of 10th, 30th, 50th, and 90th percentile infiltration maps are used. The mean infiltration rates within the grid domain (Figure 6.3-1) are 2.88, 7.79, 11.65, and 27.42 mm/yr, respectively, for the four infiltration maps (output DTN: LB0701UZMTHCAL.001), which are averaged over a smaller model domain than the UZ flow model domain (Figure 6.1-1), resulting in a smaller mean infiltration value.

The ambient temperature condition was calibrated using the three-dimensional thermal model grid of Figure 6.3-1 (DTN: LB0303THERMESH.001 [DIRS 165168]), a dual-permeability mesh. The simulations were performed using TOUGH2 V1.6 (LBNL 2003 [DIRS 161491]) with the EOS3 module. In addition to the prescribed temperature conditions on top and bottom boundaries, the infiltration was described using one of the four infiltration scenarios for present-day climate of 10th, 30th, 50th, and 90th percentile infiltration maps. The model incorporated the parameter set of Tables B-1, B-2, B-3, and B-4 (Output DTNs: LB07043DCRXPRP.001, LB0701UZMTHCAL.001), and the thermal properties (DTN: LB0210THRMLPRP.001 [DIRS 160799]). Incorporated thermal properties include effects of lithophysal cavities for TSw layers tsw33 and tsw 35. Simulations were run to steady state for comparison with measured borehole temperatures, because as shown below, the unsaturated zone is in thermal equilibrium with the present-day climatic conditions.

To evaluate the present conditions with respect to longer-term temporal variability in climate, first consider that the last significant change in climate occurred about 10,000 years ago. The 10th-percentile case from the infiltration model for present-day climate has an average flux rate of about 3 mm/yr over the UZ flow model domain. An average effective thermal diffusivity of about 4×10^{-7} m^2/s for the unsaturated zone at Yucca Mountain can be computed from the data given by Bodvarsson et al. (2003 [DIRS 162477], Table 2 and Equation 8b). For an average water content of the rock of about 0.15, this gives an advective distance of a thermal front of about 200 m and a diffusive distance of about 500 m over 10,000 years (based on the diffusion front length scale that is the square root of twice the diffusivity times the time). Furthermore, lateral thermal diffusion between flowing fractures separated by distances less than 100 m would require less than 500 years to approach thermal equilibrium. Therefore, the unsaturated zone is in steady-state thermal equilibrium with present-day climate conditions. This conclusion is not

substantially altered by uncertainty in thermal conductivity, which has a small uncertainty range. Flux rates may be lower, but thermal diffusion results in substantial penetration of the thermal front, a distance of about 500 m, over 10,000 years.

Table 6.3-1 lists the boreholes with qualified temperature measurements and the corresponding column element names used in the three-dimensional calibration of model ambient temperature. Note that in both the three-dimensional thermal model grid and the TSPA-LA grid, each element name is 8 characters long, consisting of numbers, alphabetic characters, or symbols. The last three characters of 8-character names stand for the vertical column, which are determined uniquely for each vertical grid column. As shown in Table 6.3-1, boreholes UZ#4 and UZ#5 are so close to each other that they fall into the same grid column. Therefore, only UZ#5 is used for calibrations (i.e., using temperature data from 5 of 6 boreholes). During calibration, the corresponding simulated temperature profiles for the boreholes were extracted from the TOUGH2 output and then plotted against the measurements of temperatures along each borehole.

Table 6.3-1. Temperature Boreholes and Corresponding Element Columns of the Thermal Model Grid

Borehole	Element Column
NRG-6	h39
NRG-7A	h40
SD-12	h44
UZ#5	h45
UZ-7a	h74
UZ#4	h45

Source: DTN: LB0303THERMESH.001 [DIRS 165168].

Figures 6.3-2 to 6.3-6 show the final calibrated results with the four infiltration maps and measured temperature profile in the five temperature boreholes, respectively. The figures show that the model produces best match between measured and simulated temperatures by using the 10th percentile infiltration map. Average residual temperature for each borehole are listed in Table 6.3-2. The statistic results show that 4 out of 5 boreholes are best fitted with the 10th percentile present-day scenario, with the remaining borehole best fitted with the 50th percentile scenario. Near the ground surface in five of the boreholes, observed temperatures show significant seasonal variations. However, these seasonal changes in surface temperature have little impact on steady-state heat flow or temperature profiles in the deeper (more than 20 m) unsaturated zone. The model results show that infiltration rates applied to the model top boundary control the temperature distributions inside the model domain and can therefore be used to constrain the likely range of infiltration, as discussed in Section 6.8.

Figure 6.3-7 shows the contour plot of temperature distributions at the water table or the model bottom boundary derived from field measurement data (Sass et al. 1988 [DIRS 100644]). Figure 6.3-7 indicates that the average temperature at the water table ranges from 27°C to 33°C, and lower temperatures are located in the north of the model domain, where water table elevations and percolation fluxes are higher. For the top model boundary, the estimated temperature distributions are shown in Figure 6.3-8. Results from the calibrated ambient thermal

model (i.e., calibrated ambient temperature distribution) can be used to specify initial conditions for other mountain-scale TH simulations.

Wu et al. (1999 [DIRS 117161], Figure 12) identified that data sources were from 25 boreholes documented mainly in the report (Sass et al. (1988 [DIRS 100644]) and observed that, in general, the measured data matched reasonably with early three-dimensional model results (Bodvarsson et al. 1997 [DIRS 100103]; Ahlers et al. 1995 [DIRS 101180]). The majority of the early temperature data in *Temperature, Thermal Conductivity, and Heat Flow Near Yucca Mountain, Nevada: Some Tectonic and Hydrologic Implications* (Sass et al. 1988 [DIRS 100644]) are currently not qualified. In this report, six qualified data sets of temperature distributions along boreholes are shown to be consistent with the water table distribution developed from the more extensive data set, demonstrating the consistency of water temperature distribution with unsaturated processes. The same extensive data set is also the basis for saturated zone interpretation of Fridrich et al. (1994 [DIRS 100575], pp. 133 to 168). Fridrich et al. (1994 [DIRS 100575], p. 157) discussed the heat flow anomalies, upward and downward flows, and the uncertainty of ignoring unsaturated zone processes. Constantz et al. (2003 [DIRS 177344], pp. 20 to 22) used temperature profiles to estimate percolation rates for two boreholes (WT-2 and H-3) at the Yucca Mountain site through one-dimensional numerical models. They provided a detailed discussion on the relation between temperature gradient and fluid and heat flow processes at the site. They also investigated the effects of uncertainties in ground-surface temperatures and thermal conductivity on estimates of percolation rate. The infiltration rates for the location of boreholes WT-24 and H-3 of the 10th percentile present-day infiltration map are 2.36 and 6.25 mm/yr, respectively. The case 3 of Constantz et al. (2003 [DIRS 177344], p. 22), which determined parameters jointly at both boreholes and are closest to the three-dimensional model representation, estimated the range of percolation flux from −3.4 to 7.3 mm/yr for WT-24 and 5.5 to 13.3 mm/yr for H-3. The estimates in the current ambient thermal model are in the ranges computed by their approach. The uncertainties from temperature measurement are relatively less impact on the modeling results. The surface measurements are difficult to assess because of the variation in surface temperatures with time. However, temperatures become stable over time about 20-m below the surface, which constrains the surface temperatures. Based on the near-surface temperatures, the standard deviation in surface temperature is estimated to be about 0.1°C. Water table temperatures are not as well constrained by the temperature data used for calibration of surface water flux because temperature measurements were not recorded near the water table in these boreholes. Based on other borehole temperature measurements in the region, the standard deviation in water temperature is estimated to be about 1°C. Borehole temperature measurements are uncertain by as much as 0.5°C (Sass et al. 1988, p. 85 and Figure 2-15), although the data suggest that such large uncertainties did not occur for the boreholes used for calibration. Temperature measurements at different times found variations less than 0.1°C at depths below 20 m. The uncertainty in thermal conductivity is generally less than 15% (BSC 2004 [DIRS 169854], Table 6-7; BSC 2004 [DIRS 170033], Table 6-13).

The effects of thermal conductivity may be estimated from the analytical solution using a homogeneous thermal diffusivity of 4×10^{-7} m^2/s and considering 15% variations. This calculation uses a depth of 600 m and percolation flux rates of 10 mm/yr and 30 mm/yr. The temperature sensitivity is greatest at 300 m because of the fixed boundary temperatures at the surface and the water table. Using a water table temperature of 31°C and a surface temperature of 17°C, the temperature variations at 300 m depth caused by 15% variations in thermal diffusivity

are less than 1% for 10 mm/yr flux and less than 2% for 30 mm/yr flux. Therefore, the uncertainty in water table temperatures is the largest uncertainty for temperature modeling. Because the temperature at any depth is a linear function of the water table temperature, the computed mean value case is essentially the same as the probabilistic mean case. Uncertainty results in a range of the predicted measurements. While it is generally possible to change the boundary conditions and/or thermal diffusivity to achieve a better fit to the data than given by the mean case prediction, it is also necessary to recognize that this is just one case in a continuum of probabilistic results. For example, if the 10% + sigma case gives a better fit to the data than the mean case, then it is generally true that the 10% − sigma is then a poorer fit, and this case is just as likely as the 10% + sigma case. Any given probabilistic case that provides a better fit to the data than the mean case is always balanced by a case of equal probability that gives a poorer fit. Therefore, the average residual between the prediction and the measurement is not substantially affected by this uncertainty.

Uncertainty in unsaturated zone rock properties/data may also cause variation in predicted temperature. However, the influence may be limited compared to variations in infiltration rates. In this section, only the most significant parameter, the infiltration rate, is examined.

Table 6.3-2. Average Residual Temperature in Selected Boreholes

Boreholes	Number of Samples	10th Percentile[a]	30th Percentile	50th Percentile	90th Percentile
UZ-7a	11	−1.7[b]	−2.9	-3.8	−6.5
NRG-6	9	1.4	0.9	0.5[b]	−1.0
NRG-7a	5	−0.2[b]	−1.0	−1.7	−4.1
SD-12	17	−2.1[b]	−4.1	−5.5	−10.8
UZ-5	9	−1.6[b]	−2.3	−2.9	−4.7

[a]Percentile infiltration map of present-day climate.
[b]Scenario with the least residual.

Source: Statistics compiled from Output DTN: LB0701PAWFINFM.001.

NOTE: Residual temperature takes average of percentage of difference between calculated and measured temperature relative to the calculated value (°C).

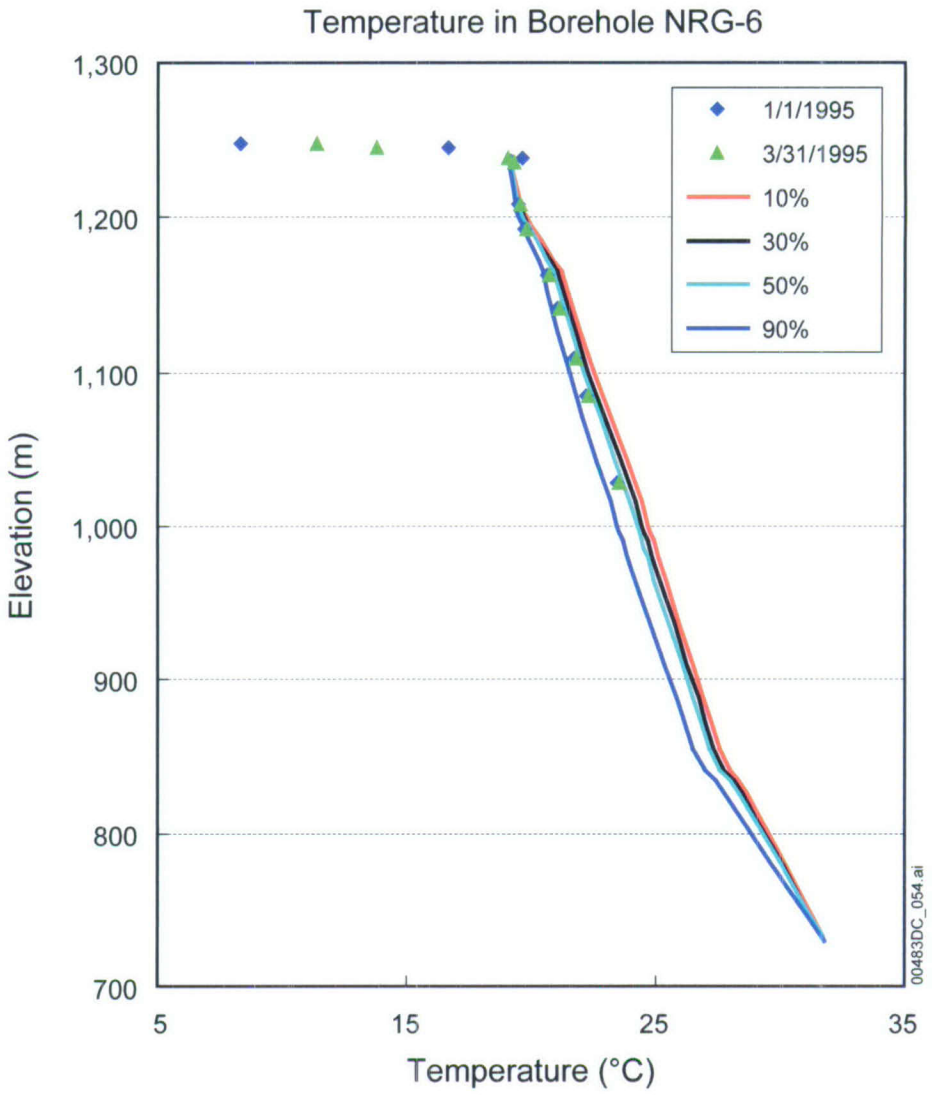

Sources: DTNs: GS031208312232.005 [DIRS 179284]; GS031208312232.004 [DIRS 182187]; GS031208312232.007 [DIRS 178751]; GS031208312232.006 [DIRS 182186]; GS031208312232.003 [DIRS 171287].

Output DTN: LB0701UZMTHCAL.001.

Figure 6.3-2. Comparisons between Measured and Modeled Ambient Temperature Profiles in Borehole NRG-6 for the Four Infiltration Maps of 10th, 30th, 50th and 90th Percentile Present-Day Infiltration Rate

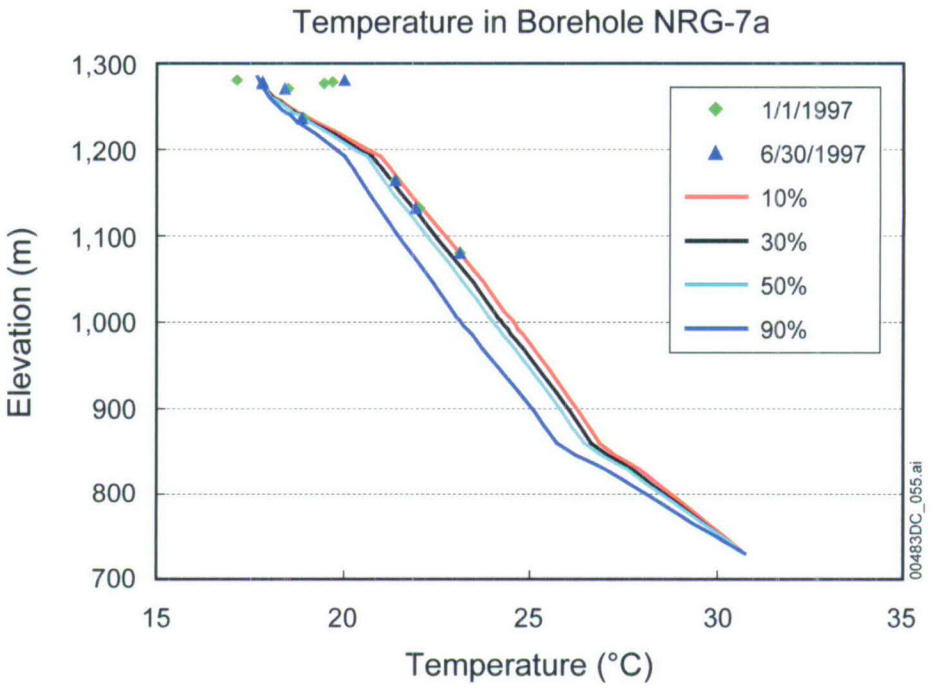

Sources: DTNs: GS031208312232.005 [DIRS 179284]; GS031208312232.004 [DIRS 182187]; GS031208312232.007 [DIRS 178751]; GS031208312232.006 [DIRS 182186]; GS031208312232.003 [DIRS 171287].

Output DTN: LB0701UZMTHCAL.001.

Figure 6.3-3. Comparisons between Measured and Modeled Ambient Temperature Profiles in Borehole NRG-7A for the Four Infiltration Maps of 10th, 30th, 50th and 90th Percentile Present-Day Infiltration Rate

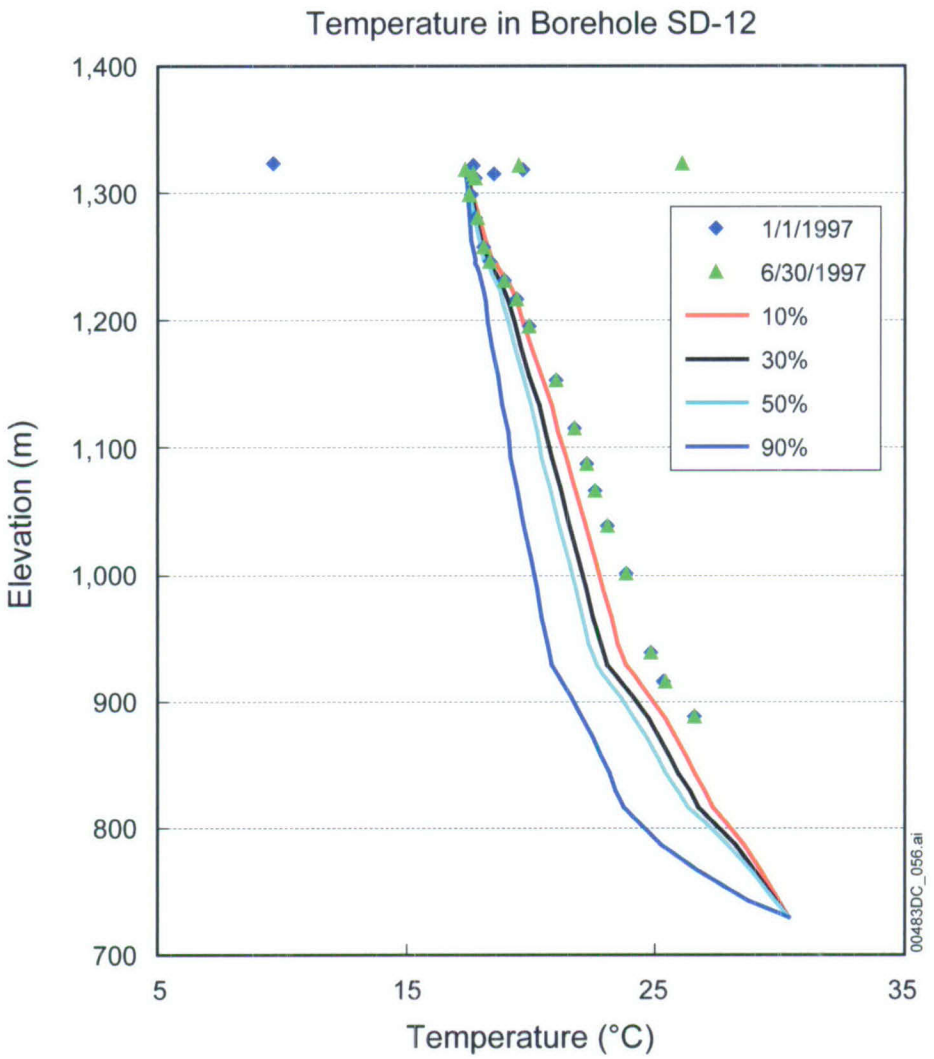

Sources: DTNs: GS031208312232.005 [DIRS 179284]; GS031208312232.004 [DIRS 182187]; GS031208312232.007 [DIRS 178751]; GS031208312232.006 [DIRS 182186]; GS031208312232.003 [DIRS 171287].

Output DTN: LB0701UZMTHCAL.001.

Figure 6.3-4. Comparisons between Measured and Modeled Ambient Temperature Profiles in Borehole SD-12 for the Four Infiltration Maps of 10th, 30th, 50th and 90th Percentile Present-Day Infiltration Rate

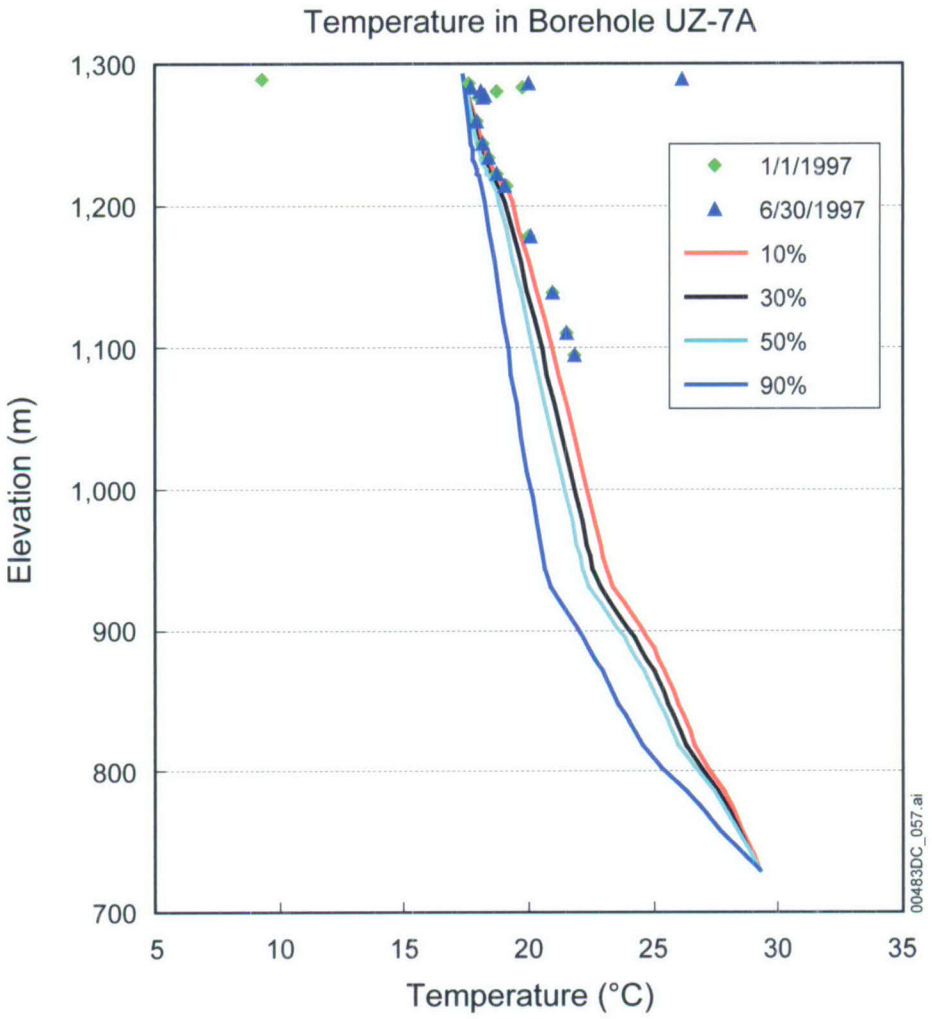

Sources: DTNs: GS031208312232.005 [DIRS 179284]; GS031208312232.004 [DIRS 182187]; GS031208312232.007 [DIRS 178751]; GS031208312232.006 [DIRS 182186]; GS031208312232.003 [DIRS 171287].

Output DTN: LB0701UZMTHCAL.001.

Figure 6.3-5. Comparisons between Measured and Modeled Ambient Temperature Profiles in Borehole UZ-7A for the Four Infiltration Maps of 10th, 30th, 50th and 90th Percentile Present-Day Infiltration Rate

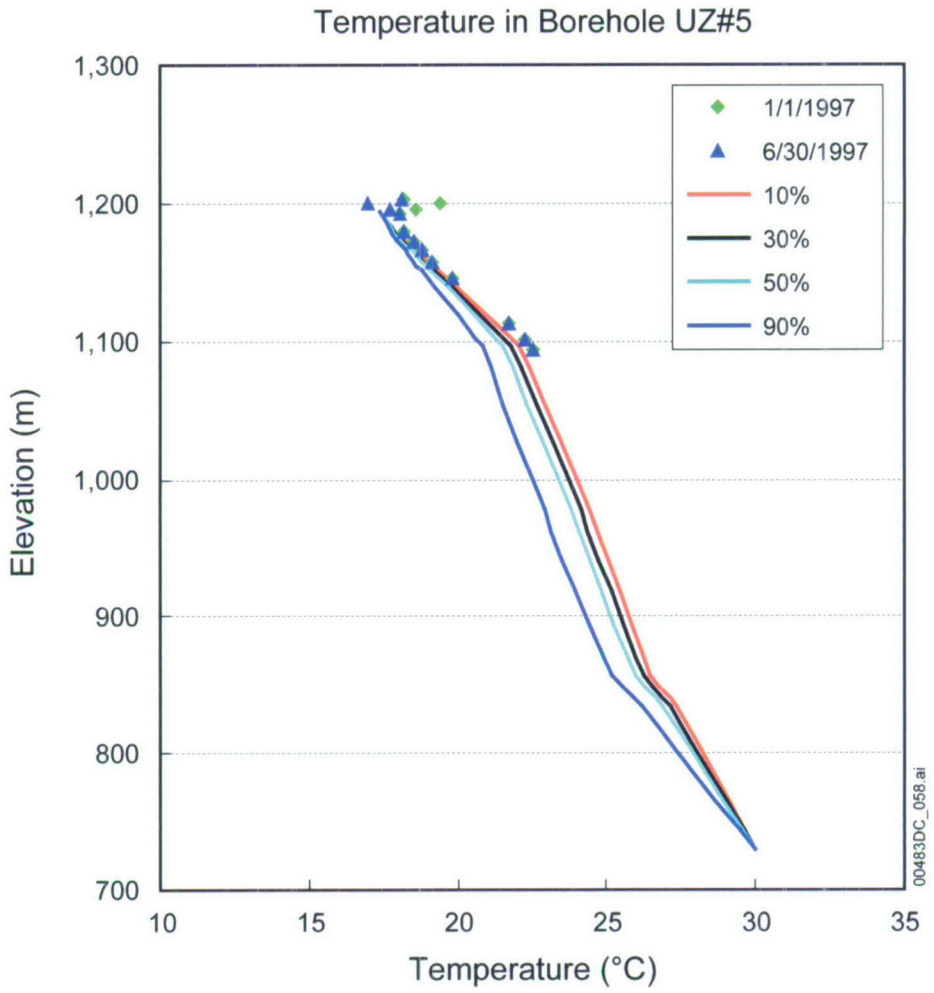

Sources: DTNs: GS031208312232.005 [DIRS 179284]; GS031208312232.004 [DIRS 182187]; GS031208312232.007 [DIRS 178751]; GS031208312232.006 [DIRS 182186]; GS031208312232.003 [DIRS 171287].

Output DTN: LB0701UZMTHCAL.001.

Figure 6.3-6. Comparisons between Measured and Modeled Ambient Temperature Profiles in Borehole UZ#5 for the Four Infiltration Maps of 10th, 30th, 50th and 90th Percentile Present-Day Mean Infiltration Rate

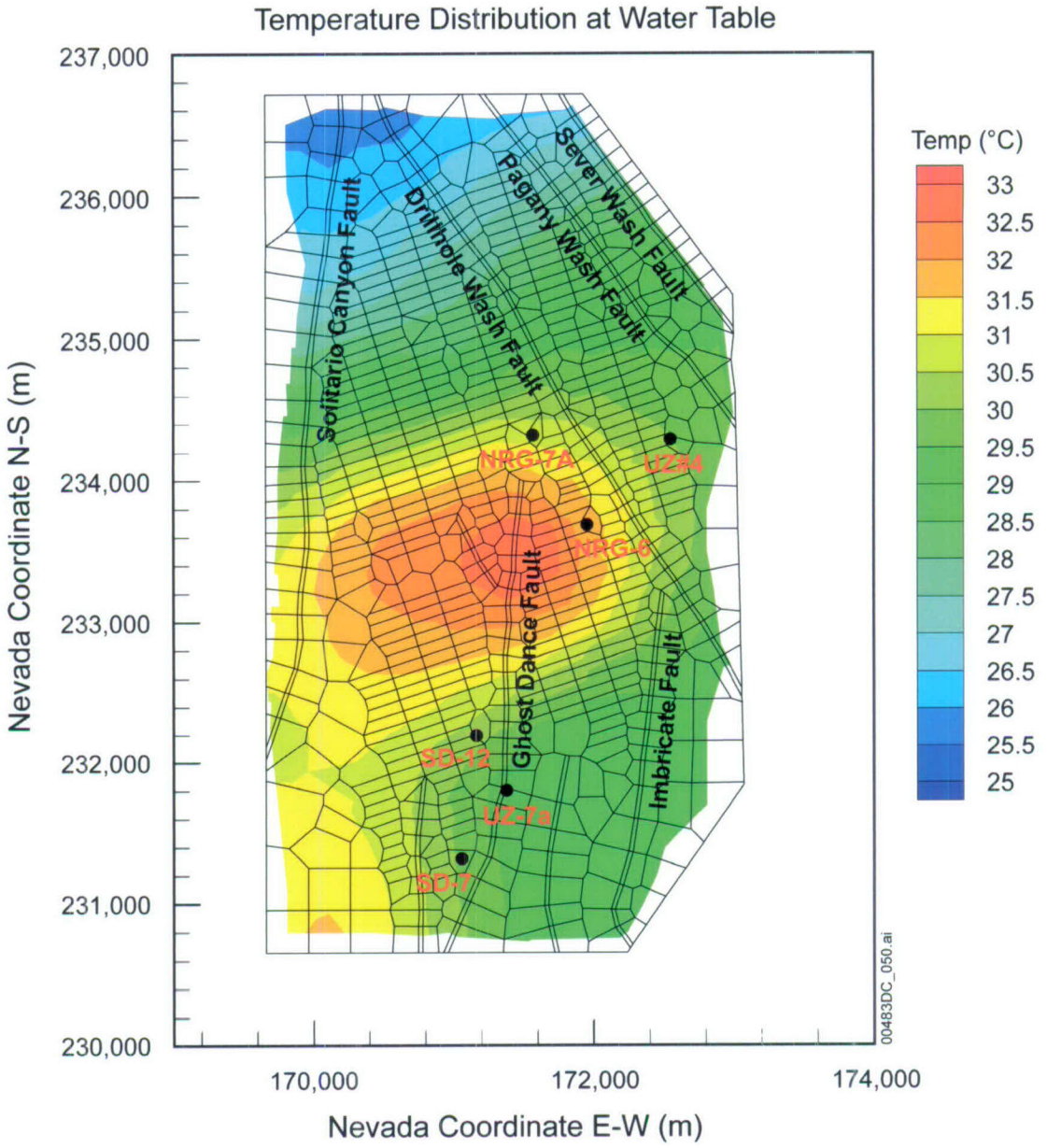

DTN: LB0303THERMSIM.001 [DIRS 165167].

Figure 6.3-7. Ambient Temperature Distributions at the Water Table for the Bottom Boundary Condition Used in the Ambient Thermal Model Simulations

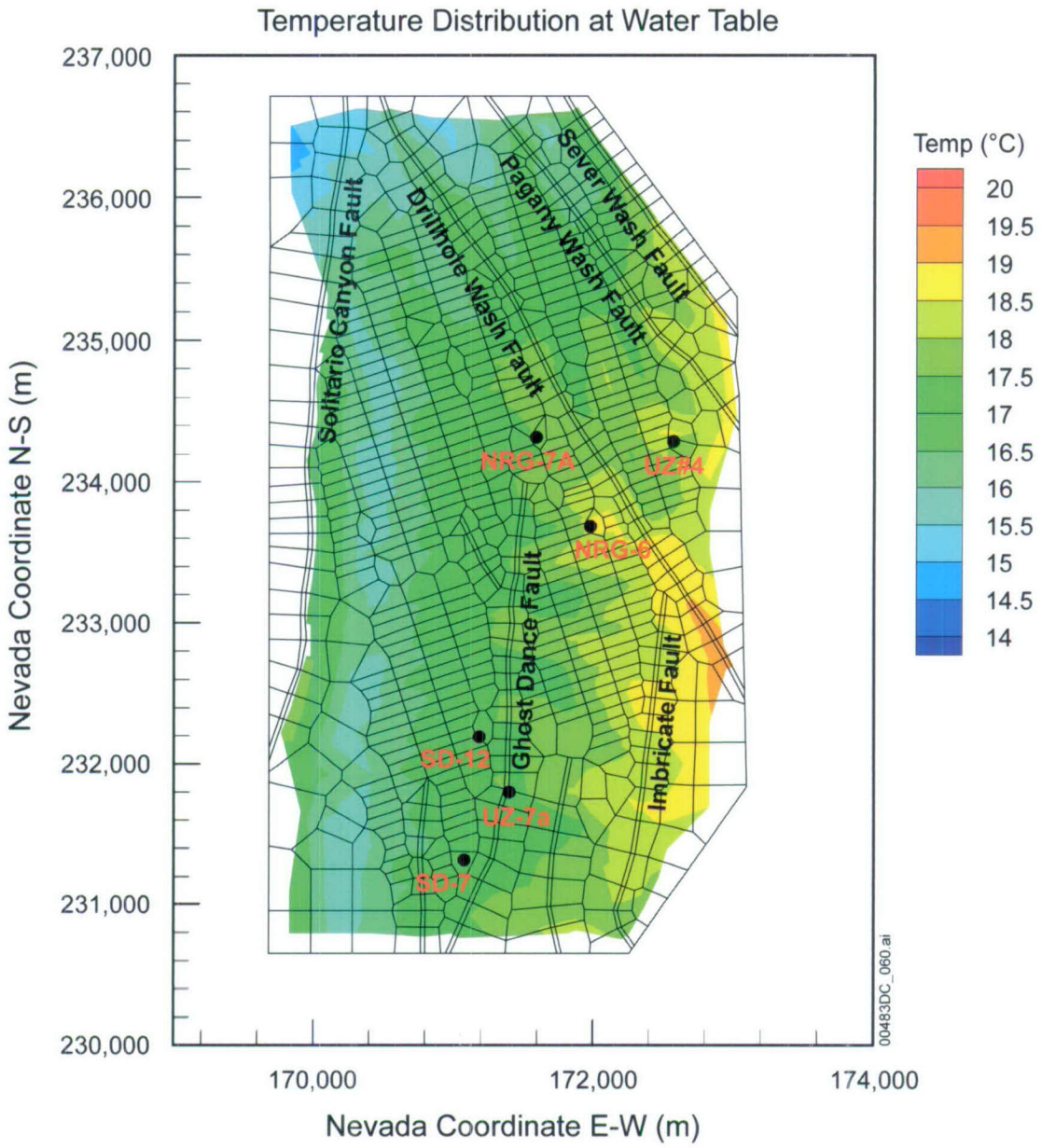

DTN: LB0303THERMSIM.001 [DIRS 165167].

Figure 6.3-8. Temperature Distributions at the Mountain Surface, the Top Model Boundary for the Present-Day Mean Infiltration Scenario

6.4 THREE-DIMENSIONAL PNEUMATIC CALIBRATION

Subsurface pneumatic responses to surface barometric pressure fluctuations at Yucca Mountain are controlled by gas flow through a complex network of fractures, pore spaces, faults, and stratigraphic structures. However, this response is dominated by the permeability of large pore spaces and fractures, which are predominantly dry under the ambient conditions associated with low infiltration and arid climates found at Yucca Mountain. A three-dimensional calibration of the UZ model to the pneumatic measurements at different locations and depths is necessary and provides more realistic estimations of large-scale fracture permeability for the unsaturated zone

system than one-dimensional or two-dimensional calibrations. This information is particularly useful for modeling studies of thermal loading, gas flow and transport of gaseous phase radionuclides for the site (Ahlers et al. 1999 [DIRS 109715]; Wu et al. 2006 [DIRS 180289]). The current model only investigates the 10% and 30% infiltration scenarios. The 50% and 90% infiltration scenarios are considered to be less realistic present-day infiltration maps than the 10% and 30%, based on geochemical and other evidences found at Yucca Mountain. Therefore, the parameters obtained from the calibration based on those 50% and 90% infiltration data would be of little significance in terms of reflecting the real parameters of the rocks at the site.

6.4.1 Calibration Approaches

The three-dimensional UZ models were manually calibrated against pneumatic pressure measurements at two representative boreholes, UZ-7a and SD-12. Among them, UZ-7a represents the boreholes located within major fault zones, whereas SD-12 represents the boreholes that are significantly distant from any major faults. Table 6.4-1 lists the sensors and their associated information of both boreholes.

Table 6.4-1. Observation Sensors and Associated Information of Boreholes UZ-7a and SD-12, used in the Pneumatic Calibration

Sensor Elevation (m)	Hosting Rock	File for Observation data	Date Range	Corresponding Observation Grid Cells
Borehole UZ-7a[1]				
1243.0	tcw12	Uz7a1343.prn	12/1/95 to 1/29/96	ANd70
1232.3	tcw13	Uz7a1337.prn	12/1/95 to 1/29/96	ANd76
1221.6	ptn24	Uz7a1331.prn	12/1/95 to 1/29/96	ANd84
1213.4	ptn26	Uz7a1325.prn	12/1/95 to 1/29/96	ANd86
1177.8	tsw32	Uz7a1319.prn	12/1/95 to 1/29/96	ANd92
Borehole USW SD-12[2]				
1258.5	tcw12	Sd12_214_PT1679.txt	12/1/95 to 1/29/96	ANA18
1232.0	ptn26	Sd12_301_PT1667.txt	12/1/95 to 1/29/96	ANA28
1217.1	tsw32	Sd12_350_PT1661.txt	12/1/95 to 1/29/96	ANA32
1001.3	tsw35	Sd12_1058_PT1619.txt	12/1/95 to 1/29/96	ANA50

Sources: DTNs: [1]LB0612MTSCHPFT.001 [DIRS 180296], [2]LB0612MTSCHP50.001 [DIRS 180294].

NOTE: The first 30-day data were used for calibration, whereas the second 30-day data were used for validation (see Section 7.4).

The parameter sets obtained from the one-dimensional/two-dimensional calibration (DTN: LB0612MTSCHPFT.001 [DIRS 180296]) were the basis (or starting point) of the three-dimensional calibration, which takes the following steps:

1. Calculate the three-dimensional steady state flow field of the UZ for given infiltration scenario using EOS3 module of TOUGH2 V1.6 (2003 [DIRS 161491]).

2. Create the time-dependent gas-pressure boundary conditions at every top boundary cells (land surface cells) by scaling, using the routine TBgas3D V2.0 (2002 [DIRS 160107]), the observed atmospheric barometric pressure data (DTN: LB0302AMRU0035.001 [DIRS 162378]) with the steady-state gas pressures obtained in Step 1.

3. Simulate one-year, three-dimensional gas flow of the unsaturated zone (ignoring liquid flow) with response to the boundary conditions created in Step 2 and save the simulated pneumatic responses in the observation grid cells;

4. Visually compare the simulated pneumatic pressures with the observed data of the first 30 days (12/01/1996 to 12/30/1996) and determine if an acceptable match between the simulated and the observed data has been obtained;

5. If an acceptable match has not been obtained, modify the fracture permeability of the responsible layers and go to Step 1 to start another iteration of calibration. Otherwise, finish the calibration.

In addition, the numerical mesh and other conditions used in the three-dimensional modeling are described below:

The three-dimensional mesh used in this gas flow simulation is the same three-dimensional thermal grid mesh (Figure 6.3-1) used for the thermal simulation. (The mesh is described in Section 6.3 above). The grid domain covers approximately 20 km^2 of the area, which is smaller than the TSPA-LA grid (Figure 6.1-1). Similar to the TSPA-LA grid, this grid also uses a finer mesh in the vicinity of the repository area.

The bottom water table boundary is treated as a Dirichlet-type boundary. The gas pressure conditions at the bottom boundary are determined based on measured pressures for boreholes USW SD-7 and SD-12 (DTNs: LB991091233129.001 [DIRS 125868]; LB0303GASFLW3D.001 [DIRS 180351]). All lateral boundaries are treated as no-flow boundaries.

In the time-dependent gas-flow simulation (Step 3), the liquid phase flow was neglected to save simulation time without losing much gas-flow accuracy. The impact of liquid-phase flow to the gas flow system is small for gas-flow simulation results, mainly because of the very dry conditions found in the unsaturated zone. It was found that the single-phase (gas) and two-phase (water and gas) flow simulations produce almost identical results in calculated gas pressures. The gas-flow-only condition in the simulation is realized by forcing the relative-permeability of liquid phase to equal 0 (using the linear relative permeability function and choosing appropriate parameters).

6.4.2 Calibration of the UZ Model for the Scenario of the 10-Percentile Infiltration Map

This calibration starts with the one-dimensional/two-dimensional (fault zone) calibrated mountain-scale fracture permeability set, the matrix permeability, matrix van Genuchten alpha, fracture van Genuchten alpha, and active fracture model gamma (DTN: LB0612MTSCHPFT.001 [DIRS 180296]) corresponding to the 10-percentile infiltration map (DTN: SN0609T0502206.028 [DIRS 178753]). Following the steps described in Section 6.4.1, the fracture permeability of some geological layers needs to be adjusted (Table 6.4-2) to match the observed pneumatic data in borehole SD-12. The smaller fracture permeability in TSw units obtained in the three-dimensional calibration, compared with the one-dimensional/two-dimensional (fault zone) calibration results, reflects the significant lateral gas flow through the intensively fractured tsw units from the nearby major faults to the

observation sensors in borehole SD-12. Such three-dimensional gas flow features cannot be captured by any one-dimensional model. As a result, the one-dimensional calibration has to raise the fracture permeability in the TSw unit artificially to compensate for the effects of missing the lateral gas flow in the model. On the other hand, the pneumatic responses to the surface-barometer pressure fluctuations in the fault zone are mainly (if not solely) controlled by the fast vertical gas flow within the zone, and the fracture permeability of normal rocks (outside of fault zones) has little effect on them. These features have already been captured by the parameters obtained from the two-dimensional (fault zone) calibration. Therefore, the match for borehole UZ-7a, which is located within the fault zone, is always good, as expected. Figures 6.4-1 and 6.4-2 show the calibrated model responses against the observed pneumatic pressure responses at several depths in boreholes UZ-7a and SD-12, respectively. Overall, the calibrated model reproduced the pattern variations observed in the pneumatic responses very well.

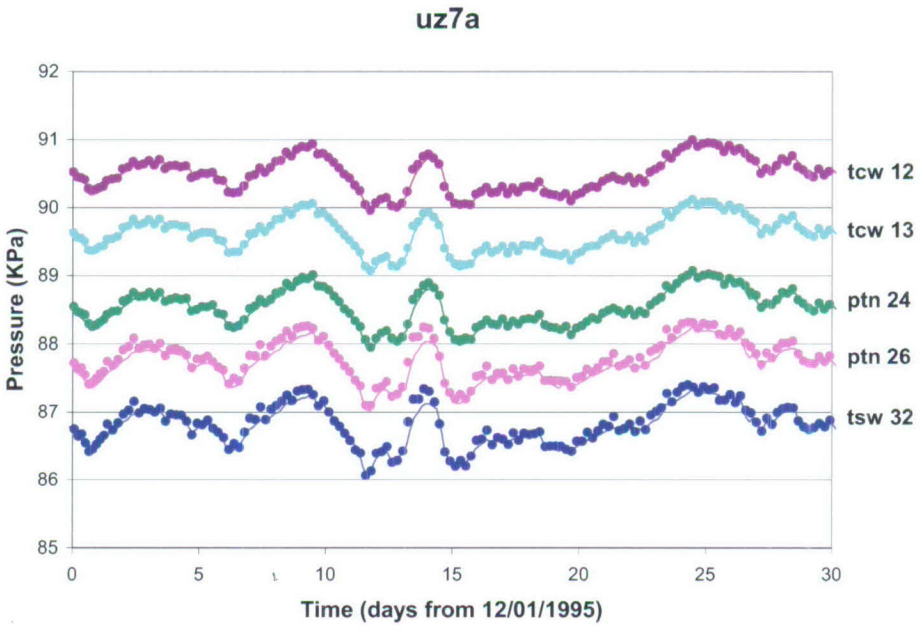

Output DTN: LB07043DGASCAL.001.

NOTE: Both observations and simulations have been vertically offset for clear display. Note the observed data from DTN: LB0612MTSCHPFT.001 [DIRS 180296].

Figure 6.4-1. Comparison of Simulated (solid line) and Observed (solid dots) Gas Pressures at Borehole UZ-7a during the First 30-Day Period

Table 6.4-2. Changes In Fracture Permeability Because of Three-dimensional Calibration (10% Scenario)

Rock	One-dimensional Calibrated Fracture Permeability (m^2)	Three-dimensional Calibrated Fracture Permeability (m^2)
tcw11	1.0000×10^{-12}	2.0000×10^{-12}
tsw31	8.1280×10^{-11}	4.0640×10^{-12}
tsw32	7.0790×10^{-11}	3.5395×10^{-12}
tsw33	7.7620×10^{-11}	3.8810×10^{-12}
tsw34	3.3100×10^{-11}	3.3110×10^{-12}
tsw35	9.1200×10^{-11}	9.1200×10^{-12}
tsw36	1.3490×10^{-10}	1.3490×10^{-11}
tsw37	1.3490×10^{-10}	1.3490×10^{-11}

Output DTN: LB07043DGASCAL.001.

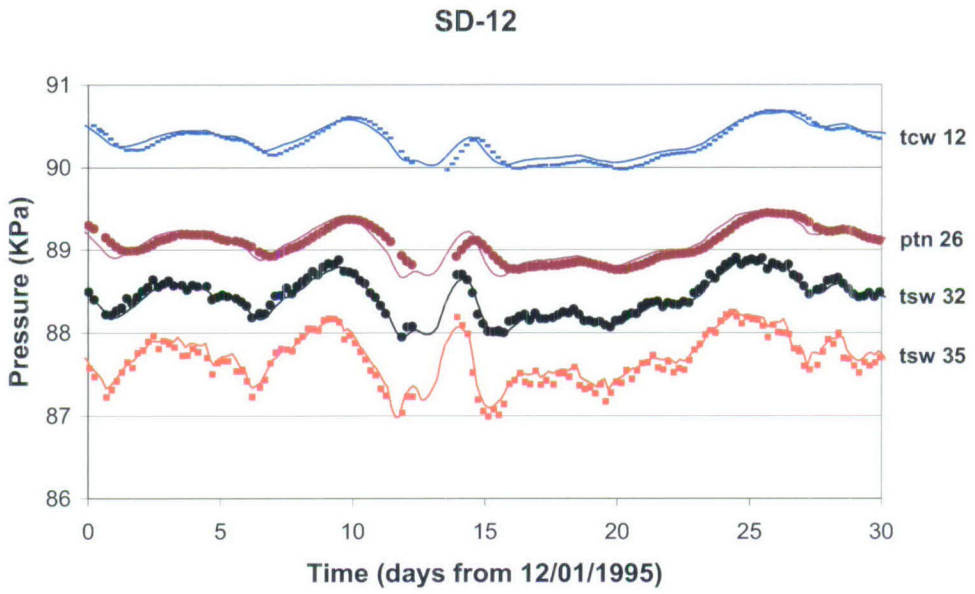

Output DTN: LB07043DGASCAL.001.

NOTE: Both observations and simulations have been vertically offset for clear display. Note the observed data from DTN: LB0612MTSCHPFT.001 [DIRS 180296].

Figure 6.4-2. Comparison of Simulated (solid line) and Observed (solid dots) Gas Pressures at Borehole SD-12 during the First 30-Day Period

6.4.3 Calibration of the UZ Model for 30-Percentile Infiltration Map

This calibration follows the same steps as used for the 10th-percentile case. The initial guess of the fracture permeability and other rock properties come from the one-dimensional/ two-dimensional (fault zone) calibrated mountain-scale fracture permeability set and the matrix permeability, matrix van Genuchten alpha, fracture van Genuchten alpha, and active fracture model gamma (DTN: LB0612MTSCHPFT.001 [DIRS 180296]) corresponding to the 30-percentile infiltration map (DTN: SN0609T0502206.028 [DIRS 178753]). Similar to the 10-percentile case, the match for borehole UZ-7a is always good, but the fracture permeability of some geological layers needs to be adjusted (Table 6.4-3) to match the observed pneumatic data in borehole SD-12. Similarly to the situation of the 10th-percentile infiltration case, the smaller fracture permeability in TSw units obtained in the three-dimensional calibration, compared with the one-dimensional / two-dimensional (fault zone) calibration results, reflects the significant lateral gas flow through the intensively fractured TSw units from the nearby major faults to the observation sensors in borehole SD-12. Such three-dimensional gas flow features cannot be captured by any one-dimensional model. As a result, the one-dimensional calibration has to raise the fracture permeability in the TSw unit artificially to compensate the effects of missing the lateral gas-flow in the model. On the other hand, the pneumatic responses to the surface-barometer-pressure fluctuations in the fault zone are mainly (if not solely) controlled by the fast vertical gas flow within the zone and are virtually unaffected by the fracture permeability of normal rock (outside fault zones). These features have already been captured by the parameters obtained from the two-dimensional (fault zone) calibration. Therefore, the match for borehole UZ-7a, located within the fault zone, is always good, as expected. Figures 6.4-3 and 6.4-4 show the calibrated model responses against the observed pneumatic pressure responses at several depths in boreholes UZ-7a and SD-12, respectively. Note that the tcw11 is no longer in the change list for this 30th-percentile case. Overall, the calibrated model reproduced the pattern variations observed in the pneumatic responses very well (Figure 6.4-3 and Figure 6.4-4).

Table 6.4-3. The Changed Fracture Permeability Because of Three-dimensional Calibration (30% scenario)

Rock	One-dimensional Calibrated Fracture Permeability (m^2)	Three-dimensional Calibrated Fracture Permeability (m^2)
tsw31	8.1280×10^{-11}	1.6256×10^{-12}
tsw32	7.0790×10^{-11}	1.4158×10^{-12}
tsw33	7.7620×10^{-11}	1.5524×10^{-12}
tsw34	3.3110×10^{-11}	3.3110×10^{-12}
tsw35	9.1200×10^{-11}	9.1200×10^{-12}
tsw36	1.3490×10^{-10}	1.3490×10^{-11}
tsw37	1.3490×10^{-10}	1.3490×10^{-11}

Output DTN: LB07043DGASCAL.001.

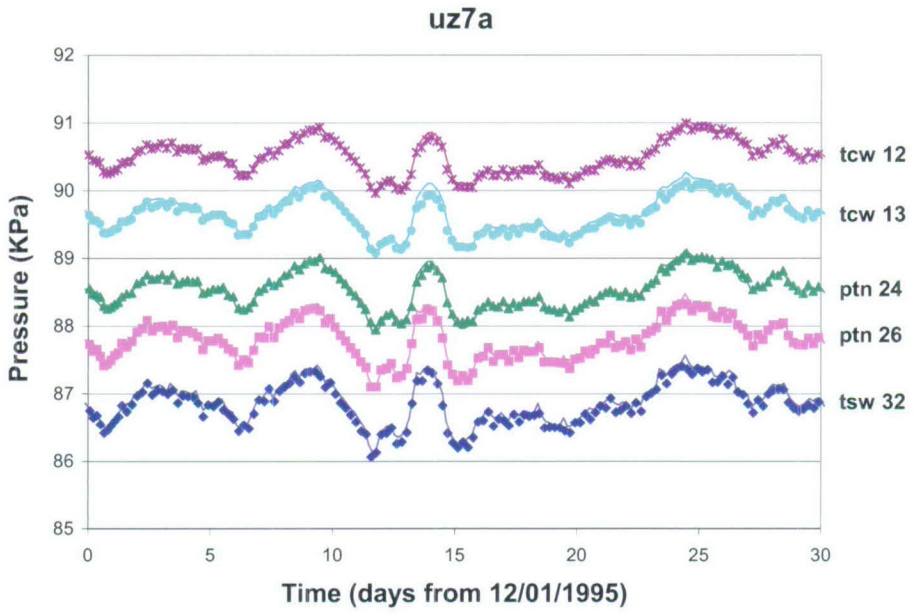

Output DTN: LB07043DGASCAL.001.

NOTE: Both observations and simulations have been vertically offset for clear display. The observed data is from DTN: LB0612MTSCHPFT.001 [DIRS 180296].

Figure 6.4-3. Comparison of Simulated (solid line) and Observed (solid dots) Gas Pressures at Borehole UZ-71 during the First 30-day Period

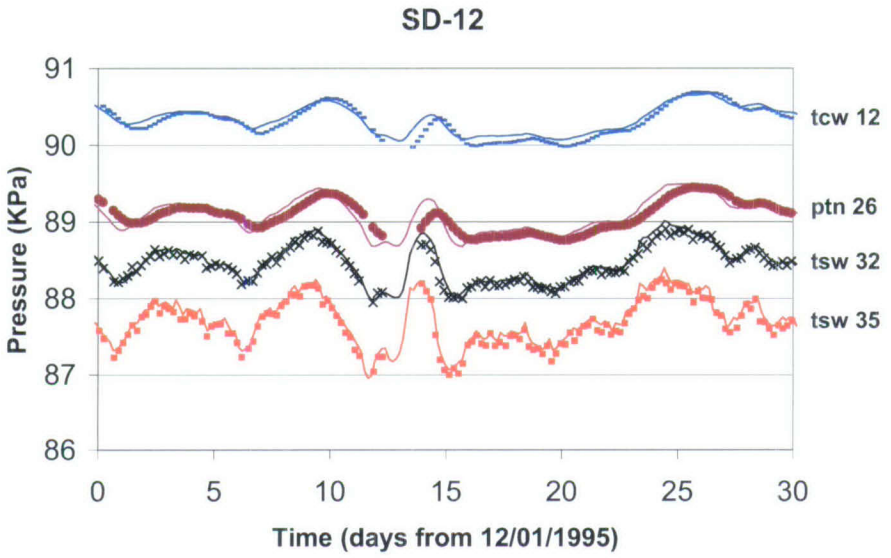

Output DTN: LB07043DGASCAL.001.

NOTE: Both observations and simulations have been vertically offset for clear display. The observed data is from DTN: LB0612MTSCHPFT.001 [DIRS 180296].

Figure 6.4-4. Comparison of Simulated (solid line) and Observed (solid dots) Gas Pressures at Borehole SD-12 during the First 30-day Period

6.5 ANALYSIS AND MODELING OF PORE-WATER CHLORIDE DATA

This study consists of modeling and analyzing geochemical data in the Yucca Mountain unsaturated zone. It utilizes geochemical models to evaluate the hydrological systems, through assessing spatial distribution of surface net infiltration and the impact of variations on its magnitude. It is part of the model calibration effort to support the conceptual model of UZ flow and to build confidence in the predictive capability of the model.

Geochemical data provide additional information by which to analyze the unsaturated zone system. Solutes can be transferred from the atmosphere to the ground surface by precipitation and dry deposition. The chemistry of rain water undergoes drastic changes as it comes in to contact with the earth surface. The distribution of chemical constituents within both liquid and solid phases of the unsaturated zone system depends on such factors as hydrological and geochemical processes of surface precipitation and evapotranspiration, the fracture–matrix interaction of flow and transport, large-scale mixing via lateral transport, and the history of climate changes and recharge. The premise for using chloride for the calibration is that chloride is a conservative species. Evaporation of water leaves chloride behind, and chloride does not interact with other minerals. Chloride in samples from Yucca Mountain has four main sources: (1) salts or fluids present in fractures; (2) salts or fluids present in intergranular pores; (3) isolated fluid inclusions within mineral grains; and (4) chemically bound chloride in hydrous minerals such as biotite and hornblende (Lu et al. 2003 [DIRS 168915]). Chloride from the

above sources (3) and (4) is not believed to contribute to the pore-water chloride, because in those case it is trapped within the mineral grain.

Chloride distribution in the unsaturated zone groundwater provides important information for UZ model calibration and validation. Pore-water chloride concentration data are used in this section to calibrate the UZ model and to bound the infiltration flux, flow pathways, and transport time. This concentration data are analyzed and modeled by three-dimensional chemical transport simulations, using a dual-permeability modeling approach. (UZ flow models of this chloride transport use the three-dimensional model property set in Appendix B). Percolation flux strongly depends on infiltration rates and their spatial distribution. The present-day infiltration rate, estimated across the study area, ranges from 3.03 to 26.78 mm/yr, averaged over the UZ model domain (output DTN: LB0706UZWATSAT.001; Table 6.1-2). The climate over the past 100,000 years has been used to estimate the possible range in infiltration rates over the next 10,000 years (Sonnenthal and Bodvarsson 1999 [DIRS 117127]).

The use of present-day flow field and steady-state simulations discounts the possibility of there being a residual impact resulting from higher infiltration rates during the Pleistocene Epoch. Precipitation last reached a maximum around 21 ka. Higher levels of precipitation (compared to the modern climate lasted for at least another 10,000 years, and at 10,000 years may have been 50% higher than the modern precipitation rate (Tyler et al. 1996 DIRS [108774]). In transient simulations of postglacial change in infiltration and chloride fluxes, Sonnenthal and Bodvarsson (1999 [DIRS 117127], Sections 5.7 and 5.8) show that surface concentrations reached their modern values after 10,000 years of modern infiltration and chloride fluxes. Depths that have been reached by the present-day chloride-rich waters vary considerably. Under ridge tops and side slopes, modern waters reached the water table, whereas under regions of very low infiltration, the front of the chloride-rich plume has barely reached the PTn, leaving much of the underlying TSw unaffected. The residual impact of past climates with higher infiltration rates than present-day climate is a concern for the chloride model, because chloride mass from the previous 10,000 years and earlier remains to be washed out of the unsaturated zone. Consequently, the waters in the current unsaturated zone system are a mixture of two end members—very old water and recent infiltrated water. Given a linear mixing, current chloride concentration of pore water represents an intermediate value between the concentrations of the two end-members. Since a higher infiltration rate in the distant past corresponds to an end member with low pore-water concentration, the other end member must represent a pore-water concentration higher than current measurement values. In other words, current field-measured chloride concentration has been affected by old water residing in the unsaturated zone, leading to a lower concentration than the case would have without the residual old water. As a result, the infiltration rate calibrated using field-measured chloride data results in wetter climate—corresponding to a conservative, higher infiltration rate for the present-day climate.

6.5.1 Available Data

6.5.1.1 Pore-Water Chemical Concentration Data

Chloride transport processes were modeled as part of this model analysis. The chloride concentrations used in the modeling were measured from pore waters extracted from field samples. Collected from a total of twelve surface-based boreholes, the ESF, and the ECRB. (The

boreholes were SD-6, SD-7, SD-9, SD-12, NRG-6, NGR-7a, UZ-14, UZ#16, UZ-7a, WT-24, G-2, and UZ-N55. Data sources for each borehole are listed in Table 6.5-1.)

Table 6.5-1. Chloride Data Sources

Boreholes/Facilities	DTN
SD-6	GS981008312272.004 [DIRS 153677] A LA0002JF12213U.001 [DIRS 154760] B
SD-7	GS000608312271.001 [DIRS 153407] C GS970908312271.003 [DIRS 111467] D GS961108312271.002 [DIRS 121708] F GS981008312272.004 [DIRS 153677] A LA0002JF12213U.001 [DIRS 154760] B LAJF831222AQ98.011 [DIRS 145402] H
SD-9	GS970908312271.003 [DIRS 111467] D GS961108312271.002 [DIRS 121708] F LA0002JF12213U.001 [DIRS 154760] B LAJF831222AQ98.011 [DIRS 145402] HGS020408312272.003 [DIRS 160899] O
SD-12	GS000608312271.001 [DIRS 153407] C GS970908312271.003 [DIRS 111467] D GS961108312271.002 [DIRS 121708] F GS981008312272.004 [DIRS 153677] A LA0002JF12213U.001 [DIRS 154760] B
NRG-6	GS010708312272.002 [DIRS 156375] I LA0002JF12213U.001 [DIRS 154760] B LAJF831222AQ98.011 [DIRS 145402] H
NRG-7a	GS961108312271.002 [DIRS 121708] F GS981008312272.004 [DIRS 153677] A GS010708312272.002 [DIRS 156375] I LA0002JF12213U.001 [DIRS 154760] B LAJF831222AQ98.011 [DIRS 145402] H GS020408312272.003 [DIRS 160899] O
UZ-14	GS010708312272.002 [DIRS 156375] I GS961108312271.002 [DIRS 121708] F GS990208312272.001 [DIRS 146134] J LA0002JF12213U.001 [DIRS 154760] B LAJF831222AQ98.011 [DIRS 145402] H
UZ#16	GS010708312272.002 [DIRS 156375] I GS990208312272.001 [DIRS 146134] J LA0002JF12213U.001 [DIRS 154760] B LAJF831222AQ98.011 [DIRS 145402] H
UZ-N55	LA0002JF12213U.001 [DIRS 154760] B GS010708312272.002 [DIRS 156375] I
UZ-7a	GS981008312272.004 [DIRS 153677] A LA0002JF12213U.001 [DIRS 154760] B
WT-24	GS981008312272.004 [DIRS 153677] A LA0002JF12213U.001 [DIRS 154760] B LAJF831222AQ98.011 [DIRS 145402] H
G-2	LAJF831222AQ98.011 [DIRS 145402] H

Table 6.5-1. Chloride Data Sources (Continued)

Boreholes/Facilities	DTN
ECRB	LA9909JF831222.004 [DIRS 145598] K LA0002JF12213U.002 [DIRS 156281] L GS020408312272.003 [DIRS 160899] O
ESF	GS961108312261.006 [DIRS 107293] M LA0002JF12213U.002 [DIRS 156281] L LA9909JF831222.010 [DIRS 122733] N

NOTE: Letters following the DIRS numbers are not a part of the DTN number. Each letter corresponds to the appearance of the same DTN.

6.5.1.2 Chloride Flux

Sources contributing to the chloride flux in recharge waters are precipitation, run-on, and runoff. The portion of these waters that form net infiltration is small. Infiltration rates for present-day climate scenarios are estimated to be in the range of 3.03 to 26.78 mm/yr, based on the average infiltration rates for the 10th and 90th percentile infiltration maps (Table 6.1-2). The estimated modern mean infiltration rate is approximately 5 mm/yr, and the glacial maximum infiltration rate at 28,000 years ago was about 28 mm/yr (Sonnenthal and Bodvarsson 1999 [DIRS 117127], p. 148, Figure 23).

Four case studies corresponding to four present-day climate scenarios were chosen. They represent the 10th, 30th, 50th, and 90th percentile infiltration maps. Their mean fluxes are listed in Table 6.5-2, calculated from four infiltration maps (DTN: SN0609T0502206.028 [DIRS 178753]). Also listed in the table are the notations for these infiltration scenarios, which are consistent with the notations used in the flow models (Section 6.2). The chloride transport model uses the same flow model as the notation indicates. Chloride recharge fluxes to these transport models are calculated accordingly for these climate scenarios.

Chloride recharge sources into the saturated zone include dissolved material in rain, particulate in snow, and a contribution from windblown dust (Tyler et al. 1996 [DIRS 108774]). Also, precipitate on land surfaces would experience physical processes such as evaporation, which leaves behind Cl^- in the remaining water. The chloride mass flux to the chloride transport model depends on the amount of water flux and its chloride concentration. In the model, fluxes are considered to be precipitation, runon, and runoff. Thus, the water fluxes contributing to chloride recharge can be calculated using the following equation:

$$F = F_{prec} + F_{runon} - F_{runoff} \quad \text{(Eq. 6.5-1)}$$

where F is the net flux contributing to the chloride in the recharging water (defined as net recharge in Table 6.5-2, independent of the net infiltration of Table 6.1-2), F_{prec} is the precipitation flux, F_{runon} is the runon flux, and F_{runoff} is the runoff flux. For input to TOUGH2 calculation the net recharge flux in mm/yr is converted to equivalent mass flux (kg/s). Calculating each term for F is carried out using the routine infil2grid V1.7 (2002 [DIRS 154793] and the precipitation, runoff and runon data for the present-day climate (DTN:

SN0609T0502206.028 [DIRS 178753]). Chloride flux is then calculated using the following formula:

$$F_{Cl} = C_{Cl,p} \times 10^{-6} (F_{prec} + F_{runon} - F_{runoff}) \qquad \text{(Eq. 6.5-2)}$$

where F_{Cl} is chloride flux (kg/s), F_{prec} is precipitation flux (kg/s), F_{runon} is run-on (kg/s), and F_{runoff} is runoff flux (kg/s). $C_{Cl,p}$ is chloride concentration in precipitation (mg/(kg water). (Note that actual calculations and procedures using this equation in preparing input files for chloride simulations are summarized in Appendix D2).

Table 6.5-2. Present-Day Infiltration Rates at Different Scenarios (Averaged over Model Domain)

Scenario Notations [a]	Scenarios	Precipitation (mm/yr)	Runon (mm/yr)	Runoff (mm/yr)	Net Recharge Used in Calculation of Chloride Flux [b] (mm/yr)
pd_10	10th Percentile Infiltration Map	163.44	277.00	279.03	161.41
pd_30	30th Percentile Infiltration Map	153.89	600.21	606.09	148.01
pd_50	50th Percentile Infiltration Map	189.68	995.78	1005.62	179.84
pd_90	90th Percentile Infiltration Map	147.05	862.39	871.02	138.43

Source: [a]Fluxes calculated as described in Appendix D, Section D2, data from Output DTN: LB0706UZWATSAT.001]

NOTE: [b]Net water flux contributing to the chloride recharge is calculated by Equation 6.5-1.

Surface chloride concentrations are discussed by Sonnenthal and Bodvarsson (1999 [DIRS 117127], pp. 113 to 114). The range of 0.55 to 0.73 mg/L was considered to bound the average value. Triay et al. (1996 [DIRS 101014]) obtained a mean chloride concentration in precipitation of 0.55 mg/L, which is probably close to the minimum value expected. A similar value was obtained by combining a mean annual precipitation of about 170 mm/yr with a present-day chloride surface flux of 106 mg/(m^2-yr) yielding a mean chloride concentration of about 0.62 mg/L (Fabryka-Martin et al. 1997 [DIRS 100144]), which includes a windblown dust component. The contribution from windblown dust may be 33% of the total chloride flux in the Great Basin of Nevada and Utah (Tyler et al. 1996 [DIRS 108774]). Even though the contribution from windblown dust is considered in the flux, as in part of the measured precipitation, the upper limit of concentration can be bounded by adding 33% more chloride to the 0.55 mg/L concentration to yield a maximum of about 0.73 mg/L. The upper limit is less well defined than the lower limit, which is more easily set from the concentrations in precipitation. Clearly, this variation in this 0.73 mg/L chloride concentration before evapotranspiration is much less than the over an order-of-magnitude range in estimates of infiltration rate, and therefore the surface chloride concentration is a moderately well-constrained boundary value for modeling studies (Sonnenthal and Bodvarsson (1999 [DIRS 117127], pp. 113 to 114). A value of 0.55 mg/L (Sonnenthal and Bodvarsson 1999 [DIRS 117127]; Triay et al. 1996 [DIRS 101014]) is used in the present simulations, applied to all infiltrating water in the form of precipitation, run-on, and runoff (Sonnenthal and Bodvarsson 1999 [DIRS 117127], p. 148). The concentration of recharge water is factored into the above equation as a linear coefficient in the chloride flux

formulation. Given a fixed water flux, increasing its concentration will effectively yield a higher chloride infiltration flux, leading to shifting of the simulated curves to a higher concentration direction. As the chloride concentration increases, the infiltration rate necessary to maintain the same chloride flux must decrease. Thus, using a chloride concentration of 0.55 mg/L rather than a higher value will result in a conservative estimation of precipitation.

Chloride measurement can be made with precision. Rock properties have been calibrated with field moisture data, and sensitivity analyses show that parameter uncertainties have much less effect on UZ flow than infiltration uncertainty, as discussed in Section 6.10.1. The chloride measurements are expected to yield a mean value that smoothes out the heterogeneous effects of point samples and, therefore, is considered comparable to numerical simulation results from implicit spatial averaging.

6.5.2 Three-Dimensional Simulations

Chloride transport within the UZ hydrological system was simulated under two-phase isothermal flow conditions of water and air. A three-dimensional dual-permeability model and the T2R3D V1.4 (1999 [DIRS 146654]) of the TOUGH2 family of codes were employed for these simulations. Steady-state liquid-flow fields were obtained using the EOS9 module of T2R3D (1999 [DIRS 146654]). (The water and chloride fluxes used for the simulation can be found in output DTN: LB0706UZWATSAT.001.) Hydrological properties and grid are the same as for the three-dimensional flow model of this report. Chemical concentration distributions were then computed from transport equations, using the decoupled T2R3D module (LBNL 1999 [DIRS 146654]). Flow boundary conditions, simulation grids, and the basic hydrological properties of the rock matrix and fractures are the same as those used in the three-dimensional UZ flow simulation. Boundary conditions for chemical components were treated similarly to those for flow simulations, with mass flux prescribed at the top boundary and no-flow and water table conditions at the lateral and bottom boundaries, respectively. Dispersivities for both fracture and matrix continua in the simulation were assumed to be zero (Sonnenthal and Bodvarsson 1999 [DIRS 117127], Section 5.3, p. 129). The diffusion coefficient for Cl^- is set to 2.032×10^{-9} m^2/s in *Handbook of Chemistry and Physics* (Lide 2002 [DIRS 160832], p. 5-96) for the chemical ions in dilute water at 25°C, which approximates the average of the surface temperature and water table temperature. The tortuosity was set to 0.7 for fracture and 0.2 for matrix, respectively (Grathwohl 2000 [DIRS 141512], Section 2.2.3, p. 31, and Figure 2.6). Here, tortuosity (<1) is defined as the ratio of the shortest distance to the effective path length in a porous medium.

6.5.2.1 Modeling Results

Modeling results are shown in Figures 6.5-1 to 6.5-11 for comparisons with data from boreholes, and the ESF and the ECRB drift facilities. These figures plot the computed chloride profiles for four present-day infiltration rates (10th, 30th, 50th, and 90th percentile maps). Visual examination in general demonstrates that the computed profiles for the 10th percentile infiltration case has overall the closest matches between the calculated concentrations and the field-measured chloride data, while matches in the higher infiltration scenarios become poorer and poorer when infiltration rates increase from the 30th, to the 50th, and then to the 90th percentile cases. Figures 6.5-2, 6.5-5, and 6.5-7 show that the 10th percentile and 30th percentile

generally match the measured field data equally well. Figures 6.5-9 and 6.5-11 indicate that the 30th and the 50th percentile maps provide better matches to measured field data. Point-based concentration measurement residuals are calculated for 14 boreholes and facilities (G-2, NRG-6, NRG-7a, SD-12, SD-6, SD-7, SD-9, UZ-14, UZ-16, WT-24, UZ-7a, UZ-N55, ESF, and ECRB). Results show that 10 are best fitted for 10th percentile scenario, with the remaining four (G-2, UZ-14, UZ-16, and ESF) best fitted for 30th percentile scenario. (Figure for UZ-N55 is not shown in the current analysis) (Table 6.5-3).

The field-measured pore-water chloride data for boreholes are mainly collected from the PTn unit, perched water sites, and the CHn unit. The repository host unit TSw is represented by the ESF and ECRB, with the ESF data in three narrow segments. Even though scattered in spatial distribution, in terms of match to the field-measured pore-water chloride data, the simulated results for the vertical profiles of the boreholes are consistent with those of the ESF and ECRB. These results are used in the estimates of likely range of infiltration in Section 6.8.

Table 6.5-3. Residual Chloride Concentration in Boreholes and Facilities

Boreholes or Facilities	Number of Samples	10th Percentile[a]	30th Percentile	50th Percentile	90th Percentile
G-2	1	0.25	0.13[b]	0.24	0.58
NRG-6	13	0.23[b]	0.58	0.73	1.26
NRG-7a	10	0.30[b]	0.52	0.57	1.03
SD-12	14	0.13[b]	0.55	0.62	1.10
SD-6	3	0.38[b]	0.78	0.88	1.29
SD-7	10	0.30[b]	0.65	0.74	1.18
SD-9	17	0.24[b]	0.48	0.57	1.06
UZ-14	71	0.32	0.30[b]	0.31	0.68
UZ-16	44	0.85	0.19[b]	0.22	0.65
WT-24	3	0.22[b]	0.60	0.70	1.08
UZ-7a	3	0.28[b]	0.85	0.97	1.49
UZ-N55	6	0.44[b]	0.46	0.64	1.17
ESF	31	0.57	0.29[b]	0.43	0.94
ECRB	26	0.20[c]	0.47	0.55	1.01

Source: Compiled from Output DTN: LB0701PAWFINFM.001.

[a]Percentile infiltration map of present-day climate.

[b]Scenario with the least residual.

NOTE: Residual concentration represents the absolute difference between calculated and measured chloride concentration (mg/L, in log scale).

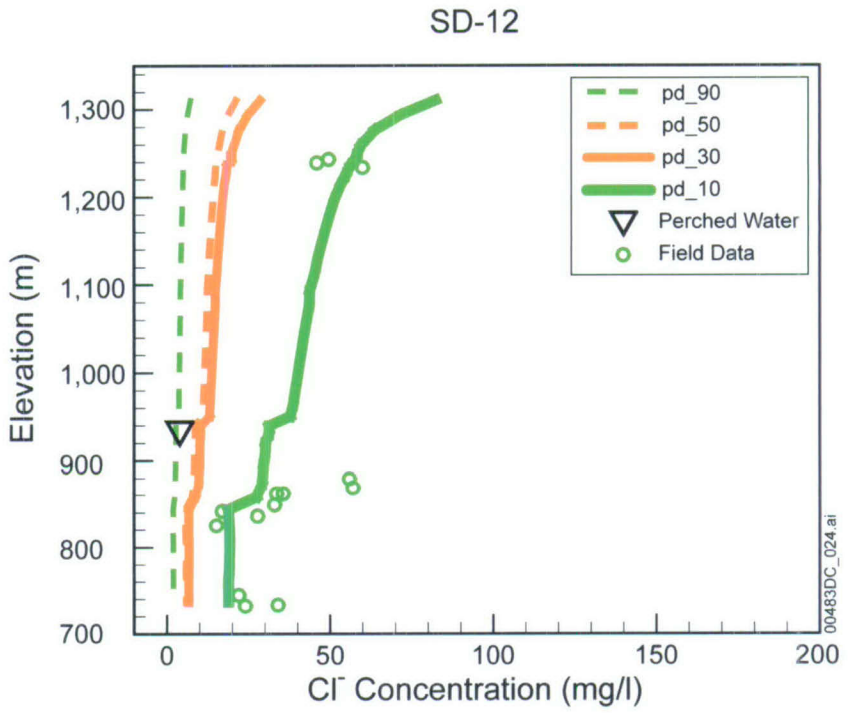

Sources: DTNs: GS000608312271.001 [DIRS 153407]; GS970908312271.003 [DIRS 111467]; GS961108312271.002 [DIRS 121708]; GS981008312272.004 [DIRS 153677]; LA0002JF12213U.001 [DIRS 154760].

Output DTN: LB0701UZMCLCAL.001.

Figure 6.5-1. Chloride Concentration (mg/L) Profiles at Borehole USW SD-12 for Present-Day 10th, 30th, 50th, and 90th Percentile Infiltrations

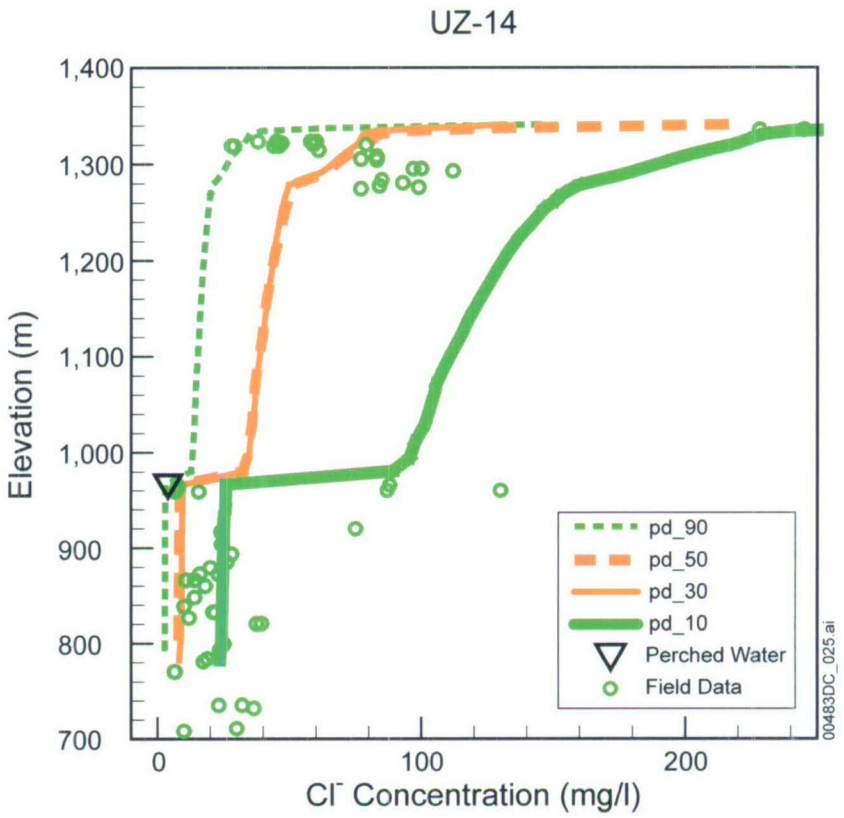

Source DTNs: GS010708312272.002 [DIRS 156375]; GS961108312271.002 [DIRS 121708]; GS990208312272.001 [DIRS 146134]; LA0002JF12213U.001 [DIRS 154760]; LAJF831222AQ98.011 [DIRS 145402].

Output DTN: LB0701UZMCLCAL.001.

Figure 6.5-2. Chloride Concentration (mg/L) Profiles at Borehole USW UZ-14 for Present-Day 10th, 30th, 50th, and 90th Percentile Infiltrations

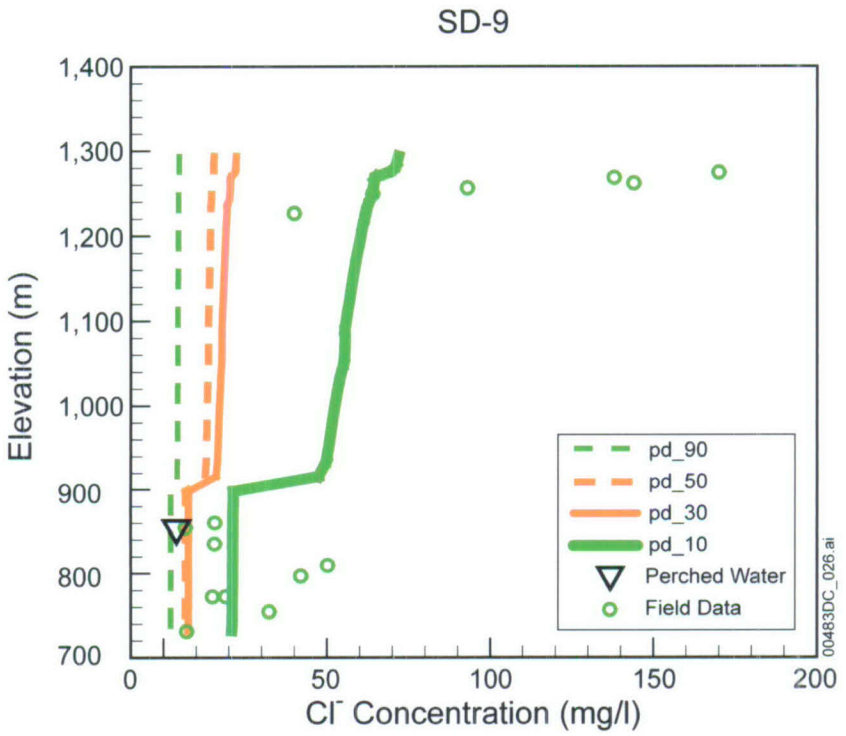

Source DTNs: GS970908312271.003 [DIRS 111467]; GS961108312271.002 [DIRS 121708]; LA0002JF12213U.001 [DIRS 154760]; LAJF831222AQ98.011 [DIRS 145402]; GS020408312272.003 [DIRS 160899].

Model Results–Output DTN: LB0701UZMCLCAL.001.

Figure 6.5-3. Chloride Concentration (mg/L) Profiles at Borehole USW SD-9 for Present-Day 10th, 30th, 50th, and 90th Percentile Infiltrations

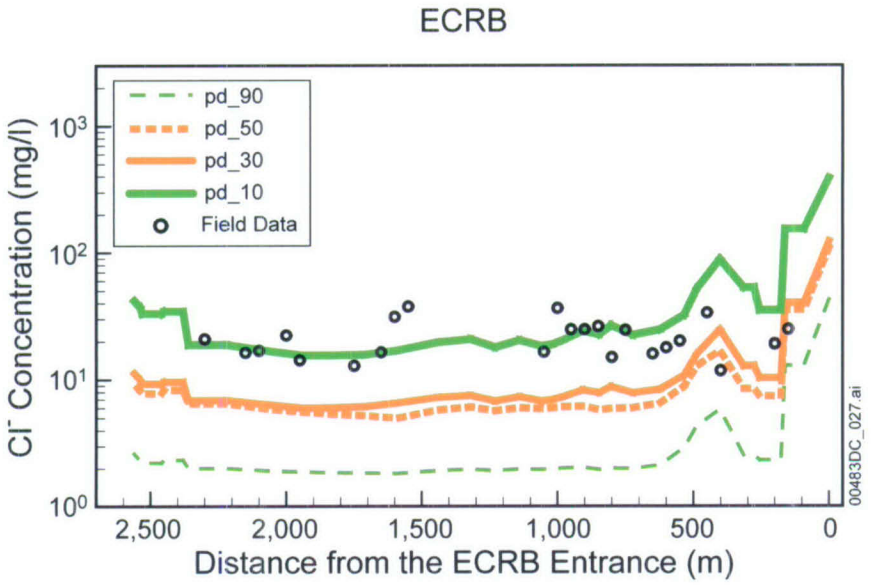

Source DTNs: LA9909JF831222.004 [DIRS 145598]; LA0002JF12213U.002 [DIRS 156281]; GS020408312272.003 [DIRS 160899].

Model Results–output DTN: LB0701UZMCLCAL.001.

Figure 6.5-4. Chloride Concentration (mg/L) Profiles at the ECRB for Present-Day 10th, 30th, 50th, and 90th Percentile Infiltrations

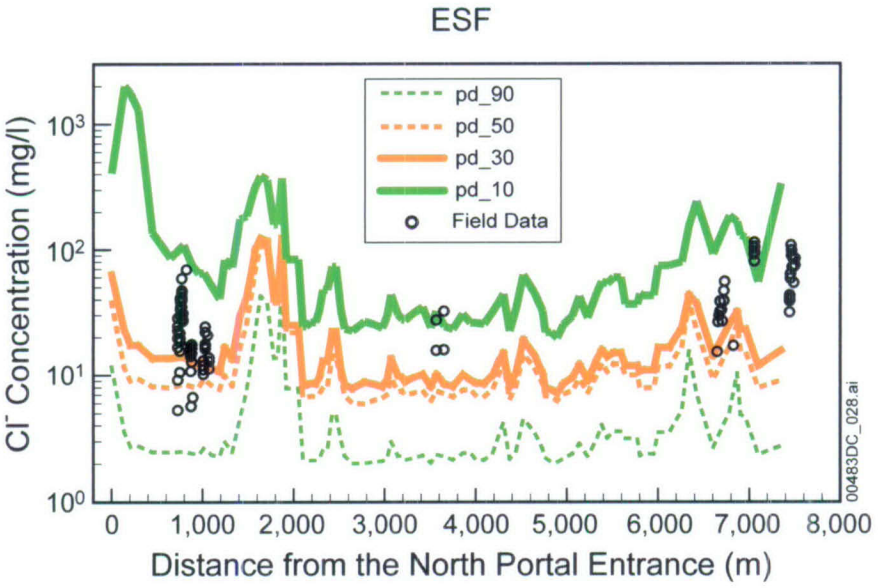

Source DTNs: GS961108312261.006 [DIRS 107293]; LA0002JF12213U.002 [DIRS 156281]; LA9909JF831222.010 [DIRS 122733].

Model Results–Output DTN: LB0701UZMCLCAL.001.

Figure 6.5-5. Chloride Concentration (mg/L) Profiles at the ESF for Present-Day 10th, 30th, 50th, and 90th Percentile Infiltrations

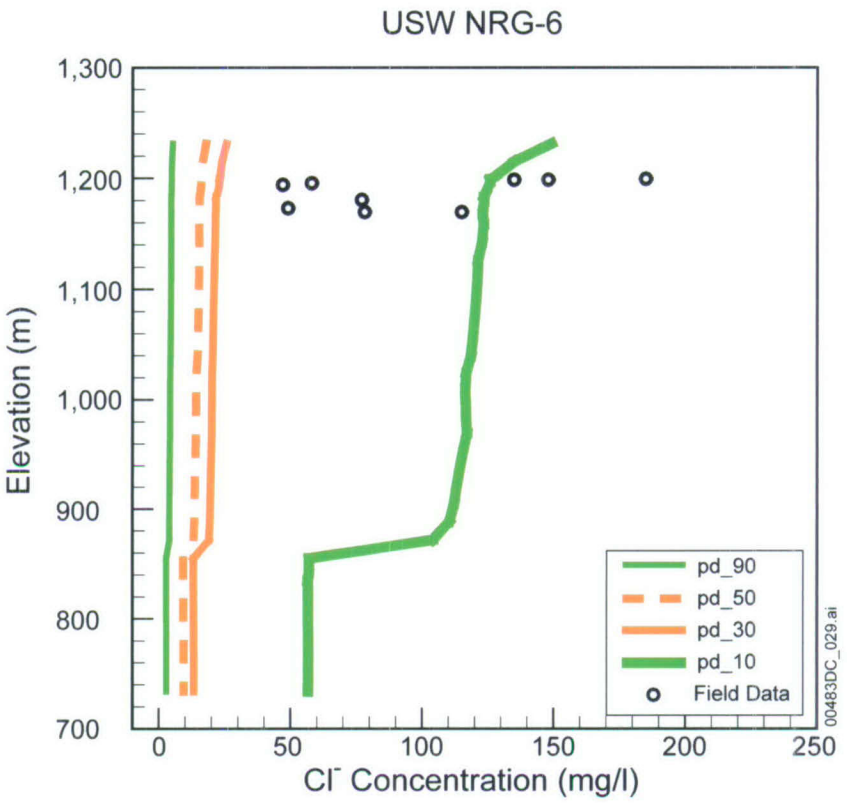

Source DTNs: GS010708312272.002 [DIRS 156375]; LA0002JF12213U.001 [DIRS 154760]; LAJF831222AQ98.011 [DIRS 145402].

Model Results–Output DTN: LB0701UZMCLCAL.001.

Figure 6.5-6. Chloride Concentration (mg/L) Profiles at Borehole USW NRG-6 for Present-Day 10th, 30th, 50th, and 90th Percentile Infiltrations

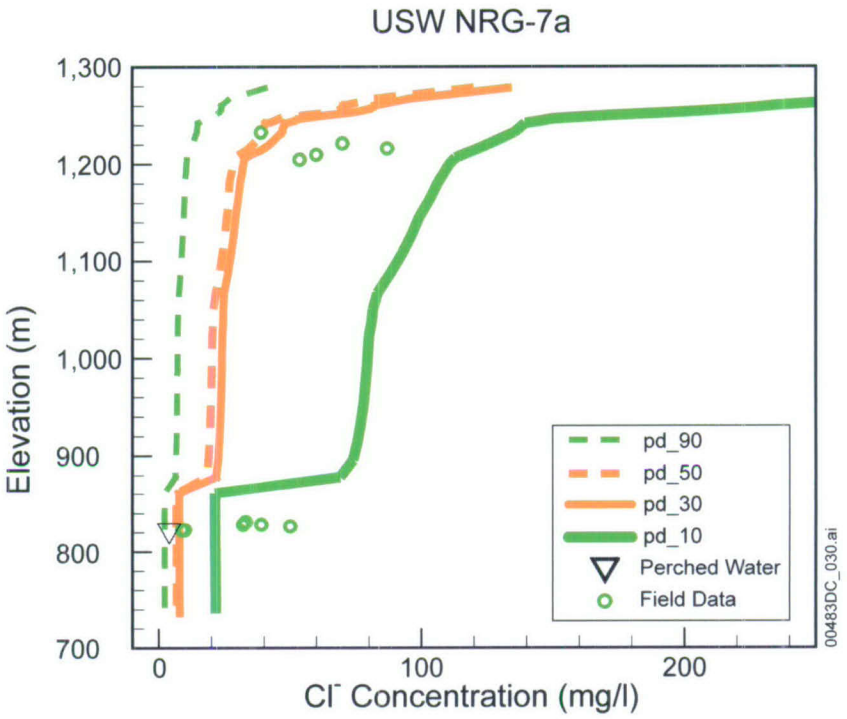

Source DTNs: GS961108312271.002 [DIRS 121708]; GS981008312272.004 [DIRS 153677]; GS010708312272.002 [DIRS 156375]; LA0002JF12213U.001 [DIRS 154760]; LAJF831222AQ98.011 [DIRS 145402]; GS020408312272.003 [DIRS 160899].

Model Results–output DTN: LB0701UZMCLCAL.001.

Figure 6.5-7. Chloride Concentration (mg/L) Profiles at Borehole USW NRG-7a for Present-Day 10th, 30th, 50th, and 90th Percentile Infiltrations

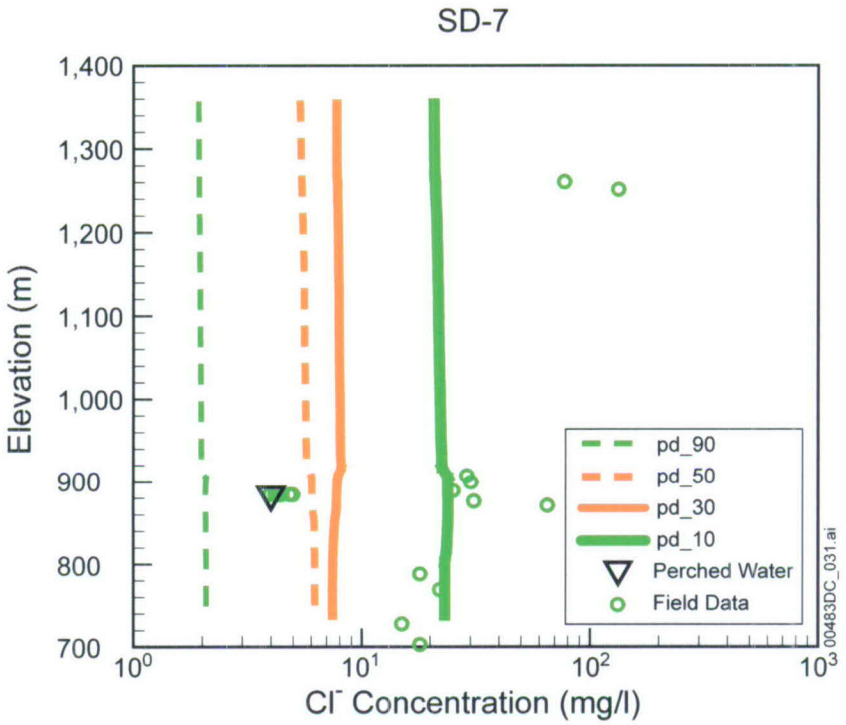

Sources: DTNs: GS000608312271.001 [DIRS 153407]; GS970908312271.003 [DIRS 111467]; GS961108312271.002 [DIRS 121708]; GS981008312272.004 [DIRS 153677]; LA0002JF12213U.001 [DIRS 154760]; LAJF831222AQ98.011 [DIRS 145402] .

Model Results–output DTN: LB0701UZMCLCAL.001.

Figure 6.5-8. Chloride Concentration (mg/L) Profiles at Borehole USW SD-7 for Present-Day 10th, 30th, 50th, and 90th Percentile Infiltrations

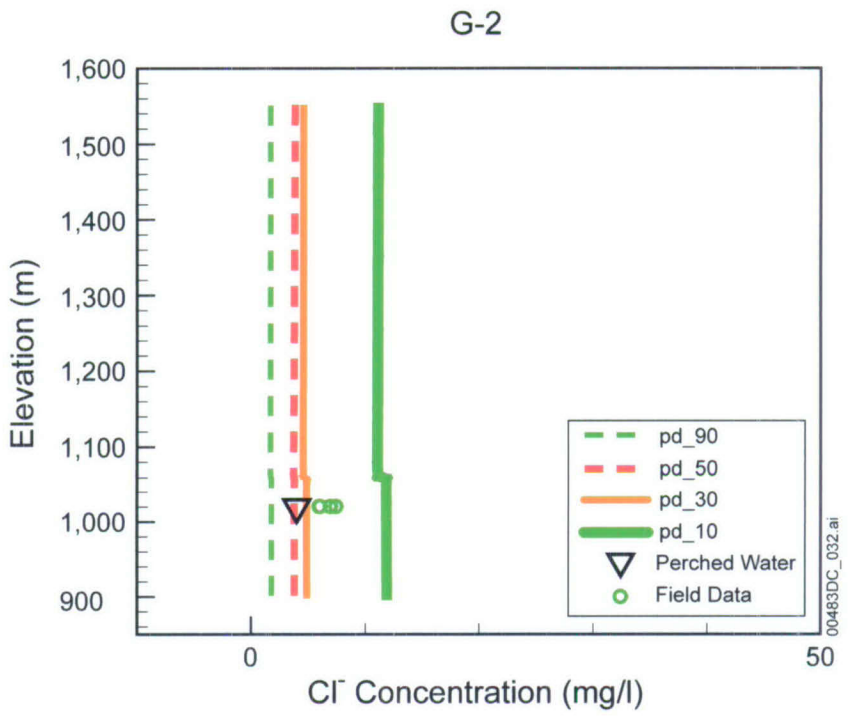

Source: DTN: LAJF831222AQ98.011 [DIRS 145402].
Model Results–output DTN: LB0701UZMCLCAL.001.

Figure 6.5-9. Chloride Concentration (mg/L) Profiles at Borehole USW G-2 for Present-Day 10th, 30th, 50th, and 90th Percentile Infiltrations

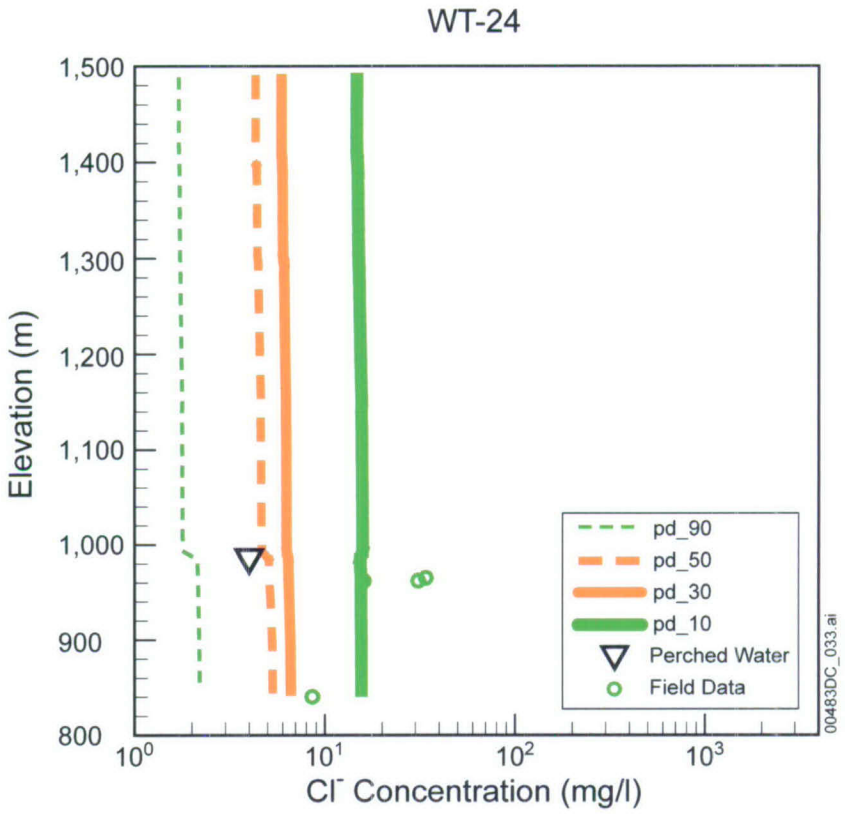

Sources: DTNs: GS981008312272.004 [DIRS 153677]; LA0002JF12213U.001 [DIRS 154760]; LAJF831222AQ98.011 Model Results–output DTN: LB0701UZMCLCAL.001.

Figure 6.5-10. Chloride Concentration (mg/L) Profiles at Borehole USW WT-24 for Present-Day 10th, 30th, 50th, and 90th Percentile Infiltrations

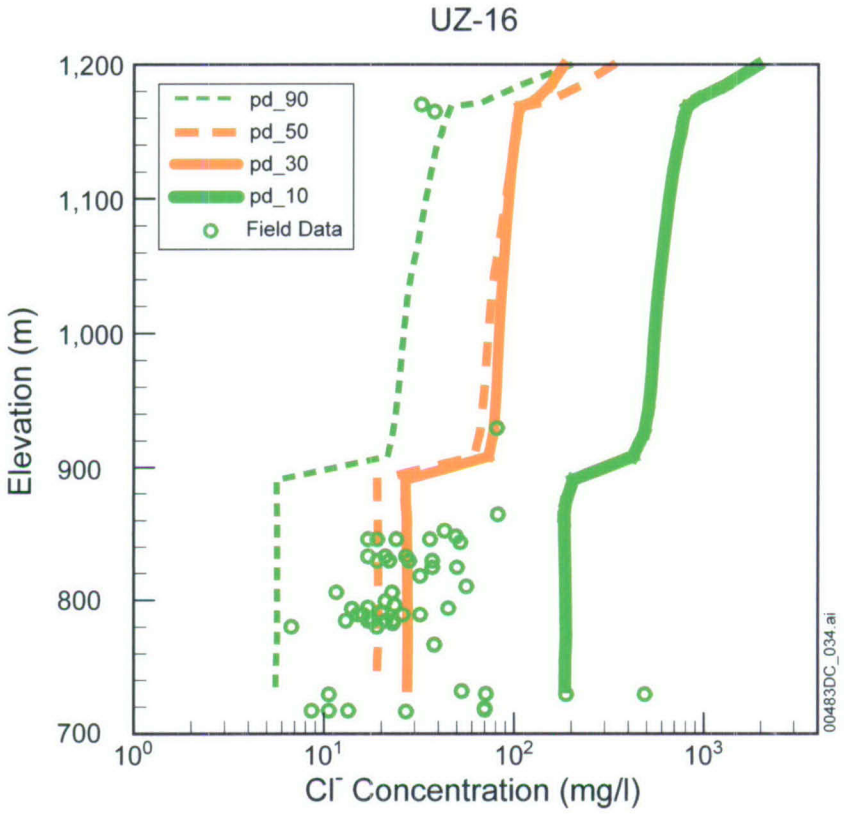

Sources: DTNs: GS010708312272.002 [DIRS 156375]; GS990208312272.001 [DIRS 146134]; LA0002JF12213U.001 [DIRS 154760]; LAJF831222AQ98.011 [DIRS 145402].

Output DTN: LB0701UZMCLCAL.001 (model results).

Figure 6.5-11. Chloride Concentration (mg/L) Profiles at Borehole USW UZ-16 for Present-Day 10th, 30th, 50th, and 90th Percentile Infiltrations

6.6 FLOW PATTERN ANALYSIS OF THREE-DIMENSIONAL UZ FLOW FIELDS

This section analyzes and summarizes the three-dimensional UZ flow fields from the 16 flow simulation scenarios under four climates. The 16 model simulations are performed using the TSPA-LA grid (Figure 6.1-1) and 16 infiltration maps (as discussed in Section 6.1.4), the four calibrated parameter sets in Appendix B, and the UZ flow model of Section 6.2.2.

6.6.1 Simulation Scenarios and Model Results

Table 6.2-6 summarizes the 16 simulation scenarios or UZ flow fields associated with parameter sets and infiltration maps. Based on the analyses and model calibration results of Sections 6.2.5, 6.3, and 6.5, the present-day 10th percentile infiltration rate is considered to be the most likely infiltration scenario. Therefore, in the sections below, the results of 10th percentile infiltration maps are used as a reference point in the analysis of the evolution of percolation flux and the proportion of fracture to matrix flow through the Yucca Mountain unsaturated zone.

As shown in Table 6.2-6, simulations with the sixteen infiltration maps cover three climatic scenarios (i.e., present-day, monsoon, and glacial transition), and additional post-10,000-year infiltration rates for the UZ flow fields.

6.6.2 Flow Fields and Analyses

Percolation flux through the unsaturated zone is one important natural-barrier factor affecting overall repository performance in TSPA calculations. The quantity as well as the spatial and temporal variations in percolation flux will directly affect (1) the amount of water flowing into waste emplacement drifts, (2) moisture conditions and the corrosion environment of waste packages within the drifts, (3) radionuclide release from the repository, and (4) radionuclide migration from the unsaturated zone to the saturated zone. Percolation fluxes through unsaturated fractured tuffs cannot be readily measured in the field, and, thus, indirect data and model results have to be used to estimate these fluxes.

Model studies (Wu et al. 1999 [DIRS 117161]; 2002 [DIRS 160195]; 2004 [DIRS 173953]) indicate that the accuracy of model predictions for percolation fluxes in the Yucca Mountain unsaturated zone depend on many factors, including (1) net infiltration rates over the surface boundary (Wu et al. 1999 [DIRS 117161], pp. 208 to 210 and Figure 13; 2002 [DIRS 160195], p. 227, Figure 6), (2) geological models and conceptualizations, (3) distribution of rock-property values for fractures and matrix, and (4) treatment of fracture–matrix flow and interaction. In this section, percolation fluxes at the repository horizon are analyzed using the 16 simulation results (Table 6.2-6) of the UZ flow models for TSPA-LA. In the analysis, the percolation flux is defined as total vertical liquid mass flux through both fractures and matrix, and is converted to millimeters per year (mm/yr) per unit area using a constant water density.

6.6.2.1 Percolation Flux at Repository Horizon

Figures 6.6-1 to 6.6-4 show examples of percolation fluxes along the repository layer or horizon for the four 10^{th} percentile infiltration scenarios of the four climates (see Appendix E for relevant data compilation, extraction and calculation for simulated percolation fluxes). Comparisons of the calculated repository percolation fluxes of Figures 6.6-1, 6.6-2, 6.6-3, and 6.6-4 with those of the surface infiltration maps (Figures 6.1-2, 6.1-3, 6.1-4, and 6.1-5, respectively) indicate that percolation fluxes at the repository are very different from surface infiltration patterns, essentially in the northern part of the model domain. Surface infiltration rates and distributions are independent of faults. Under steady-state flow conditions, percolation flux and its distribution along any horizon of the model domain would be the same or very similar if there were no lateral flow. The major differences in percolation flux at the repository level (Figures 6.6-1–6.6-4) from the surface infiltration maps (Figures 6.1-2 to 6.1-5) are (1) flow converted through faults in the very northern part of the model domain (with the north coordinate greater than 237,000 m) and (2) flow diverted into or near faults located in the rest of the model domain.

In addition to the northern model domain and the area near faults, comparisons between the surface infiltration maps (Figures 6.1-2 to 6.1-5) and the repository-level percolation flux (Figures 6.6-1 to 6.6-4) also show some indication of eastward movement for the high infiltration zones from south to north along the crest, located along the center of the model domain for the four 10th percentile infiltration scenarios. Flow redistribution in the very northern part of the

model domain (beyond the repository block) results from the repository grid layer horizon laterally intersecting the CHn zeolitic and perched water zones locally, with major flow paths being faults. Overall, percolation results as shown in Figures 6.6-1, 6.6-2, 6.6-3, and 6.6-4 display different patterns from the surface infiltrations, because of both lateral flow within the PTn unit and flow focusing into faults.

Simulated percolation fluxes in the repository layer, in addition to those shown in Figures 6.6-1, 6.6.2, 6.6-3, and 6.6-4 (for four 10th percentile infiltration rates), are presented in Appendix F, for the 30th, 50th, and 90th percentile infiltration rates of present-day, monsoon, glacial transition, and post-10,000-year climates.

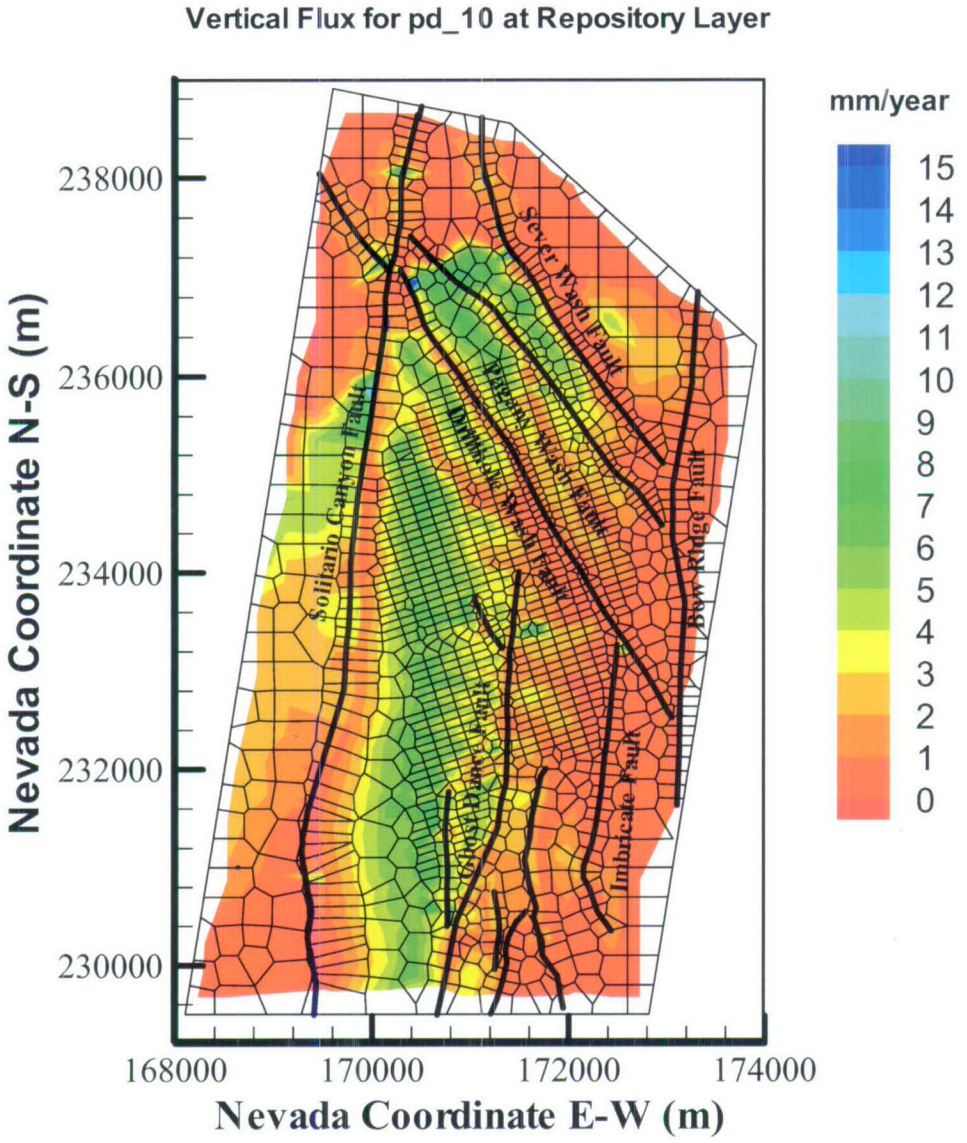

Output DTN: LB06123DPDUZFF.001.

Figure 6.6-1. Simulated Percolation Fluxes at the Repository Horizon under the Present-Day, 10th Percentile Infiltration Scenario

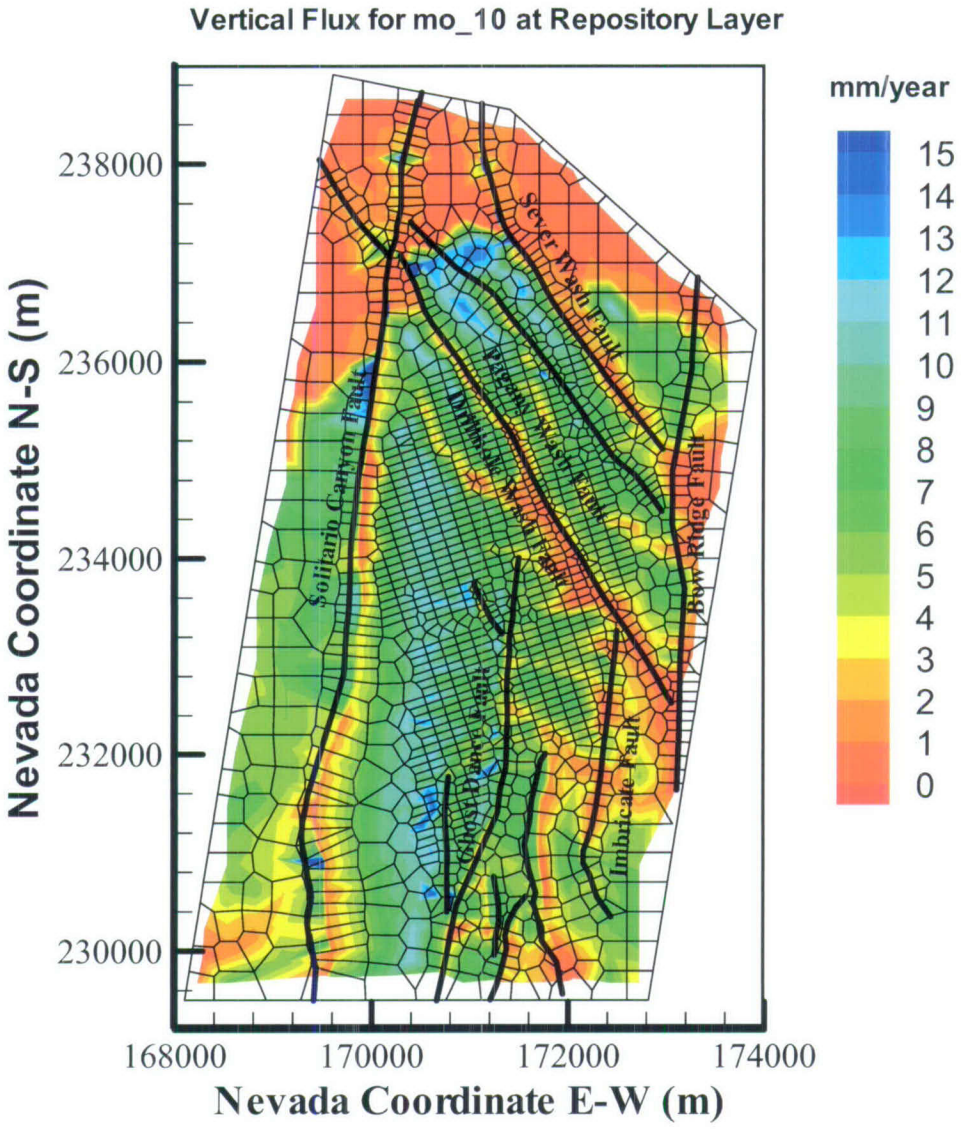

Output DTN: LB07013DMOUZFF.001.

Figure 6.6-2. Simulated Percolation Fluxes at the Repository Horizon under the Monsoon, 10th Percentile Infiltration Scenario

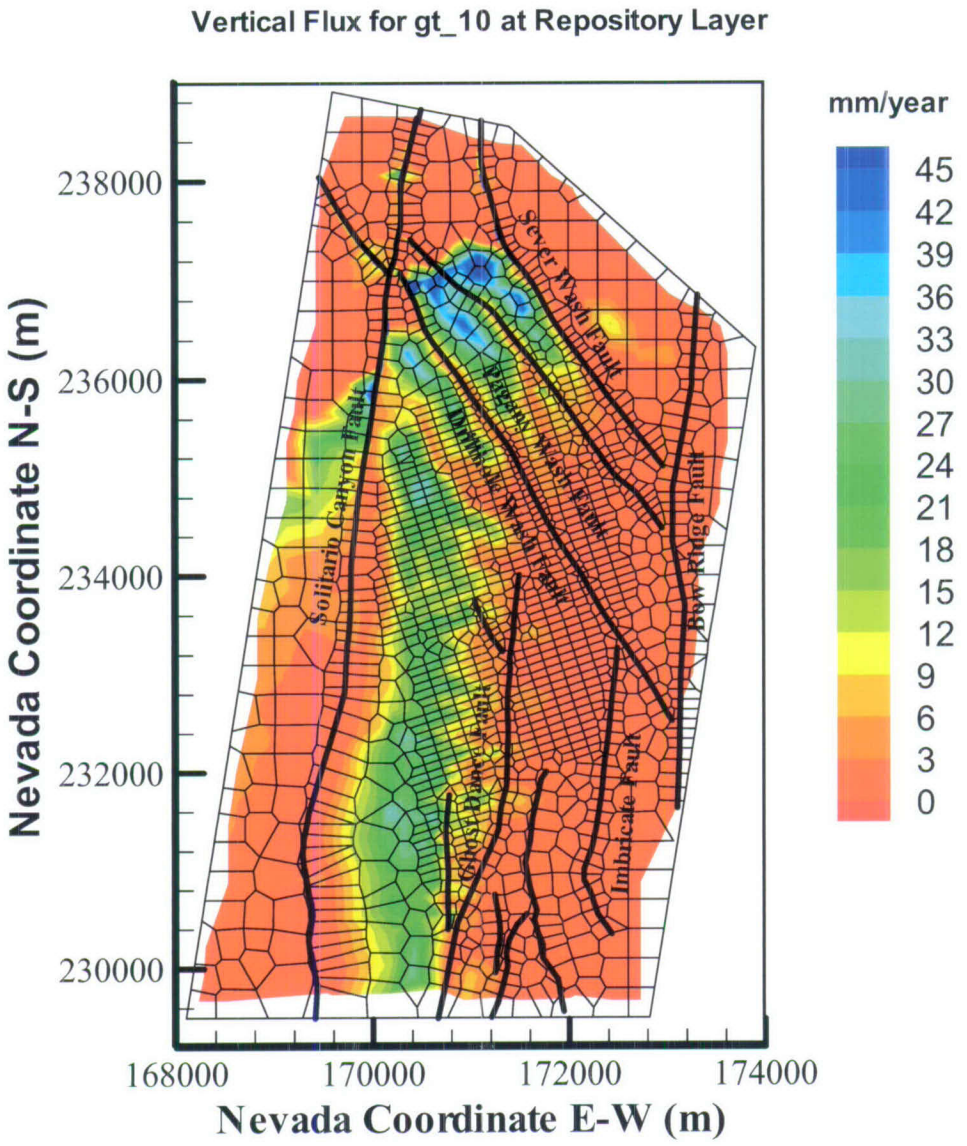

Output DTN: LB07013DGTUZFF.001.

Figure 6.6-3. Simulated Percolation Fluxes at the Repository Horizon under the Glacial Transition, 10th Percentile Infiltration Scenario

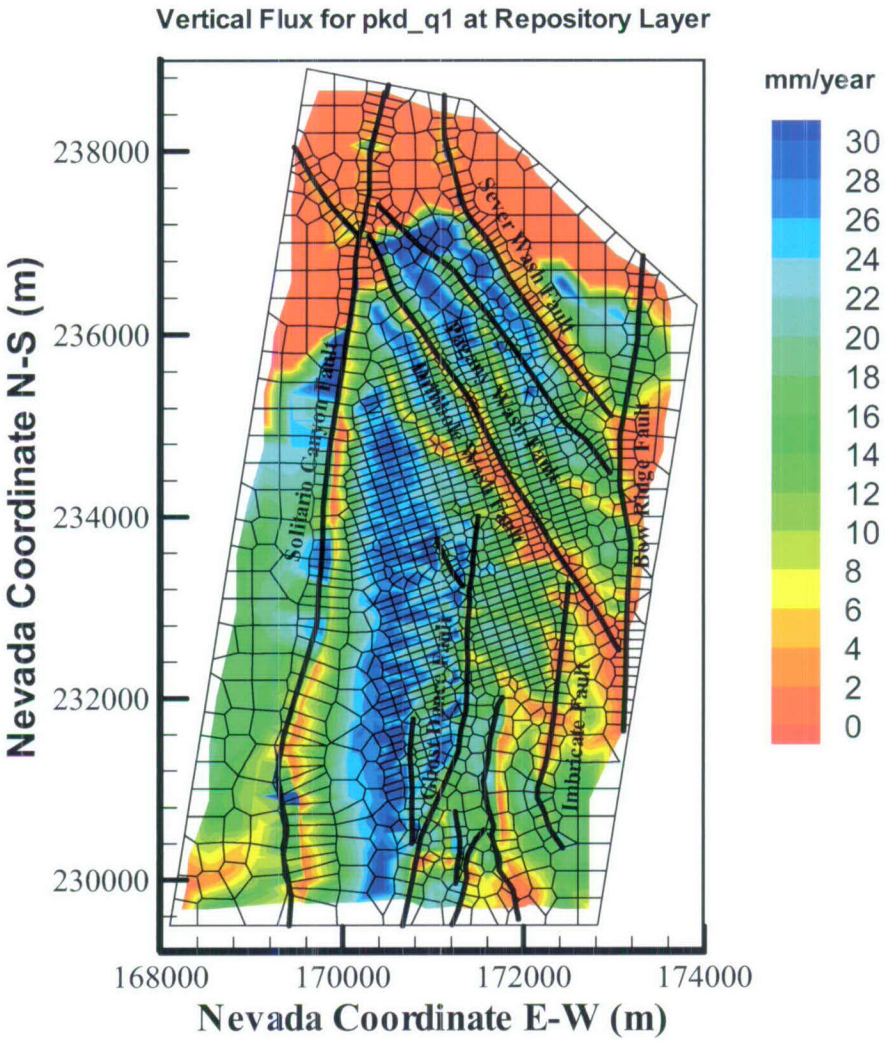

Output DTN: LB0702UZP10KFF.002.

Figure 6.6-4. Simulated Percolation Fluxes at the Repository Horizon under the Post-10,000-Year, 10th Percentile Infiltration Scenario

6.6.2.2 Percolation Flux at Water Table

Figures 6.6-5 through 6.6-8 show the simulated percolation fluxes at the water table using the four 10th percentile infiltration scenarios of the four climates present-day, monsoon, glacial transition, and post-10,000 years. When comparing the percolation fluxes at the repository (e.g., Figures 6.6-1, 6.6-2, 6.6-3, and 6.6-4), the following is found:

- In the northern half of the domain, because of the impact of perched water and lower-permeability zeolitic units, flow is focused significantly into major faults.
- In the central and southern portions of the model domain, the flow fields at the water table show lateral flow of several hundreds of meters to the east in the area directly below the southern repository. This is the area where vitric zones are located within the CHn unit.

All 16 flow fields are calculated using a fixed water table. These flow fields can also be used for a rising-water-table case in the future. This is because the water table is handled as a sink term in the model, and the flow at or above the water table is determined by the upstream or upper-layer conditions. Therefore, a water-rise situation can be handled by simply transecting the flow fields vertically at a new water table elevation. The software WTRISE V2.0 (LBNL 2003 [DIRS 163453]) is available to obtain those results. As discussed in *Saturated Zone Site-Scale Flow Model* (BSC 2004 [DIRS 170037], Section 6.4.5) and *Particle Tracking Model and Abstraction of Transport Processes* (BSC 2004 [DIRS 170041], Section 6.4.9), the water table under future wetter climates is expected to rise. The elevation of 850 m was selected (BSC 2004 [DIRS 170041], Section 6.4.9) as a nominal water table elevation under future climates consistent with the studies documented in *Saturated Zone Site-Scale Flow Model* (BSC 2004 [DIRS 170037], Section 6.4.5.1).

Twelve UZ flow fields for the three future climates (Output DTNs: LB0701MOFEHMFF.001; LB0701GTFEHMFF.001; LB0702PAFEM10K.002) of monsoon, glacial transition, and post-10,000 years are converted by WTRISE V2.0 (2003 [DIRS 163453]) to account for a higher future water table. These future UZ flow fields are generated using the three-dimensional UZ flow fields (mo_10, mo_30, mo_50, and mo_90; gt_10, gt_30, gt_50, and gt_90; pkd_q1, pkd_q2, pkd_q3, and pkd_q4) of Section 6.6.3, which have been determined using a fixed, lower water table representing the current ambient conditions. In addition, the four present-day flow fields (Output DTN: LB0612PDFEHMFF.001, as well as the 12 future climate flow fields are the converted files readable to FEHM using T2FEHM V4.0 [DIRS 163161].

The 12 new flow fields are extracted using the WTRISE code for a rising-water-table case of 850 m elevation in the future by transecting the 12 flow fields with the current water table vertically at a new water table elevation.

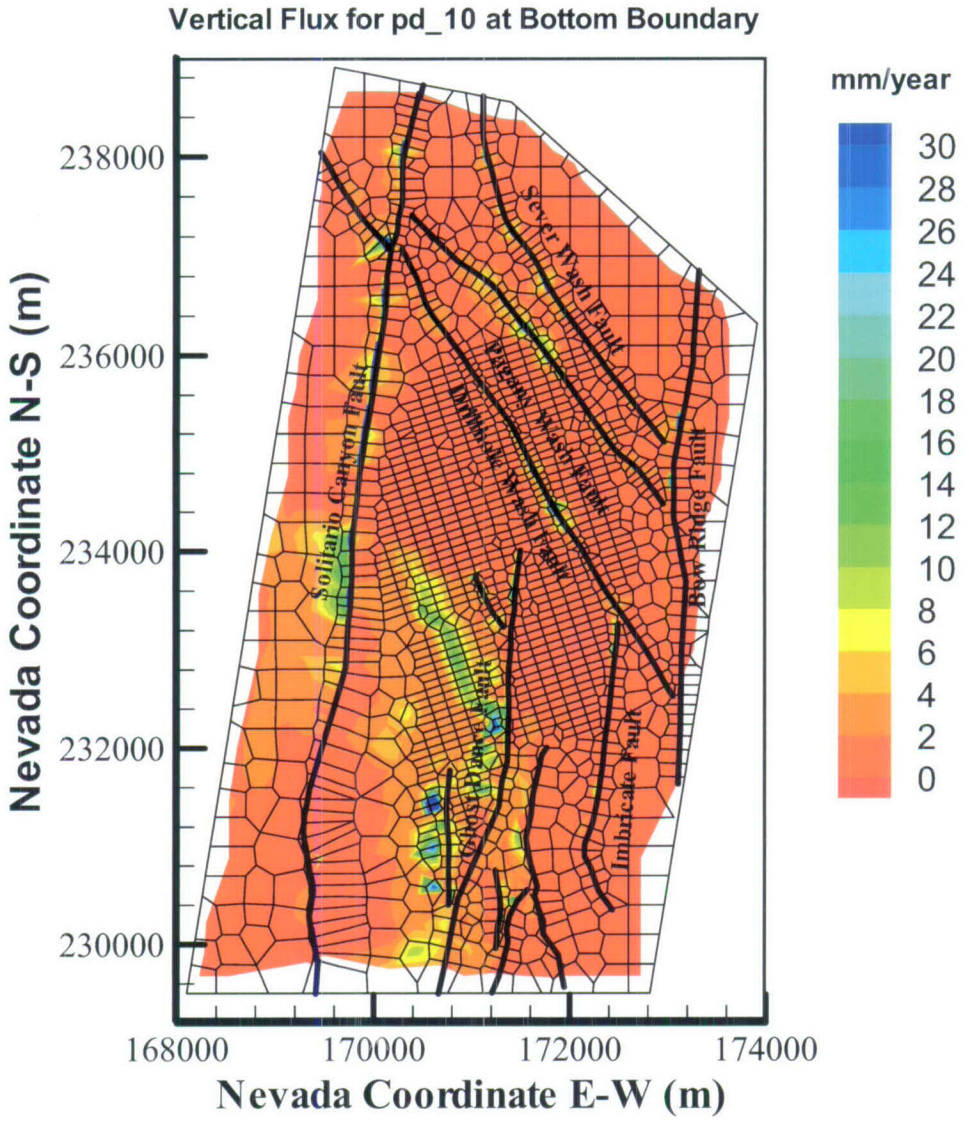

Output DTN: LB06123DPDUZFF.001.

Figure 6.6-5. Simulated Percolation Fluxes at the Water Table under the Present-Day, 10th Percentile Infiltration Scenario

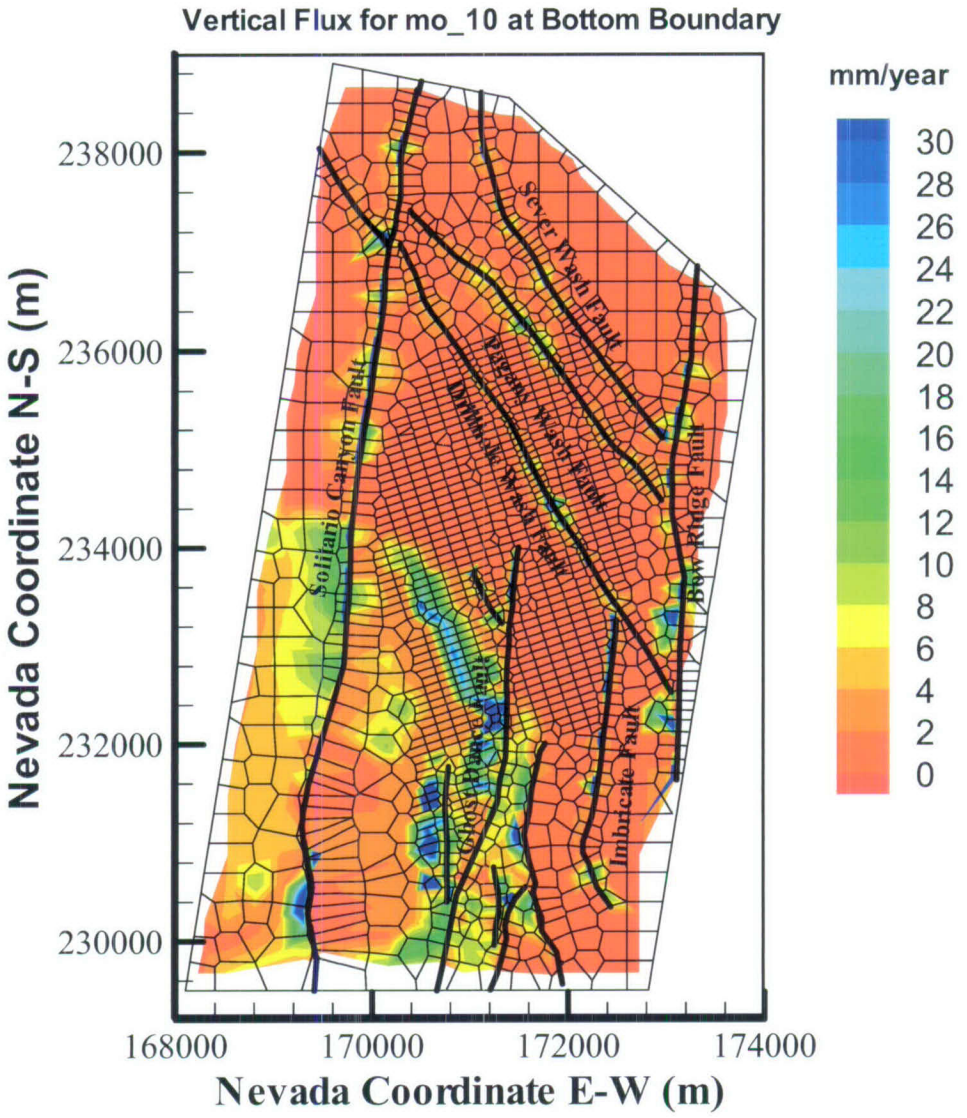

Output DTN: LB07013DMOUZFF.001.

Figure 6.6-6. Simulated Percolation Fluxes at the Water Table under the Monsoon, 10th Percentile Infiltration Scenario

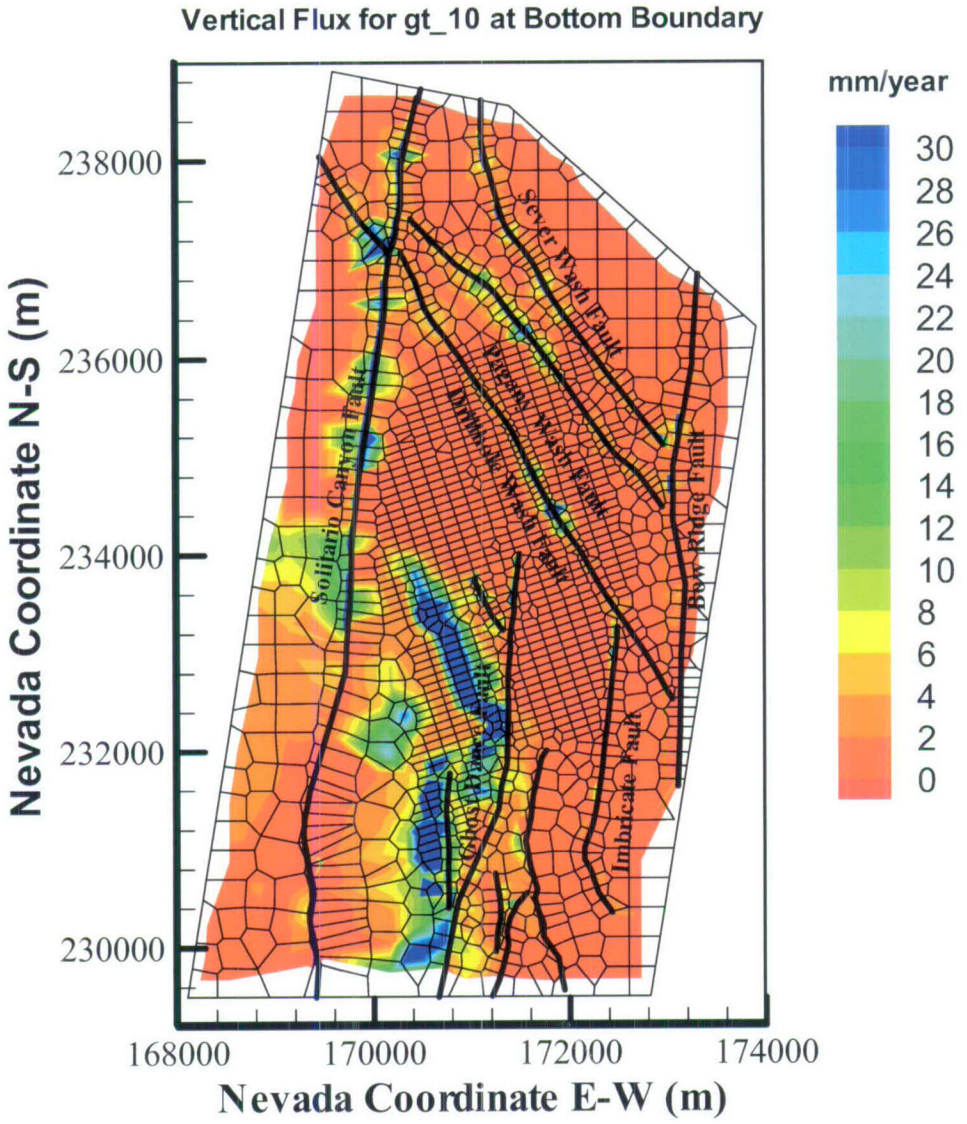

Output DTN: LB07013DGTUZFF.001.

Figure 6.6-7. Simulated Percolation Fluxes at the Water Table under the Glacial Transition, 10th Percentile Infiltration Scenario

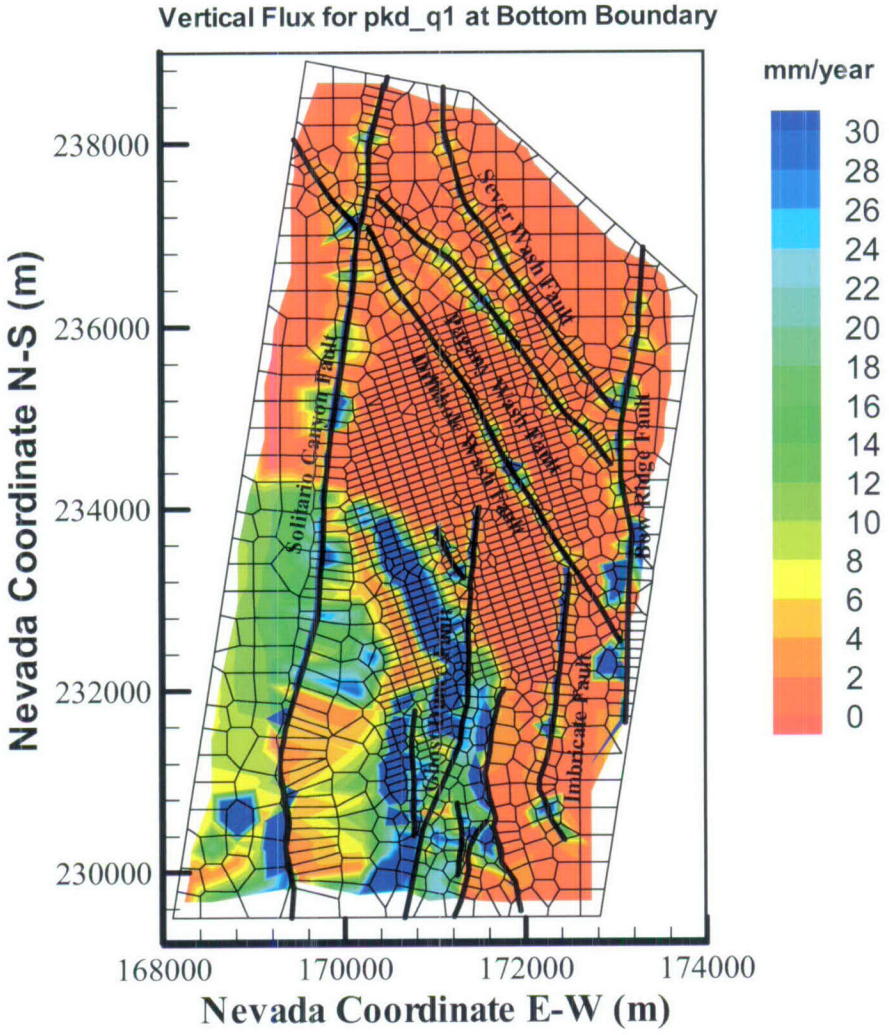

Output DTN: LB0702UZP10KFF.002.

Figure 6.6-8. Simulated Percolation Fluxes at the Repository Horizon under the Post-10,000-Year, 10th Percentile Infiltration Scenario

6.6.2.3 Matrix, Fracture, and Fault Flow Components

Tables 6.6-1, 6.6-22, and 6.6-3 list percentages of fracture-matrix flow components for non-fault zones and fault flow over the entire model domain and within the repository footprint at the three horizons of the TCw/PTn interface, the repository layer, and the water table. (In these 3 tables as well as in the rest of the documentation, the accuracy in the value of parameters is one less than the significant digits, as given, because the last significant digits are rounded.) Fracture and matrix percentages are computed for the non-fault zones only (i.e., excluding fault flow), where as fault flow percentages represent total vertical fracture-matrix flux through fault blocks over the entire model layer or the smaller region of the repository footprint at the three horizons. The three percentages sum to 100%. (Procedures for calculating the percentages are explained in Appendix E.) These statistics are calculated from vertical flow along each grid column, using the sixteen flow fields.

A statistical data as shown in Tables 6.6-1 and 6.6-2 indicate that fracture flow is dominant at both the top of the PTn unit and the repository horizons. At the repository level, fracture flow consists of about 60% to 80% of the total percolation fluxes over the entire model layer, and is mostly higher than 90% within the repository footprint. On the other hand, fault flow increases with depth. Over the entire model layer, fault flow at the TCw/PTn interface is about 1% to ~2%, increasing to 12% to 32% at the repository horizon, and reaching 44% to 65% at the water table. In comparison, fault flow over the smaller area, within the repository footprint, is low, at about 1%, at the TCw/PTN interface and repository horizon, but then increases to 16%–37% at the bottom boundary, the water table. Comparison of fault flow percentages at the TCw/PTn interface, the repository horizon, and the water table in Tables 6.6-1, 6.6-2, and 6.6-3 indicates that flow focusing into faults occurs mainly through the PTn unit and through the lower hydrogeological CHn unit.

Table 6.6-1. Comparison of the Water Flux through Matrix, Fractures of Non-fault Zones, and Faults as a Percentage of the Total Flux over the Entire Model Domain and within the Repository Footprint, at Three Different Horizons of the TCw/PTn Interface for the 16 Flow Fields

Simulation Designation	Flux at TCw/PTn Interface over Entire Model Domain (%)			Flux at TCw/PTn Interface within Repository Footprint (%)		
	Fracture	Matrix	Fault	Fracture	Matrix	Fault
pd_10	98.66	0.04	1.31	99.01	0.04	0.95
pd_30	98.33	0.05	1.62	98.76	0.04	1.20
pd_50	98.54	0.03	1.43	98.81	0.03	1.16
pd_90	98.34	0.05	1.61	98.64	0.04	1.32
mo_10	98.06	0.06	1.87	98.60	0.06	1.35
mo_30	98.13	0.07	1.80	98.61	0.06	1.33
mo_50	98.33	0.06	1.61	98.72	0.05	1.22
mo_90	98.03	0.04	1.93	98.55	0.03	1.42
gt_10	98.30	0.10	1.59	98.69	0.10	1.21
gt_30	98.11	0.11	1.78	98.59	0.10	1.32
gt_50	98.08	0.07	1.84	98.59	0.07	1.34
gt_90	97.99	0.09	1.91	98.50	0.08	1.41
pkd_q1	98.10	0.03	1.87	98.61	0.02	1.37

Table 6.6-1. Comparison of the Water Flux through Matrix, Fractures of Non–fault Zones, and Faults as a Percentage of the Total Flux over the Entire Model Domain and within the Repository Footprint at Three Different Horizons at the TCw/PTn Interface for the 16 Flow Fields (Continued)

Simulation Designation	Flux at TCw/PTn Interface over Entire Model Domain (%)			Flux at TCw/PTn Interface within Repository Footprint (%)		
	Fracture	Matrix	Fault	Fracture	Matrix	Fault
pkd_q2	98.54	0.03	1.43	98.82	0.03	1.16
pkd_q3	98.38	0.03	1.59	98.68	0.02	1.30
pkd_q4	98.02	0.06	1.93	98.53	1.42	1.42

Output DTNs: LB06123DPDUZFF.001; LB07013DMOUZFF.001; LB07013DGTUZFF.001; LB0702UZP10KFF.002; LB0705FLOWCOMP.001.

PTn=Paintbrush nonwelded hydrogeologic unit; TCw=Tiva Canyon welded hydrogeologic unit.

Table 6.6-2. Comparison of the Water Flux through Matrix, Fractures of Non-fault Zones, and Faults as a Percentage of the Total Flux over the Entire Model Domain and within the Repository Footprint at Three Different Horizons of the Repository Level for the 16 Flow Fields

Simulation Designation	Flux at Entire Repository Layer (%)			Flux at Repository Horizon within Repository Footprint (%)		
	Fracture	Matrix	Fault	Fracture	Matrix	Fault
pd_10	58.42	9.71	31.87	94.20	5.16	0.65
pd_30	67.14	7.90	24.95	95.96	2.73	1.31
pd_50	64.74	7.51	27.75	96.68	2.03	1.28
pd_90	74.04	6.69	19.27	97.76	1.24	1.00
mo_10	71.64	13.26	15.10	91.14	8.00	0.86
mo_30	73.34	9.35	17.31	94.54	4.04	1.42
mo_50	68.18	8.13	23.70	95.11	3.55	1.34
mo_90	79.63	6.33	14.04	97.89	1.03	1.08
gt_10	64.63	17.49	17.88	86.90	12.31	0.79
gt_30	71.33	10.27	18.40	93.50	5.05	1.45
gt_50	71.29	9.12	19.59	94.14	4.43	1.42
gt_90	78.97	7.43	13.60	96.95	2.06	0.99
Pkd_q1	79.14	9.02	11.84	95.79	3.32	0.89
Pkd_q2	65.34	7.24	27.42	96.88	1.84	1.29
pkd_q3	72.36	6.93	20.71	97.09	1.49	1.42
pkd_q4	79.40	6.71	13.89	97.58	1.37	1.05

Output DTNs: LB06123DPDUZFF.001; LB07013DMOUZFF.001; LB07013DGTUZFF.001; LB0702UZP10KFF.002; LB0705FLOWCOMP.001.

Table 6.6-3. Comparison of the Water Flux through Matrix, Fractures of Non-fault Zones, and Faults as a Percentage of the Total Flux over the Entire Model Domain and within the Repository Footprint at Three Different Horizons of the Water Table for the 16 Flow Fields

Simulation Designation	Flux at Entire Water Table (%)			Flux at Water Table within Repository Footprint (%)		
	Fracture	Matrix	Fault	Fracture	Matrix	Fault
pd_10	20.24	14.40	65.36	54.21	23.53	22.26
pd_30	25.56	12.78	61.66	50.58	16.50	32.92
pd_50	22.35	12.72	64.92	47.26	15.70	37.04
pd_90	28.72	7.09	64.19	57.97	5.95	36.08
mo_10	29.13	21.71	49.16	52.90	26.63	20.47
mo_30	31.25	14.83	53.91	51.38	15.93	32.69
mo_50	25.99	15.39	58.62	48.80	17.10	34.10
mo_90	29.17	8.17	62.66	58.42	5.94	35.64
gt_10	30.35	25.98	43.68	51.55	32.52	15.93
gt_30	34.57	15.44	49.99	52.30	16.85	30.85
gt_50	28.42	17.01	54.56	49.21	17.60	33.19
gt_90	31.31	10.58	58.11	57.61	7.71	34.68
pkd_q1	26.18	18.84	54.98	56.95	19.96	23.09
pkd_q2	22.84	11.93	65.23	50.42	16.87	32.70
pkd_q3	23.50	14.01	62.50	47.89	15.10	37.01
pkd_q4	29.88	8.95	61.17	58.55	6.26	35.18

Output DTNs: LB06123DPDUZFF.001; LB07013DMOUZFF.001; LB07013DGTUZFF.001; LB0702UZP10KFF.002; LB0705FLOWCOMP.001.

6.6.2.4 Distributions of Percolation Fluxes within the Repository Footprint

Percolation fluxes at the repository horizon and within the repository footprint can be further analyzed using a frequency distribution plot. This plot displays the averaged percentage of the repository area subject to a particular percolation rate. Note that the normalized flux rates are determined by normalizing an infiltration value with respect to the averaged infiltration rate for the scenario. For example, "1" stands for the normalized flux rate corresponds to 3.03, 6.74, 11.03, and 16.89 mm/yr (Tables 6.1-2 and 6.1-3), respectively, for the four 10th percentile infiltration scenarios. The information, as shown in Figures 6.6-9, 6.6-10, 6.6-11, and 6.6-12 (see Appendix E for calculation details), is important to drift-scale modeling studies of flow and transport at drifts and flow-redistributing phenomena through the TSw. Figures 6.6-9 to 6.6-12 show the frequency distribution of normalized percolation flux within the repository horizon for the four 10th percentile infiltration rates of the four climates.

Figures 6.6-9 to 6.6-12 indicate that the highest flux frequencies, occurring at 14% to 24%, have normalized fluxes of about 1.2 to 1.5, except for the case of the glacial transition 10th percentile infiltration (gt_10), which has the highest frequency flux at the lowest range of normalized fluxes. In general, the areas with normalized percolation fluxes greater than 3 are very small, taking up less than 1% of the total repository area.

The results of the 16 flow field analyses, as shown in Figure 6.6-9–6.6.-12, can be used to define a cumulative flux-frequency distribution, as shown in Figure 6.6-13 (see Appendix E for details of the calculation). The cumulative frequency of Figure 6.6-13 can be used, for example, in selecting ambient-flow-boundary conditions for drift-scale modeling. The similarity in flux distribution patterns for the 16 flow fields helps to define a flux-distribution factor for seepage estimation in the TSPA-LA calculations.

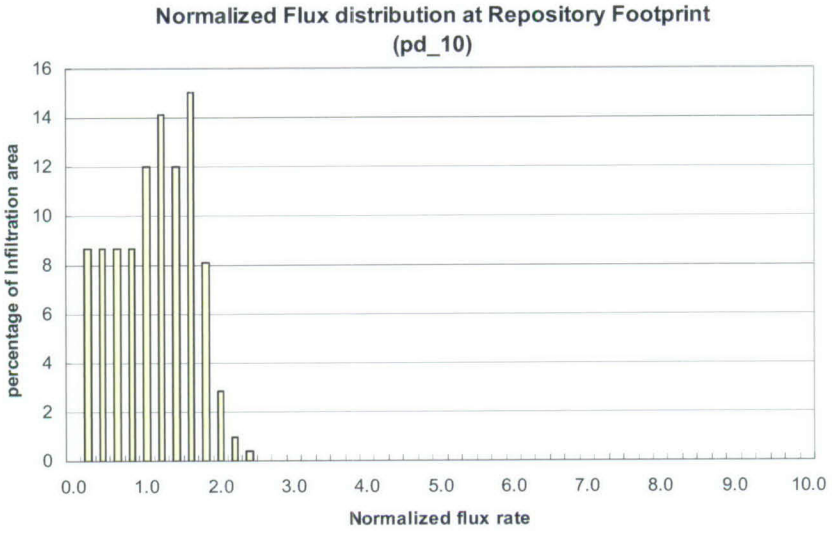

Output DTN: LB06123DPDUZFF.001.

Figure 6.6-9. Areal Frequency and Distribution of Simulated Percolation Fluxes within the Repository Domain Normalized to the Present-Day, 10th Percentile Infiltration Rate

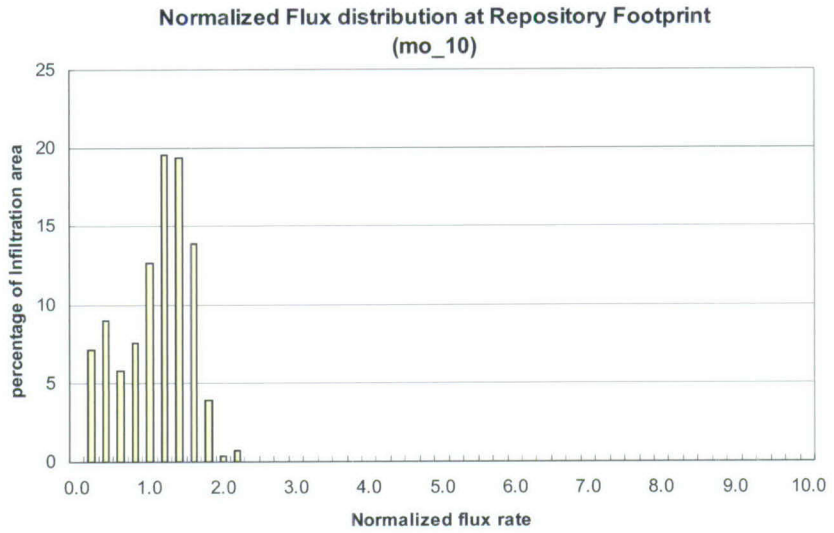

Output DTN: LB07013DMOUZFF.001.

Figure 6.6-10. Areal Frequency and Distribution of Simulated Percolation Fluxes within the Repository Domain Normalized to the Monsoon, 10th Percentile Infiltration Rate

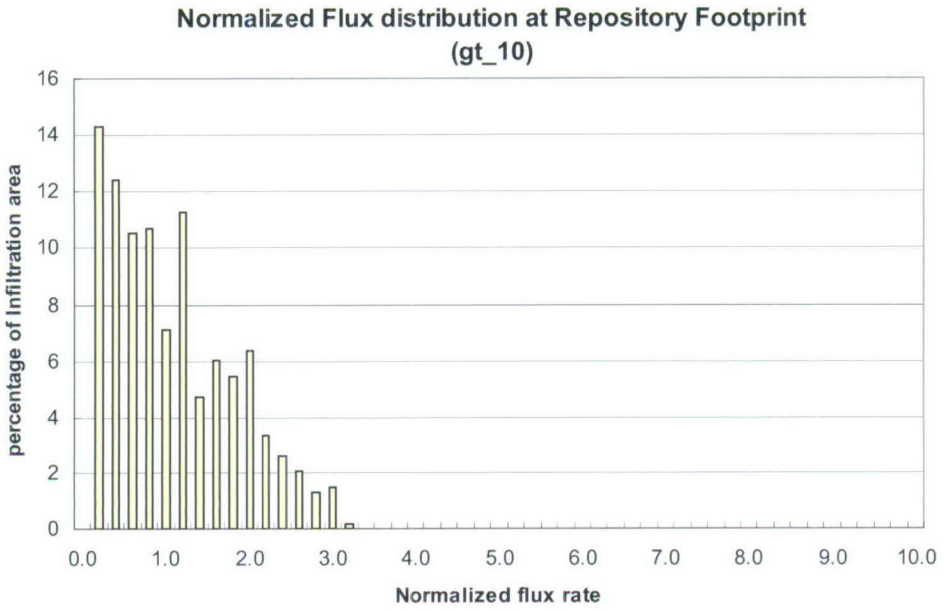

Output DTN: LB07013DGTUZFF.001.

Figure 6.6-11. Areal Frequency and Distribution of Simulated Percolation Fluxes within the Repository Domain Normalized to the Glacial Transition, 10th Percentile Infiltration Rate

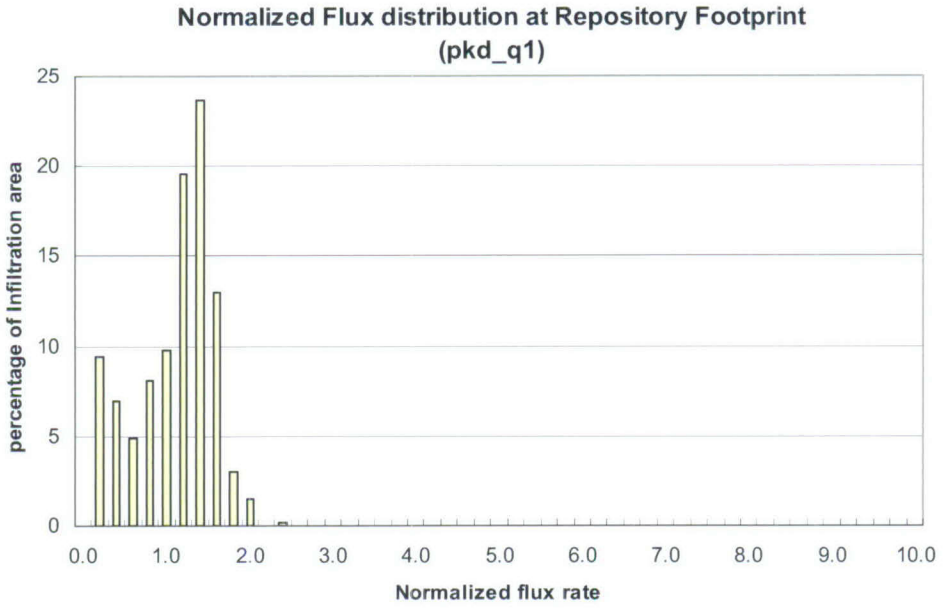

Output DTN: LB0702UZP10KFF.002.

Figure 6.6-12. Areal Frequency and Distribution of Simulated Percolation Fluxes within the Repository Domain Normalized to the Post-10,000-year, 10th Percentile Infiltration Rate

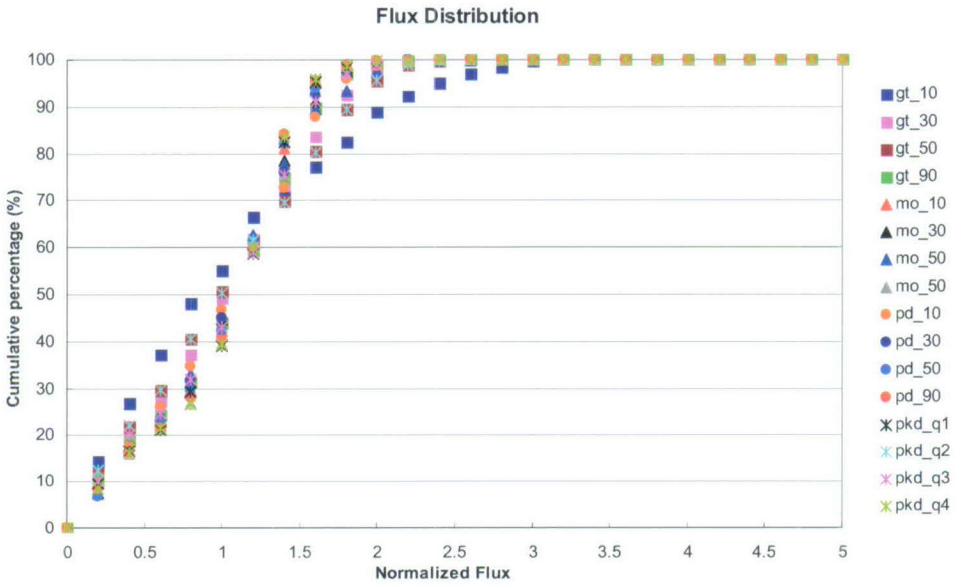

Output DTNs: LB06123DPDUZFF.001; LB07013DMOUZFF.001; LB07013DGTUZFF.001; LB0702UZP10KFF.002.

Figure 6.6-13. Cumulative Flux Distribution and Range as Functions of Normalized Percolation Flux within the Repository from the 16 Flow Fields of Four Climates

6.7 TRACER TRANSPORT TIMES

This section summarizes simulated tracer transport using the 16 UZ flow fields. The results present an evaluation of tracer or radionuclide transport processes from the repository to the water table (saturated zone) within the mountain, including the effects of different infiltration scenarios, advection, diffusion, and adsorption. Tracer-transport studies described in this section provide insight into UZ flow patterns, groundwater travel times, and tracer transport processes.

6.7.1 Methodology and Transport Parameters

Simulation results and analyses in this section are based on transport studies of conservative and reactive tracers, using the T2R3D V1.4 code (1999 [DIRS 146654]). The dual-permeability modeling approach with the three-dimensional TSPA-LA grid (Figure 6.1-1), as discussed in Section 6.1.1, is used in the transport simulations. In the tracer transport modeling, the 16 steady-state, three-dimensional flow fields of Section 6.6 are directly used as input to the T2R3D code for modeling transport from the repository to the water table.

To assess tracer transport times from the repository to the water table, tracers are treated as conservative (nonadsorbing) and reactive (adsorbing) components transported through the unsaturated zone In both cases, hydrodynamic/mechanical dispersion through the fracture–matrix system is ignored, because sensitivity studies indicate that mechanical dispersion has an insignificant effect on the cumulative breakthrough curves of tracers at the water table (Wu et al. 2002 [DIRS 160195]). A constant molecular diffusion coefficient of 3.2×10^{-11} m^2/s is used for matrix diffusion of the conservative component, and 1.6×10^{-10} m^2/s is used for the reactive

component. The range of matrix diffusion coefficients is close to the values of typical diffusion coefficients for ions, anions and cations. For example, the diffusion coefficients of ions typically range from 3.0×10^{-10} to 20.0×10^{-10} m^2/s (Langmuir 1997 [DIRS 100051], p. 65), which summarizes that those of anions $4.14 \times 10^{-10} - 52.7 \times 10^{-10}$ m^2/s, and cations $1.53 \times 10^{-10} - 93.1 \times 10^{-10}$ m^2/s (Lerman 1979 [DIRS 182304], Section 3.2, Table 3.1).

The two diffusion coefficients are multiplied by porosity and tortuosity in the simulation to account for various units. In the case of a reactive or adsorbing tracer, several K_d values are used, as given in Table 6.7-1, for different units. These values were selected to approximate those for neptunium (^{237}Np) transport (DTNs: LA0010JC831341.001 [DIRS 162476]; LA0010JC831341.002 [DIRS 153321]; LA0010JC831341.003 [DIRS 153322]; LA0010JC831341.004 [DIRS 153323]; LA0010JC831341.005 [DIRS 153320]; LA0010JC831341.006 [DIRS 153318]; LA0010JC831341.007 [DIRS 153319]). For a conservative tracer, K_d is set to zero. These molecular diffusion coefficients and K_d values are selected to represent technetium and neptunium. Model parameters such as porosity and rock grain density were taken from the matrix and thermal properties (DTNs: LB0207REVUZPRP.002 [DIRS 159672]; LB0210THRMLPRP.001 [DIRS 160799]).

Transport simulations were conducted for 1,000,000 years using 16 infiltration rates of four climates. At the start of each simulation, an initial, constant concentration source was instantaneously released from the fracture continuum gridblocks representing the repository.

Table 6.7-1. K_d Values Used for Reactive Tracer Transport in Different Hydrogeologic Units

Hydrogeologic Unit	K_d (cc/g)
Zeolitic matrix in CHn	4.0
Vitric matrix in CHn	1.0
Matrix in TSw	1.0
Fault matrix in CHn	1.0
Fractures and the matrix in the rest of units	0.0

Sources: DTNs: LA0010JC831341.001 [DIRS 162476], LA0010JC831341.002 [DIRS 153321], LA0010JC831341.003 [DIRS 153322], LA0010JC831341.004 [DIRS 153323], LA0010JC831341.005 [DIRS 153320], LA0010JC831341.006 [DIRS 153318], and LA0010JC831341.007 [DIRS 153319].

CHn = Calico Hills nonwelded hydrogeologic unit; TSw = Topopah Spring welded hydrogeologic unit.

6.7.2 Simulation Scenarios

For each flow simulation, as listed in Table 6.2-6, there are two transport runs, one for conservative (tc_*) and one for reactive (np_*) tracer transport. Table 6.7-2 summarize a total of 16 × 2 tracer-fracture-release simulation scenarios, corresponding to the 16 UZ flow fields for the 16 infiltration maps of four climates, respectively.

Table 6.7-2. Transport Simulation Scenarios: Data Files and Corresponding 16 Flow Fields and Infiltration Maps

Designation/ Transport Simulation	Designation/ Corresponding Flow Simulation	Infiltration Map Corresponding Infiltration Maps
tc_pd_10 np_pd_10	pd_10	Present-day 10th percentile infiltration (DTNs: SN0609T0502206.028 [DIRS 178753])
tc_pd_30 np_pd_30	pd_30	Present-day day 30th percentile infiltration (DTNs: SN0609T0502206.028 [DIRS 178753])
tc_pd_50 np_pd_50	pd_50	Present-day 50th percentile infiltration (DTNs: SN0609T0502206.028 [DIRS 178753])
tc_pd_90 np_pd_90	pd_90	Present-day 90th percentile infiltration (DTNs: SN0609T0502206.028 [DIRS 178753])
tc_mo_10 np_mo_10	mo_10	Monsoon 10th percentile infiltration SN0609T0502206.024 [DIS 179063]
tc_mo_30 np_mo_30	mo_30	Monsoon 30th percentile infiltration SN0609T0502206.024 [DIS 179063]
tc_mo_50 np_mo_50	mo_50	Monsoon 50th percentile infiltration SN0609T0502206.024 [DIS 179063]
tc_mo_90 np_mo_90	mo_90	Monsoon 90th percentile infiltration SN0609T0502206.024 [DIS 179063]
tc_gt_10 np_gt_10	gt_10	Glacial-transition 10th percentile infiltration SN0609T0502206.029 [DIRS 178862])
tc_gt_30 np_gt_30	gt_30	Glacial-transition 30th percentile infiltration SN0609T0502206.029 [DIRS 178862])
tc_gt_50 np_gt_50	gt_50	Glacial-transition 50th percentile infiltration SN0609T0502206.029 [DIRS 178862])
tc_gt_90 np_gt_90	gt_90	Glacial-transition 90th percentile infiltration SN0609T0502206.029 [DIRS 178862])
tc_pkd_q1 np_pkd_q1	pkd_q1	Post-10,000-yr, 10th percentile infiltration (DTN: LB0702UZP10KFF.002)
tc_pkd_q2 np_pkd_q2	pkd_q2	Post-10,000-yr, 30th percentile infiltration (DTN: LB0702UZP10KFF.002)
tc_pkd_q3 np_pkd_q3	pkd_q3	Post-10,000-yr, 50th percentile infiltration (DTN: LB0702UZP10KFF.002)
tc_pkd_q4 np_pkd_q4	pkd_q4	Post-10,000-yr, 90th percentile infiltration (DTN: LB0702UZP10KFF.002)

Output DTNs: LB06123DPDUZFF.001; LB07013DMOUZFF.001; LB07013DGTUZFF.001; LB0702UZP10KFF.002; LB0705TRAVTIME.001.

6.7.3 Simulation Results and Analyses

Tracer transport times (since release from the repository to the water table) were analyzed using a cumulative fractional breakthrough curve, as shown in Figures 6.7-1 for nonadsorbing tracer transport, and 6.7-2 for adsorbing tracer transport, for 1 million years. The fractional mass breakthrough in these figures is defined as the cumulative mass of a tracer arriving at the water table over the entire bottom model boundary over time, normalized by the total mass of the component initially introduced at the repository. The two figures show a wide range of tracer

transport times with different infiltration rates and types of tracers considered in the 32 simulations (listed in Table 6.7-2).

As indicated by Figures 6.7-1 and 6.7-2, the predominant factors in controlling tracer transport are (1) surface-infiltration rates or net water recharge and (2) adsorption effects (i.e., whether the tracer is conservative or reactive). Statistics of tracer transport times for 10% and 50% mass breakthrough at the water table for the 32 simulation scenarios are given in Table 6.7-3. Figure 6.7-3 correlates average infiltration rates and tracer transport times at 50% mass breakthrough for the 32 simulation scenarios. Figures 6.7-1, 6.7-2, 6.7-3, and the statistical data of Tables 6.7-3 and 6.7-5 show the following:

- Tracer transport times vary inversely to the average surface infiltration (net water recharge) rate over the model domain (Figure 6.7-3). When the average infiltration rate increases from 3 to 70 mm/yr, average tracer transport (50% breakthrough) times decrease by more than two orders of magnitude for both adsorbing and nonadsorbing species.

- Nonadsorbing tracers migrate (from the repository to the water table) one to two orders of magnitude faster than an adsorbing tracer under the same infiltration condition (Figure 6.7-3).

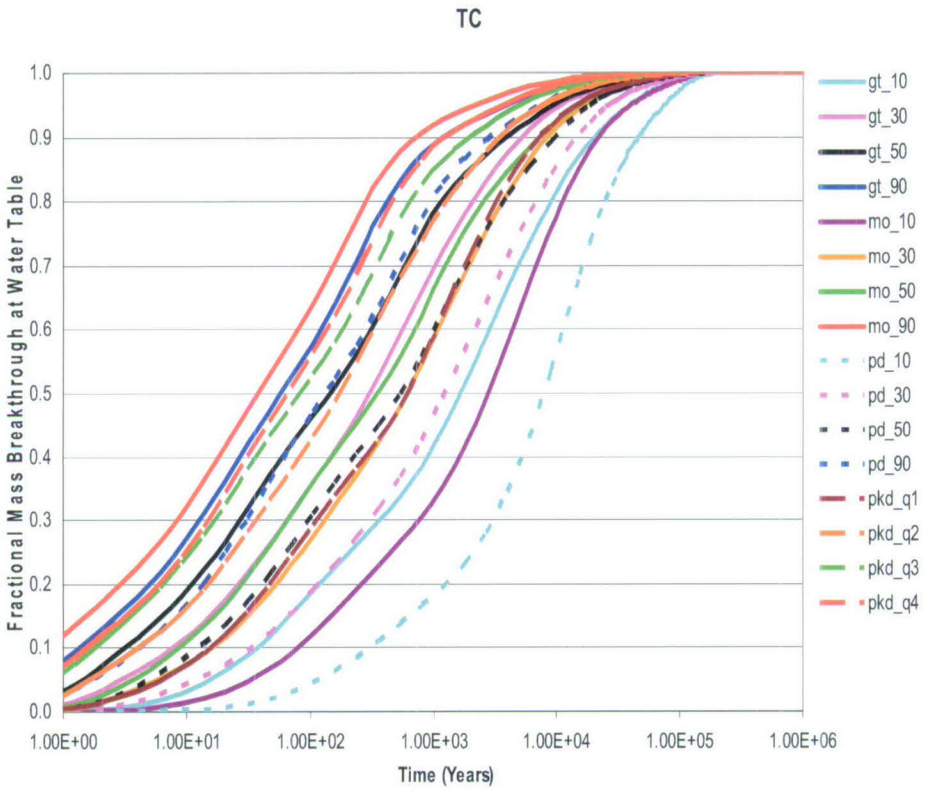

Output DTN: LB0705TRAVTIME.001.

NOTE: The tracer is released instantaneously from repository fracture elements at the start time of simulation.

Figure 6.7-1. Simulated Breakthrough Curves of Cumulative Tracer Mass Arriving at the Water Table, after Release from Fractures in the Repository, Using the 16 Flow Fields with the Sixteen Infiltration Scenarios of Present-Day, Monsoon, Glacial Transition, and Post-10,000-Year Climates for Nonadsorbing Tracers

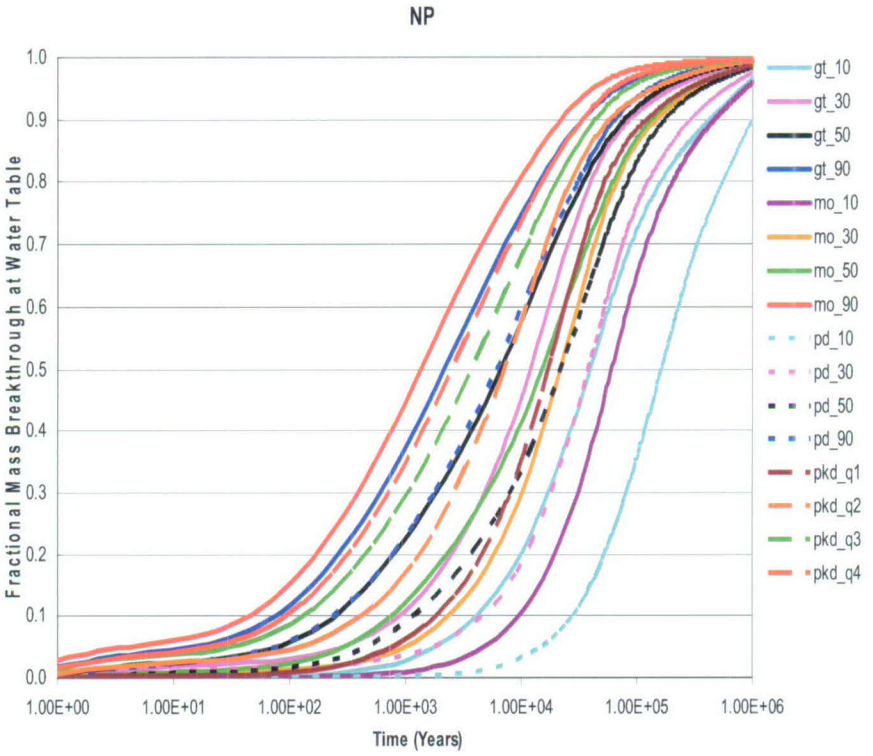

Output DTN: LB0705TRAVTIME.001.

NOTE: The tracer is released instantaneously from repository fracture elements at the start time of simulation.

Figure 6.7-2. Simulated Breakthrough Curves of Cumulative Tracer Mass Arriving at the Water Table, after Release from Fractures in the Repository, Using the 16 Flow Fields with the Sixteen Infiltration Scenarios of Present-Day, Monsoon, Glacial Transition, and Post-10,000-Year Climates for Adsorbing Tracers

Table 6.7-3. Tracer Transport Times at 10 Percent and 50 Percent Mass Breakthrough Times for 32 Transport Simulation Scenarios, Corresponding to the 16 Flow Fields with the 16 Infiltration Maps

Designation/ Transport Simulation	Types of Tracer	10% Breakthrough Times (years)	50% Breakthrough Times (years)
gt_10_tc	Nonadsorbing	37.4	1,679.1
gt_10_np	Adsorbing	4,160.7	39,688.6
gt_30_tc	Nonadsorbing	7.9	304.1
gt_30_np	Nonadsorbing	883.2	12,098.2
gt_50_tc	Adsorbing	3.2	144.1
gt_50_np	Adsorbing	251.1	6,738.2
gt_90_tc	Nonadsorbing	1.3	58.9
gt_90_np	Adsorbing	78.2	2,225.3
mo_10_tc	Nonadsorbing	79.6	2,828.1
mo_10_np	Adsorbing	9,640.5	60,724.6
mo_30_tc	Nonadsorbing	16.2	610.5
mo_30_np	Adsorbing	2,391.7	21,979.7
mo_50_tc	Nonadsorbing	8.7	349.2
mo_50_np	Adsorbing	754.9	15,325.4
mo_90_tc	Nonadsorbing	0.8	38.6
mo_90_np	Adsorbing	44.9	1,384.8
pd_10_tc	Nonadsorbing	314.4	8,081.3
pd_10_np	Adsorbing	27,884.1	166,019.7
pd_30_tc	Nonadsorbing	34.9	1,270.4
pd_30_np	Nonadsorbing	4,690.4	38,486.4
pd_50_tc	Adsorbing	12.6	536.8
pd_50_np	Adsorbing	1,186.7	22,398.8
pd_90_tc	Nonadsorbing	4.2	135.2
pd_90_np	Adsorbing	246.6	6,066.6
pkd_q1_tc	Nonadsorbing	15.8	614.1
pkd_q1_np	Adsorbing	1,869.1	17,518.2
pkd_q2_tc	Nonadsorbing	4.2	173.5
pkd_q2_np	Adsorbing	429.0	7,412.6
pkd_q3_tc	Nonadsorbing	1.8	82.5
pkd_q3_np	Adsorbing	137.9	3,756.2
pkd_q4_tc	Nonadsorbing	1.6	65.4
pkd_q4_np	Adsorbing	96.5	2,537.9

Output DTN: LB0705TRAVTIME.001.

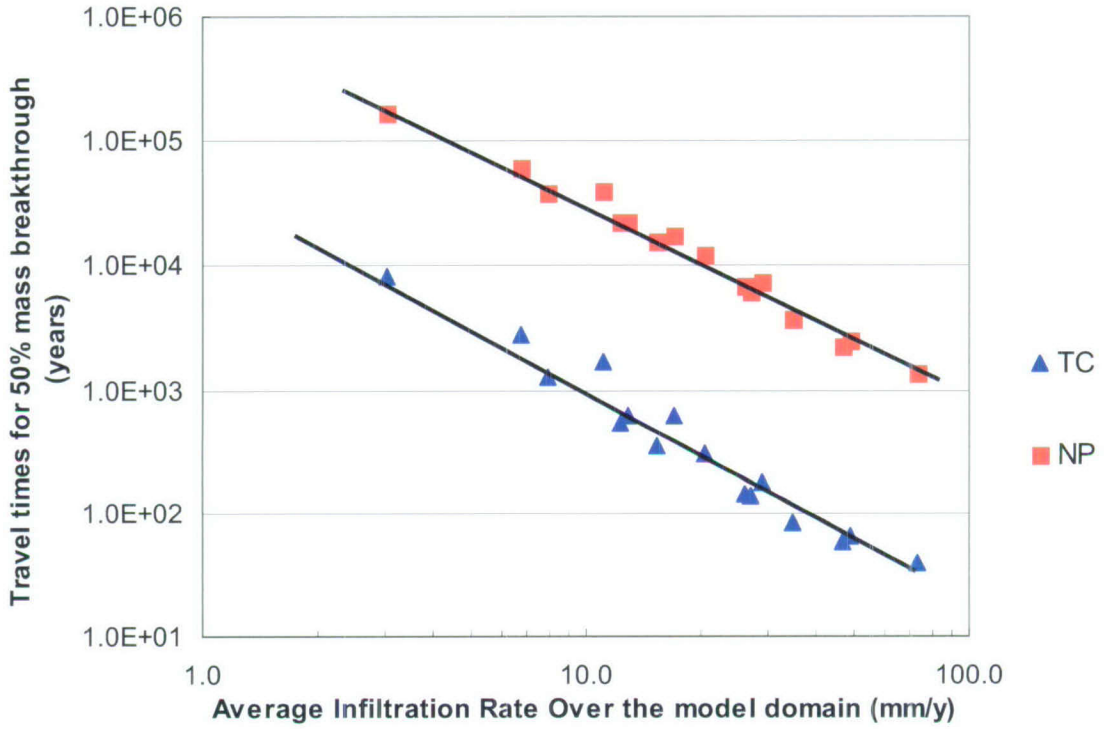

Output DTN: LB0705TRAVTIME.001.

NOTE: Some pairs of points for "A" and "B" simulations are superimposed. See Tables 6.7-4 and 6.7-5.

Figure 6.7-3. Correlation of Average Infiltration Rates and Tracer Transport Times at 50 Percent Mass Breakthrough for the 32 Tracer-Fracture-Release Simulation Scenarios

The tracer-transport-simulation results can also be used to estimate potential locations or areas where radionuclides are most likely to break through along high-flux flow paths at the water table. Figures 6.7-4, 6.7-5, 6.7-6, and 6.7-7 show cumulative and normalized mass arrival contours at the water table at 1,000 and 1,000,000 years, respectively. The cumulative mass arrival is defined as cumulative mass arriving at each grid column of the water table over time, normalized by the total initial mass released at the repository. These figures present examples of breakthrough at the water table for conservative and reactive tracer transport with the present-day, 10% percentile infiltration rate.

Figures 6.7-4 and 6.7-5 compare percentage of mass arrival contours for a conservative and reactive tracer, respectively, at the water table after 1,000 years, simulated using the present-day, 10th percentile infiltration of the base-case flow field (pd_10). The two figures clearly indicate a significant difference between the two tracer modeling results in distributions of tracer mass arrivals along the water table. Without adsorption, in 1,000 years the conservative tracer (technetium) has a much larger area of breakthrough, covering the entire area directly below the repository footprint, and spreading to the east in the north. At this time, nearly 20% of the total initial mass of conservative tracers has arrived at the water table (see Figure 6.7-1), whereas only about 1 percent of the reactive tracer (neptunium) breaks through, and only along and near the major faults, owing to adsorption effects in the rock matrix.

At a later time of 1,000,000 years, Figures 6.7-6 and 6.7-7 show very similar mass arrival contours for the two tracers below the repository footprint. This is because 90%–100% of both tracers have arrived at the water table at this time, which are transported under the same flow field. The 1,000- and 1,000,000-year contours are used to illustrate the predominantly downward percolation flow patterns, early influence of faults (especially the in-block faults), and small long-term effects of slow diffusion. The flow patterns are for hypothetical nonsorbing and sorbing tracers without taking into consideration radioactive decay, which reduces the concentrations. The information depicted in Figures 6.7-6 and 6.7-7 does not provide direct feeds to TSPA analyses; radionuclide transport is studied in detail in the downstream transport models.

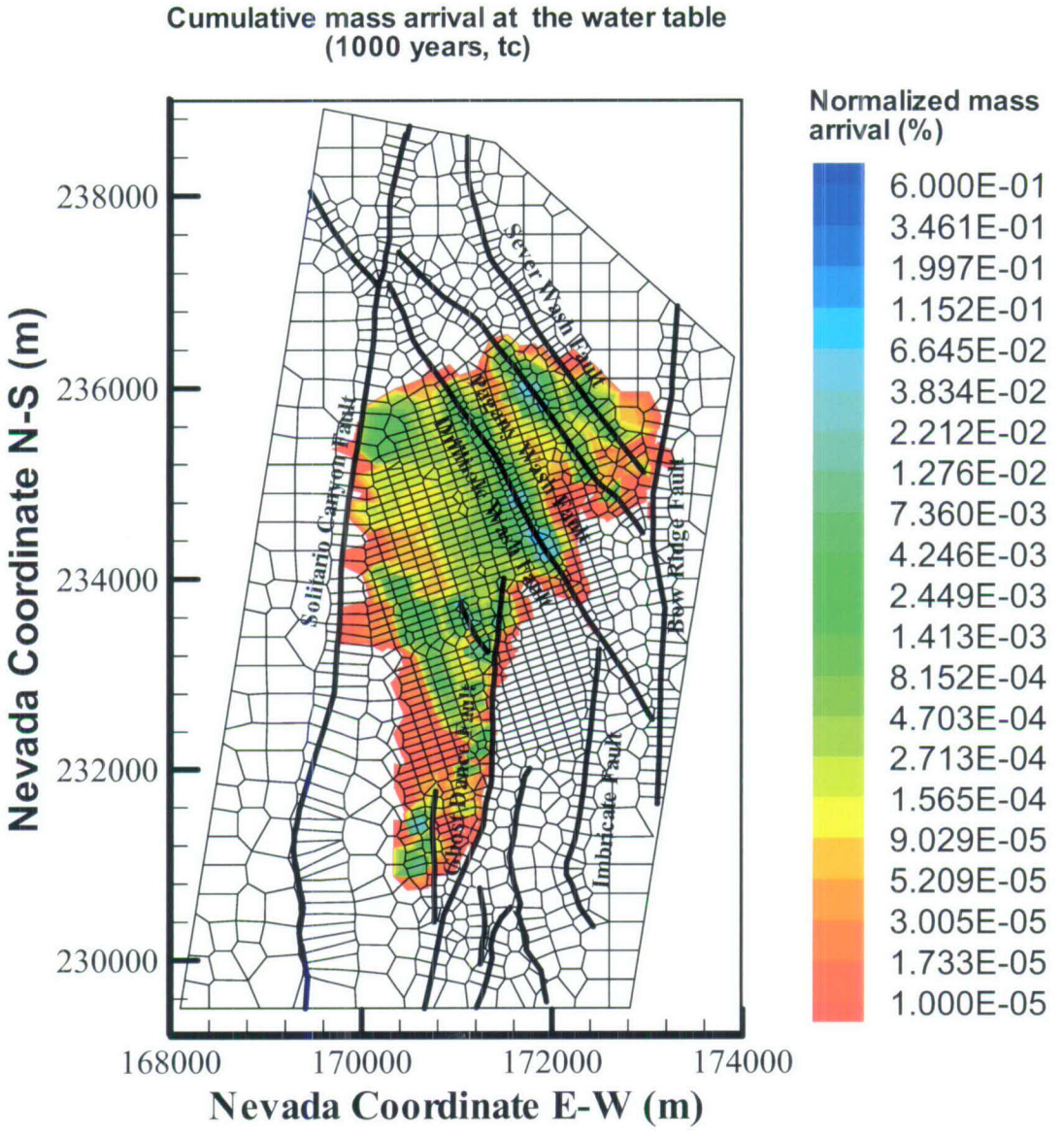

Output DTN: LB0705TRAVTIME.001.

Figure 6.7-4. Simulated Cumulative, Normalized Mass Arrival Contours of a Conservative Tracer at the Water Table after 1,000 Years, Indicating Potential Breakthrough Locations at the Time, Using the Present- Day, 10th Percentile Infiltration Scenario

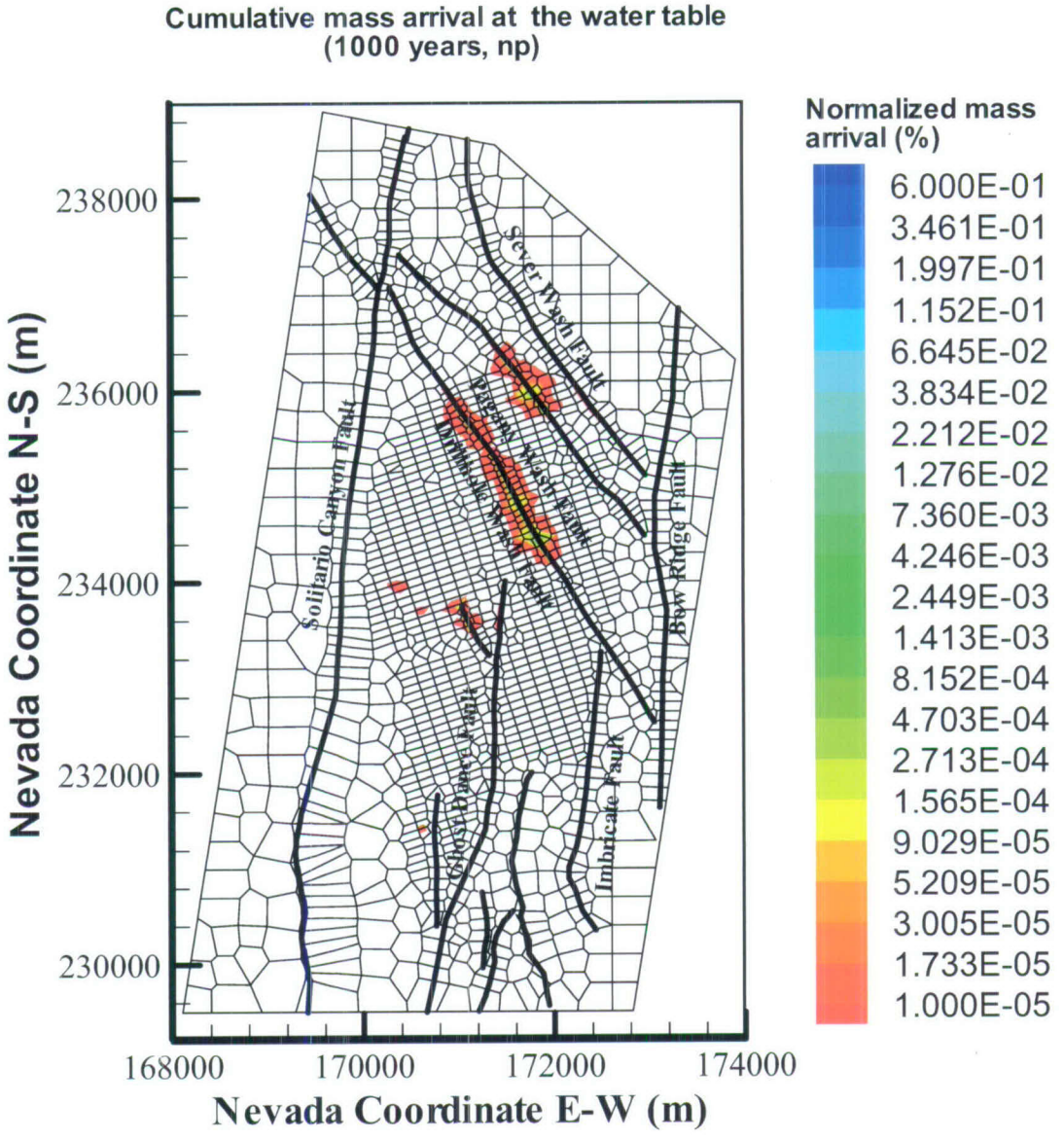

Output DTN: LB0705TRAVTIME.001.

Figure 6.7-5. Simulated Cumulative, Normalized Mass Arrival Contours of a Reactive Tracer at the Water Table after 1,000 Years, Indicating Potential Breakthrough Locations at the Time, Using the Present-Day, 10th Percentile Infiltration Scenario

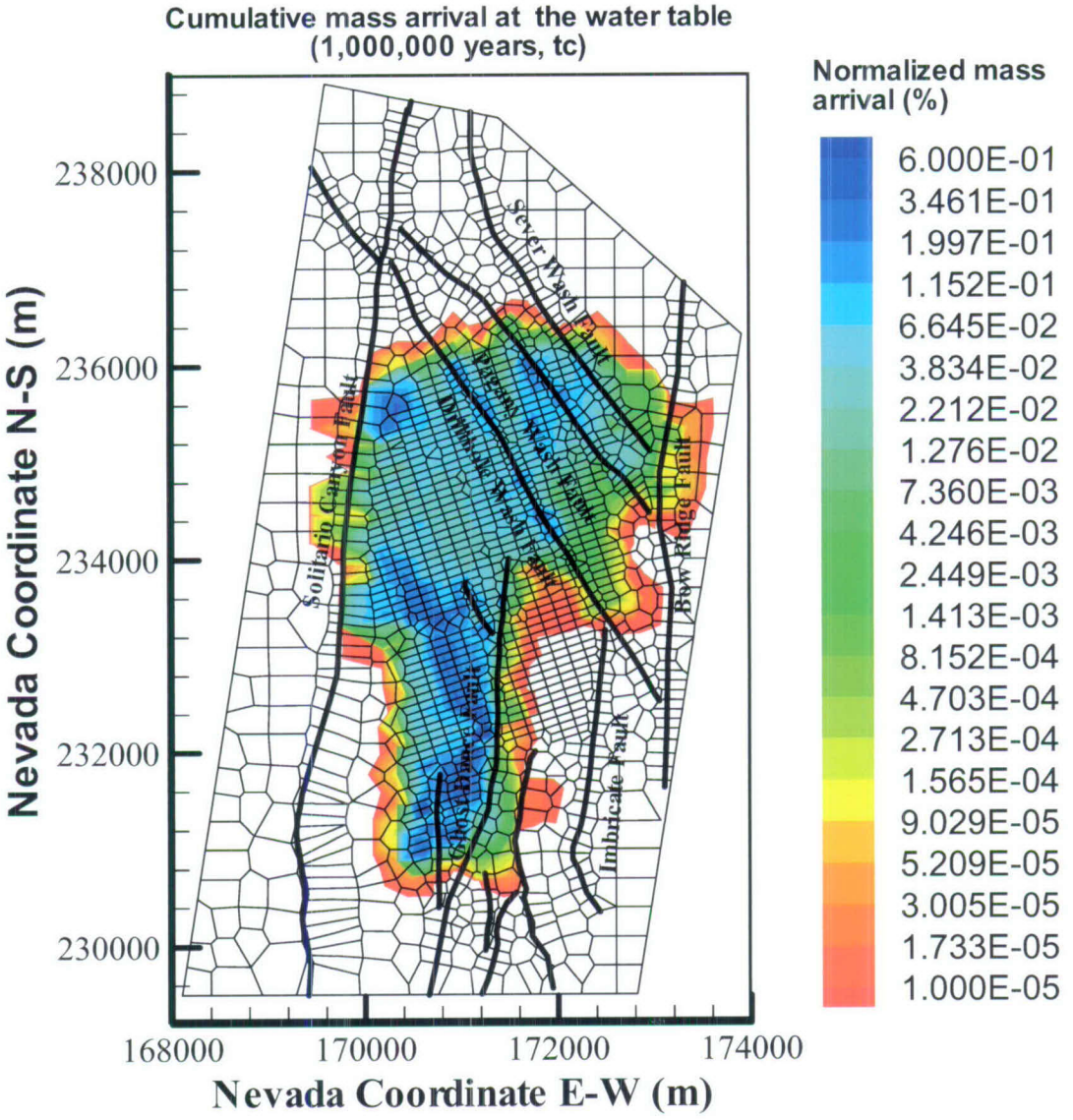

Output DTN: LB0705TRAVTIME.001.

Figure 6.7-6. Simulated Cumulative, Normalized Mass Arrival Contours of a Conservative Tracer at the Water Table after 1,000,000 Years, Indicating Potential Breakthrough Locations at the Time, Using the Present-Day, 10th Percentile Infiltration Scenario

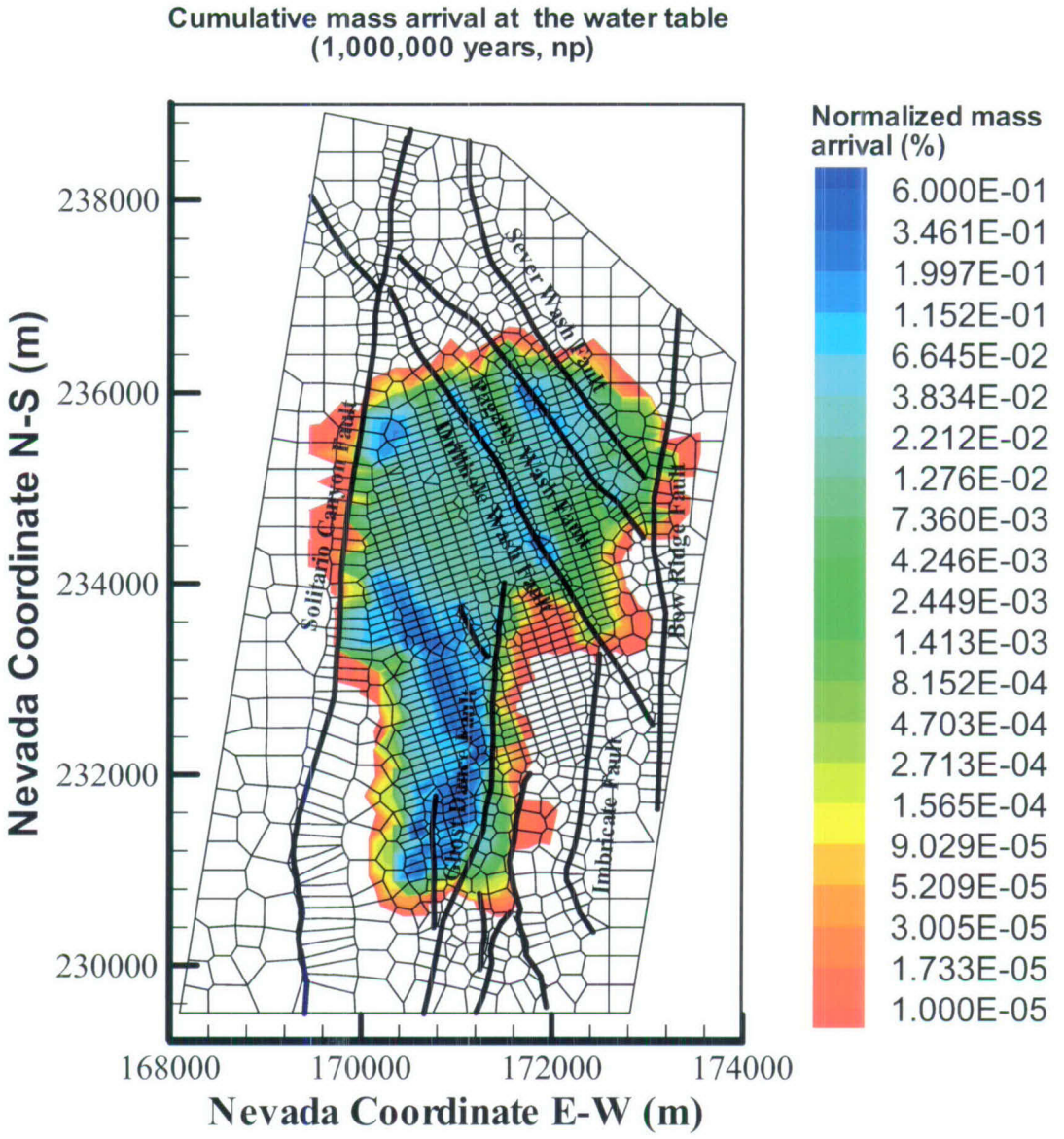

Output DTN: LB0705TRAVTIME.001.

Figure 6.7-7. Simulated Cumulative, Normalized Mass Arrival Contours of a Reactive Tracer at the Water Table after 1,000,000 Years, Indicating Potential Breakthrough Locations at the Time, Using the Present-Day, 10th Percentile Infiltration Scenario

6.8 UZ FLOW WEIGHTING FACTORS

6.8.1 Background

At Yucca Mountain, net infiltration is a key TSPA hydrologic parameter in controlling percolation rate, groundwater recharge, potential seepage into waste package, and radionuclide transport. Infiltration rates vary both spatially and temporally, owing to the nature of

precipitation events and variations in soil cover and topography. Currently estimated infiltration maps (SNL 2007 [DIRS 174294]) are based on the present-day climate and two future climates. However, no subsurface data have been used in developing these infiltration maps, although such data are important for constraining infiltration-rate estimates. A deviation from the TWP (BSC 2006 [DIRS 177465]) is to use the generalized likelihood uncertainty estimate (GLUE) methodology (Beven and Binley 1992 [DIRS 179079]) to determine physically meaningful weighting factors (or probabilities) for the selected infiltration maps, using available chloride data and temperature data in the unsaturated zone at Yucca Mountain. The application of GLUE needs a formal definition of likelihood measure, or set of likelihood measures. Beven and Binley (1992 [DIRS 179079], p. 281) pointed out that "the choice of a likelihood measure will be inherently subjective." Therefore, the determination of the weighting factors needs to address the epistemic uncertainty brought about by the application of different likelihood measures.

6.8.2 Infiltration Maps at Yucca Mountain

Yucca Mountain resides in a semiarid region of the southwestern United States, where the processes controlling net infiltration are highly variable in both time and space, and the dominant mechanisms may vary throughout the basin (SNL 2007 [DIRS 174294]). The model developed to estimate net infiltration at Yucca Mountain is referred to as the Mass Accounting System for Soil Infiltration and Flow (MASSIF). The key components considered in the model include climate input to the model (net precipitation, maximum and minimum air temperature), water transport and storage in the shallow zone, evapotranspiration, and surface run-on and runoff. A stochastic analysis was done to account for the uncertainty in the input parameters used in calculating these key components. Parameters that do not have a large contribution to infiltration uncertainty (e.g., with a relatively low uncertainty or a relatively low influence on the average net infiltration) were eliminated from the analysis (SNL 2007 [DIRS 174294]). Finally, under the present-day climate, eleven parameters were considered independently in the uncertainty analysis and two Monte Carlo simulations were done, each with 20 realizations. Forty infiltration maps, therefore, were generated with the same probability of occurrence. From these 40 maps, a cumulative distribution function (CDF) curve was obtained and annual mean net infiltration rate at different percentiles were found. Four infiltration cases (10th, 30th, 50th, 90th percentile maps) under four climate states (present-day, monsoon, glacial transition, and post-10k-yr) were considered in the UZ flow model.

However, during the process of generating infiltration maps, only climate and the shallow soil layer information have been taken into account. Data from the deep unsaturated zone provide additional information regarding infiltration/percolation processes at Yucca Mountain. The comparison between the simulated results using the four infiltration scenarios and the subsurface measured values can be used to indicate which scenario is closer to reality (Sections 6.3 and 6.5). In this study, chloride and temperature data observed from the unsaturated zone were used for determining values for the weighting factors of infiltration scenarios. Matrix saturation and water potential data were not used, because simulated distributions for the matrix saturation and water potential are not sensitive to the percolation flux in the unsaturated zone (Section 6.2.5). The pneumatic pressure data were not considered either, because the water percolation process does not significantly affect pneumatic signals in the unsaturated zone when fractures are very dry.

6.8.3 Temperature and Chloride Data

In the Yucca Mountain unsaturated zone, the temperature profiles or geothermal gradients of the unsaturated zone system are controlled by several factors, such as formation thermal conductivity and net infiltration rates, in addition to the regional weather conditions or surface temperatures. Because of the small impact of uncertainties in measured thermal conductivities on simulated heat flow, the temperature profile can be used to constrain infiltration maps and determine weighting factors. There are total of five boreholes containing qualified temperature data: NRG-6, NRG-7a, SD-12, UZ#5, and UZ-7a. The borehole locations can be found in Figure 6.1-1. Simulated temperature distribution at these five boreholes were generated from the four infiltration maps, as described in Section 6.3 (Output DTN: LB0701UZMTHCAL.001). Near the ground surface in five of the boreholes, observed temperatures show significant seasonal variations. However, these seasonal changes in surface temperature have little impact on steady-state heat flow or temperature profiles in the deeper (more than 20 m) unsaturated zone . In this study, only measurements 40 m below ground surface were considered, resulting in a total of 50 temperature data points for comparison.

In addition to limited temperature measurements, natural chemical tracers can also be used to examine infiltration history. Chloride is considered a nearly ideal natural tracer for the study of water movement in the liquid phase in geological systems. Its measurements are available at two tunnel horizontal tunnels ECRB and ESF, and twelve vertical boreholes: G-2, NRG-6, NGR-7a, SD-12, SD-6, SD-7, SD-9, UZ-14, UZ-16, UZ-7a, UZ-N55, and WT-24. Again, a map showing the tunnel and boreholes locations can be found in Figure 6.1-1. These measurements are compared with the chloride concentration outputs from the UZ chloride submodel. The simulations using the four infiltration maps are shown in Section 6.5, along with the simulated results (chloride concentrations) (Output DTN: LB0701UZMCLCAL.001). Because of the large spatial variations in chloride concentration, the comparison between the simulated and measured concentrations is done in log space. For simplicity, in this section, "the residual of chloride data" refers to the difference between the logarithm of the measured chloride concentration and the logarithm of the simulated chloride concentration.

For both data sets, because the numerical gridblock centers do not necessarily coincide with measurement points, linear interpolation is used to obtain the simulated temperatures at measurement locations.

6.8.4 UZ Flow Weighting Factors Definition/Description

The UZ flow scenarios correspond to selected present-day 10th, 30th, 50th, and 90th percentile infiltration scenarios generated by the infiltration model (DTN: SN0609T0502206.028 [DIRS 178753]). The UZ flow weighting factors (Output DTN: LB0701PAWFINFM.001, *factors.doc*) describe the probability of occurrence for each of the four infiltration scenarios, and therefore, the sum of the four weighting factors is one. The same weighting factors are expected to be used in all four climate states (present-day, monsoon, glacial transition, and post-10,000 years). The justification is given in Section 6.8.8.

6.8.5 Determination of UZ Flow Weighting Factors and Uncertainty

Among the uncertainties in the UZ flow model, the uncertainty associated with the calibrated properties is secondary or tertiary to the uncertainty in the estimates of infiltration rates. This is demonstrated by results of flow and transport sensitivity analyses (Zhang et al. 2006 [DIRS 180287]; BSC 2005 [DIRS 174116]).

6.8.5.1 GLUE Procedures for Determining the UZ Flow Weighting Factors

A generalized likelihood uncertainty estimation (GLUE) methodology described by Beven and Binley (1992 [DIRS 179079]) is used to determine the weighting factors. Although in many applications, a large number of runs were made, there is no restriction or requirement in GLUE applications. The application of this method to UZ flow weighting factors accounts for prior information on the probability of infiltration maps from the infiltration model, as well as the relative agreement between UZ flow model results (distributions of temperature and chloride concentration) and corresponding field observations. For the UZ flow weighting factors, there are many data points to support individual likelihood functions, so the GLUE method can be used to differentiate between as few as two models; and there is only one parameter (infiltration map) instead of multiple parameters (which increases parameter-space dimensions exponentially and number of runs). Because the GLUE methodology relies on UZ field observations that are only available for present-day conditions, the weighting factors are derived from infiltration and UZ flow model results for present-day conditions.

The following provides a summary of the GLUE steps that are specific to determining the UZ flow weighting factors:

Step 1. Determine the prior probability for each infiltration map (i.e., 10th, 30th, 50th, and 90th). According to *Simulation of Net Infiltration for Present-Day and Potential Future Climates* (SNL 2007 [DIRS 174294], Figure 6.5.7.1-4), 40 realizations of infiltration maps were generated with the same probability. These 40 realizations define a cumulative distribution curve for net infiltration. The 10th, 30th, 50th and 90th percentile maps can be identified from the plot. Assuming that the four selected fields are representative of all the others in this interval of the complete set of infiltration maps, the prior weight factors (or probability values) are determined based on the percentage interval of selected infiltration maps: W_1(10th percentile) = ((30% + 10%)/2) – 0 = 0.2, W_2(30th percentile) = ((50% + 30%)/2) – 0.2 = 0.2; W_3(50th percentile) = ((90% + 50%)/2) – 0.4 = 0.3 and W_4(90th percentile) = (1 – (90% + 50%)/2) = 0.3, respectively, for the present-day 10th, 30th, 50th, and 90th percentile infiltration maps. As shown in Figure 6.8-1, the prior weight for each infiltration map is the area of the corresponding shaded region.

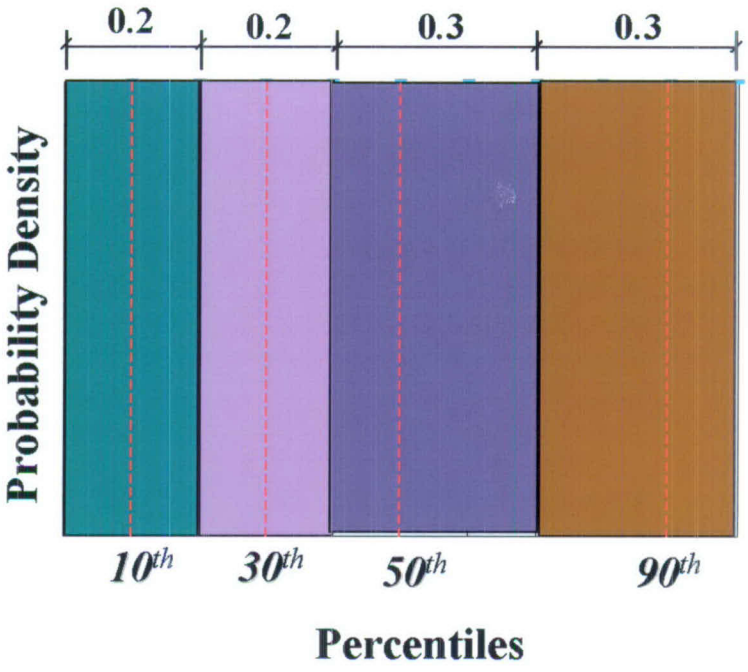

Figure 6.8-1. Prior Weights for the Selected Infiltration Maps

Step 2. Perform UZ flow calculations for each selected infiltration map. Based on the match between UZ model results and observations—temperature and chloride concentration data—calculate likelihood values, L_i^t and L_i^c, using each datum for each selected infiltration map. Section 6.8.5.2 discusses in detail the different ways to choose likelihood functions.

Step 3. Determine weighting factors, P_i, based on prior weights, W_i, and the likelihood values, L_i^t and L_i^c:

$$P_i = \frac{W_i L_i}{\sum W_i L_i} = \frac{W_i L_i^c L_i^t}{\sum W_i L_i^c L_i^t} \quad \text{(Eq. 6.8-1)}$$

Note that P_i is determined by both prior weights W_i and the likelihood values, L_i^t and L_i^c, that are measures of matches between simulated results and observed data in the unsaturated zone.

6.8.5.2 Likelihood Measures

Applying GLUE to determine the UZ flow weighting factors is different from traditional GLUE applications in the following ways: (1) Most GLUE applications involve the modeling of time series. Usually, the objective is to evaluate the parameter sets based on past time series (measured and simulated) and forecast future output. However, in this case, time series are not considered. The input to the model (infiltration) and output from the model (temperature and chloride concentration) do not change over time. (2) One common practice in GLUE methodology is to sample parameter space using some kind of Monte Carlo Simulation and assign weights to these samples. In this case, the four infiltration maps are preselected and there

is no parameter combination or sampling involved. (3) In most GLUE applications, behavioral and nonbehavioral models are distinguished, and the nonbehavioral models are rejected. However, this case considers the four infiltration maps to be "behavior" as long as each map's weight is above 0.

As pointed out by Beven and Binley (1992 [DIRS 179079], p. 281), "The choice of a likelihood measure will be inherently subjective." Different likelihood functions can result in different likelihood values, and therefore different weighting factors. Hence, care should be given to the choice of a likelihood value. As a rule of thumb, three things should be considered when choosing the likelihood measures: (1) the advantages and disadvantages of a likelihood measure, (2) the uniqueness of the problem under consideration compared to other general GLUE applications, and (3) epistemic uncertainty caused by the subjective likelihood measures.

Addressing the uncertainty aspect, it is generally desirable to include multiple likelihood functions as long as they satisfy the first two considerations in the previous paragraph. While there are different likelihood functions available in the literature, the selected likelihood functions should: (1) exhibit dramatically different mathematical forms such that a relatively large range of types of likelihood functions are considered, (2) not be theoretically inconsistent with the data and physical processes involved in calculating weighting factors, and (3) be easily calculated using the available data.

Based on these considerations, the following likelihood functions are selected (Equations 6.8-2 to 6.8-5):

1. The most common likelihood function associated with uncorrelated normal distribution of model error is (Makowski et al. 2002 [DIRS 179044], p. 194; Romanowicz and Beven 2006 [DIRS 179821]):

$$L_i = \prod_{j=1}^{N_i} \left(2\pi\sigma_j^{\,2}\right)^{-0.5} \exp\left(-\frac{\left(O_j - y_{ij}\right)^2}{2\sigma_j^{\,2}}\right) \qquad \text{(Eq. 6.8-2)}$$

where i is the index of selected infiltration maps, N_i is the total number of groups for field observations, O_j is *jth* observation, y_{ij} is the corresponding UZ model result, and σ_j is the standard deviation for measurement error in O_j. According to the likelihood concept, uncertainty in the model parameters is not caused by their random nature, but by insufficient data and their corruption by noise (Carrera and Neuman 1986 [DIRS 104368]). The maximum likelihood has the advantage in its formulation that more observation data (either data points or data types) will accentuate the better simulations, which means, greater reduction of uncertainty. Therefore, this likelihood measure is usually attractive. Also note that the above likelihood function has been often used for inverse modeling in the subsurface hydrology community, as a result of its close association with the classical statistics (Carrera and Neuman 1986 [DIRS 104368]).

2. Beven and Binley (1992 [DIRS 179079], Equation 5) provided a likelihood measure as follows:

$$L_i = \{\sum_{j=1}^{N_i} \frac{W_j}{(y_{ij} - O_j)^2}\}^N \quad \text{(Eq. 6.8-3)}$$

where W_j is the weight for observation j such that $\sum W_j = 1$. The same weight is used for all groups of observations. N is a parameter (called shape factor) chosen by the user. If $N=0$, all the infiltration maps will have the same weight, and if $N \to \infty$, the single best simulation will have a rescaled likelihood value of 1, and all others 0. In this study, likelihood values are calculated using $N=1$ and $N=0.5$, based on the following considerations: (1) $N = 1$ has been frequently used in the literature as reviewed by Beven et al. (2000 [DIRS 179825], Table 1), and (2) the use of $N = 0.5$ allows for evaluating the sensitivity of the likelihood-function value to changes in N within a certain range. Note that if $N=0$, all the infiltration maps will have the same weight. Similarly if $N \to \infty$, the best simulation will single out a rescaled likelihood value of 1, and all others 0. (As shown below, a smaller N value will result in a larger weighting factor value for an infiltration map with a higher average infiltration rate, which is conservative.)

3. The third category of likelihood measures is (Beven and Binley 1992 [DIRS 179079], Eq. 6):

$$L_i = 1/(\prod_{j=1}^{K_i} (y_{ij} - O_j)^2) \quad \text{(Eq. 6.8-4)}$$

4. The fourth category uses fuzzy measures as likelihood measures. Although there are different ways of choosing fuzzy membership functions (Beven 2006 [DIRS 179081]), Equation 6.8-5 expresses the most commonly used triangular membership function as (Franks and Beven 1997 [DIRS 179084], Eq. 8):

$$f_{ij} = 1 - \frac{|y_{ij} - O_j|}{\varepsilon} \quad \text{(Eq. 6.8-5)}$$

where ε is called acceptable error. In this case, a maximum absolute residual (the term "residual" refers to the difference between the observed (O) and simulated values (y)) from all observation location out of the four infiltration maps is taken as ε. Then, membership values at different observation points are combined using an arithmetic mean (Zak et al. 1997 [DIRS 179088]).

For the above measures, the final likelihood values are normalized as shown in Equation 6.8-6, so that the sum of the likelihood values for the four infiltration maps is one:

$$L_{i\_normalized} = L_i \Big/ \sum_{i=1}^{4} L_i \quad \text{(Eq. 6.8-6)}$$

Two types of data reflecting infiltration history are available: thermal data (temperature) and chloride concentration. The likelihood functions based on each type are calculated separately, and combined by multiplying the normalized likelihood value together, as shown in Equation 6.8-7:

$$L_i = L_i^t \bullet L_i^c \qquad \text{(Eq. 6.8-7)}$$

where L_i^c is the likelihood value calculated using chloride data, and L_i^t is the likelihood value calculated using temperature data. This treatment for different types of data ensures that the two kinds of data can be considered one at a time without affecting the final results (as shown below).

Measured chloride data are available for both boreholes (vertical) and tunnels (horizontal). The map indicating the locations of these boreholes and tunnels can be found in Figure 6.1-1. Note that the amount of information (i.e., infiltration history) contained in a certain number of observations from a tunnel is greater than the same number of observations from a borehole, due to greater horizontal area covered in a tunnel. To consider the effect, chloride data is placed into three groups, with two groups representing the two horizontal tunnels and one group representing all the area covered by boreholes. The average absolute residual (or residual squares) from each borehole is used (in the borehole group) to represent contribution from the given borehole. Then, the further average of squared average-residuals (or average of residual squares) for all the individual boreholes within the borehole group is used for likelihood value calculation. This treatment is to ensure that the likelihood calculation is not biased to boreholes with more data points, considering that each borehole represents roughly the same amount of horizontal area intercepting infiltration and should be treated equally in evaluating the infiltration maps. For the other two groups, the average of squared average-residual (or average of residual squares) is directly used for likelihood-value calculations. For likelihood measure Category 1, the average of residual squares is used. For likelihood-measure Categories 2 and 3, both the average of absolute residuals and average of residual squares are used to evaluate effects of different averaging schemes. For likelihood-measure Category 4, the average of fuzzy membership is used. To be consistent with the treatment of chloride data, the averaged residuals (or average of residual squares) for the individual borehole data are also used for temperature likelihood calculations.

As shown in Equation 6.8-7, the calculation of likelihood functions based on each type is calculated separately, and then combined by multiplying the normalized likelihood value together. An alternative way to consider the two types of data is to consider one at a time, for example:

1. Update the weights using likelihood values calculated by chloride data (L_i^c), then the posterior weights P_i^1 (after considering chloride data) is (Makowski et al. 2002 [DIRS 179044]):

$$P_i^1 = \frac{W_i L_i^c}{\sum W_i L_i^c} \qquad \text{(Eq. 6.8-8)}$$

2. Update the weights using likelihood values calculated by temperature data (L_i^t), then the final weight P_i (after considering both data) is:

$$P_i = \frac{P_i^1 L_i^t}{\sum P_i^1 L_i^t} \qquad \text{(Eq. 6.8-9)}$$

Substituting Equation 6.8-8 into Equation 6.8-9,

$$P_i = \frac{P_i^1 L_i^t}{\sum P_i^1 L_i^t} = \frac{\frac{W_i L_i^c}{\sum W_i L_i^c} L_i^t}{\sum \frac{W_i L_i^c}{\sum W_i L_i^c} L_i^t} = \frac{\frac{W_i L_i^c L_i^t}{\sum W_i L_i^c}}{\frac{\sum W_i L_i^c L_i^t}{\sum W_i L_i^c}} = \frac{W_i L_i^c L_i^t}{\sum W_i L_i^c L_i^t} \qquad \text{(Eq. 6.8-10)}$$

This result is identical to Equation 6.8-1. It shows that the weighting factors are independent of whether temperature or chloride data are used first.

Note that in the above calculations, the following likelihood function (Nash and Sutcliffe 1970 [DIRS 179820]; Beven and Binley (1992 [DIRS 179079]); Beven et al. (2000 DIRS 179825]), which is frequently used in the surface hydrology community, is not used here:

$$L_i = 1 - \frac{\sigma_e^{\ 2}}{\sigma_o^{\ 2}} \qquad \text{(Eq. 6.8-11)}$$

where $\sigma_e^{\ 2}$ and $\sigma_o^{\ 2}$ are the variance of residuals and variance of observations, respectively. This likelihood function is reasonable for data without (or with weak) trends (e.g., discharge data). However, it is not a valid goodness-of-fit measure for data sets exhibiting a considerable degree of trend. In this case, $\sigma_o^{\ 2}$ is dominated by the data trend and considerably larger than $\sigma_e^{\ 2}$, resulting in the likelihood function value not being sensitive to the goodness-of-fit. In this study, both temperature and Cl data sets exhibit spatial trends.

6.8.5.3 Results of UZ flow Weighting Factors

This section contains tabulated values (Table 6.8-1) (Output DTN: LB0701PAWFINFM.001, *factors.doc*) for the weighting factors using each of the methods discussed above, as well as the means of all the methods. The naming convention for Table 6.8-1 is as follows: the immediate number after "s" refers to the likelihood measures (see Section 6.8.5.2), "a1" refers to averaging scheme 1 (average absolute residuals) and "a2" refers to averaging scheme 2 (average residual squares).

Table 6.8-1. Calculated Weighting Factors Using Both Chloride Data and Temperature Data

Summary of Final Weights From All The Methods				
Infiltration map	**10%**	**30%**	**50%**	**90%**
S1	100%	0%	0%	0%
s2_a1_N=1	59%	21%	17%	3%
s2_a1_N=0.5	40%	24%	26%	11%
s2_a2_N=1	47%	24%	25%	4%
s2_a2_N=0.5	34%	24%	30%	12%
s3_a1	97%	3%	0%	0%
s3_a2	94%	6%	1%	0%
s4_sum	26%	24%	32%	18%
Average weighting factors	62%	16%	16%	6%

Output DTN: LB0701PAWFINFM.001, *factors.doc*.

Not only are the likelihood values, L_i^I and L_i^c, measures of matches between simulated results and observed data in the unsaturated zone, but also the prior weightings W_i (given in 6.8.5.1 Step 1) determine P_i. As shown in Table 6.8-1, the weighting factors are sensitive to the choice of likelihood measures, and the final weighting factors passed to TSPA for the four selected infiltration maps are determined as the arithmetic mean of the weightings P_i using the previously discussed methods (Equation 6.8-1).

Figure 6.8-2 shows the final likelihood of each infiltration map. Four bars represent the four infiltration maps. The individual point corresponds to the individual likelihood value from each calculation scheme. The mean infiltration rate for the 10th, 30th, 50th and 90th percentile infiltration map can be found in Table 6.1-2. Note that the weighting factors are subject to uncertainty because of the uncertainties in defining likelihood functions. The downstream users of the weighting factors should consider both the mean values and the uncertainties of these factors (Table 6.8-1). Specifically, TSPA calculations need to consider both the mean values for the weighting factors and the results of individual likelihood functions.

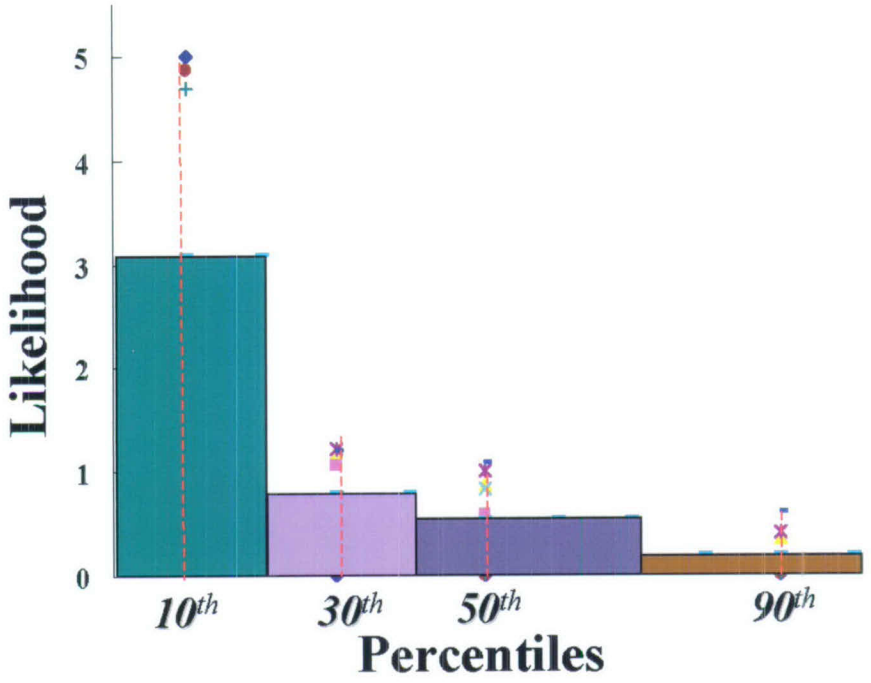

Output DTN: LB0701PAWFINFM.001. NOTE: Shaded Areas Represent Weighting Factors and Individual Points Represent Likelihood Values Resulting From Different Calculation Schemes.

Figure 6.8-2. Posterior Weighting Factors for Infiltration Map

6.8.6 Sensitivity Analysis for UZ Flow Weighting Factors

A number of sensitivity studies are performed to ensure that the results of likelihood value calculation are reasonable and robust.

6.8.6.1 Effects of Measurement Error for Temperature Data

The measurement errors (characterized by standard deviations) are used for evaluating the likelihood function given in Equation 6.8-2. For temperature measurement, the standard deviations representing measurement errors are on the order of 10^{-4}°C to ~ 10^{-3}°C (DTNs: GS031208312232.005 [DIRS 179284]; GS950208312232.003 [DIRS 105572]). A sensitivity analysis was performed for likelihood function 1 using a uniform standard deviation (0.1°C) for measurement errors to evaluate the effects of these deviations within a certain range for all the temperature observations. The resultant weighting factor values for the likelihood function are 1, 0, 0, and 0 for the 10th, 30th, 50th, and 90th percentile maps, respectively (Output DTN: LB0704UZWFINFM.001, file: *Cal_t1_sensitivity.xls*). That these are the same as those listed in Table 6.8-1 indicates that the variation of measurement errors within a reasonable range does not change the calculation results based on the first likelihood function.

6.8.6.2 Effects of Averaging Scheme

As indicated in Section 6.8.5.2, averaging residual squares, as well as squares of averaged absolute residuals, were used to evaluate the second and third likelihood functions. As an alternative, only the first, and more-commonly used, averaging scheme was considered for determining the weighting factors based on the second and third likelihood functions. Table 6.8-2 shows the final weighting-factor values averaged for all the likelihood functions. These values are very close to those listed in Table 6.8-1, indicating that the final results are not sensitive to the weighting schemes used in this study.

Table 6.8-2. Final Weighting Factors without Considering Average Absolute Residuals

Infiltration map	10%	30%	50%	90%
Average weighting factors	60%	16%	18%	7%

Output DTN: LB0704UZWFINFM.001, file: *summary_sen_average.xls*.

6.8.6.3 Results Without Considering the First and the Fourth Likelihood Functions

The first likelihood function has the effect of accentuating the best simulations, while the last likelihood function tends to differentiate the four infiltration maps least. One aspect of the sensitivity analysis is calculation of an average of the weighting factors without these two extreme cases. The results are shown in Table 6.8-3. Again, these results are very close to the results listed in Table 6.8-1.

Table 6.8-3. Weighting Factors Without Considering the First and Fourth Likelihood Functions

Infiltration map	10%	30%	50%	90%
Average	62%	17%	17%	5%

Output DTN: LB0704UZWFINFM.001, file: *summary_sen_2&3only.xls*.

6.8.6.4 Results from Individual Data Sets

To further examine the consistency between the determined weighting factor and field observations from different sources, weighting factors are also calculated based on: (1) chloride data only (Table 6.8-4), and (2) temperature data only (Table 6.8-5). As shown in these tables, the same rankings and similar weighting-factor values for different infiltration maps are obtained independently from these two data sets, involving very different physical processes in the unsaturated zone. This demonstrates the robustness of the determined weighting factors (given in Table 6.8-1). The small differences between those given in Table 6.8-1 and those given in Tables 6.8-4 and 6.8-5 are a result of combining the two data sets. The use of more data sets (closely related to the infiltration/percolation processes) is preferred in determining the weighting factors, simply because more data sets contain more information and should provide more accurate estimates for the weighting-factor values.

Table 6.8-4. Calculated Weighting Factors Using Chloride Data Only

Infiltration map	10%	30%	50%	90%
S1	100%	0%	0%	0%
s2_a1_N=1	48%	25%	21%	6%
s2_a1_N=0.5	34%	25%	28%	14%
s2_a2_N=1	41%	27%	25%	8%
s2_a2_N=0.5	30%	25%	29%	16%
s3_a1	72%	21%	7%	0%
s3_a2	62%	27%	11%	0%
s4_sum	24%	23%	32%	21%
Average	51%	22%	19%	8%

Output DTN: LB0704UZWFINFM.001, file: *summary_chloride only.xls*.

Table 6.8-5. Calculated Weighting Factors Using Temperature Data Only

Infiltration map	10%	30%	50%	90%
S1	100%	0%	0%	0%
s2_a1_n=1	31%	21%	30%	19%
s2_a1_n=0.5	25%	21%	30%	24%
s2_a2_n=1	26%	21%	35%	18%
s2_a2_n=0.5	23%	21%	33%	24%
s3_a1	89%	8%	2%	0%
s3_a2	83%	11%	5%	0%
s4_sum	22%	21%	31%	27%
Average	50%	15%	21%	14%

Output DTN: LB0704UZWFINFM.001, file: *summary_ temperature only.xls*.

6.8.7 Discussion of the Results of Unsaturated Zone Flow Weighting Factors

The expert elicitation for UZ flow (CRWMS M&O 1997 [DIRS 100335]) reviewed several methods for estimating percolation flux, including temperature. The report states that in general, the experts did not embrace the use of temperature gradients and heat flux to estimate percolation flux in the UZ (CRWMS M&O 1997 [DIRS 100335], p. 3-15). The cited drawbacks included data limitations, large spacing of measurement points, uncertainties in rock thermal conductivities, and, in particular, uncertainties in heat flux within the saturated and unsaturated zones. However, the temperature method employed for calibrating percolation flux does not need or use heat flux. The problem is thoroughly defined by the temperature boundary conditions and surface water-flux-boundary condition, in addition to the requisite material properties. While data limitations are still present, the temperature method used here does not suffer from the problem of heat flux uncertainty, cited as a major reason by the expert panel for not endorsing the method. The paper by Constantz et al. (2003 [DIRS 177344]) reviewed the use of temperature for estimating percolation flux and found the method was suitable for the sites investigated, including the deep unsaturated zones found in Southern Nevada at Frenchman's Flat and Yucca Mountain.

The expert elicitation also considered the use of chloride mass balance for estimating percolation flux. The conclusions were that the method could be used to support other methods but was insufficient for obtaining independent estimates of percolation flux (CRWMS M&O 1997 [DIRS 100335], p. 3-17). Objections to the method centered on uncertainties in the specification of chloride concentrations entering the unsaturated zone, incomplete mixing of waters during flow through the unsaturated zone, and the differences in chloride concentrations in the PTn and lower in the unsaturated zone in perched water bodies. As discussed earlier, uncertainties in the chloride concentration for water entering the UZ are estimated to be between 0.55 to 0.73 mg/L, and an overall variation of about 33%. Given that infiltration rate estimates from the 10th percentile to the 90th percentile vary by a factor of nearly 9 (Table 6.1-2), this uncertainty in chloride concentration does not preclude using the method. Incomplete mixing will result in some uncertainty in the spatial distribution of percolation flux, but will not affect the use of the method as an average flux indicator. Finally, the differences in chloride concentration between the PTn and perched water, as already discussed, is believed to be the transient chloride concentration variations that result from the incomplete penetration of the present-day chloride concentrations represented in the PTn to the locations at the base of the TSw where waters from earlier, wetter climates still affect the water chemistry.

A comparison of the GLUE-calibrated surface water flux probability distribution over the repository footprint with the expert elicitation probability distribution for percolation flux through the repository footprint is shown in Figure 6.8-3. The results show that the calibrated probability distribution is consistent with the aggregate expert percolation flux probability distribution and lies well within the bounds established by the expert panel.

6.8.7.1 Comparison with Percolation Flux

The results of the flow weighting factor analysis suggest that infiltration and deep percolation are not quantitatively similar. This is inconsistent with other findings (Stothoff and Musgrave 2006 [DIRS 182157], Section 1), which indicate that infiltration, deep percolation, and recharge are expected to be quantitatively similar when averaged over sufficiently large space and time scales. However, the methods used to perform infiltration estimates (SNL 2007 [DIRS 174294]) may have led to net infiltration rates that are biased to higher values than representative of the physical system. Net infiltration is a small component of a water balance that is dominated by precipitation and evapotranspiration (SNL 2007 [DIRS 174294], Table 6.5.7.4-1). Small errors in these quantities can have a large effect on the estimate of infiltration.

The infiltration model domain is limited to the surficial soils. Soil depth over most of the repository belongs to Soil Class 4, which varies from 0.1 to 0.5 m in the infiltration model (SNL 2007 [DIRS 174294], Figure 6.5.2.4-1 and Table 6.5.2.4-3). The soil depth is sampled according to a uniform distribution. Bare soil-evaporation occurs over a range of depths of 0.1 to 0.2 m (SNL 2007 [DIRS 174294], Table 6.5.4.2-4), sampled over a uniform distribution, and diffusive evaporation occurs over the root-zone thickness (SNL 2007 [DIRS 174294], Section 6.4.4). The root-zone thickness for Soil Class 4 is equal to the soil depth (SNL 2007 [DIRS 174294], Table 6.5.5.1-1). These facts result in a very limited zone (less than 0.5 m) for evapotranspiration processes. The model assumption is that these processes do not extend into the bedrock. This is acknowledged as a bias in that leads to an overestimate of infiltration (SNL 2007 [DIRS 174294], Section 5.5).

The recognition of a potential bias to overestimate infiltration is also acknowledged later in the report, which states (SNL 2007 [DIRS 174294], Section 8.3):

> Net infiltration estimates presented in this report include the quantification of uncertainty which bounds these estimates. While it was not the intent of this analysis to provide a "conservative" estimate of net infiltration, the results of the analysis may be conservative (over-estimate) due to the lack of certain site-specific data to constrain the results.

The calibration of the surface water flux boundary condition using subsurface data for temperature and chloride provides additional constraints for the infiltration results. This constraint has resulted in a reduction in the average percolation flux through the unsaturated zone as compared with the average infiltration model results, which is consistent with the potential conservative bias of the infiltration results.

The review on climate and infiltration with application to Yucca Mountain (Stothoff and Musgrave 2006 [DIRS 182157], Section 4) presents various regional-specific methods to estimate infiltration by Maxey-Eakin (1950 DIRS [DIRS 100598]) and Nichols (2000 [DIRS 178863]). The results of this analysis show that several methods lead to a relatively narrow range of results with average recharge being about 7 mm/yr or less for precipitation of 150 to 200 mm/yr (Stothoff and Musgrave 2006 [DIRS 182157], Figure 9). This is consistent with the GLUE-calibrated distribution of surface water flux, which has a mean value of 6.7 mm/yr using unsaturated zone domain average infiltration (Table 6.1-2) for present-day climate, and the final weighting factors (Table 6.8-1). The only exception presented by Stothoff and Musgrave (2006 [DIRS 182157], Figure 9) is called the "High-Elevation Correlation," where precipitation and recharge for high precipitation (300 to 860 mm/yr) are used to extrapolate to the range of precipitation representative of Yucca Mountain, 170 mm/yr (Stothoff and Musgrave 2006 [DIRS 182157], Section 3.3.1). Stothoff and Musgrave (2006 [DIRS 182157], Section 3.3.1) note that extrapolation beyond the range of precipitation used to develop the correlation must by done cautiously. In this case, infiltration is found to lie between 15 to 22 mm/yr. However, an extrapolation to 170 mm/yr is questionable in light of the fact that the ratio between recharge and precipitation was found to decrease substantially for precipitation levels of 200 mm/yr or less (Nichols 2000 DIRS [178863], Table C12).

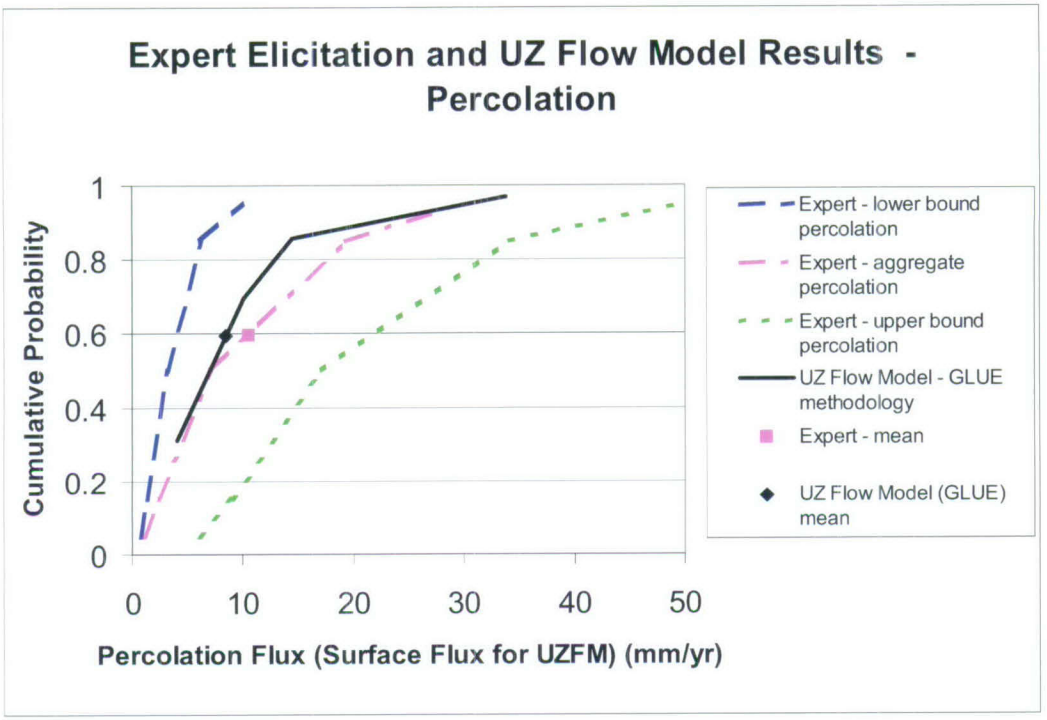

Source: CRWMS M&O 1997 [DIRS 100335], Table 3-2.

NOTE: Figure shows the expert elicitation probability distributions for percolation flux through the repository footprint.

Figure 6.8-3. Comparison of the GLUE-calibrated Surface Flux Probability Distribution over the Repository Footprint

6.8.8 Justification of Using the Same Weighting Factors for Monsoon and Glacial Transition Climates

The use of the same weighting factors for present-day, monsoon, and glacial transition climates is based on the modeling methods used for infiltration and UZ flow. Infiltration estimates are produced for future climates using the same hydrologic parameter ranges, the same methods for modeling weather patterns, and the same infiltration hydrologic model (MASSIF) as used for present-day climate. Similarly, UZ flow estimates are produced for future climates using the same parameter sets, same modeling assumptions, and same UZ flow model (TOUGH2) as used for present-day climate. Given the similarity of modeling methods across climate states, the expectation is that any deviations between the UZ flow model results for temperature and chloride, and the infiltration model results for infiltration rates under present-day climate, are also comparable for future climates. Therefore, the same weighting factors derived for present-day climate are applicable for monsoon and glacial transition climates. The probabilities associated with the weighting factors are also used to select specific cases for average percolation flux through the repository footprint for the post-10k-yr period. However, this does not impact the probability distribution for the post-10k-yr average percolation rates through the repository footprint as given in the proposed rule. This weighting factor methodology is based on UZ data that is sensitive to infiltration rate but was not considered in the development of the infiltration model. Therefore, the weighting factors derived by this method may differ from the

uncertainty identified by the infiltration model, which was based on uncertainties in climate and surface hydrological conditions.

Additional evidence supporting the weighting factor adjustment for future climates is provided by the calcite model presented in Section 7.7. Hydrogenic mineral coatings in the unsaturated zones are nonuniformly distributed and located almost entirely on fracture footwalls and cavity floors—in contrast to saturated environments, in which vein and cavity deposits usually coat all surfaces. The calcite model is a reactive transport model of the geochemical system at Yucca Mountain. In the model, advective and diffusive transport of aqueous chemical species is considered in the liquid phase. Molecular diffusive transport of gaseous species (CO_2) is considered in the gas phase. Aqueous chemical complexation and gas dissolution/exsolution are accounted for under local equilibrium, whereas mineral dissolution/precipitation can proceed at equilibrium and/or can be kinetically controlled. Gas species in the chemical computations are assumed to behave as ideal gases (i.e., fugacity equals partial pressure). Temperature effects are considered for geochemical reaction calculations, because equilibrium and kinetic data are functions of temperature.

The objective of the calcite modeling study was to investigate the relationship between percolation flux and measured calcite abundances. The U.S. Geological Survey (USGS) determined calcite abundances from a deep surface-based borehole (WT-24) (DTN: GS021008315215.007 [DIRS 162127]). Geochronology work performed by the USGS (Neymark et al. 2001 [DIRS 156889]) indicates that this calcite formed over approximately 10 million years. Thus, the calcite deposition is indicative of longer-term percolation flux behavior beyond present-day climate. Climate analyses suggest that the glacial transition climate accounts for more than half of the past 1,000,000 years (Sharpe 2003 [DIRS 161591], Tables 6-6 and 6-8). Therefore, the calcite data may be expected to be more representative of the glacial transition climate than present-day climate.

The simulated calcite abundances generally fall within the range of calcite observed in the field for a range in percolation rates of 2 to 20 mm/yr. The simulated calcite distributions capture the USGS–measured data from the WT-24 well cuttings (DTN: GS021008315215.007 [DIRS 162127]). The 20 mm/yr infiltration rate may be the upper bound for WT-24 location, whereas the infiltration rate (5.92 mm/yr) used for the flow model gives the closest match to the data (Figure 7.7-3a). The observed calcite precipitation for the top of TSw occurs mostly in the fractures, which is also captured. The range of infiltration rates at WT-24 for the 10th, 30th, 50th, and 90th percentile cases are given in *Calibrated Unsaturated Zone Properties* (SNL 2007 [DIRS 179545], Table 6-3). Using the prior probabilities from the infiltration model gives an average infiltration rate of 24.2 mm/yr, which lies outside the range of percolation rates identified as consistent with the calcite deposition data. Using the average GLUE-derived weights gives an average percolation flux of 12.2 mm/yr, which lies within the range of 2 to 20 mm/yr as found using the calcite model.

6.9 TEMPORAL DAMPING OF EPISODIC INFILTRATION PULSES

The temporal damping effect of the PTn unit on transient infiltration fluxes is examined through models with episodic infiltration pulses on the top boundary of the model. The discussion in this section is based on previous studies, as well as new simulation results from one-dimensional

models. This section and Section 8.1 on the calibrated properties address outstanding Key Technical Issue, TSPAI 2.02 AIN-1, Comment J-20.

The net infiltration at the bedrock surface (on top of the TCw unit) is conceptualized as episodic, with significant pulses occurring only once every few years. Spatially and temporally variable pulses of moisture percolate rapidly through the highly fractured tuffs of the TCw. However, at the TCw–PTn interface, where welded tuffs grade sharply into nonwelded tuffs, flow behavior changes from fracture-dominated to matrix-dominated flow. The highly porous PTn unit attenuates the episodic infiltration flux significantly such that the net episodic surface infiltration, once crossing the PTn, can be approximated as steady state (Section 6.2.2).

Effects of surface transient infiltration on capillary barriers and percolation have been analyzed using numerical models (Wu et al. 2002 [DIRS 161058]; Zhang et al. 2006 [DIRS 180273]). In the past several years, a number of modeling efforts have investigated the temporal damping effect of the PTn unit. Those efforts primarily used one-dimensional or two-dimensional flow and transport models to examine the responses of vertical flux to the pulse-infitlration boundary conditions at the land surface (Wu et al. 2000 [DIRS 154918]). In most of these models, surface infiltration pulses are assumed to be distributed with a one-week infiltration cycle of 50 years (i.e., the model top boundary is subject to nonzero infiltration for only one week every 50 years). Wu et al. (2000 [DIRS 154918]) investigated how surface transient infiltration affected capillary barriers and percolation, using both one-dimensional and two-dimensional models. Their models clearly indicate the importance of PTn-unit damping effects. The model results show that the surface transient-infiltration pulse can be significantly smoothened, temporally, after an early transient period of several hundreds of years. Guerin (2001 [DIRS 180551]) developed one-dimensional models to examine the flow and transport behavior in one-dimensional columns. These one-dimensional models correspond to several boreholes at the Yucca Mountain site. Guerin's models were run using different infiltration scenarios. From model calculations, she concluded that the PTn unit damped infiltration pulses no matter what infiltration scenarios were applied. Calibration results indicated that for most parameter changes, no notable movement of contaminant occurred below the PTn. Differences in contaminant transport behavior for the various simulations were only noted above the bottom of PTn unit. Other modeling studies indicate that the damping effect may be caused by lateral flow within the PTn unit (Wu et al. 2002 [DIRS 161058]; Liu et al. 2003 [DIRS 162478]). However, one- and two-dimensional models generally have difficulty describing the three-dimensional unsaturated flow system—for example, the lateral flow paths and flow-focusing phenomena through heterogeneous three-dimensional layers of the Yucca Mountain unsaturated zone.

A further systematic modeling study of damping effects in the unsaturated zone was conducted by Zhang et al. (2006 [DIRS 180273]), using both three-dimensional mountain-scale and one-dimensional vertical column models. The three-dimensional model incorporates a wide variety of field-specific data for the highly heterogeneous formation at the site and provides a more realistic representation of the unsaturated zone flow, while the simplified one-dimensional flow and transport models are useful for examining the long-term response of the flow system to different infiltration pulses. In the three-dimensional model, the top pulse-infiltration boundary condition is set by concentrating a total amount of net infiltration, averaged over 50 years, to the modeling domain in one week as infiltration pulses. Temporal average for infiltration pulses is assumed to be the present-day mean infiltration rate. The model's top boundary is subject to

nonzero infiltration (with a pulse of 2,609 times present-day mean infiltration) for only one week every 50 years, while during the rest period of every 50 years, the surface boundary is subject to zero infiltration. Note that related influence of soil on infiltration rate applied to the model had been excluded. Their modeling results also indicate that the PTn unit can attenuate the episodic infiltration flux significantly. Their study provides insights into unsaturated zone flow behavior under episodic infiltration conditions, as well as the role of the PTn unit in damping of pulse percolation. Model results show that the total percolation fluxes at the PTn bottom gradually approach the average value of mean infiltration rate for the whole period, and that eventually the system should reach an equilibrium condition under the uniform pulses of infiltration. In the areas without faults, vertical flux at the PTn bottom does not rapidly respond to top boundary infiltration pulses. Zhang et al.'s (2006 [DIRS 180273])results indicate that the damping effect happens at the PTn1 through PTn4 subunits. Results from the one-dimensional model with higher-rate infiltration scenarios confirm that the damping effect will not be weakened by higher rate infiltration pulses. The transport model results further reveal that the damping effect exists specifically in the PTn unit. Their results also show that most percolating water is damped by the subunits at the top of PTn, and that a small percentage of percolation flux is diverted into faults. The highly porous PTn unit attenuates episodic infiltration flux by imbibing water into the rock matrix. Flux allocation analyses suggest that the damping effect at nonfault columns is mainly caused by matrix rock water storage, absorbing and releasing water at different periods. Along fault columns, both lateral flow and rock water storage play an important role, with the importance of these two damping components being location-dependent.

In addition to modeling investigations, Salve et al. (2003 [DIRS 164470]) carried out a series of field tests for understanding flow patterns within the PTn. They examined whether the nonwelded tuffs of the PTn effectively damp pulses of infiltration, or whether preferential flow paths forming within the PTn serve to promote flow focusing. Their test results suggested that the PTn matrix has few discrete flow paths that can transmit water quickly, while the adjoining bulk matrix to the flow paths has much lower permeability. They found that episodic infiltration events appear to be damped by an initially dry PTn matrix, and that faults may convey a pulse of water over larger distances when the matrix is wet. These tests, however, are limited to a small scale in space within the PTn unit, and the test results cannot show large-scale effects of the flow system.

In the current model, two additional one-dimensional column models were developed to investigate PTn damping effects at different locations with different layer thicknesses. The two columns, f95 and i78, are located at the center and south of the model domain, respectively (See Figure 6.9-1). The PTn unit has a thickness of about 81 m at column f95 and 21 m at column i78. The combined thickness of the PTn layers exceeds 150 m at the northern end of Yucca Mountain, while at the southern end, the PTn thins to less than 30 m or even pinches out (Wu et al. 2002 [DIRS 161058]). The selected two columns are typical representation of PTn unit at the model domain. Episodic infiltration pulses with a rate of 10,079.7 mm/yr are applied on the model top boundary by one pulse infiltration period for only one week every 50 years. During the non-pulse infiltration period, a background infiltration rate of 28.1 mm/yr is applied on the model top boundary. The average infiltration rate for the whole modeling period is 32 mm/yr. These infiltration rates are determined based on the rationale that follows.

The pulse and background infiltration rates are determined from the post-10k-yr infiltration map. The mean value for the post-10k-yr period is 32 mm/yr (Section 6.1.4). Given x as the background infiltration rate, the total infiltration of 50 years is estimated as the background infiltration rate over 49 years plus 221.4 mm in the 50th year. The value of 221.4 mm is the maximum value for 333-yr return period (from DTN: SN0701T0502206.037 [DIRS 181227]). The total infiltrated water is set equal to infiltration with the mean post-10k-yr rate over 50 years, giving $49x + 221.4 = 32 \times 50$, which results in a background infiltration rate of $x = 28.1$ mm/yr. If the pulse is applied over 1 week, the total amount of water in the pulse is $221.4 - (28.1 \times 51/52) = 193.8$ mm. This pulse is at an equivalent rate (per year) of 10,079.7 mm/yr.

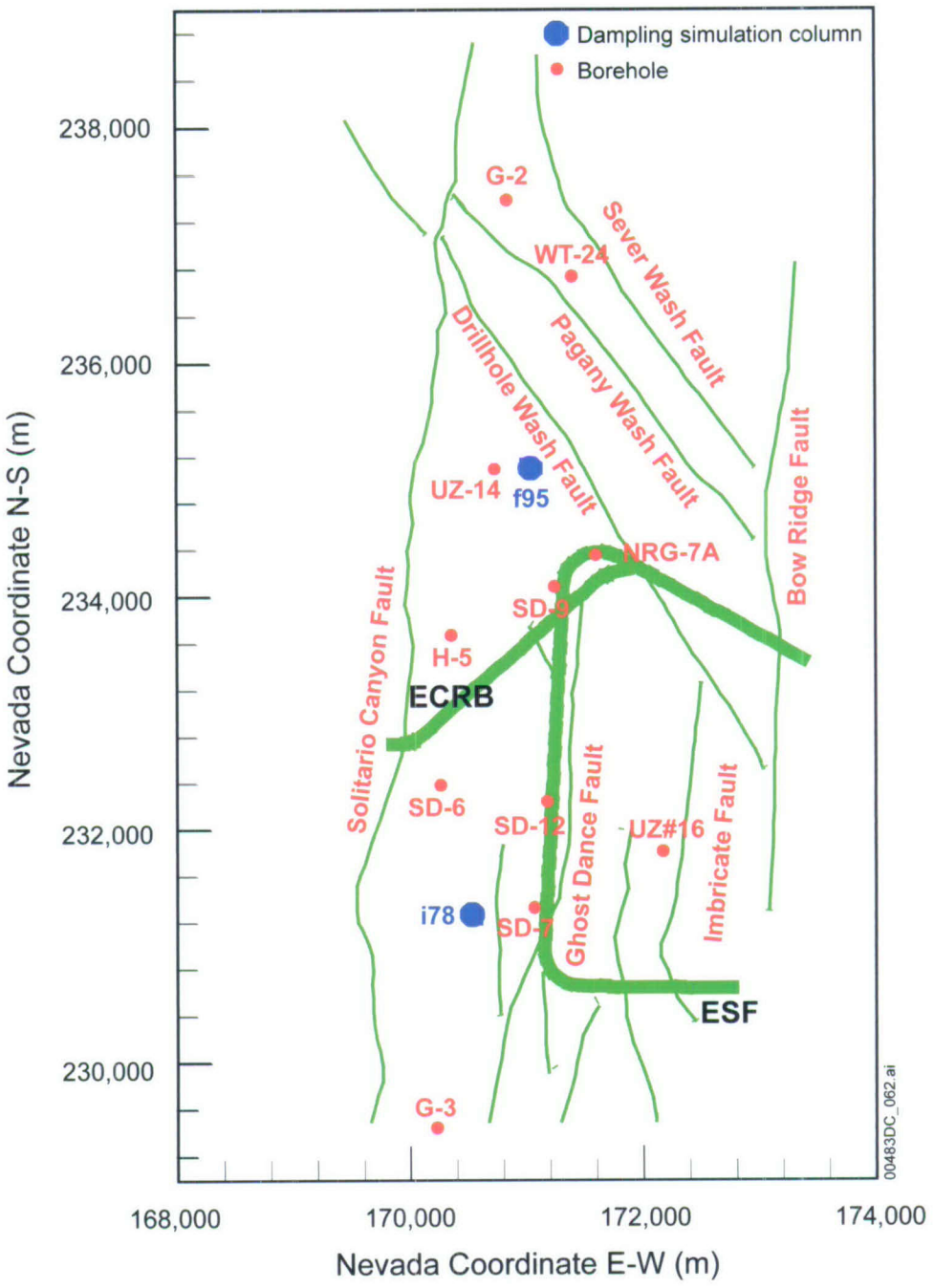

Source: DTN: LB03023DKMGRID.001 [DIRS 162354].

Figure 6.9-1. Location of the Columns for Damping Effect Simulation

Figures 6.9-2 and 6.9-3 show the variations of percolation fluxes at the bottom of the PTn and surface infiltration pulses versus time from the two one-dimensional column models. Results for both columns demonstrate the strong time damping effects of the PTn unit. Surface infiltration or pulses can be effectively smoothed temporally. The two figures present the results for up to 2,000 years following the steady-state flow of the initial condition. Figure 6-9.3 shows a relatively large fluctuation of total percolation flux compared to Figure 6-9.2. This is because i78

has a thinner layer of the PTn unit, compared to f95. In general, after rapid changes during the first several hundred years, the percolation fluxes at the bottom of the PTn unit gradually approach the average value of 32 mm/yr, and eventually the system reaches an equilibrium condition under the uniform pulses of infiltration, which could be approximated as a quasi-steady state. The variations in the case of the thinner PTn at column i78 are a maximum of 17 mm/yr and a dynamic equilibrium variation (after 500 years) of about 10 mm/yr. Relative to the mean infiltration rate of 32 mm/yr, the ratio of the variation compared with the mean is about 0.5 and 0.3, respectively. These variations may be compared with the ratio of the range (90th percentile flux minus the 10th percentile flux) to the mean for surface water flux in column i78 for the post-10k-yr period, which is about 1.1. Therefore, the episodic flow variations are small relative to other uncertainties in the problem, and the assumption of steady flow is valid.

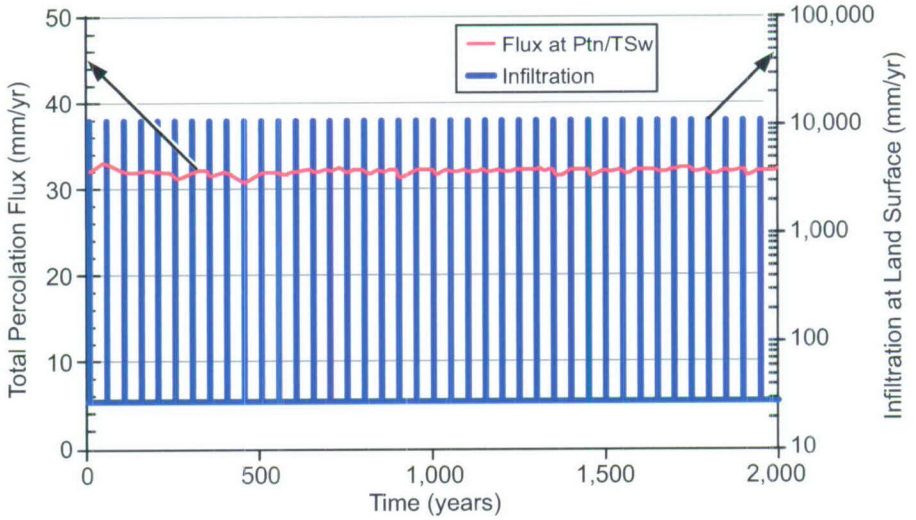

Output DTN: LB0705DAMPINGA.001, file: *f95_time_flux.xls*.

NOTE: PTn unit has a thickness of 81 m at Column f95.

Figure 6.9-2. Infiltration Pulse and Simulated Variations in Total Percolation Fluxes Versus Times at the Bottom PTn Unit for Column f95

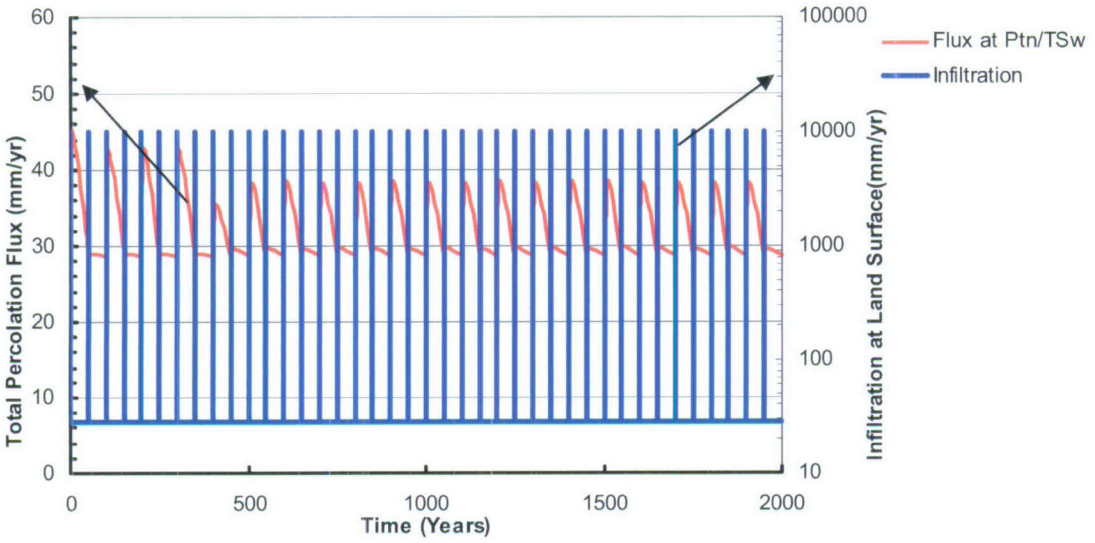

Output DTN: LB0705DAMPINGA.001, file: *i87_time_flux.xls*.
NOTE: PTn unit has a thickness of 21 m at Column i78.

Figure 6.9-3. Infiltration Pulse and Simulated Variations in Total Percolation Fluxes Versus Times at the Bottom PTn Unit for Column i78

The models provide insights into unsaturated zone flow behavior under episodic infiltration conditions, as well as the role of the PTn unit in damping pulse percolation. The modeling studies indicate that the PTn unit can attenuate the episodic infiltration flux significantly. Episodic infiltration, once crossing the PTn unit, can be approximated as steady state. The total percolation fluxes at the PTn bottom gradually approach the average value of mean infiltration rate for the whole period. This study justifies the reasonableness of assuming steady-state flow conditions below the PTn unit.

Episodic flow resulting from episodic infiltration in the unsaturated zone at Yucca Mountain has also been investigated by Manepally et al. (2007 [DIRS 182155]). In this study, longer-term transients that span up to thousands of years were investigated for a range of fluxes that roughly correspond with the post-10k-yr percolation flux range (Manepally et al. 2007 [DIRS 182155], Table 4-3; Section 6.1.4). As with the case with climate change, longer-term transients are expected to penetrate the PTn because of the finite storage capacity of the unit. The magnitude of the transients in the study by Manepally et al. (2007 [DIRS 182155], p. 5-2) were found to be characterized by a standard deviation of about 20% of the mean flux and a maximum range of 50%. By comparison, the standard deviation in the mean flux implemented for the post-10k-yr climate is about 60%, and the range is 127% of the mean flux (Tables 6.1-3 and 6.8-1) over the repository footprint. Therefore, the transient fluctutations are small in comparison with the uncertainty in the mean already incorporated in the TSPA.

6.10 UNCERTAINTIES IN PARAMETERS AND MODELS

The UZ flow model is developed to describe the unsaturated zone hydrological, geochemical, and geothermal conditions and processes. Even though model parameters and output results are based on qualified field-observation data, updated hydrogeological conceptual understanding, and integrated modeling studies in the model report, they are associated with some uncertainties. Uncertainties arise from (1) observed parameters and field data; (2) estimated present-day and future climates; (3) approximations used in hydrogeological conceptual models, such as steady-state flow conditions; (4) scale-dependent heterogeneity and model input parameters in the unsaturated zone fracture–matrix system; (5) the complexity of different unsaturated zone coupled flow and transport processes; and (6) the limitations of current modeling approaches using large volume-averages.

Numerical model representation of a real-world hydrogeologic system involves spatial discretization of a model domain into a large number of gridblocks or elements, with each element assigned the necessary attributes or properties. For the UZ models developed and used in this report, the necessary properties or model parameters are known at only a relatively few locations within the model domain. However, the range of infiltration uncertainty provided by the four infiltration uncertainty scenarios of the present-day climate covers most of the uncertainty range, because parameter uncertainties investigated in sensitivity analyses show much less effect on unsaturated zone flow than infiltration uncertainty. Uncertainties associated with these input parameters and models are discussed below in detail.

6.10.1 Input Parameter Uncertainties

To address the issue of uncertainties associated with input parameters, significant effort has been made to quantify and reduce uncertainties associated with model parameters and output results in this report. A total of four sets of model input parameters are developed (Appendix B), which cover the effect of uncertainties in 10th, 30th, 50th, and 90th percentile infiltration rates. Uncertainties with each of the present-day and three future climates are investigated using four infiltration maps (i.e., 10th, 30th, 50th, and 90th infiltration rates for the four infiltration scenarios).

Implementation of four model input property sets (Appendix B) for the three-dimensional mountain-scale UZ flow model, combined with the four different infiltration maps in each of the four climates, results in 16 three-dimensional flow fields. The effects of parameter uncertainties on UZ flow should be sufficiently covered in the model results. Additional sources of parameter uncertainties exist when using the hydrologic property sets, obtained by model calibration with the present-day climate for modeling studies under future climate conditions with higher infiltration rates. The range of infiltration uncertainty provided by the four infiltration uncertainty scenarios of the present-day climate covers most of the uncertainty range, as sensitivity analyses show that parameter uncertainties have much less effect on unsaturated zone flow than infiltration uncertainty, as discussed below.

Systematic sensitivity analyses of the UZ flow model results to model input parameters have been performed in *Parameter Sensitivity Analysis for Unsaturated Zone Flow* (BSC 2005 [DIRS 174116]), which is the source material for a journal article by Zhang et al. (2006

[DIRS 180287]). These parameter sensitivity analyses were conducted using the site-scale UZ flow model (BSC 2005 [DIRS 174116]; Zhang et al. 2006 [DIRS 180287]), by varying fracture and matrix properties using the statistical data of standard deviation from measurements. Specifically, sensitivity analyses are intended to estimate the effect of uncertainties in fracture and matrix hydrologic parameters on UZ flow and transport model predictions. Sensitivity simulations were carried out by considering uncertainties for the four important parameters: both permeabilities and van Genuchten alphas for fracture and matrix using standard deviations, associated with the three-dimensional model, base-case parameter set, by adding and subtracting one standard deviation to and from the corresponding parameter of the unit for all the units/layers and faults. These parameter variations resulted in a total of eight parameter sets. Therefore, eight new or additional three-dimensional unsaturated zone flow fields were generated to account for the uncertainties of the four hydrological parameters of fractures and the matrix.

Modeling results from the eight three-dimensional flow simulations for sensitivity analyses (BSC 2005 [DIRS 174116]; Zhang et al. 2006 [DIRS 180287]) have been compared with observed borehole matrix liquid saturation, water potential, and perched water data, as well as with the simulation results of the previous version of the UZ model (BSC 2004 [DIRS 169861]) The eight sensitivity flow fields cover a wide range of variability, in modeled liquid saturation, water potential, and percolation flux. The comparisons show that the eight modeled results show certain differences from the previous base-case simulation results (BSC 2004 [DIRS 169861]). In general, the eight new modeling results in the study (BSC 2005 [DIRS 174116]) indicate that uncertainties in matrix parameters cause larger uncertainty in simulated liquid saturation, water potential, percolation flux, and tracer transport than corresponding uncertainty in fracture properties.

The uncertainty of flow and radionuclide transport in the unsaturated zone at Yucca Mountain has been assessed using the Monte Carlo method, with matrix permeability, porosity, and sorption coefficient as random variables (Ye et al. 2006 [DIRS 180272]). Distributions were determined in the study by applying comprehensive transformations and rigorous statistics to on-site measurements of the parameters. The distribution of permeability was further adjusted based on model calibration results (BSC 2004 [DIRS 169861], Section 6.2.3). Correlation between matrix permeability and porosity was incorporated using the Latin Hypercube Sampling method. After conducting 200 Monte Carlo simulations of three-dimensional unsaturated flow and radionuclide transport for conservative and reactive tracers, an evaluation was performed on the mean, variances, and 5th, 50th, and 95th percentiles. The mean and 50th percentile were used as the mean predictions, and their associated predictive uncertainties were measured by the variances and the 5th and 95th percentiles (also known as uncertainty bounds). Mean predictions of matrix liquid saturation and water potential were in good agreement with corresponding measurements. The uncertainty bounds include a large portion of the measurements, suggesting that data variability can be partially explained by parameter uncertainty. This independent study illustrates propagation of predictive uncertainty for percolation flux, increasing downward from repository horizon to water table. Statistics from the tracer-transport breakthrough curves indicate that transport of the reactive tracer is delayed by the sorption process, and prediction of the reactive tracer is of larger uncertainty than that of the conservative tracer, because randomness in the sorption coefficient increases the prediction uncertainty. Uncertainty in radionuclide transport is related also to uncertainty in the percolation flux.

6.10.2 Model Uncertainties

Model uncertainties involved with the UZ flow model have mainly to do with the hydrogeological conceptual models used, including the steady-state flow approximation or the role played by the PTn unit, layer-wise homogeneous geological formations, perched water occurrence, fast-flow pathways, the effects of major faults, and numerical modeling approaches for handling fracture–matrix interaction. These uncertainties have been discussed, investigated, or quantified in this report, using field observation data (Sections 1.4 and 6.2), modeling analyses (Sections 6.6 and 6.7), and other arguments.

Among the approximations or conceptualizations used in the UZ flow model, the steady-state or quasi–steady-state assumption is a key issue. This assumption relies on the effect of spatial and temporal damping of transient infiltration pulses when such pulses flowing through the PTn unit. The effectiveness of the PTn unit in damping episodic flow is further examined in Section 6.9, using episodic infiltration pulses on the top boundary of the model. The analyses in Section 6.9 indicates that the steady-state flow approximation used in the UZ flow model is reasonable, because of the existence of the PTn unit. In addition, the conceptual model for steady-state flow approximation is shown in this report to be capable of matching chloride and temperature data (as well as moisture data) fairly well. This indicates that the steady-state flow below the PTn is a good approximation. Another effect of the steady-state approximation is that it does not track the delay between a change in climate at the surface and the corresponding change in percolation at depth. Doughty (1999 [DIRS 135997], Figure 7) indicates that the delay may be on the order of one thousand years in a one-dimensional simulation of responses to infiltration pulses at the Yucca Mountain unsaturated zone. However, the transients and time required to reach steady-state due to a change in climate were not investigated in this report. The intended use of the output of the UZ flow model is a set of steady state flow fields that pertain to different climate states assumed to change instantaneously in the TSPA model; therefore, transients are not needed. This method leads to conservative estimates of percolation flux in the unsaturated zone since the subsequent climates yield wetter conditions.

Additional uncertainty associated with models includes different matrix porosity values and extra storage space contributed by lithophysal cavities in the hydrogeological layers of the upper lithophysal (tsw33) and lower lithophysal (tsw35) units. This uncertainty regarding matrix porosity or lithophysal cavities should have little impact on simulation results of percolation flux under steady-state unsaturated zone flow, but would have some impact on the in situ volume of water simulated. In addition, the effect of these cavities on tracer transport from the repository to the water table is expected to be small. This is because: (1) the geological layers with cavities are located either higher than or at the repository horizon, and (2) cavities will remain dry, with little water is expected to flow through them because of strong capillary barrier effects on potential seepage into cavities.

Only the 10th, 30th, 50th, and 90th infiltrate rates of the infiltration maps for present-day, monsoon, and glacial transition climates (SNL 2007 [DIRS 174294]) are used in the report for the UZ flow model calibration, validation, and flow-field simulations. These infiltration maps are selected from the 120 infiltration maps of the three climates (DTNs: SN0609T0502206.028 [DIRS 178753]; SN0609T0502206.024 [DIRS 179063]; SN0609T0502206.029 [DIRS 178862]).

The impact evaluations on the new infiltration model as well as on downstream use of infiltration/UZ flow results are provided in Appendix H.

6.11 REPRESENTATION OF THE UZ FLOW FIELDS WITH AN ELEVATED WATER TABLE

This section discusses the simulation of water table rise within the UZ flow model. In the absence of direct hydrological data to validate the future unsaturated zone flow fields with a higher water table, justification of the simulated future flow fields must rely on the conceptual and mathematical validity of models. As described in Section 6.6.3, these future UZ flow fields were generated based on the three-dimensional UZ flow model, which was developed using a fixed water table representing the current, ambient conditions. The flow fields with the current water table can also be used to extract flow fields for a rising-water-table case in the future (i.e., a water-rise situation can be handled by simply transecting the flow fields vertically at a new water table elevation).

The use of these truncated steady-state UZ flow fields can be justified by considering the fundamentals in model formulation (i.e., the mathematical model of Richards equation, or, more specifically, Darcy's law for description of UZ flow under a future high-water-table condition). Unsaturated zone flow is simulated using Richards' equation as well as Darcy's law, and the impact of a future water table rising is limited mainly to the lower unit of the CHn below the repository horizon. Note that the water table boundary is handled as a sink term in the UZ flow model. Near or at the future elevated water table, which is within the model domain of the UZ flow model, unsaturated zone flow is vertically dominant. The flow is determined primarily by the upstream or upper-layer conditions in the UZ flow model. According to Darcy's law, in particular, the vertical flow is decided by two factors: hydraulic conductivity and hydraulic gradient. Since the hydraulic conductivity is upstream weighted in the model and the vertical hydraulic gradient is dominated by a gravity term, which is a constant, inserting a future water table boundary into the current UZ flow model will provide a good approximation for obtaining the future flow fields with an elevated water table. The truncation at the higher water table ignores the capillary fringe for a simulation with the higher water table as the lower boundary is an acceptable approximation. Under steady-state conditions for the three-dimensional unsaturated zone flow fields, flow rate or percolation flux should be the same at any horizontal cross section, regardless of capillary fringe. Current truncation method preserves steady state percolation flux at a horizon. In addition, certain lateral flow may occur at or near a future water table, which is caused by intersecting perched water low-permeability zones. These intersected perched water or low-permeability zones will have liquid saturation near 100%, as predicted by the UZ flow model, which are approximately the same conditions needed for representing a future water table boundary. Therefore, truncated flow fields at a future higher water table, using the current unsaturated zone flow fields, provide a reasonable representation for unsaturated zone flow fields under future climates for both vertical and lateral flow components.

7. VALIDATION

Validation activities for the UZ flow model and submodels were planned in *Technical Work Plan for: Unsaturated Zone Flow, Drift Seepage and Unsaturated Zone Transport Modeling, REV 04* (BSC 2006 [DIRS 177465], Section 2.2.1.1). The model validation approach for the UZ site-scale flow model is presented in *Technical Work Plan for Technical Work Plan for: Unsaturated Zone Flow, Drift Seepage and Unsaturated Zone Transport Modeling* (BSC 2006 [DIRS 177465], Section 2.2.1.1), which states that the UZ site-scale flow model requires Level I validation. The validation plan was developed under the BSC procedures in effect at the time. The BSC Level I validation is equivalent to Level I validation as described in SCI-PRO-002. The Level I validation includes the six steps of confidence building during model development as described in SCI-PRO-002 and at least one postdevelopment activities as described in SCI-PRO-006, Section 6.3.2. This model validation section deviates from the TWP (BSC 2006 [DIRS 177465], Section 2.2.1.1.2), in that temperature and chloride data are not used for validation. This is because the temperature and chloride data have been used to calibrate the flow weighting factors representing the effects of infiltration uncertainty discussed in Section 6.8. A second deviation include the Alcove 8–Niche 3 flow and transport test data as one additional validation effort. The model validation efforts of this section include confidence building during model development and corroboration with experimental data. The additional validation activities presented in this section are corroboration with information published in refereed journals and literature, analysis of model uncertainties, and corroboration with natural analogues. The models will be accepted as valid for their purposes through confidence building during model development of Section 7.1, as well as through postdevelopment validation efforts of corroboration with experimental data in Sections 7.2 to 7.8, according to the following criteria (BSC 2006 [DIRS 177465], Section 2.2.1.1.2):

- The water-potential data measured from ECRB are used for validation by comparing with simulation results of the UZ flow model. The criterion for the validation is that simulated water-potential values are within the range of measurements along the ECRB tunnel. Demonstration that this criterion has been met is shown in Section 7.2.

- WT-24 perched water elevation data is used to validate the UZ flow model. The criterion for the validation is that simulated perched elevation matches the observed value within 10 m). Demonstration that this criterion has been met is shown in Section 7.3.

- The gas-flow model was calibrated against the first 30 days of pneumatic data for borehole SD-12 (Section 6.4). Pneumatic data measured in SD-12 (for the second 30 days) and UZ-7a (for the second 30 days) are used for validation of the UZ flow model. The criterion for the validation is that simulated gas pressures and their patterns of variations consistently compare closely with the observed values. That is, the simulations will consistently reproduce increases and decreases resulting from changes in barometric pressure at the ground surface. Demonstration that this criterion has been met is shown in Section 7.4.

- Carbon-14 data from gas samples provide approximate C-14 residence times for pore water. The residence times can be interpreted as tracer transport time from the ground surface to where the gas samples were collected, based on the current conceptual model for UZ flow and transport. These data are used to validate the UZ flow model. The criterion for the validation is that simulated tracer transport times (i.e., the integral breakthrough curve at the sample-collection locations for a pulse input at the ground surface or the time for first moment of concentration) are within the range of times estimated from data in the TSw unit. Demonstration that this criterion has been met is shown in Section 7.5.

- Borehole and ECRB strontium concentrations are used to check the UZ flow model results using the strontium modeling analysis. The criterion for validation is qualitative agreement between the simulated strontium concentrations and the average of the observations at the same elevation, and agreement with the vertical trends. Demonstration that this criterion has been met is shown in Section 7.6.

- The calcite model is used to validate the UZ flow model with the abundance data of calcite mineral. The calcite model is validated by comparing one-dimensional simulation results with measurements. The criterion is that the simulated volume fraction of calcite coating for each UZ model layer falls within the range of measurements for that layer. According to the TWP (BSC 2006 [DIRS 177465], Section 1, #1), the need of model validation runs are not expected for the calcite model results, because the uncertainty is already captured in the model runs. Demonstration that this criterion has been met is shown in Section 7.7. The current calcite model has not changed from the previous *UZ Flow Models and Submodels* (BSC 2004 [DIRS 169861], Section 7.9).

- A deviation from the work plan outlined in the TWP (BSC 2006 [DIRS 177465], Section 2.2.1.1) lies in the use of the Alcove 8–Niche 3 flow and transport test data. The original plan calls for the incorporation of the data to support the development of an enhancement factor to matrix diffusion in the unsaturated zone radionuclide transport model and the UZ transport abstraction model. This plan has not been implemented, and the resulting estimate of transport times through the unsaturated zone is conservative as explained in *Radionuclide Transport Models Under Ambient Conditions* (SNL 2007 [DIRS 177396], Section 6). Therefore, the information from the Alcove 8–Niche 3 fault test is again used below to support the post-development validation of the site-scale UZ flow model. The same model validation criteria as described in the previous report (BSC 2004 [DIRS 169861], Section 7) are used for this model validation exercise (i.e., the criterion for validation is that the predicted results for the time to reach a given concentration of a conservative tracer are within a factor of 5 of the observed times, or that explanations can be found for why the observed and simulated results deviate significantly). Demonstration that this criterion was met is shown in Section 7.8. This validation exercise has not changed from the previous report (BSC 2004 [DIRS 169861], Section 7.6).

For the validation activities of this section, none of the corroborative data sets selected for use in model validation wase used in model calibration and development of Section 6. In addition, there were no other similar data sets available for model validation activities. Note that model validation efforts, presented in this section, are carried out mostly by using the present-day, 10th and/or 30th percentile infiltration rates. This is because the present-day 10th and 30th percentiles are considered more realistic representations of the present-day conditions (Section 6.2).

Confidence Buidling with Information Published in Refereed Journals and Literature. In addition to the model validation activities described in the TWP, journal publications are used to provide confidence for model validation. Some methods listed here, including temperature and chloride modeling are no longer conducted for validation (corroboration) but rather are part of the calibration or model development process. Three-dimensional unsaturated zone numerical models have been developed to simulate flow and distribution of moisture, gas, and heat at Yucca Mountain (Wu et al. 1999 [DIRS 117161]; Wu et al. 2004 [DIRS 173953]). Flow and transport processes within the unsaturated zone were characterized under current and future climates (Wu et al. 2002 [DIRS 160195]). Studies of capillary barriers in the unsaturated rock of Yucca Mountain have also been published (Wu et al. 2002 [DIRS 161058]). The perched water phenomena in the Yucca Mountain unsaturated zone have been investigated (Wu et al. 1999 [DIRS 117167]). Subsurface gas pressure variations have been used to determine the pneumatic diffusivity of important geological features (Ahlers et al. 1999 [DIRS 109715]; Wu et al. 2006 [DIRS 180289]). Subsurface borehole temperature data were used to estimate percolation flux (Bodvarsson et al. 2003 [DIRS 162477]). Chloride measurements were used to calculate infiltration rates along the ESF (Fabryka-Martin et al. 1998 [DIRS 146355]). Chloride data, in conjunction with hydrostructural and hydrogeological features, were also used to constrain infiltration rates (Liu et al. 2003 [DIRS 162478]). In addition, chloride and strontium geochemistry were investigated using three-dimensional modeling for insights into the hydrology of the unsaturated zone (Sonnenthal and Bodvarsson 1999 [DIRS 117127]). In particular, these published journal papers presented examples of using temperature, pneumatic and geochemical isotopic data to calibrate and validate the UZ flow model.

Analysis of Model Uncertainty. As discussed in Section 6.10, there are a number of uncertainties associated with the UZ flow model, including data, model, and climate uncertainties. The existence of these uncertainties stems from uncertainties in parameter and field data measurements, estimates of present-day and future climates, hydrogeological conceptual models and modeling approaches, and scale-dependent heterogeneity, and model input parameters. These data- and model- related uncertainties have been discussed, investigated or evaluated in this report using field observation data, modeling sensitivity analyses, model calibration, natural analogue information, and other arguments in Sections 6.2 through 6.9 and this section. These uncertainties are reasonably captured by simulation results using four different parameter sets and 16 infiltration maps, as discussed in Section 6.10. The effects of parameter and data uncertainties on UZ flow model results are generally encompassed by the model results for the 16 three-dimensional flow fields. Systematic sensitivity analyses of the UZ flow model results (to model input parameters) were carried out to assess uncertainties associated with parameters and models (BSC 2005 [DIRS 174116]; Zhang et al. 2006 [DIRS 180287]). In addition, the uncertainty of flow and radionuclide transport in the Yucca Mountain unsaturated zone was investigated using a Monte Carlo method with matrix

permeability, porosity, and sorption coefficient treated as random variables (Ye et al. 2006 [DIRS 180272]).

Corroboration with Natural Analogues. In addition, the key flow and transport processes pertaining to the unsaturated zone at Yucca Mountain have been investigated through natural analogues (BSC 2004 [DIRS 169218]). These natural analogue investigations contained both literature studies and analyses. One of the important case studies was the unsaturated zone flow and tracer tests at the Idaho National Engineering and Environmental Laboratory's Radioactive Waste Management Complex (BSC 2004 [DIRS 169218], Section 9.3). The field tests at the site provided calibrations of numerical models with needed in situ measured data. A consistent set of parameters was obtained from calibrating the model using the dual-permeability approach to multiple hydrographs (water potential as a function of time) from transient ponded infiltration tests. The studies demonstrated that conceptual models and large-scale, volume-averaged numerical modeling approaches used for the UZ flow model at Yucca Mountain can be applied with confidence (BSC 2004 [DIRS 169218], Section 9.3.7). The model validation effort of this section is intended to further build confidence in the UZ flow model and submodels with regard to their ability to predict flow and transport processes in the Yucca Mountain unsaturated zone system. In particular, these model validation efforts further confirm that using uniform hydrogeologic parameter values across the lateral extent of most hydrostratigraphic units in the UZ flow model provides reasonable approximations and simulation results, because of the model is capability for matching different types of data from boreholes that are a considerable distance apart.

7.1 CONFIDENCE BUILDING DURING MODEL DEVELOPMENT

To establish the scientific basis and the accuracy of intended use, SCI-PRO-006 and SCI-PRO-002 require documentation of decisions or activities that are implemented to generate confidence in the model during model development, including the following:

(1) Evaluate and select input parameters and/or data that are adequate for the model's intended use [SCI-PRO-002, Attachment 3, Level I (1)].

The selection of input parameters and/or input data for the UZ flow model and its submodels is discussed and presented in Sections 4.1, 6.1–6.5, and Appendix B. Model calibration results in Section 6 show that these selected input parameter values or input data are reasonable for simulating flow and transport processes in the Yucca Mountain unsaturated zone.

(2) Formulate defensible assumptions and simplifications that are adequate for the model's intended use [SCI-PRO-002, Attachment 3, Level I (2)].

As discussed in Sections 5 and 6.1.2, the development of the UZ flow model and its submodels is based on assumptions and simplifications that are accepted in the scientific community, which are supported by many scientific journal publications, as discussed above.

(3) Ensure consistency with physical principles, such as conservation of mass, energy, and momentum, to an appropriate degree commensurate with the model's intended use [SCI-PRO-002 Attachment 3, Level I (3)].

As discussed and shown in Section 6.1.2, the development of the UZ flow model and its submodels is consistent with all these physical principles.

(4) Discussion of the impacts of uncertainties to model results. [SCI-PRO-006, Section 6 and SCI-PRO-002, Attachment 3, Level I (4) and (6)]

Impacts of uncertainties on model results are discussed in Section 6.10.

(5) Ensure simulation conditions have been designed to span the range of intended use and avoid inconsistent outputs, or that those inconsistencies can be adequately explained and demonstrated to have little impact on results [SCI-PRO-002, Attachment 3, Level I (5)].

Simulations for UZ flow have been conducted to span the range of hydrological properties that are consistent with observed hydrological conditions and the potential range of present-day infiltration rates (Section 6.2). The simulations also span the range of potential infiltration rates for future climate conditions out to 1,000,000 years (Section 6.1.4).

(6) Ensure that model predictions (performance parameters) adequately represent the range of possible outcomes, consistent with important uncertainties and modeling assumptions, conceptualizations, and implementation [SCI-PRO-002, Attachment 3, Level I (6)].

Model predictions account for uncertainties (Section 6.10), conceptualizations (Section 6.1.2), and implementations (Sections 6.1 through 6.5). Calibration activities and/or the use of initial and boundary conditions are discussed in Sections 6.1 to 6.5, resulting in the model results consistent with field-measured data.

In addition, the justification for the representation of the flow fields with a higher water table is carried out using Method 2, Corroboration with Alternative Mathematical Models, as listed in SCI-PRO-006, Section 6.3.2. Demonstration that this criterion was met is shown in Section 7.11. This validation effort, even though not specified in the TWP (BSC 2006 [DIRS 177465], is needed to justify the use of future flow fields.

7.2 VALIDATION USING ECRB WATER-POTENTIAL MEASUREMENTS

The three-dimensional site-scale UZ flow and transport model at Yucca Mountain has been the subject of several journal articles. Integrated modeling approaches were used to simulate water flow in the unsaturated zone in conjunction with gas and heat flow, and isotopic transport (Wu et al. 1999 [DIRS 117161]; Wu et al. 2004 [DIRS 173953]). In another study, flow and transport processes within the unsaturated zone under current and future climates were characterized using a three-dimensional numerical model, which incorporates a wide variety of field data in the highly heterogeneous, unsaturated fractured porous rock (Wu et al. 2002 [DIRS 160195]). The capillary barriers in the unsaturated rock of Yucca Mountain were also studied (Wu et al. 2002 [DIRS 161058]).

An east–west cross-drift was constructed in 1997 as part of the ECRB program (see Figure 6.1-1 for the location of the ECRB tunnel). Water-potential data (DTN: GS980908312242.036 [DIRS 119820]) were collected from heat-dissipation probes installed in the tunnel wall (at a depth of 2 m) along the ECRB tunnel inside the ESF. Water-potential data were collected from heat dissipation sensors calibrated for matrix potential. Though the boreholes were dry drilled, the sensors were installed with wet cement. Thus, the sensors were fully saturated and surrounded with contact media to ensure good contact with rock, and equilibrated with the matrix potential of the rock. Following the equilibration, the probe would gradually dry out from ventilation effects. Since this was the first group of probes installed in the tunnel wall, no steps were taken to reduce the effects of ventilation drying in the tunnel. Extra steps, such as installing multiple doors, were taken during subsequent installation and monitoring of probes in the ECRB tunnel.

As part of the three-dimensional flow and transport modeling validation process, modeled water potential results were compared to field-observation data collected from the wall of the tunnel to check the accuracy of the modeling predictions. Model results (pd_10 and pd_30, Output DTN: LB06123DPDUZFF.001) of the 10th and 30th infiltration simulations of the UZ flow model was selected for validation of the UZ flow model, as discussed in Section 6.2.5. (A complete list of modeling scenarios can be found in Table 6.2-6.) The infiltration boundary condition is the present-day, mean infiltration rate (DTN: SN0609T0502206.028. [DIRS 178753]). Calibrated properties used for the three-dimensional prediction are those developed and listed in Table B-1 (Output DTN: LB07043DCRXPRP.001).

Figure 7.2-1 shows a comparison of simulated and measured matrix water potentials along the wall of the ECRB drift. (Note that water potential is defined as the absolute value of capillary pressure in this report.) As shown in the figure, observation data are available only along part of the tunnel. Most of the observed water-potential data are distributed between 0.1 (10^4 Pa) and 1 (10^5 Pa) bars, with a maximum of 3.4 bar. The model predicted approximately 1 bar for the same section of tunnel, which is higher than most of the observed data. The predicted water potentials along the ECRB from the UZ flow model ranged between 0.2 and 1.4 bars for the wall distance <1,000 m (Figure 7.2-1) for the present-day, 10th and 30th percentile infiltration scenarios (pd_10 and pd_30).

The available data for field-measured matrix water potentials at the ECRB were mostly distributed over a range between 0.1 (10^4 Pa) and 1 (10^5 Pa) bar. Near the entrance (0 to 200 m) the measured water-potential data are more scattered and are higher on average. Further inside (200 to 800 m), the data are more narrowly distributed with a lower average.

Even though the available measurement data for the ECRB drift are limited to the entrance area (0 to 780 m), they are used to evaluate the predicted water potential for the whole drift. Results indicate that the UZ flow model is able to predict the range of the water-potential data from in situ measurements for the present-day 10th percentile scenario. Near the entrance, the predicted water potentials are spanned by measured data points, and further inside, the predicted ECRB water potential lie close to the measurement data. Under the present-day 30th percentile scenario, the predicted water potential at a distance of 2,500 m is higher than the measured water potential range at a distance 0 to 780 m. However, the predicted water potentials are well within the

measured values for the section where field water potentials were measured. Therefore, the criterion of validation is in general satisfied, indicating that the model is capable of predicting the range of water potential and is reasonable for its intended use.

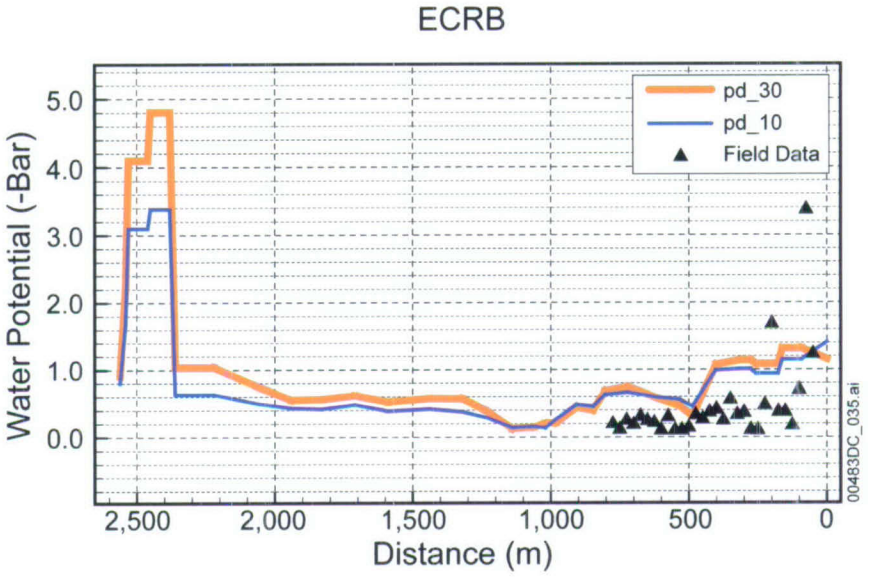

Source: DTN: GS980908312242.036 [DIRS 119820].

Output DTN: LB06123DPDUZFF.001.

Figure 7.2-1. Comparison of Predicted and Measured Water Potential along ECRB Using the Present-Day, 10th and 30th percentile Infiltration Rates (pd_10 and pd_30)

7.3 VALIDATION USING PERCHED WATER DATA AT WT-24

The perched water phenomena in the Yucca Mountain unsaturated zone were investigated with a multiphase subsurface flow model by Wu et al. (1999 [DIRS 117167]). In that paper, the simulation results were shown to agree with the observed perched water data, including water saturation, potential profile, and perched water elevation. The field-measured perched water data at borehole WT-24 is not used in the preceding model development for the calibration (Section 6.2.5) and is deliberatively held back for the purpose of the validation of perched water occurrence. Borehole WT-24 was drilled in 1997 as part of the ECRB program (see Figure 6.1-1 for borehole locations) and was monitored for saturation data (see Section 4-1 for DTNs). Also, perched water was detected within the basal vitrophyre of the TSw at an elevation of approximately 986.69 m (DTN: GS980508312313.001 [DIRS 109746]). As part of the model validation process, modeled results were compared to the field-observation perched water elevation to check the accuracy of the modeled predictions.

The UZ flow model scenario (pd_10 and pd_30, with Output-DTN: LB06123DPDUZFF.001) of the present-day, mean infiltration rate is used for the comparison. Figure 7.3-1 shows a comparison of simulated matrix water-potential results with field measurement data at Borehole WT-24. The observed elevation of perched water is also shown in the figure. As indicated there, the field-measured data for potentials are limited to the deeper section of the borehole (mostly in the CHn unit). The simulated water potential of the UZ flow model goes through the thick cluster of the field measurement data and simulated field observed perched water location

matches perched water elevations. Note that a simulated perched water zone is indicated by zero water potential. The field-measured perched water elevation is only measured at one point, at the onset of a pumping test (DTN: GS980508312313.001 [DIRS 109746]). During pumping, the perched water table was lowered by 20.66 m (DTN: GS980508312313.001 [DIRS 109746]). Actual perched water zone thickness may be larger than this fluctuation of water levels. The value of 20.66 m is very close to the simulated perched water thickness of about 30 m, as shown in Figure 7.3-1. Examination of simulated and observed perched water elevations show a difference of 2.45 m. This satisfies the validation criterion of 10 m. Since the average grid spacing is about 10 m with the UZ flow model, the 10 m criterion is sufficiently accurate in model outputs and consistent with the spatial discretization of the model.

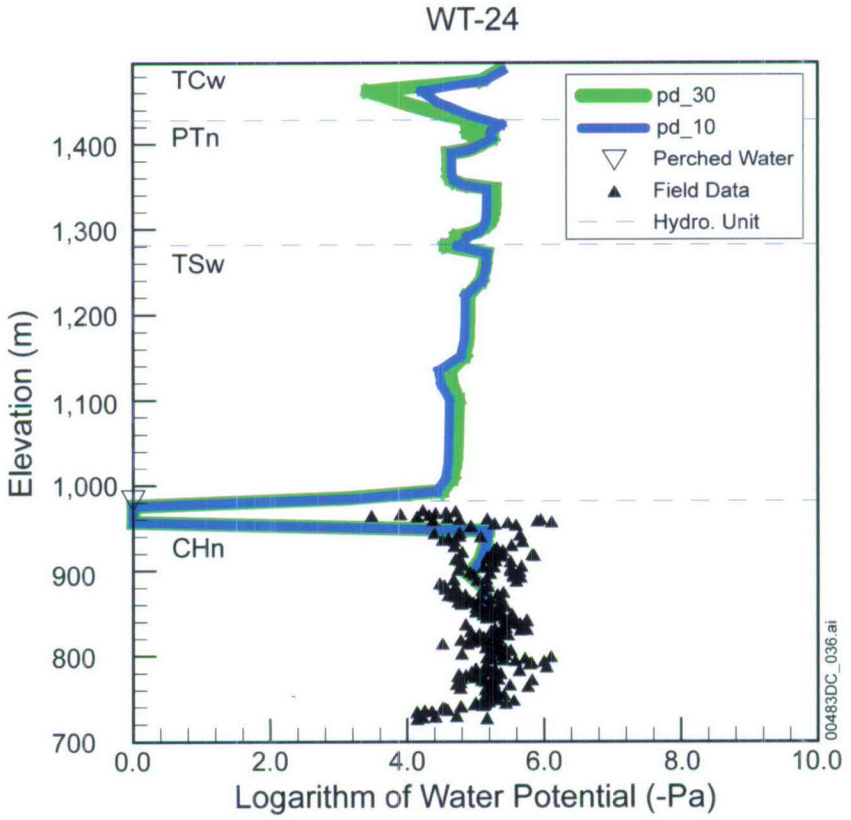

Sources: DTNs: GS980708312242.010 [DIRS 106752] (field water potential data); LB03023DSSCP9I.001 (field-measured perched water,).

Output: LB06123DPDUZFF.001

Figure 7.3-1. Comparison of Predicted (line) and Measured (gradient symbols) Matrix Water Potentials and Perched water Elevations at Borehole WT-24 Using the Present-Day, 10th and 30th Percentile Infiltration Rate (pd_10 and pd_30)

7.4 VALIDATION OF THREE-DIMENSIONAL UZ MODEL AGAINST OBSERVED PNEUMATIC PRESSURE DATA

The calibrated three-dimensional unsaturated zone gas-flow model as discussed in Section 6.4 was validated using the observed pneumatic pressure data in UZ-7a and SD-12 during the second 30-day period (immediately following the first 30 days of data used for calibration). The sensor locations, files for observation data, observation period, corresponding model mesh cells, and

host rock are listed in Table 6.4-1. The criterion for the validation is that simulated gas pressures and their pattern variations are consistent with the observed values. That is, the simulations will consistently reproduce increases and decreases resulting from changes in barometric pressure at the ground surface.

7.4.1 Validation of the UZ Model for the Scenario of the 10-Percentile Infiltration Map

Simulated results are compared with field-measured values of the 30-day validation period for the 10th percentile infiltration scenario (Figures 7.4-1 and 7.4-2) and the 30th percentile infiltration scenario (Figures 7.4-3 and 7.4-4), respectively. Overall, good agreement between the predicted gas pressures and observed data were found in both scenarios. The good match builds confidence that the calibrated properties are appropriate for gas flow simulations in either case. Comparisons between simulated and observed gas pressures at different locations of the two boreholes, shown in the two figures, prove that simulated gas pressures and their patterns of variations are consistent with observed values. In particular, the simulations consistently reproduce increases and decreases resulting from changes in barometric pressure at the ground surface. This satisfies the validation criterion for this case.

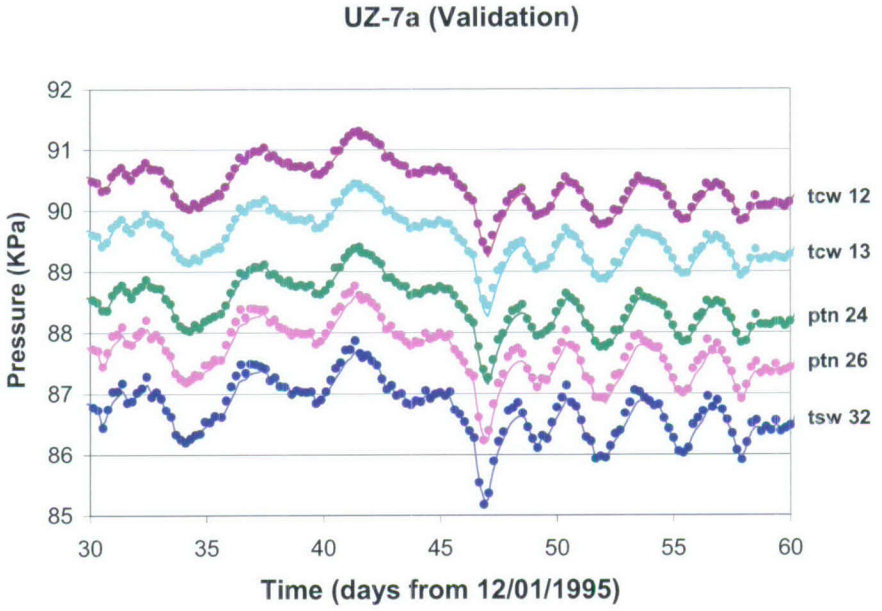

Source: DTN: LB0612MTSCHPFT.001 [DIRS 180296].

Output DTN: LB07043DGASCAL.001.

NOTE: Both observations and simulations have been vertically offset for clear display.

Figure 7.4-1. Comparison of Predicted (solid line) and Observed (solid dots) Gas Pressures at Borehole UZ-7a During the Second 30-day Period for the 10th Percentile Infiltration Scenario

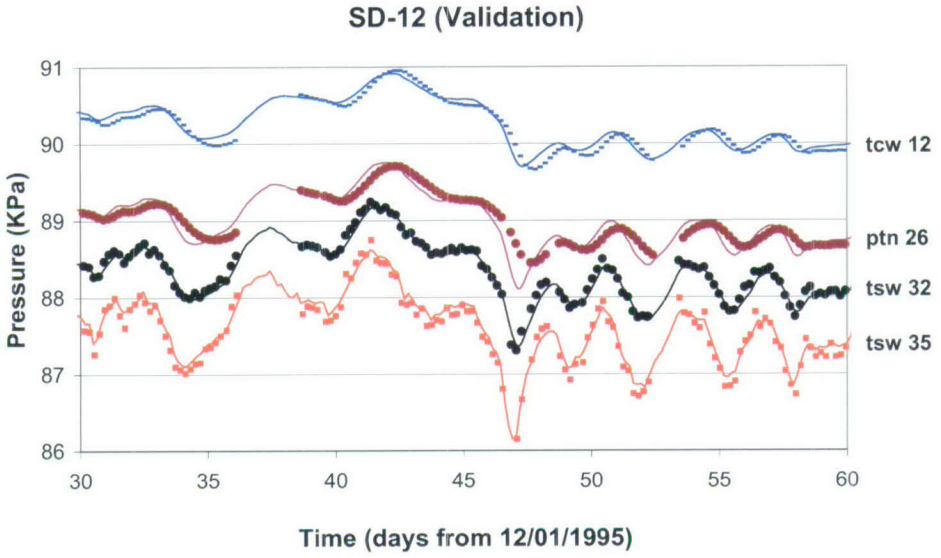

Source: DTN: LB0612MTSCHPFT.001 [DIRS 180296].

Output DTN: LB07043DGASCAL.001.

NOTE: Both observations and simulations have been vertically offset for clear display.

Figure 7.4-2. Comparison of Predicted (solid line) and Observed (solid dots) Gas Pressures at Borehole SD-12 During the Second 30-day Period for the 10th Percentile Infiltration Scenario

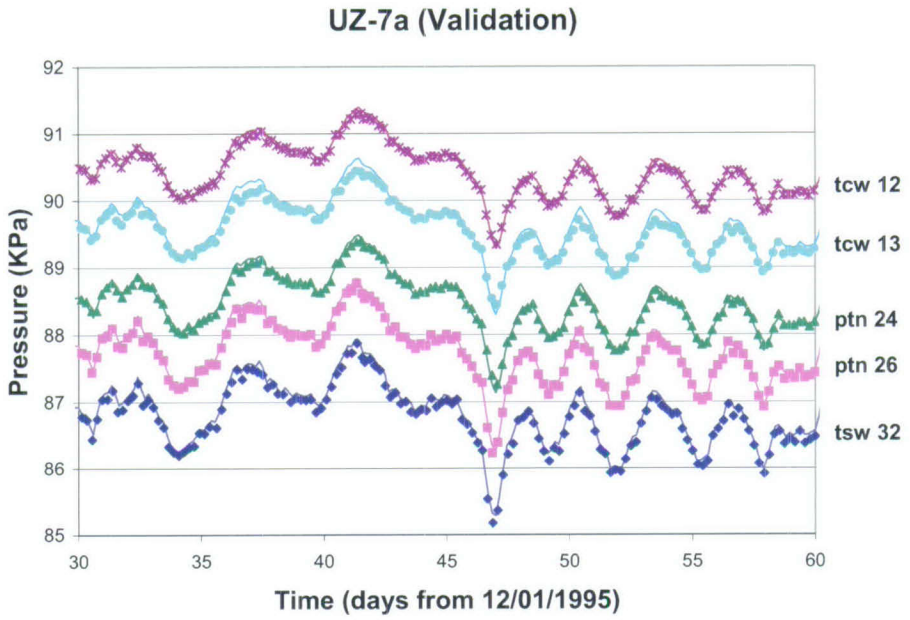

Source: DTN: LB0612MTSCHPFT.001 [DIRS 180296].

Output DTN: LB07043DGASCAL.001.

NOTE: Both observations and simulations have been vertically offset for clear display.

Figure 7.4-3. Comparison of Predicted (solid line) and Observed (solid dots or symbols) Gas Pressures at Borehole UZ-7a During the Second 30-day Period for the 30th Percentile Infiltration Scenario

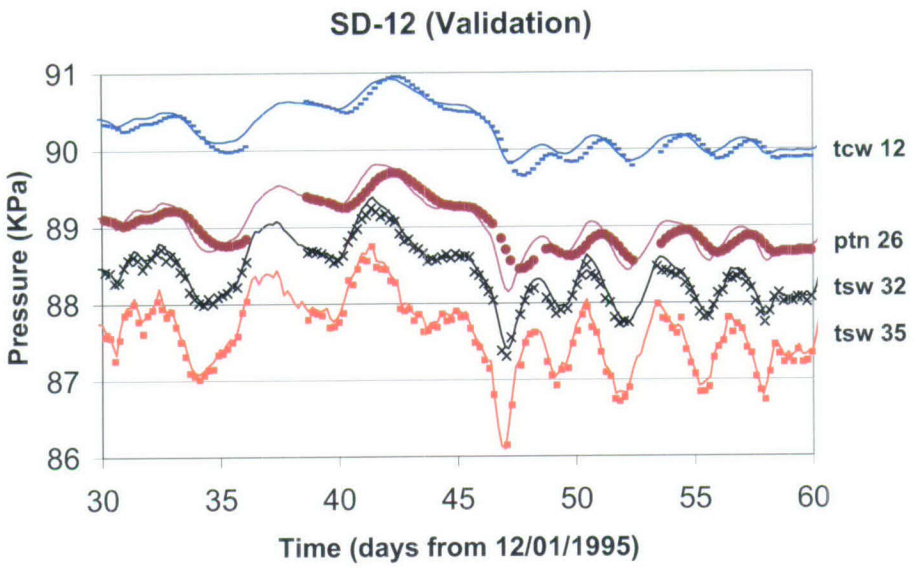

Source: DTN: LB0612MTSCHPFT.001 [DIRS 180296].

Output DTN: LB07043DGASCAL.001.

NOTE: Both observations and simulations have been vertically offset for clear display.

Figure 7.4-4. Comparison of Predicted (solid line) and Observed (solid dots or symbols) Gas Pressures at Borehole SD-12 During the Second 30-day Period for the 30th Percentile Infiltration Scenario

7.5 MODEL VALIDATION WITH ^{14}C DATA

This section describes the simulation of the solute travel times using the calibrated UZ flow models, and the comparison of the simulated travel times to the measured ^{14}C ages for borehole UZ-1 and SD-12, for validation of the UZ flow models. The criterion for the validation is that the simulated travel times for TSw units fall within the range of the measured ^{14}C ages for the TSw units.

7.5.1 Methodology

In a flow system, at a given location and time, the solute residence time (travel time) is determined within the whole system by the applicable transport processes, such as advection, diffusion and hydrodynamic dispersion. The actual residence time can be determined using a number of methods, including measuring a radioactive isotope activity and then calculating the residence time based on the decay rate. Residence time can also be simulated using a flow and conservative tracer transport model of the system (Goode 1996 [DIRS 162573]). The degree to which the model-simulated residence times fall within the range of the measured residence times can be used for validating the flow and transport model. The Yucca Mountain unsaturated zone is considered to be a quasi-steady-state flow system (Section 5). An appropriate solute residence time to use is the mean transport time required for the solute to move from the ground surface to the sample location in the subsurface system. The mean solute residence time can be considered to be constant at each location in this quasi-steady-state flow system, but spatially variable. When a tracer pulse is injected into the system through the ground surface, the tracer

concentration breakthrough at any given location in the system can be obtained from model results, and the mean travel time to that location can be computed (Goode 1996 [DIRS 162573], Eq. 1):

$$A = \frac{\int_0^\infty tc\,(t)\,dt}{\int_0^\infty c\,(t)\,dt} \qquad \text{(Eq. 7.5-1)}$$

where A is the mean travel time, t is time, and $C(t)$ is the tracer concentration. This time (A), which incorporates mixing effects brought on by multiple flow paths of different velocity, dual-permeability effects, and diffusion, is considered to be a reasonable proxy for a complete simulation of transport of an isotopic tracer with decay included. This calculated travel time can be compared to the travel time estimated from the measured ^{14}C activity for validation of the UZ flow and transport model. Equation (7.5-1), the mean travel time under steady-state conditions, is the mean value of the travel times of many particles within a control-volume element, computed in this model from the concentration breakthrough of a generic conservative tracer at the fracture-matrix gridblock in the dual-permeability model. In this way, Equation (7.5-1) is used to estimate groundwater ages, which are compared to ages estimated from ^{14}C data. For this validation exercise, computed mean travel times are based on the calibrated groundwater flow field of the UZ flow model (Output DTN: LB06123DPDUZFF.001), and are compared to ages converted from the measured ^{14}C activity (DTNs: GS961108312271.002 [DIRS 121708] for borehole USW SD-12, and MO0012CARB1314.000 [DIRS 153398] for borehole USW UZ-1) using a half life of 5,715 years (Output DTN: LB0704C14FFVAL.001).

7.5.2 Background Information of ^{14}C Isotope and the Measurements of ^{14}C Activities in Yucca Mountain

^{14}C is produced in the earth atmosphere at a constant rate by the cosmic rays that transform atmospheric ^{14}N into ^{14}C ($^{14}CO_2$). The earth atmosphere is a huge reservoir of ^{14}N, and the cosmic rays are considered relatively stable. Thus, the isotopic fraction of ^{14}C (activity) in the atmosphere is considered stable, because the production rate of the cosmic rays transforming ^{14}N into ^{14}C is balanced by the radioactive decay rate of the ^{14}C. As long as the $^{14}CO_2$ dissolves into water (chemically existing in the forms of HCO_3^-, CO_3^{2-} and aqueous CO_2) and infiltrates into the unsaturated zone, new ^{14}C is no longer produced (in the unsaturated zone), and the ^{14}C activity declines with time due to the radioactive decay. The ^{14}C in the unsaturated zone matrix pore water or gas contains the information of the residence time (i.e. the age) of the ^{14}C, and in most cases, this age is also considered a good approximation of solute and water residence time. The ^{14}C data were collected from the perched water, matrix pore water, and gas samples from the Yucca Mountain unsaturated zone (BSC 2004 [DIRS 169734], Section 5.2.2.5.4). Pore water ^{14}C data from boreholes at Yucca Mountain may not be representative of the solute residence time of the pore water, because of possible contamination by atmospheric $^{14}CO_2$ during borehole drilling, which may result in apparently younger residence times (Yang 2002 [DIRS 160839], Section 4.1.2; BSC 2004 [DIRS 169734], Section 5.2.2.5.4). ^{14}C data from gas samples from borehole UZ-1 and SD-12, on the other hand, are considered to be most representative of the in situ conditions (Yang 2002 [DIRS 160839], Section 4.1.2), because the boreholes were closed, thus preventing exchange of ^{14}C with the atmosphere. ^{14}C is also considered as the most sensitive isotope measuring the solute travel time at the Yucca Mountain unsaturated zone, due

to its half-life duration, which is on the same order of magnitude as the travel times in the unsaturated zone, and its detectable abundance. Gas samples were collected from different kinds of boreholes, including open and instrumented surface-based boreholes. Data from the latter boreholes (USW SD-12 and USW UZ-1) are regarded as more reliable indicators of solute travel time for the in situ matrix pore water (BSC 2004 [DIRS 169734], Section 5.2.2.5.4). Thus, the measured ^{14}C ages (BSC 2004 [DIRS 169734], Section 5.2.2.5.4) data from these two boreholes are used for validating the UZ flow model.

Gas-phase ^{14}C ages (Output DTN: LB0704C14FFVAL.001 for the conversion of ^{14}C activity into ages, and DTNs: GS961108312271.002 [DIRS 121708] for the ^{14}C activity of borehole USW SD-12, and MO0012CARB1314.000 [DIRS 153398] for the ^{14}C activity of borehole USW UZ-1) are interpreted to be representative of solute travel times for the *in-situ* matrix pore water. The rationale for this interpretation is provided by Yang (2002 [DIRS 160839], Section 4.1.2). The interpretation is based on the rapid exchange of gas-phase CO_2 (reaching equilibrium in hours to days) with dissolved CO_2 and HCO_3^- in pore water. Furthermore, the amount of carbon in an aqueous-phase reservoir is greater by orders of magnitude than carbon in the CO_2 gas-phase reservoir. Consequently, the aqueous phase will dominate the gaseous phase when exchange occurs, indicating the reasonableness of the interpretation (Yang 2002 [DIRS 160839], Section 4.1.2). The continuous calcite precipitation in the unsaturated zone removes carbon from groundwater. Although ^{14}C behaves a little differently from total carbon, the effect on the carbon isotopic fraction is minor, and the calcite precipitation is considered to have an insignificant impact on the ^{14}C activity in the groundwater and gas (Codell and Murphy 1992 [DIRS 100719]). Therefore, the measured gas-phase ^{14}C age is considered as representative data for the solute travel times of the matrix pore water of the Yucca Mountain unsaturated zone in the following model validation effort. Obviously, one necessary condition of this interpretation must be satisfied (i.e., there is no significant vertical gas flow through the borehole). This interpretation becomes limited if there is significant vertical gas flow through the borehole, because such flow would disturb the ^{14}C abundance distribution throughout the borehole. In fact, the boreholes (USW SD-12 and USW UZ-1) were closed, disturbation from the atmosphere can be neglected (unless leakage of atmospheric CO_2 into the borehole occurs), vertical gas flow in these two boreholes is not likely significant, and the ^{14}C abundance is not significantly disturbed.

7.5.3 Model Discussion

Two three-dimensional transport simulations were performed using T2R3D V1.4 (LBNL 1999 [DIRS 146654]). The three-dimensional flow fields of two infiltration scenarios, 10th percentile and 30th percentile, from UZ flow models (Output DTN: LB06123DPDUZFF.001) were respectively used to simulate the solute travel times in the entire model domain. The numerical grid used in this transport simulation is the same as that used in the flow simulation (Figure 6.1-1). As discussed in Section 6.7, hydrodynamic dispersion was ignored because of low water percolation fluxes. Thus, the ^{14}C transport is carried out primarily by advective and diffusive processes. An effective-diffusion-coefficient value of 1.97×10^{-10} m^2/s was used, equal to the average value of measured coefficients for tritiated water through Yucca Mountain tuffs (DTN: LA000000000034.002 [DIRS 148603]).

In this model, a tracer source was introduced as a pulse on the ground surface through fractures, and the tracer concentration in rock matrix was observed in the entire domain over the whole

simulation period (10^6 years). The simulated solute travel time of the matrix pore water, at a specific location, was then calculated using Equation 7.5-1 for each representative gridblock of borehole UZ-1 and SD-12. Then, the simulated solute travel times were compared to the measured ^{14}C ages. The simulated solute travel times of the matrix pore water for Boreholes UZ-1 and SD-12 were plotted and compared, respectively, to the available measured ^{14}C age data in Figures 7.5-1 for UZ-1 and 7.5-2 for SD-12.

Figure 7.5-1 shows that the simulated solute travel times for the matrix porewater of borehole UZ-1 with the three-dimensional UZ model and the 10th percentile infiltration map are much larger than the measured ^{14}C ages, while the simulated ages with the 30th percentile infiltration map are closer to the measurements and fall within the range of measurements for TSw units. There are larger uncertainties in the measured data of the shallow layers (i.e. PTn units), resulting from the disturbance caused by possible leakage of the atmospheric CO_2 into the borehole. Figure 7.5-2 shows that the simulated solute travel times for the matrix pore water of borehole SD-12 with the three-dimensional UZ model and the 30th percentile infiltration map falls within the range of the measured ^{14}C ages for TSw units, while the simulated solute travel times with the 10th percentile infiltration map are larger than the measurements. These results reflect the spatial uncertainties of the infiltration maps as discussed in *Simulation of Net Infiltration for Present-Day and Potential Future Climates* (SNL 2007 [DIRS 174294], Section 6.6.1.1) and are consistent with the study results that more weight should be given to the infiltration maps with percentiles lower than 50th (Section 6.8).

Table 7.5-1. Infiltration Rates of the Representative Gridblock of Borehole UZ-1 and SD-12

Boreholes	Local infiltration rates(mm/yr)		Domain-average infiltration rates (mm/yr)	
	10%	30%	10%	30%
UZ-1	0.0	0.38	3.03	7.96
SD-12	0.8	2.17	3.03	7.96

Source: Output DTN: LB06123DPDUZFF.001, *PD_10.dat* and *PD_30.dat* (domain average infiltration rates in mm/yr and location infiltration rates in kg/s), also see Table 6.1-2.

Output DTN: LB0704C14FFVAL.001 (*infiltration.xls*, converted local infiltration rates in mm/yr).

* "Local infiltration" is the infiltration at the representative gridblock in the infiltration map. The "Domain-average infiltration" is the average infiltration rate of the whole model domain of the corresponding percentile.

As mentioned in Table 7.5-1, the infiltration map shows that the local infiltration rate of the representative gridblock for borehole UZ-1 is 0.0 mm/yr (10th percentile), compared to the domain average of 3.03 mm/yr. The fact that the calculated solute travel times of this borehole with the 10th percentile infiltration map are much larger than the measured ^{14}C ages (Figure 7.5-1) may primarily be a result of the too-low local infiltration rate (compared to the actual infiltration rate). The second possible reason of this deviation is the horizontal heterogeneity in the rock hydraulic properties (permeability and porosity), which is not considered in the model. The other possible reason is the scale-dependency of the effective matrix diffusion coefficient (BSC 2004 [DIRS 170035], Section 6.2.2), which is not considered in the model. A larger effective matrix diffusion coefficient is expected to give a smaller travel time in the rock matrix.

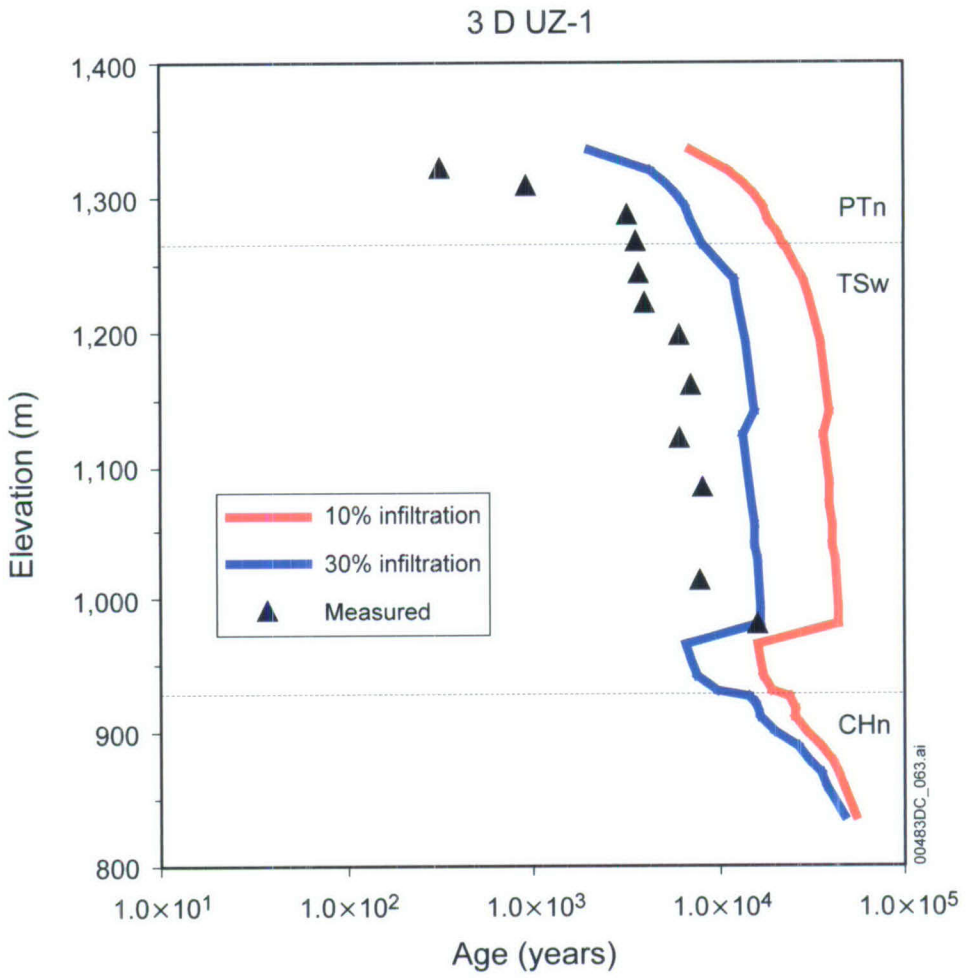

Sources: DTNs: MO0012CARB1314.000 [DIRS 153398] (Measured ^{14}C activities); MO0012MWDGFM02.002 [DIRS 153777] (borehole collar elevation and lithological layer interface elevation); LB06123DPDUZFF.001 (flow fields of 10% and 30% infiltration rate).

Output DTN: LB0704C14FFVAL.001, LB0707C14FFVAL.001, *Ages.xls* (simulated matrix porewater age, and measured ^{14}C ages converted from the measured ^{14}C activities).

Figure 7.5-1. Simulated Solute Travel Time of the Matrix Pore Water with Three-dimensional Simulation for UZ-1 Borehole Compared to the Measured ^{14}C Age

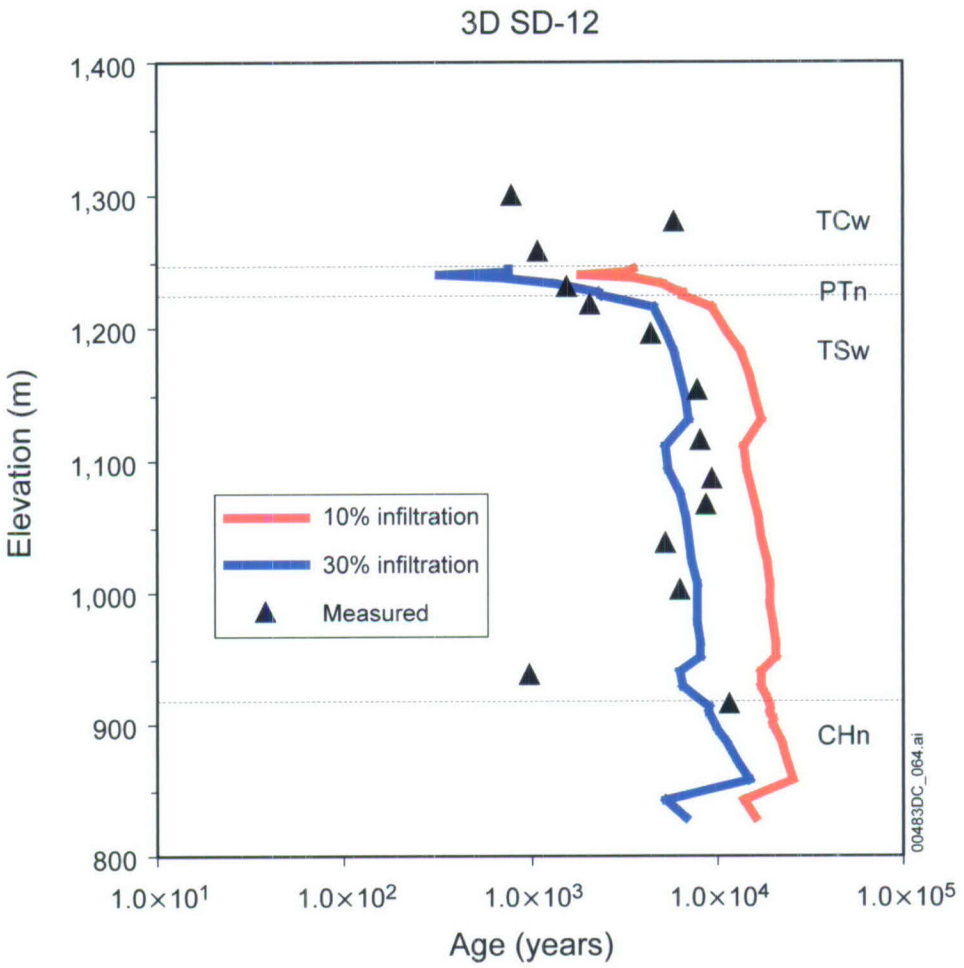

Sources: DTNs: GS961108312271.002 [DIRS 121708] (measured ^{14}C activities); MO0012MWDGFM02.002 [DIRS 153777] (borehole collar elevation and lithological layer interface elevation); Output DTN: LB06123DPDUZFF.001 (flow fields of 10% and 30% infiltration rate).

Output DTNs: LB0704C14FFVAL.001, LB0707C14FFVAL.001, *Ages.xls* (simulated matrix porewater age, and measured ^{14}C ages converted from the measured ^{14}C activities).

NOTE: Only one sample is plotted for each depth if there are multiple samples for one location.

Figure 7.5-2. Simulated Solute Travel Time of the Matrix Pore Water with Three-dimensional Simulation for SD-12 Borehole Compared to the Measured ^{14}C Age

To investigate how uncertainty in the infiltration maps affects the simulated solute travel times, a one-dimensional model was constructed for these two boreholes using the domain-average infiltration rate (10th and 30th percentile, respectively, Table 7.5-1) as an order of magnitude analysis. In comparison, the one-dimensional model reduces the uncertainties associated with spatial variation of surface infiltration rates and lateral flow with a three-dimensional model. Therefore, the one-dimensional model results are considered to be appropriate to examine the sensitivity of model simulated mean travel time to infiltration rates. The domain-average infiltration rates are higher than the respective local infiltration rate given in the 10th and 30th percentile infiltration map. The same tracer simulations described above were repeated using one-dimensional columns extracted from the three-dimensional model at locations representing SD-12 and UZ-1, and the domain-average infiltration rate (Table 7.5-1). A grid mesh of the one-dimensional simulations was made from the extracted representative gridblocks and the

connections of borehole UZ-1 and SD-12, from the three-dimensional grid mesh. Steady-state flow fields for UZ-1 and SD-12 with the domain-average infiltration rate of the 10th and 30th percentile were respectively performed using the EOS9 module of TOUGH2 V1.6 (2003 [DIRS 161491]). These steady-state flow fields (*flow9.dat* files) were then used to simulate the tracer transport processes through the representative one-dimensional columns of UZ-1 and SD-12, using T2R3D V1.4 (1999 [DIRS 146654]). The same methodology was used for tracer transport simulations and the conversion of the solute travel times of the matrix pore water from the simulated tracer concentration breakthrough, as described earlier for the three-dimensional simulations in this section. The simulated solute travel times of the pore water are plotted and compared to the measured ^{14}C age on Figure 7.5-3 (UZ-1) and Figure 7.5-4 (SD-12).

Figure 7.5-3 shows that the simulated solute travel times of borehole UZ-1 with the 30th percentile domain-average infiltration match better than that from the three-dimensional simulation (with the very low local infiltration rates), and the simulated solute travel times with the 10th percentile infiltration are also close to the measurements, but not as good as that for the 30th percentile infiltration. This finding implies that an infiltration rate between 10th and 30th percentile domain-average infiltration will make a better fit to the measured ^{14}C ages for this borehole. Figure 7.5-4 shows that the simulated solute travel times of borehole SD-12 with the 30th percentile domain-average infiltration match the measurements well, and the results with the 10th percentile domain-average infiltration fall out of range of the measurements for TSw units. These results indicate that the simulated solute travel time is sensitive to the infiltration rate, and subject to the spatial uncertainties in the infiltration maps.

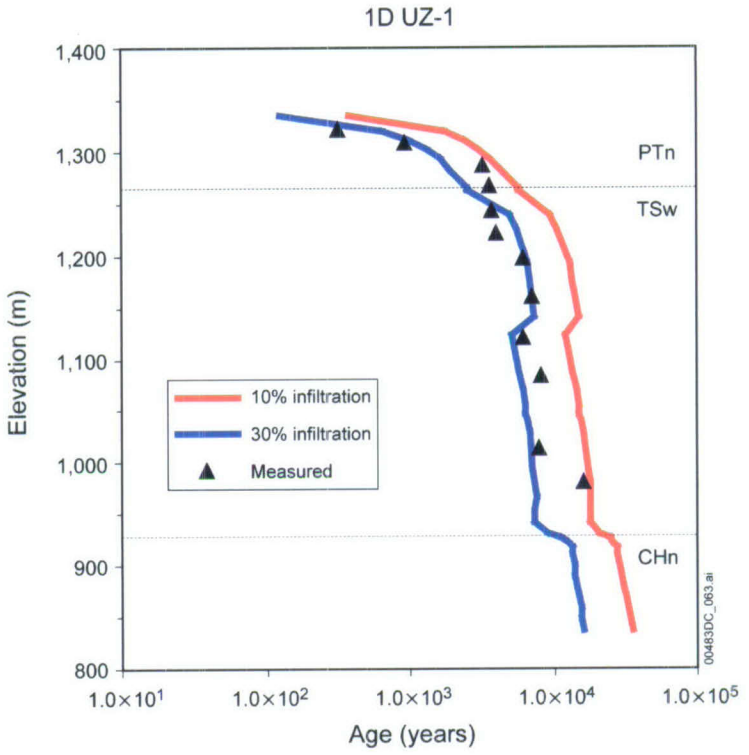

Sources: DTNs: MO0012CARB1314.000 [DIRS 153398] (Measured ^{14}C activity); MO0012MWDGFM02.002 [DIRS 153777] (borehole collar elevation and lithological layer interface elevation); Output DTN LB06123DPDUZFF.001 (flow fields of 10% and 30% infiltration rate).

Output DTN: LB0704C14FFVAL.001, LB0707C14FFVAL.001, *Ages.xls* (simulated matrix porewater age, and measured ^{14}C ages converted from the measured ^{14}C activities).

Figure 7.5-3. Simulated Solute Travel Time of the Matrix Pore Water with One-dimensional Simulation for UZ-1 Borehole Compared to the Measured ^{14}C Age

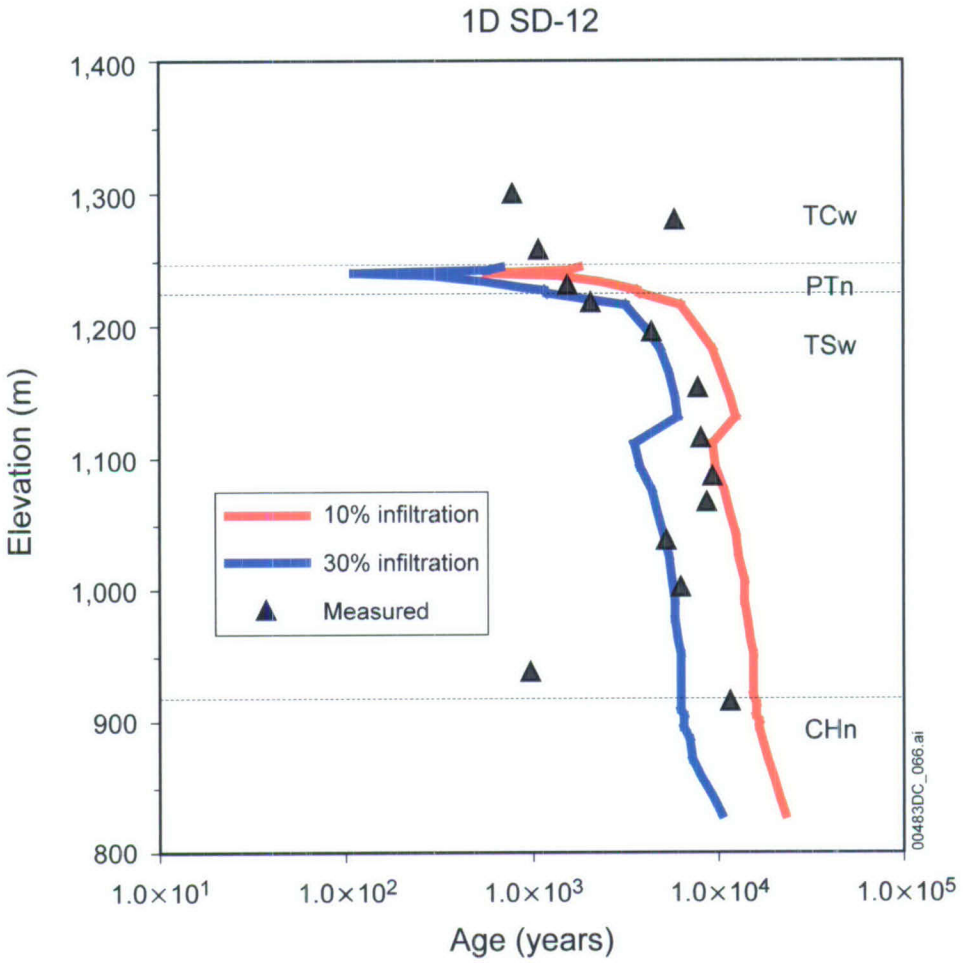

Sources: DTNs: GS961108312271.002 [DIRS 121708] (measured ^{14}C activities); MO0012MWDGFM02.002 [DIRS 153777] (borehole collar elevation and lithological layer interface elevation); Output DTN LB06123DPDUZFF.001 (flow fields of 10% and 30% infiltration rate).

Output DTN: LB0704C14FFVAL.001, LB0707C14FFVAL.001, *Ages.xls* (simulated matrix porewater age, and measured ^{14}C ages converted from the measured ^{14}C activities).

NOTE: Only one sample is plotted for each depth if there are multiple samples for one location.

Figure 7.5-4. Simulated Solute Travel Time of the Matrix Pore Water with One-dimensional Simulation for SD-12 Borehole Compared to the Measured ^{14}C Age

7.5.4 Summary

The solute travel times were simulated using a transport model based on the calibrated groundwater flow fields for the unsaturated zone, and using the 10th and the 30th percentile infiltration maps. The measured gas-phase ^{14}C ages from two instrumented boreholes (UZ-1 and SD-12) have been justified to be representative of the solute travel time for the matrix pore water. Data uncertainties were also discussed. Good matches between the calculated solute travel times and the measured ^{14}C ages was attained for borehole SD-12 with the three-dimensional UZ model and using the 30th percentile infiltration map, and an acceptable match was obtained for borehole UZ-1 using the 30th percentile infiltration map. These results reflect the spatial uncertainties in the infiltration maps as discussed in *Simulation of Net Infiltration for Present-Day and Potential Future Climates* (SNL 2007 [DIRS 174294], Section 6.6.1.1) and are

consistent with the conclusions that more weight should be given to the infiltration maps with low percentiles (Section 6.8).

In addition, sensitivities of model-simulated mean travel time to infiltration rates are studied using one-dimensional models for boreholes UZ-1 and SD-12. Results from the one-dimensional models show that the model-simulated mean travel time is sensitive to the infiltration rate. The simulated mean travel times calculated from the one-dimensional models with both 10th and 30th percentile infiltration rates are able to match the measured ^{14}C data.

However, the simulation results are subject to the uncertainties in the conceptual model and availabilities of measured data. These uncertainties include assumptions about the equilibrium of the gas-phase CO_2 and the liquid-phase carbonate, the assumption of neglecting the possible vertical gas flow inside the borehole, the possible horizontal heterogeneity in the rock hydraulic properties, and the possible scale-dependent effects of the effective matrix diffusion coefficient.

7.6 MODEL VALIDATION USING STRONTIUM GEOCHEMISTRY AND ISOTOPIC RATIOS

This section describes the use of strontium and strontium isotopic ratios ($^{87}Sr/^{86}Sr$) for validation of the UZ flow model. Validation methodology consists of work presented in peer-reviewed journals, as well as comparison of model results to data collected for pore waters. The criterion for the validation is a qualitative agreement between simulated strontium concentrations and the average of the observations at the same elevation, and an agreement with vertical trends.

7.6.1 Background

Strontium concentrations and the $^{87}Sr/^{86}Sr$ ratio in pore fluids and secondary minerals can provide important constraints on infiltration rates, flow paths, residence times, and degrees of water–rock and fracture–matrix interaction at Yucca Mountain (Stuckless et al. 1991 [DIRS 106947]; Marshall et al. 1991 [DIRS 106335]; Peterman et al. 1992 [DIRS 147110]; Peterman and Stuckless 1993 [DIRS 101149]; Johnson and DePaolo 1994 [DIRS 162560]; Vaniman and Chipera 1996 [DIRS 100089]; Sonnenthal and Bodvarsson 1999 [DIRS 117127]; and Paces et al. 2001 [DIRS 156507]). Strontium concentrations in pore waters are related to the precipitation rate and chemistry, the composition and mineralogy of windblown dust, extent of evapotranspiration, net infiltration rate, the dissolution of minerals in surface deposits, reaction with minerals or glass in the tuffs, precipitation of calcite and other carbonates, and exchange with clays and zeolites (Vaniman and Chipera 1996 [DIRS 100089]; Capo et al. 1998 [DIRS 181455]; Capo and Chadwick 1999 [DIRS 180897]; Sonnenthal and Bodvarsson 1999 [DIRS 117127]; Vaniman et al. 2001 [DIRS 157427]; Neymark et al. 2005 [DIRS 180924]). The similarity of strontium to calcium in charge and ionic radius results in strontium incorporation into calcium-bearing minerals, such as plagioclase feldspar, and secondary minerals, such as calcium-zeolites and calcium-rich smectite.

The $^{87}Sr/^{86}Sr$ ratio in pore waters depends on its initial ratio and is affected along a flow path by dissolution of strontium-bearing phases (e.g., calcite, feldspars, volcanic glass), exchange with clays or zeolites, and the mixing of waters having differing isotopic ratios (Johnson and DePaolo 1994 [DIRS 162560], p. 1,571). If such fluids have differing strontium concentrations, mixing

will result in hyperbolic curves of $^{87}Sr/^{86}Sr$ versus total strontium (Faure 1986 [DIRS 105559], p. 143), making them more complex chemically, but adding additional constraints to understanding the hydrological system. In nature, almost no fractionation of strontium isotopes occurs; however, fractionation of rubidium from strontium leads to variations in $^{87}Sr/^{86}Sr$ because of the decay of ^{87}Rb to ^{87}Sr. Because the half-life of ^{87}Rb is about 5×10^{10} years, this decay effect is insignificant over the few hundred thousand years of interest for the UZ flow system.

The effect of the rock on the isotopic composition of water thus depends on the strontium content and its isotopic ratio. The amount of rock dissolution and mineral precipitation depends on the degree to which the mineral assemblage is in disequilibrium with the water. Unaltered volcanic glass is more reactive than minerals, so that the rate of reaction of devitrified tuff with water is lower than that with glass. However, several factors can result in reduced apparent rates of reaction. The development of amorphous silica saturation in the soil zone has been proposed as a strong inhibitor of water–rock reaction in the underlying tuffs at Yucca Mountain (Meijer 2002 [DIRS 158813], pp. 803 to 804). Alteration products on the surface of fractures or on mineral grains would also lead to rates limited by diffusion through such films rather than by reaction, retarding the dissolution rate (Sonnenthal and Ortoleva 1994 [DIRS 117914], p. 407). Incongruent dissolution of volcanic glass has also been proposed as a cause for lower quantities of strontium dissolved into pore fluids in the PTn bedded tuffs (Vaniman and Chipera 1996 [DIRS 100089], p. 4,421).

7.6.2 Validation of Conceptual and Numerical Models of UZ Transport Based on Corroborative Information from Published Works

Based on chloride/strontium ratios in a relatively few number of pore-water samples that were similar to those of an estimated effective precipitation composition, and the lack of a substantial shift in $^{87}Sr/^{86}Sr$ ratio in pore salts and calcite, Sonnenthal and Bodvarsson (1999 [DIRS 117127], pp. 111 and 151) suggested that the strontium concentrations in the unsaturated zone above the zeolitic units were, in large part, inherited from surface evapotranspiration processes, with only a minor contribution from water–rock interaction. Three-dimensional unsaturated zone transport modeling, including ion exchange, showed relatively high pore-water strontium concentrations in nonzeolitic units and a strong shift to lower concentrations (by a few orders of magnitude) in zeolitic units, which was consistent with pore-water and perched water compositions in contact with the respective rock units. This comparison of modeled strontium pore water concentrations was good supporting evidence for the approximately 5 mm/yr mean infiltration rate at Yucca Mountain based on chloride concentrations in pore water (Sonnenthal and Bodvarsson 1999 [DIRS 117127], p. 107). The model also produced strontium compositions at perched water locations that were high where the perching was on the basal vitrophyre of the Topopah Spring tuff and very low where the perched water contacted zeolitic rocks. The results were consistent with several measurements made in the various boreholes that had intersected perched water bodies.

Extensive exchange of strontium with calcium in clinoptilolite is well documented in the Yucca Mountain unsaturated zone (Vaniman et al. 2001 [DIRS 157427]; Vaniman and Chipera 1996 [DIRS 100089], p. 4,431). An analysis performed by Vaniman et al. (2001 [DIRS 157427], p. 3,409) showed that the excess strontium in the zeolitic rocks from the UZ-16 borehole,

resulting from ion exchange with downward percolating water, was consistent with 10 million years of infiltration at about 5 mm/yr. Therefore, this published work provides independent corroboration of the results obtained by Sonnenthal and Bodvarsson (1999 [DIRS 117127], p. 107), based on conceptual and numerical models that form the basis for the UZ model presented here. Support for the 5 mm/yr being a long-term maximum is provided by the observation that the $^{87}Sr/^{86}Sr$ ratios in calcite are shifted to slightly higher values in calcite precipitated more recently compared to early-formed calcite, indicating some contribution of strontium from water–rock interaction (Paces et al. 2001 [DIRS 156507], p. 75). Therefore, some of the strontium in the zeolitic units must have been derived from dissolution of tuff. An increase in the $^{87}Sr/^{86}Sr$ ratio in pore water at lower infiltration rates is a result of the longer residence time that the water has in contact with rock having a much higher $^{87}Sr/^{86}Sr$ ratio.

This evidence, and the generally high strontium concentrations through the unsaturated zone above zeolitic rocks, suggests that, although some strontium is lost to precipitating calcite, a comparable amount is gained by tuff dissolution. If some of the strontium in the zeolitic rocks is in excess of that produced by infiltration, then the estimated infiltration rate, based on strontium concentrations in the zeolitic rocks, would be an upper limit.

Another piece of corroborating evidence comes from the compositions of calcite in fracture coatings. An excellent long-term record of the loss of strontium through ion exchange in the zeolites is given by the strontium concentrations in coexisting calcite, which are a few hundred parts per million through much of the unsaturated zone, and then drop to a few parts per million below zeolitic layers in the Calico Hills unit (Vaniman and Chipera 1996 [DIRS 100089], pp. 4,428 to 4,429, Table 3). This corroborates the model results showing flow through the zeolitic units and strontium exchange with calcium in zeolites, resulting in waters having very low strontium concentrations.

7.6.3 Three-Dimensional Model for Strontium Concentrations

The conceptual model for strontium in the subsurface at Yucca Mountain begins with the sources of strontium. The predominant origin of strontium from windblown carbonate dust, and lesser amounts from rainfall directly, has been well-documented for the arid Southwest (Capo and Chadwick 1999 [DIRS 180897]) and for pedogenic carbonate deposits at Yucca Mountain (Neymark et al. 2005 [DIRS 180924]. The very small effect of water–rock interaction on strontium isotopic ratios in calcite and pore waters is further validation for this conceptual model. Therefore, a reasonable approach to modeling strontium concentrations in the unsaturated zone is to consider strontium as a conservative species in the nonzeolitic units and a strongly exchangeable species in the zeolitic units (Sonnenthal and Bodvarsson 1999 [DIRS 117127], p. 143).

Strontium input at the surface was assumed to be from precipitation plus windblown dust. Two potential effective strontium concentrations in precipitation are considered. The strontium flux (J_{Sr}) at the surface was calculated similarly to the chloride flux described in Section 6.5, as follows:

$$J_{Sr} = C_{Sr,eff}(J_{prec} + J_{runon} - J_{runoff}) \quad \text{(Eq. 7.6-1)}$$

The effective concentration of strontium in precipitation ($C_{Sr,eff}$) considers both the flux from rainfall and that derived from windblown dust. Two values were chosen so that the uncertainty in this input can be evaluated. Sonnenthal and Bodvarsson (1999 [DIRS 117127]) used a value of 5.8 µg/L. $C_{Sr,eff}$ can also be calculated based on the surface dust flux, its strontium concentration, and the precipitation flux, as follows:

$$C_{Sr,eff} = \frac{C_{Sr,dust} J_{dust}}{J_{prec}} \quad \text{(Eq. 7.6-2)}$$

The concentration of strontium in dust (380 µg/g) is an average value determined for acid-leached samples collected in "sheltered" areas at Yucca Mountain (DTN: GS061208313000.005 [DIRS 181397]). This could be considered as roughly the upper maximum for the strontium that could become soluble and be transported in infiltrating water. An average dust flux of 6 g m^{-2} yr^{-1} was based on the range of values given by Reheis (2006 [DIRS 180898]) of 3 to 9 g m^{-2} yr^{-1}. Since the sum of the maximum carbonate flux (~ 2 g m^{-2} yr^{-1}) for non-limestone sediments and a maximum salt flux of also about 2 g m^{-2} yr^{-1} is less than 6 g m^{-2} yr^{-1}, and most strontium is held in the carbonate component, and less in the salts, this is likely also a maximum average value. The average precipitation rate for the 10th percentile scenario is 163.44 mm/yr, which yields a value of 13.95 µg/L for $C_{Sr,eff}$. The mean precipitation rate for the 30th percentile scenario is 153.89 mm/yr yields a value of 14.8 µg/L for $C_{Sr,eff}$.

Sr is considered to be an exchangeable species in the zeolitic units as a result of exchange of Sr for calcium in calcium-rich zeolites A strontium distribution coefficient (K_d) of 1.0 m^3/kg (DTN: LA0408AM831341.001 [DIRS 171584]) was applied to the zeolitic rocks. The latter value for the K_d is the approximate mean based on a range from 0.05 to 2.0 m^3/kg provided in the data tracking number. Because all the K_d values in this range would result in a moderate to strong shift in pore water strontium concentrations from nonzeolitic to zeolitic rocks, the effect of assuming a uniform K_d only results in uncertainty in the degree to which concentrations within and below the zeolitic units are shifted to lower values. In order to evaluate the effect of a higher K_d, two simulations were performed with a K_d value of 2.0 m^3/kg.

The lower boundary condition (saturated zone) was set to a concentration 0.036 mg/liter, based on values from the SD-6 borehole (a similar value was also reported for the saturated zone water from the J-13 well). The system was also initialized to this same value, which has no effect on the steady-state concentrations in the nonzeolitic rocks above the perched water, but sets the equilibrium value for the zeolites. All simulations were run for 2 million years using T2R3D V1.4 [DIRS 146654], with a maximum time step of 1,000 years, which resulted in a steady state concentration distribution. The model uses the same steady state fields (for 10th and 30th percentile present-day scenarios) discussed in Section 6.

The simulations conducted are as follows:

1. sr_high3_pd_10: High $C_{Sr,eff}$ (13.95 µg/liter) for present-day (pd) 10th percentile infiltration and precipitation rates. $K_{d,Sr}$ = 1.0 m^3/kg.

2. sr_high3_pd_10_kd2: High $C_{Sr,eff}$ (13.95 µg/liter) for present-day (pd) 10th percentile infiltration and precipitation rates. $K_{d,Sr}$ = 2.0 m^3/kg.

3. sr_high3_pd_30: High $C_{Sr,eff}$ (14.8 µg/liter) for present-day (pd) 30th percentile infiltration and precipitation rates. $K_{d,Sr}$ = 1.0 m^3/kg.

4. sr_high3_pd_30: High $C_{Sr,eff}$ (14.8 µg/liter) for present-day (pd) 30th percentile infiltration and precipitation rates. $K_{d,Sr}$ = 2.0 m^3/kg.

5. sr_mid2_pd_10: Lower $C_{Sr,eff}$ (5.8 µg/liter) for present-day (pd) 10th percentile infiltration and precipitation rates. $K_{d,Sr}$ = 1.0 m^3/kg.

6. sr_mid2_pd_30: Lower $C_{Sr,eff}$ (5.8 µg/liter) for present-day (pd) 30th percentile infiltration and precipitation rates. $K_{d,Sr}$ = 1.0 m^3/kg.

Inputs and outputs for the three-dimensional model simulations have been submitted to the TDMS under DTN: LB0705UZSRTRAN.001.

Modeled strontium concentrations are compared to measured values for pore salts extracted (by leaching) from two surface-based boreholes (SD-9 and SD-12; DTN: GS990308315215.004 [DIRS 145711]), perched waters, and pore waters obtained by ultracentrifugation of core samples from the ECRB and for SD-9 (DTN: GS020408312272.003 [DIRS 160899]). Comparison of concentrations determined by ultracentrifuge and by water leaches on the same samples have shown that the ultracentrifuge concentrations are higher and probably closer to the true pore water concentrations (see Figure 7.6-1a for SD-9 samples).

Comparisons of measured and modeled strontium concentrations as a function of elevation for the surface-based boreholes (SD-9 and SD-12) are shown in Figure 7.6-1(a and b). Measured concentrations in the unsaturated zone above the perched water show a range of concentrations from about 0.1 to 3 mg/L in nonzeolitic and down to about 0.005 mg/L in zeolitic. Moderately large variations exist in the measured strontium concentrations as a function of depth in the unsaturated zone above the zeolitic horizons. The high concentration, 30th percentile precipitation/infiltration and the lower (mid2) 10th percentile simulation results are closest to the measured data in boreholes SD-9 and SD-12. Looking more closely at the profiles, the near-surface data is closer to the 10th percentile precipitation/infiltration, and the deeper data (above the perched water) is closer the 30th percentile simulations at the lower effective concentration. This may be a result of climate changes where deeper waters reflect a higher proportion of older potential Pleistocene-age water (Sonnenthal and Bodvarsson 1999 [DIRS 117127]).

The sharp reduction in strontium concentrations in the perched water bodies, and in the zeolitic units below, is consistent with ion exchange in zeolitic rocks, since the decrease is much greater than the equivalent drop in chloride concentrations. Where perched water samples were collected in SD-9, the model results show a strong decrease, but not to a small value as those measured. An increase in $K_{d,Sr}$ of a factor of 2 does not make a significant difference in the results. Owing to the initialization of the pore water in the zeolitic rocks to the saturated zone value, which is higher than those measured in the perched water in SD-9, the concentrations never drop below this value, and therefore do not match the perched water or zeolitic pore waters in SD-12. Changing the initialization to a much lower value would result in a much better match, but could not be independently supported by any measured data. In SD-12, the measured and modeled

concentrations below 900 meters exhibit a reversal to higher concentrations. This reversal is consistent with lateral flow in the vitric units, rather than simple vertical flow through the zeolitic units that would result in consistently low concentrations below them.

The criterion for validation is qualitative agreement between the simulated strontium concentrations and the average of the observations at the same elevation, and agreement with the vertical trends. The comparisons shown for the surface-based boreholes therefore meet the validation criteria.

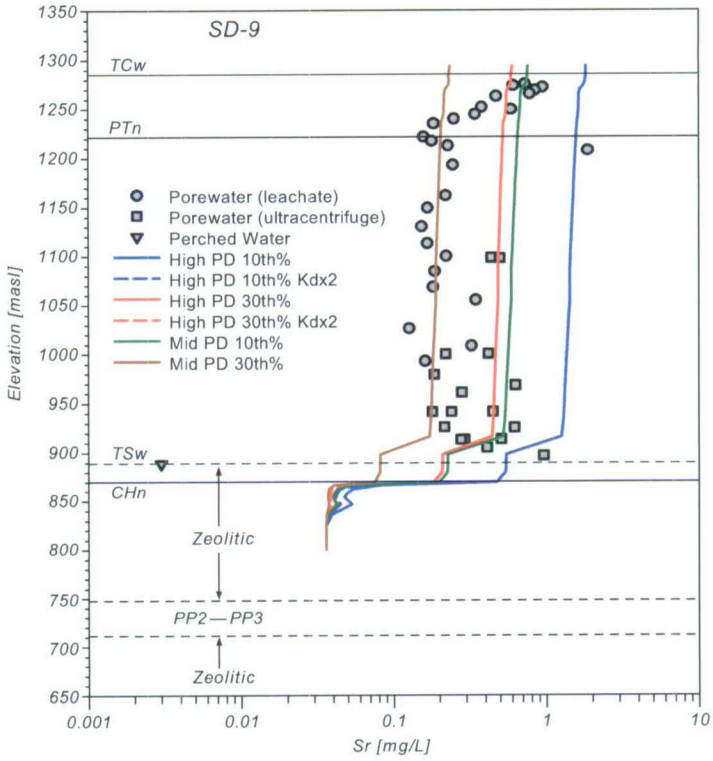

(a)

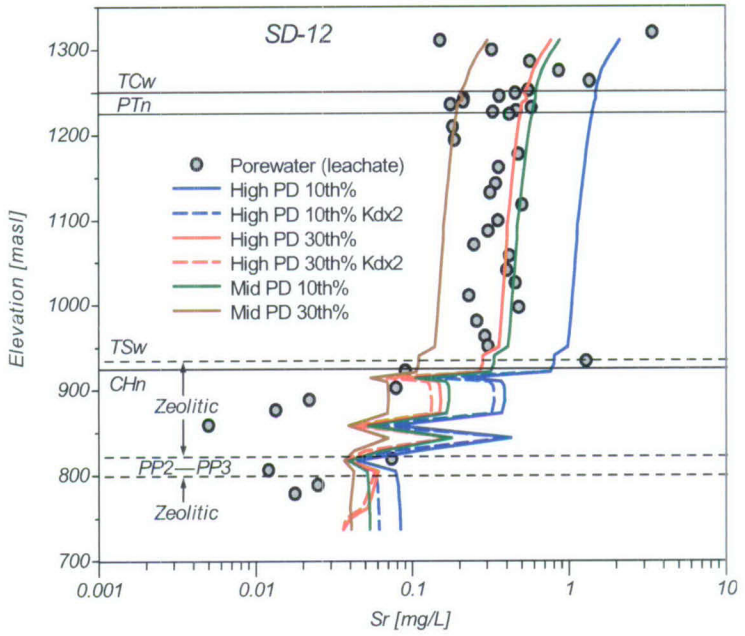

(b)

Source: DTN: GS990308315215.004 [DIRS 145711].

Model Input and Output DTN: LB0705UZSRTRAN.001.

3-D=three-dimensional; UZ=unsaturated zone; masl=meters above sea level.

Figure 7.6-1. Comparison of Measured and Modeled Strontium Concentrations as a Function of Elevation for the Surface-Based Boreholes (a) SD-9 and (b) SD-12

Measured and modeled strontium concentrations in pore waters extracted from cores taken in the ECRB are shown in Figure 7.6-2. Measured concentrations are mostly between 1 and 5 mg/L, with some samples having somewhat lower concentrations. These concentrations are generally higher than those measured in the surface-based boreholes, even those extracted by the same ultracentrifuge method. Most of the modeled strontium concentrations are also lower in this region, consistent with the lower chloride concentrations in most ECRB samples. Although the comparison of measured and modeled concentrations generally meet the order-of-magnitude criterion for the 10th percentile high concentration case, the deviations are mostly greater than that for the surface-based boreholes. Ratios for $^{87}Sr/^{86}Sr$ are not available for these samples, and, therefore, the degree to which strontium concentrations may have been shifted to higher values by water–rock interaction cannot be assessed. Bulk-rock compositions for major and trace elements for tuffs in the ECRB are virtually identical to samples collected elsewhere (Peterman and Cloke 2002 [DIRS 162576], p. 696). Consequently, a shift caused by locally greater water–rock interaction in the welded tuffs is not likely, although enhanced reaction in the PTn above is possible. Other possibilities are a larger contribution of dust-derived strontium, or that the surface-based borehole concentrations are lower than the typical samples in the unsaturated zone at the repository horizon.

Given the variability in precipitation and infiltration rates, effects of past climatic events, and local variations in dust input, the model captures the overall trends and strontium concentrations. Based on the agreement between modeled and measured borehole data, and these caveats, the strontium model has been validated sufficiently, for the 10th percentile infiltration rate, or the 30th percentile case with a high dust input.

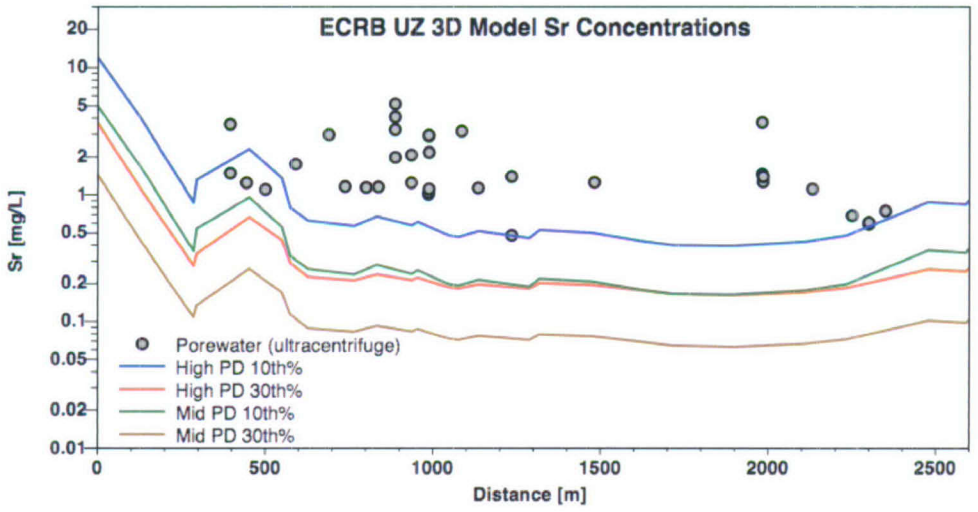

Source: DTN: GS020408312272.003 [DIRS 160899].

Model Input and Output DTN: LB0705UZSRTRAN.001.

3-D=three-dimensional; ECRB=Enhanced Characterization of the Repository Block; UZ=unsaturated zone.

Figure 7.6-2. Measured and Modeled Strontium Concentrations in Pore Waters Extracted from Cores Taken in the ECRB

7.7 CALCITE MODEL

7.7.1 Introduction

According to the TWP (BSC 2006 [DIRS 177465], Section 1), the model validation runs do not need updating from the previous work, because the infiltration rates used in calcite modeling still bound the new base-case infiltration rates. As shown in Table 6.1-2, the average rate over the model domain for the present-day 10th percentile infiltration with the UZ model grid is 3.03 mm/yr (the base-case infiltration scenario). For the WT-24 location that was used for calcite analysis, the new base-case infiltration rate is 9.25 mm/yr. These infiltration rates in the current flow model fall into the range from 2 to 20 mm/yr used in the previous calcite modeling. Therefore, Section 7.7 is basically a reproduction of Section 7.9 of the previous report (BSC 2004 [DIRS 169861]). The current content have some revisions: (1) inclusion of a commentary by Dublyansky and Smirnov (2005 [DIRS 180650]) on the journal publication of this calcite model by Xu et al. (2003 [DIRS 162124]), and the reply to the commentary paper by Sonnenthal et al. (2005 [DIRS 180639]) (see the end of this section, and Section 7.7.5.1), and (2) some clarifications for technical reviews. The conclusions of the current report have not changed from the previous report (BSC 2004 [DIRS 169861]).

The percolation flux in the unsaturated zone is an important parameter because it controls seepage into drifts that may contact waste packages. As shown in Section 6.6, it depends strongly on the infiltration flux, which is a boundary condition of the UZ flow model. Observations of precipitated calcite in the unsaturated zone constrain the infiltration flux. Therefore, comparing observed hydrogenic calcite deposits to simulations increased confidence in the model's ability to capture this boundary condition. Because direct measurements of infiltration flux is not possible, this confirmation of the boundary condition generally builds confidence in the UZ flow model. Hydrogenic calcite deposits in fractures and lithophysal cavities at Yucca Mountain have been studied to estimate past percolation fluxes (Carlos et al. 1995 [DIRS 162118]; Marshall et al. 1998 [DIRS 107415]; BSC 2004 [DIRS 169734], Section 7.7.1).

One objective of these previous studies was to investigate the relationship between percolation flux and measured calcite abundances. The U.S. Geological Survey (USGS) determined calcite abundances from a deep surface-based borehole (WT-24) (DTN: GS021008315215.007 [DIRS 162127]). Geochronology work performed by the USGS (Neymark et al. 2001 [DIRS 156889]) indicates that this calcite formed over approximately 10 million years. Hydrogenic mineral coatings in the unsaturated zone are nonuniformly distributed and located almost entirely on fracture footwalls and cavity floors—in contrast to saturated environments, in which vein and cavity deposits usually coat all surfaces.

A one-dimensional model column corresponding to the location of a deep borehole (WT-24) was chosen for modeling calcite deposition because measured calcite abundances (DTN: GS021008315215.007 [DIRS 162127]) were available for comparison. Here, the results of a reactive transport numerical model for calcite deposition under different infiltration conditions are presented. The setup and results of the problem are cited from the report by Xu et al. (2003 [DIRS 162124]). The reactive transport model used here considers the following essential factors affecting calcite precipitation: (1) infiltration, (2) the ambient geothermal

gradient, (3) gaseous CO_2 diffusive transport and partitioning in liquid and gas phases, (4) fracture–matrix interaction for water flow and chemical constituents (dual permeability), and (5) water–rock interaction. Any water–rock interaction effects (e.g., pH modification) also affect the calcite solubility, hence, its abundance in each rock unit. The dual permeability model allows us to address not only the abundances of calcite with depth, but also its relative abundance in fractures and in the rock matrix as a function of the hydrological/geochemical processes in each medium, as well as the interaction of water flowing between fractures and matrix.

Dublyansky and Smirnov (2005 [DIRS 180650]) wrote a comment paper on the journal article by Xu et al. (2003 [DIRS 162124]), which questioned inappropriate thermal boundary conditions for simulations used. In reply to the commentary paper, Sonnenthal et al. (2005 [DIRS 162127]) performed a simulation with variable bottom boundary temperatures approximating those measured in fluid inclusions. The results of this simulation is discussed later in Section 7.7.5.1.

It should be pointed out that the one-dimensional calcite data modeling and analysis do not have to do with the direct validation of the three-dimensional flow model, but this model may provide some additional evidence for the validation at a location. A steady-state one-dimensional flow field was used for the analysis, because here the primary interest is long-term calcite deposition within the TSw unit, in which flow is primary one-dimensional vertical gravity-driven.

7.7.2 Calcite Precipitation Mechanisms

Along with wind-blown dust, precipitation carries much of the calcium to the surface (Vaniman et al. 2001 [DIRS 157427]). In the soil zone, strong evapotranspiration, along with some water–rock interaction and root-zone biological processes, leads to saturation with respect to calcite. The depth to reach calcite equilibrium depends on climate and infiltration variations over time, episodic water flow, and near-surface biogeochemical conditions. During more typical smaller infiltration events, calcite may reach equilibrium close to the surface. However, large infiltration pulses of calcite-undersaturated water can dissolve near-surface calcite and reach equilibrium at a greater depth. This model validation activity concerns calcite deposition in a deep geological unit, the TSw, where the repository is located. Uncertainty in the infiltrating water composition near the surface is, thus, insignificant because calcite reaches saturation well above this unit. In addition, the constant infiltration rate and steady-state water flow conditions over geological time used in the simulations are also justified by evidence that the rate of calcite growth in the unsaturated zone has remained approximately constant over at least the past 8 million years (Paces et al. 1998 [DIRS 107408]).

The primary driving force for calcite precipitation from percolating waters in the unsaturated zone is its decreasing solubility with increasing temperature; calcite precipitates as water flows downward because of the geothermal gradient. Therefore, consideration of the ambient geothermal gradient is very important for calcite precipitation. The temperature distribution is a function of the crustal heat flow and the effect of infiltration. The modeled temperature distributions in borehole WT-24 are discussed later in Section 7.7.5.2. Pore waters extracted from deep locations of the Yucca Mountain rock matrix are close to equilibrium with respect to calcite (BSC 2004 [DIRS 169734], Section 7.7.1), and no measurements of aqueous concentrations are available from fractures because they generally have low liquid saturations.

The calcium concentration and CO_2 partial pressure in percolating water is a major factor controlling the abundances of calcite and its stability. This is a result of the decreasing solubility of CO_2 gas in water with increasing temperature, which in turn causes the following degassing process: $HCO_3^- + H^+ \rightarrow CO_2$ (g) + H_2O. Gaseous CO_2 is also redistributed by gas-phase diffusive transport. Degassing increases the pH, and then contributes to calcite precipitation: $Ca^{2+} + HCO_3^- \rightarrow CaCO_3$ (calcite) + H^+. Water and gas flow between fractures and the adjacent matrix governs the resulting calcite distribution within each medium. Calcite precipitation is also affected by other factors, such as the dissolution and precipitation of aluminosilicate minerals (mainly through modifying the pH and the CO_2 partial pressure).

7.7.3 Reactive-Transport Model

Modeling of calcite deposition in the Yucca Mountain unsaturated zone was performed using the reactive transport computer code TOUGHREACT (Xu and Pruess 1998 [DIRS 117170]; 2001 [DIRS 156280]). (This version of the code has not been qualified under LP-SI.11Q-BSC, *Software* Management, but its use for corroboration is appropriate). The code uses a sequential iteration approach similar to the report by Yeh and Tripathi (1991 [DIRS 162125]), Walter et al. (1994 [DIRS 162122]), and Xu et al. (1999 [DIRS 162123]), which solve the transport and reaction equations separately. Flow and transport are based on space discretization by means of integral finite differences. An implicit time-weighting scheme is used for individual components of the model: flow, transport, and kinetic geochemical reaction. The chemical transport equations are solved independently for each component, whereas the reaction equations are solved on a gridblock basis using Newton-Raphson iteration. Full details of the code are given in reports by Xu and Pruess (1998 [DIRS 117170]; 2001 [DIRS 156280]).

In the model, advective and diffusive transport of aqueous chemical species is considered in the liquid phase. Molecular diffusive transport of gaseous species (CO_2) is considered in the gas phase. Aqueous chemical complexation and gas dissolution/exsolution are accounted for under local equilibrium, whereas mineral dissolution/precipitation can proceed at equilibrium and/or can be kinetically controlled. Gas species in the chemical computations are assumed to behave as ideal gases (i.e., fugacity equals partial pressure). Temperature effects are considered for geochemical reaction calculations, because equilibrium and kinetic data are functions of temperature.

Changes in porosity and permeability from mineral dissolution and precipitation on water flow are not considered for the present modeling. In fact, these changes are very small. Figure 7.7-3 shows that observed calcite precipitation in TSw unit is less than 1%. These effects have not appeared to close up any fracture in the deep system. By neglecting porosity and permeability change, modelers obtain quasi-steady flow conditions. This makes it possible to consider geochemistry in great detail for a simulation period of 10 million years.

A dual permeability approach, in which fractures and matrix are treated as two separate continua, was employed for water flow and chemical transport in the unsaturated fractured tuff. In this approach, interflow (water and chemicals) is allowed between fractures and the adjacent matrix, and global flow occurs within both fracture and matrix continua. The AFM developed by Liu et al. (1998 [DIRS 105729]) was used to describe fracture–matrix interaction and preferential liquid flow in fractures.

7.7.4 Hydrogeological and Geochemical Conditions

7.7.4.1 Hydrogeological Conditions

As discussed in the geological model of Section 6.1, the Yucca Mountain unsaturated zone consists of layers of welded and nonwelded volcanic tuffs. The welded and nonwelded tuffs have vastly different hydrological properties. Welded units are characterized by relatively low porosity, low matrix permeability, and high fracture density, whereas the nonwelded tuffs have higher matrix porosity and permeability, and lower fracture density (Liu et al. 1998 [DIRS 105729]). Montazer and Wilson (1984 [DIRS 100161]) developed a conceptual model for the Yucca Mountain unsaturated zone that identified five main hydrogeological units based on the degree of welding and on the associated relationships to fracture intensity. This model has formed the basis for modeling flow in the Yucca Mountain UZ. Table 7.7-1 describes each unit, which is further divided into a number of model layers with different hydrogeological and geochemical properties (SNL 2007 [DIRS 179545]; SNL 2007 [DIRS 177404]). The CHn unit is comprised of zeolitic and vitric nonwelded tuffs underlying the basal vitrophyre of the Topopah Spring Tuff. Below the CHn are the Crater Flat undifferentiated units, consisting of the lower Bullfrog and Tram Tuffs of the Crater Flat Group. The hydrogeological units below the TSw were not considered in geochemical transport simulations, so details regarding these units are not given in Table 7.7-1. The primary interest is in calcite deposition within the TSw unit, where the repository is located (tsw4 and tsw5 model layers in Table 7.7-1). The exclusion of the underlying hydrogeological units does not affect the results in the TSw unit because flow is predominantly gravity driven, and upward chemical diffusion is subordinate to downward advective transport. Note also that the previous set of porosity and permeability (Table 7.7-1) used in calcite modeling are different from the current flow model. As mentioned before, a one-dimensional steady-state flow field was used for the calcite modeling—the amount of calcite precipitation mainly depends on infiltration rate and then the percolation flux. Therefore, effects of different porosity and permeability on calcite precipitation in TSw should be small.

Table 7.7-1. Hydrogeologic Units, Model Layers, and Hydrogeological Properties for the Yucca Mountain UZ Flow and Transport Model, as Given by the Calibrated Properties Model

Hydrogeologic Unit	Description	Model Layer	Fracture		Matrix	
			Permeability (m^2)	Porosity	Permeability (m^2)	Porosity
TCw: Tiva Canyon Welded unit	Moderately to densely welded portions of the Tiva Canyon Tuff of the Paintbrush Group	tcw1	2.41×10^{-12}	3.7×10^{-2}	3.86×10^{-15}	0.253
		tcw2	1.00×10^{-10}	2.6×10^{-2}	2.74×10^{-19}	0.082
		tcw3	5.42×10^{-12}	1.9×10^{-2}	9.23×10^{-17}	0.203
PTn: Paintbrush Nonwelded unit	Variably welded Paintbrush Tuff and its associated bedded tuffs, including those located at the bottom of the Tiva Canyon and top of the Topopah Spring Tuffs	ptn1	1.86×10^{-12}	1.4×10^{-2}	9.90×10^{-13}	0.387
		ptn2	2.00×10^{-11}	1.5×10^{-2}	2.65×10^{-12}	0.439
		ptn3	2.60×10^{-13}	3.2×10^{-3}	1.23×10^{-13}	0.254
		ptn4	4.67×10^{-13}	1.5×10^{-2}	7.86×10^{-14}	0.411
		ptn5	7.03×10^{-13}	7.9×10^{-3}	7.00×10^{-14}	0.499
		ptn6	4.44×10^{-13}	4.6×10^{-3}	2.21×10^{-13}	0.492

Table 7.7-1. Hydrogeologic Units, Model Layers, and Hydrogeological Properties for the Yucca Mountain UZ Flow and Transport Model, as Given by the Calibrated Properties Model (Continued)

Hydrogeologic Unit	Description	Model Layer	Fracture		Matrix	
			Permeability (m^2)	Porosity	Permeability (m^2)	Porosity
TSw: Topopah Spring welded unit	Moderately to densely welded portions of the Topopah Spring Tuff down to, and including, the densely welded basal vitrophyre	tsw1	3.21×10^{-11}	7.1×10^{-3}	6.32×10^{-17}	0.053
		tsw2	3.56×10^{-11}	1.2×10^{-2}	5.83×10^{-16}	0.157
		tsw3	3.86×10^{-11}	8.5×10^{-3}	3.08×10^{-17}	0.154
		tsw4	1.70×10^{-11}	1.0×10^{-2}	4.07×10^{-18}	0.110
		tsw5	4.51×10^{-11}	1.5×10^{-2}	3.04×10^{-17}	0.131
		tsw6	7.01×10^{-11}	2.0×10^{-2}	5.71×10^{-18}	0.112
		tsw7	7.01×10^{-11}	2.0×10^{-2}	4.49×10^{-18}	0.094
		tsw8	5.92×10^{-13}	1.6×10^{-2}	4.53×10^{-18}	0.037
		tsw9	4.57×10^{-13}	5.9×10^{-3}	5.46×10^{-17}	0.173

Source: DTN: LB997141233129.001 [DIRS 104055].

7.7.4.2 Geochemical Model

Minerals considered in the simulations are calcite, gypsum, goethite, tridymite, cristobalite-α, quartz, amorphous silica, hematite, fluorite, albite, K-feldspar, anorthite, calcium-smectite, Mg-smectite, Na-smectite, illite, kaolinite, opal-CT, stellerite, heulandite, mordenite, clinoptilolite, and glass (Xu et al. 2003 [DIRS 162124]). This full assemblage of minerals and the corresponding aqueous species are hereafter termed the "extended-case geochemical system." This assemblage has complexities and uncertainties in terms of thermodynamics and kinetics of mineral solid solutions (clays, zeolites, and feldspars), effects on pH, and the partial pressure of CO_2. A simpler set of minerals and aqueous species (base-case geochemical system) disregards all aluminosilicates, as well as iron- and magnesium-bearing minerals.

Calcite and gypsum dissolution and precipitation were assumed to take place under geochemical equilibrium, whereas dissolution and precipitation of the other minerals were treated under kinetic constraints. Initial mineral abundances were taken from DTN: LB991200DSTTHC.003 [DIRS 161276]. Potential secondary minerals (i.e., those allowed to precipitate but which may not necessarily form) were determined from field and experimental observations of water–rock interaction, and from equilibrium geochemical model calculations. Reactive surface areas of minerals on fracture walls were calculated from the fracture–matrix interface area/volume ratio, the fracture porosity, and the derived mineral volume fractions (DTN: LB0101DSTTHCR1.003 [DIRS 161278]). These areas were based on the fracture densities, fracture porosities, and mean fracture diameter. Mineral surface areas in the rock matrix were calculated using the geometric area of a cubic array of truncated spheres that make up the framework of the rock and reductions to those areas, owing to the presence of alteration phases such as clays and zeolites.

Initial pore water chemical concentrations were based on analyses of ultracentrifuged water and chemical speciation calculations presented in *Drift-Scale THC Seepage Model* (SNL 2007 [DIRS 177404]). Except for perched water that lies well below the repository horizon, water has not been observed in fractures in the unsaturated zone. Therefore, the initial composition of water in the fractures was set to be the same as the matrix pore water (Table 7.7-2). The same water composition, reequilibrated at the temperature of the top model boundary, was assumed for infiltrating water. Oxidizing conditions were considered for this water because the fracture permeability of the rock is high and the system is unsaturated (air phase is present everywhere). The CO_2 gas partial pressures used for initial and top boundary conditions of the gas transport are in equilibrium with the corresponding aqueous chemical composition. An elevated gas partial pressure (relative to an atmospheric value of 0.344×10^{-3} bar) at the upper boundary can be attributed to soil-zone CO_2 production.

Table 7.7-2. Water and Gas Chemistry Used for Initial and Boundary Conditions of the Reaction-Transport Simulations

Component	Concentration	Unit
Ca	101	mg/L
Mg	17	mg/L
Na	61.3	mg/L
K	8	mg/L
SiO_2 (aq)	70.5	mg/L
Al	1.67×10^{-5}	mg/L
HCO_3	200	mg/L
Cl	117	mg/L
SO_4	116	mg/L
F	0.86	mg/L
Fe	6.46×10^{-8}	mg/L
pH	8.32 (at 25°C) 7.75 (at 17°C)	
PCO_2	2.726×10^{-3} at 17°C	bar

Source: Xu et al. 2003 [DIRS 162124].

7.7.4.3 Simulation Setup

Simulations with the one-dimensional model were performed using three infiltration rates, a rate of 5.92 mm/yr (Xu et al. 2003 [DIRS 162124]), and bounding rates of 2 and 20 mm/yr. The corresponding (to infiltration rates) steady-state water flow conditions were used for geochemical transport simulations. Steady-state water saturation distribution is presented in Figure 7.7-1. Steady-state temperature distributions corresponding to the same three infiltration rates are shown in Figure 7.7-2. These were obtained using a top temperature of 15.6°C at the land surface and a bottom temperature of 28°C at the water table. For the three infiltration rates, the same water and gas chemistry was used for the top boundary condition. As discussed in Section 7.7.2, the infiltrating water composition applied here is considered to be the water chemistry after transformation by soil-zone processes (evapotranspiration predominantly). Calcite precipitation in the TSw unit is not sensitive to uncertainties in the infiltrating water chemistry, because it is well below the region where calcite becomes saturated. Moreover, episodic flow has been strongly dampened by the overlying weakly fractured bedded tuffs in the PTn hydrogeological unit.

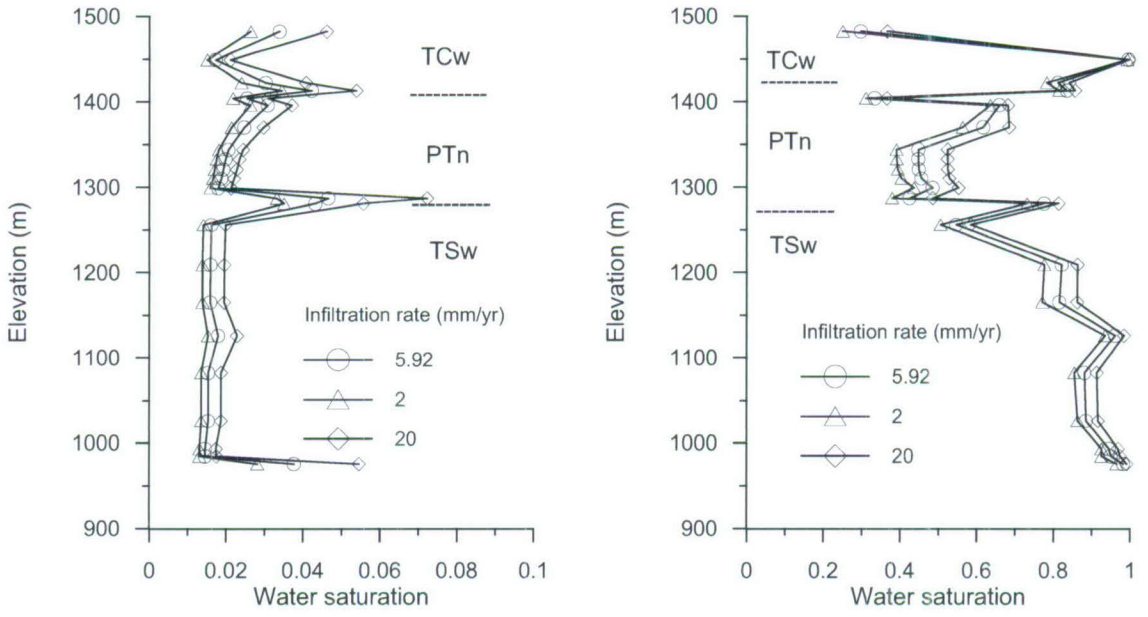

(a) Fracture (b) Matrix

Source: Xu et al. 2003 [DIRS 162124].

PTn=Paintbrush nonwelded hydrogeologic unit; TCw=Tiva Canyon welded hydrogeologic unit; TSw=Topopah Spring welded hydrogeologic unit.

Figure 7.7-1. Modeled Steady-State Water Saturations for the WT-24 Column Using Infiltration Rates: 2, 5.92, and 20 mm/yr

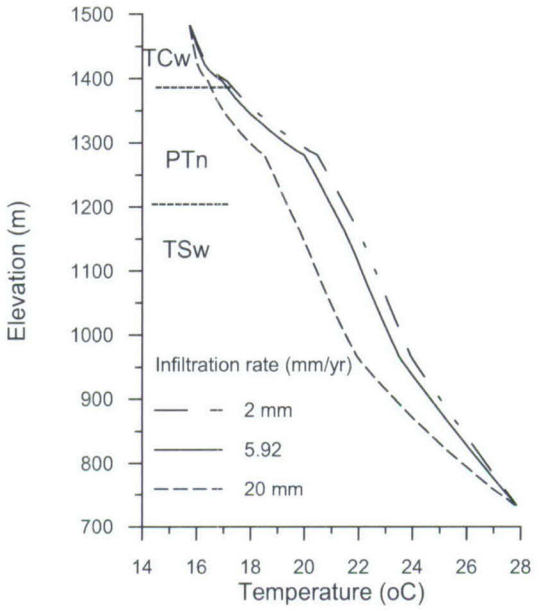

Source: Xu et al. 2003 [DIRS 162124].

PTn=Paintbrush nonwelded hydrogeologic unit; TCw=Tiva Canyon welded hydrogeologic unit; TSw=Topopah Spring welded hydrogeologic unit.

Figure 7.7-2. Modeled Temperature Profiles in Borehole WT-24 as a Function of Depth for Three Infiltration Rates

For the reactive transport simulations of calcite precipitation, a simulation time of 10 million years was selected because this calcite formed over approximately 10 million years (Neymark et al. 2001 [DIRS 156889]). Infiltration rates and temperatures were held constant throughout the time of the simulation; therefore, the results reflect the average conditions over this period of time.

7.7.5 Results and Discussion

7.7.5.1 Comparison with Measured Data

The simulated total (fracture plus matrix) calcite abundances in the WT-24 column obtained using the three different infiltration rates are presented together with measured data in Figure 7.7-3a (extended-case geochemical system) and Figure 7.7-3b (base-case geochemical system). Generally, the results obtained using the infiltration rate (5.92 mm/yr) agree better with the measured WT-24 mineral abundances than those obtained using the other infiltration rates, especially for the PTn unit. The extended-case geochemical system gives a better match to the total calcite abundances, especially for the TSw unit, indicating that some contribution of calcium from the rock is required.

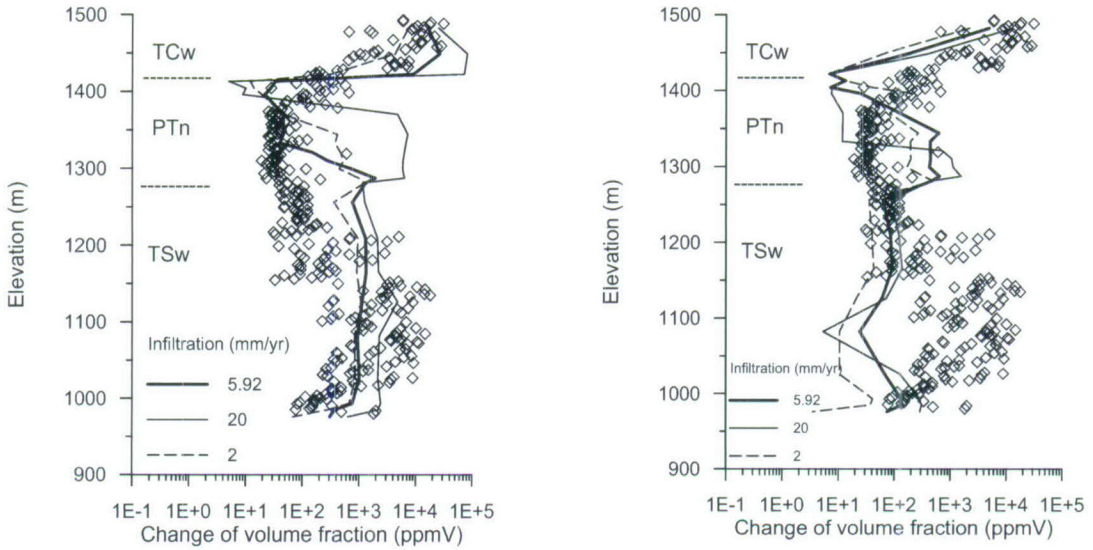

Source: Simulated results are from Xu et al. 2003 [DIRS 162124].

NOTE: Diamonds represent bulk rock calcite abundances measured by the U.S. Geological Survey (GS021008315215.007 [DIRS 162127]).

PTn=Paintbrush nonwelded hydrogeologic unit; TCw=Tiva Canyon welded hydrogeologic unit; TSw=Topopah Spring welded hydrogeologic unit.

Figure 7.7-3. Simulated Total (Fracture Plus Matrix) Calcite Abundances (in ppmV or 10^{-6} Volume Fraction) in the WT-24 Column for Different Infiltration Rates after 10 Million Years: (a) Extended-Case Geochemical System, (b) Base-Case Geochemical System

The simulated calcite abundances in the basal PTn layer for the three infiltration simulations are higher than that measured in WT-24. This results from an increase in the temperature gradient (Figure 7.7-2), resulting in a concomitant decrease in calcite solubility. The relatively larger calcite abundances in the bottom layer of the PTn have been observed at other locations such as in another deep borehole, USW G-2 (Carey et al. 1998 [DIRS 109051]). The lower measured calcite abundances may also result from lateral flow or by-passing of percolation, which is not captured in the one-dimensional simulations.

As shown in Figure 7.7-3, model results for the welded TSw unit generally fall in the wide range of measured calcite data with the extended case, while the base-case geochemical system model presents a better match only for the upper portion of TSw, but underestimates calcite abundances in the lower TSw. Calcite deposition values obtained from the highest infiltration rate (20 mm/yr) are closer to the high bound of measured values. Those values from the 5.92 mm/yr fall in the middle of the TSw measured data range. This finding may imply that the 20 mm/yr percolation rate is the high bound for the WT-24 location, whereas the base infiltration (5.92 mm/yr) from the flow property calibration (used for the flow model) may be close to the long-term mean infiltration rate for this location. The extended-case geochemical system provides the closest match to the measured data in the TSw unit, because of the contribution of calcium from feldspars.

As mentioned in the introduction (Section 7.7.1), in reply to a commentary paper by Dublyansky and Smirnov (2005 [DIRS 180650]), Sonnenthal et al. (2005 [DIRS 180639]) performed a simulation with variable bottom boundary temperatures approximating those measured in fluid inclusions. In this reply paper (Sonnenthal et al. 2005 [DIRS 180639]), the temperature was set initially at 95°C at the base of the one-dimensional model domain (with the borehole WT-24 stratigraphy) at 10 Ma and was allowed to decrease through conductive and advective cooling into the overlying rock and atmosphere. An infiltration rate of 5.92 mm/yr was used. Somewhat greater abundances result from the higher temperature gradients, yet the overall pattern and magnitude is similar to that for the steady-state ambient temperature distribution. Higher temperatures result in lower solubilities and somewhat higher calcite abundances, yet the abundances are dominated by the Ca flux into the unsaturated zone, which is a very important factor for calcite formation.

7.7.5.2 Calcite Precipitation in Fractures and Matrix

Modeled calcite abundances in the fracture and matrix continua are very different for the various hydrogeological units (Figures 7.7-4 and 7.7-5). Figure 7.7-4 shows calcite abundances in fractures and matrix for the three infiltration rates with the extended-case geochemical system. In the PTn unit (Figures 7.7-5a and 7.7-5b), the matrix shows a similar or larger proportion of calcite than the fractures, except near the contact with the TSw, where the distribution reverses. In the uppermost part of the TSw unit (just above the repository horizon), calcite precipitation in fractures is dominant, indicating that flow is enhanced in the fractures. Calcite coatings are frequently found in fractures and lithophysal cavities (intersected with fractures) in the TSw tuffs (Paces et al. 1998 [DIRS 107408]).

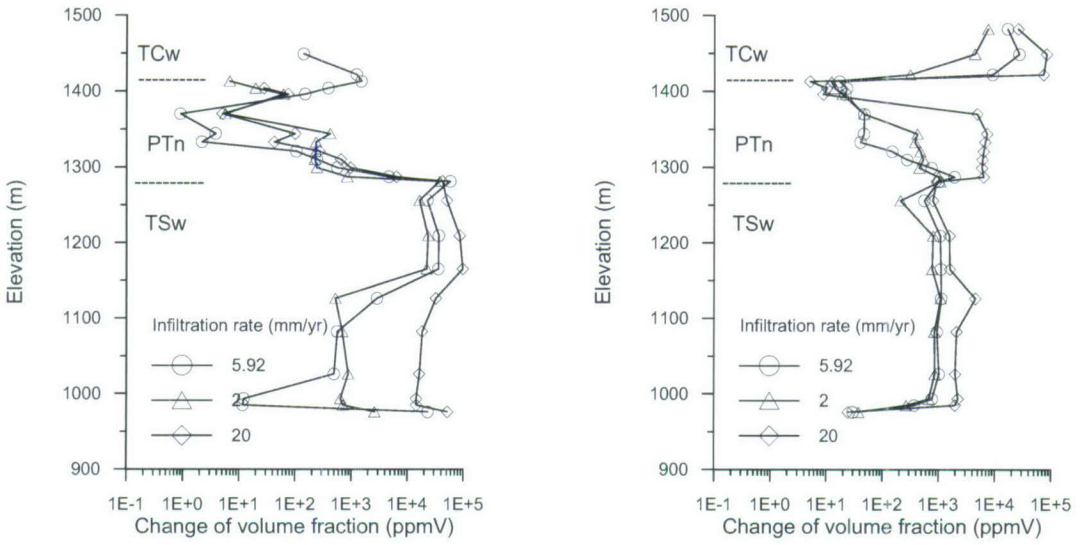

(a) Fracture

(b) Matrix

Source: Xu et al. 2003 [DIRS 162124].

PTn=Paintbrush nonwelded hydrogeologic unit; TCw=Tiva Canyon welded hydrogeologic unit; TSw=Topopah Spring welded hydrogeologic unit.

Figure 7.7-4. Modeled Calcite Abundances (in ppmV or 10^{-6} volume fraction) in Fractures and in the Matrix after 10 Million Years for Differing Infiltration Rates Using the Extended-Case Geochemical System

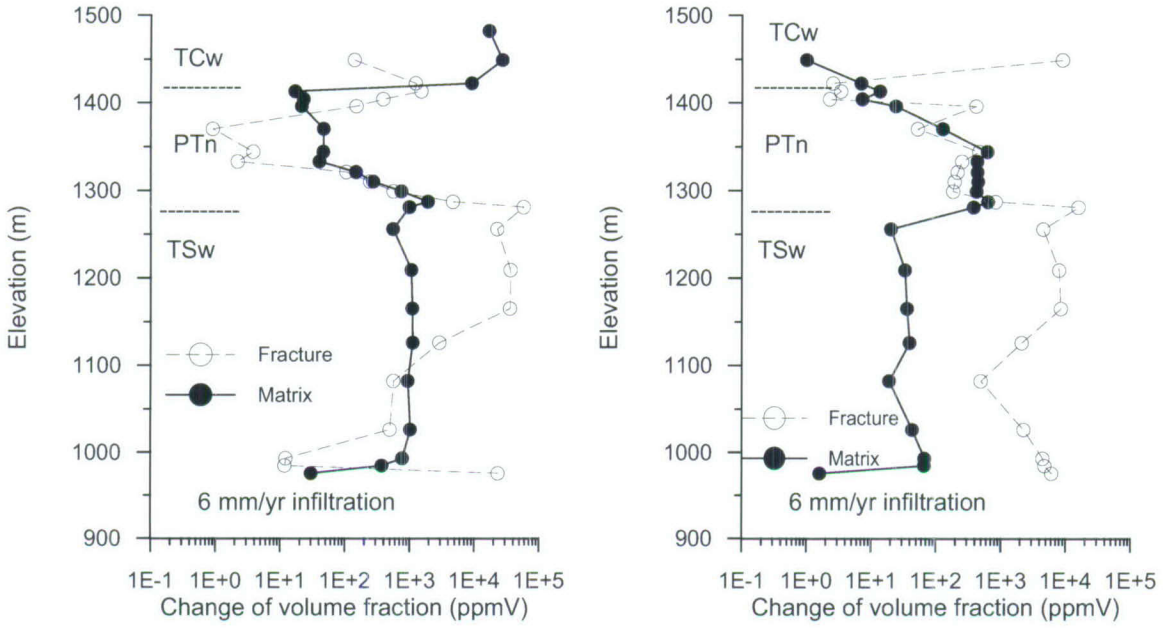

Source: Xu et al. 2003 [DIRS 162124].

PTn=Paintbrush nonwelded hydrogeologic unit; TCw=Tiva Canyon welded hydrogeologic unit; TSw=Topopah Spring welded hydrogeologic unit.

Figure 7.7-5. Modeled Calcite Abundances (in ppmV or 10^{-6} Volume Fraction) in Fractures and in the Matrix Using an Infiltration Rate of 6 mm/yr for (a) the Extended-Case and (b) Base-Case Geochemical Systems

However, the abundances in Figures 7.7-4 and 7.7-5 reflect only the proportion of calcite within the fracture and the matrix volumes individually. Figure 7.7-6 shows changes of calcite volume fraction versus infiltration rate for layer tsw4 (at an elevation of 1,126 m). In the extended case (Figure 7.7-6a), there are about equal total amounts of calcite in the matrix and fractures (the total is about twice that in the matrix, which makes up most of the volume of the rock), even though the fractures show a much larger proportion of calcite (Figure 7.7-5a). For the base-case system (Figure 7.7-6b), calcite in the fractures is about three-fourths of the total calcite in the rock, owing to the limited amount of calcium coming from the rock matrix and forming calcite. Greater simulated calcite abundances in the fractures result from the fractures carrying higher water fluxes in these strongly fractured, densely welded rocks.

The extended-case and base-case geochemical system simulations also show that from about 2 to 5.92 mm/yr, the amount of calcite precipitated in the welded Topopah Spring tuff is sensitive to the infiltration rate (Figures 7.7-6a and 7.7-6b). This dependence decreases at higher infiltration rates (5.92 mm/yr infiltration rate to 20 mm/yr), owing to a modification of the geothermal gradient from the increased percolation flux (Figure 7.7-2). The decrease in temperature at this level is about 2°C, which resulted in less calcite precipitating in the TSw and more calcite being transported below the TSw.

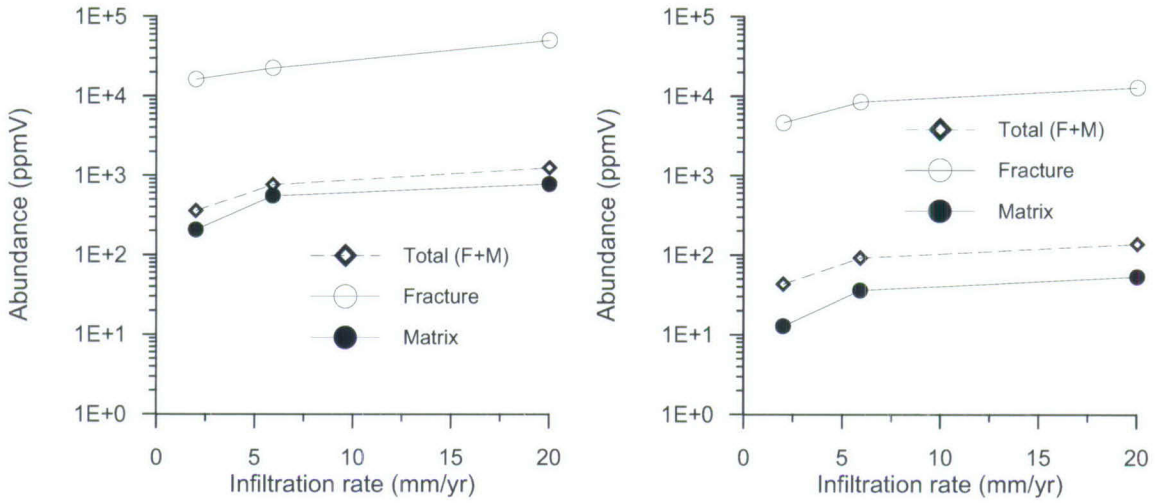

(a) Extended case

(b) Base case

Source: Xu et al. 2003 [DIRS 162124].

Figure 7.7-6. Changes in Calcite Volume Fraction (ppmV) vs. Infiltration Rates for tsw4 Layer (at an elevation of 1,126 m) for (a) the Extended-Case and (b) Base-Case Geochemical Systems

7.7.5.3 Spatial Variation in Calcite Deposition

Observed calcite abundances vary significantly in space and as a function of depth. Studies for the WT-24 column can give some general insight into calcite deposition conditions, but cannot represent the entire picture at Yucca Mountain. Calcite abundance data for borehole USW SD-6 were later published by the USGS in 2002 (DTN: GS020608315215.002 [DIRS 162126]), but modeling of calcite deposition for SD-6 has not been performed. Measured calcite data have a wide range of values (orders from 10^2 to 10^4 ppmV). To compare the two columns, which show large variability, the geometric means over a specified depth range were compared. The calcite data were grouped according to (1) every 10 m in depth (if possible) and (2) within one geological unit. The original measured calcite data and calculated geometric means versus depth are presented in Figure 7.7-7. To better compare WT-24 with SD-6, both geometric means are plotted in Figure 7.7-8. For the PTn, SD-6 has much more calcite deposition than WT-24. The thickness of the PTn unit for SD-6 is thinner than that of WT-24. For the TSw, calcite abundances in SD-6 fall in a range similar to those in WT-24. In the three-dimensional UZ flow model, a mean infiltration of 19.6 mm/yr is used in SD-6, which is higher than the 5.9 mm/yr in WT-24. This finding once again indicates that between a 5.92 and 20 mm/yr infiltration rate, the amount of calcite is not expected to differ significantly in the TSw.

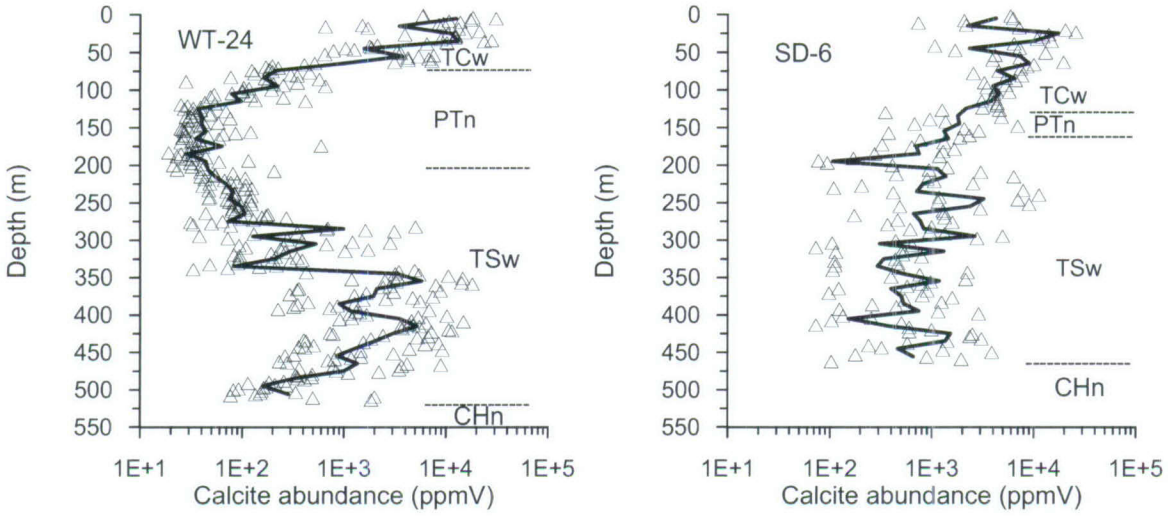

(a) WT-24 (b) SD-6

Sources: DTNs: GS021008315215.007 [DIRS 162127] for WT-24; GS020608315215.002 [DIRS 162126] for SD-6.

NOTE: Symbols represent USGS-measured calcite abundances. Solid lines represent geometric means.

PTn=Paintbrush nonwelded hydrogeologic unit; TCw=Tiva Canyon welded hydrogeologic unit; TSw=Topopah Spring welded hydrogeologic unit.

Figure 7.7-7. Calcite Abundances (in ppmV or 10^{-6} Volume Fraction) with Depth in Boreholes WT-24 and SD-6

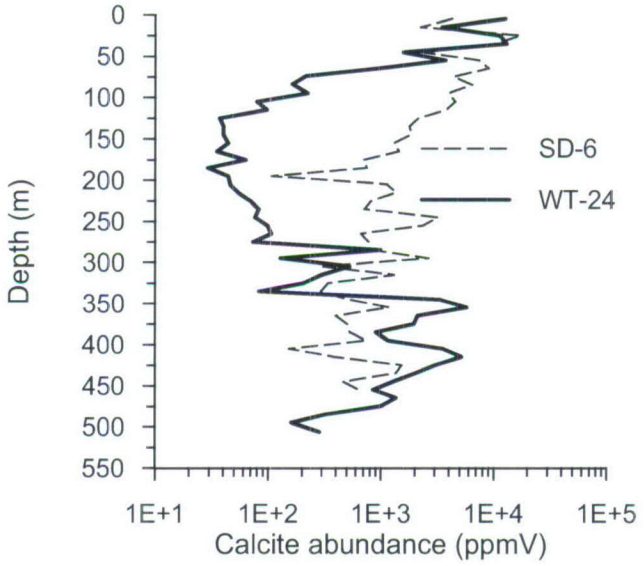

Figure 7.7-8. Geometric Means of Calcite Abundances with Depth for Boreholes WT-24 and SD-6

7.7.6 Concluding Remarks

Modeling calcite deposition provides additional evidence for validation of the UZ model. For the mean infiltration rate (2–5.92 mm/yr), simulations in Figure 7.7-3 are within the range of data for each unit (except at the PTn-TSw contact) for the more realistic extended-case geochemical system. The contact between the two units is where lateral flow may occur, which is not included in the one-dimensional model. The comparison in Figure 7.7-3 indicates that the validation criterion is met. This is because the acceptance criterion is applied only to the mean infiltration rate, which s the expected rate, and the other rates, representing extremes, would not be expected to simulate actual mean behavior. In addition, the validation is focused on the extended-case geochemical system. The excursion in the model results at the PTn-TSw contact is not important because it is an artifact of the lack of lateral flow in the one-dimensional model and would not occur in the three-dimensional UZ flow model.

Over a range of 2 to 20 mm/yr infiltration rates, the simulated calcite abundances generally fall within the range of calcite observed in the field, which satisfies the validation criterion. The simulated calcite distributions capture the USGS–measured data from the WT-24 well cuttings (DTN: GS021008315215.007 [DIRS 162127]). The 20-mm/yr infiltration rate may be the upper bound for WT-24 location, whereas the infiltration rate (2 to 5.92 mm/yr) used for the flow model gives the closest match to the data. The observed calcite precipitation for the top of TSw occurs mostly in the fractures, which is also captured. The modeling results can provide useful insight into process mechanisms such as fracture–matrix interaction, as well as conditions and parameters controlling calcite deposition. The modeled calcite abundances generally increase with increasing infiltration rate, but become less sensitive to infiltration at higher rates as a result of changes to the geothermal gradient. Therefore, between a 5.92 and 20 mm/yr infiltration rate, the amount of calcite increases only slightly in the TSw.

The calcite measurements may provide insight into the long-term average infiltration over the lifetime of the Yucca Mountain. The findings imply that perhaps lower rates are more consistent with calcite data. That is, glacial transition values in the 2 to 6 mm/yr range, with correspondingly lower present-day values, are consistent with these data. This information suggests lower long-term average rates for the site.

One-dimensional simulation is appropriate because both flow and geothermal gradient are primarily vertical. The current observed calcite is formed cumulatively over about 10 million years. A number of uncertainties are involved in the numerical simulation results, the most influential of which are variations in geothermal gradient and infiltration over time. Differences between one-dimensional and three-dimensional flow are much less than the differences in geothermal gradient and infiltration over 10 million years. Agreement between simulated and measured calcite abundance could work to establish the validity of the flow field and infiltration rates used in the UZ flow model. No significant lateral flow (above TSw and within the TSw unit) was predicted in both the previous flow model and current flow model at the WT-24 location. Therefore, the calcite analysis conclusion based on the previous flow model is still valid for the current flow model.

Finally, in reply to a commentary paper by Dublyansky and Smirnov (2005 [DIRS 180650]), Sonnenthal et al. (2005 [DIRS 180639]) preformed a simulation with variable bottom boundary temperatures approximating those measured in fluid inclusions. The results of this simulation show slightly greater abundances of calcite compared to the ambient temperature simulation, yet show similar trends with depth. The results with variable temperature boundary do not change the conclusions made above.

7.8 MODELING ANALYSIS OF ALCOVE 8/NICHE 3 FAULT TESTS

This section simulates in situ field tests of artificial infiltration along a fault at Alcove 8/Niche 3. The fault tests caused localized saturated conditions below the test spot in an otherwise UZ. Under this field condition, test data are compared to results of simulations using the same conceptual model, methodology, and modeling approach as those used in the UZ flow model. This modeling activity presents a different case of validation for the UZ flow model. The results will build confidence in the UZ flow model from a different perspective (in terms of different-scale model results and field conditions).

This modeling analysis uses both model calibration and prediction. Comparisons between simulated and observed data are useful for evaluating the validity of the methodology used in the UZ flow model for capturing UZ flow and transport processes. The criterion for validation is that the predicted results for the time required for a conservative tracer to reach a given concentration (e.g., peak concentration) are within a factor of five of the observed time. As demonstrated in Section 7.8.3.2 below (the discussion of modeling results), the criterion is met. This modeling activity is adopted from the previous version of *UZ Flow Models and Submodels* (BSC 2004 [DIRS 169861], Section 7.6).

7.8.1 Field Observations

Infiltration rate, seepage rate, and tracer concentration data from the fault test are used to corroborate model simulations. The fault test used water and two liquid tracers. The test was carried out in the upper lithophysal and middle nonlithophysal subunits in the Yucca Mountain UZ. These geological subunits correspond to model layers tsw33 and tsw34, respectively, in the UZ model. The tsw33 has some lithophysal cavities that may intersect fractures. Liquid water, first without and then with tracers, was released at the floor of an alcove along the fault (about 5 m long (DTN: GS020508312242.001 [DIRS 162129]) within tsw33. Seepage from the fault into a niche and tracer concentrations of seeping liquid were monitored as functions of time. The niche is located within tsw34, about 20 m below the floor of the alcove; the interface between tsw33 and tsw34 is about 15 m below the floor of the alcove (DTN: LB0301N3SURDAT.001 [DIRS 162130]).

A pressure head of 2 cm was maintained at the infiltration plot along the fault at the alcove. The plot consists of four trenches that have different infiltration rates as a result of subsurface heterogeneity along the fault. Figure 7.8-1 shows the total infiltration rate as a function of time (DTNs: GS020508312242.001 [DIRS 162129] and GS020908312242.002 [DIRS 162141]). For simplicity, this model considers the uniformly distributed infiltration rate along the infiltration plot to be consistent with the uniform property distribution in the UZ model. One consideration in the modeling study is to evaluate approaches used in the site-scale model. Considerable

temporal variability in the infiltration rate occurred during the test as a result of infilled materials within the fault just below the infiltration plot (Figure 7.8-1). In other words, the effective permeability of the fault just below the plot changed with time. It is also expected that most portions of the fault and the surrounding fractures away from the plot would still be unsaturated, although pressure head at the plot was positive during the test. Based on these observations, total infiltration rate (instead of a pressure head of 2 cm) was used as the boundary condition in the model.

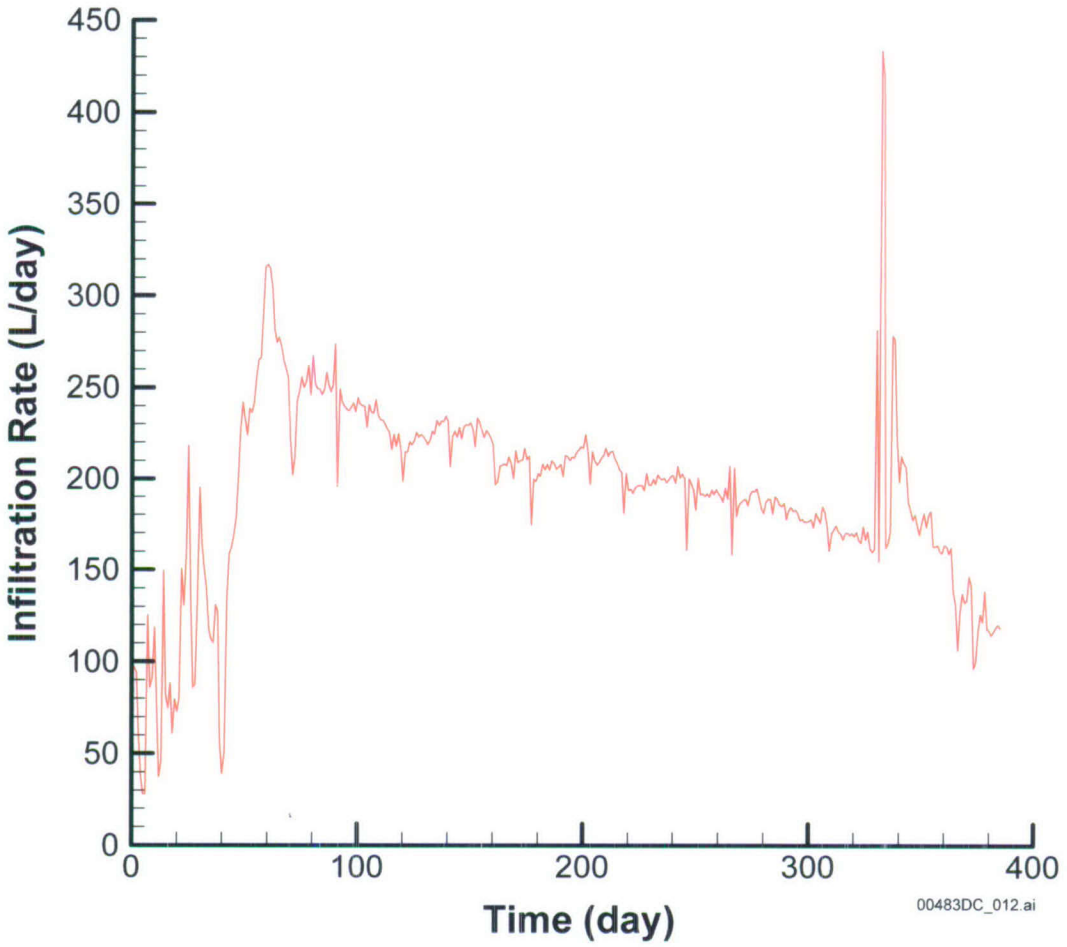

DTN: LB0303A8N3MDLG.001 [DIRS 162773] (File: *inf_sum.dat*).
NOTE: Based on DTNS: GS020508312242.001 [DIRS 162129] and GS020908312242.002 [DIRS 162141].

Figure 7.8-1. Infiltration Rate as a Function of Time

Seepage from the fault into the niche was measured during the test, with a number of trays used to cover the areas where seepage might occur. Seepage was found to be highly spatially variable. The total seepage rate as a function of time is given in Figure 7.8-2 (DTN: LB0303A8N3LIQR.001 [DIRS 162570]). Several boreholes were installed around the niche. Water arrival times at these boreholes were monitored by electrical resistivity probes. Figure 7.8-3 shows average water travel velocities determined from the arrival times from two boreholes just above the ceiling of the niche (DTN: LB0303A8N3LIQR.001 [DIRS 162570]). The fault is about 2 m from the borehole collars in Figure 7.8-3 (DTN: LB0303A8N3LIQR.001

[DIRS 162570]). Note that relatively uniform water-travel-velocity distribution within and near the fault was observed from these two boreholes.

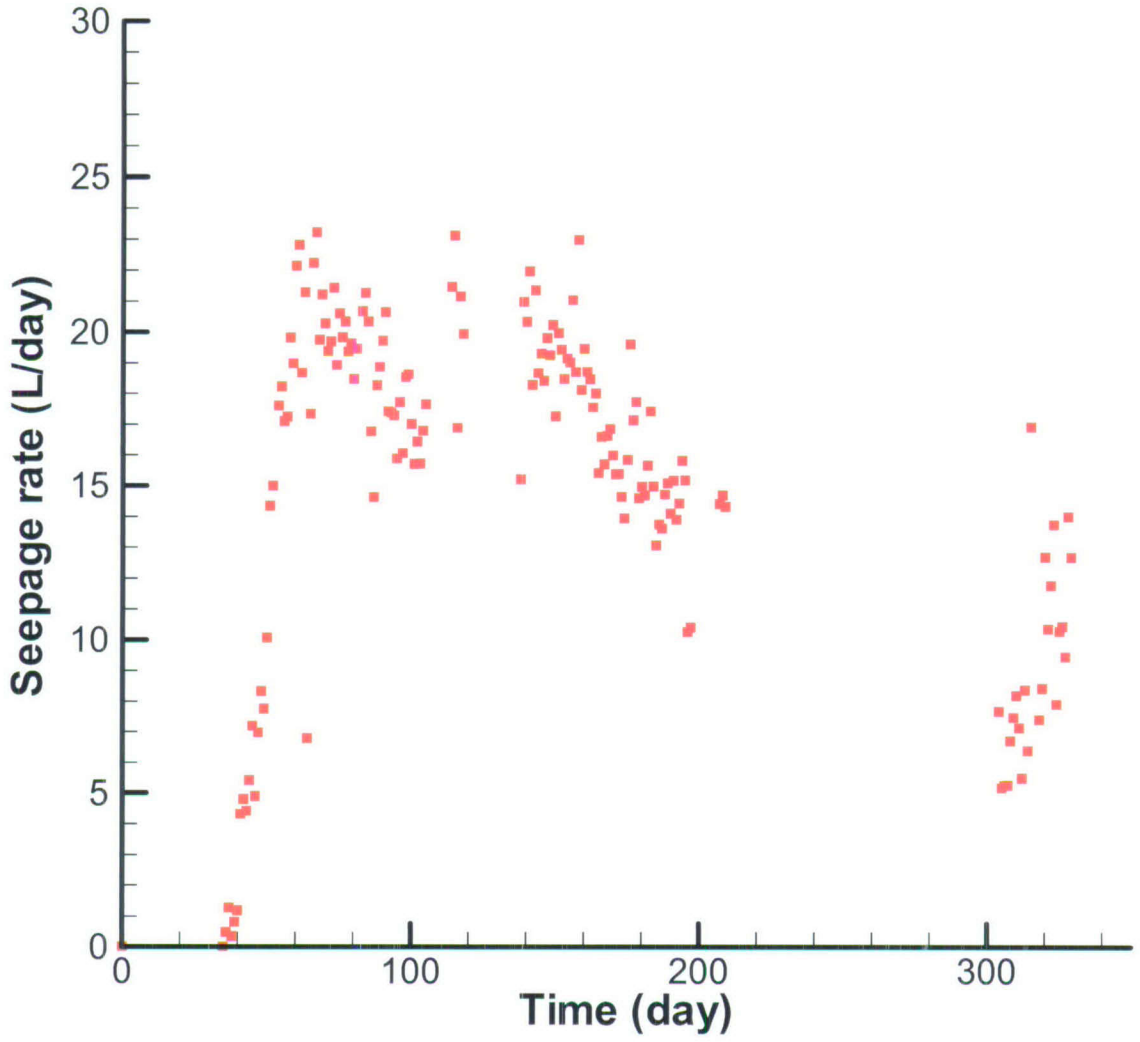

Source: DTN: LB0303A8N3LIQR.001 [DIRS 162570], file: *All_seepage.xls*.

Figure 7.8-2. Total Seepage Rate as a Function of Time

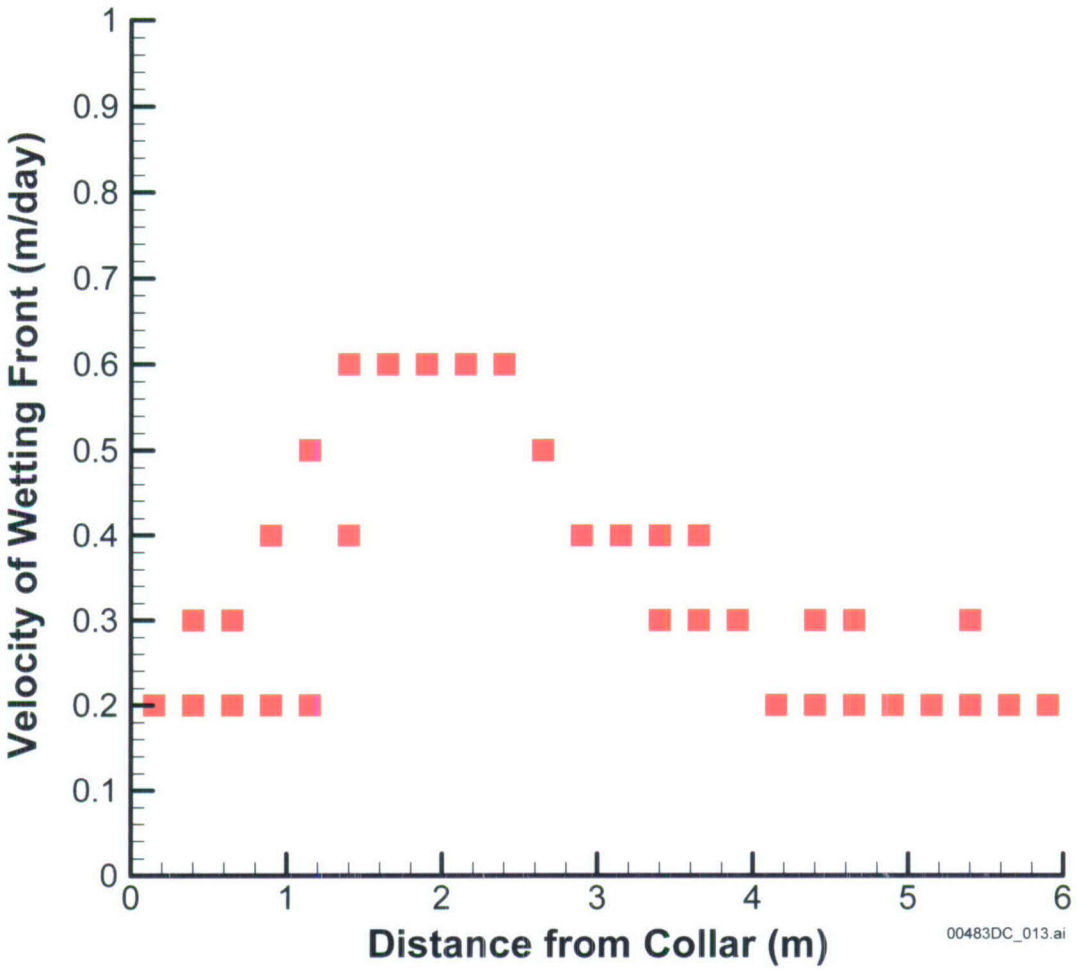

Source: DTN: LB0303A8N3LIQR.001 [DIRS 162570].

NOTE: Observation boreholes are approximately perpendicular to the fault. The distance from a borehole collar (called distance from collar) to the fault is about 2 m.

Figure 7.8-3. Water Travel Velocity Data for Boreholes 9 and 10

After 209 days, two tracers with different molecular diffusion coefficients, bromine and pentafluorobenzoic acid, were introduced into infiltrating water at the infiltration plot. Tracer concentrations in three of the trays (at the niche) capturing seeping water from the fault were measured (DTN: LB0303A8N3LIQR.001 [DIRS 162570]). Seepage rates corresponding to these three trays were not measured during the period of tracer concentration measurement. In this study, a flux-averaged breakthrough curve (concentration as a function of time) from these trays was used to represent the average breakthrough curve for all trays at the niche where seepage was captured. A constant flux value for each of the three trays was used for calculating the flux-averaged breakthrough curve shown in Figure 7.8-4. The constant flux values for the three trays were determined as the averaged value over 56 days before tracers were introduced. This flux-averaged breakthrough curve was compared with simulation results.

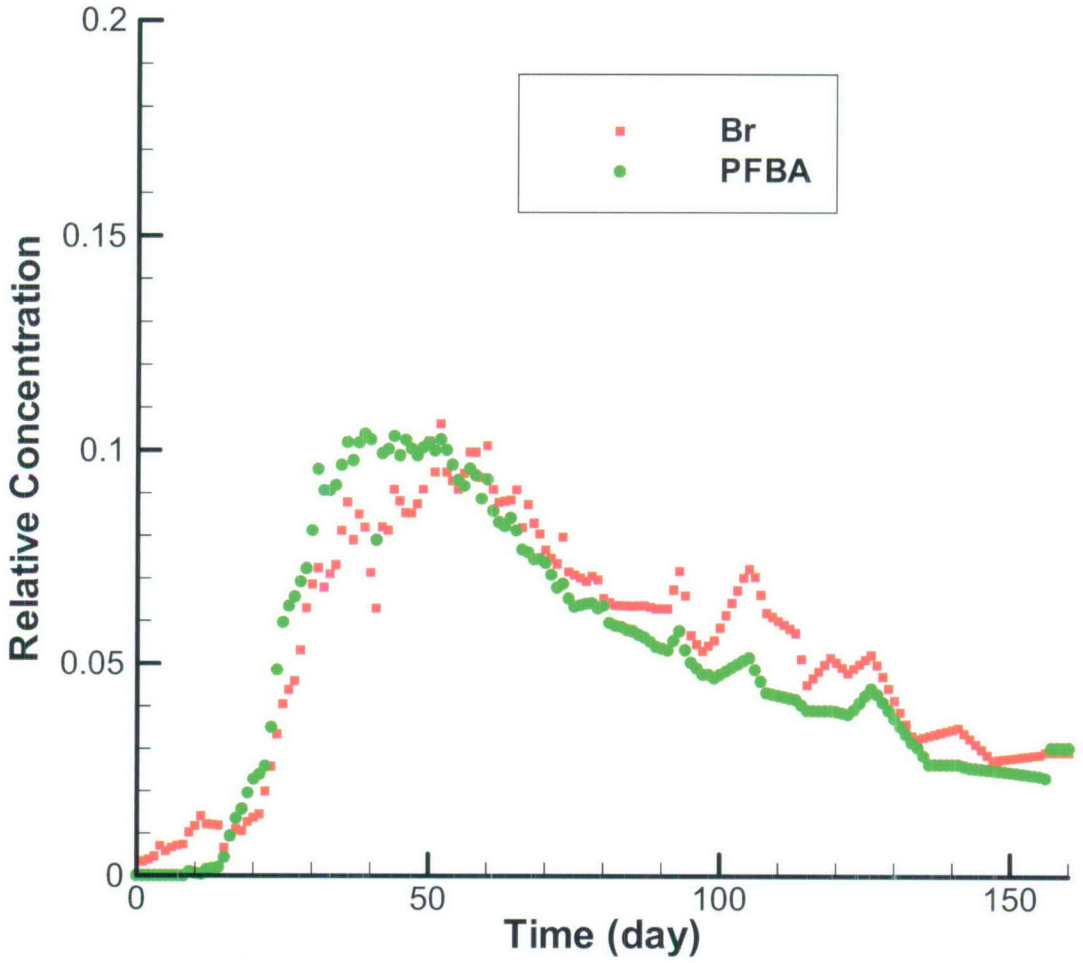

Sources: DTNs: LB0303A8N3LIQR.001 [DIRS 162570]; LB0303A8N3MDLG.001 [DIRS 162773], file: *BTC.dat*.

Figure 7.8-4. Observed Flux-Average Breakthrough Curve

7.8.2 Numerical Model

A numerical model was developed for the fault test site to compare the simulation results with the relevant field observations. (The grid was generated with a software routine Smesh.f V1.0 [DIRS 162142].) While comparison results will be presented below in Section 7.8.4, in this section, the focus is on schemes used for developing the numerical model.

A three-dimensional numerical grid is constructed for simulating the fault test (Figure 7.8-5). The fault is represented as a vertical fracture, and surrounding fractured rock is approximated as a dual-continuum system (consisting of overlapped, interacting fracture and matrix continua). Global water flow and solute transport are allowed to occur in both continua. Figure 7.8-5 shows a cross section of the grid within the fault. The thickness of the grid in the direction perpendicular to fault walls is 3 m along each side of the fault. The fracture frequency used for generating the dual-continuum grid is 1.03 for tsw33 (determined from the fracture map at the alcove floor) and 1.72 for tsw34 (determined from the fracture map at the ceiling of the niche) (DTN: GS030108314224.001 [DIRS 162131]). As shown in Figure 7.8-5, within a cross section of the grid along the fault, the grid spacing is 10 cm just above the ceiling of the niche,

enabling the seepage process to be accurately simulated. The grid spacings in the direction perpendicular to the fault are 0.024, 0.168, 0.456, 0.756, and 1.44 m, respectively. The smallest spacing is adjacent to the fault, so that water imbibition and tracer diffusion into the fractured rock from the fault can be accurately captured. Cross sections in parallel to the fault walls have identical grid meshes (Figure 7.8-5) for different distances from the fault. The niche is represented by an opening at the bottom of the grid (Figure 7.8-5), with the geometry of the opening determined from the survey data of the niche near the fault. Note that this is only an approximation of the geometry of the test site; a three-dimensional geometry of the niche with an underground tunnel connected to the niche are difficult to incorporate into the model. However, since the main concern is flow and transport processes within the fault, this geometric representation is adequate.

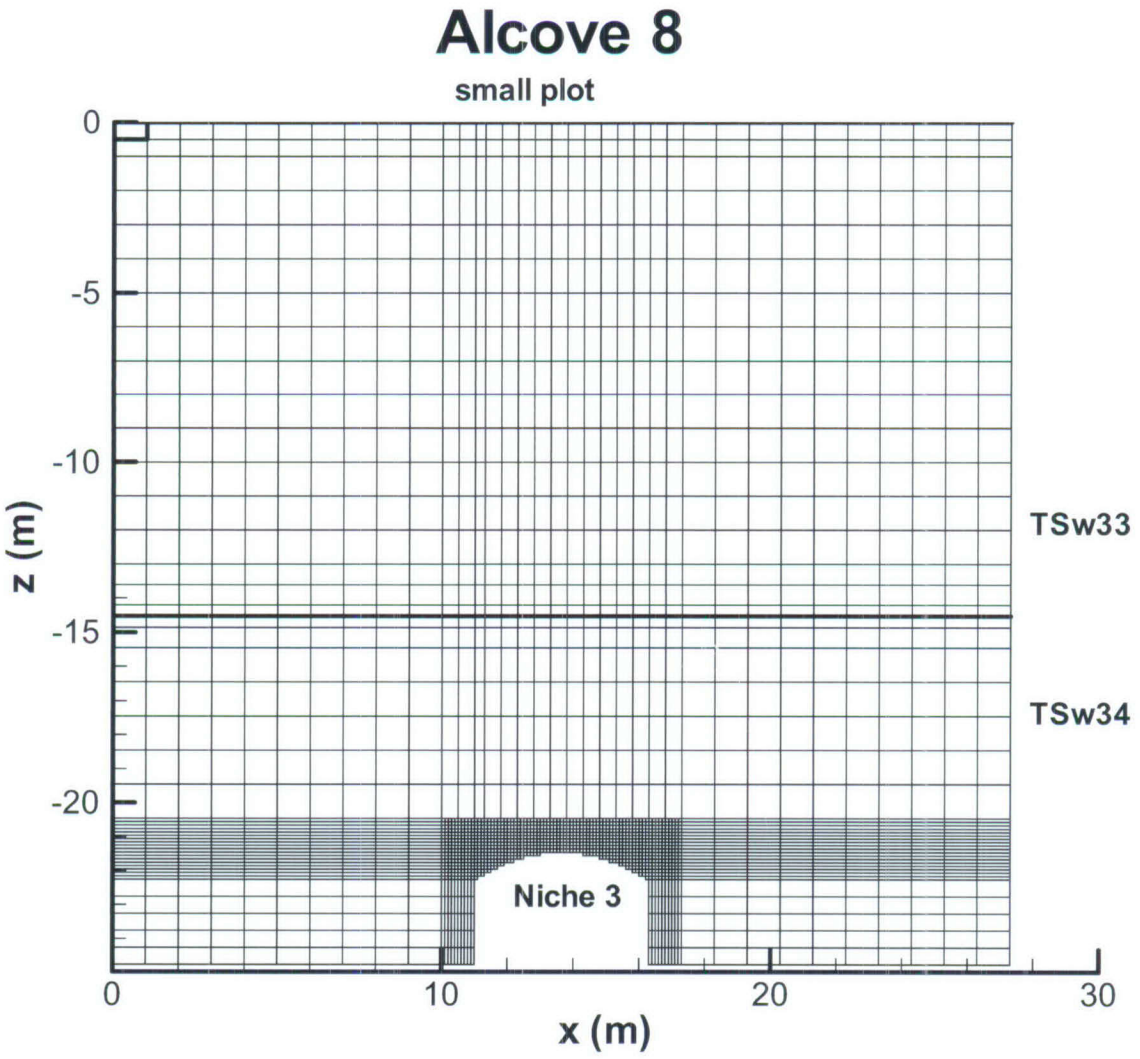

Figure 7.8-5. Cross-Sectional Schematic of the Three-Dimensional Numerical Grid Used for Modeling Studies of Alcove 8/Niche 3

Temporally variable inflow rates are imposed on the top boundary, corresponding to the infiltration plot at the alcove floor (Figure 7.8-1). The side boundary corresponds to zero-flow conditions (in the direction perpendicular to the simulation domain). The niche wall boundary is modeled by a zero capillary-pressure condition, representing capillary barrier effects (Birkholzer et al. 1999 [DIRS 105170]). The bottom boundary was assigned a constant matrix saturation of 0.85, which is consistent with field observations under ambient conditions (Flint 1998 [DIRS 100033], p. 44, Table 7). Also based on field observations in the report by Flint (1998 [DIRS 100033], p. 44), matrix saturations are initially assigned to be 0.72 for tsw33 and 0.85 for tsw34. Other initial conditions for the rock mass within the model domain are that it is solute-free and has little water saturation (1.05×10^{-2}) in both the fractures and the fault. Rock properties used in model simulations are presented in Section 7.8.3.1.

Model calibration is performed using an inverse modeling code iTOUGH2 V4.0 [DIRS 139918]. The model calibration is defined herein as the adjustment of rock hydraulic parameters to make simulation results match the corresponding data. The goodness of match is measured using the standard least squares approach, which minimizes the sum of the squared residuals weighted by the inverse of variance of the data. T2R3D V1.4 (LBNL 1999 [DIRS 146654]) is used for modeling tracer transport.

7.8.3 Model Simulations and Discussions

The numerical model was first calibrated against only the seepage and water-travel-velocity data to obtain the calibrated rock properties and the corresponding water flow field using iTOUGH2. Then, forward tracer transport simulations with different chemical transport parameters were carried out using T2R3D to evaluate the effects of matrix diffusion and other related processes on solute transport in the fault.

7.8.3.1 Calibration of Seepage-Rate Data and the Average Water-Travel-Velocity Data

Both fracture and matrix properties were assumed to be homogeneous within each geological subunit (tsw33 and tsw34). Fault properties were assumed to be the same for both units. This is based mainly on the following three considerations:

(1) Consideration of the heterogeneity within each subunit would introduce a large number of rock properties that need to be determined by more data than was available from the test site.

(2) These treatments have been used by the site-scale model of the Yucca Mountain unsaturated zone. It is of interest to examine how well this simple representation of subsurface heterogeneity can be used to model the fault test.

(3) A study by Zhou et al. (2003 [DIRS 162133]) implies that flow and transport in the Yucca Mountain unsaturated zone are mainly determined by large-scale heterogeneity, characterized by property differences between different geological units rather than by property variability within a geological unit.

Rock hydraulic properties needed as inputs into the model include fracture and matrix permeabilities, fracture and matrix porosities, fault aperture and permeabilities, van Genuchten

(1980 [DIRS 100610]) parameters (for matrix, fractures, and the fault), and the parameter of the AFM, γ, for fractures (DTNs: LB997141233129.001 [DIRS 104055]; LB980901233124.101 [DIRS 136593]; LB990861233129.001 [DIRS 110226]; and LB990501233129.001 [DIRS 106787]). Because fracture van Genuchten parameters for tsw33 and tsw34 are similar (Table 7.8.1), a simple average of these parameters was used as the corresponding parameters for the fault (. The averaged k/ϕ (where k is fracture permeability and ϕ is the corresponding fracture porosity) was calculated as fault permeability. Note that because there is no matrix in the fault in the model (or ϕ =1), the weighted k/ϕ (rather than weighted k) is employed for estimating fault permeability. The aperture of the fault was estimated as the average of fracture apertures of the two subunits. Note that the AFM was developed for fracture networks rather than for a single fracture. Consequently, the AFM does not apply to the fault here. In fact, most of the parameter values mentioned above and given in Table 7.8-1 are not site specific for the fault test site. These values were used as initial guesses for model calibration against the seepage rate and water-travel-velocity data observed from the fault test. Note that not all site-specific parameters are available and the initial guess of some values were necessary. This is because the initial guess does not significantly affect the final calibrated values. To reduce the number of variables in model calibration (or inverse modeling), parameters expected to significantly affect simulated tracer transport time and seepage rate were varied in the calibration, while other parameters were kept unchanged. The varied parameters were fracture and fault permeabilities, fracture porosity, fault aperture, and fracture and fault van Genuchten α values.

Table 7.8-1. Uncalibrated Rock Properties

Rock property	Fault[e]	tsw33		tsw34	
		Fracture	Matrix	Fracture	Matrix
Permeability (m^2)	4.34×10^{-11}	5.5×10^{-13}[c]	3.08×10^{-17}[a]	0.35×10^{-13}	4.07×10^{-18}[a]
Porosity	1.00	6.6×10^{-3}[d]	0.154[a]	10^{-2}[d]	0.11[a]
Fracture frequency (m^{-1})		1.03[e]		1.5[e]	
Fracture aperture (m)	1.12×10^{-3}	1.49×10^{-3}[e]		1.14×10^{-3}[e]	
Active fracture model parameter γ	0.0	0.41[a]		0.41[a]	
van Genuchten α (Pa^{-1})	1.0×10^{-3}	11.46×10^{-3}[a]	2.13×10^{-5}[a]	5.16×10^{-4}[a]	3.86×10^{-6}[a]
van Genuchten m	0.608	0.608[a]	0.298[a]	0.608[a]	0.291[a]

Sources: [a]DTN: LB997141233129.001 [DIRS 104055].
[b]DTN: LB980901233124.101 [DIRS 136593].
[c]DTN: LB990861233129.001 [DIRS 110226].
[d]DTN: LB990501233129.001 [DIRS 106787].
[e]BSC 2004 [DIRS 169861], Table 7.6-1.

Infiltration-seepage processes in the fault and the surrounding fractured rock were determined by several mechanisms. Liquid water applied at the alcove floor (Figure 7.8-5) flowed first into the fault and then into fractured networks connected to the fault. Matrix imbibition occurred at interfaces between fractures and the matrix, and between the fault and the matrix. When water arrived at the intersection between the fault and the niche, it might not have immediately seeped into the niche until the capillary pressure became zero because of capillary barrier effects (Philip et al. 1989 [DIRS 105743]; Birkholzer et al. 1999 [DIRS 105170]). Such effects can divert flow away from the opening, resulting in only a portion of the water arriving at the niche ceiling actually seeping into the niche. Tracer transport time was determined by fracture porosity, fault aperture, and the matrix imbibition process.

Figure 7.8-6 shows a comparison between seepage-rate data and the simulation result from a model calibration (Run #1) without considering the water-travel-velocity data. In this calibration run, fracture porosity and fault aperture were not varied. A fairly good match to the observed seepage data was obtained (Figure 7.8-6); however, water travel velocity is significantly overestimated (Figure 7.8-7). Water travel velocities were calculated from water arrival times at locations about 1 m above the middle of the opening in Figure 7.8-5. The transport time was defined as the time when fault or fracture saturation was increased from the initial value of 1.05×10^{-2} to 1.06×10^{-2}. This comparison implies that seepage rate as a function of time may be mainly controlled by rock properties near seepage locations [influence zone of capillary barrier (Liu et al. 2002 [DIRS 160230], Section 3.3)]. On the other hand, water travel velocities are determined by rock properties from the infiltration plot to the locations where water travel velocities are monitored. Table 7.8-2 gives the calibrated properties obtained from Run #1.

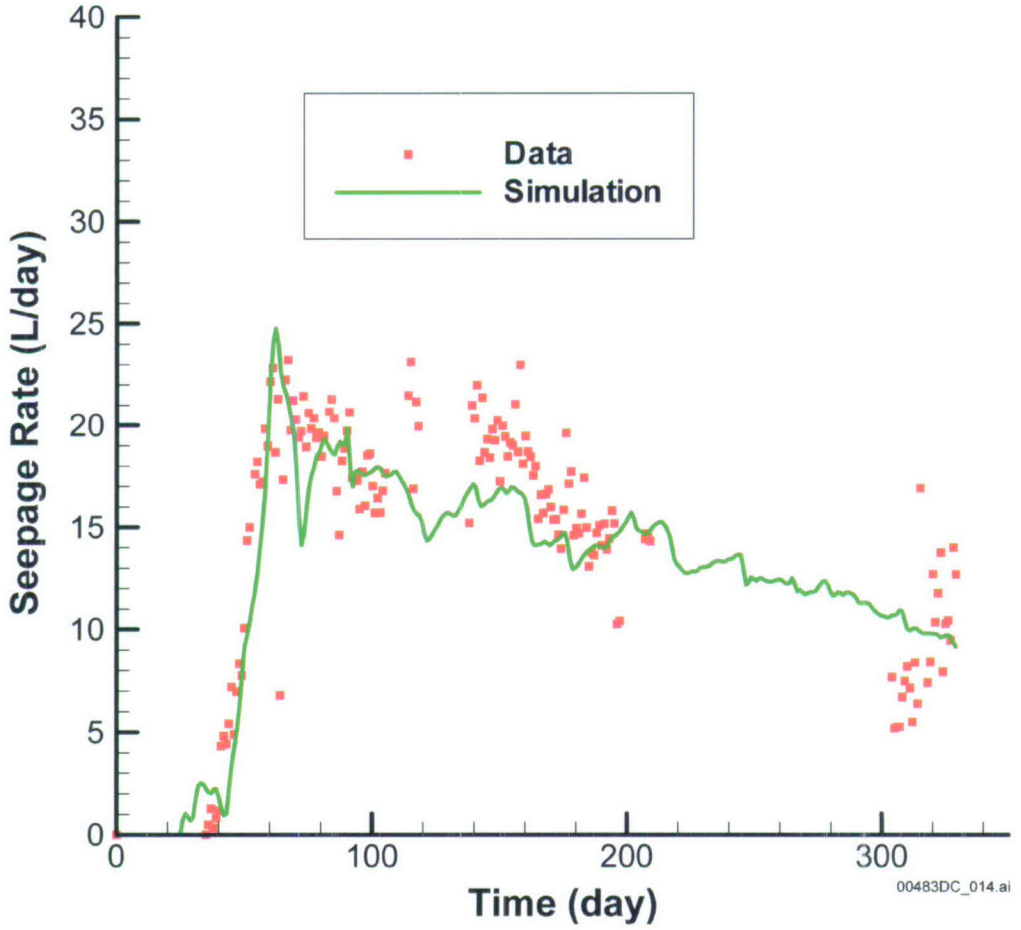

Sources: DTNs: LB0303A8N3LIQR.001 [DIRS 162570], file: *All_seepage.dat*; LB0303A8N3MDLG.001 [DIRS 162773], file: *lrun1i.tec*.

Figure 7.8-6. A Comparison between Simulated Seepage Rates as a Function of Time (Run #1) and Field Observations

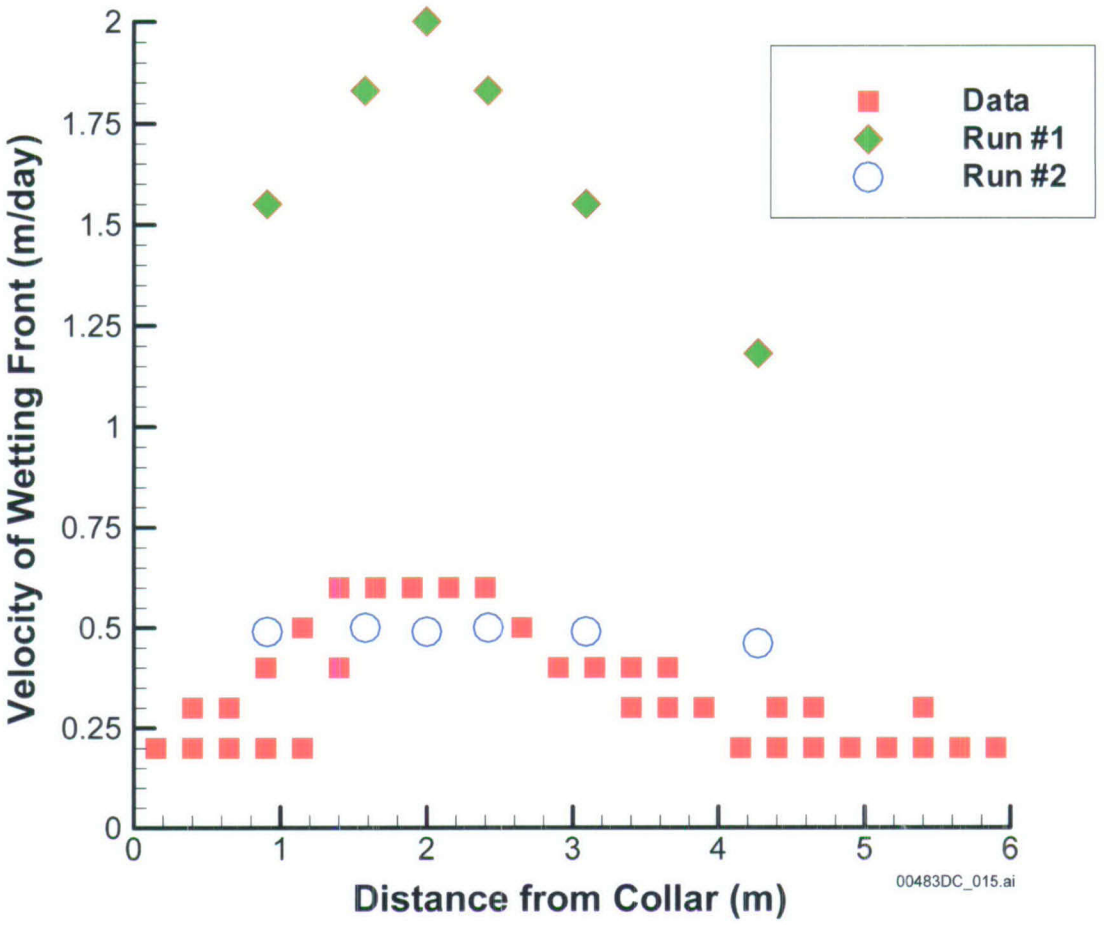

Sources: DTNs: LB0303A8N3LIQR.001 [DIRS 162570]; LB0303A8N3MDLG.001 [DIRS 162773], files: *WV_Irun1Ni.tec*; *WV_Irun4Ni.tec*.

Figure 7.8-7. A Comparison among Calculated Water Travel Velocities from Two Calibration Runs and the Velocity Data Observed from the Fault Test

Table 7.8-2. Rock Properties Calibrated from Seepage Rate Data (Run #1)

Rock Property	Fault	tsw33	tsw34
Fracture Permeability (m^2)	6.67×10^{-11}	8.93×10^{-13}	3.16×10^{-14}
Fracture van Genuchten α (Pa^{-1})	1.15×10^{-3}	1.67×10^{-3}	4.59×10^{-3}

Source: DTN: LB0303A8N3MDLG.001 [DIRS 162773], file: *Irun1i.par*.

[a] All other rock properties are the same as those in Table 7.8.1. Rock names "tswF3", "NetF3," and "NetF4" in file *Irun1i.par* correspond to "Fault", "tsw33" and "tsw34", respectively, in this table.

The overestimation of the water travel velocities may result from the following: (1) some cavities in tsw33 are connected to fractures and might contribute to increasing the storage in the fracture continuum; (2) in reality, the fault is a zone rather than a single fracture. The effective aperture from this zone may be much larger than the assumed aperture value for the fault (Table 7.8-1). Neither of these factors was considered in Run #1 (first calibration). Taking these factors into consideration, the new calibration (Run #2) allowed both fault aperture and fracture porosity in tsw33 to be varied. The resultant values are 3 cm for fault aperture and 0.066 for

fracture porosity of tsw33 (Table 7.8-3). While the actual width of the fault zone is unknown, the estimated equivalent fault aperture (3 cm) is used. The estimated fracture porosity is consistent with those estimated from water release tests performed in the same geological unit (BSC 2004 [DIRS 170004], Section 6.11.3.2).

Table 7.8-3. Rock Properties Calibrated from Both Seepage Rate and Water Travel Velocity Data (Run #2)

Rock property	Fault	tsw33	tsw34
Fracture Permeability (m^2)	1.12×10^{-10}	1.23×10^{-12}	5.01×10^{-13}
Fracture Porosity		0.066	
Fracture aperture (m)	0.03		
Fracture van Genuchten α (Pa^{-1})	1.24×10^{-3}	2.19×10^{-3}	1.09×10^{-3}

Source: Output DTN: LB0303A8N3MDLG.001 [DIRS 162773], file *Irun4Ni.par*.

NOTE: All other rock properties are the same as those in Table 7.8.1. Rock names "tswF3", "NetF3," and "NetF4" in file *Irun1i.par* correspond to "Fault", "tsw33," and "tsw34", respectively, in this table.

Figure 7.8-7 shows a comparison among calculated water travel velocities from two calibration runs and the velocity data observed from the fault test. The simulated water travel velocities from Run #2 are much closer to the observed data than those from Run #1 (especially near the fault). However, the water travel velocities away from the fault are still overestimated. One possible explanation is that matrix imbibition from fractures above the niche were underestimated because the dual-continuum approach considerably underestimates the pressure gradient near a fracture matrix interface during transient flow conditions (Pruess and Narasimhan 1985 [DIRS 101707]). While this problem can be resolved with the MINC model of the report by Pruess and Narasimhan (1985 [DIRS 101707]), the computational intensity of the inverse model problem under consideration would be significantly increased. Note that a model calibration involves a great number of forward simulation runs. Considering (1) the transient flow effects would be considerably reduced later in the test, and (2) the focus here is on flow and transport within and near faults, simulated flow field and calibrated rock properties from Run #2 were used for simulating tracer transport at the test site. Figure 7.8-8 also shows a comparison between simulated seepage rates as a function of time (Run #2) and field observations. The match is reasonable. Figure 7.8-8 matches both wetting-front velocity and seepage-rate, and it is, therefore, considered a better calibration than Figure 7.8-6, which only matches the seepage rate data. Note that to give a reasonable prediction of solute transport, the water flow must be correctly modeled.

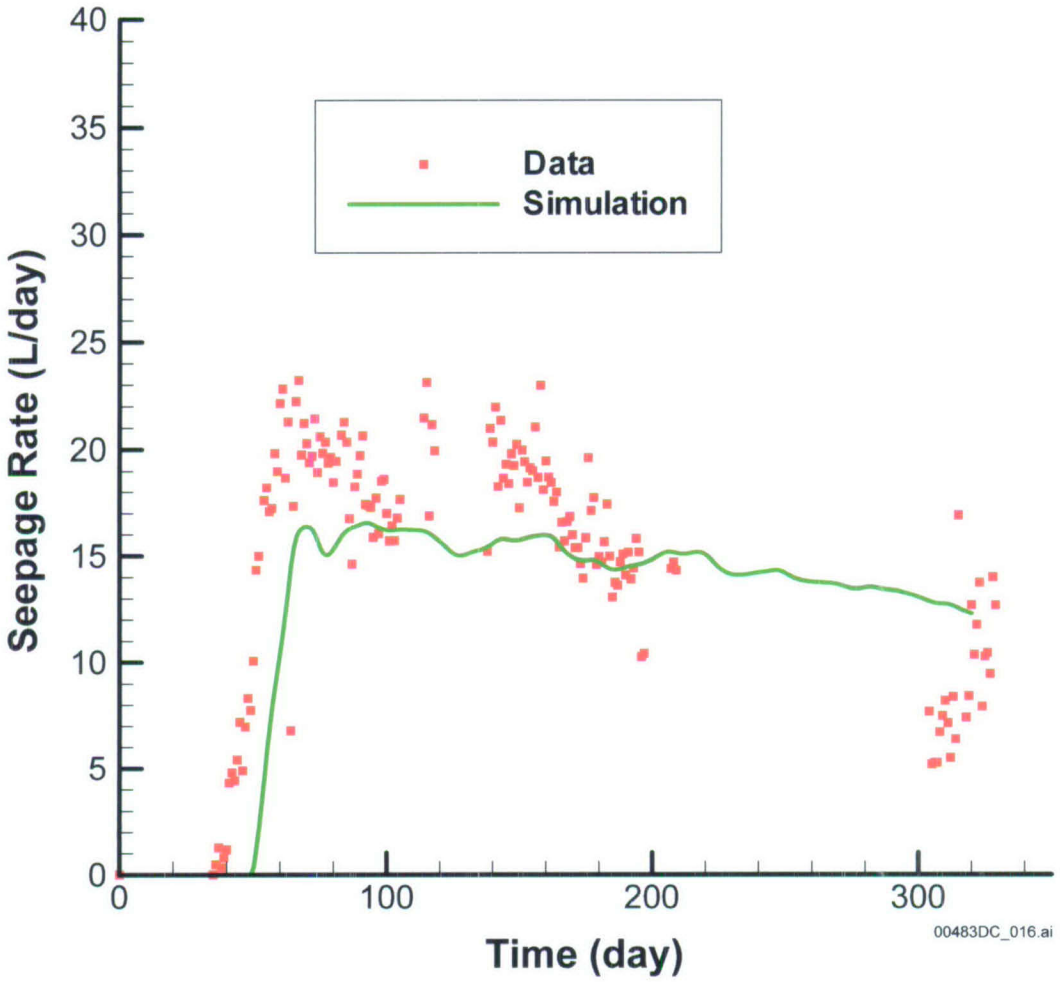

Sources: DTNs: LB0303A8N3LIQR.001 [DIRS 162570], file: *All_seepage.dat*; LB0303A8N3MDLG.001 [DIRS 162773], file: *Irun4Ni.tec*.

Figure 7.8-8. A Comparison between Simulated Seepage Rates as a Function of Time (Run #2) and Field Observations

7.8.3.2 Effects of Matrix Diffusion

Tracer transport within the fault is controlled by several processes, including advection, diffusion into the matrix blocks (matrix diffusion), mass exchange between the fault and the surrounding fracture networks, and dispersion. Special attention in this study is given to evaluating the relative importance of matrix diffusion. To do so, the flow field obtained from calibration Run #2 was used to simulate tracer transport processes and compare simulation results with field observations (Figure 7.8-4). The breakthrough curve is obtained from the output of T2R3D V1.4 [DIRS 146654] using software routine Bkread.f V1.0 [DIRS 162143].

Two conservative tracers with different molecular diffusion coefficients (2.08×10^{-9} m^2/s for bromine (Lide 2002 [DIRS 160832]) and 7.60×10^{-10} m^2/s for pentafluorobenzoic acid (Benson and Bowman 1996 [DIRS 153427]) were used in the fault test. Based on analyses of the relevant diffusion experiment results, Moridis et al. (2003 [DIRS 161902], Table 1) reported that the tortuosity factor for the tuff matrix can be approximated by the corresponding matrix porosity.

Therefore, the average matrix porosity for tsw33 and tsw34 (0.13) was used as the tortuosity factor. The effective diffusion coefficient for the matrix diffusion process is the product of the molecular diffusion coefficient and tortuosity factor.

Figure 7.8-9 shows comparisons between simulated breakthrough curves at the niche for two different fault-matrix interface areas and the observed data. One simulation corresponds to an interface area defined in the original numerical grid, which considers the fault as a fracture with two vertical walls. The criterion for validation is that the predicted results for the time required for a conservative tracer to reach a given concentration (e.g., peak concentration) are within a factor of five of the observed time. Note that this criterion is met (Figure 7.8-9). The other sensitivity simulation corresponds to an interface area increased by 45 times over that in the first simulation. In these two simulations, the dispersivity is assumed to be zero. (The relative importance of the dispersion will be discussed later.) Since the diffusive flux from the fault to the matrix is proportional to the product of the tortuosity factor and the fault-matrix interface area, changes in the interface area for a given tortuosity factor are equivalent to changes in tortuosity factor for a given interface area. For simplicity, the tortuosity factor value was changed in actual simulations, but the numerical grid (defining the interface area) was kept unchanged. Note that changes in the interface area do not significantly alter the flow field during the period of the tracer test. Tracers were introduced into infiltrating water at about 200 days after infiltration started, resulting in the matrix near the fault being almost saturated during the tracer test and the matrix imbibition being insignificant. As shown in Figure 7.8-9, the simulated breakthrough curve with the original interface area is very different from the observed data. It exhibits much larger concentration peak values and much earlier arrival times for these peaks. The observed data are favorably matched by the simulated result with increased interface area, indicating that matrix diffusion significantly affects the overall solute transport behavior and is underestimated by the simulation using the original interface area.

The need to increase interface areas between fractures (or faults) and the matrix in matching the field observations of tracer transport in fractured rock has been recently reported by several researchers. Shapiro (2001 [DIRS 162132]) interpreted concentration measurements for tritium and dichlorodifluoromethane collected from a glacial drift and fractured crystalline rock over 4 km^2 in central New Hampshire. Shapiro (2001 [DIRS 162132]) found that the effective diffusion coefficient at the kilometer scale is at least three orders of magnitude greater than laboratory estimates of diffusion in crystalline rock. Neretnieks (2002 [DIRS 162140]) presented comparisons between several analytical solutions and tracer test results at the Äspö site and reported a need for a factor 30 to 50 times larger for the fracture-matrix interface area than expected. Neretnieks (2002 [DIRS 162140]) also indicated that nine other research groups reached a similar conclusion in their interpretation of the same test data set. The results in this study are consistent with these previous findings.

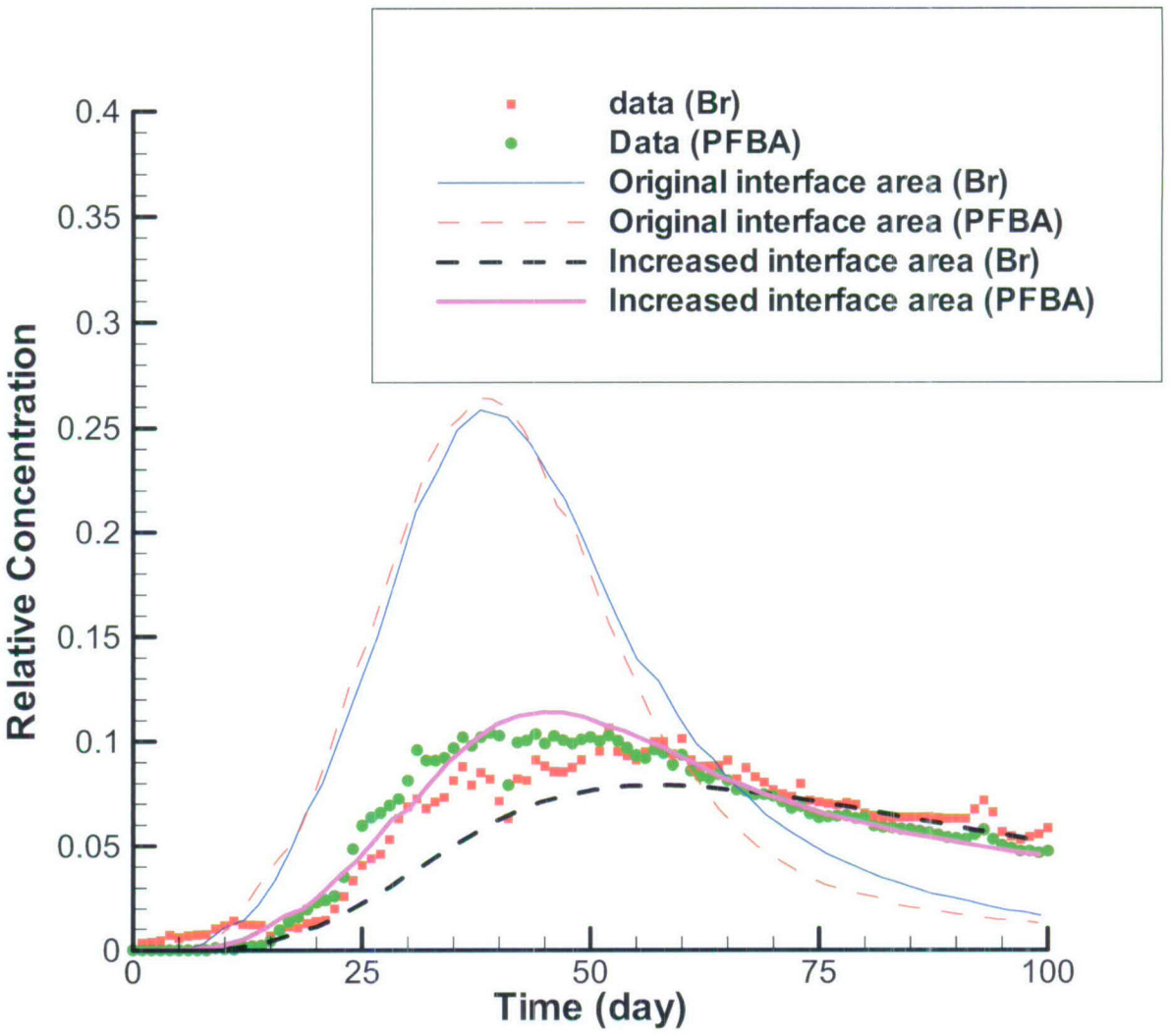

Source: DTN: LB0303A8N3MDLG.001 [DIRS 162773], files: *BTC.dat*; *BTC_odis.dat*.

Figure 7.8-9. Comparisons between Simulated Breakthrough Curves at the Niche for Two Different Fault-Matrix Interface Areas and the Observed Data

Several mechanisms regarding the increase in the interface area have been reported in the literature. They include: (1) advective mass exchanges from high-permeability fractures to low-permeability fractures (Shapiro 2001 [DIRS 162132], Section 7), (2) diffusion into stagnant water zones (Neretnieks 2002 [DIRS 162140]), and (3) enhanced fracture-matrix interface areas for fractures with small-trace lengths that do not contribute to global flow and are not considered in the survey data (and, therefore, not included in the numerical grid). In addition to these potential mechanisms, two other factors also contribute to the increase in the interface area. First, in the relevant analytical and numerical solutions to tracer transport, fracture walls are assumed to be flat surfaces. However, it is now well known that fracture walls are rough and characterized by fractal geometry (National Research Council 1996 [DIRS 139151], pp. 105 to 111). Consequently, the actual interface areas between fractures (and faults) and the matrix are larger than what are calculated using flat fracture walls. Second, a fault zone may include a great number of crushed matrix blocks that have smaller sizes than the fracture spacing in a non–fault zone. These crushed matrix blocks can make a significant contribution to the matrix diffusion within the fault, but are not considered in the numerical grid, where the fault is simply treated as a vertical fracture. To compensate for the effects of these mechanisms mentioned above, an increase in fault-matrix interface areas is obviously needed.

Although simulation results with the increased interface area reasonably match the observed data (Figure 7.8-9), the concentration difference at a given time for the two tracers is generally overestimated by the model. One plausible explanation is that the crushed matrix blocks within the fault zone have much smaller sizes than the fracture spacing. This, however, is not considered in the model, in which the matrix block size is characterized by fracture spacing. The smaller sizes correspond to the shorter times needed by the equilibrating tracer concentration at the center and outer surface of a matrix block, reducing the difference between the effects of matrix diffusion on overall solute transport behavior for different molecular-diffusion coefficients. This can be further illustrated by an extreme case: an infinitely small block size within the fault and without mass exchange between the fault and nonfault fractured rock. In this case, the concentrations of the matrix block within the fault can be equilibrated simultaneously with those at the outer surface of the block for two tracers with different molecular diffusion coefficients. Consequently, although the existence of this kind of matrix block can still significantly retard tracer transport within the fault, identical breakthrough curves may be observed at Niche 3 for the two tracers. This issue was not further explored in the current modeling study because the matrix block size distribution within the fault cannot be independently estimated or observed.

Compared with matrix diffusion, the macrodispersion process is not considered to be significant within the fault for this particular test. Field measurements indicate that water travel-velocity distribution is quite uniform within and near the fault (Figure 7.8-3), whereas macrodispersion results from variability in water velocity. These experimental observations are consistent with the findings from the model analyses: the observed data were very difficult to match when a considerable degree of dispersion was included in the model. For example, Figure 7.8-10 shows simulated breakthrough curves with a longitudinal dispersivity value of 1 m and a transverse dispersivity value of 0.1 m (and with the increased fault-matrix interface area), compared to results in Figure 7.8-9 (without considering dispersion). Larger dispersivity values generally correspond to earlier arrival times of peak concentrations and to a larger difference between these peak concentrations for the two different tracers.

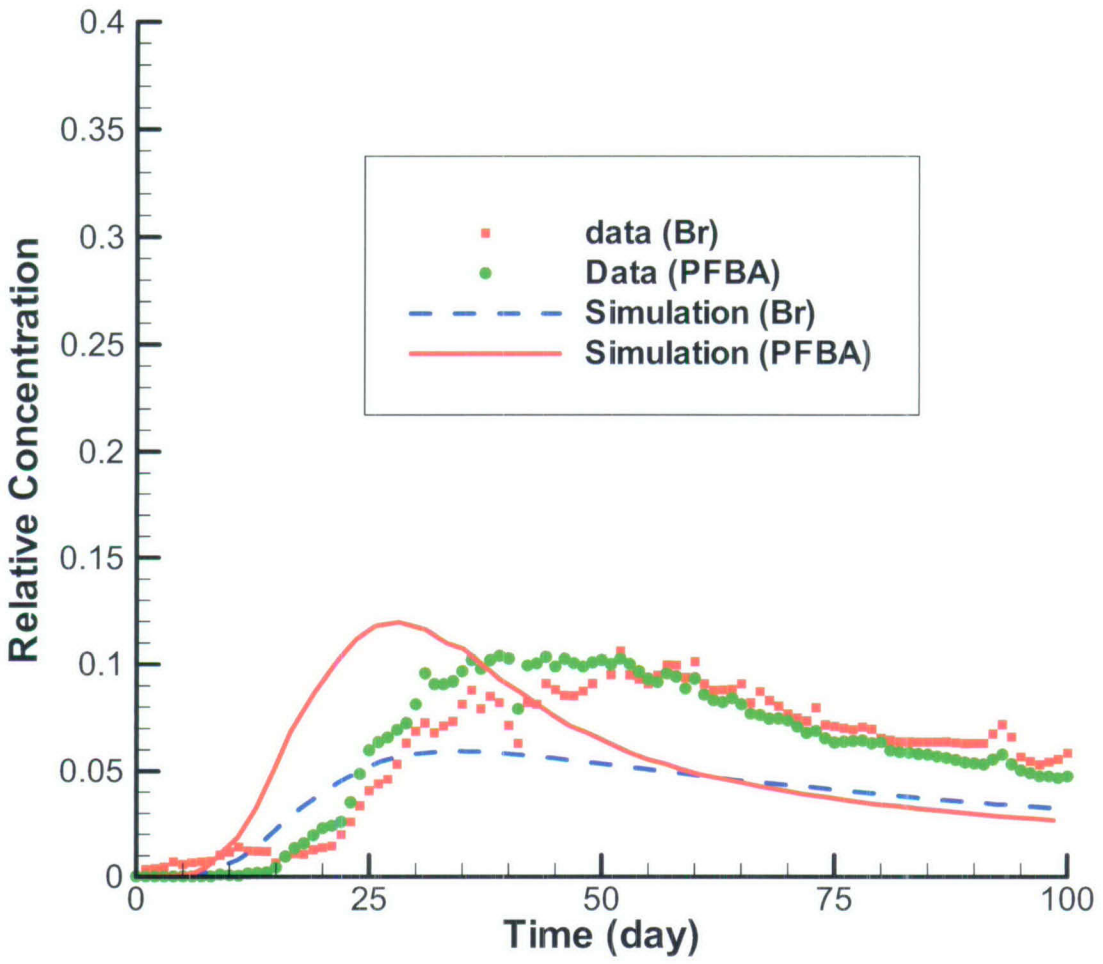

Source: DTN: LB0303A8N3MDLG.001 [DIRS 162773], files: *BTC.dat*; *BTC_dis.dat*.

Figure 7.8-10. Comparisons between Simulated Breakthrough Curves (Considering Dispersion) at the Niche for the Increased Fault-Matrix Interface Areas and the Observed Data

7.8.3.3 Implication for Radionuclide Transport in the Yucca Mountain Unsaturated Zone

Matrix diffusion has been identified as a key mechanism for retarding radionuclide transport in both unsaturated and saturated fractured rock (e.g., Bodvarsson et al. 2001 [DIRS 160133]; Neretnieks 2002 [DIRS 162140]). The enhancement of the fracture (fault)–matrix interface area (or effective matrix diffusion coefficient) seems to be common for matching field-scale solute transport observations, as suggested by this study and previous studies (Shapiro 2001 [DIRS 162132]; Neretnieks 2002 [DIRS 162140]). The current site-scale model for the Yucca Mountain unsaturated zone does not include the effects of this enhancement. Consequently, the estimated performance of the repository, estimated based on the site-scale model, may be conservative.

The other related issue is the effects of cavities (existing in several geological layers at the Yucca Mountain site) on water flow and radionuclide transport processes. One may intuitively expect the cavities connected to fractures to act as capillary barriers under unsaturated conditions, because the cavity openings are much larger than fracture apertures. However, this study and

analyses of water-release tests performed in the related geological units at the Yucca Mountain site suggest that cavities are accessible by water within fracture networks, and, therefore, are retarding the downward water flow and radionuclide transport processes. This is also supported by field observation that mineral coatings exist in many cavities (BSC 2004 [DIRS 169734], Section 5.2.2.5.4). The coating is a signature for liquid-water flow paths. Although the cavity openings are larger than fracture apertures, the roughness of cavity walls may result in film flow (along cavity walls) from fractures to the cavities (Tokunaga and Wan 1997 [DIRS 139195]).

7.9 SUMMARY OF VALIDATION

This section summarizes the validation activities and results for the UZ flow model and its submodels. The validation is carried out according to the TWP (BSC 2006 [DIRS 177465], Section 2.2.1.1). The model validation efforts in this section consists of: (1) confidence building during model development, (2) corroboration with experimental data and modeling studies, (3) corroboration with information published in refereed journals and literature, (4) analysis of model uncertainties, and (5) corroboration with natural analogues. As demonstrated in this section, the model validation criteria have been met, and the UZ flow model is valid for its intended use in TSPA-LA.

8. CONCLUSIONS

This report documents the development, results, and analyses of the current UZ flow model and its submodels. These models and modeling analyses include the following:

- A three-dimensional UZ calibration and flow model for generating 16 flow fields
- A three-dimensional, mountain-scale, ambient TH model
- A three-dimensional gas flow model
- A chloride submodel
- A calcite submodel
- A tracer transport analysis
- Model validation activities and results.

The UZ flow model and its submodels are developed to simulate past, present, and future hydrogeological, geothermal, and geochemical conditions and processes within the Yucca Mountain unsaturated zone to support various site-characterization activities. In particular, as part of the output of this report, 16 three-dimensional, steady-state flow fields of the Yucca Mountain unsaturated zone system have been generated for TSPA-LA calculations. Moreover, this report has documented the UZ flow model and its submodels in terms of modeling approaches, hydrogeological conceptual models, data source and incorporation, methodology of model calibrations, model parameter estimations and modifications, and model results and analyses of the 16 flow fields. This report also includes associated analyses on tracer transport with the 16 flow fields. The development and calibration of the mountain-scale ambient thermal, gas flow, chloride, strontium, and calcite submodels are mainly for building confidence in the UZ flow model, with the output data and tracking numbers listed in Table 8-1.

Table 8-1. Output Data and Data Tracking Numbers

Data Tracking Number	Location in this report			Description
	Section(s)	Figure(s)	Table(s)	
LB06123DPDUZFF.001[a]	6.1-4, 6.2-5, 6.6.2 Appendix E, F	6.1-2, 6.2-2, 6,2-3, 6.2-4, 6.6-1, 6.6-5, 6.6-9, 6.6-13,	6.1-2, 6.2-6, 6.2-7, 6.6-1, 6.6-2, 6.6-3,	Results of three-dimensional UZ flow fields for present-day climate of 10th, 30th, 50th, and 90th percentile infiltration maps to be used by TSPA-LA
LB07013DMOUZFF.001[a]	6.1-4, 6.2-5 Appendix E, F	6.1-3, 6.6-2, 6.6-6, 6.6-10, 6.6-13,	6.1-2, 6.2-6, 6.2-7, 6.6-1, 6.6-2, 6.6-3,	Results of three-dimensional UZ flow fields for monsoon climate of 10th, 30th, 50th, and 90th percentile infiltration maps to be used by TSPA-LA
LB07013DGTUZFF.001[a]	6.1-4, 6.2-5 Appendix E, F	6.1-4, 6.6-3, 6.6-7, 6.6-11, 6.6-13,	6.1-2, 6.2-6, 6.2-7, 6.6-1, 6.6-2, 6.6-3,	Results of three-dimensional UZ flow fields for glacial transition climate of 10th, 30th, 50th, and 90th percentile infiltration maps

Table 8-1. Output Data and Data Tracking Numbers (Continued)

Data Tracking Number	Location in this report			Description
	Section(s)	Figure(s)	Table(s)	
LB0702UZP10KFF.002 [a]	6.1-4, 6.2-5 Appendix E, F	6.1-5, 6.6-4, 6.6-8, 6.6-12, 6.6-13,	6.1-3, 6.2-6, 6.2-7, 6.6-1, 6.6-2, 6.6-3,	Results of three-dimensional UZ flow fields for post-10,000-year climate of 10th, 30th, 50th, and 90th percentile infiltration maps
LB0705TRAVTIME.001	6.7	6.7-1 to 6.7-7	6.7-2 and 6.7-3	Tc and Np Transport simulation scenarios for travel times, input/output files; using 16 three-dimensional UZ flow fields
LB0701UZMTHCAL.001	6.3, 9.4	6.3-2 to 6.3-8		Three-dimensional unsaturated zone ambient thermal model, Input/output, supporting files, and simulation results
LB07043DGASCAL.001	6.4, 7.4	6.3-2, 6.4-3, 6.4-4, 7.4-1, 7.4-2, 7.4-3, 7.4-4	6.4-2	Three-dimensional gas flow model for calibration and validation, input/out, supporting files, and simulation results
LB0704C14FFVAL.001	7.5, 9.4	7.5-1, 7.5-2, 7.5-3, 7.5-4		C-14 simulations, input/output files, and simulation results
LB07043DCRXPRP.001	6.2,6.3, 6.4, 6.4.1, 7.2, 9.4		6.2-2 to 6.2-6, 6.4-2, 6.4-3 Appendix B B-1 to B-4	Three-Dimensional site scale model calibrated property sets: Data Summaries
LB0701UZMCLCAL.001	6.5, 9.4	6.5-1 to 6.5-11		Chloride transport simulation results, input/output files
LB0705UZSRTRAN.001	7.6, 9.4	7.6-1, 7.6-2		Unsaturated zone strontium transport model, input/output files, and simulation results
LB0612PDFEHMFF.001	6.6.2.2			Four three-dimensional UZ flow fields of present-day climate 10th, 30th, 50th, and 90th percentile infiltration rates, Converted from TOUGH2 to T2FEHM format
LB0701MOFEHMFF.001	6.6.2.2			Four three-dimensional UZ flow fields of monsoon climate 10th, 30th, 50th, and 90th percentile infiltration rates, Converted from TOUGH2 to T2FEHM format

Table 8-1. Output Data and Data Tracking Numbers (Continued)

Data Tracking Number	Location in this report			Description
	Section(s)	Figure(s)	Table(s)	
LB0701GTFEHMFF.001	6.6.2.2			Four three-dimensional UZ flow fields of glacial transition climate 10th, 30th, 50th, and 90th percentile infiltration rates, Converted from TOUGH2 to T2FEHM format
LB0702PAFEM10K.002	6.6.2.2			Four three-dimensional UZ flow fields of post-10,000-year climate 10th, 30th, 50th, and 90th percentile infiltration rates, Converted from TOUGH2 to T2FEHM format
LB0612PDPTNTSW.001	Appendix E.1			PTn/TSw Interface Percolation Flux Maps for Present-Day Climate of 10th, 30th, 50th, and 90th Percentile Infiltration Scenarios
LB0701MOPTNTSW.001	Appendix E.1			PTn/TSw Interface Percolation Flux Maps for Monsoon Climate of 10th, 30th, 50th, and 90th Percentile Infiltration Scenarios
LB0701GTPTNTSW.001	Appendix E.1			PTn/TSw Interface Percolation Flux Maps for Glacial transition Climate of 10th, 30th, 50th, and 90th Percentile Infiltration Scenarios
LB0702UZPTN10K.002	Appendix E.1			PTn/TSw Interface Percolation Flux Maps for Post-10k-yr Climate of 10th, 30th, 50th, and 90th Percentile Infiltration Scenarios
LB0705FLOWCOMP.001	6.6.3			Fracture, matrix and fault flow components and percentages for the 16 UZ flow fields
LB0705DAMPINGA.001	6.9	6.9-1, 6.9-2		One-dimensional simulations for PTn damping effect on percolation fluxes
LB0701PAWFINFM.001	6.8	6.8-3	6.8-1	UZ flow weighting factors
LB0704UZWFINFM.001	6.8			Supporting files and results for calculating and sensitivity studies on UZ flow weighting factors

Table 8-1. Output Data and Data Tracking Numbers (Continued)

Data Tracking Number	Location in this report			Description
	Section(s)	Figure(s)	Table(s)	
LB0708WTTEMDAT.001	Appendix I			Results of the data qualification for temperature data used to generate water table boundary condition.

[a] These three-dimensional UZ flow fields will be directly used for TSPA-LA and are not discussed in this report.

PTn = Paintbrush nonwelded hydrogeologic unit; RIT = Repository Integration Team; TSPA-LA = Total System Performance Assessment for License Application; TSw = Topopah Spring welded hydrogeologic unit; UZ = unsaturated zone.

8.1 UZ FLOW MODEL CALIBRATION

Field-measured saturation, water potential, and perched water data have been used to calibrate the UZ flow model (Section 6.2). Such calibrations are part of the important iterative processes of model development to increase confidence in model predictions of site conditions. This report continues this model calibration effort using the one-dimensional calibrations reported in *Calibrated Unsaturated Zone Properties* (SNL 2007 [DIRS 179545]), and in the previous three-dimensional modeling effort (BSC 2004 [DIRS 169861]). This work focuses particularly on three-dimensional model forward calibrations using the updated infiltration maps (Section 6.1.4). This section, and Section 6.9 on damping of episodic flow, addresses outstanding Key Technical Issue, TSPAI 2.02 AIN-1, Comment J-20.

Calibration was conducted using four sets of rock-property parameters (SNL 2007 [DIRS 179545]) associated with present-day 10th, 30th, 50th, and 90th percentile infiltration rates, and the current geological model and numerical grid (BSC 2004 [DIRS 169855]). In addition, a permeability-barrier conceptual model was adopted for modeling water-perching occurrences. Under the permeability barrier concept, fracture and matrix rock properties were locally modified to better match data in several grid layers near the observed perched zones.

The model calibration efforts (Section 6.2) conclude that the UZ flow model can reproduce moisture conditions in the Yucca Mountain unsaturated zone in terms of liquid saturations, water potentials, and perched water occurrence, as verified by observations. In general, the modeled results from the twelve flow-field simulations of present-day, monsoon, and glacial transition climates using the perched water conceptual model are in good agreement with the measured water-perching elevations at seven boreholes.

The UZ flow model provides results of steady-state fluid (Sections 6.2 and 6.6) and heat flow (Section 6.3) as well as transient tracer transport (Section 6.7). Flow processes for model layers above the TSw and PTn units may be subject to episodic infiltration. Since the model results with these layers may not reflect actual conditions, which are time and scale dependent, the results may not be directly applicable to studies on a much smaller scale, such as the emplacement drift. In this report, the uncertainties in the results, owing to input-parameter and model-gridding uncertainties, are evaluated by generating a number of flow fields with various parameter sets, infiltration maps, and conceptual models.

8.2 GEOTHERMAL MODEL CALIBRATION

The ambient geothermal model simulates large-scale UZ geothermal and heat flow conditions (Section 6.3). The three-dimensional ambient thermal model was calibrated against qualified temperature data measured from five boreholes, using the four present-day infiltration parameter set with a three-dimensional dual-permeability thermal grid. Simulated temperature results for the present-day 10th percentile infiltration are in best agreement with the observed temperature profiles from the boreholes. Such results provide the ambient temperature distributions that determine boundary and initial conditions for the mountain-scale and drift-scale TH, THC, and THM coupled-processes models, as well as estimates to deep percolation flux in the unsaturated zone.

8.3 GAS FLOW MODEL

A three-dimensional pneumatic simulation has been performed as a part of the UZ flow model calibration and validation effort (Section 6.4). Results of gas flow simulations are compared to the measured pneumatic data from three boreholes, including SD-7, SD-12, and UZ-7a, for the purposes of calibration and validation. As a result of calibration, fracture permeability in several TSw layers was reduced by a factor of 10 to 20, leading to an overall good match between the three-dimensional model prediction and measurement of pneumatic data under three-dimensional flow conditions. The gas-flow calibration results add confidence that the UZ flow model is reliable and appropriate for modeling gas flow in the unsaturated zone.

8.4 CHLORIDE SUBMODEL

Chloride is a naturally occurring conservative tracer, entering the groundwater system as a solute with the infiltration flux. Thus, chloride data can be used to examine the long-term infiltration rate and percolation flux in the flow model. The chloride flux to the Yucca Mountain unsaturated zone is calculated based on the precipitation, runon, and runoff at the ground surface of the mountain.

The chloride transport modeling considered four present-day scenarios: 10th, 30th, 50th, and 90th percentile infiltration rates (Section 6.5). Each scenario compares simulation results against measured data. The comparisons show that the chloride transport model with the present-day, 10th percentile infiltration yields the closest and most consistent match with field data. This indicates that the present-day 10th percentile infiltration rate of 3.03 mm/yr over the UZ model domain is a good estimate for the net infiltration rate under the present-day climate.

8.5 CALCITE SUBMODEL

Calcite precipitation has been modeled in unsaturated fractured rocks, considering several essential factors: (1) infiltration rate, (2) ambient geothermal gradient, (3) gaseous CO_2 diffusive transport and partitioning between liquid and gas phases, (4) fracture–matrix interaction for water flow and chemical constituents, and (5) water–rock interaction (Section 7.7).

Modeling of calcite deposition can be used to build some constraints on the infiltration-percolation flux. The modeling also provides additional evidence for validation of the UZ model. Over a range of 2 to 20 mm/yr infiltration rates, the simulated calcite

distributions capture the measured data from the WT-24 well cuttings. The 20 mm/yr infiltration rate may be the upper bound for the WT-24 location, whereas the infiltration rate (5.92 mm/yr) at the borehole locations is a good match to the data. The observed calcite precipitation for the top of TSw occurs mostly in the fractures, which is also captured by the modeling. Modeled results can also provide useful insight into process mechanisms such as fracture–matrix interaction, as well as conditions and parameters controlling calcite deposition. The modeled calcite abundances generally increase with increasing infiltration rate, but become less sensitive to infiltration at higher rates as a result of its impact on the geothermal gradient. Data from borehole SD-6 are roughly consistent with the relation between infiltration rate and calcite abundances, although a locally higher thermal gradient in the PTn can also be a factor in calcite distribution.

8.6 UZ FLOW FIELDS

Sixteen three-dimensional UZ flow fields (10th, 30th, 50th, and 90th percentiles for each of the present-day, monsoon, glacial transition, and post-10,000-yr climates) were produced for TSPA-LA calculations (Sections 6.2 and 6.6). These flow fields were converted for use by FEHM in the TSPA-LA calculations. The flow fields were generated based on (1) the TSPA-LA grid (BSC 2004 [DIRS 169855]), (2) 16 infiltration maps representing four climates, (3) the four parameter sets, and (4) the permeability-barrier, perched water conceptual model with the calibrated perched water parameters. The purpose of studying a large number of flow fields for various modeling scenarios was to cover the TSPA-LA scenarios and to account for possible current and future site conditions, as well as model and property uncertainties. The main uncertainties currently considered in the UZ flow model include fracture and matrix properties, present-day and future net infiltration rates over the mountain, conceptual models for perched water occurrence, and the role of PTn in lateral flow.

An in-depth analysis of simulated percolation fluxes at the repository level and at the water table was conducted for all 16 flow-field simulation scenarios. Comparisons between repository level and water table percolation fluxes and their distributions (using surface infiltration maps) indicate different scales of lateral flow or diversion, mainly through the PTn and CHn units, when water travels from the surface to the water table. Large-scale lateral flow occurs in the CHn unit, through the low-permeability zeolitic or perched water zones. Significant flow diversion and redistribution into faults within the PTn unit as well as the CHn unit is predicted.

Fracture–matrix flow components at the repository horizon and at the water table were also analyzed for the 16 simulations. The statistics show that at the repository horizon fracture flow is dominant in the welded tuffs for all 16 flow fields. At the repository level, fracture flow consists of about 70% to 80% of the total percolation fluxes over the entire model layer, and is even higher within the repository footprint. Fault-flow fraction increases with depth over all UZ model layers, from 1% to ~2% at the TCw/PTn interface, 12% to 32% at the repository horizon, and 44% to 65% at the water table. Comparison of fault flow percentages at the TCw/PTn interface, the repository horizon, and the water table (in Tables 6.6-1, 6.6-2, and 6.6-3) indicates that flow focusing into faults occurs mainly through the lower hydrogeological CHn unit, and the PTn unit.

8.7 TRACER TRANSPORT TIMES

A total of 32 tracer transport simulations were carried out to obtain insight into the impacts of infiltration rates, UZ flow model conceptual models, and retardation effects on tracer migration from the repository to the water table (Section 6.7). The 16 UZ flow fields were incorporated into these 32 transport runs. For each flow field, there were two tracer transport runs, one for conservative (or nonadsorbing) and the other for reactive (or adsorbing) tracer transport, with tracer release from repository fracture blocks. These tracer-transport studies indicate that there exists a wide range of tracer transport times associated with different infiltration rates and the type of tracers. The most important factors for tracer-transport times are found to be: (1) surface net infiltration rates, and (2) adsorption effects in the CHn unit.

Statistics of tracer transport times at 10% and 50% mass breakthrough at the water table from the 32 simulations show that tracer-transport times vary inversely to the average surface infiltration (net water recharge) rate over the model domain. When the average infiltration rate increases from 3 to 70 mm/yr, average tracer transport (50% mass breakthrough) times decrease by more than two orders of magnitude for adsorbing and nonadsorbing species. Nonadsorbing tracers migrate (from the repository to the water table) one to two orders of magnitude faster than an adsorbing tracer under the same infiltration condition.

8.8 UZ FLOW WEIGHTING FACTORS

A generalized likelihood uncertainty estimation (GLUE) methodology was used to determine the weighting factors (Section 6.8). The generation of the UZ flow weighting factors accounts for prior information available from the infiltration model for the probability of infiltration maps, as well as matches between UZ flow model results (distributions of temperature and chloride concentration) and corresponding field data. Such weighting factors were derived from infiltration and UZ flow model results for present-day conditions.

8.9 ANALYZING TRANSIENT-PULSE INFILTRATION

How episodic surface infiltration affects deep percolation was investigated by examining variations in percolation fluxes at the bottom of the PTn versus time, using two one-dimensional column models (Section 6.9). Results from the two column models show that surface infiltration pulses can be effectively smoothed temporally once traveling to the bottom of the PTn unit. In general, after rapid changes during the first several hundred years of pulse infiltration, the percolation fluxes at the bottom of the PTn gradually approach the average value of net infiltration.

8.10 MODEL VALIDATION

Model validation efforts have been documented in this report (Section 7). Validation activities for the UZ flow model mainly include corroboration with experimental data and modeling studies, using the following corroboration with experimental data: (1) ECRB observation data; (2) WT-24 perched water data; (3) gas flow data from boreholes SD-12 and UZ-7a; and (4) borehole-measured ^{14}C data and Alcove 8—Niche 3 flow and transport data. In addition, validation efforts are also made for the strontium model and calcite model, using field-observed data from surface-based boreholes or from the ESF.

In these validation examples, the simulation results of the UZ flow model and submodels are shown to be able to match different types of available observation data, such as water potentials, perched water locations, tracer and geochemical concentrations, and pneumatic pressures. The criteria of the model validation of the TWP (BSC 2006 [DIRS 177465]) are, in general, satisfied. These efforts have provided validation of the UZ flow model and its submodels for their accuracy and reliability in describing hydrological, thermal, and chemical conditions, and predicting flow and transport processes in the unsaturated zone system of Yucca Mountain.

8.11 LIMITATIONS

The UZ flow model and submodels are appropriate tools for characterizing flow and transport processes in the Yucca Mountain unsaturated zone. The accuracy and reliability of the UZ flow model predictions are dependent on the accuracy of estimated model properties, other types of input data, and hydrogeological conceptual models. These models are limited mainly by the current understanding of Yucca Mountain system, including the geological and conceptual models, the volume-average modeling approach, and the available field and laboratory data.

Past site investigations have shown that large variabilities exists in the flow and transport parameters over the spatial and temporal scales of the mountain. Even though considerable progress has been made in this area, uncertainty associated with the UZ flow model input parameters exists. The major uncertainties in the UZ model parameters are: (1) the accuracy of estimated current, past, and future net infiltration rates over the mountain; (2) quantitative descriptions of the heterogeneity of welded and nonwelded tuffs, their flow properties, and detailed spatial distributions within Yucca Mountain, especially below the repository; (3) fracture properties in zeolitic units and faults from field studies; (4) evidence of lateral diversion caused by zeolites in the CHn units and within the PTn units; and (5) transport properties (e.g., adsorption or K_d coefficients in different rock types, matrix molecular diffusion coefficients in different units for different radionuclides, dispersivities in fracture and matrix systems). These uncertainties exist, but they have been addressed with the modeling studies in this report. In particular, most uncertainties are captured within the range of flow field generated.

8.12 HOW ACCEPTANCE CRITERIA ARE ADDRESSED

The following information describes how this analysis addresses the acceptance criteria in *Yucca Mountain Review Plan, Final Report* (NRC 2003 [DIRS 163274], Section 2.2.1.3.6.3). Only those acceptance criteria that are applicable to this report (Section 4.2) are discussed. In most cases, the applicable acceptance criteria are not addressed solely by this report; rather, the acceptance criteria are fully addressed when this report is considered in conjunction with other analysis and model reports that describe flow in the unsaturated zone. Where a subcriterion includes several components, only some of those components may be addressed. How these components are addressed is summarized below.

Acceptance Criteria from Section 2.2.1.3.6, *Flow Paths in the Unsaturated Zone*

Acceptance Criterion 1: ***System Description and Model Integration Are Adequate.***

Subcriterion (1): The UZ flow model and submodels described in this report support the TSPA-LA. This model adequately incorporates important design features (drift layout and spacing), physical phenomena (geologic, hydrologic, geochemical, and thermal properties of the Yucca Mountain unsaturated zone strata), and couplings (ambient thermal-hydrological and hydrological-chemical) (Sections 6.1 to 6.9). The UZ flow model uses assumptions that are consistent with related UZ abstractions and analysis reports (Section 5).

Subcriterion (2): The models adequately incorporate the aspects of geology, hydrology, geochemistry, physical phenomena, and couplings important for determining flow paths in the unsaturated zone through use of Yucca Mountain field data, calibration to site-specific data, and verification via a number of physical processes and tests (Sections 6.2 to 6.10, and 7.1 to 7.8). Conditions and assumptions supporting the related abstraction of flow paths in the unsaturated zone are identified in Section 5. These assumptions are consistent with the system and model description in Sections 6.1 and 6.3, and related abstractions.

Subcriterion (3): The process-level model of flow in the unsaturated zone uses assumptions, technical bases, data and models that are appropriate and consistent with other abstractions. Specifically, the TSPA-LA uses the UZ flow model simulations to provide input to other models such as ambient and thermal drift-scale models, the mountain-scale thermal-hydrological model, and the radionuclide transport model. Also, the UZ flow model applies other upstream models that form the project basis for climate projections, infiltration, hydrology, and geology in the unsaturated and saturated zones (Section 6.1). This model and submodels simulate ambient conditions and perform predictive studies of changes in the mountain caused by climatic, ambient thermal, and geochemical perturbations based on Yucca Mountain data collected over the last decade (Sections 6.1 to 6.5). The descriptions and technical basis are transparent and traceable to the data sources and references provided in Section 4.1.

Subcriterion (4): Parameters and properties employed in the UZ flow model were obtained from the same documents that provided the parameters and properties used for the UZ transport model (e.g., SNL 2007 [DIRS 179545] and BSC 2004 [DIRS 170029]; DTN: MO0012MWDGFM02.002 [DIRS 153777]) (Section 6.1); therefore, their bases and justification are consistent. Ambient thermal-hydrologic effects are incorporated in this model and are consistent with the approach taken for these effects in the radionuclide transport model (Sections 6.1, 6.3, and 6.5). Similar numerical model approaches were used for the flow and transport models as described in *Conceptual Model and Numerical Approaches for Unsaturated Zone Flow and Transport* (BSC 2004 [DIRS 170035]) (Section 6).

Subcriterion (5): Detailed documentation concerning the included features, events, and processes are provided in Section 6.1. The description of geological features included in the model are discussed in Section 6.1.1. Processes included in the model are discussed in Section 6.1.2. Further discussion of processes included in the model is given in *Conceptual Model and Numerical Approaches for Unsaturated Zone Flow and Transport* (BSC 2004 [DIRS 170035])

(Section 6.1). The events included in the model are related to climate change and are described in Section 6.1.4 in terms of the effects of climate change on the infiltration boundary condition.

Subcriterion (6): The infiltration boundary condition is output from an approved model that considers future climate changes. Parameter estimates used in this process-level model are representative of the temporal (time-related climate changes) and spatial (geologic strata and linear variations over the grid) discretizations considered in the model (Sections 6.1 and 6.2).

Subcriterion (7): Average parameter estimates are consistent with the temporal (time-related climate changes) and spatial discretizations adopted by the UZ flow model (Sections 6.1.1 and 6.1.5).

Subcriterion (8): Section 6.11 describes the representation of the UZ flow fields after a climate-induced water table rise.

Subcriterion (9): This report was developed in accordance with the QARD (DOE 2006 [DIRS 177092]), which commits to NUREGs 1297 and 1298. Moreover, compliance with the DOE procedures, which are designed to ensure compliance with the QARD (DOE 2006 [DIRS 177092]), is verified by audits by QA and other oversight activities. Accordingly, the guidance in NUREGs 1297 and 1298 has been followed as appropriate.

Acceptance Criterion 2: *Data Are Sufficient for Model Justification.*

Subcriterion (1): Hydrological and ambient thermal-hydrological or hydrological-chemical values used in the models discussed in this report are adequately justified in Sections 4.1, 6.1.3, 6.1.4, 6.1.5, 6.2.3, 6.3, 6.4, 6.8, 6.9, 6.10 and, in the validation sections, 7.1 through 7.8. These sections provide adequate descriptions of how the data were used, interpreted, and synthesized into the parameters.

Subcriterion (2): The quality of the data used in this report is assured by the QA program (Section 2). Approved QA procedures identified in the TWP (BSC 2006 [DIRS 177465], Section 4) have been used to conduct and document the activities described in this analysis report.

Subcriterion (3): The UZ flow model, temperature model, and geochemistry submodels have been developed to simulate past, present, and future hydrological, geothermal, and geochemical conditions in the Yucca Mountain unsaturated zone. Flow fields are computed using four parameter sets and sixteen infiltration maps with relevant spatial variability, such as future climate states that influence net infiltration amounts (Sections 6.0, 6.1, 6.2, and 6.7). As demonstrated by results of calculations for the 16 flow fields, representative values for deep-percolation flux rates are determined through use of the 10th, 30th, 50th, and 90th percentile infiltration rates for each of four climate scenarios (summarized in Section 6.1.4). The three-dimensional UZ flow model was calibrated using field-measured liquid saturation, water potential, perched water, pneumatic, and isotopic tracer data (Section 6.2). The top and bottom boundaries of the model are treated as Dirichlet-type conditions with specified constant but spatially varying temperature and gas pressure (Section 6.1.3). Surface infiltration, as discussed in Section 6.1.4, is applied using a source term, accounting for varying climate scenarios, in the fracture gridblocks on the top boundary.

Subcriterion (5): Parameter uncertainty is discussed in Section 6.10. Sensitivity analyses for fracture and matrix permeabilities and fracture and matrix van Genuchten capillary strength are presented in *Parameter Sensitivity Analysis for Unsaturated Zone Flow* (BSC 2005 [DIRS 174116]). These investigations combined with the main results for UZ flow presented in this report confirm that (a) infiltration uncertainty has the greatest influence over UZ flow behavior as compared with uncertainty for any hydrologic parameters; (b) uncertainty in matrix hydrologic parameters have more influence on flow behavior than uncertainty in fracture hydrologic parameters; (c) uncertainty in matrix hydrologic properties are only significant if the change results in a greater fraction of the total flow in the matrix.

Subcriterion (6): Approved QA procedures identified in the TWP (BSC 2006 [DIRS 177465], Section 4) and in Section 1 have been used to conduct and document the activities described in this model report.

Subcriterion (7): The conceptual model used in this report incorporates processes to describe subsurface flow and transport in the unsaturated zone in a heterogeneous system of layered, anisotropic, fractured volcanic rock. Understanding of such processes has been promoted by a continuous effort of data collection and analysis as well as modeling studies (Section 6.2.2). Mathematical models used in the UZ flow model are TOUGH2 V1.6 [DIRS 161491] and T2R3D V1.4 [DIRS 146654]. These codes were selected because they have been baselined through YMP QA procedure IT-PRO-0011 for modeling flow and transport in heterogeneous fractured rock (e.g., Wu et al. 2002 [DIRS 160195]) (Section 6.1.2). The robustness of results is demonstrated through the calibration and validation processes and comparison to alternative models as described in Sections 6.2 to 6.9, and 7.

Acceptance Criterion 3: ***Data Uncertainty is Characterized and Propagated Through the Model Abstraction.***

Subcriterion (1): The multiple flow fields generated by the UZ model capture the uncertainties in the parameter values and boundary conditions, as summarized in Sections 6.10 and 8.11. By choosing flow fields that consistently match site data and analogue models, model and parametric uncertainties are reasonably accounted for and do not result in an under-representation of the risk estimate (Section 6.10).

Subcriterion (2): The technical bases for the parameter values used in this model are provided in Section 6.2.

Subcriterion (3): Statistical correlations between parameters in this model are indirectly included through the calibration process discussed in Section 6.2.

Subcriterion (4): Boundary conditions (ground surface, and water table) applied to this model and sensitivity analyses performed on this model are representative of climate projections for sixteen cases (present-day, monsoon, glacial transition, and post-10k-yr climates of 10th, 30th, 50th, and 90th percentiles) (Section 6.1.3). Surface infiltration as a function of climate scenario, as discussed in Section 6.1.4, is applied using a source term in the surface fracture gridblocks. These boundary conditions are used for both sensitivity analyses with the alternative model parameters and base case flow field calculations.

Acceptance Criterion 4: ***Model Uncertainty is Characterized and Propagated Through the Model Abstraction.***

Subcriterion (1): The UZ flow model report includes investigation of alternative modeling approaches. Alternative approaches include climate and climate related changes (Section 6.1.4 and throughout the report), PTn damping effect on transient infiltration pulses (Section 6.9) and water table rise (Section 6.11).

Subcriterion (2): The bounds of uncertainty created by the process-level models are directly included in the UZ flow model abstraction as discussed in Section 6.10.1.

Subcriterion (3): The model uncertainties have been discussed, investigated, or quantified in this report using field observation data, modeling sensitivity analyses, natural analogue information, and other arguments (Sections 6.2 to 6.9). Model uncertainty is reasonably captured by computations using alternative parameter sets as discussed in Section 6.10. The effects of parameter and data uncertainties on UZ flow are sufficiently covered in the model results for the 16 three-dimensional flow fields, so that no under-representation of the risk estimate will occur (Section 6.10.1).

Acceptance Criterion 5: ***Model Abstraction Output Is Supported by Objective Comparisons*:**

Subcriterion (1): The models implemented in this TSPA abstraction provide results consistent with output from detailed process-level models and/or empirical observations, because the abstraction consists of selected process-model results for UZ flow, as discussed in Section 8.6.

Subcriterion (2): Abstractions of process-level models conservatively bound process-level predictions, because the abstraction consists of selected process-model results for UZ flow, as discussed in Section 8.6.

Subcriterion (3): The flow model abstraction and process model are the same model. Sensitivity analyses for fracture and matrix permeabilities and fracture and matrix van Genuchten capillary strength are presented in *Parameter Sensitivity Analysis for Unsaturated Zone Flow* (BSC 2005 [DIRS 174116]). Comparisons of the flow model output with empirical observations are made in Sections 6.2, 6.3, 6.4, 6.5, 7.2, 7.3, 7.4, 7.5, 7.6, 7.7, and 7.8. As discussed in Section 7, a comparison with the Idaho National Engineering and Environmental Laboratory's Radioactive Waste Management Complex natural analogue is presented in the *Natural Analogue Synthesis Report* (BSC 2004 [DIRS 169218], Section 9.3).

9. INPUTS AND REFERENCES

The following is a list of the references cited in this document. Column 2 represents the unique six digit numerical identifier (the Document Input Reference System number), which is placed in the text following the reference callout (e.g., BSC 2003 [DIRS 165991]). The purpose of these numbers is to assist in locating a specific reference. Within the reference list, multiple sources by the same author (e.g., BSC 2002) are sorted alphabetically by title.

9.1 DOCUMENTS CITED

101180 Ahlers, C.F.; Bandurraga, T.M.; Bodvarsson, G.S.; Chen, G.; Finsterle, S.; and Wu, Y-S. 1995. *Summary of Model Calibration and Sensitivity Studies Using the LBNL/USGS Three-Dimensional Unsaturated Zone Site-Scale Model.* Milestone 3GLM107M. Berkeley, California: Lawrence Berkeley National Laboratory. ACC: MOL.19960208.0092.

109715 Ahlers, C.F.; Finsterle, S.; and Bodvarsson, G.S. 1999. "Characterization and Prediction of Subsurface Pneumatic Response at Yucca Mountain, Nevada." *Journal of Contaminant Hydrology, 38,* (1-3), 47-68. New York, New York: Elsevier. TIC: 244160.

103750 Altman, W.D.; Donnelly, J.P.; and Kennedy, J.E. 1988. *Qualification of Existing Data for High-Level Nuclear Waste Repositories: Generic Technical Position.* NUREG-1298. Washington, D.C.: U.S. Nuclear Regulatory Commission. TIC: 200652.

103597 Altman, W.D.; Donnelly, J.P.; and Kennedy, J.E. 1988. *Peer Review for High-Level Nuclear Waste Repositories: Generic Technical Position.* NUREG-1297. Washington, D.C.: U.S. Nuclear Regulatory Commission. TIC: 200651.

156269 Bear, J. 1972. *Dynamics of Fluids in Porous Media.* Environmental Science Series. Biswas, A.K., ed. New York, New York: Elsevier. TIC: 217356.

153427 Benson, C.F. and Bowman, R.S. 1996. "Erratum, Tri- and Tetrafluorobenzoates as Nonreactive Tracers in Soil and Groundwater." *Soil Science Society of America Journal, 60,* 1780. Madison, Wisconsin: Soil Science Society of America. TIC: 246741.

179081 Beven, K. 2006. "A Manifesto for the Equifinality Thesis." *Journal of Hydrology, 320,* 18-36. New York, New York: Elsevier. TIC: 259046.

179079 Beven, K. and Binley, A. 1992. "The Future of Distributed Models: Model Calibration and Uncertainty Prediction." *Hydrological Processes, 6,* (3), 279-298. New York, New York: John Wiley & Sons. TIC: 258993.

179825 Beven, K.; Freer, J.; Hankin, B.; and Schulz, K. 2000. "The Use of Generalised Likelihood Measures for Uncertainty Estimation in High-Order Models of Environmental Systems." *Nonlinear and Nonstationary Signal Processing.* Fitzgerald, W.J.; Smith, R.L.; Walden, A.T.; and Young, P.C.; eds. Pages 115-151. New York, New York: Cambridge University Press. TIC: 259258.

105170 Birkholzer, J.; Li, G.; Tsang, C-F.; and Tsang, Y. 1999. "Modeling Studies and Analysis of Seepage into Drifts at Yucca Mountain." *Journal of Contaminant Hydrology, 38,* (1-3), 349-384. New York, New York: Elsevier. TIC: 244160.

100103 Bodvarsson, G.S.; Bandurraga, T.M.; and Wu, Y.S., eds. 1997. *The Site-Scale Unsaturated Zone Model of Yucca Mountain, Nevada, for the Viability Assessment.* LBNL-40376. Berkeley, California: Lawrence Berkeley National Laboratory. ACC: MOL.19971014.0232.

120055 Bodvarsson, G.S.; Boyle, W.; Patterson, R.; and Williams, D. 1999. "Overview of Scientific Investigations at Yucca Mountain—The Potential Repository for High-Level Nuclear Waste." *Journal of Contaminant Hydrology, 38,* (1-3), 3-24. New York, New York: Elsevier. TIC: 244160.

162477 Bodvarsson, G.S.; Kwicklis, E.; Shan, C.; and Wu, Y.S. 2003. "Estimation of Percolation Flux from Borehole Temperature Data at Yucca Mountain, Nevada." *Journal of Contaminant Hydrology, 62-63,* 3-22. New York, New York: Elsevier. TIC: 254205.

160133 Bodvarsson, G.S.; Liu, H.H.; Ahlers, C.F.; Wu, Y-S.; and Sonnenthal, S. 2001. "Parameterization and Upscaling in Modeling Flow and Transport in the Unsaturated Zone of Yucca Mountain." Chapter 11 of *Conceptual Models of Flow and Transport in the Fractured Vadose Zone.* Washington, D.C.: National Academy Press. TIC: 252777.

158726 BSC (Bechtel SAIC Company) 2001. *UZ Flow Models and Submodels.* MDL-NBS-HS-000006 REV 00 ICN 01. Las Vegas, Nevada: Bechtel SAIC Company. ACC: MOL.20020417.0382.

165991 BSC 2003. *Analysis of Infiltration Uncertainty.* ANL-NBS-HS-000027 REV 01. Las Vegas, Nevada: Bechtel SAIC Company. ACC: DOC.20031030.0003.

170038 BSC 2004. *Analysis of Hydrologic Properties Data.* ANL-NBS-HS-000042 REV 00. Las Vegas, Nevada: Bechtel SAIC Company. ACC: DOC.20041005.0004; DOC.20050815.0003.

170035 BSC 2004. *Conceptual Model and Numerical Approaches for Unsaturated Zone Flow and Transport.* MDL-NBS-HS-000005 REV 01. Las Vegas, Nevada: Bechtel SAIC Company. ACC: DOC.20040922.0006; DOC.20050307.0009.

169855 BSC 2004. *Development of Numerical Grids for UZ Flow and Transport Modeling.* ANL-NBS-HS-000015 REV 02. Las Vegas, Nevada: Bechtel SAIC Company. ACC: DOC.20040901.0001.

169864 BSC 2004. *Drift Scale THM Model.* MDL-NBS-HS-000017 REV 01. Las Vegas, Nevada: Bechtel SAIC Company. ACC: DOC.20041012.0001; DOC.20060103.0002.

170029 BSC 2004. *Geologic Framework Model (GFM2000).* MDL-NBS-GS-000002 REV 02. Las Vegas, Nevada: Bechtel SAIC Company. ACC: DOC.20040827.0008.

170004 BSC 2004. *In Situ Field Testing of Processes.* ANL-NBS-HS-000005 REV 03. Las Vegas, Nevada: Bechtel SAIC Company. ACC: DOC.20041109.0001; DOC.20051010.0001.

164327 BSC 2004. *In-Drift Natural Convection and Condensation.* MDL-EBS-MD-000001 REV 00. Las Vegas, Nevada: Bechtel SAIC Company. ACC: DOC.20041025.0006; DOC.20050330.0001; DOC.20051122.0005.

170031 BSC 2004. *Mineralogic Model (MM3.0) Report.* MDL-NBS-GS-000003 REV 01. Las Vegas, Nevada: Bechtel SAIC Company. ACC: DOC.20040908.0006.

169218 BSC 2004. *Natural Analogue Synthesis Report.* TDR-NBS-GS-000027 REV 01. Las Vegas, Nevada: Bechtel SAIC Company. ACC: DOC.20040524.0008.

170041 BSC 2004. *Particle Tracking Model and Abstraction of Transport Processes.* MDL-NBS-HS-000020 REV 01. Las Vegas, Nevada: Bechtel SAIC Company. ACC: DOC.20041020.0016.

172452 BSC 2004. *Performance Confirmation Plan.* TDR-PCS-SE-000001 REV 05. Las Vegas, Nevada: Bechtel SAIC Company. ACC: DOC.20041122.0002.

170037 BSC 2004. *Saturated Zone Site-Scale Flow Model.* MDL-NBS-HS-000011 REV 02. Las Vegas, Nevada: Bechtel SAIC Company. ACC: DOC.20041122.0001.

171764 BSC 2004. *Seepage Calibration Model and Seepage Testing Data.* MDL-NBS-HS-000004 REV 03. Las Vegas, Nevada: Bechtel SAIC Company. ACC: DOC.20040922.0003; DOC.20051121.0012.

167652 BSC 2004. *Seepage Model for PA Including Drift Collapse.* MDL-NBS-HS-000002 REV 03. Las Vegas, Nevada: Bechtel SAIC Company. ACC: DOC.20040922.0008; DOC.20051205.0001.

170007 BSC 2004. *Simulation of Net Infiltration for Present-Day and Potential Future Climates.* MDL-NBS-HS-000023 REV 00. Las Vegas, Nevada: Bechtel SAIC Company. ACC: DOC.20041109.0004.

170033 BSC 2004. *Thermal Conductivity of Non-Repository Lithostratigraphic Layers.* MDL-NBS-GS-000006 REV 01. Las Vegas, Nevada: Bechtel SAIC Company. ACC: DOC.20041022.0004.

169854 BSC 2004. *Thermal Conductivity of the Potential Repository Horizon.* MDL-NBS-GS-000005 REV 01. Las Vegas, Nevada: Bechtel SAIC Company. ACC: DOC.20040928.0006.

169861 BSC 2004. *UZ Flow Models and Submodels.* MDL-NBS-HS-000006 REV 02. Las Vegas, Nevada: Bechtel SAIC Company. ACC: DOC.20041101.0004; DOC.20050629.0003.

169862 BSC 2004. *Ventilation Model and Analysis Report.* ANL-EBS-MD-000030 REV 04. Las Vegas, Nevada: Bechtel SAIC Company. ACC: DOC.20041025.0002.

169734 BSC 2004. *Yucca Mountain Site Description.* TDR-CRW-GS-000001 REV 02 ICN 01. Two volumes. Las Vegas, Nevada: Bechtel SAIC Company. ACC: DOC.20040504.0008.

172232 BSC 2005. *Drift-Scale Coupled Processes (DST and TH Seepage) Models.* MDL-NBS-HS-000015 REV 02. Las Vegas, Nevada: Bechtel SAIC Company. ACC: DOC.20050114.0004; DOC.20051115.0002.

174191 BSC 2005. *Features, Events, and Processes in UZ Flow and Transport.* ANL-NBS-MD-000001 REV 04. Las Vegas, Nevada: Bechtel SAIC Company. ACC: DOC.20050809.0002.

174101 BSC 2005. *Mountain-Scale Coupled Processes (TH/THC/THM) Models.* MDL-NBS-HS-000007 REV 03. Las Vegas, Nevada: Bechtel SAIC Company. ACC: DOC.20050825.0007.

174116 BSC 2005. *Parameter Sensitivity Analysis for Unsaturated Zone Flow.* ANL-NBS-HS-000049 REV 00. Las Vegas, Nevada: Bechtel SAIC Company. ACC: DOC.20050808.0005; DOC.20060329.0020.

177465 BSC 2006. *Technical Work Plan for: Unsaturated Zone Flow, Drift Seepage and Unsaturated Zone Transport Modeling.* TWP-MGR-HS-000004 REV 04. Las Vegas, Nevada: Bechtel SAIC Company. ACC: DOC.20060824.0001.

180897 Capo, R.C. and Chadwick, O.A. 1999. "Sources of Strontium and Calcium in Desert Soil and Calcrete." *Earth and Planetary Science Letters, 170,* 61-72. New York, New York: Elsevier. TIC: 259393.

181455 Capo, R.C.; Stewart, B.W.; and Chadwick, O.A. 1998. "Strontium Isotopes as Tracers of Ecosystem Processes: Theory and Methods." *Geoderma, 82,* 197-225. New York, New York: Elsevier. TIC: 259540.

109051 Carey, J.W.; Chipera, S.J.; Vaniman, D.T.; and Bish, D.L. 1998. *Three-Dimensional Mineralogic Model of Yucca Mountain, Nevada: Rev 2.0.* Deliverable SP32BSM4. Los Alamos, New Mexico: Los Alamos National Laboratory, Earth and Environmental Sciences Division. ACC: MOL.20000110.0159.

162118 Carlos, B.A.; Chipera, S.J.; and Bish, D.L. 1995. "Calcite and Zeolite Fracture Coatings in Topopah Spring Tuff Along Drill Hole Wash, Yucca Mountain, Nevada." *High Level Radioactive Waste Management, Proceedings of the Sixth Annual International Conference, Las Vegas, Nevada, April 30-May 5, 1995.* Pages 100-102. La Grange Park, Illinois: American Nuclear Society. TIC: 215781.

104368 Carrera, J. and Neuman, S.P. 1986. "Estimation of Aquifer Parameters Under Transient and Steady State Conditions: 1. Maximum Likelihood Method Incorporating Prior Information." *Water Resources Research, 22,* (2), 199-210. Washington, D.C.: American Geophysical Union. TIC: 245915.

100719 Codell, R.B. and Murphy, W.M. 1992. "Geochemical Model for 14C Transport in Unsaturated Rock." High Level Radioactive Waste Management, Proceedings of the Third International Conference, Las Vegas, Nevada, April 12-16, 1992. 2, 1959-1965. La Grange Park, Illinois: American Nuclear Society. TIC: 204231.

177344 Constantz, J.; Tyler, S.W.; and Kwicklis, E. 2003. "Temperature-Profile Methods for Estimating Percolation Rates in Arid Environments." *Vadose Zone Journal, 2,* (1), 12-24. Madison, Wisconsin: Soil Science Society of America. TIC: 258470.

100335 CRWMS M&O 1997. *Unsaturated Zone Flow Model Expert Elicitation Project.* Las Vegas, Nevada: CRWMS M&O. ACC: MOL.19971009.0582.

135997 Doughty, C. 1999. "Investigation of Conceptual and Numerical Approaches for Evaluating Moisture, Gas, Chemical, and Heat Transport in Fractured Unsaturated Rock." *Journal of Contaminant Hydrology, 38,* (1-3), 69-106. New York, New York: Elsevier. TIC: 244160.

116801 Driscoll, F.G. 1986. *Groundwater and Wells.* 2nd Edition. St. Paul, Minnesota: Johnson Filtration Systems. TIC: 217555.

180650 Dublyansky, Y.V. and Smirnov, S.Z. 2005. "Commentary: Assessment of Past Infiltration Fluxes through Yucca Mountain on the Basis of the Secondary Mineral Record—Is it a Viable Methodology?" *Journal of Contaminant Hydrology, 77,* 209-217. New York, New York: Elsevier. TIC: 259337.

100144 Fabryka-Martin, J.T.; Flint, A.L.; Sweetkind, D.S.; Wolfsberg, A.V.; Levy, S.S.; Roemer, G.J.C.; Roach, J.L.; Wolfsberg, L.E.; and Duff, M.C. 1997. *Evaluation of Flow and Transport Models of Yucca Mountain, Based on Chlorine-36 Studies for FY97.* LA-CST-TIP-97-010. Los Alamos, New Mexico: Los Alamos National Laboratory. ACC: MOL.19980204.0916.

146355 Fabryka-Martin, J.T.; Wolfsberg, A.V.; Roach, J.L.; Winters, S.T.; and Wolfsberg, L.E. 1998. "Using Chloride to Trace Water Movement in the Unsaturated Zone at Yucca Mountain." *High-Level Radioactive Waste Management, Proceedings of the Eighth International Conference, Las Vegas, Nevada, May 11-14, 1998.* Pages 264-268. La Grange Park, Illinois: American Nuclear Society. TIC: 237082.

105559 Faure, G. 1986. *Principles of Isotope Geology.* 2nd Edition. New York, New York: John Wiley & Sons. TIC: 237212.

164506 Flint, A.L.; Flint, L.E.; Kwicklis, E.M.; Bodvarsson, G.S.; and Fabryka-Martin, J.M. 2001. "Hydrology of Yucca Mountain, Nevada." *Reviews of Geophysics, 39,* (4), 447-470. Washington, D.C.: American Geophysical Union. TIC: 254964.

100033 Flint, L.E. 1998. *Characterization of Hydrogeologic Units Using Matrix Properties, Yucca Mountain, Nevada.* Water-Resources Investigations Report 97-4243. Denver, Colorado: U.S. Geological Survey. ACC: MOL.19980429.0512.

163967 Flint, L.E.; Flint, A.L.; and Selker, J.S. 2003. "Influence of Transitional Volcanic Strata on Lateral Diversion at Yucca Mountain, Nevada." *Water Resources Research, 39,* (4), 4-1 to 4-17. Washington, D.C.: American Geophysical Union. TIC: 254439.

179084 Franks, S.W. and Beven, K.J. 1997. "Estimation of Evapotranspiration at the Landscape Scale: A Fuzzy Disaggregation Approach." *Water Resources Research, 33,* (12), 2929-2938. Washington, D.C.: American Geophysical Union. TIC: 252296.

100575 Fridrich, C.J.; Dudley, W.W., Jr.; and Stuckless, J.S. 1994. "Hydrogeologic Analysis of the Saturated-Zone Ground-Water System, Under Yucca Mountain, Nevada." *Journal of Hydrology, 154,* 133-168. Amsterdam, The Netherlands: Elsevier. TIC: 224606.

162573 Goode, D.J. 1996. "Direct Simulation of Groundwater Age." *Water Resources Research, 32,* (2), 289-296. Washington, D.C.: American Geophysical Union. TIC: 252291.

141512 Grathwohl, P. 2000. *Diffusion in Natural Porous Media: Contaminant Transport, Sorption/Desorption and Dissolution Kinetics.* Boston, Massachusetts: Kluwer Academic Publishers. TIC: 247983.

180551 Guerin, M. 2001. "Tritium and ^{36}Cl as Constraints on Fast Fracture Flow and Percolation Flux in the Unsaturated Zone at Yucca Mountain." *Journal of Contaminant Hydrology, 51,* 257-288. New York, New York: Elsevier. TIC: 259334.

162560 Johnson, T.M. and DePaolo, D.J. 1994. "Interpretation of Isotopic Data in Groundwater-Rock Systems: Model Development and Application to Sr Isotope Data from Yucca Mountain." *Water Resources Research, 30,* (5), 1571-1587. Washington, D.C.: American Geophysical Union. TIC: 252320.

100051 Langmuir, D. 1997. *Aqueous Environmental Geochemistry.* Upper Saddle River, New Jersey: Prentice Hall. TIC: 237107.

182304 Lerman, A. 1979. *Geochemical Processes, Water and Sediment Environments.* New York, New York: John Wiley & Sons. TIC: 259641.

160832 Lide, D.R., ed. 2002. *CRC Handbook of Chemistry and Physics.* 83rd Edition. Boca Raton, Florida: CRC Press. TIC: 253582.

160230 Liu, H.H.; Bodvarsson, G.S.; and Finsterle, S. 2002. "A Note on Unsaturated Flow in Two-Dimensional Fracture Networks." *Water Resources Research, 38,* (9), 15-1 to 15-9. Washington, D.C.: American Geophysical Union. TIC: 253307.

105729 Liu, H.H.; Doughty, C.; and Bodvarsson, G.S. 1998. "An Active Fracture Model for Unsaturated Flow and Transport in Fractured Rocks." *Water Resources Research, 34,* (10), 2633-2646. Washington, D.C.: American Geophysical Union. TIC: 243012.

162478 Liu, J.; Sonnenthal, E.L.; and Bodvarsson, G.S. 2003. "Calibration of Yucca Mountain Unsaturated Zone Flow and Transport Model Using Porewater Chloride Data." *Journal of Contaminant Hydrology, 62-63,* 213-235. New York, New York: Elsevier. TIC: 254205.

168915 Lu, G.; Sonnenthal, E.L.; and Bodvarsson, G.S. 2003. "Implications of Halide Leaching on ^{36}Cl Studies at Yucca Mountain, Nevada." *Water Resources Research, 39,* (12), 3-1 through 3-15. Washington, D.C.: American Geophysical Union. TIC: 255498.

179044 Makowski, D.; Wallach, D.; and Tremblay, M. 2002. "Using a Bayesian Approach to Parameter Estimation; Comparison of the GLUE and MCMC Methods." *Agronomie, 22,* 191-203. Paris, France: INRA, EDP Sciences. TIC: 258914.

182155 Manepally, C.; Bradbury, K.; Colton, S.; Dinwiddle, C.; Green, R.; McGinnis, R.; Sims, D.; Smart, K.; and Walter, G. 2007. *The Nature of Flow in the Faulted and Fractured Paintbrush Nonwelded Hydrogeologic Unit.* San Antonio, Texas: Center for Nuclear Waste Regulatory Analyses. ACC: LLR.20070725.0014.

107415 Marshall, B.D.; Paces, J.B.; Neymark, L.A.; Whelan, J.F.; and Peterman, Z.E. 1998. "Secondary Minerals Record Past Percolation Flux at Yucca Mountain, Nevada." *High-Level Radioactive Waste Management, Proceedings of the Eighth International Conference, Las Vegas, Nevada, May 11-14, 1998.* Pages 127-129. La Grange Park, Illinois: American Nuclear Society. TIC: 237082.

106335 Marshall, B.D.; Peterman, Z.E.; Futa, K.; and Stuckless, J.S. 1991. "Strontium Isotopes in Carbonate Deposits at Crater Flat, Nevada." *High Level Radioactive Waste Management, Proceedings of the Second Annual International Conference, Las Vegas, Nevada, April 28-May 3, 1991. 2,* 1423-1428. La Grange Park, Illinois: American Nuclear Society. TIC: 204272.

100598 Maxey, G.B. and Eakin, T.E. 1950. *Ground Water in White River Valley, White Pine, Nye, and Lincoln Counties, Nevada.* Water Resources Bulletin No. 8. Carson City, Nevada: State of Nevada, Office of the State Engineer. TIC: 216819.

158813 Meijer, A. 2002. "Conceptual Model of the Controls on Natural Water Chemistry at Yucca Mountain, Nevada." *Applied Geochemistry, 17,* (6), 793-805. New York, New York: Elsevier. TIC: 252808.

100161 Montazer, P. and Wilson, W.E. 1984. *Conceptual Hydrologic Model of Flow in the Unsaturated Zone, Yucca Mountain, Nevada.* Water-Resources Investigations Report 84-4345. Lakewood, Colorado: U.S. Geological Survey. ACC: NNA.19890327.0051.

161902 Moridis, G.J.; Hu, Q.; Wu, Y-S.; and Bodvarsson, G.S. 2003. "Preliminary 3-D Site-Scale Studies of Radioactive Colloid Transport in the Unsaturated Zone at Yucca Mountain, Nevada." *Journal of Contaminant Hydrology, 60,* (3-4), 251-286. New York, New York: Elsevier. TIC: 253921.

179820 Nash, J.E. and Sutcliffe, I.V. 1970. "River Flow Forecasting through Conceptual Models Part I - A Discussion of Principles." *Journal of Hydrology, 10,* 282-290. Amsterdam, The Netherlands: North-Holland Publishing. TIC: 259256.

139151 National Research Council. 1996. *Rock Fractures and Fluid Flow, Contemporary Understanding and Applications.* Washington, D.C.: National Academy Press. TIC: 235913.

162140 Neretnieks, I. 2002. "A Stochastic Multi-Channel Model for Solute Transport—Analysis of Tracer Tests in Fractured Rock." *Journal of Contaminant Hydrology, 55,* (3-4), 175-211. New York, New York: Elsevier. TIC: 253977.

156889 Neymark, L.A.; Amelin, Y.V.; Paces, J.B.; Peterman, Z.E.; and Whelan, J.F. 2001. "Age Constraints on Fluid Inclusions in Calcite at Yucca Mountain." *"Back to the Future - Managing the Back End of the Nuclear Fuel Cycle to Create a More Secure Energy Future," Proceedings of the 9th International High-Level Radioactive Waste Management Conference (IHLRWM), Las Vegas, Nevada, April 29, May 3, 2001.* La Grange Park, Illinois: American Nuclear Society. TIC: 247873.

180924 Neymark, L.A.; Paces, J.B.; Marshall, B.D.; Peterman, Z.E.; and Whelan, J.F. 2005. "Geochemical and C, O, Sr, and U-series Isotopic Evidence for the Meteoric Origin of Calcrete at Solitario Wash, Crater Flat, Nevada, USA." *Environmental Geology, 48,* 450-465. New York, New York: Springer-Verlag. TIC: 258003.

178863 Nichols, W.D. 2000. *Regional Ground-Water Evapotranspiration and Ground-Water Budgets, Great Basin, Nevada.* U.S. Geological Survey Professional Paper 1628. Reston, Virginia: U.S. Geological Survey. ACC: LLR.20070213.0076.

163274 NRC (U.S. Nuclear Regulatory Commission) 2003. *Yucca Mountain Review Plan, Final Report.* NUREG-1804, Rev. 2. Washington, D.C.: U.S. Nuclear Regulatory Commission, Office of Nuclear Material Safety and Safeguards. TIC: 254568.

107408 Paces, J.B.; Neymark, L.A.; Marshall, B.D.; Whelan, J.F.; and Peterman, Z.E. 1998. "Inferences for Yucca Mountain Unsaturated-Zone Hydrology from Secondary Minerals." *High-Level Radioactive Waste Management, Proceedings of the Eighth International Conference, Las Vegas, Nevada, May 11-14, 1998.* Pages 36-39. La Grange Park, Illinois: American Nuclear Society. TIC: 237082.

156507 Paces, J.B.; Neymark, L.A.; Marshall, B.D.; Whelan, J.F.; and Peterman, Z.E. 2001. *Ages and Origins of Calcite and Opal in the Exploratory Studies Facility Tunnel, Yucca Mountain, Nevada.* Water-Resources Investigations Report 01-4049. Denver, Colorado: U.S. Geological Survey. TIC: 251284.

164181 Pan, L.; Warrick, A.W.; and Wierenga, P.J. 1997. "Downward Water Flow Through Sloping Layers in the Vadose Zone: Time-Dependence and Effect of Slope Length." *Journal of Hydrology, 199,* (1-2), 36-52. New York, New York: Elsevier. TIC: 254555.

162576 Peterman, Z.E. and Cloke, P.L. 2002. "Geochemistry of Rock Units at the Potential Repository Level, Yucca Mountain, Nevada (includes Erratum)." *Applied Geochemistry, 17,* (6, 7), 683-698, 955-958. New York, New York: Pergamon. TIC: 252516; 252517; 254046.

101149 Peterman, Z.E. and Stuckless, J.S. 1993. "Isotopic Evidence of Complex Ground-Water Flow at Yucca Mountain, Nevada, USA." *High Level Radioactive Waste Management, Proceedings of the Fourth Annual International Conference, Las Vegas, Nevada, April 26-30, 1993. 2,* 1559-1566. La Grange Park, Illinois: American Nuclear Society. TIC: 208542.

147110 Peterman, Z.E.; Stuckless, J.S.; Marshall, B.D.; Mahan, S.A.; and Futa, K. 1992. "Strontium Isotope Geochemistry of Calcite Fracture Fillings in Deep Core, Yucca Mountain, Nevada -- A Progress Report." *High Level Radioactive Waste Management, Proceedings of the Third International Conference, Las Vegas, Nevada, April 12-16, 1992. 2,* 1582-1586. La Grange Park, Illinois: American Nuclear Society. TIC: 204231.

105743 Philip, J.R.; Knight, J.H.; and Waechter, R.T. 1989. "Unsaturated Seepage and Subterranean Holes: Conspectus, and Exclusion Problem for Circular Cylindrical Cavities." *Water Resources Research, 25,* (1), 16-28. Washington, D.C.: American Geophysical Union. TIC: 239117.

101707 Pruess, K. and Narasimhan, T.N. 1985. "A Practical Method for Modeling Fluid and Heat Flow in Fractured Porous Media." *Society of Petroleum Engineers Journal, 25,* (1), 14-26. Dallas, Texas: Society of Petroleum Engineers. TIC: 221917.

160778 Pruess, K.; Oldenburg, C.; and Moridis, G. 1999. *TOUGH2 User's Guide, Version 2.0.* LBNL-43134. Berkeley, California: Lawrence Berkeley National Laboratory. TIC: 253038.

180504 Quan, H. and Zhang, J. 2003. "Estimate of Standard Deviation for a Log-Transformed Variable Using Arithmetic Means and Standard Deviations." *Statistics in Medicine, 22,* 2723-2736. New York, New York: John Wiley & Sons. TIC: 259048.

180898 Reheis, M.C. 2006. "A 16-year Record of Eolian Dust in Southern Nevada and California, USA: Controls on Dust Generation and Accumulation." *Journal of Arid Environments, 67,* 487-520. New York, New York: Elsevier. TIC: 259394.

104252 Richards, L.A. 1931. "Capillary Conduction of Liquids Through Porous Mediums." *Physics, 1,* 318-333. New York, New York: American Physical Society. TIC: 225383.

179821 Romanowicz, R.J. and Beven, K.J. 2006. "Comments on Generalised Likelihood Uncertainty Estimation." *Reliability Engineering and System Safety, 91,* 1315-1321. New York, New York: Elsevier. TIC: 259255.

102097 Rousseau, J.P.; Kwicklis, E.M.; and Gillies, D.C., eds. 1999. *Hydrogeology of the Unsaturated Zone, North Ramp Area of the Exploratory Studies Facility, Yucca Mountain, Nevada.* Water-Resources Investigations Report 98-4050. Denver, Colorado: U.S. Geological Survey. ACC: MOL.19990419.0335.

100178 Rousseau, J.P.; Loskot, C.L.; Thamir, F.; and Lu, N. 1997. Results of Borehole Monitoring in the Unsaturated Zone Within the Main Drift Area of the Exploratory Studies Facility, Yucca Mountain, Nevada. Milestone SPH22M3. Denver, Colorado: U.S. Geological Survey. ACC: MOL.19970626.0351.

164470 Salve, R.; Oldenburg, C.M.; and Wang, J.S.Y. 2003. "Fault-Matrix Interactions in Nonwelded Tuff of the Paintbrush Group at Yucca Mountain." *Journal of Contaminant Hydrology, 62-63,* 269-286. New York, New York: Elsevier. TIC: 254205.

100644 Sass, J.H.; Lachenbruch, A.H.; Dudley, W.W., Jr.; Priest, S.S.; and Munroe, R.J. 1988. *Temperature, Thermal Conductivity, and Heat Flow Near Yucca Mountain, Nevada: Some Tectonic and Hydrologic Implications.* Open-File Report 87-649. Denver, Colorado: U.S. Geological Survey. TIC: 203195.

162132 Shapiro, A.M. 2001. "Effective Matrix Diffusion in Kilometer-Scale Transport in Fractured Crystalline Rock." *Water Resources Research, 37,* (3), 507-522. Washington, D.C.: American Geophysical Union. TIC: 253979.

161591 Sharpe, S. 2003. *Future Climate Analysis—10,000 Years to 1,000,000 Years After Present.* MOD-01-001 REV 01. Reno, Nevada: Desert Research Institute. ACC: MOL.20030407.0055.

181244 SNL (Sandia National Laboratories) 2007. *Abstraction of Drift Seepage.* MDL-NBS-HS-000019 REV 01 ADD 01. Las Vegas, Nevada: Sandia National Laboratories. ACC: DOC.20041103.0003; DOC.20070807.0001.

179545 SNL 2007. *Calibrated Unsaturated Zone Properties.* ANL-NBS-HS-000058 REV 00. Las Vegas, Nevada: Sandia National Laboratories. ACC: DOC.20070530.0013.

177404 SNL 2007. *Drift-Scale THC Seepage Model.* MDL-NBS-HS-000001 REV 05. Las Vegas, Nevada: Sandia National Laboratories.

177407 SNL 2007. *EBS Radionuclide Transport Abstraction.* ANL-WIS-PA-000001 REV 03. Las Vegas, Nevada: Sandia National Laboratories.

181383 SNL 2007. *Multiscale Thermohydrologic Model.* ANL-EBS-MD-000049 REV 03 AD01. Las Vegas, Nevada: Sandia National Laboratories. ACC: DOC.20050711.0001.

181006 SNL 2007. *Particle Tracking Model and Abstraction of Transport Processes.* MDL-NBS-HS-000020 REV 02 ADD 01. Las Vegas, Nevada: Sandia National Laboratories. ACC: DOC.20050808.0006.

177464 SNL 2007. *Postclosure Nuclear Safety Design Bases.* ANL-WIS-MD-000024 REV 01. Las Vegas, Nevada: Sandia National Laboratories.

177396 SNL 2007. *Radionuclide Transport Models Under Ambient Conditions.* MDL-NBS-HS-000008 REV 02 ADD 01. Las Vegas, Nevada: Sandia National Laboratories. ACC: DOC.20041101.0002; DOC.20050823.0003; DOC.20070718.0003.

181650 SNL 2007. *Saturated Zone Flow and Transport Model Abstraction.* MDL-NBS-HS-000021 REV 03 AD 01. Las Vegas, Nevada: Sandia National Laboratories.

177391 SNL 2007. *Saturated Zone Site-Scale Flow Model.* MDL-NBS-HS-000011 REV 03. Las Vegas, Nevada: Sandia National Laboratories. ACC: DOC.20070626.0004.

174294 SNL 2007. *Simulation of Net Infiltration for Present-Day and Potential Future Climates.* MDL-NBS-HS-000023 REV 01. Las Vegas, Nevada: Sandia National Laboratories. ACC: DOC.20070530.0014.

177392 SNL 2007. *Site-Scale Saturated Zone Transport.* MDL-NBS-HS-000010 REV 03. Las Vegas, Nevada: Sandia National Laboratories. ACC: DOC.20070822.0003.

177413 SNL 2007. *THC Sensitivity Study of Heterogeneous Permeability and Capillarity Effects.* ANL-NBS-HS-000047 REV 01. Las Vegas, Nevada: Sandia National Laboratories. ACC: DOC.20070807.0006.

179466 SNL 2007. *Total System Performance Assessment Data Input Package for Requirements Analysis for Subsurface Facilities.* TDR-TDIP-PA-000001 REV 00. Las Vegas, Nevada: Sandia National Laboratories.

178871 SNL 2007. *Total System Performance Assessment Model /Analysis for the License Application.* MDL-WIS-PA-000005 REV 00. Las Vegas, Nevada: Sandia National Laboratories.

117914 Sonnenthal, E. and Ortoleva, P.J. 1994. "Numerical Simulations of Overpressured Compartments in Sedimentary Basins." *Basin Compartments and Seals.* Ortoleva, P.J., ed. AAPG Memoir 61. 403-416. Tulsa, Oklahoma: American Association of Petroleum Geologists. TIC: 235940.

180639 Sonnenthal, E.; Xu, T.; and Bodvarsson, G. 2005. "Reply to "Commentary: Assessment of Past Infiltration Fluxes through Yucca Mountain on the Basis of the Secondary Mineral Record—Is it a Viable Methodology?", by Y.V. Dublyansky and S.Z. Smirnov." *Journal of Contaminant Hydrology, 77,* 225-231. New York, New York: Elsevier. TIC: 259335.

117127 Sonnenthal, E.L. and Bodvarsson, G.S. 1999. "Constraints on the Hydrology of the Unsaturated Zone at Yucca Mountain, NV from Three-Dimensional Models of Chloride and Strontium Geochemistry." *Journal of Contaminant Hydrology, 38,* (1-3), 107-156. New York, New York: Elsevier. TIC: 244160.

182157 Stothoff, S. and Musgrove, M. 2006. *Literature Review and Analysis: Climate and Infiltration.* CNWRA 2007-002. San Antonio, Texas: Center for Nuclear Waste Regulatory Analyses. ACC: LLR.20070725.0015.

106947 Stuckless, J.S.; Peterman, Z.E.; and Muhs, D.R. 1991. "U and Sr in Ground Water and Calcite, Yucca Mountain, Nevada: Evidence Against Upwelling Water." *Science, 254,* 551-554. Washington, D.C.: American Association for the Advancement of Science. TIC: 224423.

139195 Tokunaga, T.K. and Wan, J. 1997. "Water Film Flow Along Fracture Surfaces of Porous Rock." *Water Resources Research, 33,* (6), 1287-1295. Washington, D.C.: American Geophysical Union. TIC: 242739.

101014 Triay, I.R.; Meijer, A.; Conca, J.L.; Kung, K.S.; Rundberg, R.S.; and Strietelmeier, B.A. 1996. *Summary and Synthesis Report on Radionuclide Retardation for the Yucca Mountain Site Characterization Project.* Milestone 3784. Los Alamos, New Mexico: Los Alamos National Laboratory. ACC: MOL.19961231.0099.

108774 Tyler, S.W.; Chapman, J.B.; Conrad, S.H.; Hammermeister, D.P.; Blout, D.O.; Miller, J.J.; Sully, M.J.; and Ginanni, J.M. 1996. "Soil-Water Flux in the Southern Great Basin, United States: Temporal and Spatial Variations Over the Last 120,000 Years." *Water Resources Research, 32,* (6), 1481-1499. Washington, D.C.: American Geophysical Union. TIC: 235938.

100610 van Genuchten, M.T. 1980. "A Closed-Form Equation for Predicting the Hydraulic Conductivity of Unsaturated Soils." *Soil Science Society of America Journal, 44,* (5), 892-898. Madison, Wisconsin: Soil Science Society of America. TIC: 217327.

100089 Vaniman, D.T. and Chipera, S.J. 1996. "Paleotransport of Lanthanides and Strontium Recorded in Calcite Compositions from Tuffs at Yucca Mountain, Nevada, USA." *Geochimica et Cosmochimica Acta, 60,* (22), 4417-4433. New York, New York: Pergamon Press. TIC: 231351.

157427 Vaniman, D.T.; Chipera, S.J.; Bish, D.L.; Carey, J.W.; and Levy, S.S. 2001. "Quantification of Unsaturated-Zone Alteration and Cation Exchange in Zeolitized Tuffs at Yucca Mountain, Nevada, USA." *Geochimica et Cosmochimica Acta, 65,* (20), 3409-3433. New York, New York: Elsevier. TIC: 251574.

162122 Walter, A.L.; Frind, E.O.; Blowes, D.W.; Ptacek, C.J.; and Molson, J.W. 1994. "Modeling of Multicomponent Reactive Transport in Groundwater. 1. Model Development and Evaluation." *Water Resources Research, 30,* (11), 3137-3148. Washington, D.C.: American Geophysical Union. TIC: 252320.

108835 Wang, J.S.Y. and Narasimhan, T.N. 1985. "Hydrologic Mechanisms Governing Fluid Flow in a Partially Saturated, Fractured, Porous Medium." *Water Resources Research, 21,* (12), 1861-1874. Washington, D.C.: American Geophysical Union. TIC: 225290.

106793 Wang, J.S.Y. and Narasimhan, T.N. 1993. "Unsaturated Flow in Fractured Porous Media." Chapter 7 of *Flow and Contaminant Transport in Fractured Rock.* Bear, J.; Tsang, C-F.; and de Marsily, G., eds. San Diego, California: Academic Press. TIC: 235461.

153972 Wu, Y-S. and Pruess, K. 2000. "Numerical Simulation of Non-Isothermal Multiphase Tracer Transport in Heterogeneous Fractured Porous Media." *Advances in Water Resources, 23,* (7), 699-723. New York, New York: Elsevier. TIC: 249626.

173953 Wu, Y-S.; Lu, G.; Zhang, K.; and Bodvarsson, G.S. 2004. "A Mountain-Scale Model for Characterizing Unsaturated Flow and Transport in Fractured Tuffs of Yucca Mountain." *Vadose Zone Journal, 3,* 796-805. Madison, Wisconsin: Soil Science Society of America. TIC: 257371.

180274 Wu, Y-S.; Mukhopadhyay, S.; Zhang, K.; and Bodvarsson, G.S. 2006. "A Mountain-Scale Thermal–Hydrologic Model for Simulating Fluid Flow and Heat Transfer in Unsaturated Fractured Rock." *Journal of Contaminant Hydrology, 86,* 128-159. New York, New York: Elsevier. TIC: 259285.

160195 Wu, Y-S.; Pan, L.; Zhang, W.; and Bodvarsson, G.S. 2002. "Characterization of Flow and Transport Processes within the Unsaturated Zone of Yucca Mountain, Nevada, Under Current and Future Climates." *Journal of Contaminant Hydrology, 54,* (3-4), 215-247. New York, New York: Elsevier. TIC: 253316.

180289 Wu, Y-S.; Zhang, K.; and Liu, H-H. 2006. "Estimating Large-Scale Fracture Permeability of Unsaturated Rock Using Barometric Pressure Data." *Vadose Zone Journal, 5,* 1129-1142. Madison, Wisconsin: Soil Science Society of America. TIC: 259277.

154918 Wu, Y-S.; Zhang, W.; Pan, L.; Hinds, J.; and Bodvarsson, G.S. 2000. *Capillary Barriers in Unsaturated Fractured Rocks of Yucca Mountain, Nevada.* LBNL-46876. Berkeley, California: Lawrence Berkeley National Laboratory. TIC: 249912.

161058 Wu, Y-S.; Zhang, W.; Pan, L.; Hinds, J.; and Bodvarsson, G.S. 2002. "Modeling Capillary Barriers in Unsaturated Fractured Rock." *Water Resources Research, 38,* (11), 35-1 through 35-12. Washington, D.C.: American Geophysical Union. TIC: 253854.

117161 Wu, Y.S.; Haukwa, C.; and Bodvarsson, G.S. 1999. "A Site-Scale Model for Fluid and Heat Flow in the Unsaturated Zone of Yucca Mountain, Nevada." *Journal of Contaminant Hydrology, 38,* (1-3), 185-215. New York, New York: Elsevier. TIC: 244160.

117167 Wu, Y.S.; Ritcey, A.C.; and Bodvarsson, G.S. 1999. "A Modeling Study of Perched Water Phenomena in the Unsaturated Zone at Yucca Mountain." *Journal of Contaminant Hydrology, 38,* (1-3), 157-184. New York, New York: Elsevier. TIC: 244160.

117170 Xu, T. and Pruess, K. 1998. *Coupled Modeling of Non-Isothermal Multi-Phase Flow, Solute Transport and Reactive Chemistry in Porous and Fractured Media: 1. Model Development and Validation.* LBNL-42050. Berkeley, California: Lawrence Berkeley National Laboratory. TIC: 243735.

156280 Xu, T. and Pruess, K. 2001. "Modeling Multiphase Non-Isothermal Fluid Flow and Reactive Geochemical Transport in Variably Saturated Fractured Rocks: 1. Methodology." *American Journal of Science, 301,* 16-33. New Haven, Connecticut: Yale University, Kline Geology Laboratory. TIC: 251482.

162123 Xu, T.; Samper, J.; Ayora, C.; Manzano, M.; and Custodio, E. 1999. "Modeling of Non-isothermal Multi-component Reactive Transport in Field Scale Porous Media Flow Systems." *Journal of Hydrology, 214,* (1-4), 144-164. New York, New York: Elsevier. TIC: 254290.

162124 Xu, T.; Sonnenthal, E.; and Bodvarsson, G. 2003. "A Reaction-Transport Model for Calcite Precipitation and Evaluation of Infiltration Fluxes in Unsaturated Fractured Rock." *Journal of Contaminant Hydrology, 64,* (1-2), 113-127. New York, New York: Elsevier. TIC: 254008.

160839 Yang, I.C. 2002. "Percolation Flux and Transport Velocity in the Unsaturated Zone, Yucca Mountain, Nevada." *Applied Geochemistry, 17,* (6), 807-817. New York, New York: Elsevier. TIC: 253605.

180272 Ye, M.; Pan, F.; Wu, Y-S.; Hu, B.X.; Shirley, C.; and Yu, Z. 2007. "Assessment of Radionuclide Transport Uncertainty in the Unsaturated Zone of Yucca Mountain." *Advances in Water Resources, 30,* 118-134. New York, New York: Elsevier. TIC: 259284.

162125 Yeh, G-T. and Tripathi, V.S. 1991. "A Model for Simulating Transport of Reactive Multispecies Components: Model Development and Demonstration." *Water Resources Research, 27,* (12), 3075-3094. Washington, D.C.: American Geophysical Union. TIC: 236255.

179088 Zak, S.K.; Beven, K.; and Reynolds, B. 1997. "Uncertainty in the Estimation of Critical Loads: A Practical Methodology." *Water, Air, and Soil Pollution, 98,* 297-316. Boston, Massachusetts: Kluwer Academic Publishers. TIC: 259047.

180287 Zhang, K.; Wu, Y-S.; and Houseworth, J.E. 2006. "Sensitivity Analysis of Hydrological Parameters in Modeling Flow And Transport in the Unsaturated Zone of Yucca Mountain, Nevada, USA." *Hydrogeology Journal, 14,* 1599-1619. New York, New York: Springer-Verlag. TIC: 259279.

180273 Zhang, K.; Wu, Y-S.; and Pan, L. 2006. "Temporal Damping Effect of the Yucca Mountain Fractured Unsaturated Rock on Transient Infiltration Pulses." *Journal of Hydrology, 327,* 235-248. New York, New York: Elsevier. TIC: 259283.

162133 Zhou, Q.; Liu, H-H.; Bodvarsson, G.S.; and Oldenburg, C.M. 2003. "Flow and Transport in Unsaturated Fractured Rock: Effects of Multiscale Heterogeneity of Hydrogeologic Properties." *Journal of Contaminant Hydrology, 60,* (1-2), 1-30. New York, New York: Elsevier. TIC: 253978.

9.2 CODES, STANDARDS, REGULATIONS, AND PROCEDURES

173273 10 CFR 63. 2005. Energy: Disposal of High-Level Radioactive Wastes in a Geologic Repository at Yucca Mountain, Nevada. ACC: MOL.20050405.0118.

178394 70 FR 53313. Implementation of a Dose Standard After 10,000 Years. Internet Accessible.

177092 DOE (U.S. Department of Energy) 2006. *Quality Assurance Requirements and Description.* DOE/RW-0333P, Rev. 18. Washington, D.C.: U.S. Department of Energy, Office of Civilian Radioactive Waste Management. ACC: DOC.20060602.0001.

LP-SI.11Q-BSC, Rev. 0, ICN 2. *Software Management.* Washington, D.C.: U.S. Department of Energy, Office of Civilian Radioactive Waste Management. ACC: DOC.20060123.0007.

SCI-PRO-001, *Qualification of Unqualified Data.*

SCI-PRO-002, *Planning for Science Activities.*

SCI-PRO-006, *Models.*

9.3 SOURCE DATA, LISTED BY DATA TRACKING NUMBER

153407 GS000608312271.001. Pore-Water Hydrochemistry and Isotopic Data for Boreholes USW NRG-6, USW NRG-7A, USW SD-7, USW SD-9, USW SD-12, USW UZ-14 and UE-25 UZ#16 from 10/1/96 to 1/31/97. Submittal date: 06/23/2000.

156375 GS010708312272.002. Chemical Data for Pore Water from Tuff Cores of USW NRG-6, USW NRG-7/7A, USW UZ-14, USW UZ-N55 and UE-25 UZ#16. Submittal date: 09/05/2001.

160899 GS020408312272.003. Collection and Analysis of Pore Water Samples for the Period from April 2001 to February 2002. Submittal date: 04/24/2002.

162129 GS020508312242.001. Trench Fault Infiltration in Alcove 8 Using Permeameters from March 5, 2001 to June 1, 2001. Submittal date: 05/22/2002.

162126 GS020608315215.002. Carbon Dioxide Abundances, Carbon Dioxide Concentrations, and Normative Calcite Concentrations for Cuttings from Borehole USW SD-6, USW WT-24, and ECRB Cross Drift Boreholes, Determined by Carbon Dioxide Evolution, May 25, 2000 and September 8, 2000. Submittal date: 06/26/2002.

162141 GS020908312242.002. Trenched Fault Infiltration in Alcove 8 Using Permeameters from June 1, 2001 to March 26, 2002. Submittal date: 09/17/2002.

162127 GS021008315215.007. Carbon Dioxide and Normative Calcite Concentrations in Powdered Cuttings from Borehole USW WT-24 Determined by CO2 Evolution between July 1998 and August 1999. Submittal date: 11/07/2002.

162131 GS030108314224.001. Geotechnical Data for Alcove 8 (ECRB) and Niche 3 (ESF): Full Periphery Geologic Map (Drawing OA-46-356). Submittal date: 02/05/2003.

171287 GS031208312232.003. Deep Unsaturated Zone Surface-Based Borehole Instrumentation Program Data from Boreholes USW NRG-7A, UE-25 UZ #4, USW NRG-6, UE-25 UZ #5, USW UZ-7A and USW SD-12 for the Time Period 10/01/97 - 03/31/98. Submittal date: 07/29/2004.

182187 GS031208312232.004. Deep Unsaturated Zone Surface-Based Borehole Instrumentation Program Data from Boreholes USW NRG-7A, UE-25 UZ #4, UE-25 UZ #5, USW UZ-7A and USW SD-12 for the Time Period 7/1/97 - 9/30/97. Submittal date: 01/14/2004.

179284 GS031208312232.005. Deep Unsaturated Zone Surface-Based Borehole Instrumentation Program Data from Boreholes USW NRG-7A, UE-25 UZ#4, UE-25 UZ#5, USW UZ-7A and USW SD-12 for the Time Period 1/1/97 - 6/30/97. Submittal date: 05/24/2004.

182186 GS031208312232.006. Deep Unsaturated Zone, Surface-Based Borehole Instrumentation Program - Data For Boreholes USW NRG-7A, USW NRG-6, UE-25 UZ#4, UE-25 UZ #5, USW UZ-7A, and USW SD-12, for the Period 8/16/96 through 12/31/96. Submittal date: 05/24/2004.

178751 GS031208312232.007. Deep Unsaturated Zone Surface-Based Borehole Instrumentation Program Data for Boreholes USW NRG-7A, USW NRG-6, UE-25 UZ#4, UE-25 UZ#5, USW UZ-7A and USW SD-12 for the Time Period 4/1/96 through 8/15/96. Submittal date: 05/24/2004.

178750 GS031208312232.008. Deep Unsaturated Zone Surface-Based Borehole Instrumentation Program Data from Boreholes USW NRG-7A, USW NRG-6, UE-25 UZ#4, UE-25 UZ#5, USW UZ-7A, and USW SD-12 for the Time Period 10/01/95 through 3/31/96. Submittal date: 05/24/2004.

181234 GS040108312312.001. Water-Level, Discharge Rate and Related Data from the Pump Tests Conducted at Well USW UZ-14, August 12 through August 30, 1993. Submittal date: 02/12/2004.

181397 GS061208313000.005. Geochemical Composition of Dust Samples from Sheltered Areas in the Vicinity of Yucca Mountain, Phase V, Collected February 10, 2005, and Analyzed March 24, 2005-May 12, 2005. Submittal date: 12/12/2006.

105572 GS950208312232.003. Data, Including Water Potential, Pressure and Temperature, Collected from Boreholes USW NRG-6 and USW NRG-7A from Instrumentation through March 31, 1995. Submittal date: 02/13/1995.

107244 GS950408318523.001. Temperature, Thermal Conductivity, and Heat Flow Near Yucca Mountain, Nevada. Submittal date: 04/21/1995.

106756 GS951108312232.008. Data, Including Water Potential, Pressure and Temperature, Collected from Boreholes UE-25 UZ#4 & UZ#5 from Instrumentation through September 30, 1995, and from USW NRG-6 & NRG-7A from April 1 through September 30, 1995. Submittal date: 11/21/1995.

107293 GS961108312261.006. Gas Chemistry, ESF Alcoves 2 and 3, 11/95 - 4/96; Water Chemistry, Alcove 2 (Tritium), Alcove 3, and ESF Tunnel; and Pneumatic Pressure Response from Boreholes in Exploratory Studies Facility Alcoves 2 and 3, 10/95 - 5/96. Submittal date: 11/12/1996.

121708 GS961108312271.002. Chemical and Isotopic Composition of Pore Water and Pore Gas, 1994–96, from Boreholes USW UZ-1, USW UZ-14, UE-25 UZ#16, USW NRG-6, USW NRG-7A, USW SD-7, USW SD-9, ESF-AL#3-RBT#1, and ESF-AL#3-RBT#4, and ESF Rubble. Submittal date: 12/04/1996.

107253 GS970108312271.001. Interpretations of Chemical and Isotopic Composition Data and Geochemical Modeling (Netpath) in the Unsaturated Zone, Yucca Mountain, Nevada. Submittal date: 01/24/1997.

111467 GS970908312271.003. Unsaturated Zone Hydrochemistry Data, 2-1-97 to 8-31-97, Including Chemical Composition and Carbon, Oxygen, and Hydrogen Isotopic Composition: Porewater from USW NRG-7A, SD-7, SD-9, SD-12 and UZ-14; and Gas from USW UZ-14. Submittal date: 09/08/1997.

109746 GS980508312313.001. Water-Level and Related Data Collected in Support of Perched-Water Testing in Borehole USW WT-24, September 10, 1997 through February 3, 1998. Submittal date: 05/07/1998.

106752 GS980708312242.010. Physical Properties of Borehole Core Samples, and Water Potential Measurements Using the Filter Paper Technique, for Borehole Samples from USW WT-24. Submittal date: 07/27/1998.

106748 GS980808312242.014. Physical Properties of Borehole Core Samples and Water Potential Measurements Using the Filter Paper Technique for Borehole Samples from USW SD-6. Submittal date: 08/11/1998.

119820 GS980908312242.036. Water Potentials Measured with Heat Dissipation Probes in ECRB Holes from 4/23/98 to 7/31/98. Submittal date: 09/22/1998.

153677 GS981008312272.004. Analysis for Chemical Composition of Pore Water from Boreholes USW UZ-7A, USW WT-24, USW SD-6, USW SD-7, and USW SD-12 During FY 1997 and 1998. Submittal date: 10/28/1998.

146134 GS990208312272.001. Analysis for Chemical Composition of Pore Water from Borehole USW UZ-14 and UE-25 UZ#16 and Groundwater from UE-25 UZ#16. Submittal date: 02/23/1999.

145711 GS990308315215.004. Strontium Isotope Ratios and Strontium Concentrations in Rock Core Samples and Leachates from USW SD-9 and USW SD-12. Submittal date: 03/25/1999.

148603 LA000000000034.002. Diffusion of Sorbing and Non-Sorbing Radionuclides. Submittal date: 06/22/1993.

154760 LA0002JF12213U.001. Chemistry Data for Porewater Extracted from Drillcore from Surface-Based Boreholes USW NRG-6, USW NRG-7A, USW UZ-7A, USW UZ-14, UE-25 UZ#16, USW UZ-N55, USW SD-6, USW SD-7, USW SD-9, USW SD-12, and USW WT-24. Submittal date: 02/15/2000.

156281 LA0002JF12213U.002. Chemistry Data for Porewater Extracted from ESF, Cross Drift and Busted Butte Drill Core. Submittal date: 02/15/2000.

162476 LA0010JC831341.001. Radionuclide Retardation Measurements of Sorption Distribution Coefficients for Barium. Submittal date: 10/19/2000.

153321 LA0010JC831341.002. Radionuclide Retardation Measurements of Sorption Distribution Coefficients for Cesium. Submittal date: 10/19/2000.

153322 LA0010JC831341.003. Radionuclide Retardation Measurements of Sorption Distribution Coefficients for Strontium. Submittal date: 10/19/2000.

153323 LA0010JC831341.004. Radionuclide Retardation Measurements of Sorption Distribution Coefficients for Selenium. Submittal date: 10/19/2000.

153320 LA0010JC831341.005. Radionuclide Retardation Measurements of Sorption Distribution Coefficients for Uranium. Submittal date: 10/19/2000.

153318 LA0010JC831341.006. Radionuclide Retardation Measurements of Sorption Distribution Coefficients for Plutonium. Submittal date: 10/19/2000.

153319 LA0010JC831341.007. Radionuclide Retardation Measurements of Sorption Distribution Coefficients for Neptunium. Submittal date: 10/19/2000.

171584 LA0408AM831341.001. Unsaturated Zone Distribution Coefficients (Kds) for U, Np, Pu, Am, Pa, Cs, Sr, Ra, and Th. Submittal date: 08/24/2004.

145598 LA9909JF831222.004. Chloride, Bromide, and Sulfate Analyses of Busted Butte and Cross Drift Tunnel Porewaters in FY99. Submittal date: 09/29/1999.

122733 LA9909JF831222.010. Chloride, Bromide, Sulfate, and Chlorine-36 Analyses of ESF Porewaters. Submittal date: 09/29/1999.

145402 LAJF831222AQ98.011. Chloride, Bromide, Sulfate and Chlorine-36 Analyses of Springs, Groundwater, Porewater, Perched Water and Surface Runoff. Submittal date: 09/10/1998.

161278 LB0101DSTTHCR1.003. Attachment III - Mineral Reactive Surface Areas: TPTPMN and DST THC Models for AMR N0120/U0110 REV01, "Drift-Scale Coupled Processes (Drift-Scale Test and THC Seepage) Models.". Submittal date: 01/26/2001.

159525 LB0205REVUZPRP.001. Fracture Properties for UZ Model Layers Developed from Field Data. Submittal date: 05/14/2002.

159672 LB0207REVUZPRP.002. Matrix Properties for UZ Model Layers Developed from Field and Laboratory Data. Submittal date: 07/15/2002.

161285 LB0208UZDSCPMI.001. Drift-Scale Calibrated Property Sets: Mean Infiltration Supporting Files. Submittal date: 08/27/2002.

160799 LB0210THRMLPRP.001. Thermal Properties of UZ Model Layers: Data Summary. Submittal date: 10/25/2002.

162379 LB03013DSSCP3I.001. 3-D Site Scale Calibrated Properties: Data Summaries. Submittal date: 01/27/2003.

162130 LB0301N3SURDAT.001. Niche 3107 Measurements and Elevations Used for Grid Generation. Submittal date: 01/29/2003.

162354 LB03023DKMGRID.001. UZ 3-D Site Scale Model Grids. Submittal date: 02/26/2003.

162378 LB0302AMRU0035.001. Model Validation and Parameter Uncertainty: Supporting Files. Submittal date: 02/07/2003.

162570 LB0303A8N3LIQR.001. Alcove 8 - Niche 3 Seepage Data Compilation. Submittal date: 03/19/2003.

162773 LB0303A8N3MDLG.001. Alcove 8 - Niche 3 Seepage Modeling: Simulations. Submittal date: 03/31/2003.

180351 LB0303GASFLW3D.001. Time-Dependent Gas Pressure Distributions in UZ Flow-Fields. Submittal date: 03/28/2003.

165168 LB0303THERMESH.001. Thermal Model Mesh. Submittal date: 03/28/2003.

165167 LB0303THERMSIM.001. UZ Thermal Modeling: Simulations. Submittal date: 03/28/2003.

179180 LB0610UZDSCP30.001. Drift-Scale Calibrated Property Set for the 30-Percentile Infiltration Map. Submittal date: 11/02/2006.

178586 LB0611MTSCHP10.001. Mountain Scale Calibrated Property Set for the 10-Percentile Infiltration Map. Submittal date: 11/28/2006.

180293 LB0611MTSCHP30.001. Mountain Scale Calibrated Property Set for the 30-Percentile Infiltration Map. Submittal date: 11/28/2006.

180294 LB0612MTSCHP50.001. Mountain Scale Calibrated Property Set for the 50-Percentile Infiltration Map. Submittal date: 12/19/2006.

180295 LB0612MTSCHP90.001. Mountain Scale Calibrated Property Set for the 90-Percentile Infiltration Map. Submittal date: 12/20/2006.

180296 LB0612MTSCHPFT.001. Calibrated UZ Fault Property Sets. Submittal date: 12/07/2006.

136593 LB980901233124.101. Pneumatic Pressure and Air Permeability Data from Niche 3107 and Niche 4788 in the ESF from Chapter 2 of Report SP33PBM4: Fracture Flow and Seepage Testing in the ESF, FY98. Submittal date: 11/23/1999.

106787 LB990501233129.001. Fracture Properties for the UZ Model Grids and Uncalibrated Fracture and Matrix Properties for the UZ Model Layers for AMR U0090, "Analysis of Hydrologic Properties Data". Submittal date: 08/25/1999.

110226 LB990861233129.001. Drift Scale Calibrated 1-D Property Set, FY99. Submittal date: 08/06/1999.

125868 LB991091233129.001. One-Dimensional, Mountain-Scale Calibration for AMR U0035, "Calibrated Properties Model". Submittal date: 10/22/1999.

161276 LB991200DSTTHC.003. Mineral Initial Volume Fractions: Attachment II of AMR N0120/U0110, "Drift-Scale Coupled Processes (Drift-Scale Test and THC Seepage) Models.". Submittal date: 03/11/2000.

104055 LB997141233129.001. Calibrated Basecase Infiltration 1-D Parameter Set for the UZ Flow and Transport Model, FY99. Submittal date: 07/21/1999.

182332 LL0705PA038MST.030. Model preparation and analysis files for ANL-EBS-MD-000049 Multiscale. Submittal date: 08/31/2007.

152554 MO0004QGFMPICK.000. Lithostratigraphic Contacts from MO9811MWDGFM03.000 to be Qualified Under the Data Qualification Plan, TDP-NBS-GS-000001. Submittal date: 04/04/2000.

153398 MO0012CARB1314.000. Water - Carbon 13 and Carbon 14 Abundance. Submittal date: 12/01/2000.

153777 MO0012MWDGFM02.002. Geologic Framework Model (GFM2000). Submittal date: 12/18/2000.

155989 MO0109HYMXPROP.001. Matrix Hydrologic Properties Data. Submittal date: 09/17/2001.

181613 MO0706SPAFEPLA.001. FY 2007 LA FEP List and Screening. Submittal date: 06/20/2007.

109059 MO9906GPS98410.000. Yucca Mountain Project (YMP) Borehole Locations. Submittal date: 06/23/1999.

179063 SN0609T0502206.024. Monsoon Net Infiltration Results. Submittal date: 09/18/2006.

178753 SN0609T0502206.028. Present-Day Net Infiltration Results. Submittal date: 09/22/2006.

178862 SN0609T0502206.029. Glacial Transition Net Infiltration Results. Submittal date: 09/28/2006.

181227 SN0701T0502206.037. Massif Calculation of Net Infiltration at Yucca Mountain, Rev 1. Submittal date: 02/13/2007.

105067 SNT02110894001.002. Geologic Core Logs for USW SD-7. Submittal date: Submittal date: 07/15/1996.

9.4 OUTPUT DATA, LISTED BY DATA TRACKING NUMBER

LB06123DPDUZFF.001. 3-D UZ Flow Fields for Present-Day Climate of 10th-, 30th-, 50th- and 90th -Percentile Infiltration Maps. Submittal date: 12/19/2006.

LB0612PDFEHMFF.001. Flow-Field Conversions from TOUGH2 to FEHM Format for Present Day 10-, 30-, 50-, and 90-Percentile Infiltration Maps. Submittal date: 12/19/2006.

LB0612PDPTNTSW.001. Vertical Flux at PTN/TSW Interface for Present-Day Climate of 10th, 30th, 50th, and 90-Percentile Infiltration Maps. Submittal date: 12/19/2006.

LB07013DGTUZFF.001. 3-D UZ Flow Fields for Glacial Transition Climate of 10th-, 30th-, 50th-, and 90th-Percentile Infiltration Maps. Submittal date: 01/03/2007. TBV-7848 LB0706UZWATSAT.001. Post-processing of water saturation and water potential data for 3-D Site Scale UZ flow model outputs for present-day, monsoon, and glacial transition climates. Submittal date: 07/16/2008.

LB07013DMOUZFF.001. 3-D UZ Flow Fields for Monsoon Climate of 10th-, 30th-, 50th-, and 90th-Percentile Infiltration Maps. Submittal date: 01/03/2007. TBV-7849

LB0701GTFEHMFF.001. Flow-Field Conversions from TOUGH2 to FEHM Format for Glacial Transition Climate 10th-, 30th-, 50th-, and 90th-Percentile Infiltration Maps. Submittal date: 01/05/2007.

LB0701GTPTNTSW.001. Vertical Flux at PTN/TSW Interface for Glacial Transition Climate of 10th, 30th, 50th, and 90th-Percentile Infiltration Maps. Submittal date: 01/03/2007.

LB0701MOFEHMFF.001. Flow-Field Conversions from TOUGH2 to FEHM Format for Monsoon Climate 10th-, 30th-, 50th-, and 90th-Percentile Infiltration Maps. Submittal date: 01/05/2007.

LB0701MOPTNTSW.001. Vertical Flux at PTN/TSW Interface for Monsoon Climate of 10th, 30th, 50th and 90th-Percentile Infiltration Maps. Submittal date: 01/03/2007.

LB0701PAWFINFM.001. Weighting Factors for Infiltration Maps. Submittal date: 01/25/2007.

LB0701UZMCLCAL.001. Chloride Flux Profiles in the Unsaturated Zone for Present Day 10th-, 30th-, 50th- and 90th-Percentile Infiltration Maps. Submittal date: 01/22/2007. TBV-7850

LB0701UZMTHCAL.001. Input and Output of 3-D UZ Ambient Thermal Model for Present-Day Climate of 10th-, 30th-, 50th- and 90th-Percentile Infiltration Maps. Submittal date: 01/22/2007.

LB0702PAFEM10K.002. Flow Field Conversions to FEHM Format for Post 10,000 Year Peak Dose Fluxes in the Unsaturated Zone for Four Selected Infiltration Rates. Submittal date: 02/15/2007.

LB0702UZP10KFF.002. 3-D UZ Flow Fields for Post-10,000 Climate Infiltration Maps. Submittal date: 02/15/2007.

LB0702UZPTN10K.002. Vertical Flux at PTN/TSW Interface for Post-10K-Year Climate Infiltration Maps. Submittal date: 02/15/2007.

LB07043DCRXPRP.001. Mountain Scale 3D Calibrated Property Set for the 10-Percentile, 30-Percentile, 50-Percentile, and the 90-Percentile Infiltration Maps. Submittal date: 05/10/2007.

LB07043DGASCAL.001. Mountain Scale 3D Gas Calibrated Property Set for the 10-Percentile and the 30-Percentile Infiltration Maps. Submittal date: 04/24/2007.

LB0704C14FFVAL.001. Simulations of Matrix Pore-Water Residence Time (Age). Submittal date: 04/17/2007.

LB0704UZWFINFM.001. Sensitivity Studies on UZ Flow Weighting Factors. Submittal date: 04/24/2007.

LB0705DAMPINGA.001. Data of Damping Effect Analyses. Submittal date: 05/18/2007

LB0705FLOWCOMP.001. Fracture and Matrix Flow Components. Submittal date: 06/01/2007

LB0705TRAVTIME.001. Simulated Breakthrough Curves and Travel Times. Submittal date: 05/18/2007.

LB0705UZSRTRAN.001. Data of the Simulated Steady State SR Concentration. Submittal date: 05/31/2007.

9.5 SOFTWARE CODES

154787 2kgrid8.for V. 1.0. 2002. DOS V4.00.1111, OSFI V4.0. STN: 10503-1.0-00.

162143 Bkread.f V. 1.0. 2002. SunOS 5.5.1. 10894-1.0-00.

153471 bot_sum.f V. 1.0. 2000. SUN AND DEC. 10349-1.0-00.

147027 get_temp_v0.f V. 1.0. 2000. DEC Alpha w/OSF1 V4.0. 10222-1.0-00.

154793 infil2grid V. 1.7. 2002. DOS V4.00.1111, OSFI V4.0. STN: 10077-1.7-00.

139918 iTOUGH2 V. 4.0. 1999. SUN O.S. 5.5.1, OS V4.0. STN: 10003-4.0-00.

162142 Smesh.f V. 1.0. 2002. SunOS 5.5.1. 10896-1.0-00.

163161 T2FEHM V. 4.0. 2003. DEC ALPHA / OSF1 V4.0/ V5.1. 10997-4.0-00.

146654 T2R3D V. 1.4. 1999. UNIX, WINDOWS 95/98NT 4.0. STN: 10006-1.4-00.

160107 TBgas3D V. 2.0. 2002. SUN O.S. 5.5.1. STN: 10882-2.0-00.

147030 toptemp_v0.f V. 1.0. 2000. DEC Alpha w/OSF1 V4.0. 10224-1.0-00.

161491 TOUGH2 V. 1.6. 2003. DOS Emulation (win95/98), SUN OS 5.5.1., OSF1 V4.0. STN: 10007-1.6-01.

161256 TOUGHREACT V. 3.0. 2002. DEC ALPHA/OSF1 V5.1, DEC ALPHA/OSF1 V5.0, Sun UltraSparc/Sun OS 5.5.1, PC/Linux Redhat 7.2. STN: 10396-3.0-00.

154785 WINGRIDDER V. 2.0. 2002. WINDOWS NT 4.0. STN: 10024-2.0-00.

163453 WTRISE V. 2.0. 2003. PC/WINDOWS 2000/98; DEC ALPHA/OSF1 V5.1. 10537-2.0-00.

APPENDIX A
MATHEMATICAL EQUATIONS

This appendix lists the equations used in the UZ flow model for unsaturated liquid flow under isothermal conditions. They include Darcy's law (Bear 1972 [DIRS 156269]), Richards equation (Richards 1931 [DIRS 104252], van Genuchten model (1980 [DIRS 100610]), and active fracture model (Liu et al. 1998 [DIRS 105729]).

For fracture continuum or matrix continuum in the dual continuum system, the basic mass balance equations solved by TOUGH2 can be written in the following form:

$$\frac{d}{dt}\int_{V_n} M_f \, dV_n = \int_{\Gamma_n} \mathbf{F}_f \bullet \mathbf{n} \, d\Gamma_n + \int_{V_n} (q_f + q_{fm}) dV_n \qquad \text{(Eq. A-1)}$$

$$\frac{d}{dt}\int_{V_n} M_m \, dV_n = \int_{\Gamma_n} \mathbf{F}_m \bullet \mathbf{n} \, d\Gamma_n + \int_{V_n} (q_m - q_{fm}) dV_n \qquad \text{(Eq. A-2)}$$

where subscripts f, m stand for fracture continuum and matrix continuum, respectively. (Notation $p = f$ or m is used in the following discussion.) The integration is over an arbitrary subdomain V_n of the flow system under study, which is bounded by the closed surface Γ_n. **F** denotes mass flux, and **n** is a normal vector on surface element Γ_n, pointing inward into V_n. The quantity M represents mass per volume with $M_p = \phi_p S_p \rho$ (where ϕ_p is porosity, S_p is saturation, and ρ is liquid density), q_p denotes sinks and sources per unit volume and q_{fm} is fracture–matrix exchange flux per unit volume, a coupling term for describing fluid flow between the fracture and the matrix continuum. The q_{fm} takes positive values if the exchange flux is from matrix to fracture, and negative if from fracture to matrix; see Equation EA-13 below.

Darcy's law is expressed as:

$$\mathrm{F}_p = \rho \mathrm{u}_p = -k_p \frac{k_{rp}\rho}{\mu}(\nabla P_p - \rho g) \qquad \text{(Eq. A-3)}$$

where $\mathbf{u}_p$ is the Darcy velocity (volume flux), k_p is absolute permeability, k_{rp} is relative permeability, μ is viscosity, g is gravity acceleration constant, and P_p is capillary pressure. For Darcy's law written in this form, the variation of gas pressure is neglected. The capillary pressure is related to the gas pressure by the following equation:

$$P_p = -P_{pg} + P_{pl} \qquad \text{(Eq. A-4)}$$

where P_{pl} is water phase pressure and P_{pg} is the gas pressure.

By combining mass-balance equations (Equations A-1 to A-2) with Darcy's law (Equation A-3), Richards equation (Richards 1931 [DIRS 104252]; Pruess et al. 1999 [DIRS 160778], Equation A.17, p. 147) is obtained for the fracture and matrix continuum described as:

$$\frac{\partial}{\partial t}\theta_f = div\left[K_f \nabla \psi_f\right] + q_f + q_{fm} \qquad \text{(Eq. A-5)}$$

$$\frac{\partial}{\partial t}\theta_m = div[K_m \nabla \psi_m] + q_m - q_{fm} \quad \text{(Eq. A-6)}$$

where $K_p = k_p k_{rp} \rho g / \mu$ is hydraulic conductivity, $\psi_p = z + P_p/(\rho g)$ is the total water potential, z is elevation, and $\theta_p = \phi_p S_p$ is specific volumetric moisture content for fractures or matrix.

The water capillary pressure for the matrix continuum is described by the well-known van Genuchten relation (van Genuchten 1980 [DIRS 100610]), described as:

$$P_m(S_{em}) = \frac{1}{\alpha_m}[S_{em}^{-1/m_m} - 1]^{1/n_m} \quad \text{(Eq. A-7)}$$

where P_m is matrix capillary pressure; α_m (Pa^{-1}), n_m, and $m_m = 1 - 1/n_m$ are van Genuchten parameters for the matrix continuum; and S_{em} is the effective matrix water saturation. And effective fracture water saturation S_{ef} is:

$$S_{ep} = \frac{S_p - S_{rp}}{1 - S_{rp}} \quad \text{(Eq. A-8)}$$

where S_p is the water saturation of fracture or matrix and S_{rp} is the residual fracture or matrix saturation.

The relative permeability k_{rm} for the matrix continuum is given as:

$$k_{rm} = S_{em}^{1/2}[1 - \{1 - S_{em}^{1/m}\}^m]^2 \quad \text{(Eq. A-9)}$$

The water capillary pressure P_f for the fracture continuum is determined by:

$$P_f(S_{ef}) = \frac{1}{\alpha_f}[S_{ef}^{(\gamma-1)/m_f} - 1]^{1/n_f} \quad \text{(Eq. A-10)}$$

where S_{ef} is the effective water saturation of all connected fractures (defined in Equation A-8); α_f (Pa^{-1}), n_f, and $m_f = 1 - 1/n_f$ are van Genuchten parameters for the fracture continuum; and γ is the active fracture parameter (Liu et al. 1998 [DIRS 105729]).

The relative permeability k_{rf} for the fracture continuum is given as:

$$k_{rf} = S_{ef}^{(1+\gamma)/2}[1 - \{1 - S_{ef}^{(1-\gamma)/m_f}\}^{m_f}]^2 \quad \text{(Eq. A-11)}$$

In an unsaturated fracture network, the ratio of the interface area contributing to flow and transport between fractures and the matrix, to the total interface area determined geometrically from the fracture network, is called the fracture–matrix interface-area reduction factor. The reduction factor R is introduced by Liu et al. (1998 [DIRS 105729]) with the following expression:

$$R \cong S_{ef}^{\,1+\gamma} \qquad \text{(Eq. A-12)}$$

The interface area between fracture continuum and matrix continuum, used to calculate q_{fm}, is multiplied by the factor R in the active fracture model (Liu et al. 1998 [DIRS 105729]).

The fracture–matrix exchange flux introduced in Equations A-1 to A-2 can be approximated as quasi-steady, with the rate of matrix-fracture flux proportional to the difference in (local) average pressure:

$$q_{fm} \propto R\,A\,\frac{\psi_m - \psi_f}{l_f} \qquad \text{(Eq. A-13)}$$

where A is the total interface area between fracture and matrix (area/volume), and l_f is the characteristic distance for fracture–matrix flow (BSC 2004 [DIRS 169855]).

INTENTIONALLY LEFT BLANK

APPENDIX B
CALIBRATED PARAMETER SETS USED IN SIMULATIONS OF GENERATING THE SIXTEEN FLOW FIELDS AND TRACER TRANSPORT

This appendix presents the four parameter sets for the UZ flow model. Tables B-1, B-2, B-3, and B-4 list the calibrated three-dimensional UZ flow-model parameters used for generating the 16 UZ flow fields and tracer-transport simulations.

Table B-1. Calibrated Parameters for the Present-Day, 10th Percentile Infiltration Scenario, Used for Simulations with the 10th Percentile Infiltration Scenarios of the Present-Day, Monsoon, and Glacial Transition, Post-10,000 yr Climates

Model Layer	k_M (m^2)	m_M (–)	α_M (1/Pa)	k_F (m^2)	m_F (–)	α_F (1/Pa)	γ (–)
tcw11	3.744×10^{-15}	0.388	1.011×10^{-5}	2.000×10^{-12}	0.633	5.271×10^{-3}	0.400
tcw12	5.517×10^{-20}	0.280	2.564×10^{-6}	1.000×10^{-10}	0.633	1.574×10^{-3}	0.400
tcw13	5.648×10^{-17}	0.259	2.257×10^{-6}	1.000×10^{-12}	0.633	1.236×10^{-3}	0.400
ptn21	4.595×10^{-15}	0.245	7.764×10^{-5}	1.000×10^{-11}	0.633	8.700×10^{-4}	0.001
ptn22	5.448×10^{-12}	0.219	1.157×10^{-4}	1.000×10^{-13}	0.633	1.572×10^{-3}	0.001
ptn23	1.692×10^{-14}	0.247	2.467×10^{-5}	2.140×10^{-13}	0.633	5.179×10^{-3}	0.001
ptn24	6.939×10^{-12}	0.182	9.034×10^{-4}	1.172×10^{-12}	0.633	1.860×10^{-3}	0.001
ptn25	2.353×10^{-13}	0.300	6.769×10^{-5}	3.079×10^{-13}	0.633	1.334×10^{-3}	0.001
ptn26	3.162×10^{-11}	0.126	1.000×10^{-3}	1.000×10^{-13}	0.633	1.343×10^{-3}	0.001
tsw31	9.780×10^{-17}	0.218	2.802×10^{-5}	4.064×10^{-12}	0.633	1.000×10^{-4}	0.129
tsw32	4.545×10^{-16}	0.290	1.710×10^{-5}	3.540×10^{-12}	0.633	1.000×10^{-4}	0.400
tsw33	1.856×10^{-17}	0.283	7.259×10^{-6}	3.881×10^{-12}	0.633	1.589×10^{-3}	0.400
tsw34	3.162×10^{-18}	0.317	2.546×10^{-6}	3.311×10^{-12}	0.633	3.162×10^{-4}	0.400
tsw35	1.092×10^{-17}	0.216	4.447×10^{-6}	9.120×10^{-12}	0.633	3.162×10^{-4}	0.400
tsw36	3.162×10^{-18}	0.442	2.507×10^{-6}	1.349×10^{-11}	0.633	7.435×10^{-4}	0.400
tsw37	3.162×10^{-18}	0.442	2.507×10^{-6}	1.349×10^{-11}	0.633	7.435×10^{-4}	0.400
tsw38	3.785×10^{-18}	0.286	1.878×10^{-6}	8.100×10^{-13}	0.633	2.122×10^{-3}	0.400
tsw3z	3.500×10^{-17}	0.059	4.610×10^{-6}	8.100×10^{-13}	0.633	1.500×10^{-3}	0.250
tsw3v	1.488×10^{-13}	0.293	4.717×10^{-5}	8.100×10^{-13}	0.633	1.500×10^{-3}	0.250
ch1z	3.500×10^{-17}	0.349	2.120×10^{-7}	2.500×10^{-14}	0.633	1.400×10^{-3}	0.250
ch1v	2.206×10^{-12}	0.240	1.198×10^{-4}	2.200×10^{-13}	0.633	2.100×10^{-3}	0.250
ch2v	1.549×10^{-12}	0.158	3.361×10^{-4}	2.200×10^{-13}	0.633	1.900×10^{-3}	0.250
ch3v	1.549×10^{-12}	0.158	3.361×10^{-4}	2.200×10^{-13}	0.633	1.900×10^{-3}	0.250
ch4v	1.549×10^{-12}	0.158	3.361×10^{-4}	2.200×10^{-13}	0.633	1.900×10^{-3}	0.250
ch5v	1.549×10^{-12}	0.158	3.361×10^{-4}	2.200×10^{-13}	0.633	1.900×10^{-3}	0.250
ch2z	5.200×10^{-18}	0.257	2.250×10^{-6}	2.500×10^{-14}	0.633	8.900×10^{-4}	0.250
ch3z	5.200×10^{-18}	0.257	2.250×10^{-6}	2.500×10^{-14}	0.633	8.900×10^{-4}	0.250
ch4z	5.200×10^{-18}	0.257	2.250×10^{-6}	2.500×10^{-14}	0.633	8.900×10^{-4}	0.250
ch5z	5.200×10^{-18}	0.257	2.250×10^{-6}	2.500×10^{-14}	0.633	8.900×10^{-4}	0.250
ch6z	8.200×10^{-19}	0.499	1.560×10^{-7}	2.500×10^{-14}	0.633	1.400×10^{-3}	0.250
ch6v	3.922×10^{-13}	0.147	1.721×10^{-5}	2.200×10^{-13}	0.633	1.900×10^{-3}	0.250
pp4z	3.015×10^{-17}	0.474	6.310×10^{-6}	2.500×10^{-14}	0.633	2.818×10^{-4}	0.146
pp3d	9.240×10^{-14}	0.407	1.722×10^{-5}	2.200×10^{-13}	0.633	2.467×10^{-3}	0.199
pp2d	1.684×10^{-15}	0.309	4.842×10^{-6}	2.200×10^{-13}	0.633	3.168×10^{-3}	0.199
pp1z	5.012×10^{-17}	0.272	3.162×10^{-5}	2.500×10^{-14}	0.633	1.534×10^{-4}	0.146
bf3d	1.000×10^{-14}	0.193	3.202×10^{-5}	2.200×10^{-13}	0.633	2.931×10^{-3}	0.199
bf2z	8.100×10^{-17}	0.617	1.180×10^{-7}	2.500×10^{-14}	0.633	8.900×10^{-4}	0.250

Table B-1. Calibrated Parameters for the Present-Day, 10th Percentile Infiltration Scenario, Used for Simulations with the 10th Percentile Infiltration Scenarios of the Present-Day, Monsoon, and Glacial Transition, Post-10,000 yr Climates (Continued)

Model Layer	k_M (m^2)	m_M (–)	α_M (1/Pa)	k_F (m^2)	m_F (–)	α_F (1/Pa)	γ (–)
tr3d	1.000×10^{-14}	0.193	3.202×10^{-5}	2.200×10^{-13}	0.633	2.931×10^{-3}	0.199
tr2z	8.100×10^{-17}	0.617	1.180×10^{-7}	2.500×10^{-14}	0.633	8.900×10^{-4}	0.250
pcM38/pcF38	3.000×10^{-19}	0.286	1.878×10^{-6}	3.000×10^{-18}	0.286	1.878×10^{-6}	0.000
pcM39/pcF39	6.200×10^{-18}	0.059	4.610×10^{-6}	6.200×10^{-17}	0.059	4.610×10^{-6}	0.000
pcM1z/pcF1z	9.300×10^{-20}	0.349	2.120×10^{-7}	9.300×10^{-19}	0.349	2.120×10^{-7}	0.000
pcM2z/pcF2z	2.400×10^{-18}	0.257	2.250×10^{-6}	2.400×10^{-17}	0.257	2.250×10^{-6}	0.000
pcM5z/pcF5z	2.400×10^{-18}	0.257	2.250×10^{-6}	2.400×10^{-18}	0.257	2.250×10^{-6}	0.000
pcM6z/pcF6z	1.100×10^{-19}	0.499	1.560×10^{-7}	1.100×10^{-19}	0.499	1.560×10^{-7}	0.000
pcM4p/pcF4p	7.700×10^{-19}	0.474	6.310×10^{-6}	7.700×10^{-19}	0.474	6.310×10^{-6}	0.000
tcwFf				1.000×10^{-10}	0.633	1.000×10^{-2}	0.379
ptnFf				3.941×10^{-11}	0.633	2.865×10^{-3}	0.100
tswFf				1.000×10^{-10}	0.633	3.200×10^{-3}	0.200
chnFf				3.700×10^{-13}	0.633	2.300×10^{-3}	0.200

Output DTN: LB07043DCRXPRP.001.

Table B-2. Calibrated Parameters for the Present-Day, 30th Percentile Infiltration Scenario, Used for Simulations with the 30th Percentile Infiltration Scenarios of the Present-Day, Monsoon, and Glacial Transition, Post-10,000 yr Climates

Model Layer	k_M (m^2)	m_M (–)	α_M (1/Pa)	k_F (m^2)	m_F (–)	α_F (1/Pa)	γ (–)
tcw11	3.879×10^{-15}	0.388	1.220×10^{-5}	1.207×10^{-12}	0.633	4.989×10^{-3}	0.400
tcw12	1.154×10^{-19}	0.280	2.879×10^{-6}	1.000×10^{-10}	0.633	2.178×10^{-3}	0.400
tcw13	4.388×10^{-16}	0.259	2.611×10^{-6}	6.656×10^{-13}	0.633	1.853×10^{-3}	0.400
ptn21	2.132×10^{-14}	0.245	9.823×10^{-5}	2.552×10^{-12}	0.633	2.679×10^{-3}	0.001
ptn22	1.283×10^{-11}	0.219	1.224×10^{-4}	1.000×10^{-14}	0.633	1.374×10^{-3}	0.001
ptn23	4.058×10^{-14}	0.247	2.415×10^{-5}	1.513×10^{-13}	0.633	1.225×10^{-3}	0.001
ptn24	7.644×10^{-12}	0.182	7.437×10^{-4}	1.392×10^{-12}	0.633	2.937×10^{-3}	0.001
ptn25	9.635×10^{-13}	0.300	6.277×10^{-5}	1.000×10^{-14}	0.633	1.091×10^{-3}	0.001
ptn26	1.862×10^{-11}	0.126	8.106×10^{-4}	8.377×10^{-14}	0.633	9.505×10^{-4}	0.001
tsw31	3.215×10^{-17}	0.218	2.898×10^{-5}	1.626×10^{-12}	0.633	1.000×10^{-4}	0.088
tsw32	3.011×10^{-16}	0.290	1.587×10^{-5}	1.416×10^{-12}	0.633	1.000×10^{-4}	0.400
tsw33	1.856×10^{-17}	0.283	6.559×10^{-6}	1.552×10^{-12}	0.633	1.577×10^{-3}	0.400
tsw34	3.162×10^{-18}	0.317	1.709×10^{-6}	3.311×10^{-12}	0.633	3.162×10^{-4}	0.400
tsw35	1.112×10^{-17}	0.216	3.380×10^{-6}	9.120×10^{-12}	0.633	5.749×10^{-4}	0.400
tsw36	3.162×10^{-18}	0.442	7.321×10^{-7}	1.349×10^{-11}	0.633	1.091×10^{-3}	0.400
tsw37	3.162×10^{-18}	0.442	7.321×10^{-7}	1.349×10^{-11}	0.633	1.091×10^{-3}	0.400
tsw38	1.266×10^{-17}	0.286	3.105×10^{-6}	8.100×10^{-13}	0.633	8.871×10^{-4}	0.400
tsw3z	3.500×10^{-17}	0.059	4.610×10^{-6}	8.100×10^{-13}	0.633	1.500×10^{-3}	0.250
tsw3v	2.225×10^{-13}	0.293	4.693×10^{-5}	8.100×10^{-13}	0.633	1.500×10^{-3}	0.250
ch1z	3.500×10^{-17}	0.349	2.120×10^{-7}	2.500×10^{-14}	0.633	1.400×10^{-3}	0.250
ch1v	2.593×10^{-12}	0.240	1.109×10^{-4}	2.200×10^{-13}	0.633	2.100×10^{-3}	0.250

Table B-2. Calibrated Parameters for the Present-Day, 30th Percentile Infiltration Scenario, Used for Simulations with the 30th Percentile Infiltration Scenarios of the Present-Day, Monsoon, and Glacial Transition, Post-10,000 yr Climates (Continued)

Model Layer	k_M (m^2)	m_M (–)	α_M (1/Pa)	k_F (m^2)	m_F (–)	α_F (1/Pa)	γ (–)
ch2v	6.774×10^{-11}	0.158	3.328×10^{-4}	2.200×10^{-13}	0.633	1.900×10^{-3}	0.250
ch3v	6.774×10^{-11}	0.158	3.328×10^{-4}	2.200×10^{-13}	0.633	1.900×10^{-3}	0.250
ch4v	6.774×10^{-11}	0.158	3.328×10^{-4}	2.200×10^{-13}	0.633	1.900×10^{-3}	0.250
ch5v	6.774×10^{-11}	0.158	3.328×10^{-4}	2.200×10^{-13}	0.633	1.900×10^{-3}	0.250
ch2z	5.200×10^{-18}	0.257	2.250×10^{-6}	2.500×10^{-14}	0.633	8.900×10^{-4}	0.250
ch3z	5.200×10^{-18}	0.257	2.250×10^{-6}	2.500×10^{-14}	0.633	8.900×10^{-4}	0.250
ch4z	5.200×10^{-18}	0.257	2.250×10^{-6}	2.500×10^{-14}	0.633	8.900×10^{-4}	0.250
ch5z	5.200×10^{-18}	0.257	2.250×10^{-6}	2.500×10^{-14}	0.633	8.900×10^{-4}	0.250
ch6z	8.200×10^{-19}	0.499	1.560×10^{-7}	2.500×10^{-14}	0.633	1.400×10^{-3}	0.250
ch6v	2.708×10^{-13}	0.147	1.844×10^{-5}	2.200×10^{-13}	0.633	1.900×10^{-3}	0.250
pp4z	3.513×10^{-17}	0.474	6.310×10^{-6}	2.500×10^{-12}	0.633	2.818×10^{-4}	0.400
pp3d	1.021×10^{-13}	0.407	1.478×10^{-5}	2.200×10^{-12}	0.633	1.652×10^{-3}	0.400
pp2d	1.693×10^{-15}	0.309	3.895×10^{-6}	2.200×10^{-13}	0.633	1.652×10^{-3}	0.400
pp1z	2.570×10^{-17}	0.272	3.162×10^{-5}	2.500×10^{-14}	0.633	1.581×10^{-4}	0.400
bf3d	6.309×10^{-14}	0.193	6.179×10^{-5}	2.200×10^{-13}	0.633	1.652×10^{-3}	0.400
bf2z	8.100×10^{-17}	0.617	1.180×10^{-7}	2.500×10^{-14}	0.633	8.900×10^{-4}	0.250
tr3d	6.309×10^{-14}	0.193	6.179×10^{-5}	2.200×10^{-13}	0.633	1.652×10^{-3}	0.400
tr2z	8.100×10^{-17}	0.617	1.180×10^{-7}	2.500×10^{-14}	0.633	8.900×10^{-4}	0.250
pcM38/pcF38	3.000×10^{-19}	0.286	3.105×10^{-6}	3.000×10^{-18}	0.286	3.105×10^{-6}	0.000
pcM39/pcF39	6.200×10^{-18}	0.059	4.610×10^{-6}	6.200×10^{-17}	0.059	4.610×10^{-6}	0.000
pcM1z/pcF1z	9.300×10^{-20}	0.349	2.120×10^{-7}	9.300×10^{-19}	0.349	2.120×10^{-7}	0.000
pcM2z/pcF2z	2.400×10^{-18}	0.257	2.250×10^{-6}	2.400×10^{-17}	0.257	2.250×10^{-6}	0.000
pcM5z/pcF5z	2.400×10^{-18}	0.257	2.250×10^{-6}	2.400×10^{-18}	0.257	2.250×10^{-6}	0.000
pcM6z/pcF6z	1.100×10^{-19}	0.499	1.560×10^{-7}	1.100×10^{-19}	0.499	1.560×10^{-7}	0.000
pcM4p/pcF4p	7.700×10^{-19}	0.474	6.310×10^{-6}	7.700×10^{-19}	0.474	6.310×10^{-6}	0.000
tcwFf				1.000×10^{-10}	0.633	1.000×10^{-2}	0.212
ptnFf				4.955×10^{-11}	0.633	4.645×10^{-3}	0.166
tswFf				9.802×10^{-11}	0.633	3.725×10^{-4}	0.390
chnFf				3.700×10^{-13}	0.633	2.300×10^{-3}	0.200

Output DTN: LB07043DCRXPRP.001.

Table B-3. Calibrated Parameters for the Present-Day, 50th Percentile Infiltration Scenario, Used for Simulations with the 50th Percentile Infiltration Scenarios of the Present-Day, Monsoon, and Glacial Transition, Post-10,000 yr Climates

Model Layer	k_M (m^2)	m_M (–)	α_M (1/Pa)	k_F (m^2)	m_F (–)	α_F (1/Pa)	γ (–)
tcw11	3.900×10^{-15}	0.388	1.225×10^{-5}	1.320×10^{-12}	0.633	5.012×10^{-3}	0.400
tcw12	1.159×10^{-19}	0.280	3.043×10^{-6}	1.000×10^{-10}	0.633	2.188×10^{-3}	0.400
tcw13	4.408×10^{-16}	0.259	2.711×10^{-6}	5.770×10^{-13}	0.633	1.862×10^{-3}	0.400
ptn21	2.143×10^{-14}	0.245	8.824×10^{-5}	1.151×10^{-12}	0.633	2.692×10^{-3}	0.001
ptn22	1.698×10^{-11}	0.219	1.228×10^{-4}	1.000×10^{-14}	0.633	1.380×10^{-3}	0.001

Table B-3. Calibrated Parameters for the Present-Day, 50th Percentile Infiltration Scenario, Used for Simulations with the 50th Percentile Infiltration Scenarios of the Present-Day, Monsoon, and Glacial Transition, Post-10,000 yr Climates (Continued)

Model Layer	k_M (m^2)	m_M (–)	α_M (1/Pa)	k_F (m^2)	m_F (–)	α_F (1/Pa)	γ (–)
ptn23	6.151×10^{-14}	0.247	2.387×10^{-5}	1.096×10^{-13}	0.633	1.230×10^{-3}	0.001
ptn24	2.296×10^{-11}	0.182	8.079×10^{-4}	4.810×10^{-12}	0.633	2.951×10^{-3}	0.001
ptn25	6.415×10^{-13}	0.300	5.714×10^{-5}	1.000×10^{-14}	0.633	1.096×10^{-3}	0.001
ptn26	3.162×10^{-11}	0.126	9.919×10^{-4}	3.741×10^{-14}	0.633	9.550×10^{-4}	0.001
tsw31	1.037×10^{-16}	0.218	1.070×10^{-5}	6.457×10^{-11}	0.633	1.000×10^{-4}	0.075
tsw32	1.700×10^{-16}	0.290	2.703×10^{-5}	5.623×10^{-11}	0.633	1.000×10^{-4}	0.393
tsw33	3.779×10^{-17}	0.283	6.416×10^{-6}	6.166×10^{-11}	0.633	1.585×10^{-3}	0.393
tsw34	3.162×10^{-18}	0.317	1.501×10^{-6}	2.630×10^{-11}	0.633	3.162×10^{-4}	0.400
tsw35	1.937×10^{-17}	0.216	3.716×10^{-6}	7.244×10^{-11}	0.633	5.780×10^{-4}	0.400
tsw36	4.452×10^{-18}	0.442	6.578×10^{-7}	1.072×10^{-10}	0.633	1.096×10^{-3}	0.400
tsw37	4.452×10^{-18}	0.442	6.578×10^{-7}	1.072×10^{-10}	0.633	1.096×10^{-3}	0.400
tsw38	2.163×10^{-17}	0.286	3.691×10^{-6}	8.100×10^{-13}	0.633	8.913×10^{-4}	0.400
tsw3z	3.500×10^{-17}	0.059	4.610×10^{-6}	8.100×10^{-13}	0.633	1.500×10^{-3}	0.250
tsw3v	2.237×10^{-13}	0.293	4.840×10^{-5}	8.100×10^{-13}	0.633	1.500×10^{-3}	0.250
ch1z	3.500×10^{-17}	0.349	2.120×10^{-7}	2.500×10^{-14}	0.633	1.400×10^{-3}	0.250
ch1v	3.162×10^{-12}	0.240	1.354×10^{-4}	2.200×10^{-13}	0.633	2.100×10^{-3}	0.250
ch2v	1.585×10^{-11}	0.158	3.190×10^{-4}	2.200×10^{-13}	0.633	1.900×10^{-3}	0.250
ch3v	1.585×10^{-11}	0.158	3.190×10^{-4}	2.200×10^{-13}	0.633	1.900×10^{-3}	0.250
ch4v	1.585×10^{-11}	0.158	3.190×10^{-4}	2.200×10^{-13}	0.633	1.900×10^{-3}	0.250
ch5v	1.585×10^{-11}	0.158	3.190×10^{-4}	2.200×10^{-13}	0.633	1.900×10^{-3}	0.250
ch2z	5.200×10^{-18}	0.257	2.250×10^{-6}	2.500×10^{-14}	0.633	8.900×10^{-4}	0.250
ch3z	5.200×10^{-18}	0.257	2.250×10^{-6}	2.500×10^{-14}	0.633	8.900×10^{-4}	0.250
ch4z	5.200×10^{-18}	0.257	2.250×10^{-6}	2.500×10^{-14}	0.633	8.900×10^{-4}	0.250
ch5z	5.200×10^{-18}	0.257	2.250×10^{-6}	2.500×10^{-14}	0.633	8.900×10^{-4}	0.250
ch6z	8.200×10^{-19}	0.499	1.560×10^{-7}	2.500×10^{-14}	0.633	1.400×10^{-3}	0.250
ch6v	5.141×10^{-13}	0.147	1.671×10^{-5}	2.200×10^{-13}	0.633	1.900×10^{-3}	0.250
pp4z	1.886×10^{-17}	0.474	6.545×10^{-6}	2.500×10^{-14}	0.633	2.818×10^{-4}	0.365
pp3d	1.790×10^{-13}	0.407	1.776×10^{-5}	2.200×10^{-13}	0.633	1.660×10^{-3}	0.400
pp2d	1.000×10^{-15}	0.309	4.581×10^{-6}	2.200×10^{-13}	0.633	1.660×10^{-3}	0.400
pp1z	2.570×10^{-17}	0.272	3.162×10^{-5}	2.500×10^{-14}	0.633	1.413×10^{-4}	0.365
bf3d	6.109×10^{-14}	0.193	1.000×10^{-4}	2.200×10^{-13}	0.633	1.660×10^{-3}	0.400
bf2z	8.100×10^{-17}	0.617	1.180×10^{-7}	2.500×10^{-14}	0.633	8.900×10^{-4}	0.250
tr3d	6.109×10^{-14}	0.193	1.000×10^{-4}	2.200×10^{-13}	0.633	1.660×10^{-3}	0.400
tr2z	8.100×10^{-17}	0.617	1.180×10^{-7}	2.500×10^{-14}	0.633	8.900×10^{-4}	0.250
pcM38/pcF38	3.000×10^{-19}	0.286	3.691×10^{-6}	3.000×10^{-18}	0.286	3.691×10^{-6}	0.000
pcM39/pcF39	6.200×10^{-18}	0.059	4.610×10^{-6}	6.200×10^{-17}	0.059	4.610×10^{-6}	0.000
pcM1z/pcF1z	9.300×10^{-20}	0.349	2.120×10^{-7}	9.300×10^{-19}	0.349	2.120×10^{-7}	0.000
pcM2z/pcF2z	2.400×10^{-18}	0.257	2.250×10^{-6}	2.400×10^{-17}	0.257	2.250×10^{-6}	0.000
pcM5z/pcF5z	2.400×10^{-18}	0.257	2.250×10^{-6}	2.400×10^{-18}	0.257	2.250×10^{-6}	0.000
pcM6z/pcF6z	1.100×10^{-19}	0.499	1.560×10^{-7}	1.100×10^{-19}	0.499	1.560×10^{-7}	0.000
pcM4p/pcF4p	7.700×10^{-19}	0.474	6.545×10^{-6}	7.700×10^{-19}	0.474	6.545×10^{-6}	0.000

Table B-3. Calibrated Parameters for the Present-Day, 50th Percentile Infiltration Scenario, Used for Simulations with the 50th Percentile Infiltration Scenarios of the Present-Day, Monsoon, and Glacial Transition, Post-10,000 yr Climates (Continued)

Model Layer	k_M (m^2)	m_M (–)	α_M (1/Pa)	k_F (m^2)	m_F (–)	α_F (1/Pa)	γ (–)
tcwFf				1.000×10^{-10}	0.633	1.000×10^{-2}	0.287
ptnFf				5.162×10^{-11}	0.633	4.645×10^{-3}	0.166
tswFf				1.000×10^{-10}	0.633	3.162×10^{-4}	0.200
chnFf				3.700×10^{-13}	0.633	2.300×10^{-3}	0.200

Output DTN: LB07043DCRXPRP.001.

Table B-4. Calibrated Parameters for the Present-Day, 90th Percentile Infiltration Scenario, Used for Simulations with the 90th Percentile Infiltration Scenarios of the Present-Day, Monsoon, and Glacial Transition, Post-10,000 yr Climates

Model Layer	k_M (m^2)	m_M (–)	α_M (1/Pa)	k_F (m^2)	m_F (–)	α_F (1/Pa)	γ (–)
tcw11	3.900×10^{-15}	0.388	1.225×10^{-5}	9.062×10^{-13}	0.633	5.012×10^{-3}	0.400
tcw12	3.162×10^{-19}	0.280	3.047×10^{-6}	1.000×10^{-10}	0.633	2.188×10^{-3}	0.400
tcw13	4.408×10^{-16}	0.259	2.449×10^{-6}	5.547×10^{-13}	0.633	1.862×10^{-3}	0.400
ptn21	2.143×10^{-14}	0.245	7.830×10^{-5}	2.515×10^{-13}	0.633	2.692×10^{-3}	0.001
ptn22	3.162×10^{-11}	0.219	1.371×10^{-4}	1.000×10^{-14}	0.633	1.380×10^{-3}	0.001
ptn23	8.681×10^{-14}	0.247	2.394×10^{-5}	1.126×10^{-13}	0.633	1.230×10^{-3}	0.001
ptn24	3.162×10^{-11}	0.182	6.918×10^{-4}	1.000×10^{-11}	0.633	2.951×10^{-3}	0.001
ptn25	2.208×10^{-12}	0.300	7.380×10^{-5}	1.000×10^{-14}	0.633	1.096×10^{-3}	0.001
ptn26	3.162×10^{-11}	0.126	5.708×10^{-4}	1.000×10^{-14}	0.633	9.550×10^{-4}	0.001
tsw31	2.623×10^{-15}	0.218	3.381×10^{-5}	6.457×10^{-11}	0.633	1.000×10^{-4}	0.001
tsw32	2.303×10^{-16}	0.290	3.430×10^{-5}	5.623×10^{-11}	0.633	1.000×10^{-4}	0.400
tsw33	3.974×10^{-17}	0.283	1.092×10^{-5}	6.166×10^{-11}	0.633	1.585×10^{-3}	0.400
tsw34	6.310×10^{-18}	0.317	1.353×10^{-6}	2.630×10^{-11}	0.633	3.164×10^{-4}	0.400
tsw35	7.535×10^{-17}	0.216	3.084×10^{-5}	7.244×10^{-11}	0.633	3.162×10^{-4}	0.400
tsw36	7.497×10^{-18}	0.442	4.181×10^{-7}	1.072×10^{-10}	0.633	1.096×10^{-3}	0.400
tsw37	7.497×10^{-18}	0.442	4.181×10^{-7}	1.072×10^{-10}	0.633	1.096×10^{-3}	0.400
tsw38	4.399×10^{-17}	0.286	4.777×10^{-6}	8.100×10^{-13}	0.633	8.913×10^{-4}	0.400
tsw3z	3.500×10^{-17}	0.059	4.610×10^{-6}	8.100×10^{-13}	0.633	1.500×10^{-3}	0.250
tsw3v	2.237×10^{-13}	0.293	4.860×10^{-5}	8.100×10^{-13}	0.633	1.500×10^{-3}	0.250
ch1z	3.500×10^{-17}	0.349	2.120×10^{-7}	2.500×10^{-14}	0.633	1.400×10^{-3}	0.250
ch1v	2.512×10^{-12}	0.240	1.280×10^{-4}	2.200×10^{-13}	0.633	2.100×10^{-3}	0.250
ch2v	3.162×10^{-11}	0.158	2.419×10^{-4}	2.200×10^{-13}	0.633	1.900×10^{-3}	0.250
ch3v	3.162×10^{-11}	0.158	2.419×10^{-4}	2.200×10^{-13}	0.633	1.900×10^{-3}	0.250
ch4v	3.162×10^{-11}	0.158	2.419×10^{-4}	2.200×10^{-13}	0.633	1.900×10^{-3}	0.250
ch5v	3.162×10^{-11}	0.158	2.419×10^{-4}	2.200×10^{-13}	0.633	1.900×10^{-3}	0.250
ch2z	5.200×10^{-18}	0.257	2.250×10^{-6}	2.500×10^{-14}	0.633	8.900×10^{-4}	0.250
ch3z	5.200×10^{-18}	0.257	2.250×10^{-6}	2.500×10^{-14}	0.633	8.900×10^{-4}	0.250
ch4z	5.200×10^{-18}	0.257	2.250×10^{-6}	2.500×10^{-14}	0.633	8.900×10^{-4}	0.250
ch5z	5.200×10^{-18}	0.257	2.250×10^{-6}	2.500×10^{-14}	0.633	8.900×10^{-4}	0.250
ch6z	7.200×10^{-19}	0.499	1.560×10^{-7}	2.500×10^{-14}	0.633	1.400×10^{-3}	0.250

Table B-4. Calibrated Parameters for the Present-Day, 90th Percentile Infiltration Scenario, Used for Simulations with the 90th Percentile Infiltration Scenarios of the Present-Day, Monsoon, and Glacial Transition, Post-10,000 yr Climates (Continued)

Model Layer	k_M (m^2)	m_M (–)	α_M (1/Pa)	k_F (m^2)	m_F (–)	α_F (1/Pa)	γ (–)
ch6v	3.397×10^{-13}	0.147	2.195×10^{-5}	2.200×10^{-13}	0.633	1.900×10^{-3}	0.250
pp4z	1.000×10^{-17}	0.474	6.310×10^{-6}	2.500×10^{-14}	0.633	2.818×10^{-4}	0.001
pp3d	1.712×10^{-13}	0.407	1.900×10^{-5}	2.200×10^{-13}	0.633	1.660×10^{-3}	0.400
pp2d	6.310×10^{-16}	0.309	2.417×10^{-6}	2.200×10^{-13}	0.633	1.660×10^{-3}	0.400
pp1z	5.012×10^{-17}	0.272	3.162×10^{-5}	2.500×10^{-14}	0.633	1.413×10^{-4}	0.001
bf3d	1.585×10^{-14}	0.193	1.585×10^{-4}	2.200×10^{-13}	0.633	1.585×10^{-4}	0.400
bf2z	8.100×10^{-17}	0.617	1.180×10^{-7}	2.500×10^{-14}	0.633	8.900×10^{-4}	0.250
tr3d	1.585×10^{-14}	0.193	1.585×10^{-4}	2.200×10^{-13}	0.633	1.585×10^{-4}	0.400
tr2z	8.100×10^{-17}	0.617	1.180×10^{-7}	2.500×10^{-14}	0.633	8.900×10^{-4}	0.250
pcM38/pcF38	3.000×10^{-19}	0.286	4.777×10^{-6}	3.000×10^{-18}	0.286	4.777×10^{-6}	0.000
pcM39/pcF39	6.200×10^{-18}	0.059	4.610×10^{-6}	6.200×10^{-17}	0.059	4.610×10^{-6}	0.000
pcM1z/pcF1z	9.300×10^{-20}	0.349	2.120×10^{-7}	9.300×10^{-19}	0.349	2.120×10^{-7}	0.000
pcM2z/pcF2z	2.400×10^{-18}	0.257	2.250×10^{-6}	2.400×10^{-17}	0.257	2.250×10^{-6}	0.000
pcM5z/pcF5z	2.400×10^{-18}	0.257	2.250×10^{-6}	2.400×10^{-18}	0.257	2.250×10^{-6}	0.000
pcM6z/pcF6z	1.100×10^{-19}	0.499	1.560×10^{-7}	1.100×10^{-19}	0.499	1.560×10^{-7}	0.000
pcM4p/pcF4p	7.700×10^{-19}	0.474	6.310×10^{-6}	7.700×10^{-19}	0.474	6.310×10^{-6}	0.000
tcwFf				1.000×10^{-10}	0.633	4.868×10^{-3}	0.284
ptnFf				2.983×10^{-11}	0.633	2.800×10^{-3}	0.200
tswFf				6.310×10^{-11}	0.633	4.564×10^{-4}	0.338
chnFf				3.700×10^{-13}	0.633	2.300×10^{-3}	0.200

Output DTN: LB07043DCRXPRP.001.

APPENDIX C
LOCATION COORDINATES AND SURFACE ELEVATIONS OF SELECTED BOREHOLES USED IN MODEL CALIBRATION AND STUDIES

Table C-1. Coordinates and Surface Elevations of Selected Boreholes

Borehole	Easting (ft)	Northing (ft)	Elevation (ft)	Easting (m)	Northing (m)	Elevation (m)
NRG-6	564187	766726	4,093	171964.2	233698.1	1,247.5
NRG-7A	562984	768880	4,209	171597.5	234354.6	1,282.9
SD-6	558608	762421	4,906	170263.7	232385.9	1,495.3
SD-7	561240	758950	4,475	171066.0	231328.0	1,364.0
SD-9	561818	767998	4,275	171242.1	234085.8	1,303.0
SD-12	561606	761957	4,343	171177.5	232244.5	1,323.8
UZ#4	566140	768716	3,941	172559.5	234304.6	1,201.2
UZ#5	566136	768593	3,954	172558.3	234267.1	1,205.2
UZ-7a	562270	760693	4,230	171379.9	231859.2	1,289.3
UZ-14	560142	771310	4,427	170731.3	235095.3	1,349.4
UZ#16	564857	760535	4,002	172168.4	231811.3	1,219.8
H-5	558908	766634	4,852	170355.2	233670.0	1,478.9
G-2	560504	778826	5,098	170841.6	237386.2	1,553.9
G-3	558483	752780	4,858	170225.6	229447.3	1,480.7
WT-24	562329	776703	4,900	171397.9	236739.1	1,493.5

Source: DTN: MO0012MWDGFM02.002 [DIRS 153777], *contacts00el.dat.*

INTENTIONALLY LEFT BLANK

APPENDIX D
PROCESSING OF SATURATIONS AND WATER POTENTIALS OF SECTION 6.2 AND CALCULATIONS OF CHLORIDE FLUX OF SECTION 6.5

This appendix presents details for postprocessing of the simulation results of Sections 6.2 and data analyses of Section 6.5.

D.1 WATER SATURATION AND WATER POTENTIAL CALCULATIONS

This part of the appendix presents details on the postprocessing of the simulation results and data analyses of water saturations, water potentials, and perched waters of Sections 6.2 in the three-dimensional UZ flow model calibration.

This postprocessing includes boreholes NRG-7a, SD-6, SD-7, SD-9, SD-12, UZ-14, UZ#16, WT-24 and G-2. The locations of the boreholes are shown in Figure 6.1-1. The field data used include matrix liquid saturations, matrix water potentials, and perched water elevations, as observed from boreholes (Table 6.2-1).

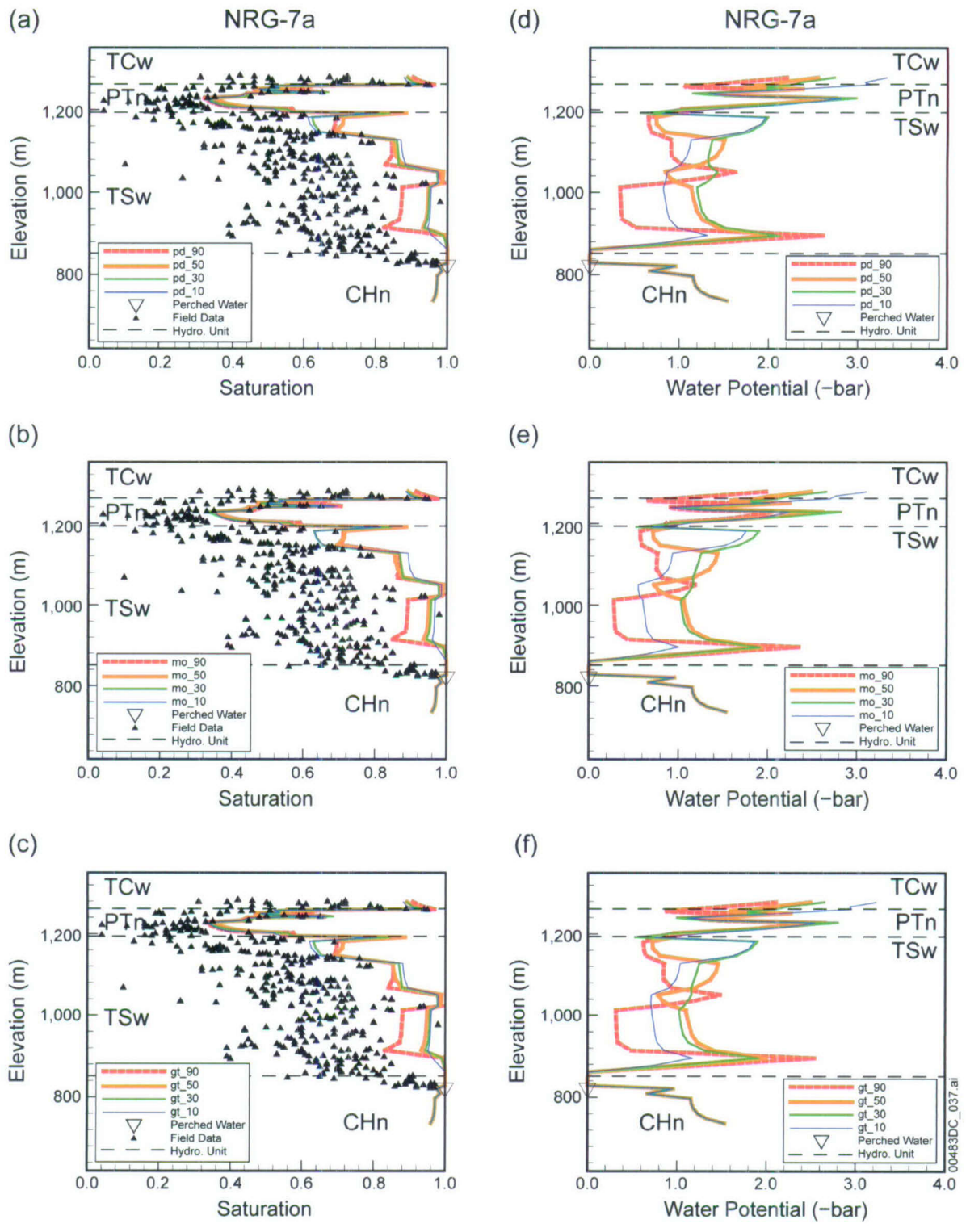

Sources: DTN: MO0109HYMXPROP.001 [DIRS 155989]; Rousseau et al. 1997 [DIRS 100178].
Output DTN: LB0706UZWATSAT.001.

Figure D.1-1. Comparison of Observed Matrix Liquid Saturations—Plots (a) to (c)—and Water Potentials —Plots (d) to (f)—at Borehole NRG-7a with Simulated Results, for the Present-Day (pd), Monsoon (mo) and Glacial Transition (gt) Infiltration Rates

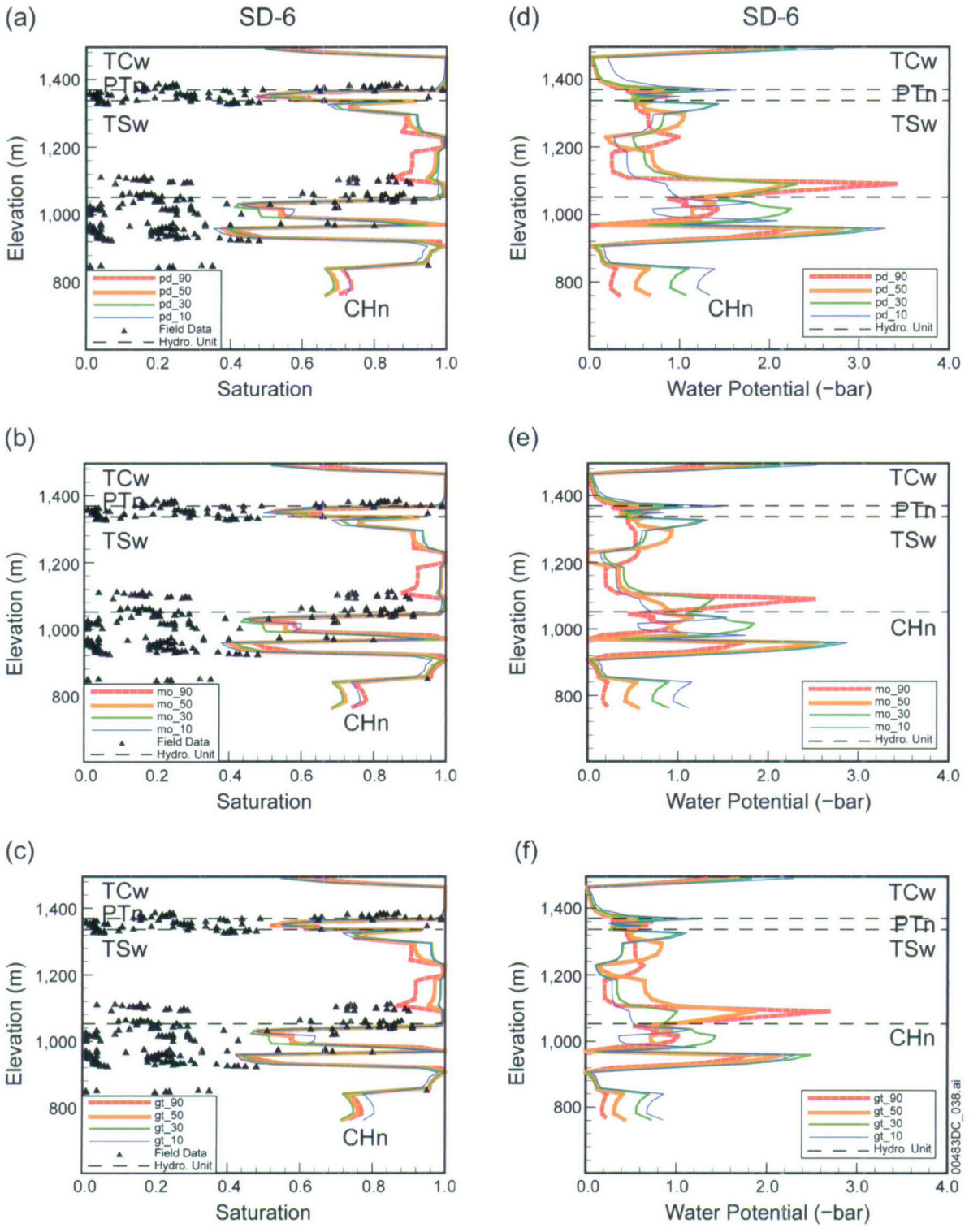

Source: DTN: GS980808312242.014 [DIRS 106748].

Output DTN: LB0706UZWATSAT.001.

Figure D.1-2. Comparison of Observed Matrix Liquid Saturations—Plots (a) to (c)—and Water Potentials—Plots (d) to (f)—at Borehole SD-6 with Simulated Results for the Present-Day (pd), Monsoon (mo) and Glacial Transition (gt) Infiltration Rates

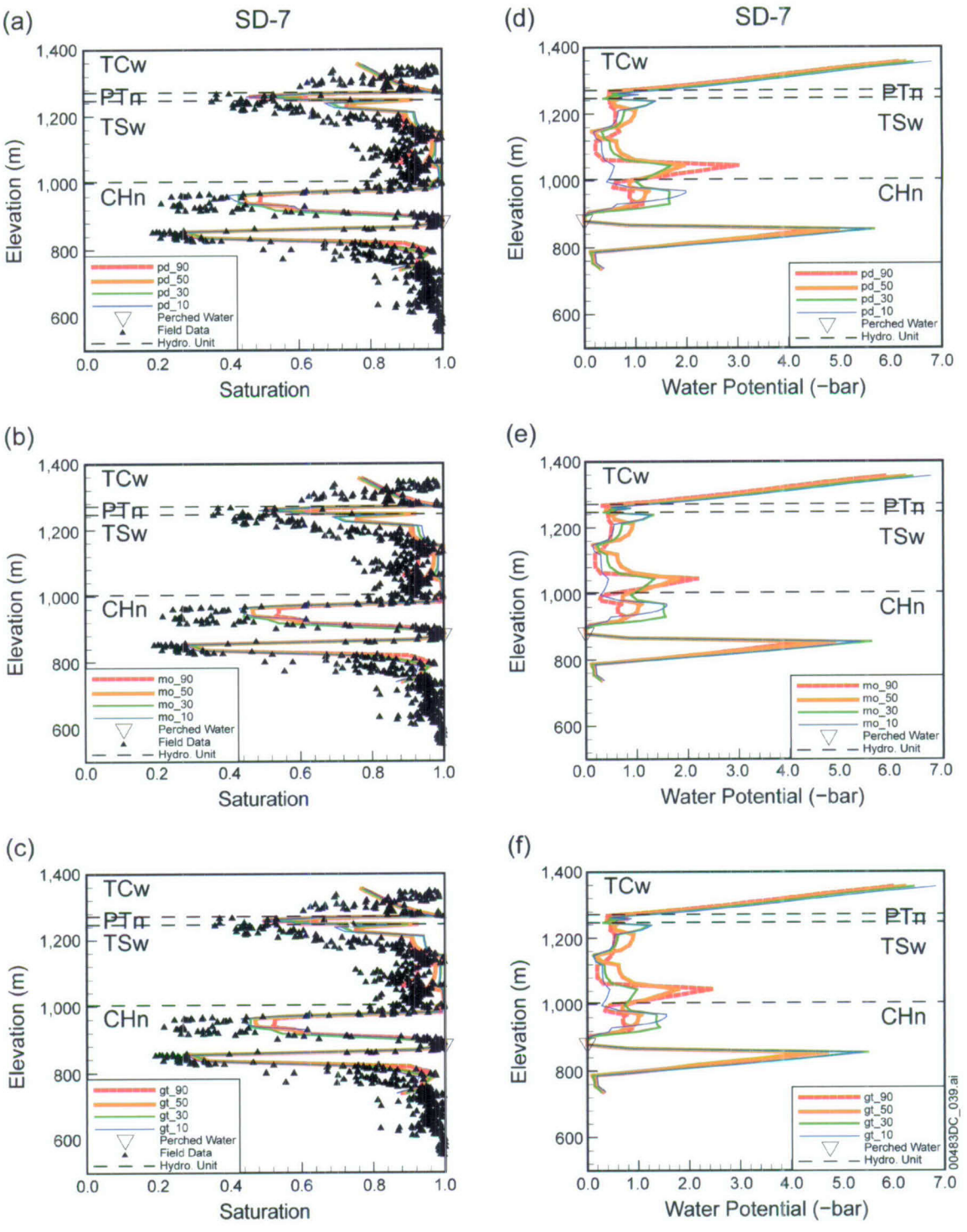

Sources: DTNs: MO0109HYMXPROP.001 [DIRS 155989]; SNT02110894001.002 [DIRS 105067].

Output DTN: LB0706UZWATSAT.001.

Figure D.1-3. Comparison of Observed Matrix Liquid Saturations—Plots (a) to (c)—and Water Potentials—Plots (d) to (f)—at Borehole SD-7 with Simulated Results for the Present-Day (pd), Monsoon (mo) and Glacial Transition (gt) Infiltration Rates

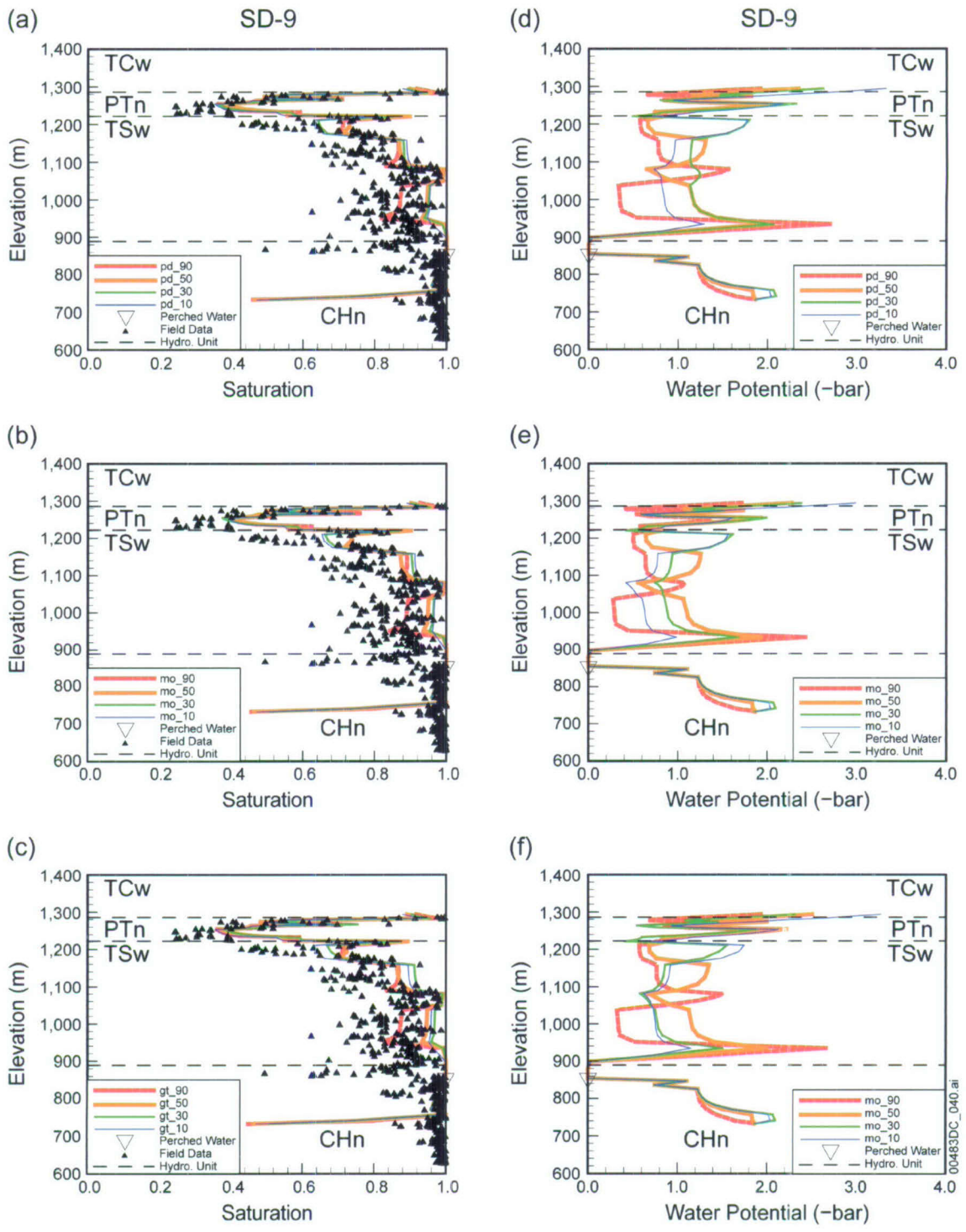

Sources: DTN: MO0109HYMXPROP.001 [DIRS 155989]; Rousseau et al. 1999 [DIRS 102097].

Output DTN: LB0706UZWATSAT.001.

Figure D.1-4. Comparison of Observed Matrix Liquid Saturations—Plots (a) to (c)—and Water Potentials—Plots (d) to (f)—at Borehole SD-9 with Simulated Results for the Present-Day (pd), Monsoon (mo) and Glacial Transition (gt) Infiltration Rates

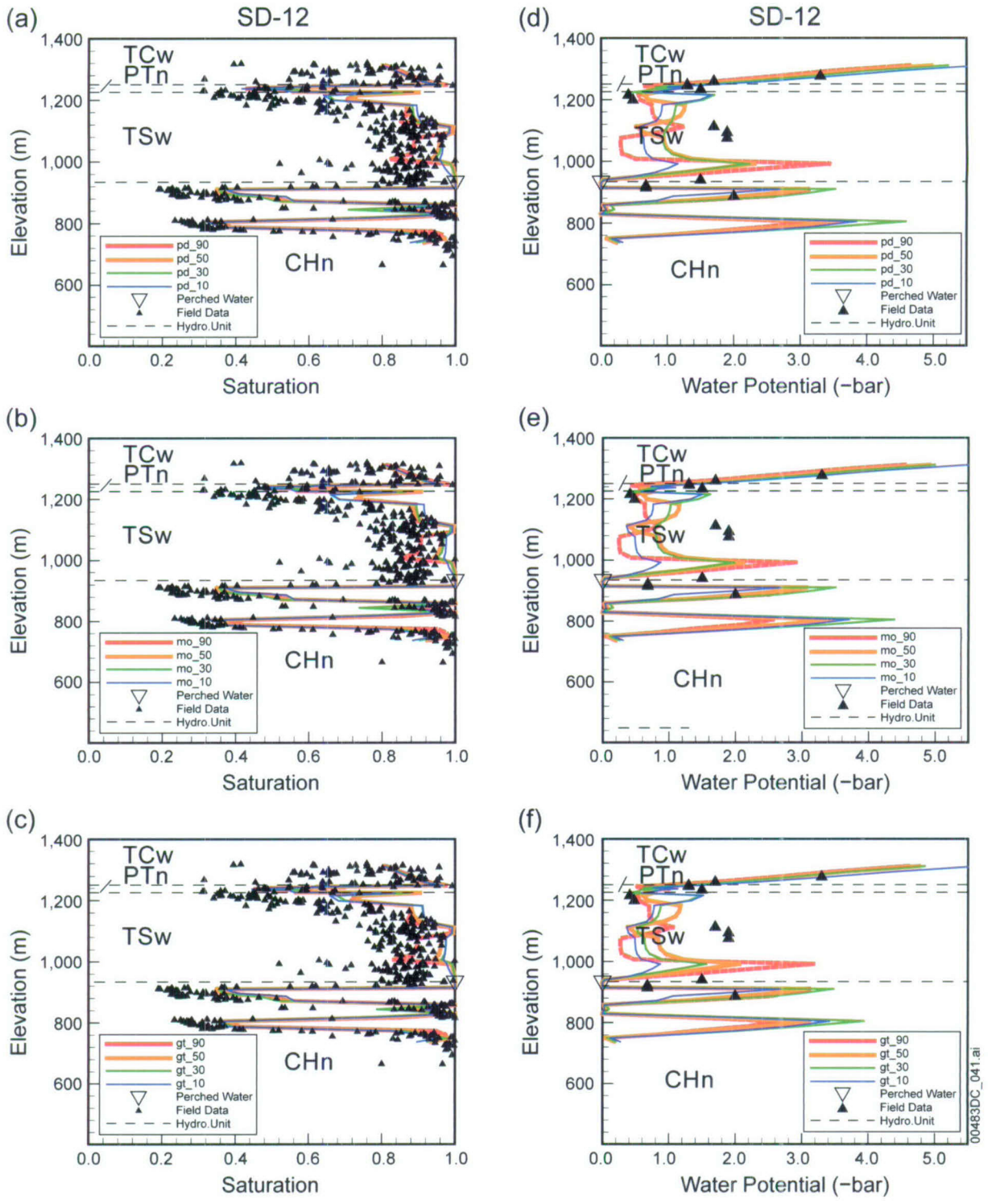

Sources: Rousseau et al. 1997 [DIRS 100178]; DTNs: MO0109HYMXPROP.001 [DIRS 155989]; GS031208312232.003 [DIRS 171287].

Output DTN: LB0706UZWATSAT.001.

Figure D.1-5. Comparison of Observed Matrix Liquid Saturations—Plots (a) to (c)—and Water Potentials—Plots (d) to (f)—at Borehole SD-12 with Simulated Results for the Present-Day (pd), Monsoon (mo) and Glacial Transition (gt) Infiltration Rates

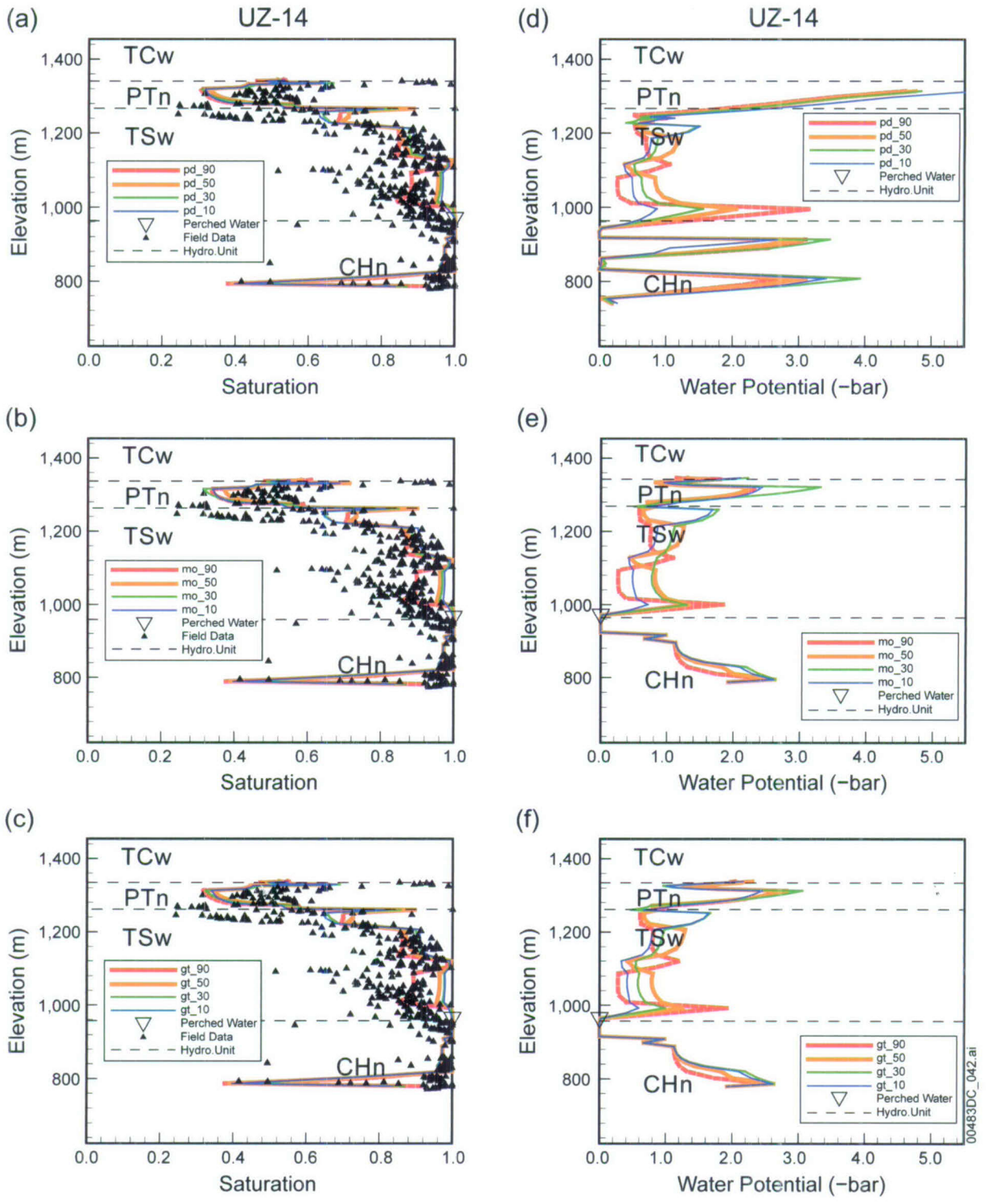

Sources: DTNs: MO0109HYMXPROP.001 [DIRS 155989]; GS040108312312.001 [DIRS 181234].
Output DTN: LB0706UZWATSAT.001.

Figure D.1-6. Comparison of Observed Matrix Liquid Saturations—Plots (a) to (c)—and Water Potentials—Plots (d) to (f)—at Borehole UZ-14 with Simulated Results for the Present-Day (pd), Monsoon (mo) and Glacial Transition (gt) Infiltration Rates

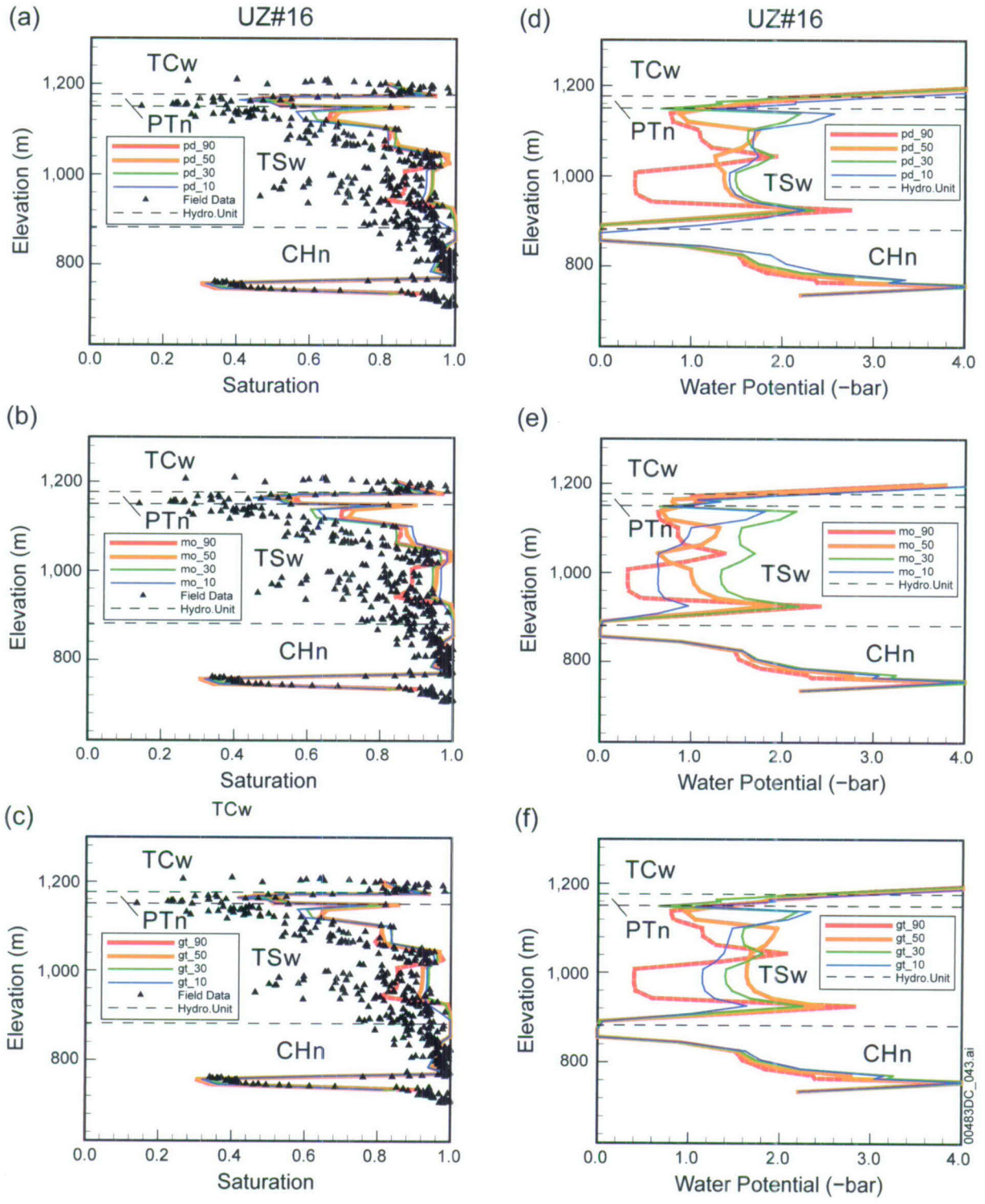

Source: DTN: MO0109HYMXPROP.001 [DIRS 155989].

Output DTN: LB0706UZWATSAT.001.

Figure D.1-7. Comparison of Observed Matrix Liquid Saturations—Plots (a) to (c)—and Water Potentials—Plots (d) to (f)—at Borehole UZ#16 with Simulated Results for the Present-Day (pd), Monsoon (mo) and Glacial Transition (gt) Infiltration Rates

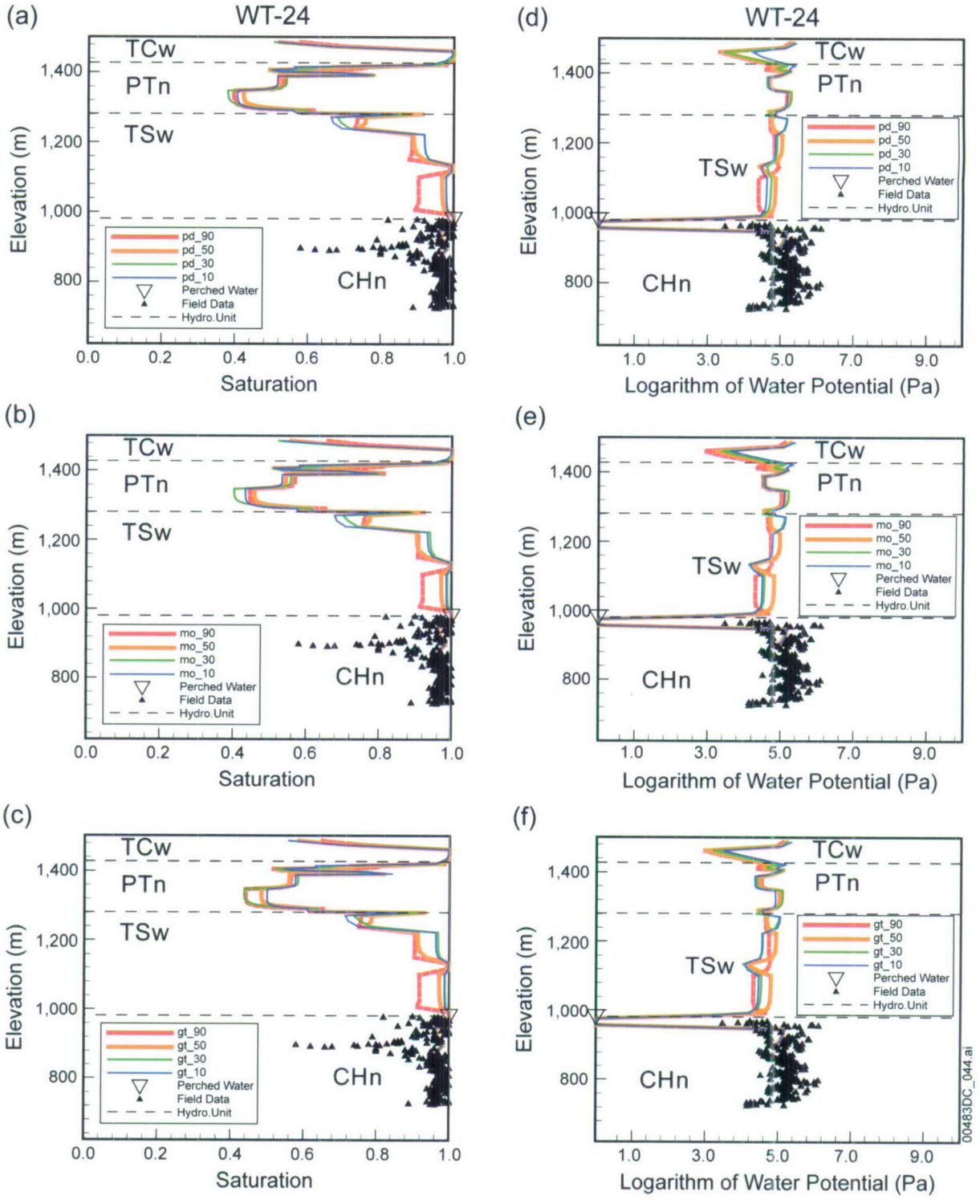

Sources: DTNs: GS980708312242.010 [DIRS 106752]; GS980508312313.001 [DIRS 109746].
Output DTN: LB0706UZWATSAT.001.

Figure D.1-8. Comparison of Observed Matrix Liquid Saturations—Plots (a) to (c)—and Water Potentials—Plots (d) to (f)—at Borehole WT-24 with Simulated Results for the Present-Day (pd), Monsoon (mo) and Glacial Transition (gt) Infiltration Rates

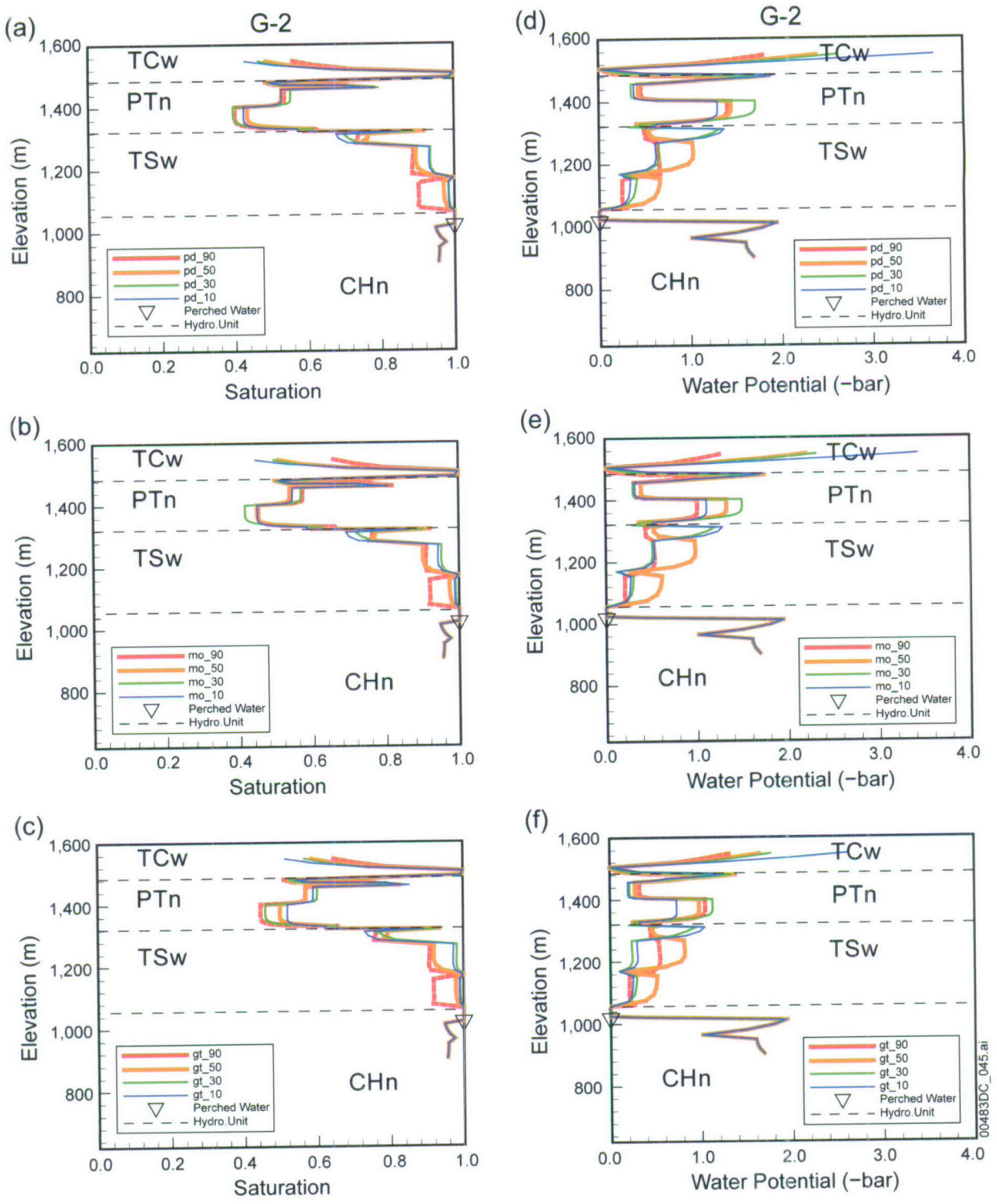

Source: DTN: GS980508312313.001 [DIRS 109746].

Output DTN: LB0706UZWATSAT.001.

Figure D.1-9. Comparison of Simulated Matrix Liquid Saturations—Plots (a) to (c)—and Water Potentials—Plots (d) to (f)—at Borehole G-2 for the Present-Day (pd), Monsoon (mo) and Glacial Transition (gt) Infiltration Rates

D.2 CHLORIDE FLUX CALCULATION

This section presents the details of calculations for preprocessing of the chloride sources in the data analyses of Section 6.5. The water and chloride fluxes used in the calculation are in Output DTN: LB0706UZWATSAT.001. The hydrological properties and grid used are the same as the three-dimensional flow model of this report.

D.2.1 FORMULATION

The chloride flux is calculated using the following formulation:

$$F_{Cl} = C_{Cl,p} \times 10^{-6} (F_{prec} + F_{runon} - F_{runoff}) \qquad \text{(Eq. D.2-1)}$$

where F_{Cl} is chloride flux (kg Cl^-/s), F_{prec} is precipitation flux (kg water/s), F_{runon} is runon (kg water/s), and F_{runoff} is runoff flux (kg water/s). $C_{Cl,p}$ is chloride concentration in precipitation and was assumed to be 0.55 mg/(kg water)l Cl^- (Sonnenthal and Bodvarsson 1999 [DIRS 117127], p. 148). These water flux terms (precipitation, runon, and runoff) are generated using software routine infil2grid V1.7 [DIRS 154793], employing the net infiltration data from the present-day infiltration map for 10th, 30th, 50th, and 90th percentile infiltrations (from DTN: SN0609T0502206.028 [DIRS 178753]). These water fluxes are organized in TOUGH2 source flux input file called GENER file, whose format is given below in Appendix D.2.2. Using Equation D.2-1, they were subsequently used to obtain the chloride mass fraction, which is also in the GENER format for the transport simulation using T2R3D V1.4 ([DIRS 146654]) of the TOUGH2 family of codes. These GENER files are organized in Output DTN: LB0706UZWATSAT.001.

D.2.2 GENER FILE FORMAT IN THE CALCULATIONS

The format of GENER file of TOUGH2 code is defined below:

Line 1: NGENER (an integer for the total number of GENER terms)
Line 2: Notation giving mean flux
Lines from 3 to NGENER:

ELEMENT, COMPONENT, FLUX, ENTHALPY
Format (A8, 28x, A5, F10.4, F10.4).

D.2.3 CALCULATION PROCEDURES

Chloride flux is calculated by taking the following steps:

Step 1: Open three input files using Excel. Then copy/paste the files into one worksheet in the order of precipitation, run-on, and runoff.

Step 2: Identify columns representing precipitation, run-on, and runoff.

Step 3: Use Equation D.2-1 to calculate chloride fluxes.

APPENDIX E
CALCULATION OF VERTICAL FLUXES, DISTRIBUTION, AND PERCENTAGE OF FRACTURE-MATRIX FLOW

Vertical fluxes at the PTn/TSw interface, at the repository layer, and at the water table are extracted and calculated in an approach discussed in this appendix. All the fluxes files are extracted from the 16 flow fields of Table 6.2-6. In particular, the output files are as follows. For present-climate *pd_10.out*, *pd_30.out*, *pd_50.out*, and *pd_90.out* (Output DTN: LB06123DPDUZFF.001); for monsoon climate, *mo_10.out*, *mo_30.out*, *mo_50.out*, and *mo_90.out* (Output DTN: LB07013DMOUZFF.001); for glacial transition climate, *gt_10.out*, *gt_30.out*, *gt_50.out*, and *gt_90.out* (Output DTN: LB07013DGTUZFF.001); for post-10k-yr climate, *pkd_q1.out*, *pkd_q2*, *pkd_q3.out*, and *pkd_q4.out* (Output DTN: LB0702UZP10KFF.002). This section documents the process for extracting fluxes from one output file (*gt-10.out*). This process is repeated for the 16 flow fields in Table 6.2-6.

E.1 EXTRACTION OF VERTICAL FLUX AT THE PAINTBRUSH NONWELDED HYDROGEOLOGIC (PTN) BOTTOM

Extracting vertical fluxes at the bottom of PTn or the top of the TSw hydrogeologic (TSw) unit requires the model mesh file, GENER, and a flow-field output file. There are four files (DTNs: LB0612PDPTNTSW.001; LB0701MOPTNTSW.001; LB0701GTPTNTSW.001; LB0702UZPTN10K.002) generated for PTn/TSw fluxes with the four climates.

In addition, the following four files are also required for identifying gridblocks, element coordinates, and connection areas in the PTn bottom and TSw top layers. The four files are *PTN_BOT.XY, PTN.BOT, TSW.TOP,* and *CONN.area.*

PTN_BOT.XY contains three columns and 2,042 rows. The three columns consist of gridblock name, x coordinate, and y coordinate. Each row corresponds to one gridblock located at the bottom layer of the PTn unit.

PTN.BOT: contains the list of 2024 gridblocks located at the bottom layer of the PTn unit.

TSW.TOP: contains the list of 2024 gridblocks located at the top layer of the TSw unit.

CONN.area: contains connection areas for all PTn bottom/TSw top vertical connections.

These four files will be used for extracting all vertical fluxes at the PTn bottom for flow fields generated by different infiltration scenarios. The extracting steps are as follows:

Step 1: Extracting flow components:

Find vertical fracture–fracture flux and matrix–matrix flux using UNIX commends (with flow field of *gt_10.out* as an example):

fgrep —f TSW.TOP gt_10.out > tsw_top.conn
fgrep —f PTN.BOT tsw_top.conn > ptn-tsw.conn
grep —v 'F0' ptn-tsw.conn > ptn-tsw_M.conn

The nonvertical connections (data rows 1,933 to 2,377) are then deleted, using a text editing application, from *ptn-tsw_M.conn*, which contains only vertical matrix–matrix flux at the PTn bottom.

The vertical fracture–fracture flux at the PTn bottom is obtained by the following steps:

grep -v 'M0' ptn-tsw.conn>ptn-tsw_F.conn

Delete data rows 1,933 to 2,377 from *ptn-tsw_F.conn* to exclude nonvertical connections.

Step 2: Importing flow components to the spreadsheet:

Use Microsoft Excel to sum the vertical fluxes from the fracture–fracture and matrix–matrix fluxes for all vertical connections as follows:

1. Open *ptn-tsw_M.conn,* and *ptn-tsw_F.conn*

2. Copy the columns for the gridblock name of connected pairs and the fluxes in these two files to a working spreadsheet (*total_ptn_flux.xls*). The connections in these files are in the same sequence.

Step 3: Handling PTn absence:

In the UZ flow model grid, Tiva Canyon welded hydrogeologic and PTn units are absent in a number of grid columns. For these columns, infiltration rates are directly added to the top layers of the TSw. Therefore, these infiltration rates are considered as bottom PTn fluxes.

Use command fgrep –f *TSW.TOP GENER>gt_10.inf* to extract infiltration data that are directly applied on TSw top. File *gt_10.inf* consists of two columns: Column 1 is the name of gridblocks directly connected to the model top boundary; Column 2 is its corresponding infiltration rate (in kg/s). Note that the *GENER* files are different for different infiltration scenarios.

There are a total of 110 direct connections to the top boundary from the TSw unit.

Step 4: Importing additional files and summation

Import *gt_10.inf* to the working spreadsheet, *total_ptn_flux.xls*.

Import *PTN_BOT.XY* to *total_ptn_flux.xls*.

Import *CONN.area* to *total_ptn_flux.xls*. (Note that all connections in different files should be in the same sequence.)

Sum fluxes along fracture–fracture, matrix–matrix connections, and infiltration corrections for related connections.

Transform the unit of total vertical flux from kg/s to mm/yr by performing $q_n = q_o*31557600.0/\text{area}$, where q_n is the vertical flux in mm/yr, q_o is the vertical flux in kg/s, and area is the corresponding connection area.

The calculations are all done using the Excel standard formula function.

Export the columns of x and y coordinates and total fluxes (mm/yr) to a text file, *gt_10_ptn.q*.

Use Tecplot to plot the vertical flux distribution map at the PTn bottom using the data file *gt_10_ptn.q*.

Table E.1-1 lists the files used to extract vertical fluxes at the PTn bottom.

Table E.1-1. Files Used in Extracting Vertical Flux at the PTn Bottom

Input Files	Mesh file	*MESH_LA.2K1*
	Model output	*gt_10.out*
	Processing used files	*PTN_BOT.XY, PTN.BOT,TSW.TOP CONN.area, GENER*
Working Files		*tsw_top.conn, ptn_tsw.conn, ptn_tsw_F.conn, ptn_tsw_M.conn, , gt_10.inf*
Working Spreadsheet and Output Files		*total_ptn_flux.xls, gt_10_ptn.q*

E.2 EXTRACTION OF VERTICAL FLUX AT THE REPOSITORY LAYER

Extraction of vertical fluxes at the repository layer requires the model MESH file and model output flow field file.

In addition, the following four mesh-related files are needed for identifying gridblocks, their coordinates, and connection areas: *REPO.XY, REPO.DAT, REPO+1.DAT,* and *CONN_rep.area.*

REPO.XY: this file contains three columns: grid block name, x, and y. There are a total of 2,042 rows for all the gridblocks located at the entire repository horizon.

REPO.DAT: this file contains 2,042 rows and only one column listing the names of the gridblocks located along the entire repository horizon.

REPO+1.DAT: this file contains 2,042 rows and one column listing the names of the gridblocks located at the layer just above the repository horizon.

CONN_rep.area: this file contains connection areas for all vertical connections at the repository layer.

These four files will be used to extract all vertical fluxes through the repository horizon, using different infiltration scenarios.

Step 1: Find vertical fracture–fracture flux and matrix–matrix flux using the following Unix commands:

- fgrep -f REPO+1.DAT gt_10.out>repo+1.conn

- fgrep -f REPO.DAT repo+1.conn>repo.conn
- grep -v 'F0' repo.conn>repo_M.conn
- grep -v 'M' repo.conn>repo_F.conn.

Step 2: Remove rows of nonvertical connections:

Use a text editor to remove rows of nonvertical connections from *repo_F.conn* and *repo_M.conn*. For vertical connections, the last three characters in the block names of two connected blocks are the same. The vertical connections are the first 2,042 connections in *repo_M.conn* and *repo_F.conn*.

Step 3: Import flow components to spreadsheet:

Open files: *repo_M.conn,* and *repo_F.conn,* in Excel, and copy the columns for gridblock name of connected cells and flux in these files to a working spreadsheet (*total_rep_flux.xls*). Ensure that all connections are in the same sequence.

Step 4: Incorporate additional files and summation:

- Import *CONN_rep.area* and *REPO.XY* to the spreadsheet

- Transform unit of flux from kg/s to mm/yr by performing:
  $q_n = q_o * 31557600.0/\text{area}$
  where q_n is vertical flux in mm/yr, q_o is vertical flux in kg/s, and area is corresponding connection area

The above calculations are performed using the Excel formulas function

- Export the columns of x and y coordinates and total flux (mm/yr) to a text file, *gt_10_rep.q*.

- Use Tecplot to plot the vertical flux distribution map at repository horizon, using the data file, *gt_10_rep.q*.

Table E.2-1 lists the files used to extract vertical fluxes at the repository layer:

Table E.2-1. Files Used to Extract Vertical Fluxes at the Repository Layer

Input Files	Mesh file	*MESH_LA.2K1*
	Model output	*gt_10.out*
	Processing used files	*REPO.XY, REPO.DAT, REPO+1.DAT* *CONN_rep.area*
Working Files		*repo_M.conn, repo_F.conn*
Working Spreadsheet and Output Files		*total_rep_flux.xls, gt_10_rep.q*

E.3 EXTRACTION OF VERTICAL FLUX AT THE DOMAIN BOTTOM

In addition to the mesh file, extraction of vertical flux at model domain bottom needs TOUGH2 output flow field file, and two files containing the bottom grid coordinates and vertical connection area (file *BT.XY* and *CONN_bt.area,*). *BT.XY* contains three columns: grid block name, x, and y. There are a total of 2,042 rows for all of the gridblocks located at the domain bottom. *CONN_bt.area* contains connection areas along all vertical connections at the domain bottom.

These two files will be used to extract all vertical fluxes through the bottom of different infiltration scenarios.

Step 1: Find vertical fracture–fracture flux and matrix–matrix flux using the following Unix commands:

- grep 'BT' gt_10.out>bt.conn
- grep 'F0' bt.conn>bt_F.conn
- grep 'M0' bt.conn>bt_M.conn.

Step 2: Sum the fracture–fracture and matrix–matrix vertical fluxes.

Use Microsoft Excel to open files *bt_M.conn* and *bt_F.conn,* and copy the columns for gridblock name of connected cells and flux in the two files to a working spreadsheet (*total_bt_flux.xls*). Note that *bt_M.conn* contains 2,042 matrix–matrix connections and *bt_F.con* has 2,042 fracture–fracture connections.

- Import "*CONN_bt.area*" and "*BT.XY*" to the spreadsheet.
- Transform unit of flux from kg/s to mm/yr by performing $q_n = q_o * 31557600.0/\text{area}$, where q_n is vertical flux in mm/yr, q_o is vertical flux in kg/s, and area is the corresponding connection area.

All of the above calculations are performed using the Excel standard formula function.

- Export the columns of x, y, and total flux (mm/yr) to a text file, *gt_10_bt.q.*
- Use Tecplot to plot the vertical flux distribution map at domain bottom using the data file, *gt_10_bt.q.*

Table E.3-1 lists the files used in extracting the vertical fluxes at the domain bottom:

Table E.3-1. Files Used in Extracting Vertical Fluxes at the Domain Bottom

Input Files	Mesh file	*MESH_LA.2K1*
	Model output	*gt_10.out*
	Processing used files	*BT.XY, CONN_bt.area*
Working Files		*bt_F.conn, bt_M.conn*
Working Spreadsheet and Output Files		*total_bt_flux.xls, gt_10_bt.q*

E.4 CALCULATION OF PERCENTAGE OF FLUX IN FRACTURES, MATRIX, AND FAULTS

Step 1: Calculate the total flux in fractures at the entire repository horizon as follows:

- Copy the columns of fracture–fracture flux and total flux, and paste them into a working spreadsheet from *total_rep_flux.xls* (see Section E.2 for more information about this file).
- Sum the cells in columns of fracture–fracture flux for total fracture flux (qf).
- Sum the cells in the column of total flux to obtain total vertical flux at the repository horizon (q).
- Percentage is computed by qf/q*100%.

Step 2: Calculate total flux in the matrix at the repository layer:

- Total matrix flux (qm), qm =q-qf. Its percentage is qm/q*100%.

The total fracture and matrix flux computed in Step 1 and 2 includes flux through faults. To exclude flux through faults, the total fracture and matrix flux should be deducted with fault flux computed in step3.

Step 3: Calculate total flux in faults at the repository layer.

- Export the columns of the connected gridblock names, fracture, matrix, and total flux to a text file from *total_rep_flux.xls.*
- Edit the text by deleting characters at columns 1 to 5 and columns 7 to 8 from data column of gridblock names. Those gridblocks with upper–case letters in their names at Column 6 are fault blocks.

- Import the text file to a working spreadsheet. Use the Excel sort function to sort the data by the sixth character of the gridblock name.
- Delete the rows with lower–case letters at column 6 of the gridblock names.
- Sum the total flux column. Total fault flux is obtained (qfa).
- Sum the fracture flux and matrix flux column to obtain overlap part of fracture flux and matrix flux with fault flux. Use these results to exclude fault flux from fracture and matrix flux computed at step 1 and 2.
- Fault flux percentage is calculated by qfa/q*100%.

Step 4: Calculate the total vertical flux in fractures and the matrix at water table

- Sum the columns of fracture–fracture flux and total flux in working file *total_bt_flux.xls* (Section E.2, Step 2). Total fracture–fracture flux (qf) and total flux (q) are obtained.
- Fracture flux percentage is computed by qf/q*100%.
- Matrix flux percentage is computed by (1-qf/q)*100%.

The calculated total fracture and matrix flux include fault flux. The fault flux can be excluded by reducing the amount of fault flux computed at Step 5.

Step 5: Calculate the total flux in faults at the water table:

Total flux in faults at the water table is calculated in the same way as the calculation of total flux in faults at the repository horizon, except the flux data is from *total_bt_flux.xls*.

E.5 EXTRACTION OF VERTICAL FLUX WITHIN THE REPOSITORY FOR CUMULATIVE FLUX DISTRIBUTION

The list of gridblock names is needed for extracting the vertical flux through the repository footprint. There are a total of 532 gridblocks within the repository zone; the gridblock names are listed in *REPO_Z*.

- Export flux data at the repository horizon from the spreadsheet *total_rep_flux.xls* (E.2, Step 3) to a text file *total_rep_q.dat*.
- Use Unix command:

  fgrep –f *REPO_Z total_rep_q.dat>rep_zone_q.dat*
  to extract fluxes through gridblocks within the repository zone.

- Import *rep_zone_q.dat* to a spreadsheet and copy the columns of fluxes to a working spreadsheet.

- Calculate flux frequency using the histogram function under the Data Analysis menu of Excel, and plot the frequency distribution using the Graph function.

E.6 CUMULATIVE FLUX DISTRIBUTION

- Copy all cumulative flux distribution frequency data (from Section E.5) to a working spreadsheet

- Plot the cumulative flux distribution curve using the Excel graph function.

APPENDIX F
SIMULATED PERCOLATION FLUXES AT REPOSITORY HORIZON AND WATER TABLE FOR 10TH, 30TH, 50TH, AND 90TH PERCENTILE INFILTRATION RATES OF PRESENT-DAY, MONSOON, GLACIAL TRANSITION, AND POST-10,000-YEAR CLIMATES

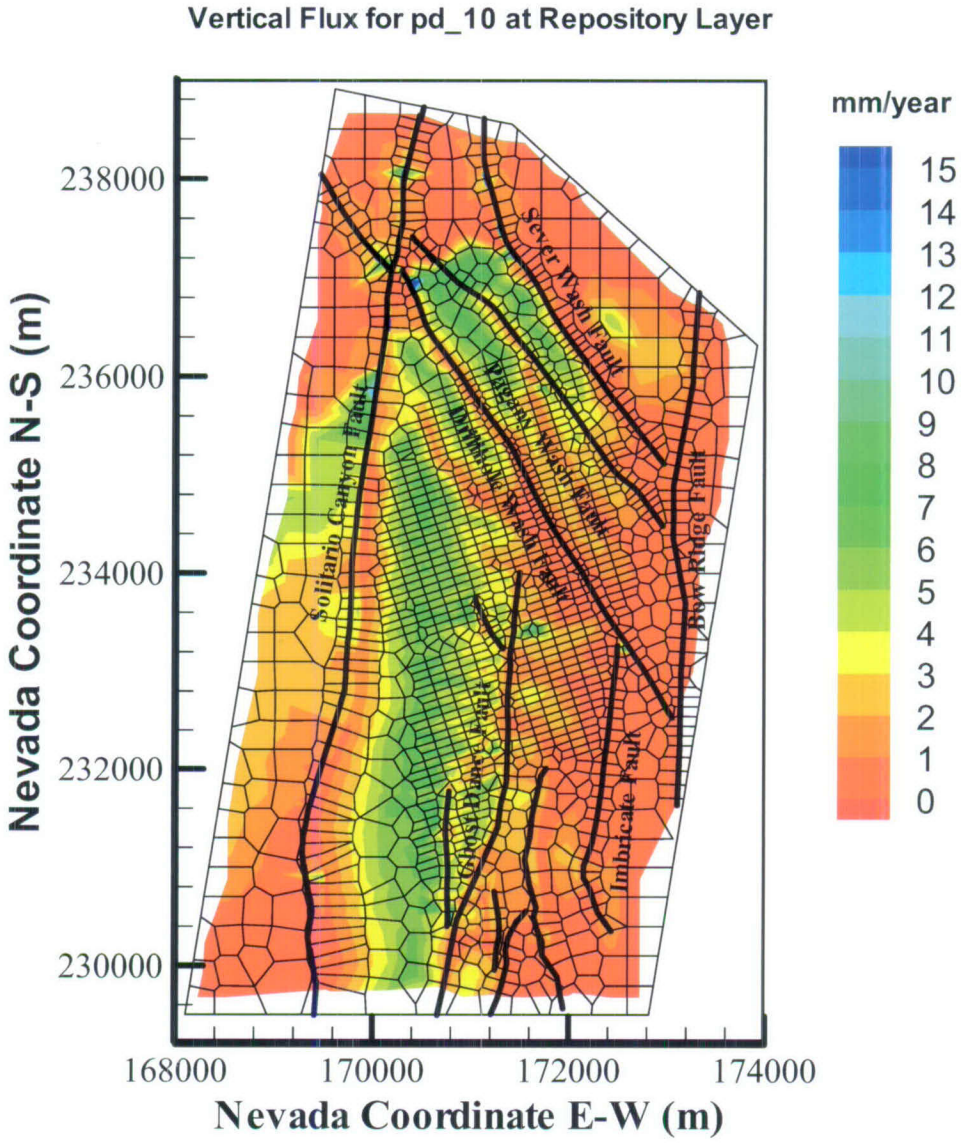

Output DTN: LB06123DPDUZFF.001.

Figure F-1. Simulated Percolation Fluxes at the Repository Horizon under the Present-Day, 10th Percentile Infiltration Scenario

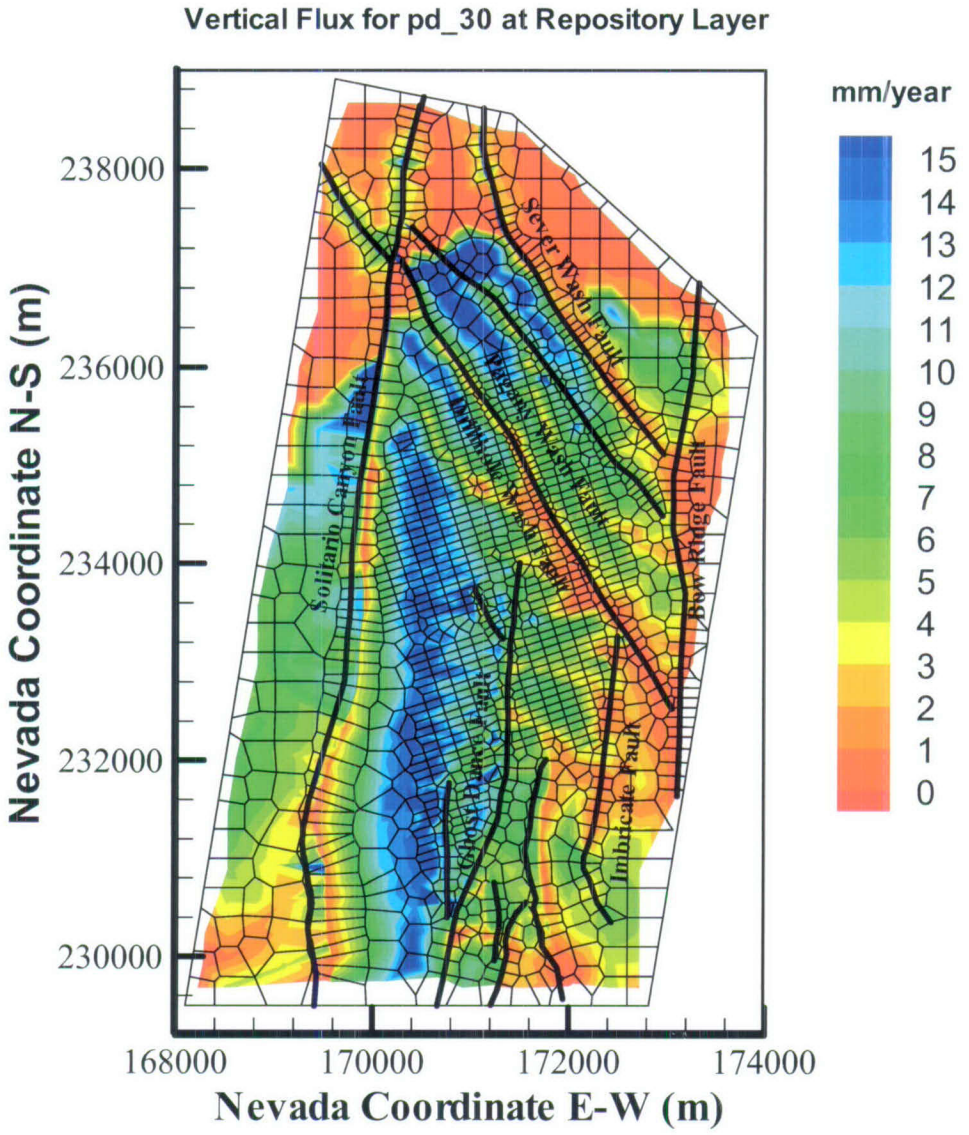

Output DTN: LB06123DPDUZFF.001.

Figure F-2. Simulated Percolation Fluxes at the Repository Horizon under the Present-Day, 30th Percentile Infiltration Scenario using the Results of Simulation pd_30

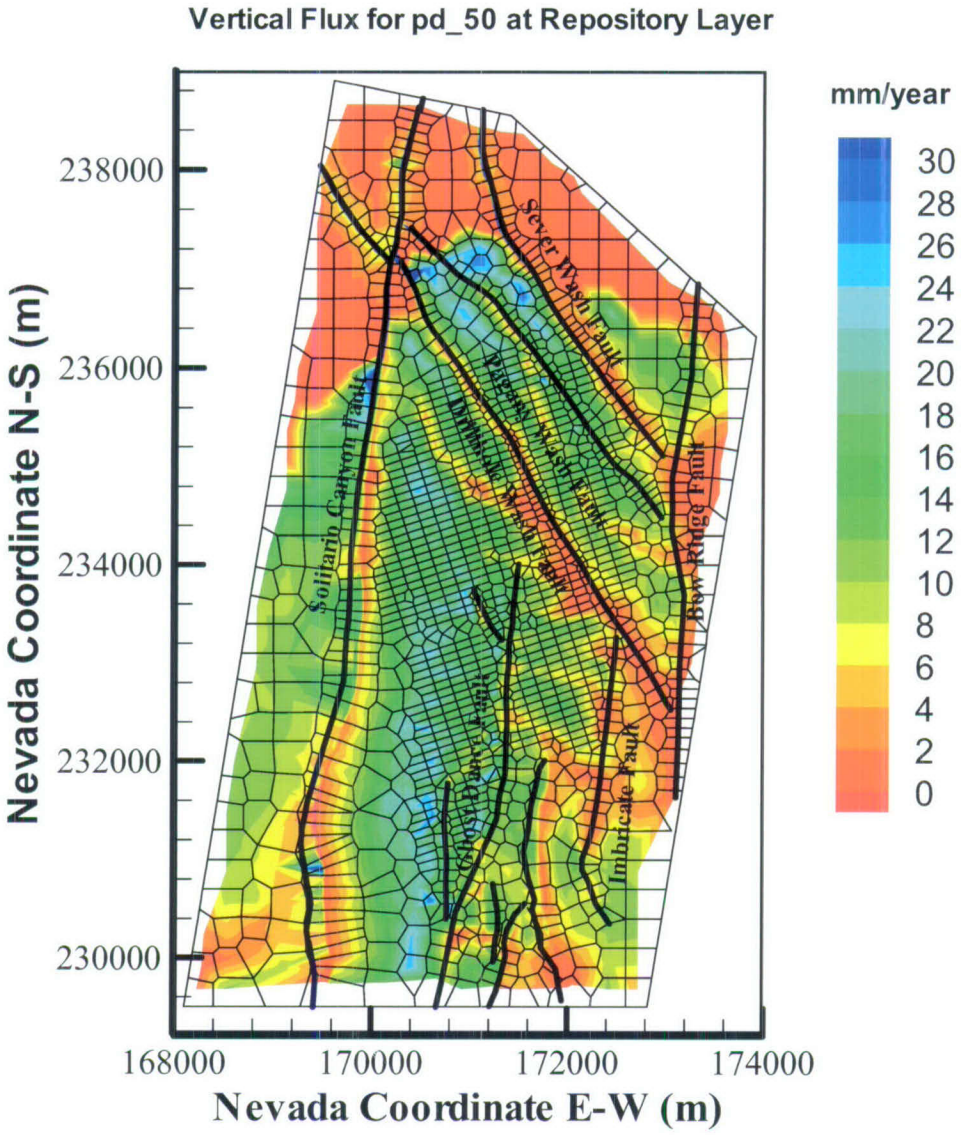

Output DTN: LB06123DPDUZFF.001.

Figure F-3. Simulated Percolation Fluxes at the Repository Horizon under the Present-Day, 50th Percentile Infiltration Scenario using the Results of Simulation pd_50

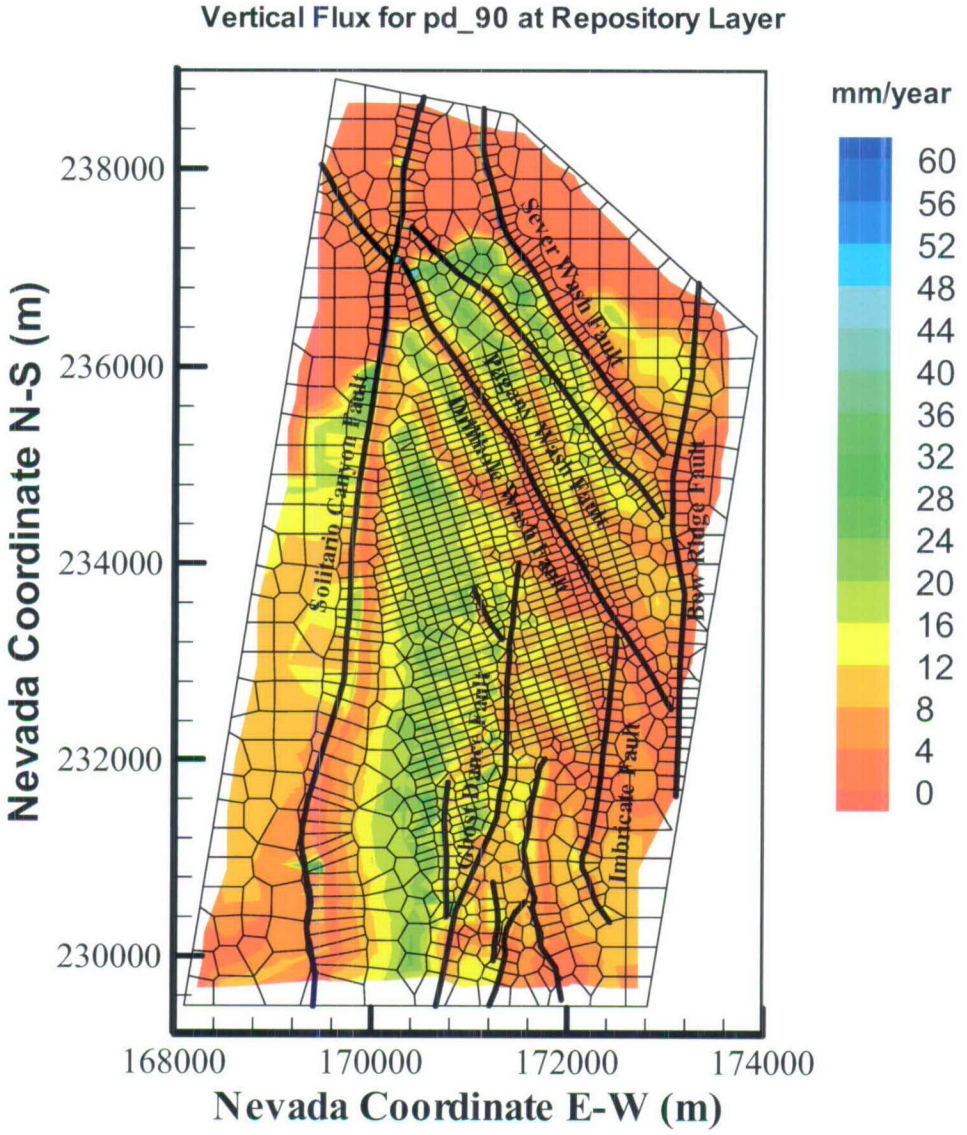

Output DTN: LB06123DPDUZFF.001.

Figure F-4. Simulated Percolation Fluxes at the Repository Horizon under the Present-Day, 90th Percentile Infiltration Scenario using the Results of Simulation pd_90

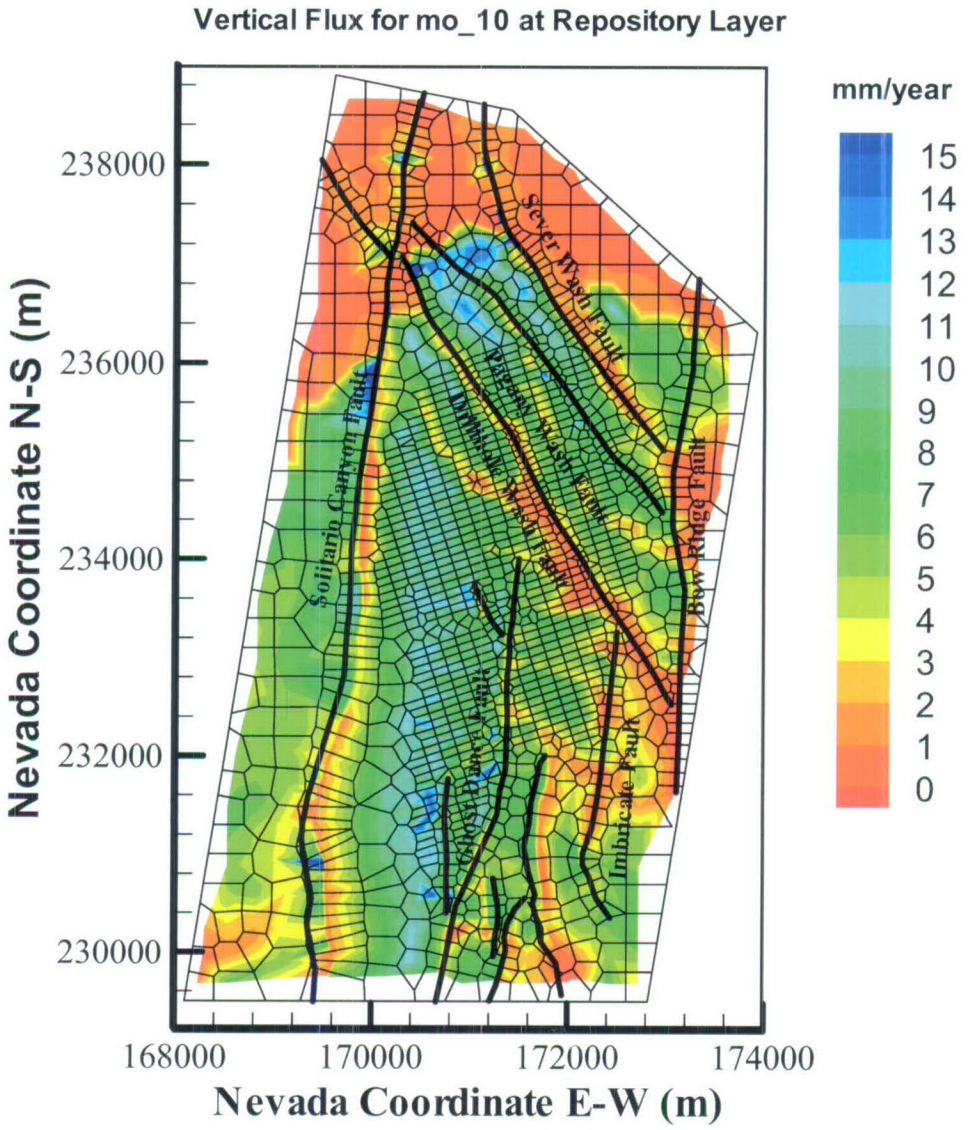

Output DTN: LB07013DMOUZFF.001.

Figure F-5. Simulated Percolation Fluxes at the Repository Horizon under the Monsoon, 10th Percentile Infiltration Scenario

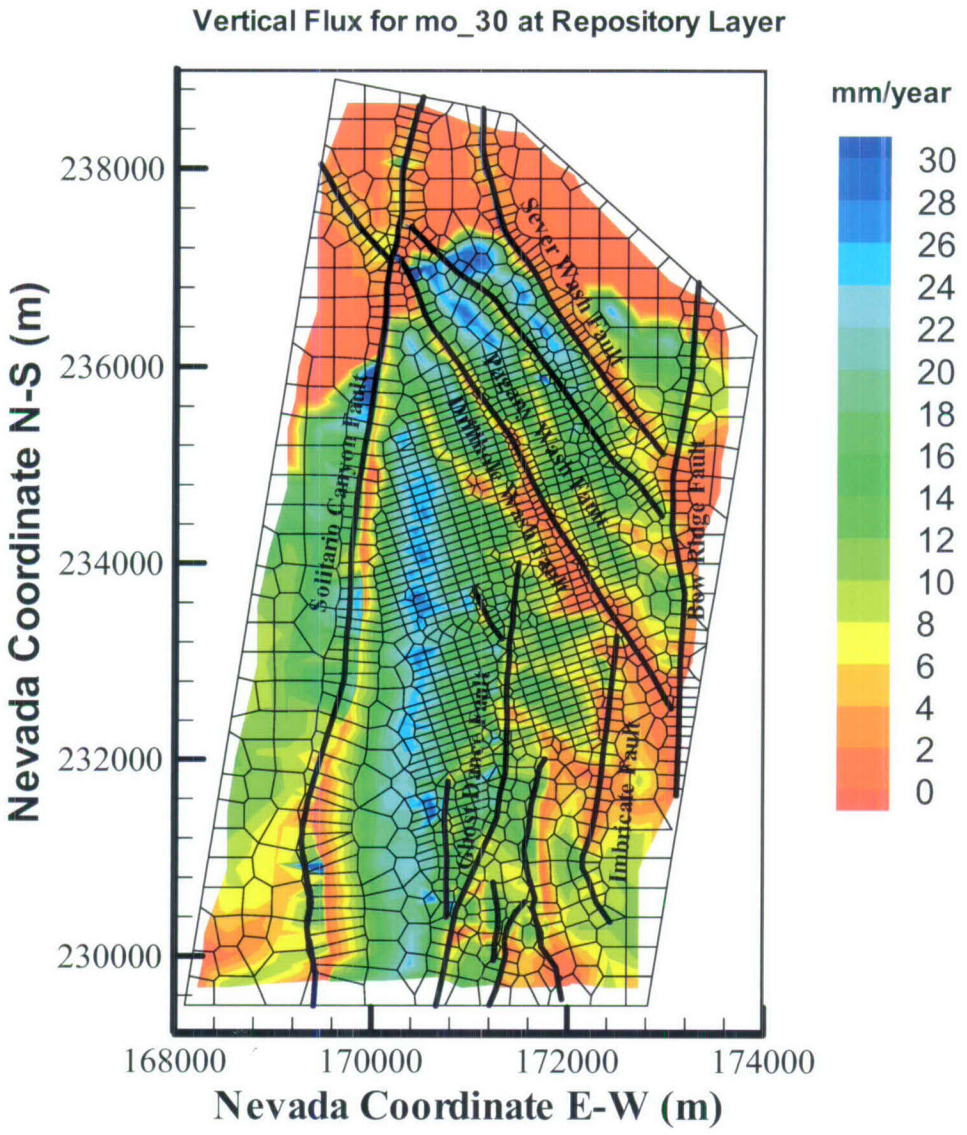

Output DTN: LB07013DMOUZFF.001.

Figure F-6. Simulated Percolation Fluxes at the Repository Horizon under the Monsoon, 30th Percentile Infiltration Scenario using the Results of Simulation mo_30

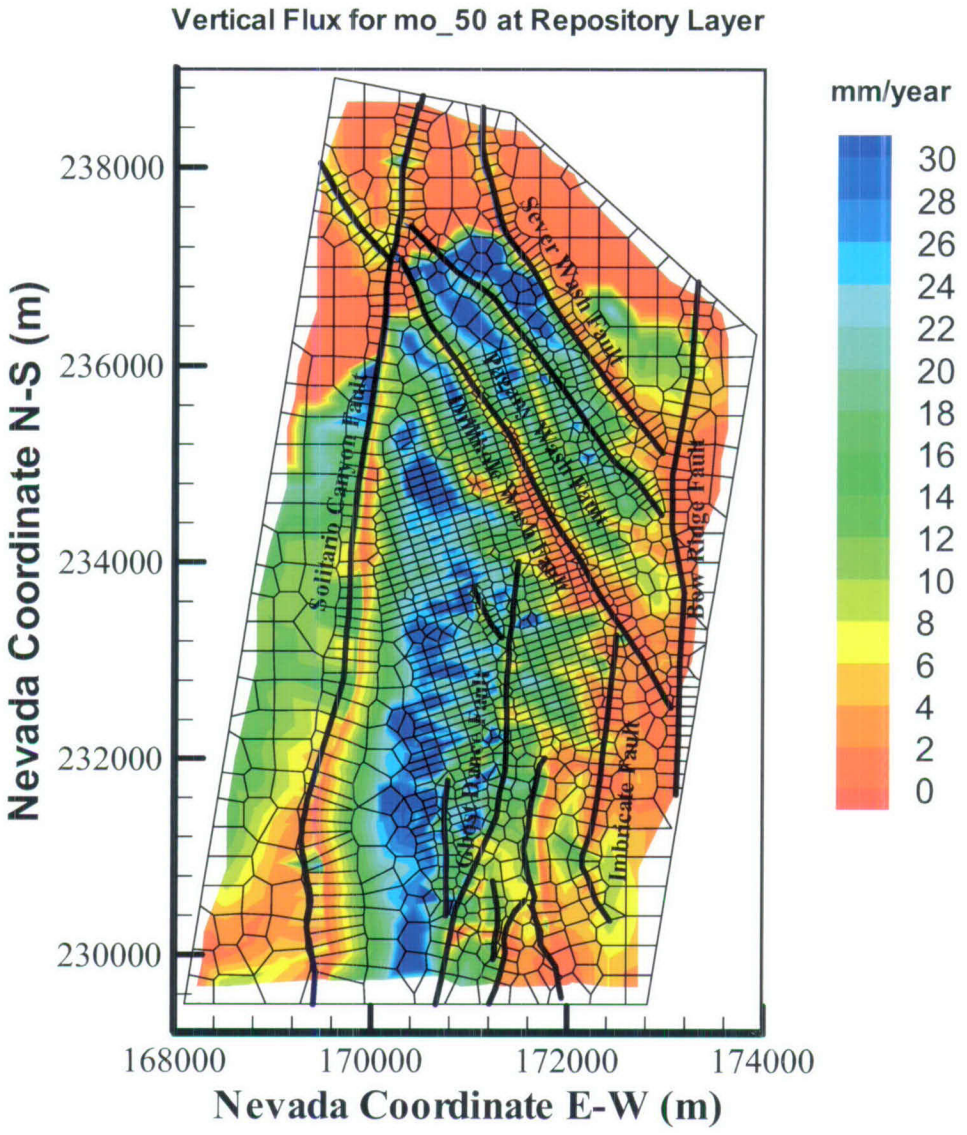

Output DTN: LB07013DMOUZFF.001.

Figure F-7. Simulated Percolation Fluxes at the Repository Horizon under the Monsoon, 50th Percentile Infiltration Scenario using the Results of Simulation mo_50

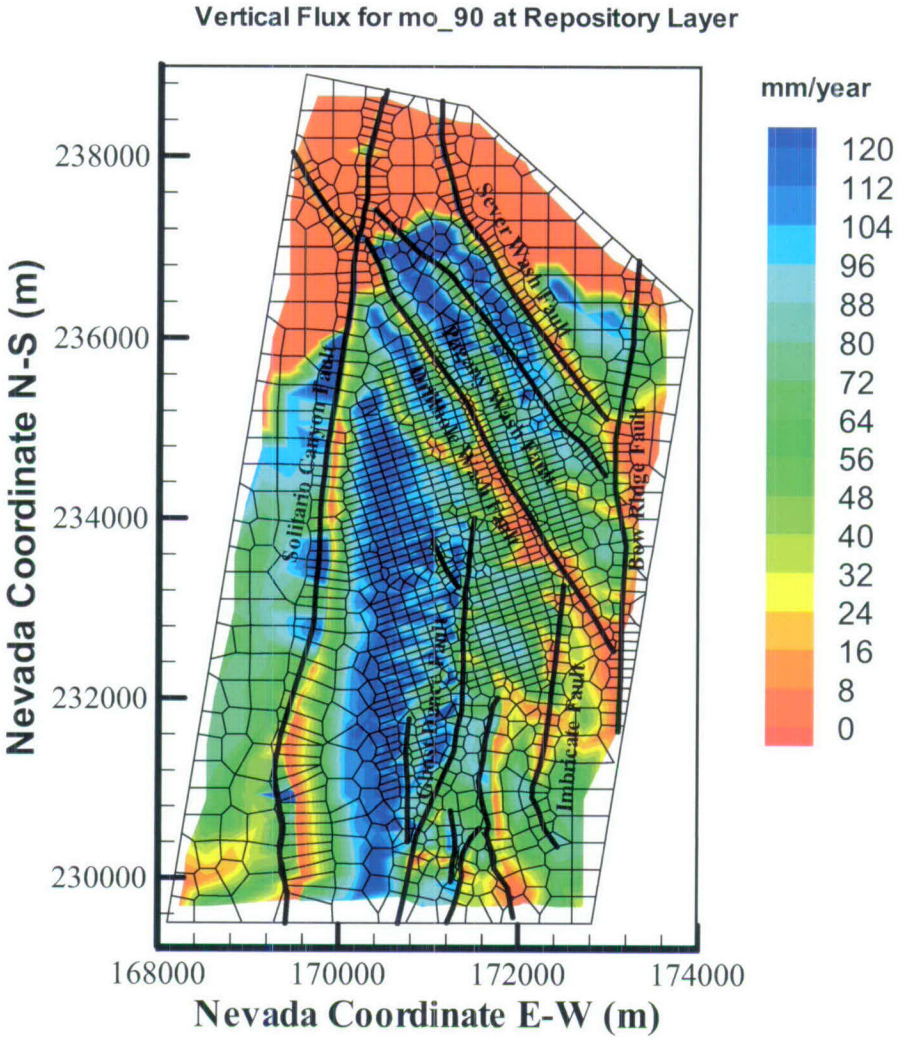

Output DTN: LB07013DMOUZFF.001.

Figure F-8. Simulated Percolation Fluxes at the Repository Horizon under the Monsoon, 90th Percentile Infiltration Scenario using the Results of Simulation mo_90

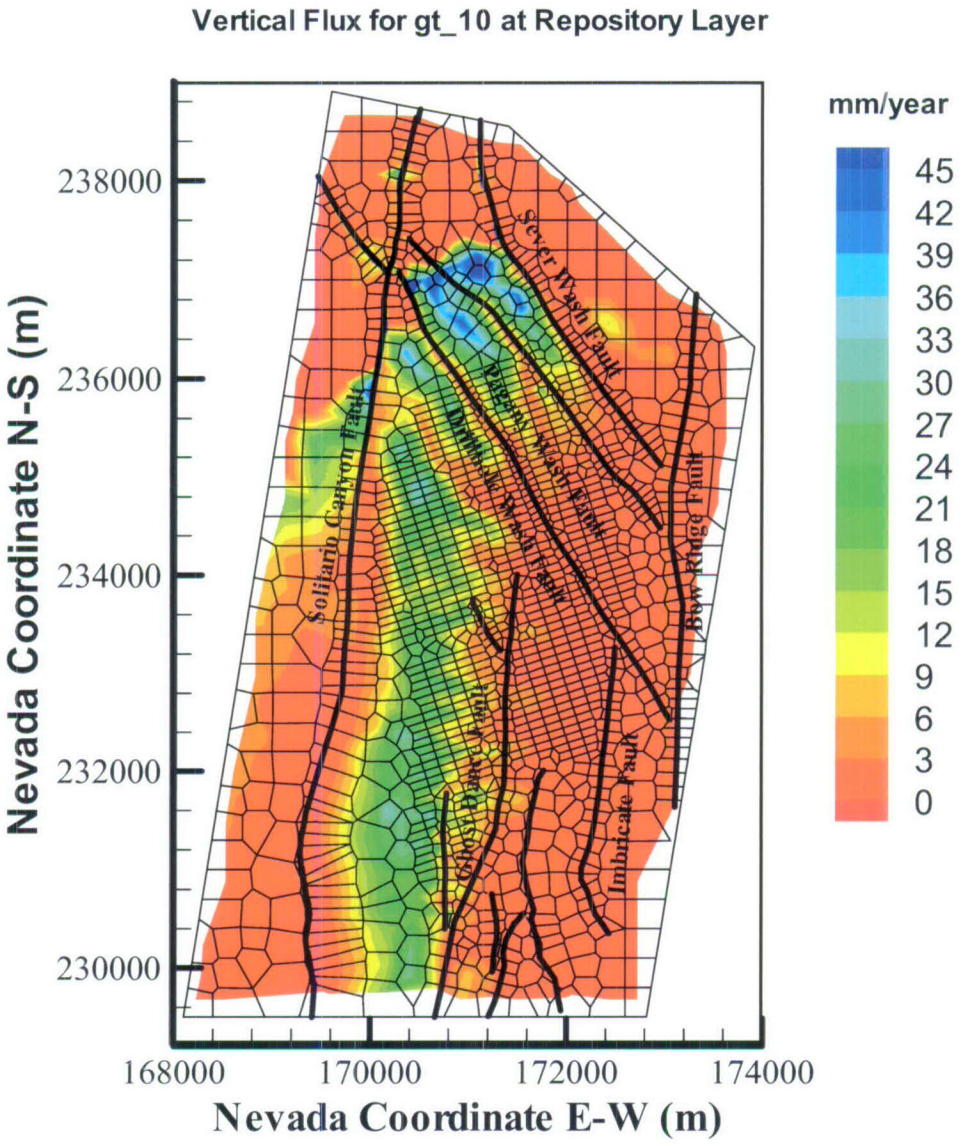

Output DTN: LB07013DGTUZFF.001.

Figure F-9. Simulated Percolation Fluxes at the Repository Horizon under the Glacial-transition, 10th Percentile Infiltration

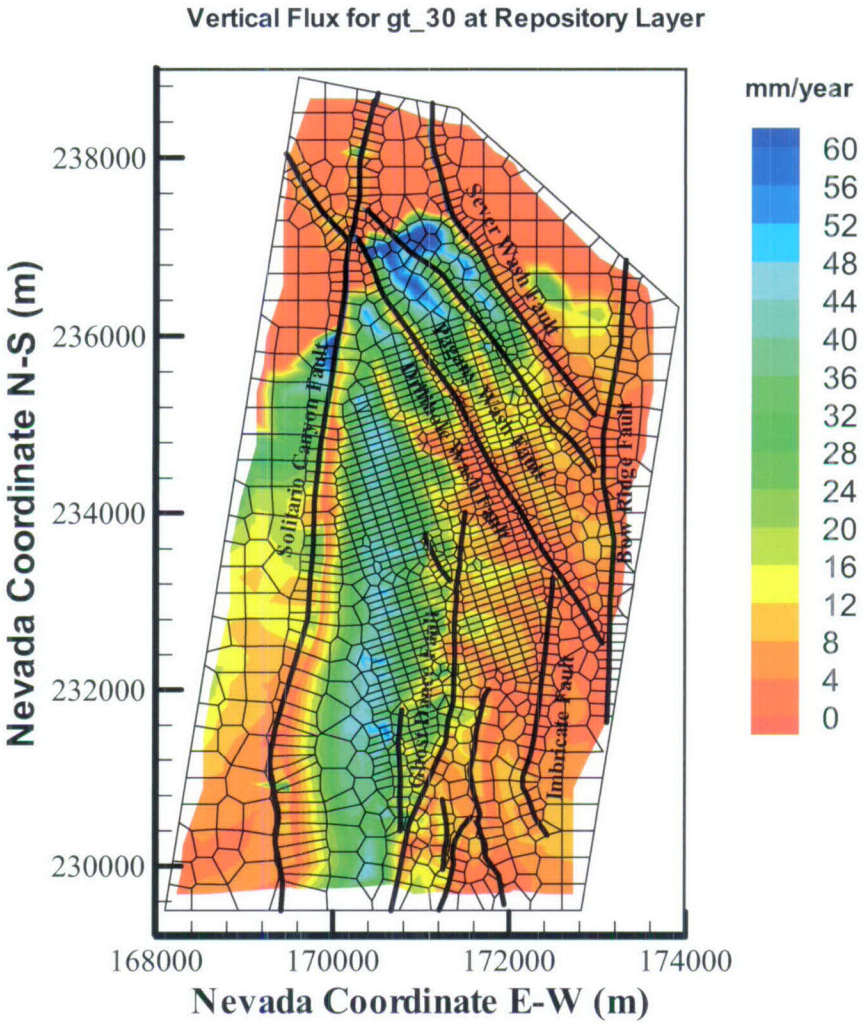

Output DTN: LB07013DGTUZFF.001.

Figure F-10. Simulated Percolation Fluxes at the Repository Horizon under the Glacial-transition, 30th Percentile Infiltration Scenario using the Results of Simulation gt_30

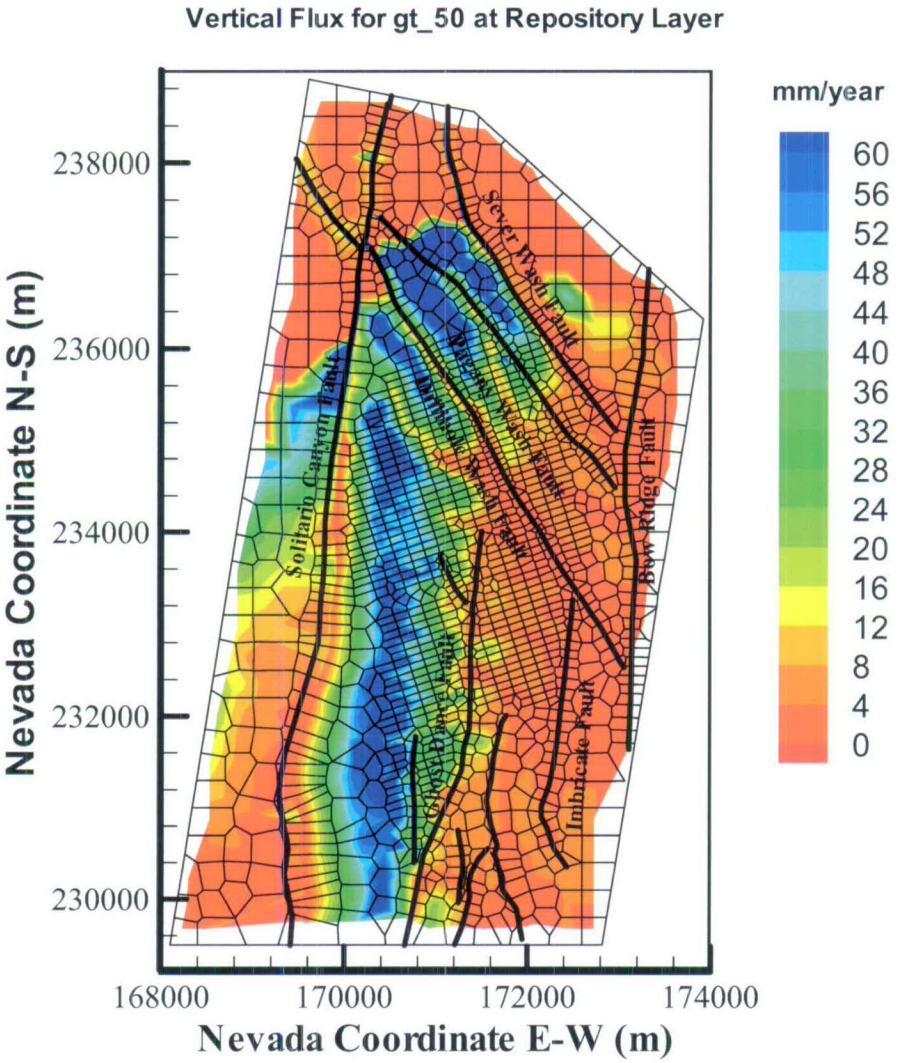

Output DTN: LB07013DGTUZFF.001.

Figure F-11. Simulated Percolation Fluxes at the Repository Horizon under the Glacial-transition, 50th Percentile Infiltration Scenario using the Results of Simulation gt_50

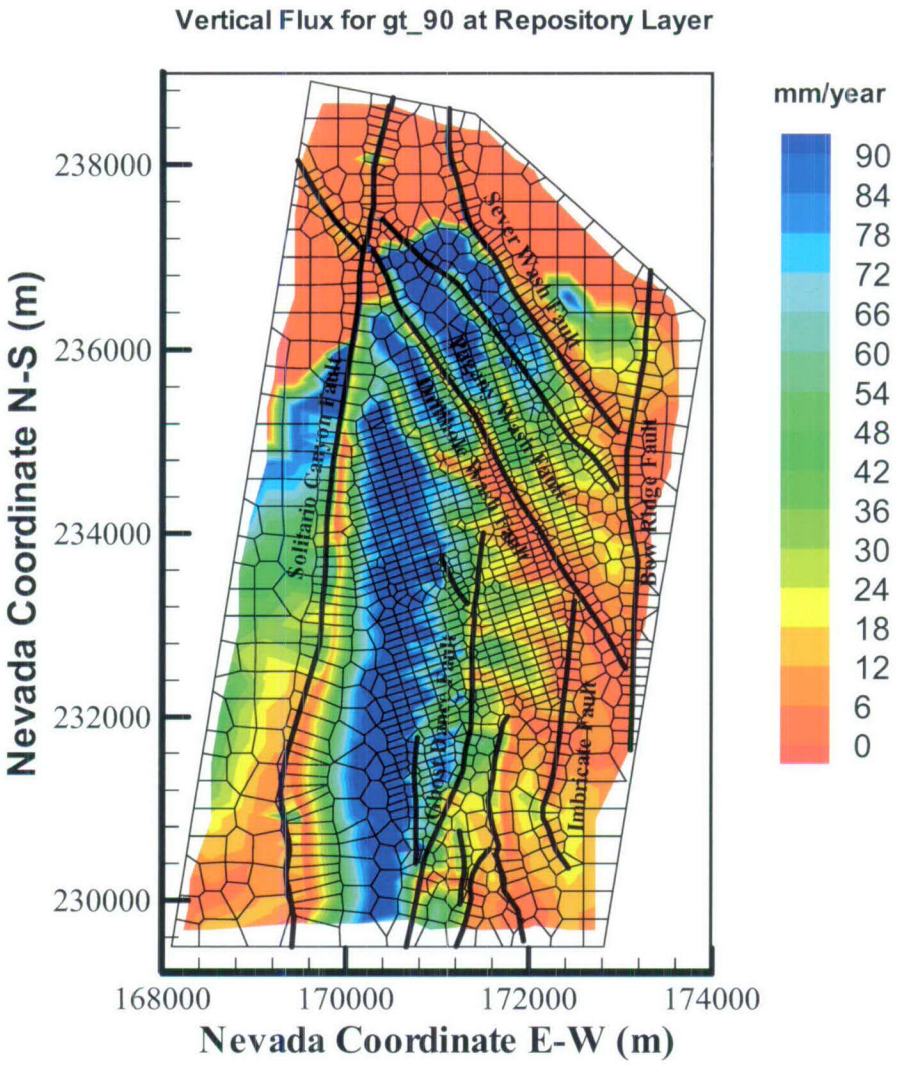

Output DTN: LB07013DGTUZFF.001.

Figure F-12. Simulated Percolation Fluxes at the Repository Horizon under the Glacial-transition, 90th Percentile Infiltration Scenario using the Results of Simulation gt_90

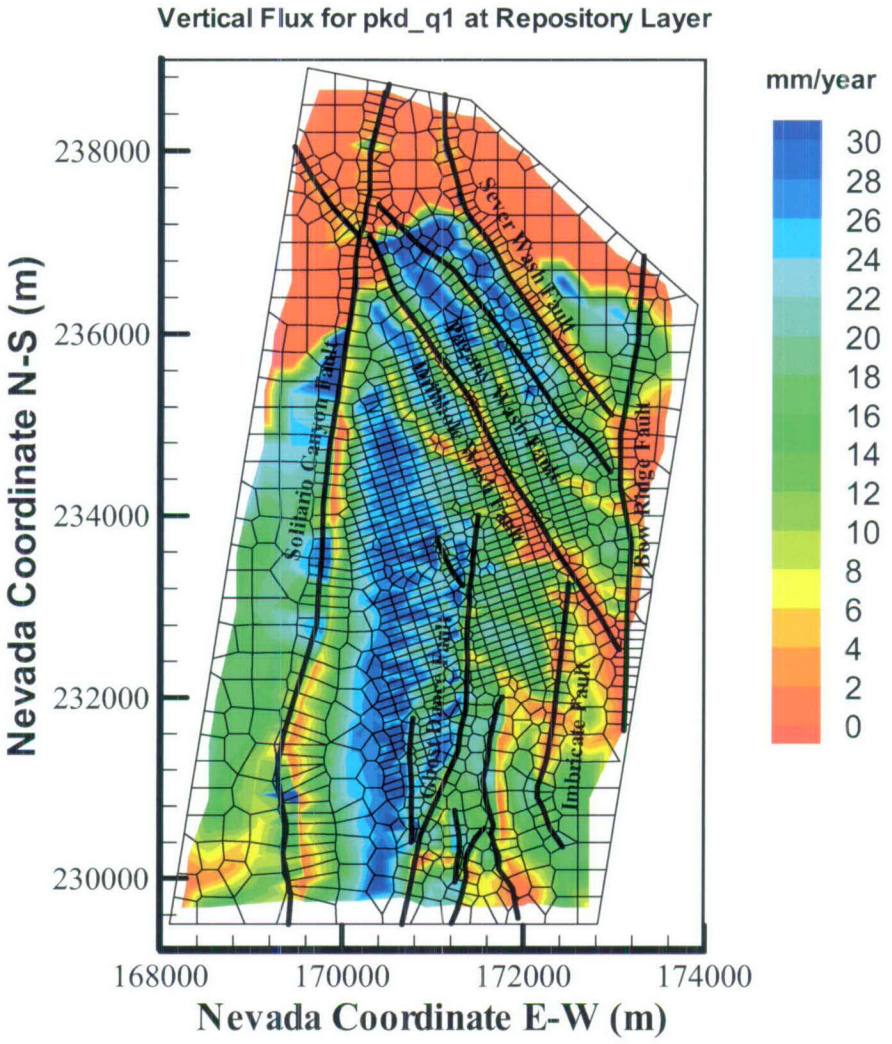

Output DTN: LB0702UZP10KFF.002.

Figure F-13. Simulated Percolation Fluxes at the Repository Horizon under the Post-10,000 Year, 10th Percentile Infiltration Scenario

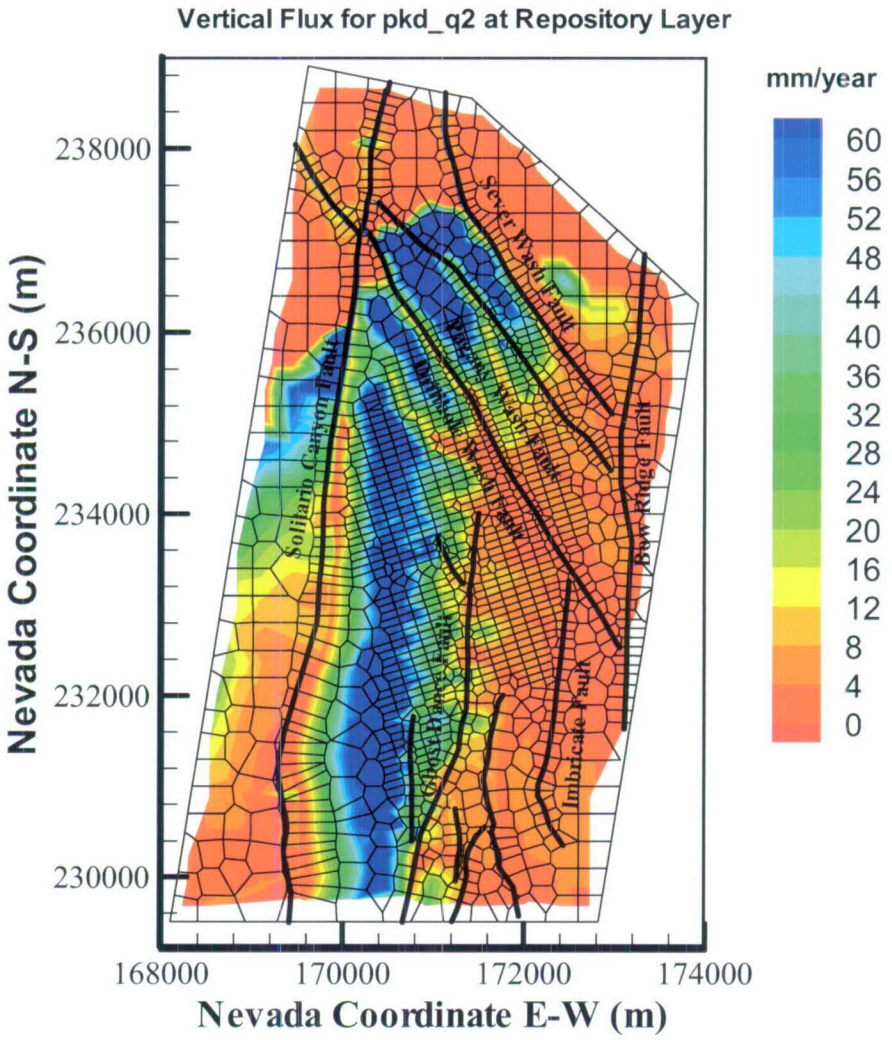

Output DTN: LB0702UZP10KFF.002.

Figure F-14. Simulated Percolation Fluxes at the Repository Horizon under the Post-10,000-Year, 30th Percentile Infiltration Scenario using the Results of Simulation pkd_q2

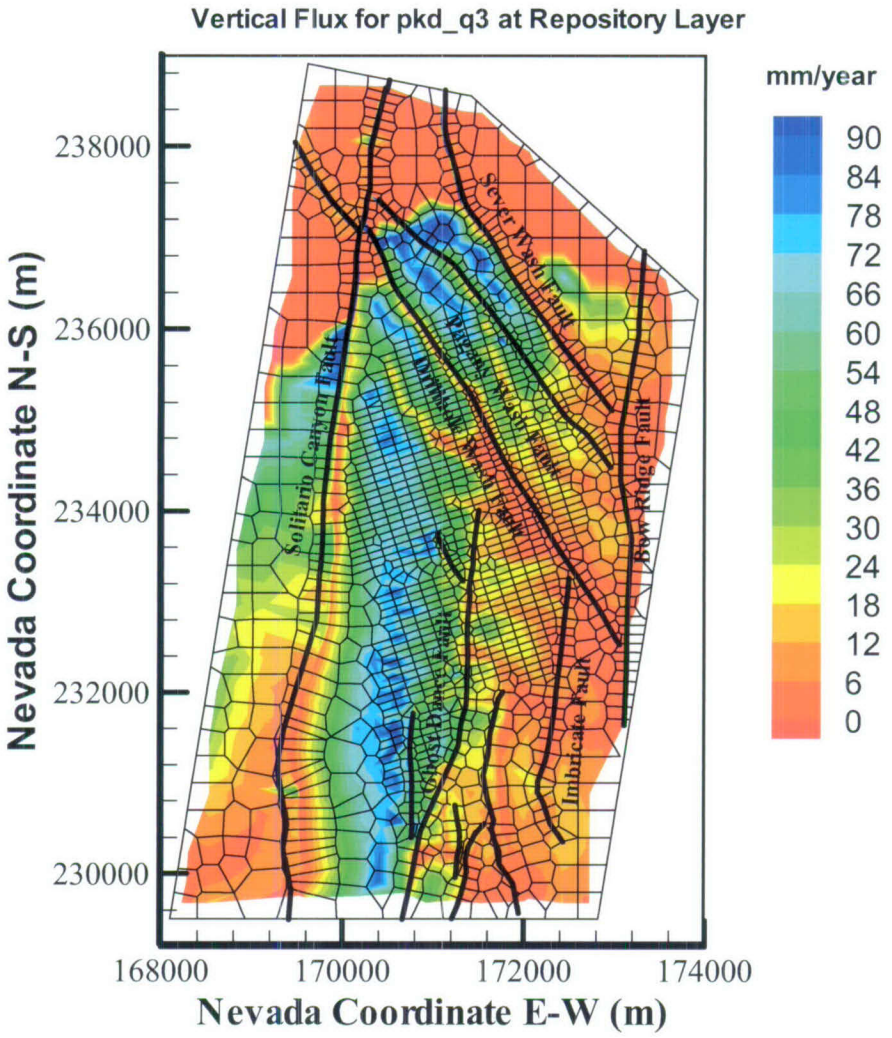

Output DTN: LB0702UZP10KFF.002.

Figure F-15. Simulated Percolation Fluxes at the Repository Horizon under the Post-10,000-Year, 50th Percentile Infiltration Scenario using the Results of Simulation pkd_q3

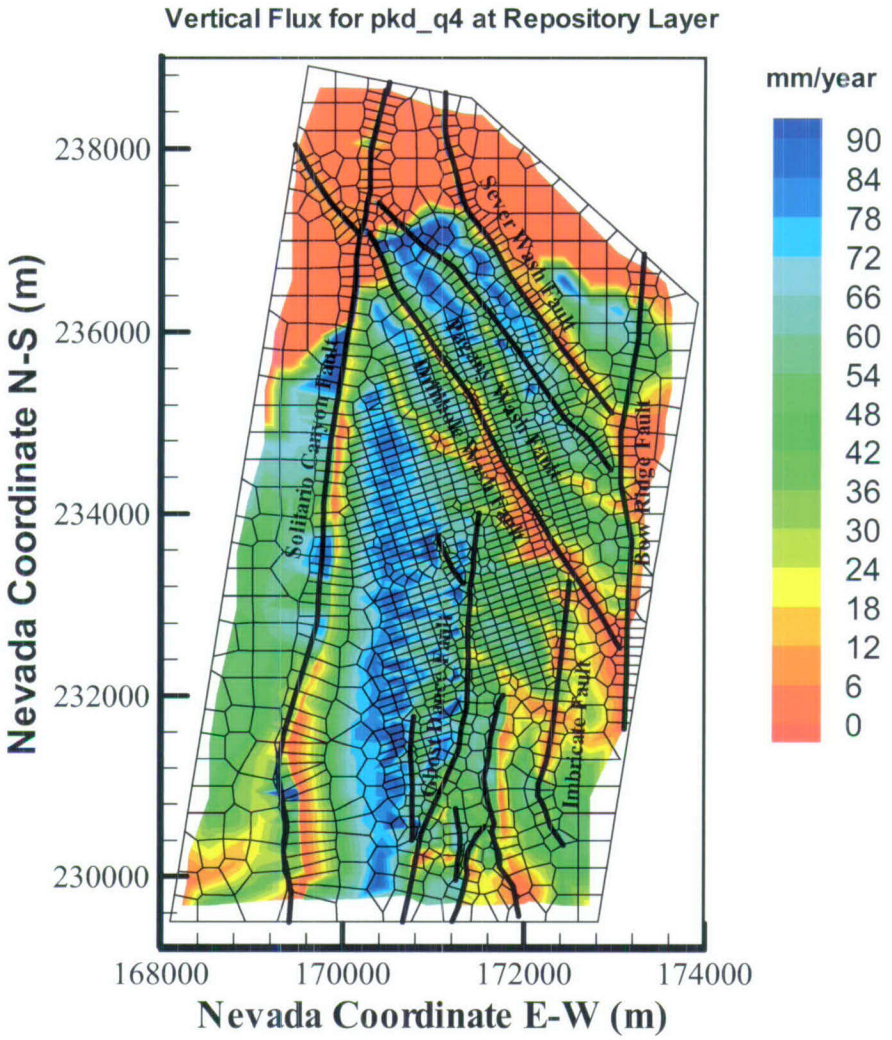

Output DTN: LB0702UZP10KFF.002.

Figure F-16. Simulated Percolation Fluxes at the Repository Horizon under the Post-10,000-Year, 90th Percentile Infiltration Scenario using the Results of Simulation pkd_q4

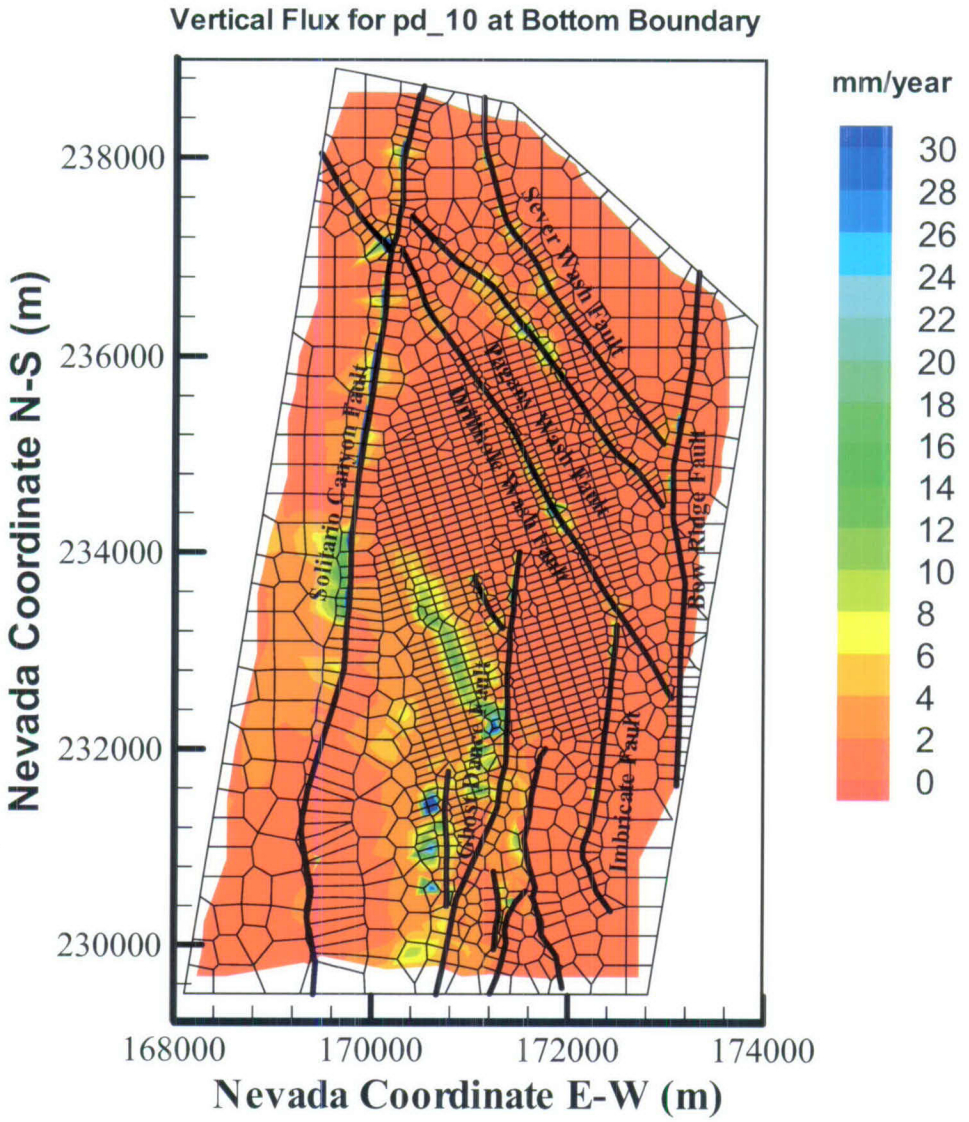

Output DTN: LB06123DPDUZFF.001.

Figure F-17. Simulated Percolation Fluxes at the Water Table under the Present-Day, 10th Percentile Infiltration Scenario

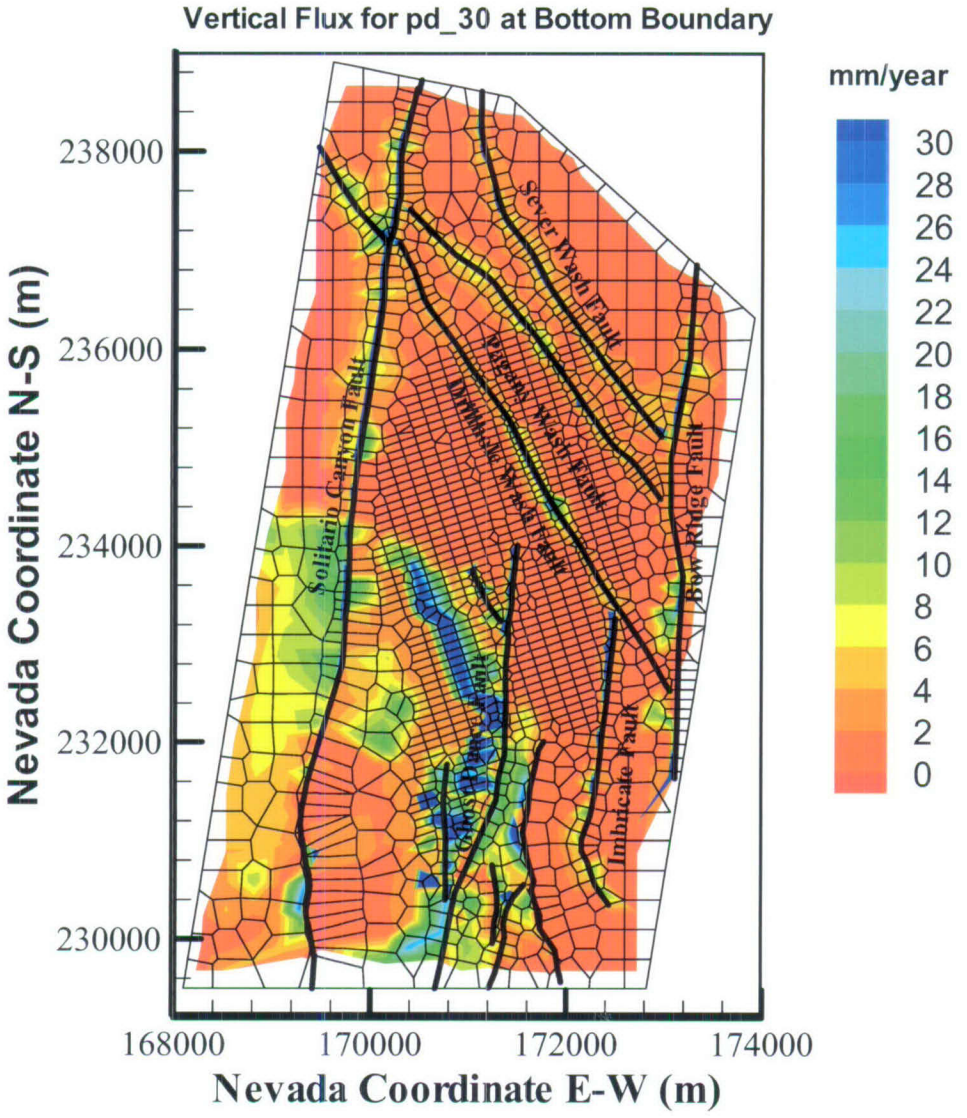

Output DTN: LB06123DPDUZFF.001.

Figure F-18. Simulated Percolation Fluxes at the Water Table under the Present-Day, 30th Percentile Infiltration Scenario using the Results of Simulation pd_30

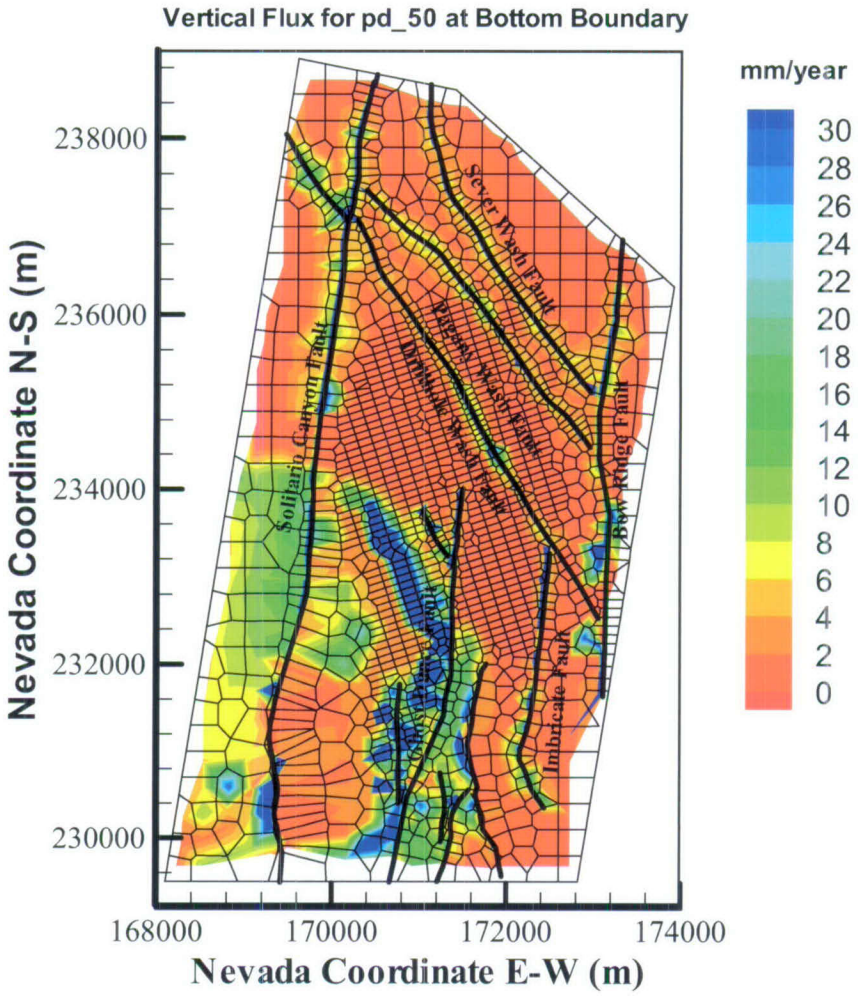

Output DTN: LB06123DPDUZFF.001.

Figure F-19. Simulated Percolation Fluxes at the Water Table under the Present-Day, 50th Percentile Infiltration Scenario using the Results of Simulation pd_50

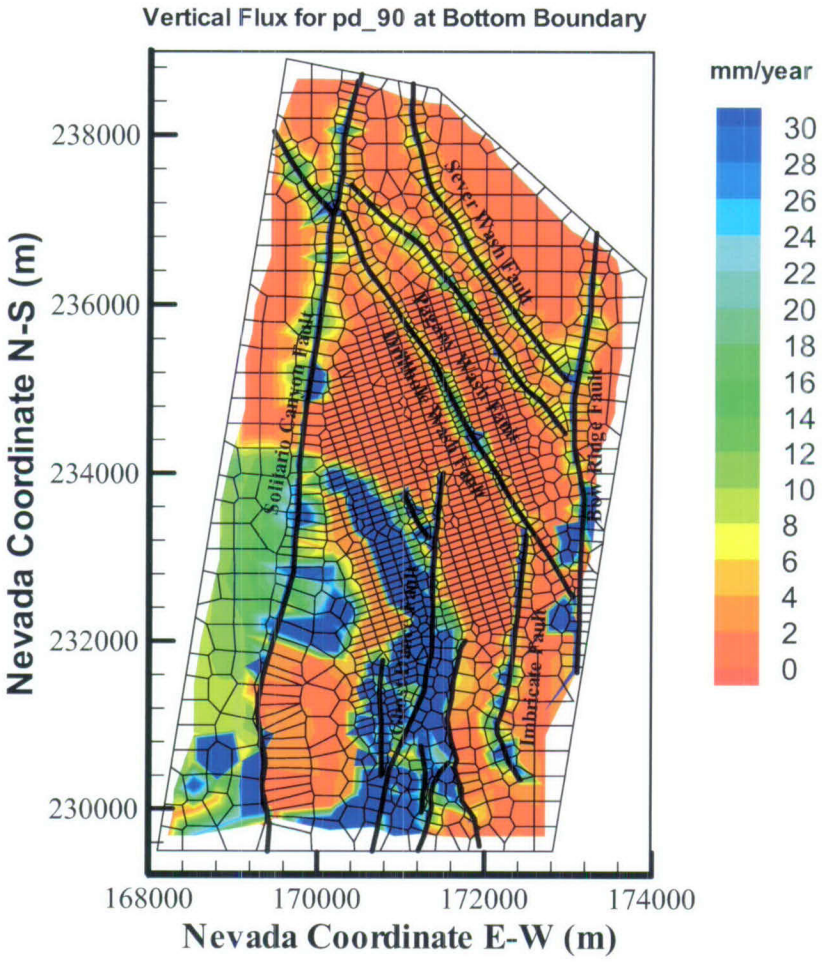

Output DTN: LB06123DPDUZFF.001.

Figure F-20. Simulated Percolation Fluxes at the Water Table under the Present-Day, 90th Percentile Infiltration Scenario using the Results of Simulation pd_90

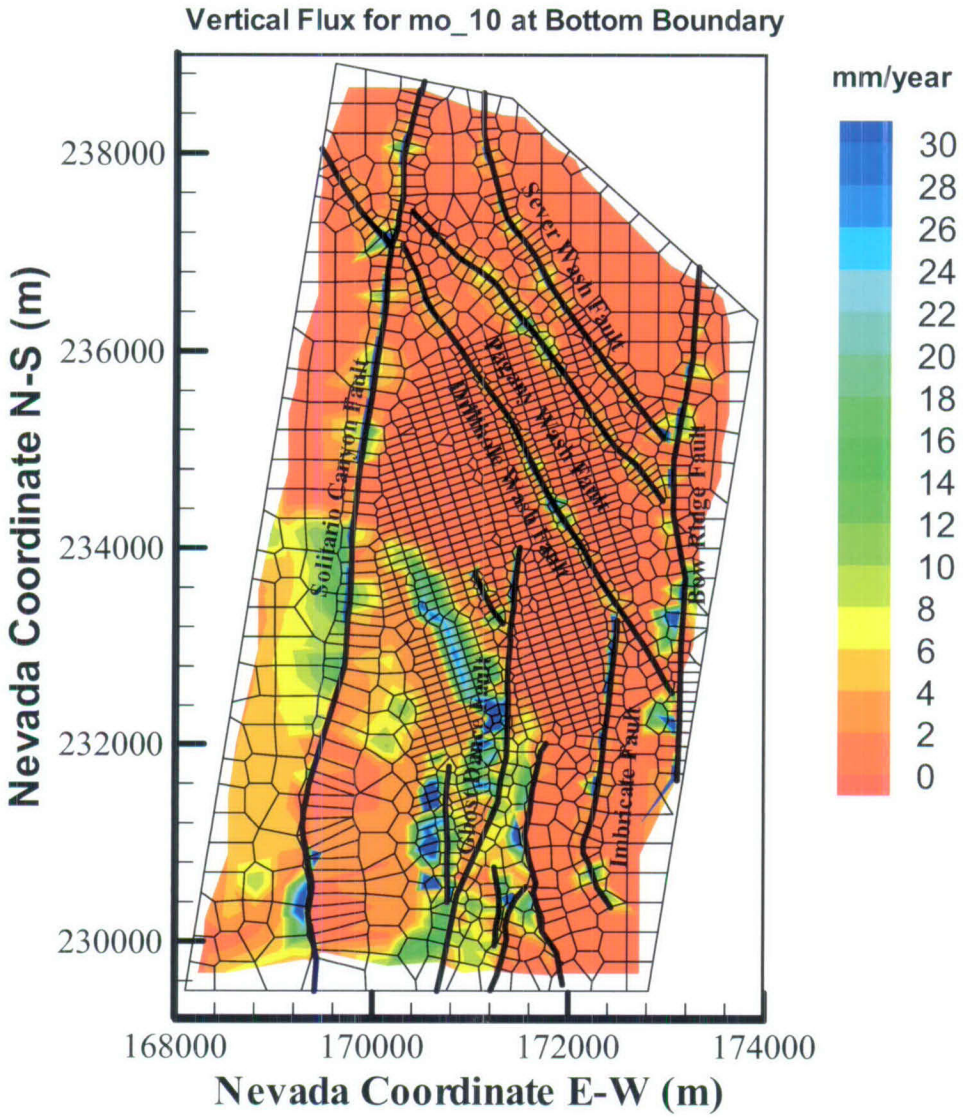

Output DTN: LB07013DMOUZFF.001.

Figure F-21. Simulated Percolation Fluxes at the Water Table under the Monsoon, 10th Percentile Infiltration Scenario

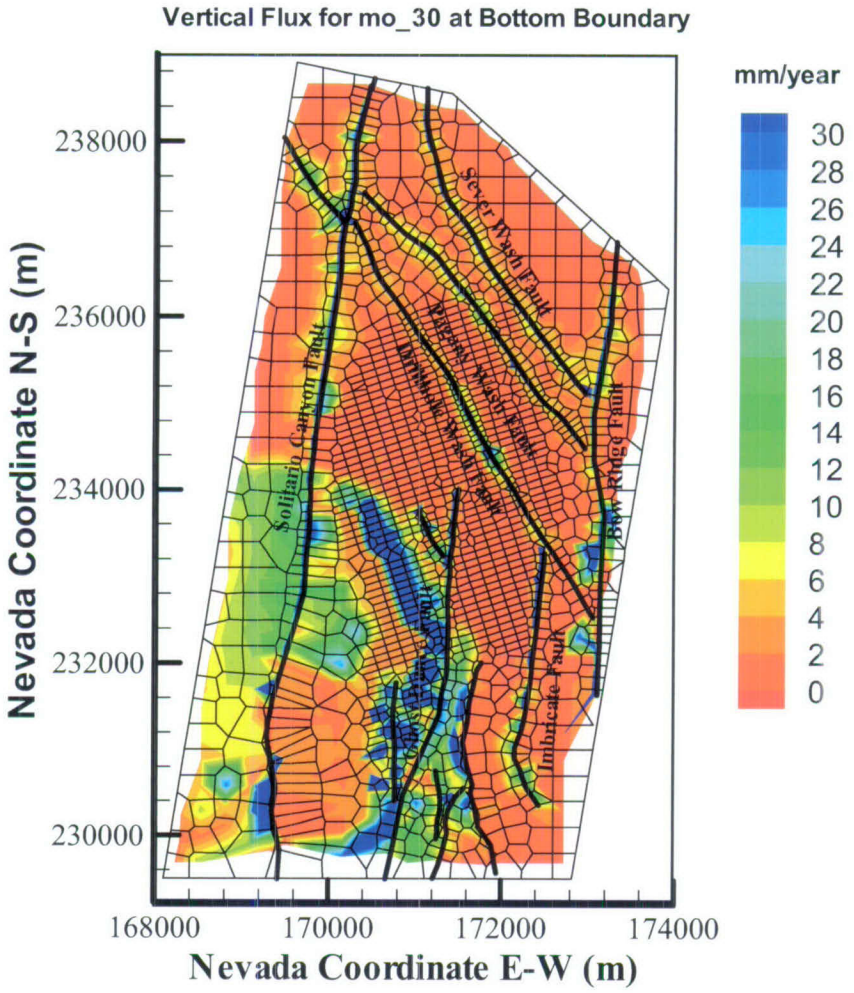

Output DTN: LB07013DMOUZFF.001.

Figure F-22. Simulated Percolation Fluxes at the Water Table under the Monsoon, 30th Percentile Infiltration Scenario using the Results of Simulation mo_30

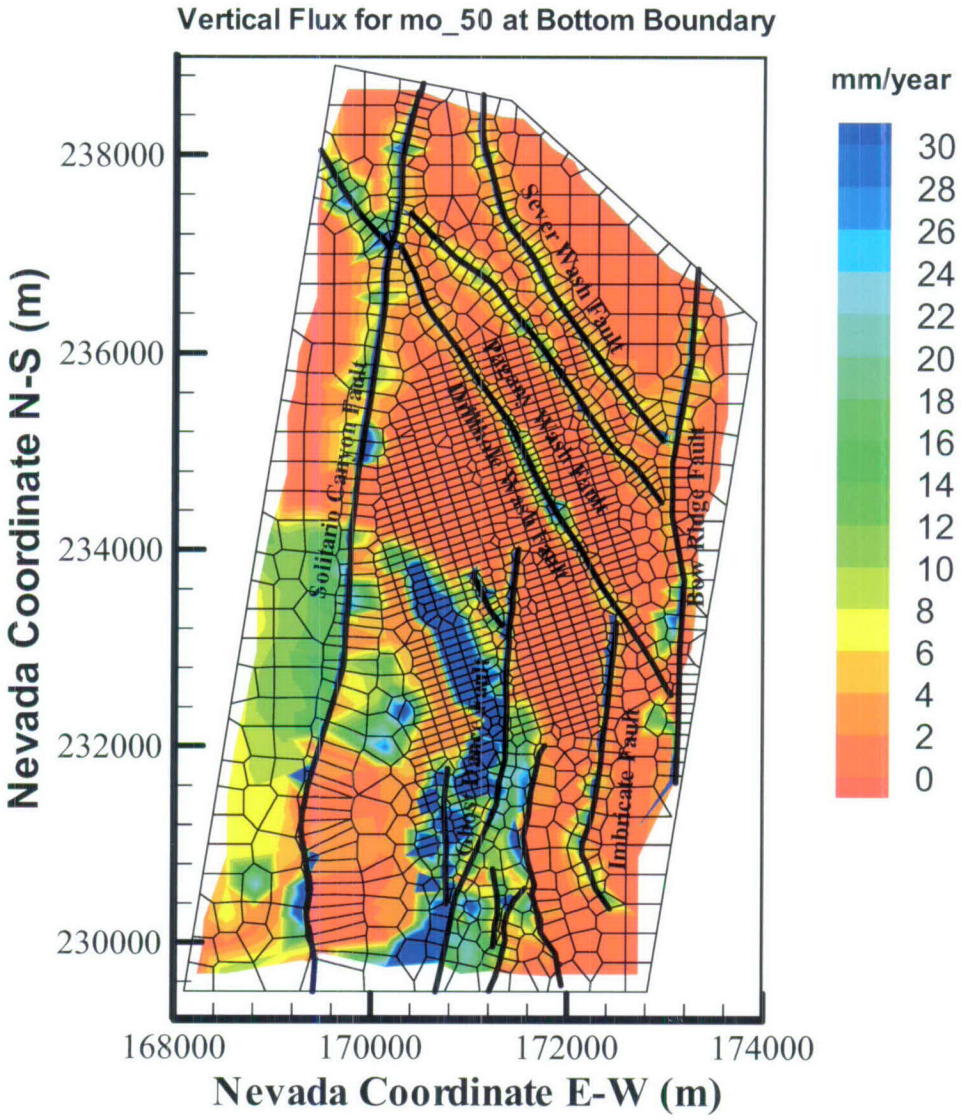

Output DTN: LB07013DMOUZFF.001.

Figure F-23. Simulated Percolation Fluxes at the Water Table under the Monsoon, 50th Percentile Infiltration Scenario using the Results of Simulation mo_50

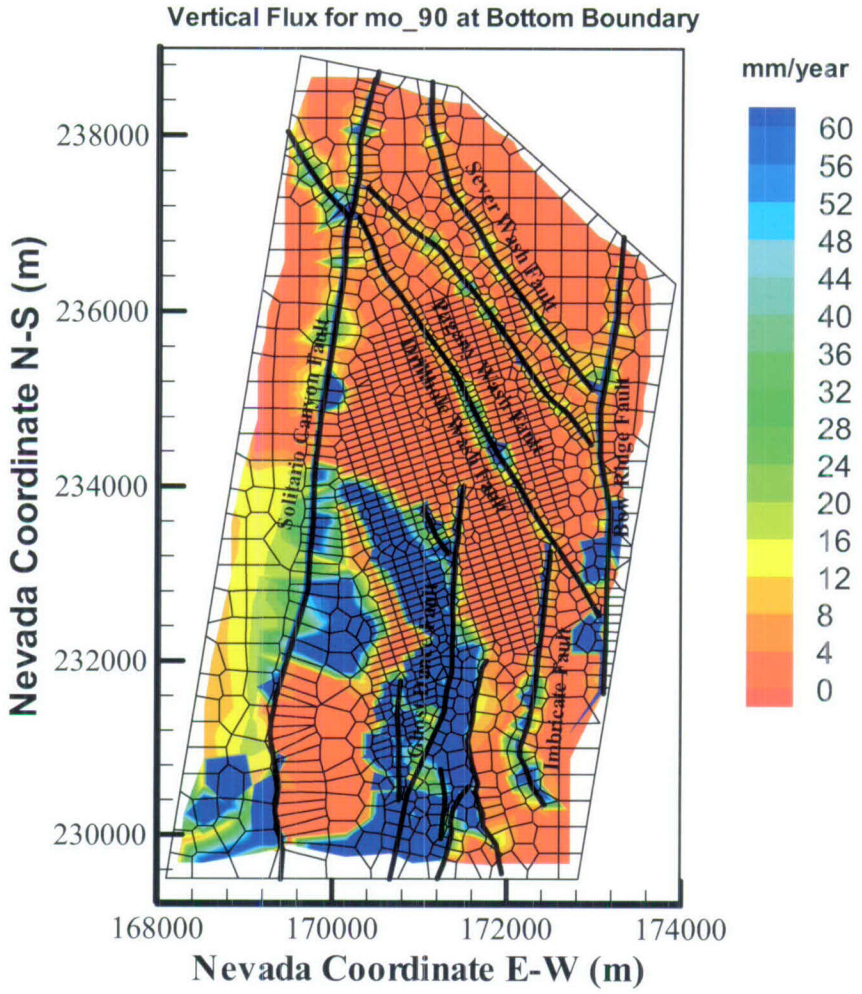

Output DTN: LB07013DMOUZFF.001.

Figure F-24. Simulated Percolation Fluxes at the Water Table under the Monsoon, 90th Percentile Infiltration Scenario using the Results of Simulation mo_90

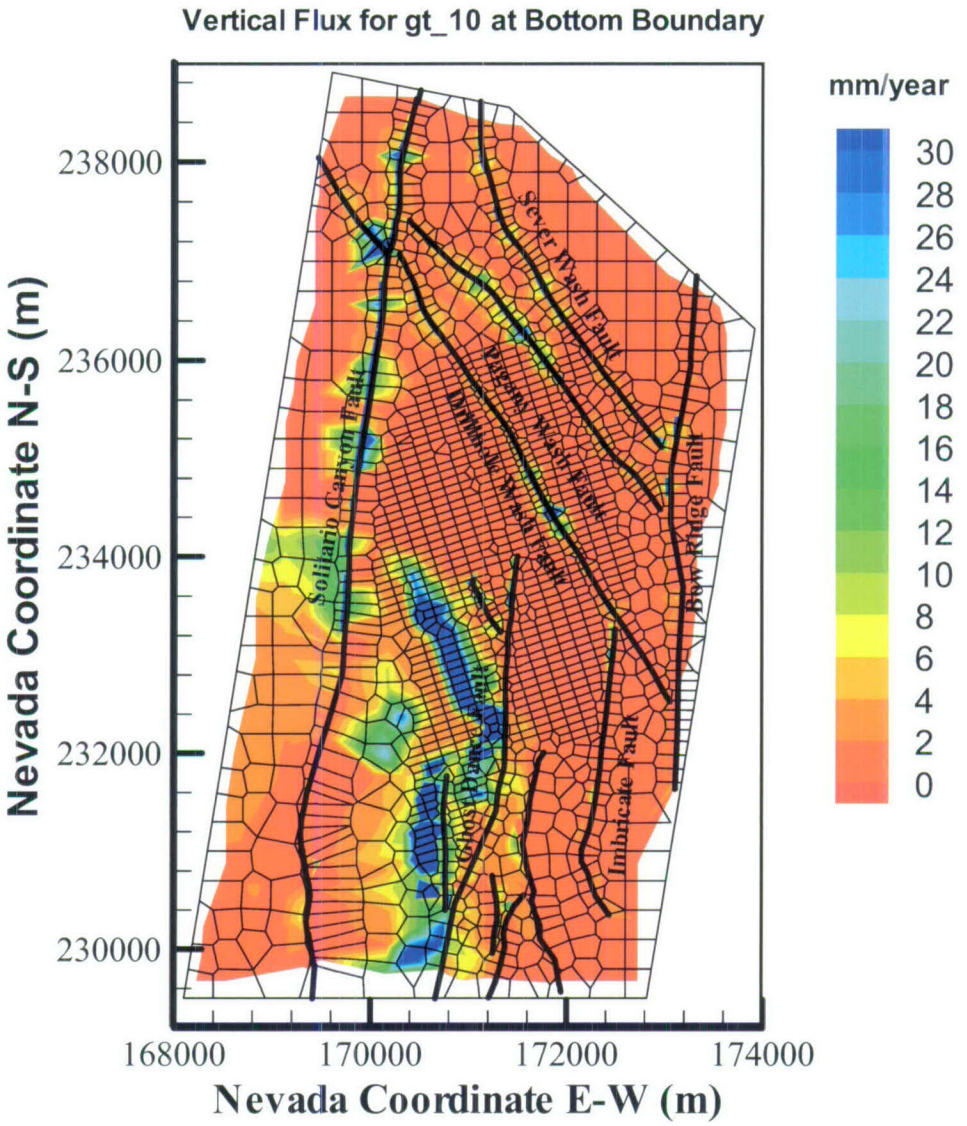

Output DTN: LB07013DGTUZFF.001.

Figure F-25. Simulated Percolation Fluxes at the Water Table under the Glacial-transition, 10th Percentile Infiltration Scenario

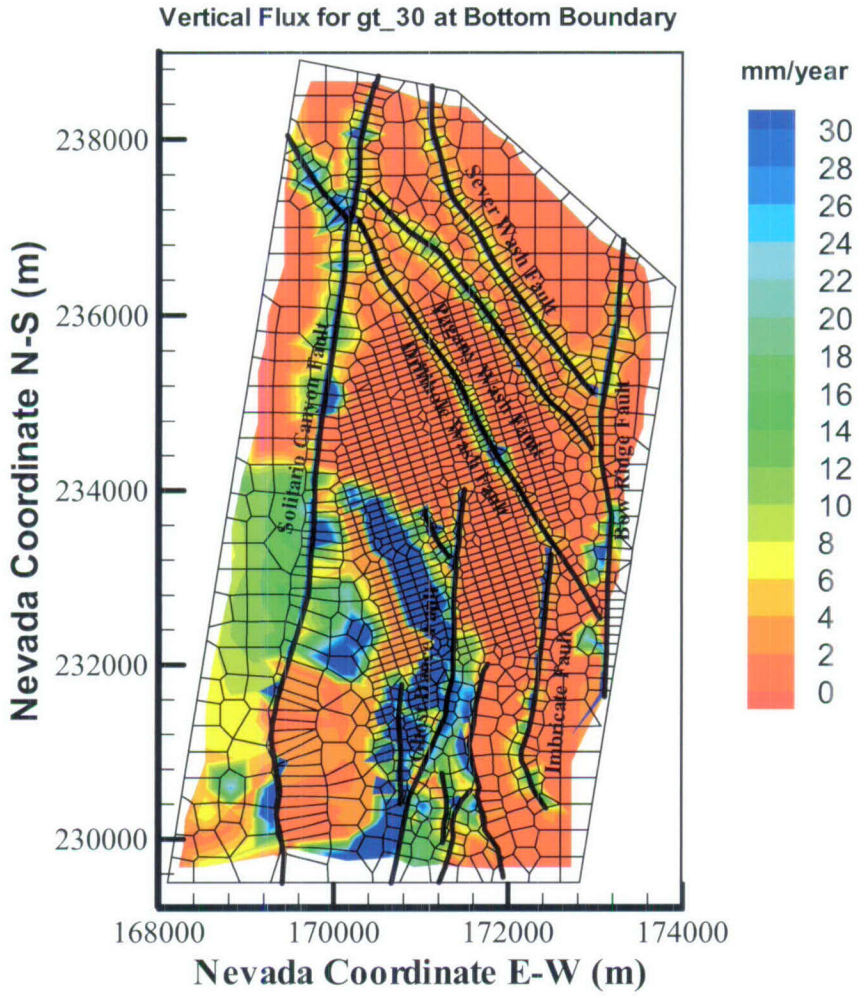

Output DTN: LB07013DGTUZFF.001.

Figure F-26. Simulated Percolation Fluxes at the Water Table under the Glacial-transition, 30th Percentile Infiltration Scenario Infiltration Scenario using the Results of Simulation gt_30

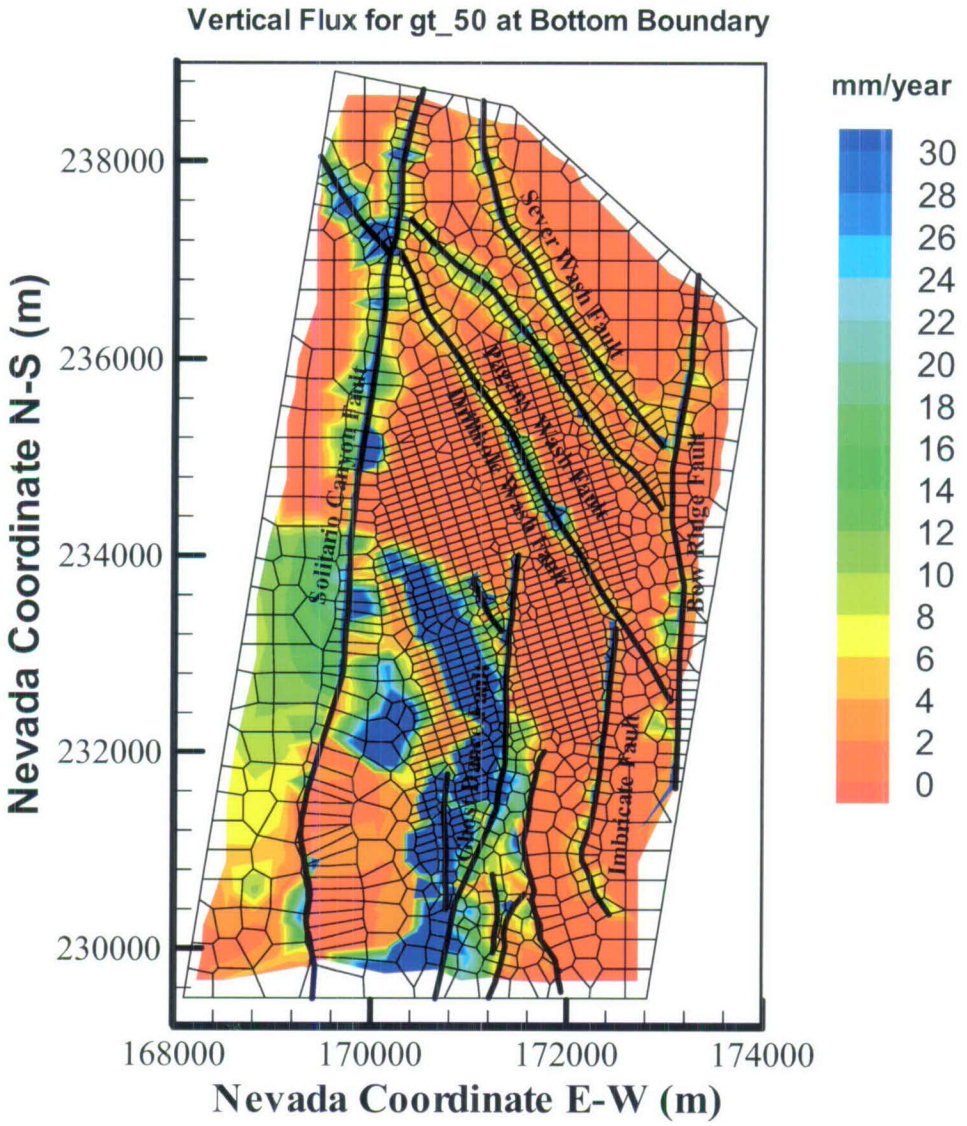

Output DTN: LB07013DGTUZFF.001.

Figure F-27. Simulated Percolation Fluxes at the Water Table under the Glacial-transition, 50th Percentile Infiltration Scenario using the Results of Simulation gt_50

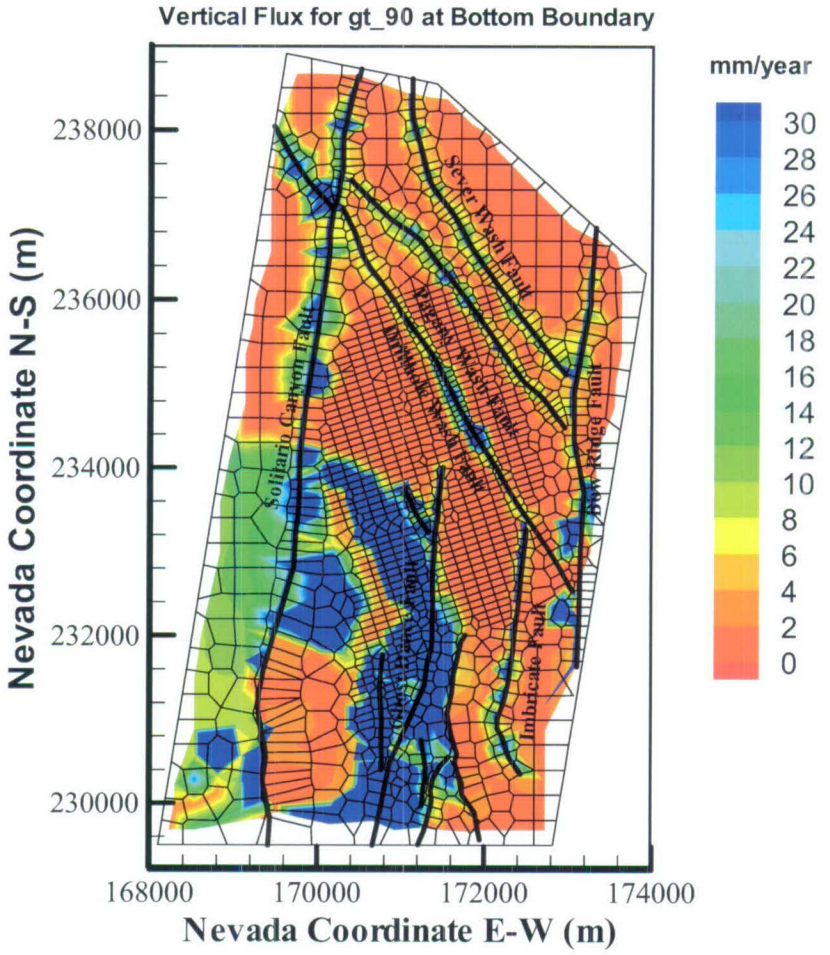

Output DTN: LB07013DGTUZFF.001.

Figure F-28. Simulated Percolation Fluxes at the Water Table under the Glacial-transition, 90th Percentile Infiltration Scenario using the Results of Simulation gt_90

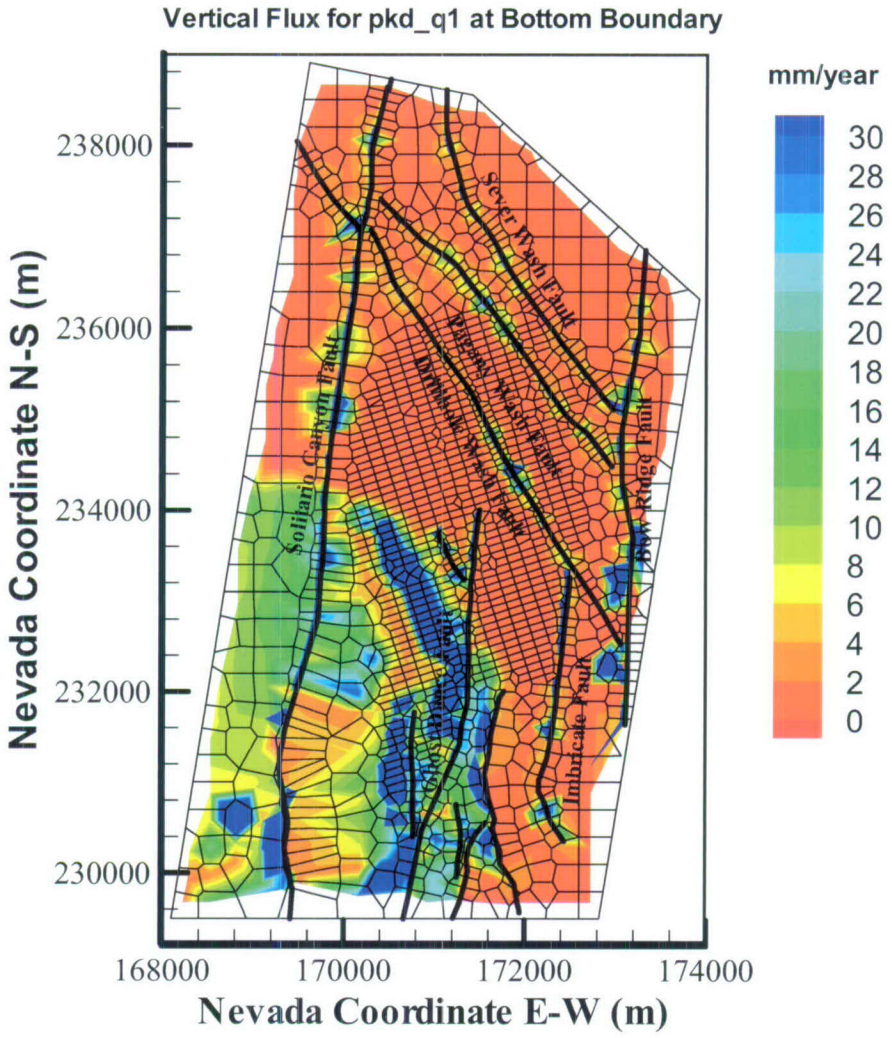

Output DTN: LB0702UZP10KFF.002.

Figure F-29. Simulated Percolation Fluxes at the Water Table under the Post-10,000-Year, 10th Percentile Infiltration Scenario

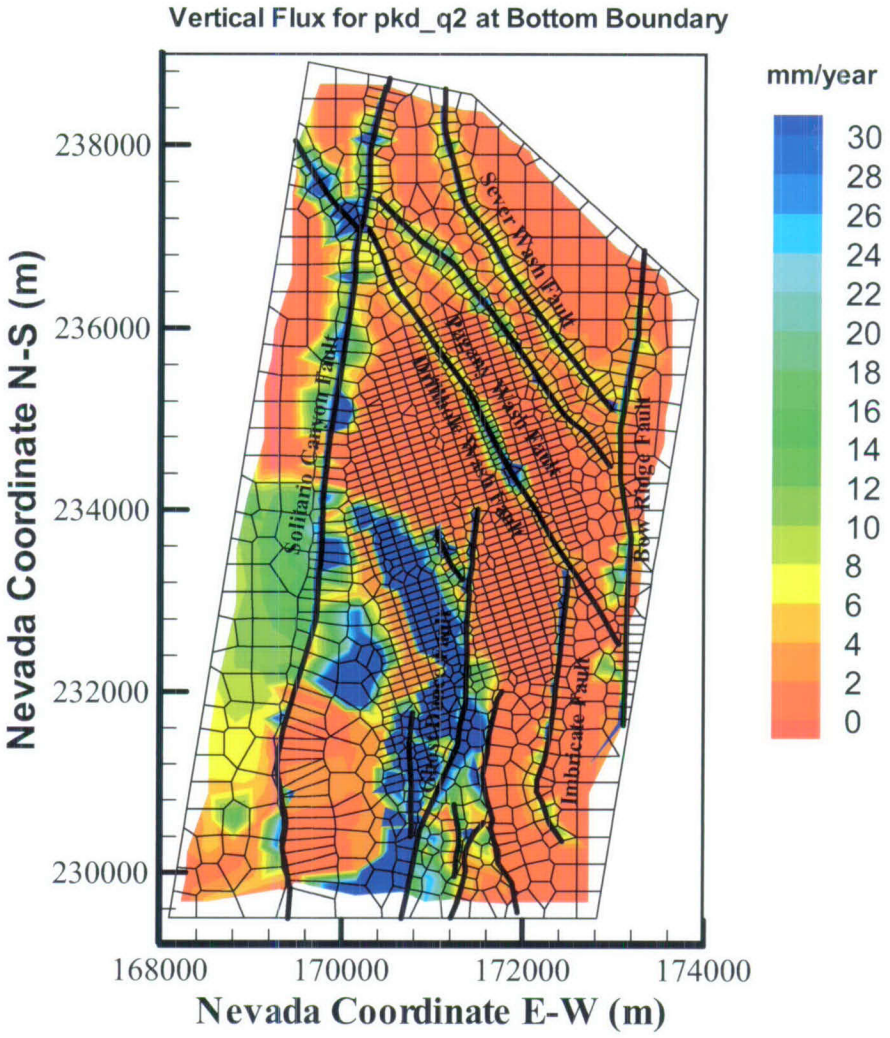

Output DTN: LB0702UZP10KFF.002.

Figure F-30. Simulated Percolation Fluxes at the Water Table under the Post-10,000-Year, 30th Percentile Infiltration Scenario using the Results of Simulation pkd_q2

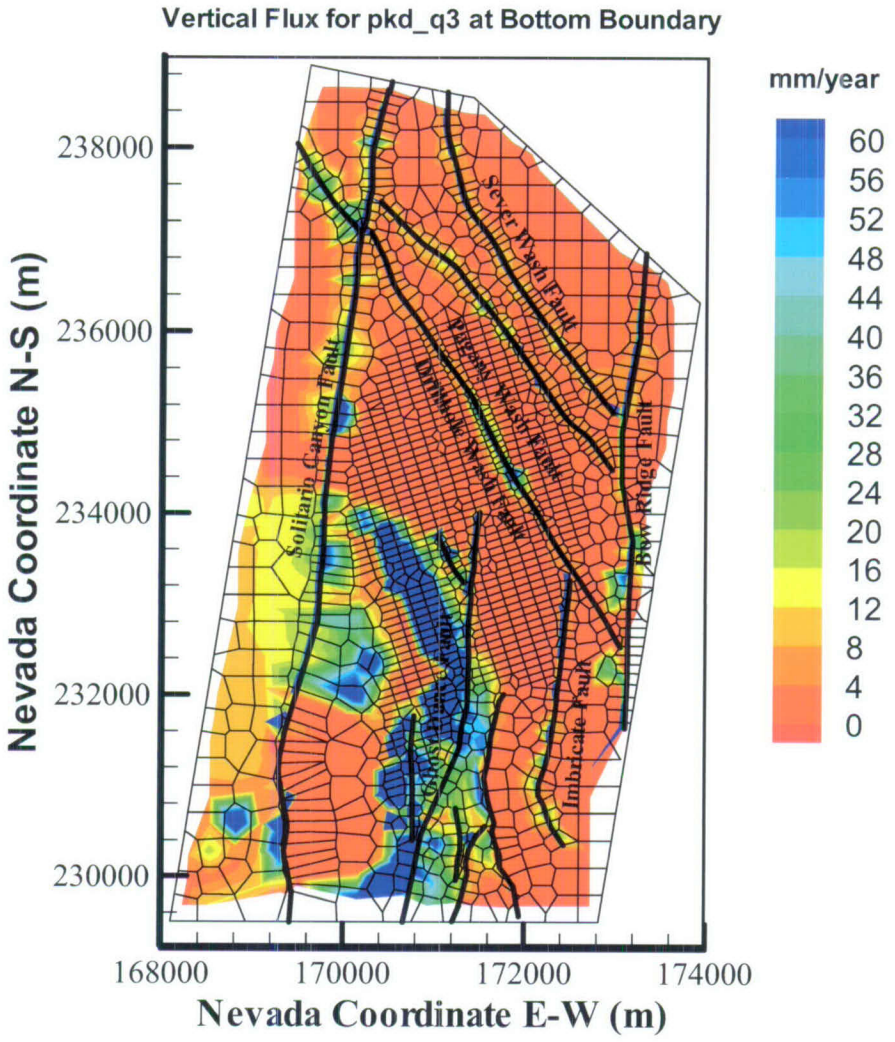

Output DTN: LB0702UZP10KFF.002.

Figure F-31. Simulated Percolation Fluxes at the Water Table under the Post-10,000-Year, 50th Percentile Infiltration Scenario using the Results of Simulation pkd_q3

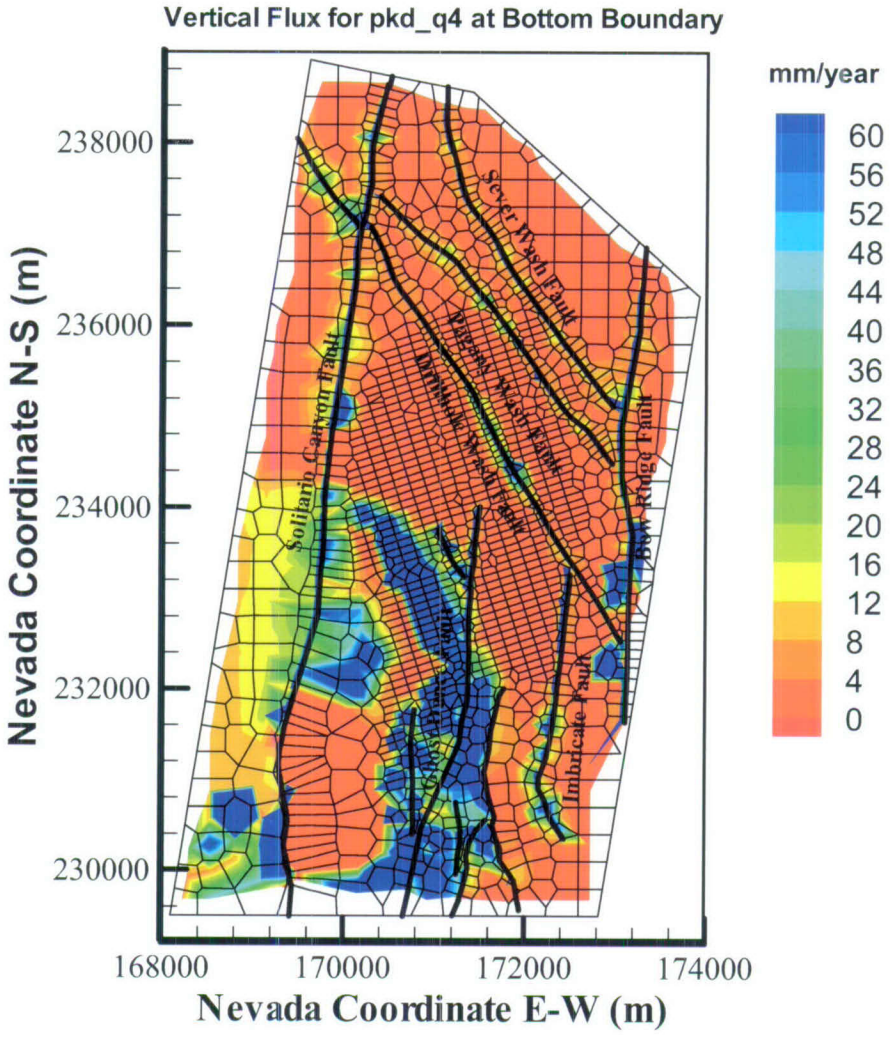

Output DTN: LB0702UZP10KFF.002.

Figure F-32. Simulated Percolation Fluxes at the Water Table under the Post-10,000-Year, 90th Percentile Infiltration Scenario using the Results of Simulation pkd_q4

APPENDIX G
SUPPORTING FILES FOR CALCULATION OF FLOW WEIGHTING FACTORS

G.1 LIKELIHOOD CALCULATION USING TEMPERATURE DATA

This section describes likelihood calculations performed using simulated temperature data (based on present-day 10th, 30th, 50th, and 90th percentile infiltration maps) and measured temperature data (Output DTN: LB0701UZMTHCAL.001). All the files discussed in this appendix are available in Output DTN: LB0701UZMTHCAL.001.

For these calculations, the following nine files are used as inputs.

Name	Size	Type	Modified
h-4_all.xls	27 KB	Microsoft Excel Wor...	1/8/2007 1:07 PM
H-5_all.xls	32 KB	Microsoft Excel Wor...	1/8/2007 1:07 PM
NRG-6_all.xls	24 KB	Microsoft Excel Wor...	1/8/2007 1:07 PM
NRG-7A_all.xls	33 KB	Microsoft Excel Wor...	1/8/2007 1:07 PM
SD-12_all.xls	33 KB	Microsoft Excel Wor...	1/8/2007 1:07 PM
UZ#4_all.xls	30 KB	Microsoft Excel Wor...	1/8/2007 1:07 PM
UZ#5_all.xls	25 KB	Microsoft Excel Wor...	1/8/2007 1:07 PM
UZ-7A_all.xls	34 KB	Microsoft Excel Wor...	1/8/2007 1:07 PM
wt-18_all.xls	32 KB	Microsoft Excel Wor...	1/8/2007 1:07 PM

Sources: Output DTN: LB0701UZMTHCAL.001; DTNs: GS031208312232.005 [DIRS 179284] (NRG-6, NRG-7a, SD-12, UZ#5, UZ-7a), GS950208312232.003 [DIRS 105572], (NRG-6 01-01-95 data).

Figure G.1-1. Excel File List of Temperature Data

Of the nine files available for use in the calculations, data for boreholes H-5, H-4, and WT-18 are not qualified, so they were not used. Boreholes UZ#4 and are within the same gridblock; therefore, only borehole UZ#5 was used.

The following steps were performed to find the standard deviation of temperature data for locations NRG-6, NRG-7a, SD-12, UZ#5, and UZ-7a.

For NRG-6, use the temperature data around 3:00 on 01/01/95 data, consistent with Output DTN: LB0701UZMTHCAL.001, to find the corresponding standard deviation of the data and copy it to an Excel file.

If there is more than one thermometer data available from around 3:00 (a.m./p.m.), use data from the first thermometer (e.g., take THM723 data at depth 350 ft).

Take THM735 data at depth 180 ft
Take THM741 data at depth 130 ft
Take THM747 data at depth 40 ft
Take THM749 data at depth 30 ft.

Because measured data points do not coincide with simulation points, linear interpretation is used to calculate the simulation values at locations where measured data are available. If those locations are outside simulation domain, the measured data at those locations will not be considered in the calculation.

For NRG-7a, use the first temperature data on 01/01/97 data. Find the corresponding standard deviation of the data, copy to Excel file.

If there is more than one thermometer data available from around 3:00 (a.m./p.m.), use data from the first thermometer (e.g., take THM405 data at depth 668 ft).

Take THM411 data at depth 494 ft
Take THM417 data at depth 388 ft
Take THM423 data at depth 153 ft
Take THM449 data at depth 40 ft.

For SD-12, use the first temperature data on 01/01/97 data. Find the corresponding standard deviation of the data, copy to the Excel file.

If there is more than one thermometer data available from around 3:00 (a.m./p.m.), use data from the first thermometer (e.g., take THM1605 data at depth 1,430 ft).

Take THM1611 data at depth 1,336 ft
Take THM1618 data at depth 1,265 ft
Take THM1623 data at depth 1,058 ft
Take THM1629 data at depth 935 ft.

For UZ#5, use the first temperature data on 01/01/97 data. Find the corresponding standard deviation of the data, copy to Excel file.

If there is more than one thermometer data at that time, data from the first one is used.

For UZ-7a, use the first temperature data on 01/01/97 data, for comparison with simulated data (Output DTN: LB0701UZMTHCAL.001). Find the corresponding standard deviation of the data, copy to Excel file.

If there is more than one thermometer data at that time, use data from the first thermometer.

Original data files are named using the convention *_*all.xls*, where * represents the borehole number. After standard deviations are incorporated, these files with interpolation points are renamed using the convention *_*data.xls*. Once again, * represents the borehole number.

For each borehole, perform the following interpolation using the five *_*data.xls* files (*NRG-6_data.xls*, *NRG-7A_data.xls*, *SD-12_data.xls*, *UZ#5_data.xls*, and *UZ-7A_data.xls*).

For each observation point (with an elevation of x), find two adjacent or immediate simulation points (in terms of elevation or location, x1<x<x2, x1, x2 are the two elevations of these two simulation point, y1, and y2 are the simulated temperatures, respectively), then perform a linear interpolation to calculate the simulated temperature y at the elevation x:

$$y = y_1 + \frac{y_2 - y_1}{x_2 - x_1}(x - x_1)$$

Repeat this for all four infiltration maps. The temperature data below ground surface within 40 m are not considered due to the large uncertainty.

After the interpolations are complete, combine these observation points with their temperature data (observed and simulated from the four infiltration maps) into one file. Calculations of likelihood value are done in these files. These files are named: *Cal_t#_*.xls*, where # is a number to distinguish different ways of calculating likelihood function, and "*" refers to how the data were handled.

Likelihood calculation:

The number in the data file name refers to the way of calculating likelihood values, based on different likelihood functions, described as below:

1. For likelihood function 1, the calculation is done in Output DTN: LB0701PAWFINFM.001, *Cal_t1.xls*.

2. For likelihood function 2, calculate both *N=1* and *N=0.5* using two averaging schemes in Output DTN: LB0701PAWFINFM.001, *Cal_t2_average1.xls*: a) average the residual term, and b) average the residual square.

3. For likelihood function 3, calculations are done in Output DTN: LB0701PAWFINFM.001, *Cal_t3_average1.xls* and *Cal_t3_average2.xls*, respectively.

4. For likelihood function 4, use the arithmetic mean for the likelihood measure calculations. Likelihood values using arithmetic mean (calculation is done at: *Cal_t4_sum.xls*).

G.2 LIKELIHOOD CALCULATION USING CHLORIDE CONCENTRATION DATA

Simulated (from 10th, 30th, 50th and 90th percentile infiltration maps) and measured chloride data (for the 10th, 30th, 50th and 90th percentile infiltration maps) are from Output DTN: LB0701UZMCLCAL.001. Figure G.1-2-1 lists the data files that were used in the likelihood calculation using chloride data. For these calculations, Excel data files were created (Output DTN: LB0701PAWFINFM.001). The file names correspond to the drift and borehole locations where the data were collected. The borehole data in the Excel files are taken from file *Borehole2006clv3.txt*.

Name	Size	Type	Modified
Borehole2006clv3...	242 KB	Text Document	1/17/2007 1:55 PM
CL_ECRB2006v3.txt	38 KB	Text Document	1/17/2007 1:15 PM
Cl_ECRB-Dec172...	10 KB	Tecplot Document	1/17/2007 1:50 PM
CL_ESF2006v3.txt	57 KB	Text Document	1/17/2007 1:15 PM
Cl_ESF-Dec17200...	11 KB	Tecplot Document	1/17/2007 1:17 PM
cl_SD12.lay	11 KB	Tecplot Document	1/17/2007 1:59 PM
cl_SD6.lay	11 KB	Tecplot Document	1/17/2007 1:35 PM
cl_SD7.lay	11 KB	Tecplot Document	1/17/2007 1:36 PM
cl_SD9.lay	10 KB	Tecplot Document	1/17/2007 1:37 PM
cl_UZ14.lay	10 KB	Tecplot Document	1/17/2007 1:38 PM
cl_UZ16.lay	10 KB	Tecplot Document	1/17/2007 1:39 PM
cl_WT24.lay	10 KB	Tecplot Document	1/17/2007 1:39 PM
contacts00el.dat	22 KB	DAT File	1/11/2001 12:00 AM
ECRB.wmf	20 KB	WMF File	1/17/2007 1:50 PM
ESF.wmf	31 KB	WMF File	1/17/2007 1:50 PM
G-2.lay	10 KB	Tecplot Document	1/17/2007 1:40 PM
G-2.wmf	18 KB	WMF File	1/17/2007 1:48 PM
LB0612PDFEHMF...	31 KB	Microsoft Word Doc...	1/17/2007 11:25 AM
LB0701UZMCLCA...	29 KB	Microsoft Word Doc...	1/17/2007 1:03 PM
NRG-6.lay	12 KB	Tecplot Document	1/17/2007 1:41 PM
NRG-6.wmf	16 KB	WMF File	1/17/2007 1:47 PM
NRG-7a.lay	14 KB	Tecplot Document	1/17/2007 1:42 PM
NRG-7a.wmf	17 KB	WMF File	1/17/2007 1:47 PM
SD-12.wmf	18 KB	WMF File	1/17/2007 1:59 PM
SD-6.wmf	16 KB	WMF File	1/17/2007 1:49 PM
SD-7.wmf	20 KB	WMF File	1/17/2007 1:49 PM
SD-9.wmf	18 KB	WMF File	1/17/2007 1:49 PM
UZ-14.wmf	23 KB	WMF File	1/17/2007 1:48 PM
UZ-16.wmf	19 KB	WMF File	1/17/2007 1:48 PM
UZ-7a.lay	11 KB	Tecplot Document	1/17/2007 1:45 PM
UZ-7a.wmf	12 KB	WMF File	1/17/2007 1:46 PM
UZ-N55.lay	11 KB	Tecplot Document	1/17/2007 1:44 PM
UZ-N55.wmf	11 KB	WMF File	1/17/2007 1:46 PM
WT-24.wmf	19 KB	WMF File	1/17/2007 1:48 PM

Figure G.1-2-1. List of files from Output DTN: LB0701UZMCLCAL.001

The boreholes data are taken from file *Borehole2006clv3.txt*, and for ECRB and ESF, data are taken from: *CL_ECRB2006v3.txt* and *CL_ESF2006v3.txt*, respectively.

Each Excel file contains 5 or 6 sheets:

1. "Measured data"—Aall measurements for this borehole or tunnel. Check data that are taken from multiple sources, repeated data are taken out

2. "Simulated data"—All simulation results from the 4 infiltration maps

3. "All data"—Simulated data with interpolated data at measurement locations. The interpolation method is the same as temperature data. For each observation point (with an elevation of x), find two adjacent or immediate simulation points (in terms of elevation or location, x1<x<x2, x1, x2 are the two elevations of these two simulation point, y1, and y2 are the simulated chloride concentrations, respectively), then do a linear interpolation to calculate the simulated chloride concentration y at the elevation x:

$$y = y_1 + \frac{y_2 - y_1}{x_2 - x_1}(x - x_1)$$

This is done for all infiltration maps.

4. "Calculation data"—Data for later calculation, including both measurements and simulation results (from interpolation) at measurement locations

5. "Log data"—The logarithm of chloride data. Because of the large variation of chloride data, all the calculations are done on the log space. This sheet also calculates the absolute difference between the log of the measured data and the log of the simulated data.

6. "Average data"—Sometimes there are multiple measurements at the same location, so the average is taken as the measurement of this location. If this is the case for some data in this borehole/tunnel, the borehole/tunnel contains this sheet for the averaged measurements.

The final processed data, either sheet 5 or 6, are copied into one file: *All.xls*.

Figure G.2-1-3 shows all the files used in the calculation (for likelihood values based on chloride data).

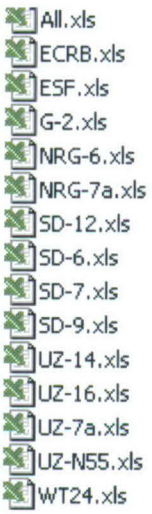

Figure G.2-1-3. List of Excel Files of Chloride Data

Similar to likelihood calculation from temperature data, all the calculations are performed in the same directory.

The number in the data file name refers to the way of calculating likelihood values, based on different likelihood functions, described as below (e.g., using likelihood function 1, the file is named as: *Cal_c1.xls*). "c" refers to "based on chloride data."

Also similar to temperature data, use group chloride data for the ECRB, ESF, and boreholes and for likelihood calculations, since the area covered by each borehole is much smaller than the area a horizontal tunnel (like ECRB or ESF) covers. The grouping schemes, or averaging schemes, are the same as the temperature averaging schemes. The following steps are performed to prepare likelihood function calculation borehole and tunnel location for each: 1) Averaging data within the tunnel is done on the same sheet; 2) Copy the averaged data from each borehole to a new sheet "boreholes;" 3) Average these data on this sheet "boreholes;" and 4) Copy the averaged data from ECRB, ESF, and boreholes to "all", and perform the calculations described below. All the likelihood measures (including averaging schemes) are the same as the temperature data.

1. For likelihood function 1, the method requires calculation of standard deviation of each data point. The standard deviation of chloride data is 5%, as stated "the analytical error is ±5% from: S00316_001 DATA REPORT (DTN: GS970108312271.001 [DIRS 107253])

   The method by which to transfer the deviation of a variable to the deviation of its log-transformed variable is taken from a journal article by Quan and Zhang (2003 [DIRS 180504]) that assumes log-normal distribution:

$$\hat{\sigma}_{\log}^{2} = \log\left(1 + \frac{\hat{\sigma}^{2}}{\hat{\mu}^{2}}\right)$$

$$\sigma / \hat{\mu} = 0.05$$

   This is done for all data points in the Excel file.

2. Again, using the same weights for the three groups, calculate *N=1* and *N=0.5*, with two averaging schemes: a) Average the residual terms (the calculation is done in: *Cal_c2_average1.xls*, and b) Average the residual square. The calculation is done in: *Cal_c2_average2.xls*.

3. Again, for the third likelihood function, two averaging schemes described above are used in: *Cal_c3_average1.xls* and *Cal_c3_average2.xls*, respectively.

4. For the fourth likelihood function, the calculation is done in *Cal_c4_sum.xls*.

Final likelihood calculation

At this point, the likelihood values from the different suggested functions are combined for calculation of the final likelihood values.

For the four infiltration maps at 10th, 30th, 50th and 90th percentiles on the cumulative distribution function (cdf) curve of annual infiltration, the prior probability or weighting factor (P_i) for each map is determined based on the location of the map on the cdf curve (Table G1-1).

Table G.1-1. Prior Weights for the Four Selected Infiltration Maps

Infiltration map	10th percentile (%)	30th percentile (%)	50th percentile (%)	90th percentile (%)
P_i	0.2 (0.2 to 0)	0.2 (0.4 to 0.2)	0.3 (0.7 to 0.4)	0.3 (1 to 0.7)

Source: Section 6.8.5.1.

The posterior weighting factors after chloride data are taken into account can be calculated as:

$$P_i^1 = \frac{P_i L_{ci}}{\sum_{i=1}^{N} P_i L_{ci}}$$

where L_{ci} is the likelihood value calculated from *chloride* data for infiltration map i. Then, accounting for temperature data, the final weight is:

$$P_i^f = \frac{P^1{}_i L_{ti}}{\sum_{i=1}^{N} P^1{}_i L_{ti}}$$

where L_{ti} is the likelihood value calculated from *temperature* data for infiltration map i.

By combining the above two equations, the final weight can be calculated in one equation:

$$P_i^f = \frac{P_i L_{ci} L_{ti}}{\sum_{i=1}^{4} P_i L_{ci} L_{ti}}$$

The final calculations are performed in DTN: LB0701PAWFINFM.001.

The calculation for each method is done in a separate spreadsheet (e.g., for likelihood function 1 as described before, the calculation is done on the spreadsheet S1, for likelihood function 2, averaging scheme 1, n=1, the calculation is done on the spreadsheet: S2_a1_n=1, etc.)

For likelihood function 4, take the arithmetic mean, and maximum residual as ε, based on the two sensitivity analysis that show that the results are not too sensitive to the choices of the two options.

Sensitivity Studies

To evaluate sensitivity to temperature data, the results documented in Output DTN: LB0701PAWFINFM.001, files: *Cal_t1.xls* and *summary.xls* were used. These sensitivity studies are documented in Output DTN : LB0704UZWFINFM.001, as described below:

Effects of Measurement Error on Temperature Data

Make a copy of *Cal_t1.xls* and rename it *Cal_t1_sensitivity.xls*. For the 10th, 30th, 50th and 90th percentile spreadsheet, change the values in column "SD" to 0.1. Then copy the results to "sum" sheet.

Effects of Averaging Scheme

Make a copy of *summary.xls* and rename it as *summary_sen_average.xls*. Make a copy of spreadsheet "all" and rename it as "average2". Delete the three lines with "s2_a1_n=1", "s2_a1_n=0.5" and "s3_a1". The remaining lines are used to calculate final averaged results.

Results Without Considering the First and the Fourth Likelihood Functions

Make a copy of *summary.xls* and rename it *summary_sen_2&3only.xls*. Make a copy of spreadsheet "all" and rename it as "all_cut." Delete the three lines with "S1" and "s4_sum." The remaining lines are used to calculate final averaged results.

Results from individual data sets

Make a copy of *summary.xls* and rename it *summary_temperature only.xls*. Delete all chloride data entries to ensure the file contains final results for temperature only.

Make a copy of *summary.xls* and rename it *summary_chloride only.xls*. Delete all temperature data entries to ensure the file contains final results for chloride only.

APPENDIX H
EVALUATION OF THE IMPACT OF THE CURRENT INFILTRATION MODEL ON DOWNSTREAM PRODUCTS

H1. INTRODUCTION

The following impact evaluation implements the work described in *Technical Work Plan for Unsaturated Zone Flow, Drift Seepage, and Unsaturated Zone Transport Modeling* (BSC 2006 [DIRS 177465]) to review and evaluate the impact of the current infiltration model on downstream products. The evaluation approach deviates from the work plan with respect to the list of products evaluated, and the nature and extent of analyses needed to determine impact, as discussed below.

A list of license application products was compiled, starting with the work plan, and subsequently other affected products not included in the work plan were added. The additions include documents that link through the DIRS database to the output DTNs from the previous infiltration model, *Simulation of Net Infiltration for Present-Day and Potential Future Climates* (BSC 2004 [DIRS 170007]), plus other products that are further downstream and link indirectly to the previous model. The developed list (Table H-1) does not include interface drawings or engineering calculations.

The license application products listed in Table H-1 are divided into three groups: (1) those currently being revised or updated that incorporate the current infiltration results, (2) those not incorporating the current infiltration results for which impacts are slight, and (3) those for which impact evaluations are needed. Impact evaluations for Group 1 are not needed because current infiltration model results are being applied in the revisions or updates.

The Group 2 products from Table H-1 are evaluated individually in the following sections. The impacts of current infiltration model results on these products is inherently limited, because of the nature of the products and the types of information produced for total system performance assessment (TSPA) and screening of features, events, and processes (FEPs). Impact evaluations for Group 3 products are provided in this report at an appropriate level of detail. These evaluations were developed by comparing average features and the range of variation for the current (MASSIF-based; SNL 2007 [DIRS 174294]) percolation flow fields with the previous (INFIL-based; BSC 2004 [DIRS 170007]) fields. The Group 3 evaluations include the potential impacts on FEP exclusion arguments, which were not covered in the TWP. Impacts on the saturated zone flow and transport models are discussed in *Site-Scale Saturated Zone Transport* (SNL 2007 [DIRS 177392]), *Saturated Zone Site-Scale Flow Model* (SNL 2007 [DIRS 177391]), and *Saturated Zone Flow and Transport Model Abstraction* (SNL 2007 [DIRS 181650]).

H2. GENERAL COMPARISON OF CURRENT INFILTRATION MODEL RESULTS WITH THE PREVIOUS MODEL

The current infiltration data (MASSIF-based) are similar to the previous infiltration model (INFIL-based), comparing the lower, mean and upper bound maps from the previous infiltration model (BSC 2004 [DIRS 170007]) to the 10th, 30th and 50th percentile maps from the current revision of the infiltration model (SNL 2007 [DIRS 174294]). The 90th percentile field from the current infiltration model is exceptional because it exceeds all of the infiltration fields from the previous model that were identified for use by TSPA.

To examine these relationships more closely, cumulative distributions from the previous and current models, for percolation in the host rock within the repository footprint, are compared in Figures H-1 through H-3 for the present-day, monsoon, and glacial transition climate states. Percolation flux in the host rock is a result from the UZ flow model and is selected for comparison here (rather than net infiltration at the ground surface) because it is used directly as a boundary condition for drift-scale coupled process models (e.g., multiscale model) and for the drift seepage abstraction in TSPA. In addition, percolation flux at the repository horizon is an important determinant of radionuclide mobility in the UZ transport abstraction.

These percolation data were developed by sorting the percolation flux values at the repository horizon in the 560 columns of the UZ flow model grid for both the previous (INFIL based; BSC 2004 [DIRS 170007]) and current (MASSIF based; SNL 2007 [DIRS 174294]) versions of the model. The 560 columns include the contingency area (SNL 2007 [DIRS 181383], Section 6.2.12) that was not included in previous representations of the repository footprint. The distributions (Figures H-1 through H-3) preserve the full uncertainty and variability of the UZ flow model, and represent the same spatial domain.

Statistical approaches are used to compare the previous and current percolation fields (Tables H-2 and H-3): (1) compare mean values for the previous model, for the three climate states, with mean values for the current 10th, 30th, and 50th percentile fields (Table H-2); and (2) compare the ranges of spatial variation for the previous model with the same ranges for the current model (Table H-3). As noted above, the 90th percentile field from the current model is exceptional, but this field is assigned a relatively low weight in TSPA. A set of composite-weighted flux values is used for each climate state (Table H-2) that combines the averages of 10th, 30th, 50th, and 90th percentile fields from the current model, using the same sampling weights used in TSPA. These weights are combined in Table H-2 with flux values from different sources (as indicated) to develop composite-weighted values for the present-day, monsoon, and glacial transition climate states that can be readily compared to supplement the impact evaluation for Group 3 products. These modal values reasonably represent flux conditions likely to be assigned in TSPA to particular waste package locations in the repository. They are useful for evaluating the sensitivity of near-field behaviors such as thermally driven coupled processes, that do not depend on the far-field distribution of percolation flux.

For the previous model (BSC 2004, [DIRS 170007]), the overall spatial variation of percolation flux at the repository horizon within the repository footprint ranged from zero (discounting small negative values) to 294 mm/yr, whereas the current model (SNL 2007 [DIRS 174294]) ranges from 0.15 to 136 mm/yr (Table H-3). Current data for the 10th, 30th, and 50th percentile fields are mostly encompassed by the previous data for the "low" and "high" uncertainty states. Extreme values from the previous data (>95th percentile for the Mean and High uncertainty states) bracket all the current data (including the 90th percentile field). While these comparisons are only statistical, they show that application of the current values in TSPA falls mostly within the range of uncertainty and variability that existed when the Group 2 and Group 3 products were developed.

An important aspect of Figures H-1 through H-3 is that the differences between previous and current model results, for the comparisons described above, are typically smaller than the differences between the uncertainty states for either the previous or current data (Table H-3).

Thus, by including uncertainty states, the results used for TSPA encompass the smaller differences between the previous and current models.

For Group 1 products (Table H-1), the full range of infiltration and percolation flux data, based on the current infiltration model, is propagated to TSPA. Also, the calibrated hydrologic properties for hydrostratigraphic units at Yucca Mountain are recalibrated using the current infiltration data. Hence, there is no impact from discrepancy between the current and previous infiltration data on the inputs to the TSPA compliance case, and no further need to discuss Group 1 products in this evaluation.

H3. EVALUATION OF IMPACT ON GROUP 2 PRODUCTS

H3.1 Performance Confirmation Plan (TDR-PCS-SE-000001 Rev. 05)

The activities described in *Performance Confirmation Plan* (BSC 2004 [DIRS 172452]) are not impacted by the results of the infiltration model. Infiltration is cited in this report as a motivation and driver for several of the testing and monitoring activities, such as precipitation monitoring and seepage monitoring. However, the procedures and objectives detailed in the report for the testing and monitoring activities will not be impacted by the differences in model predictions of infiltration. Table 5-1 in *Performance Confirmation Plan* (BSC 2004 [DIRS 172452]) provides a summary of the current test plans. *Performance Confirmation Plan* (BSC 2004 [DIRS 172452], p. 3-21) also refers to the predicted amount of seepage and fraction of waste packages contacted by drips, which are functions of the previous infiltration estimates, but the general procedure for monitoring seepage is not impacted by the predictions of infiltration.

H3.2 PARAMETER SENSITIVITY ANALYSIS FOR UZ FLOW (ANL-NBS-HS-000049 REV. 00)

The purpose of this report is to document a series of sensitivity analyses conducted using the site-scale UZ flow model. The sensitivity analyses are intended to evaluate how uncertainties in hydrologic parameters affect unsaturated zone flow. The work scope presented in this scientific analysis encompasses sensitivity analyses related to hydrologic-properties uncertainties in the UZ flow model. These sensitivity analyses are conducted using the base-case site-scale UZ flow model with distributions of the hydrologic properties for the mean glacial-transition infiltration rate. The glacial transition mean infiltration rate was chosen as being a "typical" long-term infiltration rate for this sensitivity analysis. Over the UZ model domain, the previous average glacial transition infiltration rate over the UZ model domain was 17 mm/yr (BSC 2004 [DIRS 169861], Table 6.1-2). For the current infiltration maps, the most-probable (10th percentile) glacial transition average infiltration rate over the UZ model domain is 11 mm/yr (see Table 6.1-2). However, in the current model, long-term behavior is dominated by the post-10,000 yr period. For this period, the most probable (10th percentile) average infiltration rate over the UZ model domain is also 17 mm/yr (see Table 6.1-3). This case represents over 60% of the sampling probability for infiltration uncertainty in the post-10k-yr period. Therefore, the sensitivity studies using the previous infiltration maps are still representative of the long-term behavior. In addition, the results of the previous sensitivity analysis for unsaturated zone flow are still valid because the differences in the average infiltration over the UZ model domain are

small, and the conceptual models and processes implemented in the UZ flow models have not changed.

H3.3 CONCEPTUAL MODEL AND NUMERICAL APPROACHES FOR UNSATURATED ZONE FLOW AND TRANSPORT (MDL-NBS-HS-000005 REV. 01)

The purpose of this model report is to document the conceptual and numerical models used for modeling UZ fluid (water and air) flow and solute transport processes. This work was planned in *Technical Work Plan for: Unsaturated Zone Flow, Drift Seepage and Unsaturated Zone Transport Modeling* (BSC 2006 [DIRS 177465], Sections 1.2.5, 2.1.1, 2.1.2, and 2.2.1). The conceptual and numerical modeling approaches described in this report are mainly used for models of UZ flow and transport in fractured, unsaturated rock under ambient conditions. As such, no direct inputs are used in the development of this report.

The previous infiltration map data are used for the active–fracture-model validation work. These validation calculations are for ^{14}C travel times at two boreholes, SD-12 and UZ-1, and for fracture-coating observations. The ^{14}C calculations were performed using a one-dimensional model for present-day infiltration only. However, a three-dimensional model has also been used to investigate the ^{14}C predictions against the data from UZ-1 and SD-12 in *UZ Flow Models and Submodels* (see Section 7.5). These calculations used the current infiltration maps for present-day climate. Therefore, the effects of the current infiltration rates have been investigated for ^{14}C age predictions. The results of the fracture-coating frequency analysis were shown to be insensitive to infiltration rate over a range from 8.2 to 17.3 mm/yr (BSC 2004 [DIRS 170035], Section 7.4.2). Therefore, the magnitude of change in infiltration rates shown in Figure H-1 are expected to have a negligible impact on the fracture-coating validation case.

H3.4 SEEPAGE CALIBRATION MODEL AND SEEPAGE TESTING DATA (MDL-NBS-HS-000004 REV. 03)

The seepage calibration model was used for the estimation of seepage-relevant parameters through calibration of the model against seepage-rate data from liquid-release tests performed in several niches along the Exploratory Studies Facility (ESF) Main Drift and in the Cross-Drift. In these tests, water was released from boreholes a few meters above the niche crowns, and the amount of water seeping into the openings was measured. The liquid-release rates were much higher than the background percolation at Yucca Mountain. As a result, the test data and the calibration results are not sensitive to background percolation, and moderate differences in estimates of present-day infiltration, which governs background percolation, have no significant effect on the product output of the seepage calibration model (BSC 2004 [DIRS 171764], Section 6.6.2.3). For these reasons, the seepage calibration model results are still directly relevant, and no further sensitivity analyses are needed.

H3.5 SEEPAGE MODEL FOR PA INCLUDING DRIFT COLLAPSE (MDL-NBS-HS-000002 REV. 03)

The seepage model for performance assessment (SMPA) conducts seepage predictions for sections of emplacement drifts sections using many combinations of the three most important

seepage-relevant parameters: the fracture permeability, the capillary strength parameter $1/\alpha$, and the percolation flux. The model produces look-up tables of seepage flow rates into a drift (and their uncertainty) to be used in the TSPA seepage assessment. Like the other two seepage-relevant parameters, percolation flux is parametric in the SMPA (i.e., it is an independent parameter) and the model is configured to provide seepage estimates for a wide range of flux conditions (from 1 mm/yr up to 1,000 mm/yr). For these reasons, the SMPA look-up tables are still directly relevant, and no further sensitivity analyses are needed. Changes in infiltration, and the related changes in percolation flux estimates, are accounted for in the TSPA seepage module by feeding revised flux distributions into the SMPA-generated look-up tables. The range of percolation data expected using current data is evaluated and accommodated by changes in the seepage abstraction, as described by *Abstraction of Drift Seepage* (SNL 2007 [DIRS 181244]).

H3.6 RADIONUCLIDE TRANSPORT MODELS UNDER AMBIENT CONDITIONS (MDL-NBS-HS-000008 REV. 02 ADD 01)

The infiltration results are used in this report to generate simulations of transport behavior as a basis for model comparison with the UZ particle tracking abstraction model. Therefore, even though this document is being revised, it was deemed unnecessary to perform the simulations again using the current infiltration results for the purposes of code comparison. The range of infiltration between the current and previous infiltration results is similar (Table H-2), so the use of the previous infiltration results as a basis for code comparison is adequate.

H3.7 PARTICLE TRACKING MODEL AND ABSTRACTION OF TRANSPORT PROCESSES (MDL-NBS-HS-000020 REV. 02 ADD. 01)

For purposes of model comparison and validation, the infiltration results used in this report need to be consistent with the infiltration rates used by the process model (SNL 2007 [DIRS 177396]). As described above, the use of the previous infiltration results was deemed adequate for the purposes of code comparison, since the range of infiltration is similar between the previous and current infiltration results. Therefore, the use of the previous infiltration results in this report is justified. Simulations showing the results of the particle tracking model with current infiltration data are provided in *Particle Tracking Model and Abstraction of Transport Processes* (SNL 2007 [DIRS 181006]).

H4. EVALUATION OF IMPACT ON GROUP 3 PRODUCTS

H4.1 Ventilation Model/Analysis Report (ANL-EBS-MD-000030 REV. 04)

Evaluation—The ventilation model calculates heat-removal efficiency for preclosure ventilation. It does not include effects from latent or sensible heat transfers associated with the presence of water, because these are small compared to air convection, thermal radiation, and solid-conduction in the near-field environment. To verify this model simplification, Section 6.9.1 of this report evaluates an alternative model, whereby latent heat from *in situ* porewater evaporation, and vapor removal by ventilation, contribute significantly to heat removal from the repository. Using a location-specific value of 15.71 mm/yr (rounded) for present-day percolation, and assuming a capture zone of width equal to two drift diameters, the calculation shows that

1.4% of the waste-generated heat could be removed as latent heat by evaporation over a 50 yr period. Even with a higher value of the percolation flux (see Figure H-1 for the uncertainty range) the effect on ventilation is limited to a few percent. The difference in weighted values of present-day flux from the previous flow model compared to the current one (Table H-2) is insignificant to this result. The effect of evaporation is to increase efficiency, which could be compensated by reducing the air flow rate. For these reasons no further calculation of the sensitivity of ventilation efficiency to the local percolation flux is needed.

Ventilation FEPs—Ventilation model results are used to include various FEPs including (DTN: MO0706SPAFEPLA.001 [DIRS 181613]):

- Preclosure Ventilation (1.1.02.02.0A)
- Repository Dryout Due to Waste Heat (2.1.08.03.0A)
- Chemical Characteristics of Water in Drifts (2.1.09.01.0A)
- Heat Generation in EBS (2.1.11.01.0A)
- Thermal Effects on Flow in the EBS (2.1.11.09.0A)
- Thermally Driven Flow (Convection) in Drifts (2.1.11.09.0C).

No FEP exclusion arguments are directly supported by the ventilation model report, so there are no associated impacts to evaluate.

H4.2 Drift-Scale Coupled Processes (DST and TH Seepage) Models (MDL-NBS-HS-000015 REV. 02)

Evaluation of Flux Values Used—This model report includes a thermal-hydrologic (TH) simulation of the Drift-Scale Test (DST), and a series of simulations and sensitivity analyses that describe the potential for seepage into repository drifts during the thermal period. For the DST, the results provide validation of certain fundamental aspects of TH modeling. For repository seepage, simulation results show that: (1) seepage does not occur when the drift-wall temperature is at or above boiling temperature (96°C); and (2) thermal seepage is less than simulated ambient seepage, because part of the incident percolation flux is diverted by evaporation in the rock. These findings constitute the TSPA implementation of a thermal seepage model; a cutoff temperature of 100°C is used, and ambient seepage fractions and percentages are used to bound thermal seepage (SNL 2007 [DIRS 181244], Section 6.5.2.2). In the following discussion, "thermal seepage model" refers to the implementation of these findings in TSPA, and the underlying simulations and analysis in the subject report.

Base-case percolation flux values of 6, 16, and 25 mm/yr were used in thermal seepage modeling and sensitivity analyses, for the present-day, monsoon, and glacial transition climate states, respectively. Sensitivity analyses increased these values by factors of 5, 10, 20, 40, and 100. The results described above were consistent for all flux conditions, and the effect of greater percolation flux on the thermal regime was to hasten cooling rather than to cause seepage while the drift-wall temperature was above 96°C. Because of this behavior, and the use of an extensive range of flux values for sensitivity analyses, there is no significant impact from the current infiltration and percolation data on this model report.

Evaluation of Hydrologic Property Values Used—The key properties controlling seepage are bulk permeability, capillary strength, and percolation flux. Permeability for the host rock units is based on *in situ* measurements and is not a calibrated parameter (see for example, DTN: LB0610UZDSCP30.001 [DIRS 179180], file: *Calibrated Parameter_R113_30%.doc*). Therefore the permeability description of the host rock is unaffected by changes in the infiltration or percolation flux estimates. The capillary-strength parameter is independently calibrated within the seepage model reports, *Seepage Model for PA Including Drift Collapse* (BSC 2004 [DIRS 167652] and *Seepage Calibration Model and Seepage Testing Data* (BSC 2004 [DIRS 171764]) and is also unaffected by changes in the infiltration or percolation flux estimates (see Section H.3).

Thermal Seepage FEPs—Thermal seepage model results are used to include various FEPs including the following (DTN: MO0706SPAFEPLA.001 [DIRS 181613]):

- Preclosure Ventilation (1.1.02.02.0A)
- Fractures (1.2.02.01.0A)
- Climate Change (1.3.01.00.0A)
- Water Influx at the Repository (2.1.08.01.0A)
- Enhanced Influx at the Repository (2.1.08.02.0A)
- Mechanical Effects of Excavation and Construction in the Near-Field (2.2.01.01.0A)
- Stratigraphy (2.2.03.01.0A)
- Rock Properties of Host Rock and Other Units (2.2.03.02.0A)
- Unsaturated Groundwater Flow in the Geosphere (2.2.07.02.0A)
- Focusing of Unsaturated Flow (Fingers, Weeps) (2.2.07.04.0A)
- Fracture Flow in the UZ (2.2.07.08.0A)
- Matrix Imbibition in the UZ (2.2.07.09.0A)
- Condensation Zone Forms around Drifts (2.2.07.10.0A)
- Resaturation of Geosphere Dryout Zone (2.2.07.11.0A)
- Flow Diversion around Repository Drifts (2.2.07.20.0A)
- Natural Geothermal Effects on Flow in the UZ (2.2.10.03.0B)
- Two-Phase Buoyant Flow/Heat Pipes (2.2.10.10.0A)
- Geosphere Dryout Due to Waste Heat (2.2.10.12.0A)

The thermal seepage model is used to determine that dewatering from preclosure activities is insignificant and can be excluded (Changes in Fluid Saturations in the Excavation Disturbed Zone, 2.2.01.03.0A). No other FEP exclusion arguments are directly supported by the thermal seepage model report.

H4.3 Drift-Scale THM Model (MDL-NBS-HS-000017 REV. 01)

Evaluation—This model report evaluates coupling between thermomechanical and hydrologic responses in the host rock around a repository emplacement drift. The coupled calculations used only one set of percolation values: 6, 16, and 25 mm/yr for the three climate states. The model results show that the effect of mechanical deformation on percolation flux is small, primarily because changes in fracture intrinsic permeability are compensated by changes in relative permeability (BSC 2004 [DIRS 169864], Section 6.6.2). As stated in the report, the precise

magnitude of the flux does not affect the conclusions significantly. The base-case flux values used in drift-scale thermal-hydrologic-mechanical (THM) modeling (6, 16, and 25 mm/yr) can be shown to be similar to the current data (e.g., by comparison to the composite values for the three climate states) (Table H-2). This means that the THM model is just as representative of host-rock behavior with the current flux data, as with the previous data. For these reasons the THM model results are still directly relevant and applicable to FEP exclusion arguments.

THM FEPs – The drift-scale THM model describes host-rock responses that are not included in TSPA. The report is cited in the arguments to exclude the following FEPs (DTN: MO0706SPAFEPLA.001 [DIRS 181613]):

- Effects of Subsidence (2.2.06.04.0A)
- Seismic Activity Changes Porosity and Permeability of Rock (2.2.06.01.0A)
- Seismic Activity Changes Porosity and Permeability of Faults (2.2.06.02.0A)
- Seismic Activity Changes Porosity and Permeability of Fractures (2.2.06.02.0B)
- Thermally Induced Stress Changes in the Near-Field (2.2.01.02.0A)
- Radionuclide Transport in the Excavation Disturbed Zone (2.2.01.05.0A)
- Repository-Induced Thermal Effects on Flow in the UZ (2.2.10.01.0A)
- Thermal-Mechanical Stresses Alter Characteristics of Fractures near Repository (2.2.10.04.0A)
- Thermal-Mechanical Stresses Alter Characteristics of Faults near Repository (2.2.10.04.0B)

Many of these exclusion arguments are thermal-mechanical and do not depend on the percolation flux. The effects of THM changes in fracture permeability in the near field on the potential for seepage and radionuclide transport are excluded, based on arguments that do not depend closely on the percolation flux.

H4.4 Mountain-Scale Coupled Processes (TH/THC/THM) Models (MDL-NBS-HS-000007 Rev. 03)

This family of mountain-scale models includes a three-dimensional TH model, a two-dimensional TH profile model, a two-dimensional thermal-hydrologic-chemical (THC) profile model, and a two-dimensional THM profile model. The two-dimensional TH profile model forms the basis of the THM and THC models that consist of all or part of the same profile. As TSPA supporting work, these models are used only in disposition of FEPs (see below).

The three-dimensional mountain-scale TH model occupies the same spatial domain as the UZ flow model and uses the same infiltration flux boundary conditions. The average values of net infiltration for this model (Table H-2) are comparable to averages from the current data for the repository footprint (10th percentile), for both surface infiltration and host-rock percolation. However, this model is not used directly in FEP screening and is not discussed further here.

The two-dimensional mountain-scale TH model uses a spatial profile of net infiltration extracted from the previous infiltration data used as a boundary condition for the previous UZ flow model as discussed above. Accordingly, the flux boundary condition is spatially variable. The averages for this profile, for the three climate states, are closely comparable to the weighted composite values for both the previous and current data for the repository footprint (Table H-2). The higher percentiles of the current data include average flux values, which are approximately 3 times the upper limit of the two-dimensional TH model (74.49 versus 28.8 mm/yr; Table H-2). Such conditions tend to quench the thermal-hydrologic response and hasten the return to pre-heating conditions. The same profile boundary condition is used for the two-dimensional mountain-scale THM model. Greater fluxes (e.g., 3 times greater) would not approach the unsaturated hydraulic conductivity of the host rock, even if permeability were decreased as much as a factor of 5 by THM processes (BSC 2005 [DIRS 174101], Section 6.5.12). Thus the finding that mountain-scale THM processes do not affect the vertical percolation flux in the host rock holds for greater values of the flux.

The two-dimensional mountain-scale THC model uses a segment of the two-dimensional profile discussed above. This is a north-south profile, and lateral diversion at interfaces between stratigraphic units is not significant, so percolation is predominantly downward in the model. The average fluxes along the profile (ranging up to 106 mm/yr in the glacial transition climate) are roughly comparable to the averages for the current 50th and 90th percentile flux fields for all three climate states (Table H-3). As such, the two-dimensional mountain-scale THC model does not exhibit significant diversion effects and represents a relatively wet profile, whether compared to the previous or current infiltration/percolation data sets.

Mountain-Scale FEPs—The mountain-scale coupled-process models are used in exclusion arguments for five FEPs as discussed below (DTN: MO0706SPAFEPLA.001 [DIRS 181613]):

- **Repository-Induced Thermal Effects on Flow in the UZ** (2.2.10.01.0A) The mountain-scale two-dimensional TH model shows that the limited extent of flow redistribution found at the mountain scale is consistent with drift-scale results (BSC 2005 [DIRS 174101], Section 6.5.13).

- **Mineralogic Dehydration Reactions** (2.2.10.14.0A) Results from the two-dimensional mountain-scale TH model suggests that temperature at the base of the TSw will remain below 77°C in the southern portion of the repository, and below 74°C in the northern portion (BSC 2005 [DIRS 174101], Section 6.2). Therefore the temperature changes induced by the repository will not cause significant zeolite dehydration or volume changes in the zeolitic rock (DTN: MO0706SPAFEPLA.001 [DIRS 181613]).

- **Thermo-Chemical Alteration in the UZ (Solubility, Speciation, Phase Changes, Precipitation/Dissolution)** (2.2.10.06.0A) Trends in the two-dimensional mountain-scale THC model results, particularly in the variation of chloride and pH, are similar to drift-scale simulations. Variations in chloride are driven mainly by evaporation and are found to return to near-ambient values upon rewetting (BSC 2005 [DIRS 174101], Section 6.4.3.3.2).

- **Geochemical Interactions and Evolution in the UZ** (2.2.08.03.0B) Fluctuations in host-rock water composition during the thermal period will be relatively short-lived (much less than 10,000 yr) and of limited magnitude compared to the existing ambient variability of *in situ* water composition. Trends in two-dimensional mountain-scale THC model results, particularly in the variation of chloride and pH, are similar to drift-scale simulations (BSC 2005 [DIRS 174101], Section 6.4.3.3.2)

- **Thermal-Mechanical Stresses Alter Characteristics of Rocks Above and Below the Repository** (2.2.10.05.0A) THM-induced changes in the two-dimensional mountain-scale THM model hydrological properties have no significant impact on the vertical percolation flux through the repository horizon (BSC 2005 [DIRS 174101, Sections 6.5.10 to 6.5.14).

These arguments do not depend closely on the percolation flux, for the various reasons discussed above. No further impact evaluation is needed to confirm the applicability of documented FEP screening arguments based on the mountain-scale models, developed using the previous (INFIL-based) infiltration and percolation data.

H5. SUMMARY

This evaluation has grouped the potential impacts of current (MASSIF-based) infiltration and host-rock percolation flux data on technical products that will support the postclosure TSPA (Table H-1). Some of these products (Group 1) are being revised or modified to consider the current data and require no evaluation. Other products (Group 2) cite the previous (INFIL-based) infiltration data but do not use them directly in models, analyses, or calculations. Some Group 2 products use the previous infiltration data, but the actual values are not critical for the purposes of the analysis or calculation. The evaluations for these products focus on the manner of use and the possibility that conclusions or other content would be changed if current data were used.

The last category of products (Group 3) consists of those that used the previous data directly in models, analyses, or calculations. Each of these products is discussed, and values used are tabulated and characterized in Table H-2. Use of the previous data in analysis of FEPs is also considered for Group 3. The impact of the current data (compared with the previous data in Figures H-1 through H-3) on Group 2 and 3 products is generally negligible, because of similarity between the data sets, and the manner of data use in scoping or screening arguments. This conclusion is not surprising, because the models and analyses that are more sensitive to infiltration or percolation flux are being recalculated for TSPA and fall into Group 1.

Table H-1. Summary of Products Impacted by Changes in the Infiltration Model

Product	Title	Use	Impact Evaluation Status
Group 1 Products - Infiltration Data Updated			
SNL 2007 [DIRS 181383]	Multiscale Thermohydrologic Model	TSPA	None needed
SNL 2007 [DIRS 177413]	THC Sensitivity Study of Heterogeneous Permeability and Capillarity Effects	FEPS	None needed
SNL 2007 [DIRS 177404]	Drift-Scale THC Seepage Model	FEPs	None needed
This document	UZ Flow Models and Submodels	TSPA	None needed
SNL 2007 [DIRS 181650]	Saturated Zone Flow and Transport Model Abstraction	TSPA	None needed
BSC 2004 [DIRS 164327]	In-Drift Convection and Condensation Model	TSPA	None needed
SNL 2007 [DIRS 178871]	Total System Performance Assessment Model/Analysis for License Application	SAR	None needed
SNL 2007 [DIRS 179545]	Unsaturated Zone Calibrated Properties	TSPA supporting	None needed
SNL 2007 [DIRS 177407]	EBS Radionuclide Transport Abstraction	TSPA	None needed
BSC 2006 [DIRS 177464]	Postclosure Nuclear Safety Design Basis	SAR	None needed
Group 2 Products - Impact Evaluation Provided			
BSC 2004 [DIRS 172452]	Performance Confirmation Plan	SAR	Cites percolation flux data only with respect to future confirmation studies
BSC 2005 [DIRS 174116]	Parameter Sensitivity Analysis for Unsaturated Zone Flow	TSPA supporting	Parametric with respect to percolation flux
BSC 2004 [DIRS 170035]	Conceptual Model and Numerical Approaches for Unsaturated Zone Flow and Transport	TSPA supporting	Parametric with respect to percolation flux
BSC 2004 [DIRS 171764]	Seepage Calibration Model and Seepage Testing Data	TSPA supporting	Parametric with respect to percolation flux. Based on experiments with flux as an independent parameter.
BSC 2004 [DIRS 167652]	Seepage Model for PA Including Drift Collapse	TSPA supporting	Parametric with respect to percolation flux. Range of flux is addressed by SNL 2007 [DIRS 181244].
SNL 2007 [DIRS 177396]	Radionuclide Transport Models Under Ambient Conditions	TSPA supporting	Infiltration used for model comparison only.
SNL 2007 [DIRS 181006]	Particle Tracking Model and Abstraction of Transport Processes	TSPA	Infiltration used for model comparison only.
Group 3 Products - Specific Impact Evaluation Provided			
BSC 2004 [DIRS 169862]	Ventilation Model and Analysis Report	TSPA supporting	The single flux value used is adequate for its intended purpose.
BSC 2005 [DIRS 172232]	Drift Scale Coupled Processes (DST and TH Seepage) Models	TSPA supporting	Parametric with respect to Percolation Flux, but Uses Older Calibrated Hydrologic Properties.
BSC 2004 [DIRS 169864]	Drift Scale THM Model	FEPs	Only Used Values of 6, 16, and 25 mm/yr for 3 Climate States. Uses Older Calibrated Hydrologic Properties.
BSC 2005 [DIRS 174101]	Mountain Scale Coupled Processes (TH/THC/THM) Models	FEPs	Uses mean INFIL-model based maps for 3 climate states, in 2D and 3D models. Also uses calibrated hydrologic properties from INFIL-based data. Flux values are similar to values from the updated model, and are therefore adequate for the intended use.

Table H-2. Average Flux Values for Comparison of Previous and Current Model Results

All fluxes in mm/yr	Present- Day	Monsoonal	Glacial-Transition	Weights	
Current Models for Infiltration and UZ Flow, Percolation Flux at PTn-TSw Interface					
Quantile	**Avg. Flux in Footprint [a]**				
0.1	4.1	7.8	12.2	0.6191	Weights: Table 6.8-1 (average values) Fluxes: SNL 2007 [DIRS 181383], Table 6.2-5.
0.3	10.2	16.1	26.3	0.1568	
0.5	14.6	19.5	36.2	0.1645	
0.9	34.1	92.4	69.7	0.0596	
Weighted	**8.6**	**16.1**	**21.8**	1.0000	
Previous Models for Infiltration and UZ Flow, Infiltration Flux at Ground Surface					
Case	**Avg. Flux in Footprint [a]**				
Lower	0.25	4.20	1.92	0.24	Fluxes and weights: BSC 2003 [DIRS 165991], Tables 6-4 and 6-7 (not including contingency area).
Mean	4.20	11.86	18.57	0.41	
Upper	10.80	19.53	35.23	0.35	
Weighted	**5.6**	**12.7**	**20.4**	1.00	
Previous Models for Infiltration and UZ Flow, Percolation Flux at PTn-TSw Interface					
Case	**Avg. Flux in Repository Footprint [a]**				
Lower	0.40	4.30	1.90	0.24	Fluxes: SNL 2007 [DIRS 181244], Table 6.6-11 Weights: BSC 2003 [DIRS 165991], Table 6-7
Mean	3.80	11.70	17.90	0.41	
Upper	11.10	20.30	35.10	0.35	
Weighted	**5.5**	**12.9**	**20.1**	1.00	
Drift-Scale Coupled Processes (DST and TH Seepage) Models (MDL-NBS-HS-000015 Rev. 02, Section 4.1.1.4)					
Values Used	6.0	16.0	25.0		Base values shown; model also includes sensitivity runs that multiply these values by factors of up to 100 (BSC 2005 [DIRS 172232], Section 6.2.1.4).
Drift-Scale THM Model (MDL-NBS-HS-000017 Rev. 01; Section 4.1.1.2)					
Values Used	6.0	16.0	25.0		
Mountain-Scale Coupled Processes (TH/THC/THM) Models (MDL-NBS-HS-000007 Rev. 03)					
Values Used	3.6	10.4	16.1	Average over three-dimensional TH model domain (Table 6.1-2)	
Values Used	5.8	17	28.8	Average over two-dimensional TH and THM model profiles (Section 6.1.4 and Table 6.5.6-1)	
Values Used	8.7	32.3	101.6	Average over segment of two-dimensional TH profile used for THC (Section 6.4.2.3)	
Ventilation Model and Analysis Report (ANL-EBS-MD-000030 Rev. 04, Section 6.9.1)					
Value Used	15.71	From mean flux field at location selected for sensitivity analysis.			

NOTE: [a] Refers to the 560-column footprint including the contingency area, for the previous and current data.

Table H-3. Ranges of Flux Values for Comparison of Previous and Current Model Results

Spatial Variability Quantile	Current Host-Rock Percolation (nominal percentiles of selected realizations)				Previous Host-Rock Percolation (uncertainty state)		
	10th	30th	50th	90th	Lower	Mean	Upper
PRESENT-DAY CLIMATE							
Minimum	0.13	0.34	0.60	1.32	-0.97	0.11	0.15
0.05	0.59	1.74	2.36	4.94	0.00	0.52	1.83
0.10	0.90	2.66	3.61	7.35	0.00	1.07	3.13
0.50	3.97	10.10	14.90	35.40	0.16	3.34	9.61
0.90	5.99	14.60	20.00	44.80	1.16	7.00	19.10
0.95	6.43	15.30	21.00	47.20	1.65	8.52	22.28
Maximum	8.10	19.00	26.60	58.70	4.24	39.90	80.44
MONSOONAL CLIMATE							
Minimum	0.43	0.55	0.53	3.08	0.02	0.21	0.18
0.05	1.23	2.42	2.71	11.90	0.63	1.38	3.31
0.10	1.90	4.06	4.12	18.00	0.98	2.60	5.39
0.50	8.01	15.90	19.10	96.90	3.96	9.26	16.15
0.90	10.70	23.60	28.60	122.00	7.59	22.09	36.43
0.95	11.10	25.00	32.00	128.00	8.61	26.92	41.43
Maximum	14.60	31.20	49.90	160.00	29.74	152.78	164.76
GLACIAL TRANSITION CLIMATE							
Minimum	0.15	0.43	0.45	1.20	0.00	0.36	0.48
0.05	0.83	2.89	3.30	7.00	0.10	2.49	6.10
0.10	1.51	5.14	5.24	12.20	0.25	3.86	9.56
0.50	9.17	24.30	32.80	70.20	1.51	14.12	28.15
0.90	22.90	41.80	59.20	99.70	4.31	34.09	65.46
0.95	26.20	44.60	63.40	106.00	5.38	41.18	75.27
Maximum	36.20	54.90	79.90	136.00	17.84	233.45	294.13

Source: DTN: LL0705PA038MST.030 [DIRS 182332], *Perc. flux footprint summary April2007.xls*.

NOTE: Percolation fields (current and previous) sorted to the same 560 columns from the UZ flow model.

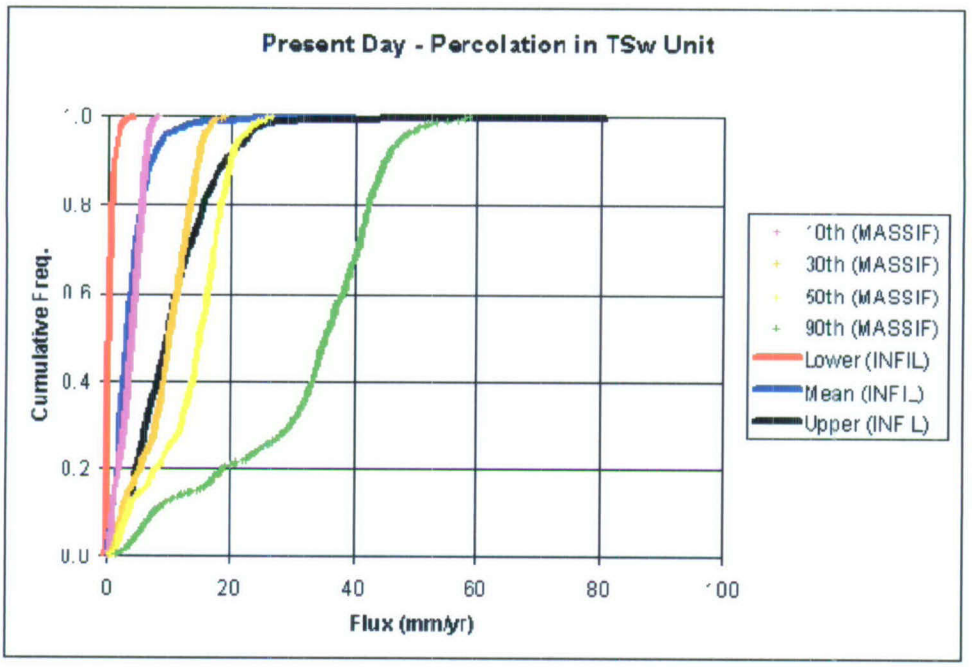

Source: DTN: LL0705PA038MST.030 [DIRS 182332], *Perc. flux footprint summary April2007.xls.*

Figure H-1. Cumulative Distributions for Present-Day Percolation in the Host Rock, Comparing the Impact of Infiltration Model Inputs from the Current versus Previous Model

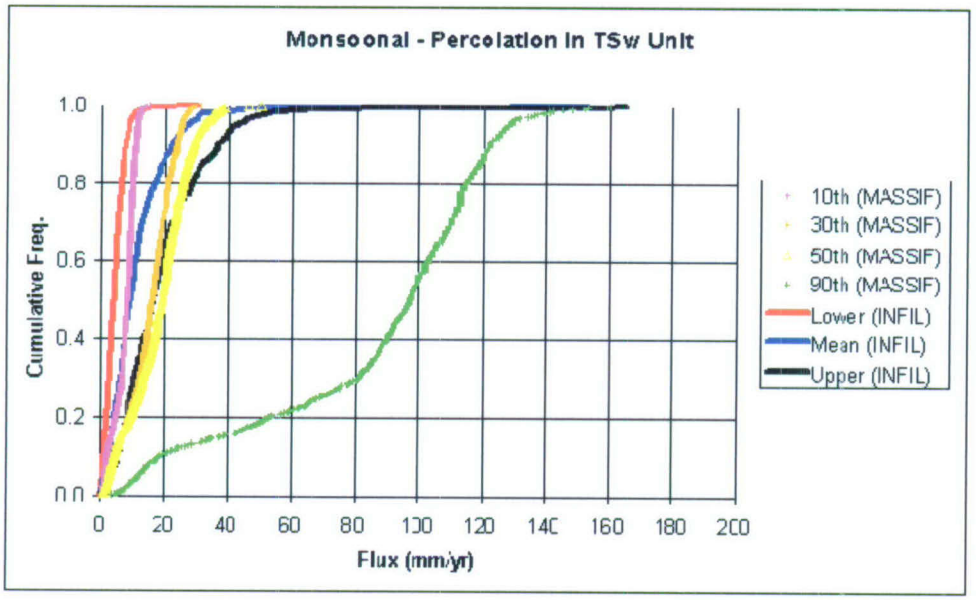

Source: DTN: LL0705PA038MST.030 [DIRS 182332], *Perc. flux footprint summary April2007.xls.*

Figure H-2. Cumulative Distributions for Monsoonal Percolation in the Host Rock, Comparing the Impact of Infiltration Model Inputs from the Current versus Previous Model

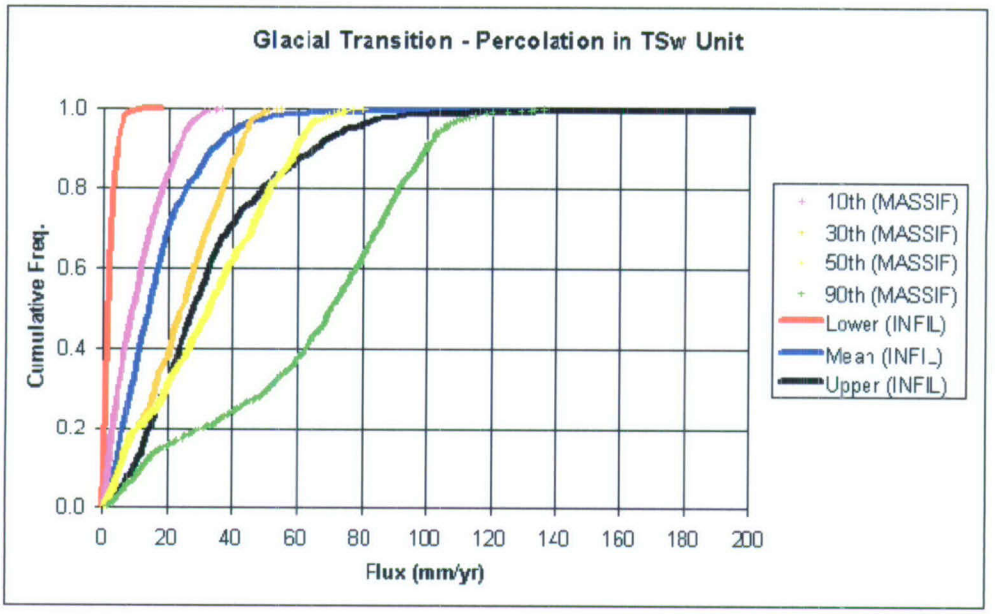

Source: DTN: LL0705PA038MST.030 [DIRS 182332], *Perc. flux footprint summary April2007.xls.*

Figure H-3. Cumulative Distributions for Glacial-Transition Percolation in the Host Rock, Comparing the Impact of Infiltration Model Inputs from the Current versus Previous Model

INTENTIONALLY LEFT BLANK

APPENDIX I
QUALIFICATION OF UNQUALIFIED DATA

I-1. PURPOSE

This appendix documents qualification of data used to calculate the lower-temperature boundary of UZ models as described in Section 6.3.3. The values to be qualified are temperature measurements in DTN: GS950408318523.001 [DIRS 107244]. These data are long-term temperature measurement data for 34 boreholes at Yucca Mountain, originally developed by Sass et al. (1988 [DIRS 100644]). Since the data were collected in the 1980s, they were not qualified according to the current QA procedures.

I-2. QUALIFICATION PLAN AND CRITERIA

The data qualification plan states that the qualification process will be conducted according to Method 2 "Corroborating Data" (SCI-PRO-001, Attachment 3), because qualified data are available to conduct data comparison that can be shown to substantiate or confirm parameter values. In addition, the data qualification plan states that Qualification Process Attributes 1, 3, 4, and 10 (SCI-PRO-001, Attachment 4) will be used.

The criteria stated in the data qualification plan are as follows:

> The difference of the temperature values between the unqualified data and the qualified data at the same (or nearby) locations are within the range of ±2.0°C or less than 5% of the temperature value. Because no boreholes exactly overlap between these two data sets, unqualified temperature data from the closest borehole (or several nearby boreholes if they are within a similar distance) to that in the qualified data set will be picked for temperature comparison. These distances between boreholes from the two data sets will be treated as a weighting factor when evaluating temperature differences. In addition, the data at the deepest depth of the boreholes that have qualified measurements will be selected for temperature comparison, to avoid complication from possible influence of near-surface noises.

I-3. DATA QUALIFICATION DETAIL

I-3.1. ATTRIBUTE 1: QUALIFICATIONS OF PERSONNEL OR ORGANIZATIONS GENERATING THE DATA ARE COMPARABLE TO QUALIFICATION REQUIREMENTS OF PERSONNEL GENERATING SIMILAR DATA UNDER AN APPROVED PROGRAM THAT SUPPORTS THE YMP LICENSE APPLICATION PROCESS OR POSTCLOSURE SCIENCE (SCI-PRO-001, ATTACHMENT 4):

The unqualified data (DTN: GS950408318523.001 [DIRS 107244]) and qualified data (DTNs: GS031208312232.005 [DIRS 179284], GS031208312232.004 [DIRS 182187], GS031208312232.007 [DIRS 178751], GS031208312232.006 [DIRS 182186], GS950208312232.003 [DIRS 105572], GS031208312232.003 [DIRS 171287]) were collected by USGS; USGS meets the qualification requirements under the approved program that supports the YMP License Application.

I-3.2. ATTRIBUTE 3: THE EXTENT TO WHICH THE DATA DEMONSTRATE THE PROPERTIES OF INTEREST (E.G., PHYSICAL, CHEMICAL, GEOLOGIC, MECHANICAL) (SCI-PRO-001, ATTACHMENT 4):

The temperature boundary at the water table, needed by UZ models, is a constant temperature (or steady state) boundary condition at that deep subsurface, which should not be subject to seasonal or daily variations in any significant way. The small variations in measured temperature values within boreholes with qualified measurements demonstrate this property (Table I-1).

Table I-1. Variations of Temperature Data Measured in the Boreholes That Were Qualified

Borehole	Depth (m)	Starting Data	Ending Data	T (mean, °C)	STD	CV	Number of Measurements
USW NRG-7a	203.61	10/1/1997	3/31/1998	23.1348	0.002991	0.000129266	2,918
USW NRG-7a	203.61	7/1/1997	9/30/1997	23.13445	0.002066	8.92898×10^{-5}	1,199
USW NRG-7a	203.61	1/1/1997	6/30/1997	23.13286	0.002202	9.5185×10^{-5}	1,730
USW NRG-7a	203.61	8/16/1996	12/16/1996	23.12996	0.003248	0.000140422	1,221
USW NRG-7a	203.61	4/1/1996	8/15/1996	23.12535	0.003252	0.000140631	1,217
USW NRG-7a	203.61	10/28/1994	3/31/1995	22.93948	0.23528	0.010256557	1,761
USW NRG-6	219.46	12/3/1997	3/31/1998	23.517	0.006889	0.000292918	623
USW NRG-6	219.46	8/16/1996	9/3/1996	23.51274	0.005144	0.000218765	176
USW NRG-6	219.46	4/1/1996	8/15/1996	23.50982	0.577398	0.024559869	1,318
USW NRG-6	219.46	11/17/1994	3/31/1995	23.3552	0.266532	0.011412097	1,167
UE-25 UZ #4	111.86	10/1/1997	3/31/1998	22.7222	0.001032	4.54358×10^{-5}	1,643
UE-25 UZ #4	111.86	7/2/1997	9/30/1997	22.72111	0.000897	3.94746×10^{-5}	736
UE-25 UZ #4	111.86	1/1/1997	6/30/1997	22.72064	0.00119	5.23728×10^{-5}	1,763
UE-25 UZ#4	111.86	8/16/1996	12/31/1996	22.71971	0.001034	4.54916×10^{-5}	1,457
UE-25 UZ#4	111.86	4/1/1996	8/15/1996	22.71746	0.001033	4.54514×10^{-5}	1,426
UE-25 UZ #5	111.56	10/1/1997	3/31/1998	22.50697	0.0012	5.33387×10^{-5}	1,627
UE-25 UZ #5	111.56	7/2/1997	9/30/1997	22.50481	0.000894	3.97272×10^{-5}	723
UE-25 UZ #5	111.56	1/1/1997	6/30/1997	22.50304	0.001454	6.46317×10^{-5}	1,754
UE-25 UZ#5	111.56	8/16/1996	12/31/1996	22.50045	0.001445	6.42355×10^{-5}	1,439
UE-25 UZ#5	111.56	4/1/1996	8/15/1996	22.49415	0.002805	0.000124703	1,418
USW UZ-7a	194.16	10/1/1997	3/31/1998	21.82107	0.00297	0.000136088	1,810
USW UZ-7a	194.16	7/1/1997	9/30/1997	21.82053	0.002379	0.000109018	874
USW UZ-7a	194.16	1/1/1997	6/30/1997	21.82051	0.002475	0.000113424	1,424
USW UZ-7a	194.16	8/16/1996	12/31/1996	21.82032	0.002559	0.000117286	1,300
USW UZ-7a	194.16	4/1/1996	8/15/1996	21.82309	0.002572	0.000117854	1,232
USW SD-12	435.86	10/1/1997	3/31/1998	26.5495	0.001629	6.13532×10^{-5}	1,766
USW SD-12	435.86	7/1/1997	9/30/1997	26.54842	0.001341	5.05289×10^{-5}	879
USW SD-12	435.86	1/1/1997	6/30/1997	26.5445	0.002781	0.000104773	2,628
USW SD-12	435.86	8/16/1996	12/31/1996	26.53451	0.005371	0.000202418	1,990
USW SD-12	435.86	4/1/1996	8/15/1996	26.5038	0.028535	0.001076649	953

Source: DTN: LB0708WTTEMDAT.001, file: *QualifyTData.xls*, sheet: *SummaryQ-Data.*

I-3.3. ATTRIBUTE 4: THE ENVIRONMENTAL CONDITIONS UNDER WHICH THE DATA WERE OBTAINED IF GERMANE TO THE QUALITY OF DATA (SCI-PRO-001, ATTACHMENT 4):

The temperature in the deep subsurface is stable under ambient conditions and should not change significantly within two decades. As shown in Table I-2, although the temperature increased in most boreholes, the magnitude of the change was small (the average is below about 0.02°C/yr). Therefore, these two data sets, although collected in different periods, should be comparable.

Table I-2 Average Yearly Change of Temperature

Borehole	Depth (m)	Starting Data	Ending Data	Average Change (°C/yr)
USW NRG-7a	203.61	10/28/1994	3/31/1998	0.057072
USW NRG-6	219.46	11/17/1994	3/31/1998	0.048047
UE-25 UZ #4	111.86	4/1/1996	3/31/1998	0.002375
UE-25 UZ #5	111.56	4/1/1996	3/31/1998	0.006422
USW UZ-7a	194.16	4/1/1996	3/31/1998	-0.00101
USW SD-12	435.86	4/1/1996	3/31/1998	0.022899
Mean				**0.022634**

Source: DTN: LB0708WTTEMDAT, file: *QualifyTData.xls*, sheet: *SummaryQ-Data.*

I-3.4. ATTRIBUTE 10: EXTENT AND QUALITY OF CORROBORATING DATA OR CONFIRMATORY TESTING RESULTS (SCI-PRO-001, ATTACHMENT 4)

The corroborating data were qualified under QA procedures that support the YMP License Application. The qualified data set includes data at sufficient depth (within the unsaturated zone) to be free from the influence of seasonal or daily variations of surface temperature (Table I-1).

The difference in temperature values between the unqualified data and the qualified data at the same (or nearby) locations are within the range of ±2.0°C, or less than 5% of the temperature value (Table I-3). The mean difference is –0.0752°C and the mean relative difference is –0.41% of the qualified values.

Table I-3. Differences Between Qualified and Unqualified Data

Q-Boreholes	T (Q)	T (unQ)	TunQ - TQ	(unQ-Q)/Q %	N of nearby unQ-boreholes
USW NRG-7a	23.0985	23.1530	0.0545	0.235986	6
USW NRG-6	23.4564	23.6485	0.1921	0.819022	5
UE-25 UZ #4	22.7202	21.8954	−0.8248	−3.63018	5
UE-25 UZ #5	22.5018	21.8820	−0.6198	−2.75455	5
USW UZ-7a	21.8211	21.9205	0.0994	0.455481	2
USW SD-12	26.5389	27.1863	0.6474	2.439581	4
Mean error			−0.0752	−0.4058	
Criteria			< 2.0	< 5.0	

Source: DTN: LB0708WTTEMDAT, file: *QualifyTData.xls*, sheet: *SummaryQ-Data.*

I-3.5. CALCULATION PROCEDURES

Step 1. Create a new blank Excel Workbook named *QualifyTData.xls*.

Step 2. Load the qualified temperature data sets into *QualifyTData.xls*. Each DTN has an individual worksheet (i.e., GS031208312232.005 to worksheet GS031208312232.005_T, GS031208312232.004 to GS031208312232.004_T, GS031208312232.007 to GS031208312232.007_T, GS031208312232.006 to GS031208312232.006_T, GS950208312232.003 to GS950208312232.003_T, and GS031208312232.003 to GS031208312232.003_T, respectively). In each worksheet, separate the data based on boreholes using cut and paste, so that the data of every borehole start at the same row. Furthermore, sort data for each borehole in order of depth (descending), so that the data measured at the deepest depth come first.

Step 3. Load borehole locations from DTN: MO9906GPS98410.000 [DIRS 109059] (sheet: "New Coordinates") into the worksheet entitled "YM Borehole Locations."

Step 4. Load unqualified temperature data from DTN: GS950408318523.001 [DIRS 107244]. These data are separated into several groups and stored in corresponding worksheets as follows: Data of boreholes UE-25 a#1 through UE-25 a#7 are stored in worksheet "a#1 to a#7," UE-25 b#1 in "b#1," UE-25 J-13 in "J-13," UE-25 p#1 in "p#1," UE-25 WT #3 through UE-25 WT#18 in "WT#3 to WT#18," USW G-1 through USW G-4 in "G-1 to G-4," USW H-1 through USW H-6 in "H-1 to H-6," USW UZ-1 in "UZ-1," and USW WT-1 through WT-11 in "WT-1 to WT-11," respectively. In each worksheet, calculate the coordinates (m) of each borehole, based on the coordinate data (ft) on worksheet "YM Borehole Locations" (the converting factor is 1 ft = 0.3048 m).

Step 5. Create a new worksheet called "Water Table Temp." Obtain the coordinates of all unqualified boreholes (Column A to Column D) by linking to the values calculated in Step 4 above. Calculate the coordinates (m) of all qualified boreholes based on the coordinate data (ft) in the worksheet "YM Borehole Locations" (Columns R to T). For every qualified borehole (i.e., SD-12, NRG-7a, NRG-6, UZ#4, UZ#5, and UZ-7a), calculate its horizontal distances to all unqualified boreholes (Columns E though P). Copy them (the value) to Columns Q through AB and then sort the data in order (descending) of distance for each borehole.

Step 6. Create a new worksheet called "SummaryQ-Data". In rows 10 to 19, for each qualified borehole, obtain coordinates from worksheet "Water Table Temp." The depth (the deepest available for that borehole), starting date, and ending data are taken from the corresponding worksheets that contain qualified data (i.e., all worksheets with names starting with "GS"). The average T, STD, and number of measurements are also calculated from the data in those worksheets by using the @Average(), @STDEV(), and @Count() functions of Excel. CV is calculated as STD/T. The mean temperature for the entire time period is also calculated as the average value of each time period weighted by the number of measurements.

Step 7. In Worksheet "SummaryQ-Data", get the results of Step 6 (in rows 10 through 19) and store to rows 74 through 104 to facilitate the creation of Table I-1. Note that the depth has been converted from feet to meters.

Step 8. In worksheet "SummaryQ-Data", rows 105-113, calculate the yearly change rate of temperature (=(T at the last period – T at the first period) / (ending date – starting date)). The results are summarized in Table I-2.

Step 9. In worksheet "SummaryQ-Data," rows 21-71, for each qualified borehole, obtain temperature data as well as the associated measurement date and depth of the nearby (unqualified) boreholes from the corresponding worksheets (e.g., data for UE-25 a#4 from worksheet "a#1 to a#7"). The nearby boreholes are selected based on their distances and geometric relationships to the given qualified borehole (see the figures showing the relative locations of these boreholes in the worksheet). The data in the same unqualified boreholes are selected according to the following rules:

1) If there is a value measured at the same depth as the qualified data, it will be selected. Otherwise, check Rule 2.
2) If there is a pair of data measured at depths that enclose the depth where the qualified data were measured, these two data will be selected. Otherwise, check Rule 3.
3) A pair of data, including the one measured at the depth that is closest to the depth where the qualified data were measured, will be selected. To reduce the effect of measurement error on the linear interpolation, another data point located 100 ft away from the first data point will be selected.

For data selected by Rule 2 or 3, a linear interpolation would be used to calculate the temperature at the same depth as that of the qualified data. This interpolation approach, along with the inverse-distance-weighted averaging, is similar to the interpolation techniques used to calculate the lower (temperature) boundary (at water table level) of the UZ models from the unqualified data set (DTN: GS950408318523.001 [DIRS 107244]). Both the weighting average value and the simple average value were calculated. The weighting factor is the inverse of the three-dimensional distance between the locations where the unqualified data and the qualified data were originally measured. The absolute and relative differences between the qualified value and the unqualified (average) value were calculated and stored in rows 39 to 41.

Step 10. The results obtained from Step 9 are summarized in row 1-8 and become Table I-3.

I-4. CONCLUSION

The unqualified data in DTN: GS950408318523.001 [DIRS 107244] meet all the criteria outlined in the data qualification plan and therefore are qualified for use in this report. The results of the data qualification are presented in Output DTN: LB0708WTTEMDAT (file: *QualifyTData.xls*).

Data Qualification Plan

Complete only applicable items.

QA: QA
Page ~~1 of 1~~ 10 of 2 LP 7/30/07

Section I. Organizational Information

Qualification Title

Qualification of Unqualified Borehole Temperature Data

Requesting Organization

Lawrence Berkeley National Laboratory

Section II. Process Planning Requirements

1. List of Unqualified Data to be Evaluated

The unqualified temperature data in DTN: GS950408318523.001 (file "zz_sep_306109.txt, [DIRS 107244]) were used to generate the temperature boundary conditions at the water table for UZ Flow Models and Submodels AMR (MDL-NBS-HS-000006 REV 00). These data are long-term temperature measurement data for 34 boreholes at Yucca Mountain, and originally developed by Sass et al. 1988 [DIRS 100644]. Since the data were collected in 1980's, they were not qualified according to the current QA procedures. However, these data control more volume of Yucca Mountain (in both area and depth) than the qualified temperature data available. It is necessary to use them to determine the boundary conditions at water table in the related simulations for UZ Flow Models and Submodels (MDL-NBS-HS-000006 REV 00). The quality of the data set will be evaluated against the available qualified data at nearby locations, which would provide a desired level of confidence that the data are suitable for their intended use in MDL-NBS-HS-000006 REV 03.

2. Type of Data Qualification Method(s) [Including rationale for selection of method(s) (Attachment 3) and qualification attributes (Attachment 4)]

Method 2 "Corroborating Data" (SCI-PRO-001 Attachment 3) is used because the qualified data are available to conduct data comparison that can be shown to substantiate or confirm the unqualified data.

The following qualification attributes (SCI-PRO-001 Attachment4) will be considered in this qualification:

"1. Qualifications of personnel or organizations generating the data are comparable to qualification requirements of personnel generating similar data under an approved program that supports the YMP License Application process or post closure science;"

Both the unqualified data and the qualified data were collected by USGS who meet the qualification requirements under the approved program that supports the YMP License.

"3. The extent to which the data demonstrate the properties of interest (e.g., physical, chemical, geologic, mechanical);"

The temperature boundary at water table needed by UZ models is a constant (or steady state) temperature at that deep subsurface, which should not be subject to the seasonal or daily variations in any significant way. Therefore, if the unqualified data are comparable to the qualified data at the same location (or at closer locations), the quality of the unqualified data should have desired confidence for the intended usage use in MDL-NBS-HS-000006 REV 03.

"4. The environmental conditions under which the data were obtained if germane to the quality of data;"

The temperature in deep subsurface is stable under ambient conditions and should not change significantly within two decades. Therefore, these two data sets, although collected in different periods, should be comparable.

"10. Extent and quality of corroborating data or confirmatory testing results;"

The corroborating data were qualified under QA procedures that support the YMP License. The qualified data set includes data at sufficient depth (of the UZ) to be free from the influence of seasonal or daily variations of surface temperature.

3. Data Qualification Team and Additional Support Staff Required

Lehua Pan (chairperson), Keni Zhang, Yu-Shu Wu, and Charles Haukwa

No additional staff required.

SCI-PRO-001.1-R1

Data Qualification Plan

Complete only applicable items.

QA: QA

Page ~~2 of~~ 2 of 2 LP 7/30/07

4. Data Evaluation Criteria

If the following criteria are met, values stated in block 1 above will be qualified for use in MDL-NBS-HS-000006 REV 03 for the purpose of determining the temperature boundary at water table (the lower boundary) of the UZ model:

The difference of the temperature values between the unqualified data and the qualified data at the same (or nearby) locations are within the range of ±2.0 °C or less than 5% of the temperature value. Because no boreholes exactly overlap between these two data sets, unqualified temperature data from one closest borehole (or several nearby boreholes if they are within a similar distance) to that in the qualified data set will be picked for temparature comparison.These distances between boreholes from the two data sets will be treated as a weighting factor when evaluating temperature differences. In addition, the data at the deepest depth of the boreholes that have qualified measurements will be selected for temperature comparison, to avoid complication from possible influence of near-surface noises.

The unqualified data are in DTN GS950408318523.001.

The qualified data are in DTN: GS031208312232.005, GS031208312232.004, GS031208312232.007, GS031208312232.006, GS950208312232.003, and GS031208312232.003.

5. Identification of Procedures Used

Procedure SCI-PRO-001 will be used to conduct the data qualification task. The qualification task will be conducted within a work product (UZ Flow Models and Submodels, MDL-NBS-HS-000006 REV 03) and the results of the data qualification task will be appended to MDL-NBS-HS-000006 REV 03.

6. Plan coordinated with the following known organizations providing input to or using the results of the data qualification

PA Natural Systems, LBNL

Section III. Approval

Qualification Chairperson Printed Name	Qualification Chairperson Signature	Date
Lehua Pan	Lehua Pan	7/30/07
Responsible Manager Printed Name	Responsible Manager Signature	Date
Yvonne Tsang	Yvonne Tsang	7/30/07
Stephanie Kuzio	Clifford K. Ho for S.K.	8/14/2007

SCI-PRO-001.1-R1

INTENTIONALLY LEFT BLANK

Addendum Cover Page

Complete only applicable items.

QA: QA

1. Total Pages: 16

2. Addendum to (Title):
UZ Flow Models and Submodels

3. DI (including Revision and Addendum No.):
MDL-NBS-HS-000006 REV03 AD 01

	Printed Name	Signature	Date
4. Originator	Yu-Shu Wu	Yu-Shu Wu	12/20/07
5. Independent Technical Reviewer	Susan Altman	Susan Altman	12/20/2007
5. Checker	Shaoping Chu	Shaoping Chu	12/20/07
6. QCS / QA Reviewer	Charles Beach	Charles P. Beach	12-21-07
7. Responsible Manager / Lead	Ming Zhu	Ming Zhu	12/21/07
8. Responsible Manager	Kathryn Knowles	Kathryn Knowles FOR MK Zhu	21 DEC 2007

9. Remarks

Change History

10. Revision and Addendum No.	11. Description of Change
REV 03 AD 01	Initial Issue.

SUMMARY AND ORGANIZATION

The purpose of this addendum is to modify the parent report in accordance with the governing procedure (SCI-PRO-006, *Models*) and *Technical Work Plan for: Unsaturated Zone Flow, Drift Seepage and Unsaturated Zone Transport Modeling* (BSC 2006 [DIRS 177465]). The addendum was prepared to provide information that supports the development of Safety Analysis Report Section 2.3.2 and the screening justification features, events, and processes (FEP) 2.2.07.05.0A (Flow in the UZ from episodic infiltration).

The specific modifications presented in this addendum are as follows, each representing an issue identified in the parent report and addressed herein:

(1) Figure 6.8-3 has been replaced and now includes a distribution derived by the infiltration model, providing another basis of comparison against UZ temperature and chloride data (the GLUE-modified distribution) and the distributions developed from the expert elicitation.

(2) Figure 6.9-3 has been updated with a plot using new simulation results with more output times, and citation of Output DTN: LB0705DAMPINGA.001 has been replaced with citation of new Output DTN: LB0711DAMPINGA.001.

(3) Table 8.1 is supplemented with Output DTN: LB0711DAMPINGA.001 for the new simulation in Section 6.9[a].

(4) Section 8.7 is replaced with a revision in the conclusion for tracer transport times.

The organization of this addendum corresponds to the major outline of the parent report and includes all sections mandated by the governing procedure (SCI-PRO-006), regardless of whether or not a mandated section is being modified. Mandated sections, in other words, are reproduced in this addendum for procedural compliance and convenience of cross-referencing, but may not contain actual modifications to the parent report. In such cases, the addendum section contains a bracketed statement of "No modification" under the section heading.

Conversely, sections not mandated by procedure (i.e., most subsections) are reproduced in this addendum only if they contain a modification to the corresponding section of the parent report, which is also true of any other addendum elements (i.e., figures, tables, equations, or appendices). Unless added as new elements not present in the parent report, the numbering of addendum elements such as figures, tables, equations, and appendices corresponds to the numbering in the parent report. Bracketed designators (e.g., "[a]") are added to all numbered elements in this addendum to distinguish them from corresponding elements in the parent report.

In every case, the modifications presented in this addendum are preceded by bracketed, italicized text explaining why the modification was made and how it relates to the corresponding element in the parent report. When appropriate, this explanatory text may cite page and paragraph numbers from the parent report for cross-referencing purposes.

INTENTIONALLY LEFT BLANK

CONTENTS

INTENTIONALLY LEFT BLANK

FIGURES

TABLE

INTENTIONALLY LEFT BLANK

ACRONYMS AND ABBREVIATIONS

[Acronyms and abbreviations used in this addendum are listed and defined below. Certain acronyms may be used but not defined in the addendum text itself in order to preserve the treatment of acronyms in the parent report.]

DOE	U.S. Department of Energy
DTN	data tracking number
GLUE	generalized likelihood uncertainty estimation
PTn	Paintbrush nonwelded hydrogeologic unit
TSw	Topopah Spring welded hydrogeologic unit
UZ	unsaturated zone

INTENTIONALLY LEFT BLANK

1[a]. PURPOSE

[No modification to the parent report.]

2[a]. QUALITY ASSURANCE

[No modification to the parent report.]

3[a]. USE OF SOFTWARE

[No modification to the parent report.]

4[a]. INPUTS

4.1[a] DIRECT INPUT

[No modification to the parent report.]

4.2[a] CRITERIA

[No modification to the parent report.]

4.3[a] CODES, STANDARDS, AND REGULATIONS

[No modification to the parent report.]

5[a]. ASSUMPTIONS

[No modification to the parent report.]

6[a]. MODEL DISCUSSION

[No modification to the parent report in Section 6 except those noted below for Sections 6.8.7 and 6.9]

6.8.7[a] Discussion of the Results of Unsaturated Zone Flow Weighting Factors

[The following paragraph replaces the last paragraph of Section 6.8.7 before Section 6.8.7.1 of the parent report.]

A comparison of the calibrated infiltration distribution over the repository footprint using the GLUE methodology with the expert elicitation probability distribution for percolation flux through the repository footprint is shown in Figure 6.8-3[a]. The results show that the GLUE-calibrated infiltration probability distribution is reasonably consistent with the aggregate expert percolation flux probability distribution, and covers a majority of the range established by the expert panel. Results for the infiltration model are also presented on this figure, which spans the range between the aggregate and upper bound expert elicitation distributions.

[The following figure replaces Figure 6.8-3 in the parent report. The new figure adds a distribution derived by the infiltration model, providing another basis of comparison against UZ temperature and chloride data (the GLUE-modified distribution) and the distributions developed from the expert elicitation.]

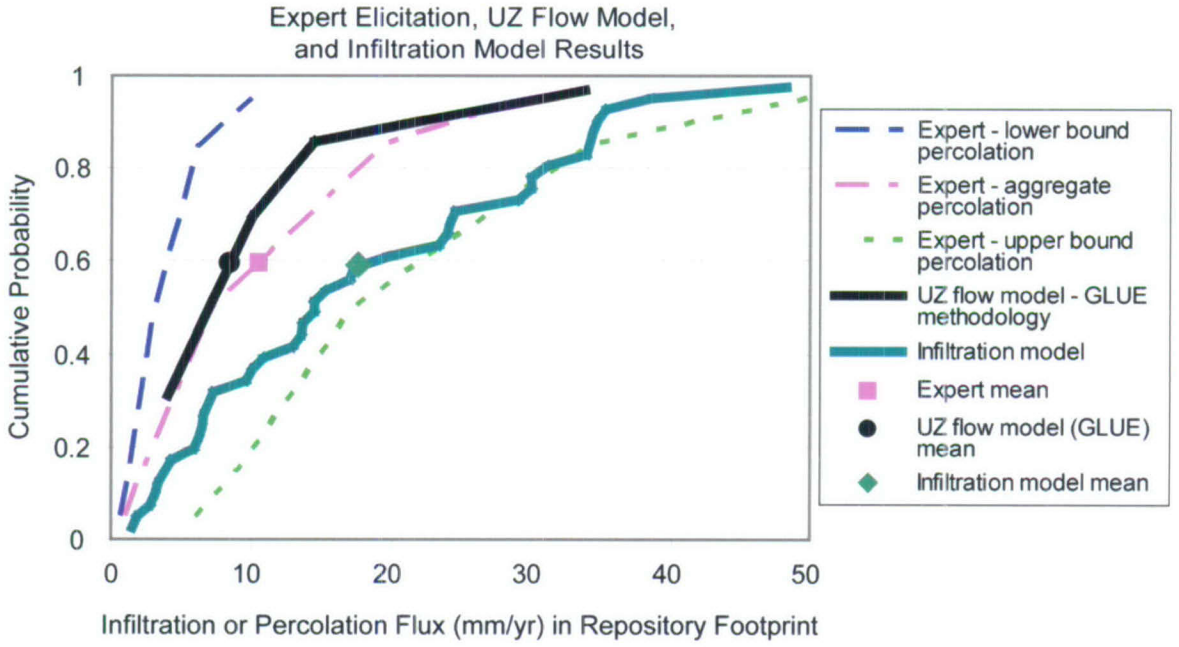

Source: CRWMS M&O 1997 [DIRS 100335] (expert elicitation results); SNL 2007 [DIRS 182145], Figure 7.2.3-1[a] (infiltration model results).

NOTE: Infiltration model results based on 2002 repository design footprint (DTN: LB0208HYDSTRAT.001 [DIRS 174491], file: *Repository02_Table.xls*). See SNL 2007 [DIRS 182145], Section 1.

Figure 6.8-3[a]. Comparison of Unsaturated Zone Flow Model Results Using GLUE Methodology and Infiltration Model Results for Infiltration in the Repository Footprint with the Expert Elicitation Results for Percolation at the Repository

6.9[a] TEMPORAL DAMPING OF EPISODIC INFILTRATION PULSES

[The following figure replaces the corresponding figure in the parent report. Citation of Output DTN: LB0705DAMPINGA.001 has been replaced with citation of new Output DTN: LB0711DAMPINGA.001 and the figure has been replotted using new simulation results with more output times. No other changes to Section 6.9 of the parent report.]

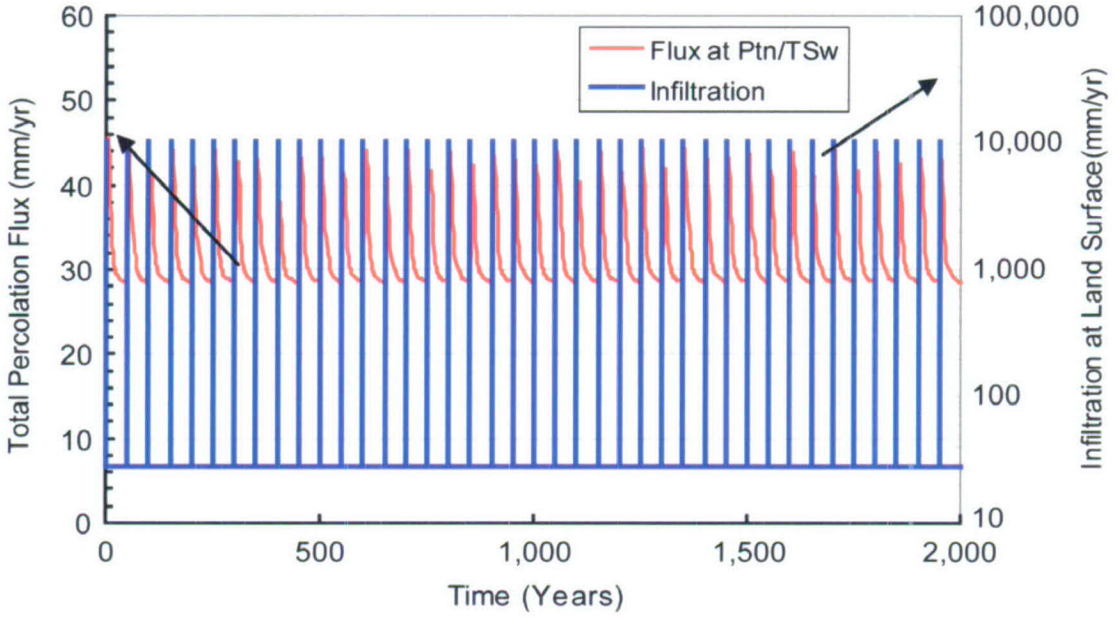

Output DTN: LB0711DAMPINGA.001, file: *i78_time_flux.xls*.

NOTE: PTn unit has a thickness of 21 m at Column i78.

Figure 6.9-3[a]. Infiltration Pulse and Simulated Variations in Total Percolation Fluxes versus Time at the Bottom PTn Unit for Column i78

7[a]. VALIDATION

[No modification to parent report.]

8[a]. CONCLUSIONS

[The following table supplements the corresponding table in the parent report. Output DTN: LB0711DAMPINGA.001 is added for the new simulations with transient pulse infiltration in Section 6.9[a] of this addendum No other changes to Section 8 of the parent report.]

Table 8-1[a]. Output Data and Data Tracking Numbers

Data Tracking Number	Location in this report			Description
	Section(s)	Figure(s)	Table(s)	
LB0711DAMPINGA.001	6.9[a]	6.9-3[a]		One-dimensional simulations showing damping effect on percolation fluxes for case with 21-m thick PTn

9[a]. INPUTS AND REFERENCES

9.1[a] DOCUMENTS CITED

[The following listings pertain only to their use in this addendum. No other changes to Section 9.1 of the parent report.]

177465 BSC (Bechtel SAIC Company) 2006. *Technical Work Plan for: Unsaturated Zone Flow, Drift Seepage and Unsaturated Zone Transport Modeling.* TWP-MGR-HS-000004 REV 04. Las Vegas, Nevada: Bechtel SAIC Company. ACC: DOC.20060824.0001.

100335 CRWMS (Civilian Radioactive Waste Management System) M&O (Management and Operating Contractor) 1997. *Unsaturated Zone Flow Model Expert Elicitation Project.* Las Vegas, Nevada: CRWMS M&O. ACC: MOL.19971009.0582.

182145 SNL (Sandia National Laboratories) 2007. *Simulation of Net Infiltration for Present-Day and Potential Future Climates.* MDL-NBS-HS-000023 REV 01 AD 01. Las Vegas, Nevada: Sandia National Laboratories.

9.2[a] CODES, STANDARDS, REGULATIONS, AND PROCEDURES

[The following listing pertains only to its use in this addendum. No other changes to Section 9.2 of the parent report.]

SCI-PRO-006, Rev. 6, ICN 0. *Models.* Washington, D.C.: U.S. Department of Energy, Office of Civilian Radioactive Waste Management. ACC: DOC.20071026.0003.

9.3[a] SOURCE DATA, LISTED BY DATA TRACKING NUMBER

[The following listing pertains only to its use in this addendum. No other changes to Section 9.3 of the parent report.]

174491 LB0208HYDSTRAT.001. 2002 UZ Model Grid Components. Submittal date: 08/26/2002.

9.4[a] OUTPUT DATA, LISTED BY DATA TRACKING NUMBER

[The following listings pertain only to their use in this addendum. No other changes to Section 9.4 of the parent report.]

LB0705DAMPINGA.001. Data of Damping Effect Analyses. Submittal date: 05/18/2007.

LB0711DAMPINGA.001. Data of Damping Effect Analyses. Submittal date: 11/16/2007.

9.5[a] SOFTWARE CODES

[No modification to the parent report.]

INTENTIONALLY LEFT BLANK

Model
Administrative Change Notice

QA: QA

Page 1 of 7

Complete only applicable items.

1. Document Number:	MDL-NBS-HS-000006	2. Revision:	03/ND 01	3. ACN:	01
4. Title:	UZ Flow Models and Submodels				
5. No. of Pages Attached	86 91	1-7-08			

6. Approvals:		
Preparer:	Yu-Shu Wu Print name and sign	12/14/07 Date
Checker:	Shaoping Chu Print name and sign	12/18/2007 Date
QCS/Lead Lab QA Reviewer:	Charles Beach Print name and sign	12-18-07 Date
Independent Technical Reviewer:	Susan Altman Print name and sign	12/18/2007 Date
Responsible Manager: 1-7-08	M. KATHRYN KNOWLES ~~Geoff Freeze~~ Print name and sign	1/7/08 Date

7. Affected Pages	8. Description of Change:
ix	Listing for Section 7.4.1: Changed listing to "Validation of the UZ Model for the Scenario of the 10th-Percentile Infiltration Map" to reflect corresponding section heading change (see entry for p. 7-9 below).
xiv	Listing for Figure 6.4-3: Changed listing to "Comparison of Simulated (solid line) and Observed (solid dots) Gas Pressures at Borehole UZ-7a during the First 30-day Period" to reflect corresponding figure caption change (see entry for p. 6-62 below). Listing for Figure 6.6-2: Changed listing to "Simulated Percolation Fluxes at the Repository Horizon under the Monsoon, 10th Percentile Infiltration Scenario" to reflect corresponding figure caption change (see entry for p. 6-88 below).
xvi	Listing for Figure 7.5-1: Changed listing to "Simulated Solute Travel Time of the Matrix Pore Water with Three-dimensional Simulation for Borehole UZ-1 Compared to the Measured ^{14}C Age" to reflect corresponding figure caption change (see entry for p. 7-16 below). Listing for Figure 7.5-2: Changed listing to "Simulated Solute Travel Time of the Matrix Pore Water with Three-dimensional Simulation for Borehole SD-12 Compared to the Measured ^{14}C Age" to reflect corresponding figure caption change (see entry for p. 7-17 below).
xvii	Listing for Figure 7.5-3: Changed listing to "Simulated Solute Travel Time of the Matrix Pore Water with One-dimensional Simulation for Borehole UZ-1 Compared to the Measured ^{14}C Age" to reflect corresponding figure caption change (see entry for p. 7-19 below). Listing for Figure 7.5-4: Changed listing to "Simulated Solute Travel Time of the Matrix Pore Water with One-dimensional Simulation for Borehole SD-12 Compared to the Measured ^{14}C Age" to reflect corresponding figure caption change (see entry for p. 7-20 below).

Model
Administrative Change Notice

Complete only applicable items.

1. Document Number:	MDL-NBS-HS-000006	2. Revision:	03	3. ACN:	01
4. Title:	UZ Flow Models and Submodels				

xxi	Listing for Table 6.4-3: Changed listing to "Modifications to Fracture Permeability Resulting from Three-Dimensional Calibration (30% scenario)" to reflect corresponding figure caption change (see entry for p. 6-61 below). Listing for Table 6.5-2: Changed listing to "Present-Day Chloride Recharge Fluxes and Precipitation, Runon, and Runoff Rates for Different Scenarios (Averaged over Model Domain)" to reflect corresponding figure caption change (see entry for p. 6-67 below). Listing for Table 6.6-1: Changed listing to "Comparison of the Water Flux through Matrix, Fractures of Non-fault Zones, and Faults as a Percentage of the Total Flux over the Entire Model Domain and within the Repository Footprint at the TCw/PTn Interface for the 16 Flow Fields" to reflect corresponding table caption change (see entry for p. 6-91 below). Changed the word "water" to "Water" (Listing for Tables 6.2-2 through 6.2-5).
xxii	Listing for Table 6.6-2: Changed listing to "Comparison of the Water Flux through Matrix, Fractures of Non-fault Zones, and Faults as a Percentage of the Total Flux over the Entire Model Domain and within the Repository Footprint at the Repository Level for the 16 Flow Fields" to reflect corresponding table caption change (see entry for p. 6-92 below). Listing for Table 6.6-3: Changed listing to "Comparison of the Water Flux through Matrix, Fractures of Non-fault Zones, and Faults as a Percentage of the Total Flux over the Entire Model Domain and within the Repository Footprint at the Water Table for the 16 Flow Fields" to reflect corresponding table caption change (see entry for p. 6-93 below).
5-1	Last paragraph, first sentence: Changed "past Modern Interglacial Climate" to "present-day interglacial climate".
6-2	Last sentence: Inserted "(CFu)" after "Crater Flat undifferentiated unit".
6-3 and 6-4	Table 6.1-1: In the "Lithostratigraphic Nomenclature" column, merged blank cells under the cells listing the "Tptrn" and "Tptpln" units; in the "UZ Model Grid Unit/Layer" column, merged blank cells under "tcw12", "ptn22", "ptn24", "tsw31," and "tsw33"; in "Hydrogeologic Unit" column, merged blank cells under "CUL, CW", "BT4", "BT3", "TC", and "TUL"; carried last row on page 6-3 onto page 6-4 to merge blank cells under "pp2" and "PP2 (devitrified)".
6-7	Last paragraph, 4th line from bottom: Inserted "model," before "the gas flow model".
6-8	First paragraph: Inserted "the" before "fracture and matrix continuum" in two instances. Last sentence: Changed "Darcy's velocity" to "Darcy velocity".
6-10	Second paragraph, 7th line: Replaced "becoming earlier" with "occurring sooner".
6-11	Second paragraph, 7th line from bottom: Split sentence into two separate sentences by deleting "even though" and ending the first sentence after "lateral diversions". Second sentence now begins with "The degree or scale . . .".
6-15	Figure 6.1-2: Replaced figure to correct misspelling of "infiltration" in figure heading.
6-16	Figure 6.1-3: Replaced figure to correct misspelling of "infiltration" in figure heading.
6-17	Figure 6.1-4: Replaced figure to correct misspelling of "infiltration" in figure heading.
6-18	Last paragraph, 4th line from bottom: Changed "flow field" to "flow fields".
6-19	Table 6.1-3: Changed "percentiles" to "percentile" in 4th row under "Scenario" column.
6-20	Figure 6.1-5: Replaced figure to correct misspelling of "infiltration" in figure heading.
6-22	Third paragraph, 3rd line: Deleted "of" before "the important iterative processes". Last paragraph, 2nd sentence: Added missing "*Analysis of*" to title of DIRS 170038.

Model
Administrative Change Notice

Complete only applicable items.

1. Document Number:	MDL-NBS-HS-000006	2. Revision:	03	3. ACN:	01
4. Title:	UZ Flow Models and Submodels				

6-25	First paragraph, 6th line: Deleted the phrase "and it is even thicker to the north of the repository".
6-26	First paragraph, 4th line: Inserted "a" before "reasonable".
6-29 and 6-30	Tables 6.2-2 through 6.2-5: Capitalized the "w" in "water" in the table captions.
6-33	Last paragraph, 5th line from bottom: Changed "source" to "sources". Last paragraph, 3rd and 4th lines from bottom: Revised "Only in situ measurement of water potentials are used among the water-potential data" to read "Only in situ measurements of water-potential are used in this analysis." Also, deleted "simulation" before "results".
6-34	Last paragraph, 3rd line: Changed "other seven" to "seven other". Last paragraph: add to the end of the paragraph: "In Figures 6.2-2 and 6.2-3, saturations simulated for the lower portion of the TSw with the pd_90 scenario are lower than the rest of the lower infiltration scenarios. This is because the simulations for each infiltration scenario use different parameter sets. Nevertheless, simulation results are still within ranges of measured saturation data."
6-38	Table 6.2-8, last column, 1st row, 5th line: Changed "averaged" to "average".
6-43	First paragraph, lines 9 through 11: Deleted sentence "As discussed in Section 6.3.4, percolation flux (or infiltration rate) is one of the factors that control thermal conditions."
6-45	Last paragraph, 2nd and 4th lines: Inserted "a" before "multiple-year temperature data set" and inserted "the" before "model bottom temperature boundary".
6-46	First paragraph, 2nd line: Replaced "against" with "when compared to". Second paragraph, 3rd line: Changed "condition" to "conditions". Fourth paragraph, 4th line: Inserted "the" before "top".
6-48	Second paragraph, line 22: Changed the range of percolation flux from "−3.4 to 7.3 mm/yr" to "3.4 to 7.3 mm/yr". Second paragraph, line 24: Changed "are" to "have".
6-57	Table 6.4-1, NOTE: Changed "30-day data" to "30 days of the data set" in two places. Second paragraph from bottom, 1st line: Inserted "the" before "given infiltration scenario". Last paragraph, 1st line: Changed "cells" to "cell".
6-58	Last paragraph of Section 6.4.1, 2nd sentence: Replaced "to" with "on". Sentence now reads: "The impact of liquid-phase flow on the gas flow system …". First paragraph of Section 6.4.2, third sentence: Changed "tsw" to "TSw" and deleted "nearby".
6-59	Figure 6.4-1: Replaced figure to correct the UZ model grid unit labeling on the curves (e.g., "tcw 12", "tsw 32", etc.) and to change the units on the y-axis label from "KPa" to "kPa". Figure 6.4-1, NOTE: Added "The hydrogeologic units shown on the figure (e.g., tcw12) are determined from a comparison of the borehole location and measurement depth with the spatial data for the hydrogeolgic units available from the UZ model grid."
6-60	Figure 6.4-2: Replaced figure to correct the UZ model grid unit labeling on the curves (e.g., "tcw 12", "tsw 35", etc.) and to change the units on the y-axis label from "KPa" to "kPa". Figure 6.4-2, NOTE: Added "The hydrogeologic units shown on the figure (e.g., tcw12) are determined from a comparison of the borehole location and measurement depth with the spatial data for the hydrogeolgic units available from the UZ model grid."

Model
Administrative Change Notice

Complete only applicable items.

1. Document Number:	MDL-NBS-HS-000006	2. Revision:	03	3. ACN:	01
4. Title:	UZ Flow Models and Submodels				

6-61	First paragraph, 12th line, deleted "nearby". Table 6.4-3: Changed table caption to "Modifications to Fracture Permeability Resulting from Three- Dimensional Calibration (30% scenario)".
6-62	Figure 6.4-3: Replaced figure to correct the UZ model grid unit labeling on the curves (e.g., "tcw 12", "tsw 32", etc.) and to change the units on the y-axis label from "KPa" to "kPa". Also changed "UZ-71" to "UZ-7a" in figure caption. Figure 6.4-3, NOTE: Added "The hydrogeologic units shown on the figure (e.g., tcw12) are determined from a comparison of the borehole location and measurement depth with the spatial data for the hydrogeolgic units available from the UZ model grid."
6-63	Figure 6.4-4: Replaced figure to correct the UZ model grid unit labeling on the curves (e.g., "tcw 12", "tsw 35", etc.) and to change the units on the y-axis label from "KPa" to "kPa". Figure 6.4-4, NOTE: Added "The hydrogeologic units shown on the figure (e.g., tcw12) are determined from a comparison of the borehole location and measurement depth with the spatial data for the hydrogeolgic units available from the UZ model grid."
6-64	First paragraph, 2nd line: Changed "case" to "cases". Second paragraph, 4th line: Changed "This" to "These". Third paragraph, 4th line: Added closing parenthesis after "(compared to the modern climate" and inserted "before present" after second "10,000 years". Last paragraph: Combined the second and third sentences.
6-65	Table 6.5-1: Added missing note "H" after entry for DTN: LAJF831222AQ98.011 in 3rd row of 2nd column (entry for SD-9).
6-66	First paragraph: Changed "28,000 years" to "21,000 years" and the sentence to: "The present-day mean infiltration rate estimated from the chloride data is approximately 5 mm/yr, and the glacial maximum infiltration rate at 21,000 years ago was about 28 mm/yr" Third paragraph, 1st line: Changed "particulate" to "particulates". Last paragraph, 3rd line: Inserted "the" before "TOUGH2".
6-67	Table 6.5-2: Changed caption to ""Present-Day Chloride Recharge Fluxes and Precipitation, Runon, and Runoff Rates for Different Scenarios (Averaged over Model Domain)". Last paragraph, 10th line: Deleted "in" before "part". Last paragraph, 8th line from bottom: Deleted "this" before "variation". Last paragraph, 3rd line from bottom: Inserted "and" before "applied".
6-83	Figure 6.6-2: Removed superscripting from "th" in "10th" in caption. Figure caption now reads: "Simulated Percolation Fluxes at the Repository Horizon under the Monsoon, 10th Percentile Infiltration Scenario".

Model
Administrative Change Notice

Complete only applicable items.

1. Document Number:	MDL-NBS-HS-000006	2. Revision:	03	3. ACN:	01
4. Title:	UZ Flow Models and Submodels				

6-91	First paragraph, 1st line: Changed "6.6-22" to "6.6-2". First paragraph, 6th and 7th lines: Changed "where as" to "whereas". Second paragraph, 1st line: Deleted "A" and capitalized "statistical". Second paragraph, 6th line: Inserted "(Table 6.6-3)" after "reaching 44% to 65% at the water table". Table 6.6-1: Changed caption to "Comparison of the Water Flux through Matrix, Fractures of Non-fault Zones, and Faults as a Percentage of the Total Flux over the Entire Model Domain and within the Repository Footprint at the TCw/PTn Interface for the 16 Flow Fields".
6-92	Table 6.6-2: Changed caption to "Comparison of the Water Flux through Matrix, Fractures of Non-fault Zones, and Faults as a Percentage of the Total Flux over the Entire Model Domain and within the Repository Footprint at the Repository Level for the 16 Flow Fields". Table 6.6-2: Changed heading in 1st row, 2nd column to "Flux at Repository Horizon over Entire Model Domain (%)".
6-93	Table 6.6-3: Changed caption to "Comparison of the Water Flux through Matrix, Fractures of Non-fault Zones, and Faults as a Percentage of the Total Flux over the Entire Model Domain and within the Repository Footprint at the Water Table for the 16 Flow Fields". Table 6.6-3: Changed heading in 1st row, 2nd column to "Flux at Water Table over Entire Model Domain (%)".
6-96	Last paragraph, 3rd line: Added missing period after first sentence.
6-97	First paragraph, 1st line: Inserted new sentence before 1st full sentence. New sentence reads: "Note that the conservative component is used to represent a radionuclide, which typically has a small diffusion coefficient due to heavy molecular weight and large size." First paragraph, 4th and 5th lines: Placed parentheses around the diffusion coefficient ranges cited for both anions and cations.
6-99	Second paragraph: Changed "Tables 6.7-3 and 6.7-5" to "Table 6.7-3".
6-110	First paragraph, 8th line: Changed "distribution" to "distributions". Second paragraph, 4th line: Changed "tunnel horizontal tunnels ECRB and ESF," to "horizontal tunnels, the ECRB and ESF,". Second paragraph, 6th line: Changed "boreholes" to "borehole".
6-114	Paragraph for third likelihood function: Added the following after Equation 6.8-4: "This is a pseudo-maximum likelihood function. It is similar to maximum likelihood in a way that in its formulation more observation data (either data points or data types) will accentuate the better simulations, which means greater reduction of uncertainty. This function can be an alternative when measurement errors are not available." Paragraph for fourth likelihood function: Changed "location" to "locations" in 3rd line after Equation 6.8-5.
6-115	Third paragraph, 8th line: Inserted "the" before "contribution". Third paragraph, 10th line: Inserted "the" before "likelihood".
6-117	Last paragraph: Replaced first three sentences with "Figure 6.8-2 shows the final likelihood of each infiltration map. Four bars represent the four infiltration maps. The weights for each map using an individual likelihood value correspond to the y-axis value for that individual likelihood function times its prior weights."

Model
Administrative Change Notice

Complete only applicable items.

1. Document Number:	MDL-NBS-HS-000006	2. Revision:	03	3. ACN:	01
4. Title:	UZ Flow Models and Submodels				

6-118	Figure 6.8-2: Replaced figure to make the plotting symbols visible in the shaded portions of the figure. Figure 6.8-2, NOTE: Placed figure note on separate line from DTN listing.
7-1	First paragraph, 9th line from bottom: Changed "include" to "includes". Second bullet, 2nd line: Inserted "water" after "perched".
7-2	Third bullet, 2nd line: Deleted "mineral". Last bullet, 9th line: Deleted "again".
7-3	First paragraph, 2nd line: Changed "wase" to "case". Second paragraph, 4th line: Added two commas. Second paragraph, next to last line: Added "hydrologic," before "temperature,".
7-4	Second paragraph, last sentence: Replaced "model is" with "model's".
7-9	Heading for Section 7.4.1: Added a "th" after "10". Heading now reads: "Validation of the UZ Model for the Scenario of the 10th-Percentile Infiltration Map". Figure 7.4-1: Replaced figure to correct the UZ model grid unit labeling on the curves (e.g., "tcw 12", "tsw 32", etc.) and to change the units on the y-axis label from "KPa" to "kPa". Figure 7.4-1, NOTE: Added "The hydrogeologic units shown on the figure (e.g., tcw12) are determined from a comparison of the borehole location and measurement depth with the spatial data for the hydrogeolgic units available from the UZ model grid."
7-10	Figure 7.4-2: Replaced figure to correct the UZ model grid unit labeling on the curves (e.g., "tcw 12", "tsw 35", etc.) and to change the units on the y-axis label from "KPa" to "kPa". Figure 7.4-2, NOTE: Added "The hydrogeologic units shown on the figure (e.g., tcw12) are determined from a comparison of the borehole location and measurement depth with the spatial data for the hydrogeolgic units available from the UZ model grid."
7-11	Figure 7.4-3: Replaced figure to correct the UZ model grid unit labeling on the curves (e.g., "tcw 12", "tsw 32", etc.) and to change the units on the y-axis label from "KPa" to "kPa". Figure 7.4-3, NOTE: Added "The hydrogeologic units shown on the figure (e.g., tcw12) are determined from a comparison of the borehole location and measurement depth with the spatial data for the hydrogeolgic units available from the UZ model grid."
7-12	Figure 7.4-4: Replaced figure to correct the UZ model grid unit labeling on the curves (e.g., "tcw 12", "tsw 35", etc.) and to change the units on the y-axis label from "KPa" to "kPa". Figure 7.4-4, NOTE: Added "The hydrogeologic units shown on the figure (e.g., tcw12) are determined from a comparison of the borehole location and measurement depth with the spatial data for the hydrogeolgic units available from the UZ model grid."
7-14	Second paragraph, 3rd line form bottom: Inserted "because" before "the boreholes".
7-15	First paragraph, 4th line: Uncapitalized the "b" in "Boreholes".
7-16	Figure 7.5-1: Changed "UZ-1 Borehole" to "Borehole UZ-1" in figure caption.
7-17	Figure 7.5-2: Changed "SD-12 Borehole" to "Borehole SD-12" in figure caption.
7-18	Second paragraph, 5th line: Inserted "the" before "10th and 30th".
7-19	Figure 7.5-3: Changed "UZ-1 Borehole" to "Borehole UZ-1" in figure caption.
7-20	Figure 7.5-4: Changed "SD-12 Borehole" to "Borehole SD-12" in figure caption.

Model
Administrative Change Notice

Complete only applicable items.

1. Document Number:	MDL-NBS-HS-000006	2. Revision:	03	3. ACN:	01
4. Title:	UZ Flow Models and Submodels				

7-25	Last paragraph, 4th line: Changed "but not to a small value as those measured in zeolitic rocks" to "but not as small a value as those measured in zeolitic rocks."
7-29	First paragraph, 6th line from bottom: Changed "content have" to "content has". Second paragraph, 5th line from bottom: Changed "is not possible" to "are not possible".
7-30	Second paragraph, added "The comment paper contended that the calcite was formed by upwelling hydrothermal waters and that the original journal article considered a constant ambient geothermal gradient for the approximately 10 million-year period, rather than a higher gradient which has been inferred from fluid inclusions." Following the first sentence. Third paragraph, last sentence: Changed "primary" to "primarily". Last paragraph, 2nd line from top: Revised sentence to "Pore waters extracted from Yucca Mountain rock matrix collected from deep locations are close to equilibrium with respect to calcite (BSC 2004 [DIRS 169734], Section 7.7.1), . . .".
7-31	Second paragraph, 6th line: Changed "solve" to "solves".
7-32	First paragraph, 9th and 10th lines: Added "Table 7.7-1 describes three of the five units, each of which is further divided . . .". First paragraph, 5th line from bottom: Inserted "values" after "permeability".
7-43	Third paragraph, 2nd line: Deleted "the" before "Yucca Mountain".
7-44	First paragraph, the last sentence changed to: "The new results are within the spread of the measured calcite abundances, and therefore the variable geothermal gradient did not change the conclusions of the first paper. Thus, the results with variable temperature boundary do not change the conclusions made above."
7-47	Figure 7.8-3: Deleted the phrase "(called distance from collar)" in figure NOTE.
7-51	First paragraph, 6th line: Removed parenthesis after "fault".
7-54	Second paragraph, 7th line from bottom: Inserted "so" before "simulated flow field".
8-7	First paragraph, last sentence: Deleted "in the CHn unit".
8-8	Third paragraph, last line: Changed "range of flow field generated" to "range of the flow fields generated".
H-2	Second paragraph, 5th line: Changed "6.2.12" to "6.2.12[a]".
H-12	Table H-2, 4th row of last column: Changed "Table 6.8-1" to "Table 6.8-1 of Section 6" and changed "Table 6.2-5" to "Table 6.2-5[a]".

CONTENTS (Continued)

Page

FIGURES (Continued)

Page

FIGURES (Continued)

Page

FIGURES (Continued)

Page

TABLES

TABLES (Continued)

Page

5. ASSUMPTIONS

Assumptions are listed in this section only if they are necessitated by lack of data in the development of the UZ flow model and its submodels. Several approximations and idealizations are used for model development, such as selection of hydrogeological conceptual models, use of numerical modeling approaches, and specification of model boundary conditions. These are discussed and justified as appropriate in Section 6. In particular, modeling idealizations and approximations used for specific modeling studies are appropriately discussed in Section 6.

This section presents the rationale and justification for assumptions, discusses whether further confirmation is needed, and references the sections in the report where these assumptions are used. The assumptions used in developing the UZ flow models and submodels are as follows:

1. In the UZ flow model, faults are assumed to be vertical or inclined 30 m wide zones, crossing the entire unsaturated zone thickness from the surface to the water table. This assumption is used for the three-dimensional UZ flow model (Sections 6.1, 6.2, 6.5, 6.6, and 6.7) and three-dimensional ambient thermal model (Sections 6.3 and 6.4).

   Basis: This assumption is consistent with the assumptions and approximations used in designing the three-dimensional UZ model grid (BSC 2004 [DIRS 169855]). Considering the large-scale averaging performed by the three-dimensional mountain-scale UZ model, in which horizontal grid spacings are typically on the order of 100 m, a 30 m width is compatible with a spatial discretization of 100 m lateral spacing in the adjacent, nonfault gridblocks. The impact of fault widths or cross-sectional areas on results of steady-state flow simulation in the unsaturated zone is equivalent to that of variation in fault permeability. The sensitivity modeling analysis (BSC 2005 [DIRS 174191]) showed that three-orders-of-magnitude variations in fault transmissivity had very small impact on UZ flow and tracer transport from the repository to the water table. Therefore, this assumption is considered adequate and requires no further confirmation.

2. In describing the top temperature boundary condition, the ambient thermal model (Section 6.3) assumes that the average surface temperature is a linear function of surface elevation. Therefore, the entire temperature ranges along the top model boundary can be determined using a linear equation whose coefficients are estimated using average annual temperature data measured from two boreholes.

   Basis: The surface temperature is controlled by the local atmosphere conditions, while variations in the mean atmospheric temperature are dependent primarily on elevation, which are handled as linear functions of elevation. Therefore, this assumption is considered reasonable and adequate, and requires no further confirmation.

3. In describing infiltration, the uncertainty distribution for the present-day interglacial climate is fully correlated with theuncertainty distribution for the future Monsoon Climate and the future Glacial Transition Climate.

- The possible flow diversion in the PTn
- The perched water zones and associated flow barriers
- The probable flow paths from the repository to the water table
- Tracer transport times and paths from the repository to the water table, and breakthrough curves and areas of tracers at the water table.

The UZ flow model described here provides a defensible and credible UZ model for evaluation of Yucca Mountain as an underground radioactive waste repository. Major activities accomplished in this revision include incorporation of updated net infiltration maps for present-day, monsoon, glacial transition, and post-10k-yr climates; updated model calibrated property sets; updated model calibration studies of three-dimensional UZ flow; evaluation of the effects of PTn and perched water; updated geochemical and geothermal conditions; updated estimates of tracer and radionuclide transport times; estimates of UZ flow weighting factors; and intensive model validation efforts.

Other activities have involved generating 16 three-dimensional flow fields (Sections 6.2 and 6.7) to evaluate the uncertainties and sensitivity of the UZ model relative to fracture and matrix parameters and infiltration rates of four climates over the mountain by using four sets of model parameters, and sixteen infiltration scenarios. A total of 16 flow fields have been submitted to the TDMS as output DTNs. The sixteen flow fields are provided for use in TSPA calculations of radionuclide transport through the unsaturated zone system, and for other activities such as drift seepage abstraction.

FEPs included through this report are discussed in Section 6.2.6 and in Table 6.2-8.

6.1 MODEL DESCRIPTION

The conceptual and numerical models used for the modeling studies are documented in this report as well as in *Conceptual Model and Numerical Approaches for Unsaturated Zone Flow and Transport* (BSC 2004 [DIRS 170035]). The conceptual and numerical models are presented in this section so that a complete discussion of the models can be made.

6.1.1 Geological Model and Numerical Grids

The geologic framework model (GFM2000) (DTN: MO0012MWDGFM02.002 [DIRS 153777]) is used for incorporating geological features into the UZ flow model and its submodels. The development and features of the three-dimensional model grids are documented in *Development of Numerical Grids for UZ Flow and Transport Modeling* (BSC 2004 [DIRS 169855]). Table 6.1-1 lists the geological units/layers for different hydrogeologic units and the associated UZ model numerical grid-layer information. These geological formations have been organized into layered hydrogeologic units based primarily on the degree of welding (Montazer and Wilson 1984 [DIRS 100161]). These are the Tiva Canyon welded hydrogeologic unit (TCw), the Paintbrush nonwelded hydrogeologic unit (PTn), the Topopah Spring welded unit (TSw), the Calico Hills nonwelded hydrogeologic unit (CHn), and the Crater Flat undifferentiated unit (CFu).

Table 6.1-1. GFM2000 Lithostratigraphy, UZ Model Layer, and Hydrogeological Unit Correlation Used in the UZ Flow Model and Submodels

Major Unit[a]	Lithostratigraphic Nomenclature[b]	UZ Model Grid Unit/Layer[c]	Hydrogeological Unit [d]
Tiva Canyon welded (TCw)	Tpcr	tcw11	CCR, CUC
	Tpcp	tcw12	CUL, CW
	TpcLD		
	Tpcpv3	tcw13	CMW
	Tpcpv2		
Paintbrush nonwelded (PTn)	Tpcpv1	ptn21	CNW
	Tpbt4	ptn22	BT4
	Tpy (Yucca)		
		ptn23	TPY
		ptn24	BT3
	Tpbt3		
	Tpp (Pah)	ptn25	TPP
	Tpbt2	ptn26	BT2
	Tptrv3		
	Tptrv2		
Topopah Spring welded (TSw)	Tptrv1	tsw31	TC
	Tptrn		
		tsw32	TR
	Tptrl, Tptf	tsw33	TUL
	Tptpul, RHHtop		
	Tptpmn	tsw34	TMN
	Tptpll	tsw35	TLL
	Tptpln	tsw36	TM2 (upper 2/3 of Tptpln)
		tsw37	TM1 (lower 1/3 of Tptpln)
	Tptpv3	tsw38	PV3
	Tptpv2	tsw39 (vit, zeo)	PV2
Calico Hills nonwelded (CHn)	Tptpv1	ch1 (vit, zeo)	BT1 or BT1*a* (altered)
	Tpbt1		
	Tac (Calico)	ch2 (vit, zeo)	CHV (vitric) or CHZ (zeolitic)
		ch3 (vit, zeo)	
		ch4 (vit, zeo)	
		ch5 (vit, zeo)	
	Tacbt (Calicobt)	ch6 (vit, zeo)	BT
	Tcpuv (Prowuv)	pp4	PP4 (zeolitic)
	Tcpuc (Prowuc)	pp3	PP3 (devitrified)

Table 6.1-1. GFM2000 Lithostratigraphy, UZ Model Layer, and Hydrogeological Unit Correlation Used in the UZ Flow Model and Submodels (Continued)

Major Unit[a]	Lithostratigraphic Nomenclature[b]	UZ Model Grid Unit/Layer[c]	Hydrogeological Unit [d]
Calico Hills nonwelded (CHn) (Continued)	Tcpmd (Prowmd)	pp2	PP2 (devitrified)
	Tcplc (Prowlc)		
	Tcplv (Prowlv)	pp1	PP1 (zeolitic)
	Tcpbt (Prowbt)		
	Tcbuv (Bullfroguv)		
Crater Flat undifferentiated (CFu)	Tcbuc (Bullfroguc)	bf3	BF3 (welded)
	Tcbmd (Bullfrogmd)		
	Tcblc (Bullfroglc)		
	Tcblv (Bullfroglv)	bf2	BF2 (nonwelded)
	Tcbbt (Bullfrogbt)		
	Tctuv (Tramuv)		
	Tctuc (Tramuc)	tr3	Not Available
	Tctmd (Trammd)		
	Tctlc (Tramlc)		
	Tctlv (Tramlv)	tr2	Not Available
	Tctbt (Trambt) and below		

Sources: [a]Montazer and Wilson 1984 [DIRS 100161]; [b]BSC 2004 [DIRS 170029]; [c]BSC 2004 [DIRS 169855]; [d]Flint 1998 [DIRS 100033].

NOTES: [c]Defined by the rock material type, represented by the code name, for grid layers or blocks belonging to the same rock unit. [d]Hydrogeologcal units or layers defined for the UZ model exclude alluvial covers. The top model boundary is at the ground surface of the mountain (or the tuff-alluvium contact in areas of significant alluvial covers).

UZ = unsaturated zone.

The three-dimensional UZ model domain, as well as the numerical grid for this study (DTN: LB03023DKMGRID.001 [DIRS 162354]), is shown in plan view in Figure 6.1-1, encompassing approximately 40 km^2 of the area over the mountain. The UZ model grid, shown in Figure 6.1-1, is referred to as the TSPA-LA grid. It is primarily designed for model calibration and simulations of three-dimensional flow fields used in TSPA-LA calculations. As shown in Figure 6.1-1, this three-dimensional model grid uses a refined mesh in the vicinity of the repository, located near the center of the model domain, covering the region from the Solitario Canyon fault to Ghost Dance fault in the west-east direction, and from borehole G-3 in the south to beyond Sever Wash fault in the north (SNL 2007 [DIRS 179466]). Also shown in Figure 6.1-1 are the locations of several boreholes used in model calibrations and analyses. The model domain is selected to focus on the study area of the repository and to investigate the effects of different infiltration scenarios and major faults on moisture flow around and below the repository. In the model grid, faults are represented in the model by vertical or inclined 30 –m wide zones (Section 5). The top model boundary is set at the ground surface or the tuff–alluvium interface; the bottom model boundary is set to the water table. The water table is set to the average water table elevation across the model domain, fully supported by borehole water table measurement data. The water table, which is the bottom boundary of the UZ model, is shown to be a relatively flat, stable surface in most of the model domain, increasing its elevation only in the north (BSC 2004 [DIRS 169855]). This rise has little effect on flow simulation results within

three-dimensional TSPA-LA flow fields. For gas flow simulation and ambient temperature calibration, the TOUGH2 V1.6 (2003 [DIRS 161491]) EOS3 module was used. Tracer transport and chloride studies were performed using the decoupled module of T2R3D V1.4 (1999 [DIRS 146654]) with flow fields generated by the EOS9 module. TOUGH2 V1.6 (2003 [DIRS 161491]) and T2R3D V1.4 (1999 [DIRS 146654]) were selected because they have been qualified and baselined for modeling flow and transport in heterogeneous fractured rock (e.g., Wu et al. (2002 [DIRS 160195]). These numerical codes were used for this work because they were qualified and baselined for use in this report, and they have the generalized capability of handling fractured rock with local and global fracture–matrix interaction, which was required for modeling studies of this report.

To model unsaturated flow and transport processes in the unsaturated zone system at Yucca Mountain, mathematical models or governing equations are needed to describe the physical processes quantitatively. The physical processes associated with flow and transport in porous media are governed by the fundamental conservation laws (i.e., conservation of mass, momentum, and energy), which govern the behavior of fluid flow, chemical migration, and heat transfer through unsaturated fractured porous media. The macroscopic continuum approach has been most commonly used in practical applications (Bear 1972 [DIRS 156269]). In this approach, the physical laws governing flow of several fluids, transport of multicomponents, and heat transfer in porous media are represented mathematically on the macroscopic level by a set of partial differential or integral equations. Fluid and heat flow and chemical-transport processes in fracture and matrix systems in the unsaturated zone are described using a macroscopic, dual-permeability continuum approach.

In addition to the conservation or continuity equations of mass and thermal energy in fracture and matrix systems, specific relationships or *mechanisms* are needed that describe how fluid flow, solute/tracer transport, and heat transfer occur in porous and fractured media. The following specific laws and constitutive relationships act as such mechanisms by governing local fluid flow, component transport, and heat-transfer processes in porous and fractured media:

1. The governing equation for describing isothermal, unsaturated liquid flow is the Richards equation (Richards 1931 [DIRS 104252]; Pruess et al. 1999 [DIRS 160778], Equation A-17, p. 146), based on the conservation of mass and Darcy's law (Bear 1972 [DIRS 156269]) with flux driven by gravity and capillary pressure gradient. The unsaturated flux is a product of the unsaturated hydraulic conductivity and the driving gradient. Hydraulic conductivity is proportional to effective permeability and fluid density, and inversely proportional to fluid viscosity. Rock and fluid properties can be treated as constants under isothermal conditions. The effective permeability (relative permeability times absolute permeability or saturated permeability) is related to water content (saturation times porosity) and capillary pressure, as described by the van Genuchten model (1980 [DIRS 100610]). The governing equations for unsaturated flow under isothermal conditions are given in Appendix A. Exceptions to the use of the Richards equation are the ambient temperature model, the gas flow model, and the calcite model, which use the two-phase (water and air, TOUGH2 EOS3 module) flow equation instead of Richards equation for the isothermal or nonisothermal water and airflow flow.

The UZ flow model and its submodels adopt the dual-continuum approach for modeling flow through fractures and the matrix. The Richards equation is applied to the fracture and matrix continuum for unsaturated flow under isothermal conditions. Fluid exchange between the fracture continuum and matrix continuum is the fracture–matrix interaction, which is simulated by the dual-permeability concept, and is further modified by an active fracture model (AFM) (Liu et al. 1998 [DIRS 105729]) in the UZ flow model.

The active fracture model (AFM) was developed within the context of the dual-continuum approach (Liu et al. 1998 [DIRS 105729]). It is based on the reasoning that, on account of fingering flow, only a portion of fractures in a connected, unsaturated fracture network contribute to liquid water flow, while other fractures are simply bypassed. The portion of the connected fractures that actively conduct water are called active fractures. Thus, the AFM uses a combination of a continuum approach and a simple filtering concept to model fracture flow. Inactive fractures are filtered out in modeling fracture–matrix interaction and flow in the fracture continuum.

Darcy's law (Appendix A) and the van Genuchten model can be generalized for multiphase flow under nonisothermal conditions. The governing equations for gas and liquid flow and heat flow are based on conservation of mass for fluid phases, and on conservation of energy for conductive and convective heat transfer processes, respectively. The full set of equations for nonisothermal, two-phase flow of gas and water in fractures and matrix are presented in a report by Pruess et al. (1999 [DIRS 160778], Appendix A).

In solving the governing equations (Appendix A), a number of known parameters are given as input to the UZ flow model. Some of those variables are treated as constants—for example, fluid viscosity under isothermal conditions. Others are provided as known parameters measured either in the laboratory or in field tests, and/or further calibrated. Examples of known parameters are rock density, porosity, and absolute permeability. Input parameters are further discussed in Section 6.1.5. In addition, boundary conditions are needed to solve governing equations (Section 6.1.3). The top boundary for the UZ flow model is subject to net infiltration from the land surface (Section 6.1.4). With these input parameters and boundary conditions, the solving of the full set of equations (Pruess et al. 1999 [DIRS 160778]) in the UZ flow model provides outputs for variables such as liquid saturation, phase pressures, capillary pressure, mass or percolation flux, and Darcy velocity, in addition to temperatures in the thermal model.

surfaces become minimal, and the one block matrix-fracture representation is expected to produce accurate solutions (Doughty 1999 [DIRS 135997]).

The utility and appropriateness of conceptual and numerical approach of dual-permeability for modeling several flow and transport processes has been discussed by Doughty (1999 [DIRS 135997]) through a one-dimensional column extracted from a three-dimensional UZ site-scale model of the unsaturated zone at Yucca Mountain, NV. Within the dual-continua models, the formulation for fracture–matrix (F–M) interface area can have a major effect on the hydrodynamic response to an infiltration pulse and tracer arrival at various horizons, with fracture responses occurring sooner as F–M interface area decreases. The number of matrix blocks also has a significant effect on response time, with the more accurate multi-matrix-gridblock models yielding slower fracture response times. For steady-state moisture flow, most of the numerical and conceptual models provide similar results for saturation and fracture flow profiles. When advection and diffusion play a significant role in tracer transport, the arrival time of tracer fronts is strongly dependent on the choice of F–M interface area formulation, as this area controls the magnitude of F–M diffusion in addition to F–M fluid flow. In general, as F–M interface area decreases, tracer travel time through the fractures decreases. For the cases studied, considering a uniform, relatively small infiltration rate, tracer front arrival time is somewhat sensitive to the choice of one or more matrix blocks, with dual-permeability models predicting earlier fracture arrival times for cases in which F–M interface area is reduced. For thermal loading, preliminary studies indicate that the dual-permeability model does capture all the significant physical processes, in which rapid fluid and heat flow occurs in the fractures before the matrix has a chance to equilibrate.

As applied in this report, the traditional dual-permeability concept is further modified using an AFM (Liu et al. 1998 [DIRS 105729]) to represent fingering effects of liquid flow through fractures and to limit flow into the matrix system. The active fracture concept has been evaluated in *Conceptual Model and Numerical Approaches for Unsaturated Zone Flow and Transport* (BSC 2004 [DIRS 170035]) and further sensitivity analyses are provided in Section 6.8. The dual-permeability conceptual model is used for describing fracture–matrix interaction with all geological units as well as faults.

As an alternative modeling approach, the discrete-fracture or "weeps" type model have extremely high uncertainties with respect to fracture distribution data within the mountain, as well as an extensive computational burden that cannot be solved currently or in the near future. On the other hand, the effective-continuum approach, although the most computationally efficient, may not capture important, nonequilibrium interaction in flow and transport between fractures and matrix in the unsaturated zone. Therefore, it may also not be appropriate for use in modeling UZ flow and transport at Yucca Mountain.

In model calibration of moisture flow and tracer transport, ambient, variably saturated flow in the unsaturated zone underlying Yucca Mountain is treated as an isothermal, steady-state flow system. This is considered to be a good approximation of the unsaturated zone below the PTn unit, because the relatively unfractured nonwelded PTn unit is expected to damp and homogenize downward-moving transient pulses arising from episodic surface infiltration events (Wu et al. 2000 [DIRS 154918]; Wu et al. 2002 [DIRS 161058]; Flint et al. 2001 [DIRS 164506]; Zhang et al. 2006 [DIRS 180273]). Additional analyses of PTn damping effects using the updated UZ model are presented in Section 6.9, to show the effectiveness of the PTn unit in redistributing

percolation flux for the units below. Therefore, estimated surface net infiltration rates may effectively be described as steady-state water recharge (Section 6.1.4).

In the development of the UZ flow model and its submodels over the past decade, the steady-state nature of the flow fields and the damping of transient pulses were evaluated in different studies. Wu et al. (1999 [DIRS 117161], p. 186) referred to the early work of Wang and Narasimhan (1985 [DIRS 108835]; 1993 [DIRS 106793], Figure 7.4.7), which suggested that effects of infiltration pulses at the surface are damped by the underlying tuff units, especially the PTn. The welded tuff of the repository horizon exhibited only small changes in saturations, pressures, and potentials from steady-state values in response to the transient pulses. Pan et al. (1997 [DIRS 164181]) investigated transient flow behavior for downward water flow through sloping layers in the vadose zone, with up-slope flow developed during heavy rain, likely enhancing the downward flow. Wu et al. (2002 [DIRS 161058], pp. 35-1 to 35-12) analyzed the capillary barrier capacities in unsaturated units and indicated that, on average, it took several thousands years for water to travel through the PTn. Wu et al. (2000 [DIRS 154918], 2002 [DIRS 161058]) and Flint et al. (2003 [DIRS 163967]) analyzed the implications of capillary barrier development in subunits of the PTn for lateral diversion of flow in the PTn. Along sloping layers, strong capillary barriers, if formed, will promote lateral diversions. The degree or scale of lateral diversion can be evaluated by: (1) comparative sensitivity studies, (2) detailed analysis of field data including geochemical evidences, and (3) long-term controlled field tests. A more recent study, conducted by Zhang et al. (2006 [DIRS 180273]) using three-dimensional and one-dimensional model results, shows that the PTn can attenuate episodic infiltration pulses significantly, most percolating water is damped by the subunits at the top of the PTn, and a small percentage of percolation flux is diverted into faults.

6.1.3 Model Boundary Conditions

The ground surface of the mountain (or the tuff-alluvium contact in areas of significant alluvial cover) is taken as the top model boundary; the water table is treated as the bottom model boundary. The top and bottom boundaries of the model are treated as Dirichlet-type conditions with specified constant, but spatially varying temperature and gas pressure. For flow simulations using the EOS9 module, only water pressure or saturation values are needed along the top and bottom model boundaries. Surface infiltration, as discussed below in Section 6.1.4, is applied using a source term in the fracture gridblocks within the second grid layer from the top. This method was adopted because the first layer is treated as a Dirichlet-type boundary, with constant pressure, saturation, and temperature to represent average atmospheric conditions at the mountain.

The water table is used as the bottom model boundary, a surface where the water pressure is a single, fixed value. Within the numerical models, only one set of model primary variables for solving Richards' equations is specified for the bottom boundary, equivalent to specifying a constant saturation. For gas and/or heat flow simulations, the bottom model boundary representing the water table is subject to fixed gas pressure, equal to the atmospheric pressure at that elevation (Sections 6.3.3 and 6.4.1). Lateral boundaries, as shown in Figure 6.1-1, are treated as no-flow (closed) boundaries, which allow flow to occur exclusively along the vertical plane. This treatment is reasonable for the eastern boundary, which is along or near the Bow Ridge fault, because high vertical permeability and lower capillary forces are expected within the faults (see fault properties estimated in *Calibrated Unsaturated Zone Properties* (SNL 2007

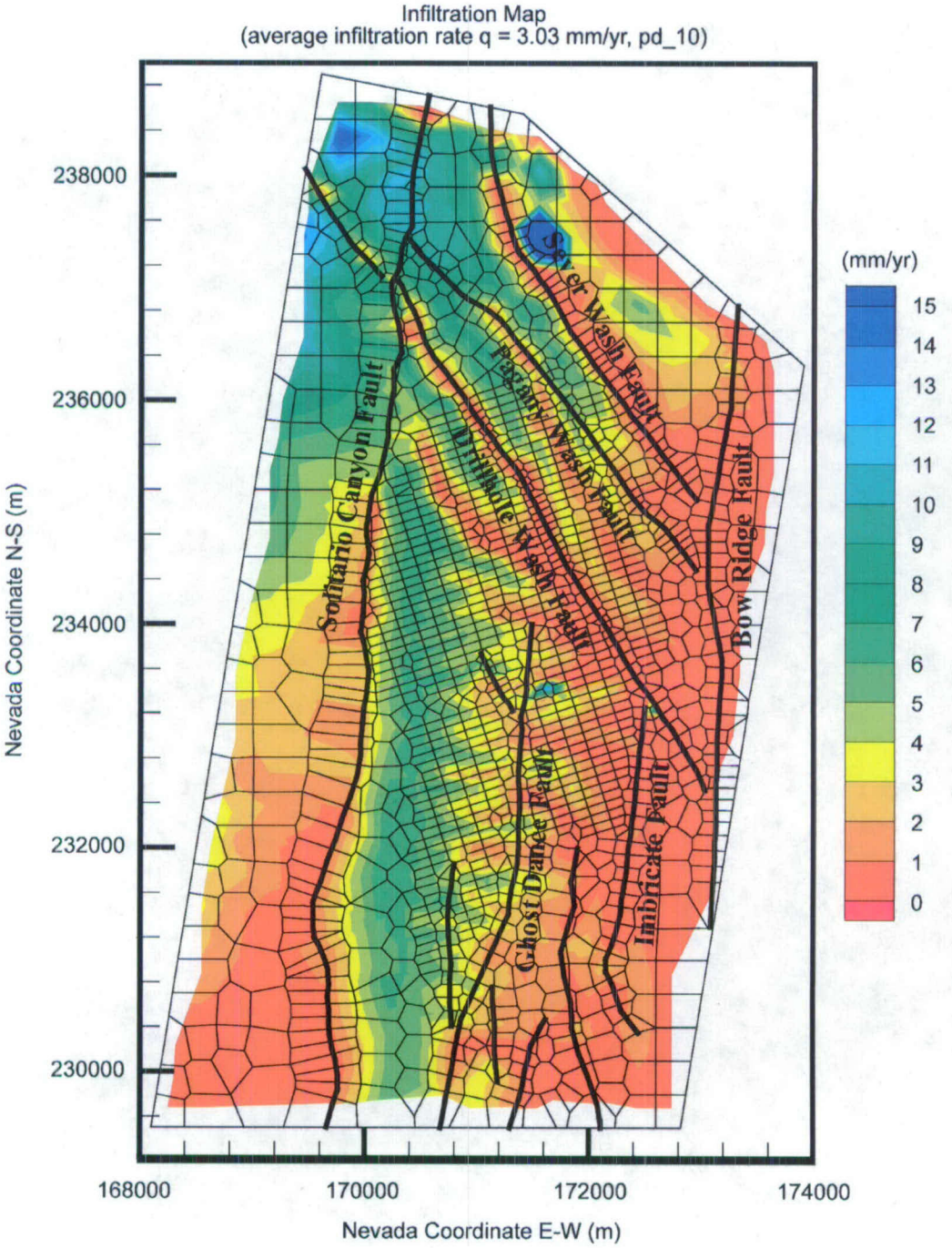

Source: DTN: SN0609T0502206.028 [DIRS 178753].

Output DTN: LB06123DPDUZFF.001.

Figure 6.1-2. Plan View of Net Infiltration Distributed over the Three-Dimensional Unsaturated Zone TSPA-LA Model Grid for the Present-Day 10th Percentile Infiltration Scenario

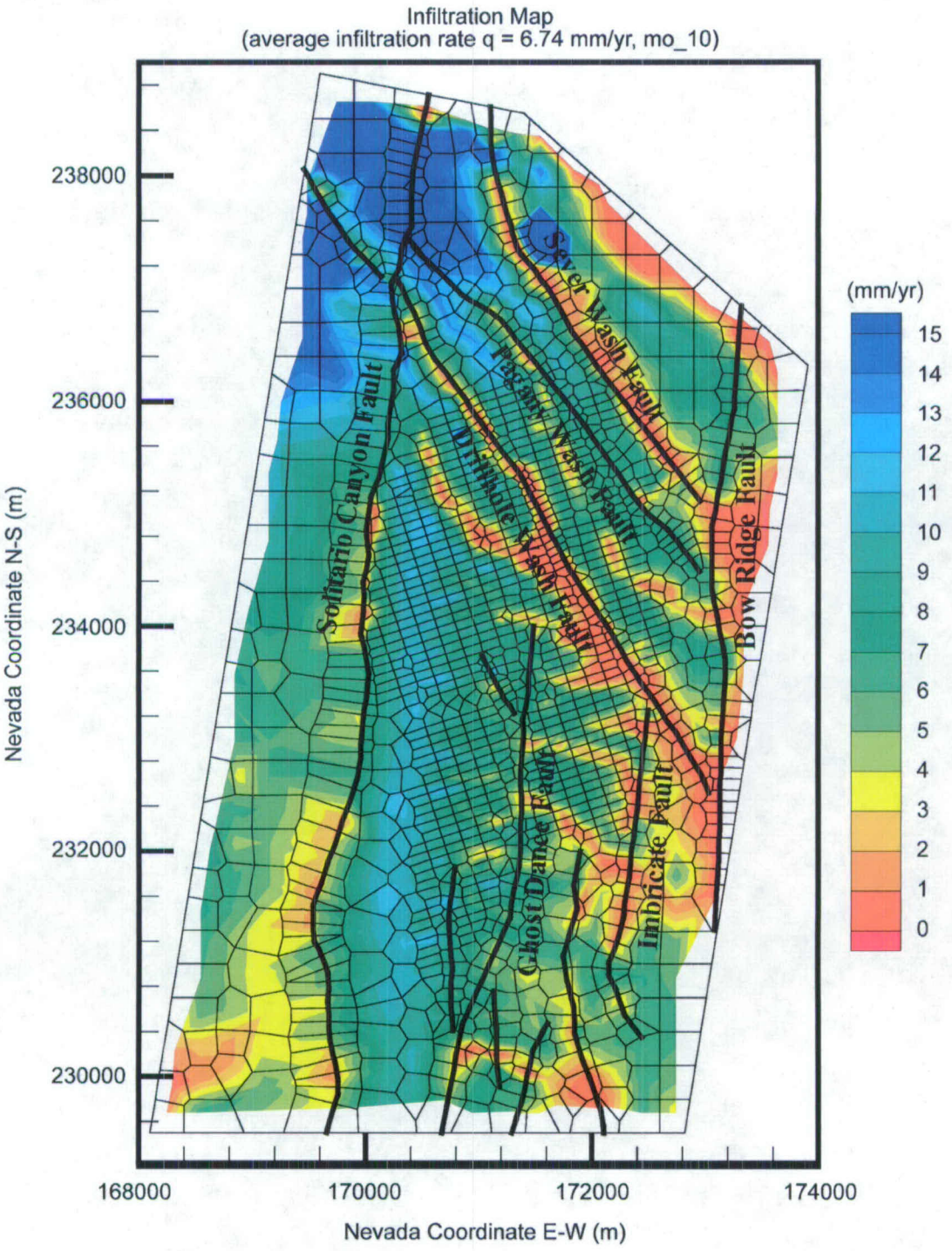

Source: DTN: SN0609T0502206.028 [DIRS 179063].

Output DTN: LB07013DMOUZFF.001.

Figure 6.1-3. Plan View of Net Infiltration Distributed over the Three-Dimensional Unsaturated Zone TSPA-LA Model Grid for the Monsoon 10th Percentile Infiltration Scenario

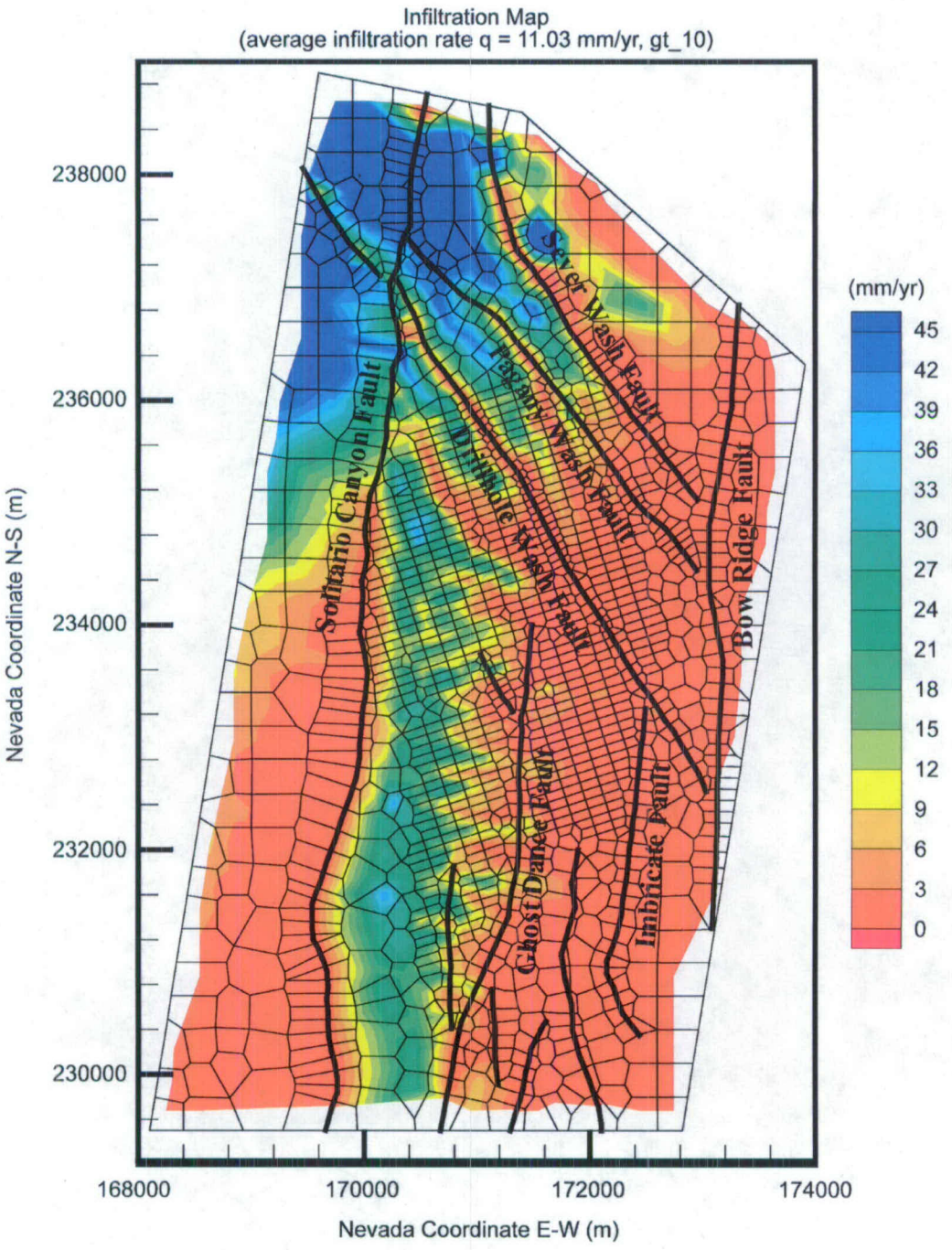

Source: DTN: SN0609T0502206.029 [DIRS 178862].

Output DTN: LB07013DGTUZFF.001.

Figure 6.1-4. Plan View of Net Infiltration Distributed over the Three-Dimensional Unsaturated Zone TSPA-LA Model Grid for the Glacial Transition 10th Percentile Infiltration Scenario

One additional climate scenario for the post-10,000-year period (post-10k-yr) was considered, using the average percolation flux ranges specified by the U.S. Nuclear Regulatory Commission (NRC) (BSC 2006 [DIRS 177465]). The stipulated distribution of average percolation flux to the repository is given as a log-uniform distribution ranging from 13 to 64 mm/yr, according to the NRC-proposed rule ([DIRS 178394], 10 CFR 63.342(c), p. 53,320). The NRC directs the Department of Energy to accordingly consider the dose calculations during the post-10k-yr time period.

Because the UZ flow model specifies flux at the upper boundary, not at an interior surface such as the repository, the appropriate flux is specified in the repository footprint projected up to the ground surface. Computations have shown that the average flux flowing to the repository is within three percent of the average flux specified at the ground surface over the projected repository area. The values for average water flux are taken to be at the same four probabilities used for present day, monsoon, and glacial transition climates. This is discussed in Section 6.8, where the calibrated probabilities for 10th, 30th, 50th, and 90th scenarios are developed. The adjusted probabilities for these cases are found to be (Table 6.8-1) 62%, 16%, 16%, and 6%, respectively. The midpoints of these probability ranges for a cumulative probability distribution are at 31%, 70%, 86%, and 97%, respectively. Using these percentiles and the log-uniform percolation flux distribution gives the values shown in Table 6.1-3, averaged over the repository footprint. An infiltration map must be developed to spatially distribute infiltration for a given average infiltration rate.

For the available 12 infiltration maps implemented for the pre-10k-yr period (10th, 30th, 50th, and 90th scenarios for each of present-day, monsoon, and glacial transition) (Table 6.1-2), the average infiltration rates through the repository footprint were first calculated. The infiltration map with a calculated average infiltration rate that most closely matches the first of the four target values (21.29, 39.52, 51.05, and 61.03 mm/yr in Table 6.1-3) for the post-10k-yr period was selected. This selection process was repeated for maps for the second through the fourth target. Then the infiltration rates for that map were scaled such that the target value for the average infiltration through the repository footprint is obtained to meet the NRC requirement. Specifically, the infiltration rates for the maps of present-day 90th percentile, glacial transition 50th percentile, glacial transition 90th percentile, and monsoon 90th percentile infiltration scenarios were then scaled such that the average infiltration flux through the repository footprint closely matched the target value. This scaled infiltration map was then used as the infiltration boundary condition for the UZ flow model to generate the post-10k-yr flow field. With the infiltration boundary condition specified, computing the post-10k-yr UZ flow fields was the same as computing the pre-10k-yr flow fields. The resulting percolation fluxes over the UZ model domain, as well as through the repository footprint for the post-10k-yr climate, are shown in Table 6.1-3. Figure 6.1-5 shows UZ flow model results for the case of the 10th percentile post-10k-yr climate.

Table 6.1-3. Average and Target Infiltration Rates for Four Selected Maps over the UZ Model Domain and within Repository Footprint for Post-10k-year Climate

Scenario	Percentile	Average Infil of Selected Map Over UZ Model Domain		Target Average Infil within Repository Footprint	
		Average (mm/yr)	Scenario	Rate (mm/yr)	Mid-point Cumulative Probability
pkd_q1	10	16.89	present-day 90th percentile	21.29	0.3096
pkd_q2	30	28.99	glacial transition 50th percentile	39.52	0.6975
pkd_q3	50	34.67	glacial transition 90th percentile	51.05	0.8582
pkd_q4	90	48.84	monsoon 90th percentile	61.03	0.9702

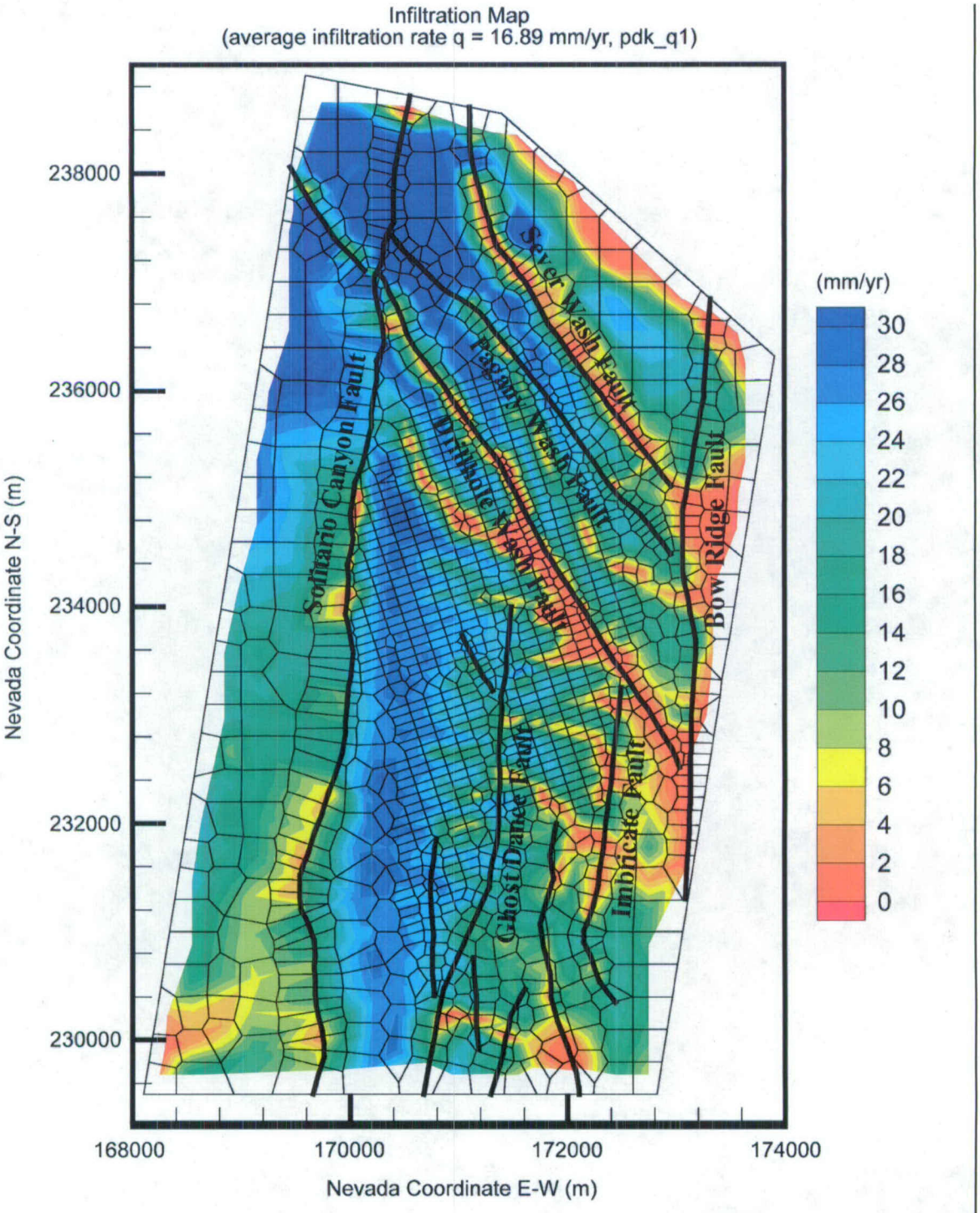

Output DTN: LB0702UZP10KFF.002.

Figure 6.1-5. Plan View of Net Infiltration Distributed over the Three-Dimensional Unsaturated Zone TSPA-LA Model Grid for the Post-10,000-yr Period Climate, 10th Percentile Infiltration Scenario

systems using a dual-permeability approach. In addition, the van Genuchten relative permeability and capillary pressure functions (van Genuchten 1980 [DIRS 100610]) are used to describe flow in fractures and matrix.

In addition to fracture and matrix properties, lithophysal cavities are found in several hydrogeological layers of upper lithophysal (tsw33) and lower lithophysal (tsw35) units. These cavities, according to their local association with fractures or matrix blocks, mainly contribute storage space to fracture or matrix systems in terms of impact on flow and transport through these tuff layers. Lithophysal cavities can be considered as part of fracture or matrix porosity, but the effect of these cavities on tracer transport from the repository to the water table is expected to be small and are not explicitly incorporated into the UZ flow model. Under steady-state flow conditions, fracture or matrix porosity does not affect UZ flow fields. This is commensurate with the main objective of the UZ flow model—development of three-dimensional steady-state UZ flow fields, which are independent of the values of fracture or matrix porosity used under steady-state flow condition. In addition, porosity has little effect on pneumatic flow, which is largely controlled by fracture properties and only negligibly by matrix porosity. However, porosity has a certain influence on transient transport. The geological layers with cavities are located either higher than or at the repository horizon, and cavities will remain dry. Little water is expected to flow through cavities, owing to the strong capillary barrier effect on seepage into cavities. Therefore, the existence of these lithophysal cavities has virtually no impact on the calibration and simulation results of the UZ flow model (Section 6.10.2).

6.2 THREE-DIMENSIONAL UZ FLOW MODEL CALIBRATION

A critical step in developing the three-dimensional UZ flow model was to use field-measured liquid saturation, water potential, perched water, and pneumatic data to calibrate the three-dimensional model. This calibration is essential for the important iterative processes of model verification, which increase confidence in model predictions for the site conditions. A detailed model-calibrating investigation is reported in *Calibrated Unsaturated Zone Properties* (SNL 2007 [DIRS 179545]), using one- and two-dimensional models for estimating model parameters with water potential, and saturation. However, these one-dimensional models cannot predict whether lateral flow or perched water occurs in several hydrogeological units of the unsaturated zone below the repository level. This section documents a further model calibration effort, focusing on three-dimensional flow patterns: perched water calibrations using the three-dimensional model grid (Figure 6.1-1).

The three-dimensional flow model calibration is conducted using the four sets of parameters of one-dimensional site-scale calibrated properties (SNL 2007 [DIRS 179545]); DTNs: LB0611MTSCHP10.001 [DIRS 178586], LB0611MTSCHP30.001 [DIRS 180293], LB0612MTSCHP50.001 [DIRS 180294], LB0612MTSCHP90.001 [DIRS 180295]), two-dimensional site-scale calibrated fault properties (DTN: LB0612MTSCHPFT.001 [DIRS 180296]), three present-day infiltration rates (see Table 6.1-2), and the geological model and numerical grid for calibration (BSC 2004 [DIRS 169855]). In addition, previously developed three-dimensional properties for the perched water zone unit (DTN: LB03013DSSCP3I.001 [DIRS 162379]) developed from *Analysis of Hydrologic Properties Data* (BSC 2004 [DIRS 170038]) and based on information from the previous version

of this report (BSC 2004 [DIRS 169861]) are adopted in this report. As shown in Section 6.2.2.2, even with

of this report (BSC 2004 [DIRS 169861]) are adopted in this report. As shown in Section 6.2.2.2, even with

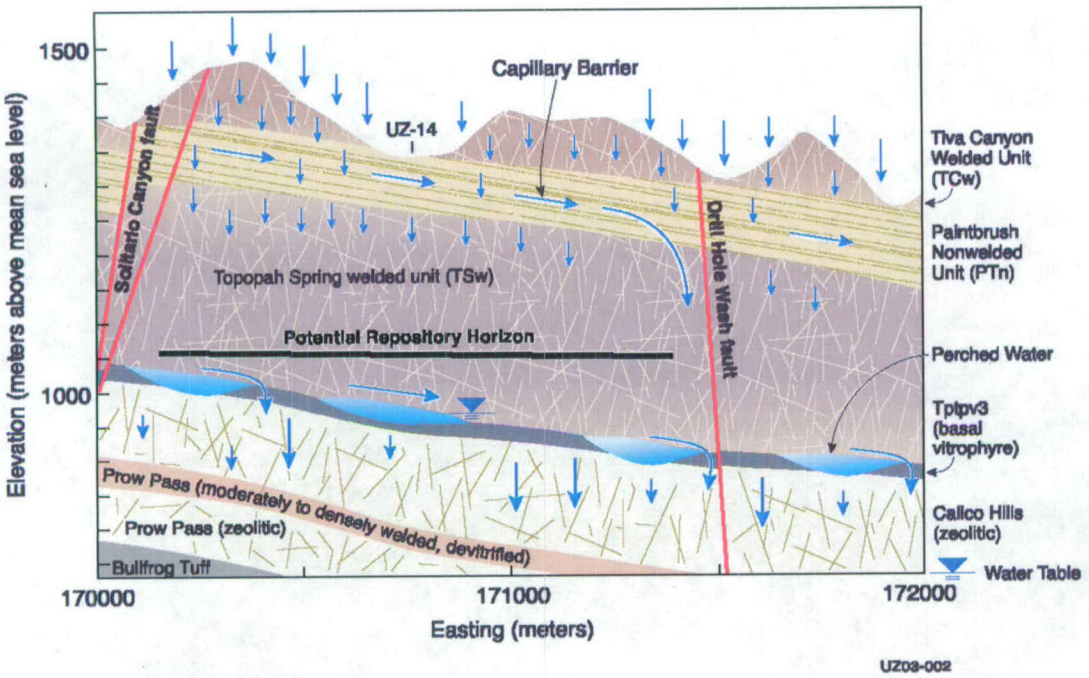

Source: For illustration purposes only.

Figure 6.2-1. Schematic Showing the Conceptualized Flow Processes and Effects of Capillary Barriers, Major Faults, and Perched Water Zones within a Typical Cross Section of the Unsaturated Zone Flow Model Domain in the East-West Direction

The PTn unit, as described by the current geological model, consists primarily of non- to partially welded tuffs. The dip of these layers is generally less than 10° to the east or southeast. The combined thickness of the PTn layers ranges from 150 m in the north of the model area to 30 m or less, even completely disappearing in several areas of the south. However, the PTn unit is present over the entire repository area, where the thickness of the PTn unit ranges from approximately 30 to 60 m. The PTn unit as a whole exhibits very different hydrogeologic properties from the TCw and TSw units that bound it above and below. The TCw and TSw units have low porosity and intense fracturing typical of the densely welded tuffs at Yucca Mountain. In contrast, the PTn has high porosity and low fracture intensity, and its matrix system has a large capacity for storing groundwater. It has been shown to effectively damp spatial and temporal variations in percolation flux (Wu et al. 2000 [DIRS 154918], pp. 30 to 32 and 39 to 41; Zhang et al. 2006 [DIRS 180273]). Therefore, water flow through the unsaturated zone is modeled to occur under steady-state conditions, while the temporal damping effect of episodic flux is studied in Section 6.9.

6.2.2.1 Capillary Barriers

The concept of capillary barriers has been advanced to explain flow behavior within the PTn at Yucca Mountain (Montazer and Wilson 1984 [DIRS 100161], pp 26 to 30). These capillary barriers are due to the large contrast in rock properties across predominantly horizontal interfaces within the PTn unit. The presence of faults and larger fractures prevents development of

extensive lateral flow or laterally extensive or continuous capillary barriers. Field data obtained from tens of boreholes have been used to characterize the distribution of rock properties within the PTn unit. In general, field data indicate that the Yucca Mountain formation is more heterogeneous vertically than horizontally, so that layer-wise representations provide a reasonable approximation of the complex geological system. Calibration using this conceptual model matches different types of observation data, as further demonstrated in the following sections. However, characterizing general flow behavior within the unsaturated zone system is complicated by the presence of faults, which interrupt the lateral continuity in the rock matrix properties of sloping layers.

The key conceptualizations made in the UZ flow model concerning lateral flow above the repository horizon are as follows: (1) the hydrogeological units/layers are internally homogeneous, and the material properties of each unit are continuous throughout each layer (Table 6.1-1) unless interrupted by faults; (2) ambient water flow in the system is at a steady-state condition; and (3) faults are represented by vertical or inclined columns of gridblocks having finite or small width. The flow patterns associated with capillary barriers within the PTn are studied in the following sections using this conceptual model.

6.2.2.2 Perched Water

Conceptual models of perched water occurrence are of particular interest in assessing the system performance of the repository and UZ flow patterns below the repository. Waste-isolation strategies and unsaturated zone natural barrier capability depend, in part, on sorption within the zeolitic portions of the CHn and on tracer transport times between the repository horizon and the water table. Several conceptual models have been proposed for the genesis of perched water at Yucca Mountain (e.g., Wu et al. 1999 [DIRS 117167]; Wu et al. 2004 [DIRS 173953]).

Perched water may occur where percolation flux exceeds the capacity of the geological media to transmit vertical flux in the unsaturated zone. Perched water has been encountered in a number of boreholes at Yucca Mountain, including UZ-14, SD-7, SD-9, SD-12, NRG-7a, G-2, and WT-24. These perched water occurrences are found to be associated with low-permeability zeolites in the CHn or the densely welded basal vitrophyre (Tptpv3, Table 6.1-1) of the TSw unit. Some possible mechanisms of water perching in the unsaturated zone of Yucca Mountain may be permeability or capillary barrier effects at faults, or a combination of both.

The permeability-barrier conceptual model for perched water occurrence has been used in UZ flow modeling studies since 1996 (Wu et al. (1999 [DIRS 117167]; Wu et al. 2004 [DIRS 173953]). In this model, perched water bodies in the vicinity of the ESF North Ramp (near Boreholes UZ- 14, SD-9, NRG-7a, G-2, and WT-24) are observed to occur above the base of the TSw, underlain by a zone of low-permeability, zeolitized rock. The perched water bodies in this northern area of the repository may be interconnected. However, the perched water zones at Boreholes SD-7 and SD-12 are considered here as local, isolated bodies. In this conceptual model, vertical and lateral water movement in the vicinity of the perched zones is considered to be controlled mainly by the fracture and matrix permeability distribution in these areas. The major aspects of the permeability-barrier conceptual model are: (1) no large-scale, vertically connected, potentially fluid-conducting fractures transect the underlying low-permeability units; (2) vertical and horizontal permeabilities within and below the perched water zone are small

- Near borehole SD-7, properties for the gridblocks in grid columns q45, i80, i81, i84, i87, o92, and o95, over grid layers of ch5z (ch5Fz/ch5Mz), ch6z (ch6Fz/ch6Mz) and pp4 (pp4Fz/pp4Mz) are replaced by (pcF5z/pcM5z), (pcF6z/pcM6z), and (pcF4p/pcM4p), respectively.

- Near borehole SD-12, properties for the gridblocks in grid columns q47, b93, b99, k61, k62 and k67, over grid layers of tsw38 (tswF8/tswM8), tsw39 (tswF9/tswM9), and ch1v (ch1Fv/ch1Mv) are replaced by (pcF38/pcM38), (pcF39/pcM39), and (pcF1z/pcM1z), respectively.

Fracture and matrix permeabilities of potential perched layers/zones, as identified above, are calibrated based on the three-dimensional model calibrated values and shown in Tables 6.2-2, 6.2-3, and 6.2-4. All properties except intrinsic permeabilities, van Genuchten's α and m parameters, and residual saturations for matrix blocks within perched zones are identical to parameters estimated from the current one-dimensional calibrations discussed in *Calibrated Unsaturated Zone Properties* (SNL 2007 [DIRS 179545]). The active-fracture parameter, γ, is set to zero for the perched zones, causing the fracture and matrix interface-area factor to be equivalent to liquid saturation (Liu et al. 1998 [DIRS 105729]). Tables 6.2-2, 6.2-3, 6.2-4, and 6.2-5 present the final four sets of calibrated rock properties at zones with perched water, with 10th, 30th, 50th, and 90th present-day infiltration scenarios, respectively. The modified "fracture" properties in the following three tables are close to those of the matrix, so that fractures in water perching layers are effectively removed.

In Tables 6.2-2 to 6.2-5, as well as those in Appendix B, the symbols and notations standing for parameters are defined as follows: k_M and k_F are intrinsic permeability of matrix and fracture systems; α_M and α_F are van Genuchten α parameters of the matrix and fracture systems; m_M and m_F are van Genuchten m parameters of the matrix and fracture systems; and γ is the AFM parameter.

Table 6.2-2. Calibrated Parameters of Perched Water Conceptual Model for the Present-Day, 10th Percentile Infiltration Scenario

Model Layer	k_M (m^2)	α_M (1/Pa)	m_M (–)	k_F (m^2)	α_F (1/Pa)	m_F (–)	γ (–)
pcM38/ pcF38	3.000×10^{-19}	1.878×10^{-6}	0.286	3.000×10^{-18}	1.878×10^{-6}	0.286	0.00
pcM39/ pcF39	6.200×10^{-18}	4.610×10^{-6}	0.059	6.200×10^{-17}	4.610×10^{-6}	0.059	0.00
pcM1z/ pcF1z	9.300×10^{-20}	2.120×10^{-7}	0.349	9.300×10^{-19}	2.120×10^{-7}	0.349	0.00
pcM2z/ pcF2z	2.400×10^{-18}	2.250×10^{-6}	0.257	2.400×10^{-17}	2.250×10^{-6}	0.257	0.00
pcM5z/ pcF5z	2.400×10^{-18}	2.250×10^{-6}	0.257	2.400×10^{-18}	2.250×10^{-6}	0.257	0.00
pcM6z/ pcF6z	1.100×10^{-19}	1.560×10^{-7}	0.499	1.100×10^{-19}	1.560×10^{-7}	0.499	0.00
pcM4p/ pcF4p	7.700×10^{-19}	6.310×10^{-6}	0.474	7.700×10^{-19}	6.310×10^{-6}	0.474	0.00

Output DTN: LB07043DCRXPRP.001.

Table 6.2-3. Calibrated Parameters of Perched Water Conceptual Model for the Present-Day, 30th Percentile Infiltration Scenario

Model Layer	k_M (m^2)	α_M (1/Pa)	m_M (-)	k_F (m^2)	α_F (1/Pa)	m_F (-)	γ (-)
pcM38/ pcF38	3.000×10^{-19}	3.105×10^{-6}	0.286	3.000×10^{-18}	3.105×10^{-6}	0.286	0.00
pcM39/ pcF39	6.200×10^{-18}	4.610×10^{-6}	0.059	6.200×10^{-17}	4.610×10^{-6}	0.059	0.00
pcM1z/ pcF1z	9.300×10^{-20}	2.120×10^{-7}	0.349	9.300×10^{-19}	2.120×10^{-7}	0.349	0.00
pcM2z/ pcF2z	2.400×10^{-18}	2.250×10^{-6}	0.257	2.400×10^{-17}	2.250×10^{-6}	0.257	0.00
pcM5z/ pcF5z	2.400×10^{-18}	2.250×10^{-6}	0.257	2.400×10^{-18}	2.250×10^{-6}	0.257	0.00
pcM6z/ pcF6z	1.100×10^{-19}	1.560×10^{-7}	0.499	1.100×10^{-19}	1.560×10^{-7}	0.499	0.00
pcM4p/ pcF4p	7.700×10^{-19}	6.310×10^{-7}	0.474	7.700×10^{-19}	6.310×10^{-7}	0.474	0.00

Output DTN: LB07043DCRXPRP.001.

Table 6.2-4. Calibrated Parameters of Perched Water Conceptual Model for the Present-Day, 50th Percentile Infiltration Scenario

Model Layer	k_M (m^2)	α_M (1/Pa)	m_M (-)	k_F (m^2)	α_F (1/Pa)	m_F (-)	γ (-)
pcM38/ pcF38	3.000×10^{-19}	3.691×10^{-6}	0.286	3.000×10^{-18}	3.691×10^{-6}	0.286	0.00
pcM39/ pcF39	6.200×10^{-18}	4.610×10^{-6}	0.059	6.200×10^{-17}	4.610×10^{-6}	0.059	0.00
pcM1z/ pcF1z	9.300×10^{-20}	2.120×10^{-7}	0.349	9.300×10^{-19}	2.120×10^{-7}	0.349	0.00
pcM2z/ pcF2z	2.400×10^{-18}	2.250×10^{-6}	0.257	2.400×10^{-17}	2.250×10^{-6}	0.257	0.00
pcM5z/ pcF5z	2.400×10^{-18}	2.250×10^{-6}	0.257	2.400×10^{-18}	2.250×10^{-6}	0.257	0.00
pcM6z/ pcF6z	1.100×10^{-19}	1.560×10^{-7}	0.499	1.100×10^{-19}	1.560×10^{-7}	0.499	0.00
pcM4p/ pcF4p	7.700×10^{-19}	6.545×10^{-6}	0.474	7.700×10^{-19}	6.545×10^{-6}	0.474	0.00

Output DTN: LB07043DCRXPRP.001.

Table 6.2-5. Calibrated Parameters of Perched Water Conceptual Model for the Present-Day, 90th Percentile Infiltration Scenario

Model Layer	k_M (m^2)	α_M (1/Pa)	m_M (-)	k_F (m^2)	α_F (1/Pa)	m_F (-)	γ (-)
pcM38/ pcF38	3.000×10^{-19}	4.777×10^{-6}	0.286	3.000×10^{-18}	4.777×10^{-6}	0.286	0.00
pcM39/ pcF39	6.200×10^{-18}	4.610×10^{-6}	0.059	6.200×10^{-17}	4.610×10^{-6}	0.059	0.00
pcM1z/ pcF1z	9.300×10^{-20}	2.120×10^{-7}	0.349	9.300×10^{-19}	2.120×10^{-7}	0.349	0.00
pcM2z/ pcF2z	2.400×10^{-18}	2.250×10^{-6}	0.257	2.400×10^{-17}	2.250×10^{-6}	0.257	0.00
pcM5z/ pcF5z	2.400×10^{-18}	2.250×10^{-6}	0.257	2.400×10^{-18}	2.250×10^{-6}	0.257	0.00
pcM6z/ pcF6z	1.100×10^{-19}	1.560×10^{-7}	0.499	1.100×10^{-19}	1.560×10^{-7}	0.499	0.00
pcM4p/ pcF4p	7.700×10^{-19}	6.310×10^{-6}	0.474	7.700×10^{-19}	6.310×10^{-6}	0.474	0.00

Output DTN: LB07043DCRXPRP.001.

The third and last parameter adjustment is the fracture permeability in the TCw and TSw units under the present-day, 10th and 30th percentile infiltration scenarios (see Section 6.4). The present-day, 10th and 30th percentile infiltration rates are used for gas flow calibration because the pneumatic tests were conducted in a small time scale of days to years at present-day conditions. This calibration, described in Section 6.4, was made from three-dimensional gas

Mass Balance and Solution Convergence: Table 6.2-7 shows the mass-balance results for the sixteen simulation scenarios. In Table 6.2-7, "inflow" is the total infiltration rate over the entire model top boundary, representing a net water recharge rate (water mass) into the system for the infiltration scenario simulated. "Outflow" is the cumulative total-flow rate out of the model and into the lower boundary representing the water table. Global mass-balance errors between inflow and outflow from the system, as shown in Table 6.2-7, are less than 0.013% for all 16 simulations, leading to the conclusion that steady-state solutions are obtained for all the simulations.

Table 6.2-7. Mass-Balance Results for Checking Steady State Status of Sixteen Flow Simulation Results

Simulation Scenarios	Inflow from Infiltration (kg/s)	Outflow to Water Table (kg/s)	Relative Error (%)
pd_10	3.821408495	3.8210676	0.0089
pd_30	10.05089517	10.0496168	0.0127
pd_50	15.50822442	15.5082076	0.0001
pd_90	33.81826331	33.8182842	0.0001
mo_10	8.511510348	8.5115148	0.0001
mo_30	16.28484915	16.2848381	0.0001
mo_50	19.41794042	19.4179219	0.0001
mo_90	92.51816511	92.5183180	0.0002
gt_10	13.93611829	13.9360979	0.0001
gt_30	25.82297803	25.8229675	0.0001
gt_50	32.81793890	32.8179286	0.0000
gt_90	58.95021503	58.9500578	0.0003
pkd_q1	21.33438025	21.3344012	0.0001
pkd_q2	36.61220864	36.6123755	0.0005
pkd_q3	43.78254941	43.7827807	0.0005
pkd_q4	61.67639555	61.6727082	0.0060

Output DTNs: LB06123DPDUZFF.001; LB07013DMOUZFF.001; LB07013DGTUZFF.001; LB0702UZP10KFF.002.

Model Calibrations and Results: As listed in Table 6.2-6, there are a total of 16 model scenarios, covering 16 infiltration rate distributions for four (present-day, monsoon, glacial transition, and post-10k-yr) climates. The four present-day cases (10th, 30th, 50th, and 90th percentiles) out of the 16 simulations are for model calibrations, and the other twelve scenarios are forward runs for providing UZ flow fields as well as sensitivity analyses. The four present-day simulations have been calibrated against the field-observed data of perched water. In addition, the observed matrix liquid saturations and water potentials (when available) are also used to examine these modeling results. A perched water body is defined as fully liquid saturated gridblocks with zero capillary pressure for calibration. The data sources used in the calibrations are listed in Section 4.1 and in Table 6.2-1. Only in situ measurements of water potentials are used in this analysis. In this section, the results of the four present-day simulations are presented and discussed in terms of: (1) comparisons with matrix liquid saturation, water potential, and perched water data; (2) examination of simulated perched water bodies; and (3) examination of simulated percolation flux and fracture–matrix flow components.

All 12 simulations for the present-day, monsoon, and glacial transition climates are checked against observed saturation, water potential, and perched water data. Only a few of these comparisons are shown here, and boreholes UZ-14 and SD-12 are selected to show the match between observed and modeled vertical-saturation profiles and perched water locations for four present-day climate simulations with perched water occurrence. Table C-1 lists the surface elevations and coordinates of selected boreholes for conversion from depth to elevation. Matches to other borehole data are similar. Most borehole observation data used in this section and the following sections are given relative to depth. In plots of this report, elevations are used to illustrate model results and comparisons. Appendix D provides more comparisons of the saturation and potential profiles of all boreholes evaluated by the model.

Matrix saturation and water potential data are not used in the GLUE analysis in Section 6.8, because, as shown below, simulated distributions for the matrix saturation and water potential are not very sensitive to the percolation flux in the unsaturated zone. Pneumatic pressure data are not considered, either, because the water percolation process does not significantly affect pneumatic signals in the unsaturated zone when fractures are very dry.

Comparisons with Liquid Saturation, Water Potential, and Perched Water Data: Measured matrix liquid saturation, water-saturation data and perched water elevations are compared against three-dimensional model results from the twelve simulations. Matrix liquid saturation, water potential, and perched water data used for comparisons are taken from nine boreholes (NRG-7a, SD-6, SD-7, SD-9, SD-12, UZ-14, UZ#16, WT-24, and G-2). The locations of these boreholes are shown in Figure 6.1-1.

The comparisons of simulated and observed matrix liquid saturations along the vertical column representing boreholes UZ-14 and SD-12 are shown, as examples, in Figures 6.2-2 and 6.2-3, from the UZ flow models with four present-day infiltration scenarios. Plots for seven other boreholes are documented in Appendix D-1. Figure 6.2-4 shows a comparison with water potentials for SD-12. In general, the modeled results from the twelve simulations with the UZ flow conceptual model are in reasonable agreement with the measured saturation and water-potential profiles, as shown in Figures 6.2-2, 6.2-3, and 6.2-4. It should be mentioned that there are some differences between simulated and observed saturation data, as shown in Figures 6.2-2, 6.2-3, and 6.2-4, which are primarily caused by formation heterogeneity and grid coarseness. In Figures 6.2-2 and 6.2-3, saturations simulated for the lower portion of the TSw with the pd_90 scenario are lower than the rest of the lower infiltration scenarios. This is because the simulations for each infiltration scenario use different parameter sets. Nevertheless, simulation results are still within ranges of measured saturation data.

Table 6.2-8. FEPs Addressed in This Report

FEP Number and FEP Name	FEP Description	Summary of Technical Basis and Approach for FEP Inclusion
1.2.02.01.0A Fractures	Groundwater flow in the Yucca Mountain region and transport of any released radionuclides may take place along fractures. The rate of flow and the extent of transport in fractures are influenced by characteristics such as orientation, aperture, asperity, fracture length, connectivity, and the nature of any linings or infills.	Fractures are included in process models for unsaturated zone flow and transport by using models based on the dual-permeability concept, with fractures represented by a distinct continuum. The fracture continuum models spatially average flow through discrete fractures. The fracture continuum interacts with the matrix continuum, which represents matrix blocks separated by the network of fractures. Fracture porosity, fracture spacing, and fracture volume fraction measured in the field and within different stratigraphic units determine geometrical parameters of fractures that are incorporated in the model.
1.2.02.02.0A Faults	Numerous faults of various sizes have been noted in the Yucca Mountain region, and specifically in the repository area. Faults may represent an alteration of the rock permeability and continuity of the rock mass, an alteration or short-circuiting of the flow paths and flow distributions close to the repository, and (or) unexpected pathways through the repository.	Stratigraphic displacement, dip-slip, strike-slip, and detachments due to faulting within the model domain are explicitly discretized in the site-scale unsaturated zone flow and transport models. Specific hydrogeologic properties are assigned to the fault zones, supported by measurements within fault zones or across faults. The net effect on flow is reflected in the unsaturated zone flow fields that include flow through faults.
1.3.01.00.0A Climate change	Climate change may affect the long-term performance of the repository. This includes the effects of long-term change in global climate (e.g., glacial–interglacial cycles) and shorter-term change in regional and local climate. Climate is typically characterized by temporal variations in precipitation and temperature.	Climate change is addressed in TSPA based on the record of climate changes in the past, which are used to predict the expected changes in climate for the future. Climate modeling is incorporated into TSPA through the unsaturated zone flow fields that use different surface water flux boundary condition maps corresponding to three different climates during the first 10,000 years. This is incorporated in TSPA through the unsaturated zone flow model output, which uses the results of the infiltration model to assign the water flux boundary conditions at the model's upper boundary. For the post-10,000-year period, the surface water flux boundary condition for the unsaturated zone flow model is assigned using the percolation flux distribution given in the proposed rule (70 Fed. Reg. 173).
1.3.07.02.0B Water table rise affects unsaturated zone	Climate change could produce increased infiltration, leading to a rise in the regional water table, possibly affecting radionuclide release from the repository by altering flow and transport pathways in the unsaturated zone. A regionally higher water table and change in unsaturated zone flow patterns might flood the repository.	The potential for water table rise caused by climate change is included in TSPA calculations using a water table rise model based on climate data, which allows the water table to change elevation instantaneously upon change in climate.
1.4.01.01.0A Climate modification increases recharge	Climate modification causes an increase in recharge in the Yucca Mountain region. Increased recharge might lead to increased flux through the repository, perched water, or water table rise.	The effects of climate changes on unsaturated zone flux through the repository are incorporated through explicit simulations of unsaturated zone flow fields corresponding to the four uncertainty cases for water flux at the upper boundary of the unsaturated zone flow model and three distinct climate states: present-day, monsoon, and glacial transition as well as the post-10,000-year period.

6.3 TEMPERATURE CALIBRATION

The percolation and moisture distributions under present-day conditions are used as initial conditions for performing thermal-hydrological studies of the unsaturated zone system, as well as repository performance studies under thermal loading conditions. The ambient geothermal and moisture conditions serve as the initial and boundary conditions of a thermal model (Wu et al. 2006 [DIRS 180274]). This section describes a three-dimensional ambient geothermal submodel of the UZ model developed to evaluate steady-state, ambient thermal, and moisture conditions of the unsaturated zone system with different infiltration rates for use in various scale TH modeling studies. Subsequent temperature calibration then provides an independent examination of percolation fluxes simulated by the UZ flow model. As discussed in Section 6.3.4, percolation flux (or infiltration rate) is one of the factors that control the ambient temperature distribution within the unsaturated zone (Bodvarsson et al. 2003 [DIRS 162477]). By matching borehole temperature measurements, the ambient TH model helps to constrain infiltration-rate ranges as well as fracture–matrix parameter values. Note that except for this section, the rest of the three-dimensional model development and calibration in this report deal with isothermal conditions. The three-dimensional calibrated isothermal unsaturated zone flow properties developed in Section 6.2 are used in the three-dimensional thermal model.

6.3.1 Three-Dimensional Thermal Model Grid

For thermal calibration as well as the gas flow calibration described in the next section, a three-dimensional grid (Figure 6.3-1), smaller than the TSPA-LA grid (Figure 6.1-1), is used (DTN: LB0303THERMESH.001 [DIRS 165168]). This grid is designed to reduce the computational burden needed in thermal modeling studies using a three-dimensional dual-permeability grid. The thermal model domain is selected to focus on geothermal conditions and thermal loading effects at and near the repository area. The model domain is considered to provide sufficient accuracy for such studies, because of the small thermal impact expected in the lateral directions from repository thermal loading.

This three-dimensional grid, featuring a smaller model domain than that of the UZ flow model (Figure 6.1-1), is referred to as the three-dimensional thermal model grid. As shown in the plan view of Figure 6.3-1, the thermal-model-grid domain covers approximately 20 km^2 of the area. Similar to the TSPA-LA grid of Figure 6.1-1, the thermal model grid (Figure 6.3-1) also uses a refined mesh in the vicinity of the repository and includes the locations of several boreholes used in temperature calibrations and analyses. In particular, the thermal model grid explicitly incorporates every repository drift by taking into account orientations, lengths, elevations, and spacings of the drifts. A grid spacing of 81 m is used in the direction perpendicular to drifts, such that each individual drift segment can be inserted into the three-dimensional thermal grid for thermal loading studies, such as in a previous report (BSC 2005 [DIRS 174101]; Wu et al. 2006 [DIRS 180274]). In the model, faults are also represented by vertical or inclined 30 m wide zones.

(DTNs: GS031208312232.008 [DIRS 178750], GS951108312232.008 [DIRS 106756], and GS950208312232.003 [DIRS 105572]), with several years of continuous temperature monitoring data. The surface temperatures, T_s, at any elevation, Z, are then computed using the routine toptemp_v0.f V1.0 (LBNL 2000 [DIRS 147030]), and are treated as constants according to the following equation (Wu et al. 1999 [DIRS 117161], Equation 4):

$$T_s = T_{ref} - \lambda[Z - Z_{ref}] \quad \text{(Eq. 6.3-1)}$$

where T_{ref} is mean surface temperature at reference elevation Z_{ref} and λ is the dry adiabatic atmospheric lapse rate in °C/m. A lapse rate of is 0.01°C/m was adopted from Driscoll (1986 [DIRS 116801], p. 50). In this formulation, the surface reference temperature used is 18.23°C at an elevation of 1,231.0 m, averaged using measured data from borehole NRG-6. The averaged temperature measurement of NRG-7a at an elevation of 1,282.2 m is 17.78°C. The calculated mean lapse rate, based on these field measurements, is 0.009°C/m, which is consistent with the value presented by Driscoll (1986 [DIRS 116801], p. 50). Because the lapse rate estimated in this report is based on a limited number of borehole temperature data, Driscoll's value, that may be more reliable, is adopted for the calculations.

Uncertainty in the predicted temperatures is mainly a result of uncertainty in the bottom boundary conditions and the thermal conductivity. The standard deviation for temperature at the ground surface is small (approximately ± 0.1°C). The temperature measurements at about 20 m below the ground surface are stable over time. Using the top boundary conditions from previous calculations should be adequate for the current ambient thermal simulation.

6.3.3 Bottom Boundary Temperature

The bottom temperature boundary condition was first estimated using the software routine of get_temp_v0.f V1.0 (2000 [DIRS 147027]) at a flat surface of an elevation of 730 m. Because the water table is no longer flat with the current UZ and TH models, the actual estimates of the water table or bottom-model-boundary temperatures were interpolated between the values at 730 m elevation and the model surface boundary. Nonqualified measured temperature profiles (Sass et al. 1988 [DIRS 100644]; DTN: GS950408318523.001 [DIRS 107244]) are qualified in Appendix I and used to confirm water table boundary temperature contours in DTN: LB0303THERMSIM.001 [DIRS 165167]. The initially estimated water table temperatures show a good match to the measurements through comparison with the qualified temperature data in boreholes NRG-6, NRG-7a, SD-12 UZ#4, UZ#5, and UZ-7A (DTNs: GS950208312232.003 [DIRS 105572], GS031208312232.005 [DIRS 179284], GS031208312232.004 [DIRS 182187], GS031208312232.007 [DIRS 178751], GS031208312232.006 [DIRS 182186], and GS031208312232.003 [DIRS 171287]).

Uncertainty in temperatures for defining the bottom temperature boundary conditions is relatively small. This is because a multiple-year temperature data set (qualified in Appendix I with Output DTN: LB0708WTTEMDAT) was used to derive the temperature distributions at the water table, the model bottom temperature boundary. The long-term variation of the measured temperatures is minor, with standard deviation < 0.1°C in 32 out of the 34 boreholes. Somewhat larger deviation over certain measurement periods was found in a couple of boreholes, with borehole NRG-7a having a maximum deviation of 0.24°C/yr, and borehole

NRG-6 of 0.58°C/yr (Appendix I, Table I-1). In addition, the data set also provides comparable temperature values when compared to the 6 qualified boreholes in the ambient thermal model. Specifically, their temperature differences obtained from borehole-location-wise proximity, are within 0.82°C, or less than 3.6% (Appendix I, Table I-3). Using the bottom temperature boundary conditions from these data is adequate for the current ambient thermal simulation.

6.3.4 Calibration of Ambient Temperatures

The temperature profiles or geothermal gradients in the unsaturated zone system are controlled by several factors, such as formation thermal conductivity and net infiltration rates, in addition to the regional weather conditions or surface temperatures. Measured thermal conductivities are relatively accurate for the different geological units at the site. Because of the fewer uncertainties involved in measured thermal conductivities related to simulated heat flow, temperature calibration may be conducted using either ambient infiltration, or model boundary temperatures, or both (Wu et al. 2006 [DIRS 180274]).

In this report, four ambient net infiltration rates for the present-day climate of 10th, 30th, 50th, and 90th percentile infiltration maps are used. The mean infiltration rates within the grid domain (Figure 6.3-1) are 2.88, 7.79, 11.65, and 27.42 mm/yr, respectively, for the four infiltration maps (output DTN: LB0701UZMTHCAL.001), which are averaged over a smaller model domain than the UZ flow model domain (Figure 6.1-1), resulting in a smaller mean infiltration value.

The ambient temperature condition was calibrated using the three-dimensional thermal model grid of Figure 6.3-1 (DTN: LB0303THERMESH.001 [DIRS 165168]), a dual-permeability mesh. The simulations were performed using TOUGH2 V1.6 (LBNL 2003 [DIRS 161491]) with the EOS3 module. In addition to the prescribed temperature conditions on the top and bottom boundaries, the infiltration was described using one of the four infiltration scenarios for present-day climate of 10th, 30th, 50th, and 90th percentile infiltration maps. The model incorporated the parameter set of Tables B-1, B-2, B-3, and B-4 (Output DTNs: LB07043DCRXPRP.001, LB0701UZMTHCAL.001), and the thermal properties (DTN: LB0210THRMLPRP.001 [DIRS 160799]). Incorporated thermal properties include effects of lithophysal cavities for TSw layers tsw33 and tsw 35. Simulations were run to steady state for comparison with measured borehole temperatures, because as shown below, the unsaturated zone is in thermal equilibrium with the present-day climatic conditions.

To evaluate the present conditions with respect to longer-term temporal variability in climate, first consider that the last significant change in climate occurred about 10,000 years ago. The 10th-percentile case from the infiltration model for present-day climate has an average flux rate of about 3 mm/yr over the UZ flow model domain. An average effective thermal diffusivity of about 4×10^{-7} m^2/s for the unsaturated zone at Yucca Mountain can be computed from the data given by Bodvarsson et al. (2003 [DIRS 162477], Table 2 and Equation 8b). For an average water content of the rock of about 0.15, this gives an advective distance of a thermal front of about 200 m and a diffusive distance of about 500 m over 10,000 years (based on the diffusion front length scale that is the square root of twice the diffusivity times the time). Furthermore, lateral thermal diffusion between flowing fractures separated by distances less than 100 m would require less than 500 years to approach thermal equilibrium. Therefore, the unsaturated zone is in

steady-state thermal equilibrium with present-day climate conditions. This conclusion is not

model (i.e., calibrated ambient temperature distribution) can be used to specify initial conditions for other mountain-scale TH simulations.

Wu et al. (1999 [DIRS 117161], Figure 12) identified that data sources were from 25 boreholes documented mainly in the report (Sass et al. (1988 [DIRS 100644]) and observed that, in general, the measured data matched reasonably with early three-dimensional model results (Bodvarsson et al. 1997 [DIRS 100103]; Ahlers et al. 1995 [DIRS 101180]). The majority of the early temperature data in *Temperature, Thermal Conductivity, and Heat Flow Near Yucca Mountain, Nevada: Some Tectonic and Hydrologic Implications* (Sass et al. 1988 [DIRS 100644]) are currently not qualified. In this report, six qualified data sets of temperature distributions along boreholes are shown to be consistent with the water table distribution developed from the more extensive data set, demonstrating the consistency of water temperature distribution with unsaturated processes. The same extensive data set is also the basis for saturated zone interpretation of Fridrich et al. (1994 [DIRS 100575], pp. 133 to 168). Fridrich et al. (1994 [DIRS 100575], p. 157) discussed the heat flow anomalies, upward and downward flows, and the uncertainty of ignoring unsaturated zone processes. Constantz et al. (2003 [DIRS 177344], pp. 20 to 22) used temperature profiles to estimate percolation rates for two boreholes (WT-2 and H-3) at the Yucca Mountain site through one-dimensional numerical models. They provided a detailed discussion on the relation between temperature gradient and fluid and heat flow processes at the site. They also investigated the effects of uncertainties in ground-surface temperatures and thermal conductivity on estimates of percolation rate. The infiltration rates for the location of boreholes WT-24 and H-3 of the 10th percentile present-day infiltration map are 2.36 and 6.25 mm/yr, respectively. The case 3 of Constantz et al. (2003 [DIRS 177344], p. 22), which determined parameters jointly at both boreholes and are closest to the three-dimensional model representation, estimated the range of percolation flux from 3.4 to 7.3 mm/yr for WT-24 and 5.5 to 13.3 mm/yr for H-3. The estimates in the current ambient thermal model are in the ranges computed by their approach. The uncertainties from temperature measurement have relatively less impact on the modeling results. The surface measurements are difficult to assess because of the variation in surface temperatures with time. However, temperatures become stable over time about 20-m below the surface, which constrains the surface temperatures. Based on the near-surface temperatures, the standard deviation in surface temperature is estimated to be about 0.1°C. Water table temperatures are not as well constrained by the temperature data used for calibration of surface water flux because temperature measurements were not recorded near the water table in these boreholes. Based on other borehole temperature measurements in the region, the standard deviation in water temperature is estimated to be about 1°C. Borehole temperature measurements are uncertain by as much as 0.5°C (Sass et al. 1988, p. 85 and Figure 2-15), although the data suggest that such large uncertainties did not occur for the boreholes used for calibration. Temperature measurements at different times found variations less than 0.1°C at depths below 20 m. The uncertainty in thermal conductivity is generally less than 15% (BSC 2004 [DIRS 169854], Table 6-7; BSC 2004 [DIRS 170033], Table 6-13).

The effects of thermal conductivity may be estimated from the analytical solution using a homogeneous thermal diffusivity of 4×10^{-7} m^2/s and considering 15% variations. This calculation uses a depth of 600 m and percolation flux rates of 10 mm/yr and 30 mm/yr. The temperature sensitivity is greatest at 300 m because of the fixed boundary temperatures at the surface and the water table. Using a water table temperature of 31°C and a surface temperature of 17°C, the temperature variations at 300 m depth caused by 15% variations in thermal diffusivity

system than one-dimensional or two-dimensional calibrations. This information is particularly useful for modeling studies of thermal loading, gas flow and transport of gaseous phase radionuclides for the site (Ahlers et al. 1999 [DIRS 109715]; Wu et al. 2006 [DIRS 180289]). The current model only investigates the 10% and 30% infiltration scenarios. The 50% and 90% infiltration scenarios are considered to be less realistic present-day infiltration maps than the 10% and 30%, based on geochemical and other evidences found at Yucca Mountain. Therefore, the parameters obtained from the calibration based on those 50% and 90% infiltration data would be of little significance in terms of reflecting the real parameters of the rocks at the site.

6.4.1 Calibration Approaches

The three-dimensional UZ models were manually calibrated against pneumatic pressure measurements at two representative boreholes, UZ-7a and SD-12. Among them, UZ-7a represents the boreholes located within major fault zones, whereas SD-12 represents the boreholes that are significantly distant from any major faults. Table 6.4-1 lists the sensors and their associated information of both boreholes.

Table 6.4-1. Observation Sensors and Associated Information of Boreholes UZ-7a and SD-12, used in the Pneumatic Calibration

Sensor Elevation (m)	Hosting Rock	File for Observation data	Date Range	Corresponding Observation Grid Cells
Borehole UZ-7a[1]				
1243.0	tcw12	Uz7a1343.prn	12/1/95 to 1/29/96	ANd70
1232.3	tcw13	Uz7a1337.prn	12/1/95 to 1/29/96	ANd76
1221.6	ptn24	Uz7a1331.prn	12/1/95 to 1/29/96	ANd84
1213.4	ptn26	Uz7a1325.prn	12/1/95 to 1/29/96	ANd86
1177.8	tsw32	Uz7a1319.prn	12/1/95 to 1/29/96	ANd92
Borehole USW SD-12[2]				
1258.5	tcw12	Sd12_214_PT1679.txt	12/1/95 to 1/29/96	ANA18
1232.0	ptn26	Sd12_301_PT1667.txt	12/1/95 to 1/29/96	ANA28
1217.1	tsw32	Sd12_350_PT1661.txt	12/1/95 to 1/29/96	ANA32
1001.3	tsw35	Sd12_1058_PT1619.txt	12/1/95 to 1/29/96	ANA50

Sources: DTNs: [1]LB0612MTSCHPFT.001 [DIRS 180296], [2]LB0612MTSCHP50.001 [DIRS 180294].

NOTE: The first 30 days of the data set were used for calibration, whereas the second 30 days of the data set were used for validation (see Section 7.4).

The parameter sets obtained from the one-dimensional/two-dimensional calibration (DTN: LB0612MTSCHPFT.001 [DIRS 180296]) were the basis (or starting point) of the three-dimensional calibration, which takes the following steps:

1. Calculate the three-dimensional steady state flow field of the UZ for the given infiltration scenario using EOS3 module of TOUGH2 V1.6 (2003 [DIRS 161491]).

2. Create the time-dependent gas-pressure boundary conditions at every top boundary cell (land surface cells) by scaling, using the routine TBgas3D V2.0 (2002 [DIRS 160107]), the observed atmospheric barometric pressure data (DTN: LB0302AMRU0035.001 [DIRS 162378]) with the steady-state gas pressures obtained in Step 1.

3. Simulate one-year, three-dimensional gas flow of the unsaturated zone (ignoring liquid flow) with response to the boundary conditions created in Step 2 and save the simulated pneumatic responses in the observation grid cells;

4. Visually compare the simulated pneumatic pressures with the observed data of the first 30 days (12/01/1996 to 12/30/1996) and determine if an acceptable match between the simulated and the observed data has been obtained;

5. If an acceptable match has not been obtained, modify the fracture permeability of the responsible layers and go to Step 1 to start another iteration of calibration. Otherwise, finish the calibration.

In addition, the numerical mesh and other conditions used in the three-dimensional modeling are described below:

The three-dimensional mesh used in this gas flow simulation is the same three-dimensional thermal grid mesh (Figure 6.3-1) used for the thermal simulation. (The mesh is described in Section 6.3 above). The grid domain covers approximately 20 km^2 of the area, which is smaller than the TSPA-LA grid (Figure 6.1-1). Similar to the TSPA-LA grid, this grid also uses a finer mesh in the vicinity of the repository area.

The bottom water table boundary is treated as a Dirichlet-type boundary. The gas pressure conditions at the bottom boundary are determined based on measured pressures for boreholes USW SD-7 and SD-12 (DTNs: LB991091233129.001 [DIRS 125868]; LB0303GASFLW3D.001 [DIRS 180351]). All lateral boundaries are treated as no-flow boundaries.

In the time-dependent gas-flow simulation (Step 3), the liquid phase flow was neglected to save simulation time without losing much gas-flow accuracy. The impact of liquid-phase flow on the gas flow system is small for gas-flow simulation results, mainly because of the very dry conditions found in the unsaturated zone. It was found that the single-phase (gas) and two-phase (water and gas) flow simulations produce almost identical results in calculated gas pressures. The gas-flow-only condition in the simulation is realized by forcing the relative-permeability of liquid phase to equal 0 (using the linear relative permeability function and choosing appropriate parameters).

6.4.2 Calibration of the UZ Model for the Scenario of the 10-Percentile Infiltration Map

This calibration starts with the one-dimensional/two-dimensional (fault zone) calibrated mountain-scale fracture permeability set, the matrix permeability, matrix van Genuchten alpha, fracture van Genuchten alpha, and active fracture model gamma (DTN: LB0612MTSCHPFT.001 [DIRS 180296]) corresponding to the 10-percentile infiltration map (DTN: SN0609T0502206.028 [DIRS 178753]). Following the steps described in Section 6.4.1, the fracture permeability of some geological layers needs to be adjusted (Table 6.4-2) to match the observed pneumatic data in borehole SD-12. The smaller fracture permeability in TSw units obtained in the three-dimensional calibration, compared with the one-dimensional/two-dimensional (fault zone) calibration results, reflects the significant lateral gas flow through the intensively fractured TSw units from the major faults to the

observation sensors in borehole SD-12. Such three-dimensional gas flow features cannot be captured by any one-dimensional model. As a result, the one-dimensional calibration has to raise the fracture permeability in the TSw unit artificially to compensate for the effects of missing the lateral gas flow in the model. On the other hand, the pneumatic responses to the surface-barometer pressure fluctuations in the fault zone are mainly (if not solely) controlled by the fast vertical gas flow within the zone, and the fracture permeability of normal rocks (outside of fault zones) has little effect on them. These features have already been captured by the parameters obtained from the two-dimensional (fault zone) calibration. Therefore, the match for borehole UZ-7a, which is located within the fault zone, is always good, as expected. Figures 6.4-1 and 6.4-2 show the calibrated model responses against the observed pneumatic pressure responses at several depths in boreholes UZ-7a and SD-12, respectively. Overall, the calibrated model reproduced the pattern variations observed in the pneumatic responses very well.

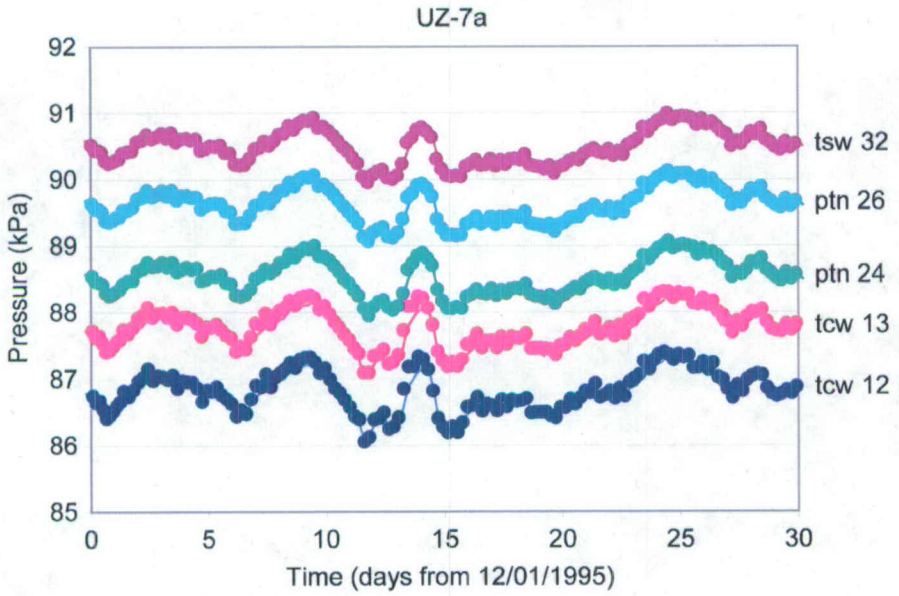

Output DTN: LB07043DGASCAL.001.

NOTE: The hydrogeologic units shown on the figure (e.g., tcw12) are determined from a comparison of the borehole location and measurement depth with the spatial data for the hydrogeolgic units available from the UZ model grid. Both observations and simulations have been vertically offset for clear display. Note the observed data from DTN: LB0612MTSCHPFT.001 [DIRS 180296].

Figure 6.4-1. Comparison of Simulated (solid line) and Observed (solid dots) Gas Pressures at Borehole UZ-7a during the First 30-Day Period

Table 6.4-2. Changes In Fracture Permeability Because of Three-dimensional Calibration (10% Scenario)

Rock	One-dimensional Calibrated Fracture Permeability (m^2)	Three-dimensional Calibrated Fracture Permeability (m^2)
tcw11	1.0000×10^{-12}	2.0000×10^{-12}
tsw31	8.1280×10^{-11}	4.0640×10^{-12}
tsw32	7.0790×10^{-11}	3.5395×10^{-12}
tsw33	7.7620×10^{-11}	3.8810×10^{-12}
tsw34	3.3100×10^{-11}	3.3110×10^{-12}
tsw35	9.1200×10^{-11}	9.1200×10^{-12}
tsw36	1.3490×10^{-10}	1.3490×10^{-11}
tsw37	1.3490×10^{-10}	1.3490×10^{-11}

Output DTN: LB07043DGASCAL.001.

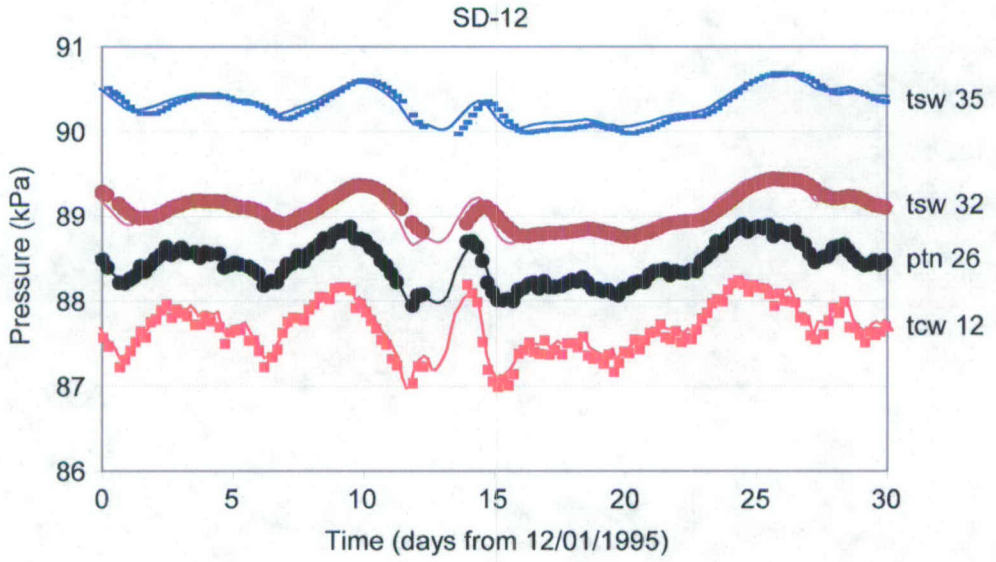

Output DTN: LB07043DGASCAL.001.

NOTE: The hydrogeologic units shown on the figure (e.g., tcw12) are determined from a comparison of the borehole location and measurement depth with the spatial data for the hydrogeolgic units available from the UZ model grid. Both observations and simulations have been vertically offset for clear display. Note the observed data from DTN: LB0612MTSCHPFT.001 [DIRS 180296].

Figure 6.4-2. Comparison of Simulated (solid line) and Observed (solid dots) Gas Pressures at Borehole SD-12 during the First 30-Day Period

6.4.3 Calibration of the UZ Model for 30-Percentile Infiltration Map

This calibration follows the same steps as used for the 10th-percentile case. The initial guess of the fracture permeability and other rock properties come from the one-dimensional/ two-dimensional (fault zone) calibrated mountain-scale fracture permeability set and the matrix permeability, matrix van Genuchten alpha, fracture van Genuchten alpha, and active fracture model gamma (DTN: LB0612MTSCHPFT.001 [DIRS 180296]) corresponding to the 30-percentile infiltration map (DTN: SN0609T0502206.028 [DIRS 178753]). Similar to the 10-percentile case, the match for borehole UZ-7a is always good, but the fracture permeability of some geological layers needs to be adjusted (Table 6.4-3) to match the observed pneumatic data in borehole SD-12. Similarly to the situation of the 10th-percentile infiltration case, the smaller fracture permeability in TSw units obtained in the three-dimensional calibration, compared with the one-dimensional / two-dimensional (fault zone) calibration results, reflects the significant lateral gas flow through the intensively fractured TSw units from the major faults to the observation sensors in borehole SD-12. Such three-dimensional gas flow features cannot be captured by any one-dimensional model. As a result, the one-dimensional calibration has to raise the fracture permeability in the TSw unit artificially to compensate the effects of missing the lateral gas-flow in the model. On the other hand, the pneumatic responses to the surface-barometer-pressure fluctuations in the fault zone are mainly (if not solely) controlled by the fast vertical gas flow within the zone and are virtually unaffected by the fracture permeability of normal rock (outside fault zones). These features have already been captured by the parameters obtained from the two-dimensional (fault zone) calibration. Therefore, the match for borehole UZ-7a, located within the fault zone, is always good, as expected. Figures 6.4-3 and 6.4-4 show the calibrated model responses against the observed pneumatic pressure responses at several depths in boreholes UZ-7a and SD-12, respectively. Note that the tcw11 is no longer in the change list for this 30th-percentile case. Overall, the calibrated model reproduced the pattern variations observed in the pneumatic responses very well (Figure 6.4-3 and Figure 6.4-4).

Table 6.4-3. Modifications to Fracture Permeability Resulting from Three-Dimensional Calibration (30% scenario)

Rock	One-dimensional Calibrated Fracture Permeability (m^2)	Three-dimensional Calibrated Fracture Permeability (m^2)
tsw31	8.1280×10^{-11}	1.6256×10^{-12}
tsw32	7.0790×10^{-11}	1.4158×10^{-12}
tsw33	7.7620×10^{-11}	1.5524×10^{-12}
tsw34	3.3110×10^{-11}	3.3110×10^{-12}
tsw35	9.1200×10^{-11}	9.1200×10^{-12}
tsw36	1.3490×10^{-10}	1.3490×10^{-11}
tsw37	1.3490×10^{-10}	1.3490×10^{-11}

Output DTN: LB07043DGASCAL.001.

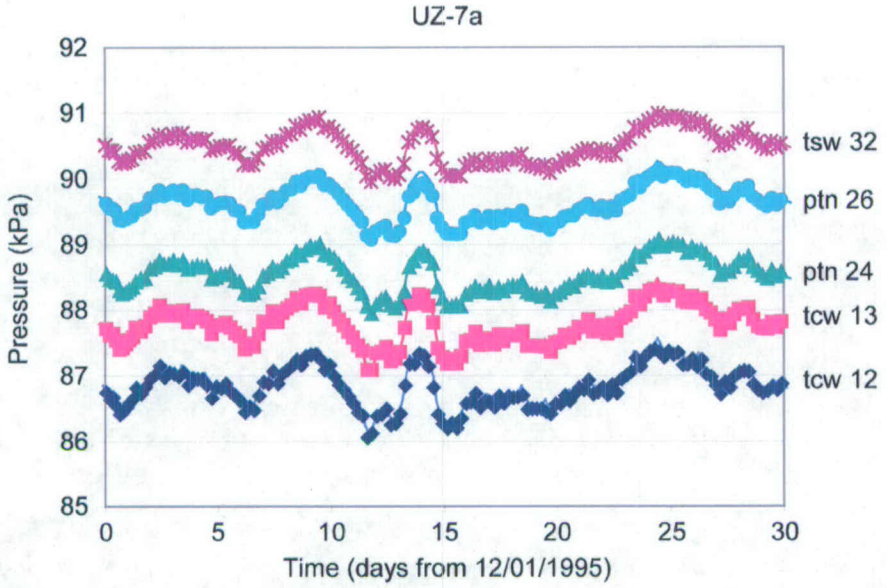

Output DTN: LB07043DGASCAL.001.

NOTE: The hydrogeologic units shown on the figure (e.g., tcw12) are determined from a comparison of the borehole location and measurement depth with the spatial data for the hydrogeolgic units available from the UZ model grid. Both observations and simulations have been vertically offset for clear display. The observed data is from DTN: LB0612MTSCHPFT.001 [DIRS 180296].

Figure 6.4-3. Comparison of Simulated (solid line) and Observed (solid dots) Gas Pressures at Borehole UZ-7a during the First 30-day Period

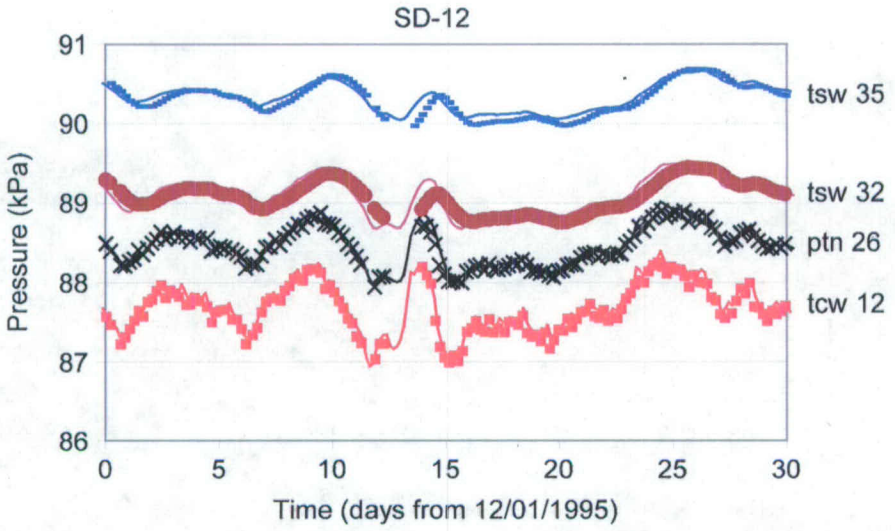

Output DTN: LB07043DGASCAL.001.

NOTE: The hydrogeologic units shown on the figure (e.g., tcw12) are determined from a comparison of the borehole location and measurement depth with the spatial data for the hydrogeolgic units available from the UZ model grid. Both observations and simulations have been vertically offset for clear display. The observed data is from DTN: LB0612MTSCHPFT.001 [DIRS 180296].

Figure 6.4-4. Comparison of Simulated (solid line) and Observed (solid dots) Gas Pressures at Borehole SD-12 during the First 30-day Period

6.5 ANALYSIS AND MODELING OF PORE-WATER CHLORIDE DATA

This study consists of modeling and analyzing geochemical data in the Yucca Mountain unsaturated zone. It utilizes geochemical models to evaluate the hydrological systems, through assessing spatial distribution of surface net infiltration and the impact of variations on its magnitude. It is part of the model calibration effort to support the conceptual model of UZ flow and to build confidence in the predictive capability of the model.

Geochemical data provide additional information by which to analyze the unsaturated zone system. Solutes can be transferred from the atmosphere to the ground surface by precipitation and dry deposition. The chemistry of rain water undergoes drastic changes as it comes in to contact with the earth surface. The distribution of chemical constituents within both liquid and solid phases of the unsaturated zone system depends on such factors as hydrological and geochemical processes of surface precipitation and evapotranspiration, the fracture–matrix interaction of flow and transport, large-scale mixing via lateral transport, and the history of climate changes and recharge. The premise for using chloride for the calibration is that chloride is a conservative species. Evaporation of water leaves chloride behind, and chloride does not interact with other minerals. Chloride in samples from Yucca Mountain has four main sources: (1) salts or fluids present in fractures; (2) salts or fluids present in intergranular pores; (3) isolated fluid inclusions within mineral grains; and (4) chemically bound chloride in hydrous minerals such as biotite and hornblende (Lu et al. 2003 [DIRS 168915]). Chloride from the above sources (3) and (4) is not believed to contribute to the pore-water chloride, because in those cases it is trapped within the mineral grain.

Chloride distribution in the unsaturated zone groundwater provides important information for UZ model calibration and validation. Pore-water chloride concentration data are used in this section to calibrate the UZ model and to bound the infiltration flux, flow pathways, and transport time. These concentration data are analyzed and modeled by three-dimensional chemical transport simulations, using a dual-permeability modeling approach. (UZ flow models of this chloride transport use the three-dimensional model property set in Appendix B). Percolation flux strongly depends on infiltration rates and their spatial distribution. The present-day infiltration rate, estimated across the study area, ranges from 3.03 to 26.78 mm/yr, averaged over the UZ model domain (output DTN: LB0706UZWATSAT.001; Table 6.1-2). The climate over the past 100,000 years has been used to estimate the possible range in infiltration rates over the next 10,000 years (Sonnenthal and Bodvarsson 1999 [DIRS 117127]).

The use of present-day flow field and steady-state simulations discounts the possibility of there being a residual impact resulting from higher infiltration rates during the Pleistocene Epoch. Precipitation last reached a maximum around 21 ka. Higher levels of precipitation (compared to the modern climate) lasted for at least another 10,000 years, and at 10,000 years before present may have been 50% higher than the modern precipitation rate (Tyler et al. 1996 DIRS [108774]). In transient simulations of postglacial change in infiltration and chloride fluxes, Sonnenthal and Bodvarsson (1999 [DIRS 117127], Sections 5.7 and 5.8) show that surface concentrations reached their modern values after 10,000 years of modern infiltration and chloride fluxes. Depths that have been reached by the present-day chloride-rich waters vary considerably. Under ridge tops and side slopes, modern waters reached the water table, whereas under regions of very low infiltration, the front of the chloride-rich plume has barely reached the PTn, leaving much of the underlying TSw unaffected. The residual impact of past climates with higher infiltration rates than present-day climate is a concern for the chloride model, because chloride mass from the previous 10,000 years and earlier remains to be washed out of the unsaturated zone. Consequently, the waters in the current unsaturated zone system are a mixture of two end members—very old water and recent infiltrated water. Given a linear mixing, current chloride concentration of pore water represents an intermediate value between the concentrations of the two end-members. Since a higher infiltration rate in the distant past corresponds to an end member with low pore-water concentration, the other end member must represent a pore-water concentration higher than current measurement values. In other words, current field-measured chloride concentration has been affected by old water residing in the unsaturated zone, leading to a lower concentration than the case would have without the residual old water. As a result, the infiltration rate calibrated using field-measured chloride data results in wetter climate—corresponding to a conservative, higher infiltration rate for the present-day climate.

6.5.1 Available Data

6.5.1.1 Pore-Water Chemical Concentration Data

Chloride transport processes were modeled as part of this model analysis. The chloride concentrations used in the modeling were measured from pore waters extracted from field samples, collected from a total of twelve surface-based boreholes, the ESF, and the ECRB. (The boreholes were SD-6, SD-7, SD-9, SD-12, NRG-6, NGR-7a, UZ-14, UZ#16, UZ-7a, WT-24, G-2, and UZ-N55. Data sources for each borehole are listed in Table 6.5-1.)

Table 6.5-1. Chloride Data Sources

Boreholes/Facilities	DTN
SD-6	GS981008312272.004 [DIRS 153677] A LA0002JF12213U.001 [DIRS 154760] B
SD-7	GS000608312271.001 [DIRS 153407] C GS970908312271.003 [DIRS 111467] D GS961108312271.002 [DIRS 121708] F GS981008312272.004 [DIRS 153677] A LA0002JF12213U.001 [DIRS 154760] B LAJF831222AQ98.011 [DIRS 145402] H
SD-9	GS970908312271.003 [DIRS 111467] D GS961108312271.002 [DIRS 121708] F LA0002JF12213U.001 [DIRS 154760] B LAJF831222AQ98.011 [DIRS 145402] H HGS020408312272.003 [DIRS 160899] O
SD-12	GS000608312271.001 [DIRS 153407] C GS970908312271.003 [DIRS 111467] D GS961108312271.002 [DIRS 121708] F GS981008312272.004 [DIRS 153677] A LA0002JF12213U.001 [DIRS 154760] B
NRG-6	GS010708312272.002 [DIRS 156375] I LA0002JF12213U.001 [DIRS 154760] B LAJF831222AQ98.011 [DIRS 145402] H
NRG-7a	GS961108312271.002 [DIRS 121708] F GS981008312272.004 [DIRS 153677] A GS010708312272.002 [DIRS 156375] I LA0002JF12213U.001 [DIRS 154760] B LAJF831222AQ98.011 [DIRS 145402] H GS020408312272.003 [DIRS 160899] O
UZ-14	GS010708312272.002 [DIRS 156375] I GS961108312271.002 [DIRS 121708] F GS990208312272.001 [DIRS 146134] J LA0002JF12213U.001 [DIRS 154760] B LAJF831222AQ98.011 [DIRS 145402] H
UZ#16	GS010708312272.002 [DIRS 156375] I GS990208312272.001 [DIRS 146134] J LA0002JF12213U.001 [DIRS 154760] B LAJF831222AQ98.011 [DIRS 145402] H
UZ-N55	LA0002JF12213U.001 [DIRS 154760] B GS010708312272.002 [DIRS 156375] I
UZ-7a	GS981008312272.004 [DIRS 153677] A LA0002JF12213U.001 [DIRS 154760] B
WT-24	GS981008312272.004 [DIRS 153677] A LA0002JF12213U.001 [DIRS 154760] B LAJF831222AQ98.011 [DIRS 145402] H
G-2	LAJF831222AQ98.011 [DIRS 145402] H
ECRB	LA9909JF831222.004 [DIRS 145598] K LA0002JF12213U.002 [DIRS 156281] L GS020408312272.003 [DIRS 160899] O

Table 6.5-1. Chloride Data Sources (Continued)

Boreholes/Facilities	DTN
ESF	GS961108312261.006 [DIRS 107293] M LA0002JF12213U.002 [DIRS 156281] L LA9909JF831222.010 [DIRS 122733] N

NOTE: Letters following the DIRS numbers are not a part of the DTN number. Each letter corresponds to the appearance of the same DTN.

6.5.1.2 Chloride Flux

Sources contributing to the chloride flux in recharge waters are precipitation, run-on, and runoff. The portion of these waters that form net infiltration is small. Infiltration rates for present-day climate scenarios are estimated to be in the range of 3.03 to 26.78 mm/yr, based on the average infiltration rates for the 10th and 90th percentile infiltration maps (Table 6.1-2). The present-day mean infiltration rate estimated from the chloride data is approximately 5 mm/yr, and the glacial maximum infiltration rate at 21,000 years ago was about 28 mm/yr (Sonnenthal and Bodvarsson 1999 [DIRS 117127], p. 148, Figure 23).

Four case studies corresponding to four present-day climate scenarios were chosen. They represent the 10th, 30th, 50th, and 90th percentile infiltration maps. Their mean fluxes are listed in Table 6.5-2, calculated from four infiltration maps (DTN: SN0609T0502206.028 [DIRS 178753]). Also listed in the table are the notations for these infiltration scenarios, which are consistent with the notations used in the flow models (Section 6.2). The chloride transport model uses the same flow model as the notation indicates. Chloride recharge fluxes to these transport models are calculated accordingly for these climate scenarios.

Chloride recharge sources into the saturated zone include dissolved material in rain, particulates in snow, and a contribution from windblown dust (Tyler et al. 1996 [DIRS 108774]). Also, precipitate on land surfaces would experience physical processes such as evaporation, which leaves behind Cl^- in the remaining water. The chloride mass flux to the chloride transport model depends on the amount of water flux and its chloride concentration. In the model, fluxes are considered to be precipitation, runon, and runoff. Thus, the water fluxes contributing to chloride recharge can be calculated using the following equation:

$$F = F_{prec} + F_{runon} - F_{runoff} \qquad \text{(Eq. 6.5-1)}$$

where F is the net flux contributing to the chloride in the recharging water (defined as net recharge in Table 6.5-2, independent of the net infiltration of Table 6.1-2), F_{prec} is the precipitation flux, F_{runon} is the runon flux, and F_{runoff} is the runoff flux. For input to the TOUGH2 calculation the net recharge flux in mm/yr is converted to equivalent mass flux (kg/s). Calculating each term for F is carried out using the routine infil2grid V1.7 (2002 [DIRS 154793]) and the precipitation, runoff and runon data for the present-day climate (DTN: SN0609T0502206.028 [DIRS 178753]). Chloride flux is then calculated using the following formula:

$$F_{Cl} = C_{Cl,p} \times 10^{-6} (F_{prec} + F_{runon} - F_{runoff}) \qquad \text{(Eq. 6.5-2)}$$

where F_{Cl} is chloride flux (kg/s), F_{prec} is precipitation flux (kg/s), F_{runon} is run-on (kg/s), and F_{runoff} is runoff flux (kg/s). $C_{Cl,p}$ is chloride concentration in precipitation (mg/(kg water). (Note that actual calculations and procedures using this equation in preparing input files for chloride simulations are summarized in Appendix D2).

Table 6.5-2. Present-Day Chloride Recharge Fluxes and Precipitation, Runon, and Runoff Rates for Different Scenarios (Averaged over Model Domain)

Scenario Notations [a]	Scenarios	Precipitation (mm/yr)	Runon (mm/yr)	Runoff (mm/yr)	Net Recharge Used in Calculation of Chloride Flux [b] (mm/yr)
pd_10	10th Percentile Infiltration Map	163.44	277.00	279.03	161.41
pd_30	30th Percentile Infiltration Map	153.89	600.21	606.09	148.01
pd_50	50th Percentile Infiltration Map	189.68	995.78	1005.62	179.84
pd_90	90th Percentile Infiltration Map	147.05	862.39	871.02	138.43

Source: [a]Fluxes calculated as described in Appendix D, Section D2, data from Output DTN: LB0706UZWATSAT.001]

NOTE: [b]Net water flux contributing to the chloride recharge is calculated by Equation 6.5-1.

Surface chloride concentrations are discussed by Sonnenthal and Bodvarsson (1999 [DIRS 117127], pp. 113 to 114). The range of 0.55 to 0.73 mg/L was considered to bound the average value. Triay et al. (1996 [DIRS 101014]) obtained a mean chloride concentration in precipitation of 0.55 mg/L, which is probably close to the minimum value expected. A similar value was obtained by combining a mean annual precipitation of about 170 mm/yr with a present-day chloride surface flux of 106 mg/(m^2-yr) yielding a mean chloride concentration of about 0.62 mg/L (Fabryka-Martin et al. 1997 [DIRS 100144]), which includes a windblown dust component. The contribution from windblown dust may be 33% of the total chloride flux in the Great Basin of Nevada and Utah (Tyler et al. 1996 [DIRS 108774]). Even though the contribution from windblown dust is considered in the flux, as part of the measured precipitation, the upper limit of concentration can be bounded by adding 33% more chloride to the 0.55 mg/L concentration to yield a maximum of about 0.73 mg/L. The upper limit is less well defined than the lower limit, which is more easily set from the concentrations in precipitation. Clearly, variation in this 0.73 mg/L chloride concentration before evapotranspiration is much less than the over an order-of-magnitude range in estimates of infiltration rate, and therefore the surface chloride concentration is a moderately well-constrained boundary value for modeling studies (Sonnenthal and Bodvarsson (1999 [DIRS 117127], pp. 113 to 114). A value of 0.55 mg/L (Sonnenthal and Bodvarsson 1999 [DIRS 117127]; Triay et al. 1996 [DIRS 101014]) is used in the present simulations, and applied to all infiltrating water in the form of precipitation, run-on, and runoff (Sonnenthal and Bodvarsson 1999 [DIRS 117127], p. 148). The concentration of recharge water is factored into the above equation as a linear coefficient in the chloride flux

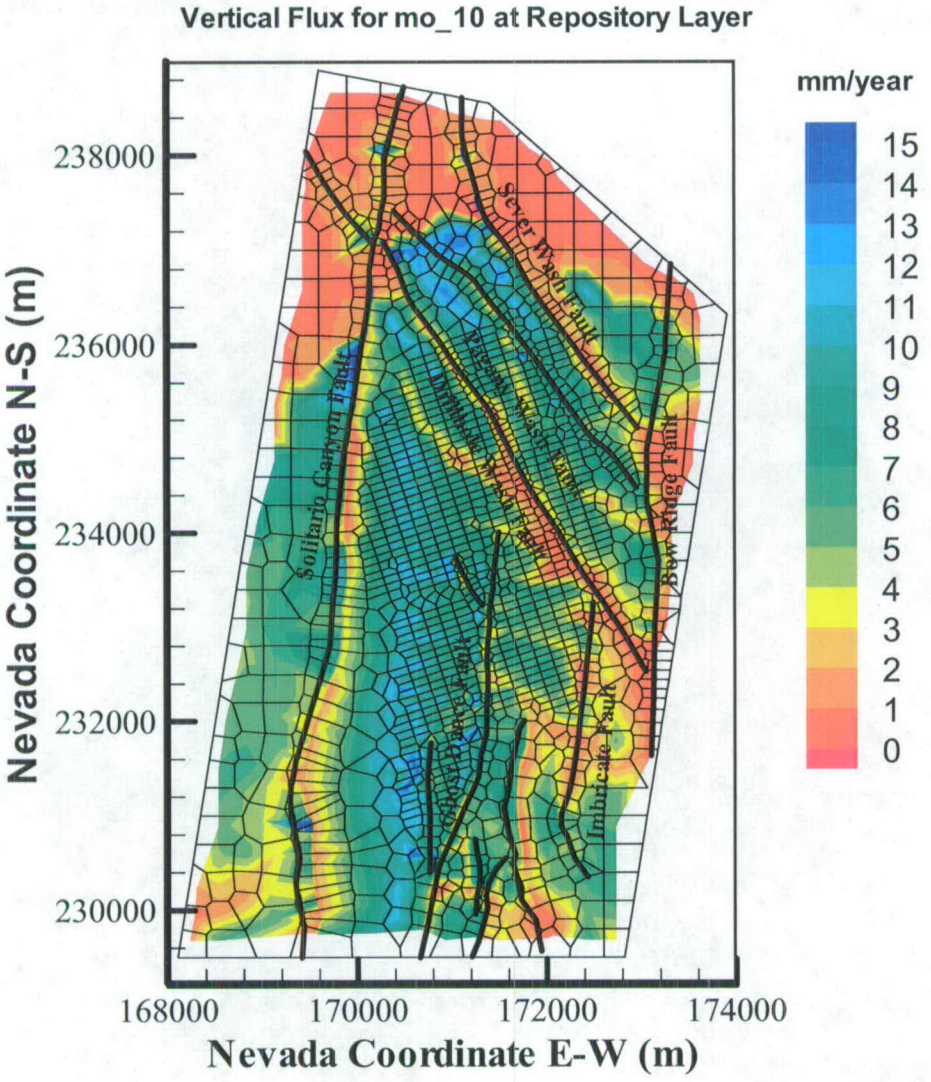

Output DTN: LB07013DMOUZFF.001.

Figure 6.6-2. Simulated Percolation Fluxes at the Repository Horizon under the Monsoon, 10th Percentile Infiltration Scenario

6.6.2.3 Matrix, Fracture, and Fault Flow Components

Tables 6.6-1, 6.6-2, and 6.6-3 list percentages of fracture-matrix flow components for non-fault zones and fault flow over the entire model domain and within the repository footprint at the three horizons of the TCw/PTn interface, the repository layer, and the water table. (In these 3 tables as well as in the rest of the documentation, the accuracy in the value of parameters is one less than the significant digits, as given, because the last significant digits are rounded.) Fracture and matrix percentages are computed for the non-fault zones only (i.e., excluding fault flow), whereas fault flow percentages represent total vertical fracture-matrix flux through fault blocks over the entire model layer or the smaller region of the repository footprint at the three horizons. The three percentages sum to 100%. (Procedures for calculating the percentages are explained in Appendix E.) These statistics are calculated from vertical flow along each grid column, using the sixteen flow fields.

Statistical data as shown in Tables 6.6-1 and 6.6-2 indicate that fracture flow is dominant at both the top of the PTn unit and the repository horizons. At the repository level, fracture flow consists of about 60% to 80% of the total percolation fluxes over the entire model layer, and is mostly higher than 90% within the repository footprint. On the other hand, fault flow increases with depth. Over the entire model layer, fault flow at the TCw/PTn interface is about 1% to ~2%, increasing to 12% to 32% at the repository horizon, and reaching 44% to 65% at the water table (Table 6.6-3). In comparison, fault flow over the smaller area, within the repository footprint, is low, at about 1%, at the TCw/PTN interface and repository horizon, but then increases to 16%–37% at the bottom boundary, the water table. Comparison of fault flow percentages at the TCw/PTn interface, the repository horizon, and the water table in Tables 6.6-1, 6.6-2, and 6.6-3 indicates that flow focusing into faults occurs mainly through the PTn unit and through the lower hydrogeological CHn unit.

Table 6.6-1. Comparison of the Water Flux through Matrix, Fractures of Non-fault Zones, and Faults as a Percentage of the Total Flux over the Entire Model Domain and within the Repository Footprint at the TCw/PTn Interface for the 16 Flow Fields

Simulation Designation	Flux at TCw/PTn Interface over Entire Model Domain (%)			Flux at TCw/PTn Interface within Repository Footprint (%)		
	Fracture	Matrix	Fault	Fracture	Matrix	Fault
pd_10	98.66	0.04	1.31	99.01	0.04	0.95
pd_30	98.33	0.05	1.62	98.76	0.04	1.20
pd_50	98.54	0.03	1.43	98.81	0.03	1.16
pd_90	98.34	0.05	1.61	98.64	0.04	1.32
mo_10	98.06	0.06	1.87	98.60	0.06	1.35
mo_30	98.13	0.07	1.80	98.61	0.06	1.33
mo_50	98.33	0.06	1.61	98.72	0.05	1.22
mo_90	98.03	0.04	1.93	98.55	0.03	1.42
gt_10	98.30	0.10	1.59	98.69	0.10	1.21
gt_30	98.11	0.11	1.78	98.59	0.10	1.32
gt_50	98.08	0.07	1.84	98.59	0.07	1.34
gt_90	97.99	0.09	1.91	98.50	0.08	1.41
pkd_q1	98.10	0.03	1.87	98.61	0.02	1.37

Table 6.6-1. Comparison of the Water Flux through Matrix, Fractures of Non–fault Zones, and Faults as a Percentage of the Total Flux over the Entire Model Domain and within the Repository Footprint at the TCw/PTn Interface for the 16 Flow Fields (Continued)

Simulation Designation	Flux at TCw/PTn Interface over Entire Model Domain (%)			Flux at TCw/PTn Interface within Repository Footprint (%)		
	Fracture	Matrix	Fault	Fracture	Matrix	Fault
pkd_q2	98.54	0.03	1.43	98.82	0.03	1.16
pkd_q3	98.38	0.03	1.59	98.68	0.02	1.30
pkd_q4	98.02	0.06	1.93	98.53	1.42	1.42

Output DTNs: LB06123DPDUZFF.001; LB07013DMOUZFF.001; LB07013DGTUZFF.001; LB0702UZP10KFF.002; LB0705FLOWCOMP.001.

PTn=Paintbrush nonwelded hydrogeologic unit; TCw=Tiva Canyon welded hydrogeologic unit.

Table 6.6-2. Comparison of the Water Flux through Matrix, Fractures of Non-fault Zones, and Faults as a Percentage of the Total Flux over the Entire Model Domain and within the Repository Footprint at the Repository Level for the 16 Flow Fields

Simulation Designation	Flux at Repository Horizon over Entire Model Domain (%)			Flux at Repository Horizon within Repository Footprint (%)		
	Fracture	Matrix	Fault	Fracture	Matrix	Fault
pd_10	58.42	9.71	31.87	94.20	5.16	0.65
pd_30	67.14	7.90	24.95	95.96	2.73	1.31
pd_50	64.74	7.51	27.75	96.68	2.03	1.28
pd_90	74.04	6.69	19.27	97.76	1.24	1.00
mo_10	71.64	13.26	15.10	91.14	8.00	0.86
mo_30	73.34	9.35	17.31	94.54	4.04	1.42
mo_50	68.18	8.13	23.70	95.11	3.55	1.34
mo_90	79.63	6.33	14.04	97.89	1.03	1.08
gt_10	64.63	17.49	17.88	86.90	12.31	0.79
gt_30	71.33	10.27	18.40	93.50	5.05	1.45
gt_50	71.29	9.12	19.59	94.14	4.43	1.42
gt_90	78.97	7.43	13.60	96.95	2.06	0.99
Pkd_q1	79.14	9.02	11.84	95.79	3.32	0.89
Pkd_q2	65.34	7.24	27.42	96.88	1.84	1.29
pkd_q3	72.36	6.93	20.71	97.09	1.49	1.42
pkd_q4	79.40	6.71	13.89	97.58	1.37	1.05

Output DTNs: LB06123DPDUZFF.001; LB07013DMOUZFF.001; LB07013DGTUZFF.001; LB0702UZP10KFF.002; LB0705FLOWCOMP.001.

Table 6.6-3. Comparison of the Water Flux through Matrix, Fractures of Non-fault Zones, and Faults as a Percentage of the Total Flux over the Entire Model Domain and within the Repository Footprint at the Water Table for the 16 Flow Fields

Simulation Designation	Flux at Water Table over Entire Model Domain (%)			Flux at Water Table within Repository Footprint (%)		
	Fracture	Matrix	Fault	Fracture	Matrix	Fault
pd_10	20.24	14.40	65.36	54.21	23.53	22.26
pd_30	25.56	12.78	61.66	50.58	16.50	32.92
pd_50	22.35	12.72	64.92	47.26	15.70	37.04
pd_90	28.72	7.09	64.19	57.97	5.95	36.08
mo_10	29.13	21.71	49.16	52.90	26.63	20.47
mo_30	31.25	14.83	53.91	51.38	15.93	32.69
mo_50	25.99	15.39	58.62	48.80	17.10	34.10
mo_90	29.17	8.17	62.66	58.42	5.94	35.64
gt_10	30.35	25.98	43.68	51.55	32.52	15.93
gt_30	34.57	15.44	49.99	52.30	16.85	30.85
gt_50	28.42	17.01	54.56	49.21	17.60	33.19
gt_90	31.31	10.58	58.11	57.61	7.71	34.68
pkd_q1	26.18	18.84	54.98	56.95	19.96	23.09
pkd_q2	22.84	11.93	65.23	50.42	16.87	32.70
pkd_q3	23.50	14.01	62.50	47.89	15.10	37.01
pkd_q4	29.88	8.95	61.17	58.55	6.26	35.18

Output DTNs: LB06123DPDUZFF.001; LB07013DMOUZFF.001; LB07013DGTUZFF.001; LB0702UZP10KFF.002; LB0705FLOWCOMP.001.

6.6.2.4 Distributions of Percolation Fluxes within the Repository Footprint

Percolation fluxes at the repository horizon and within the repository footprint can be further analyzed using a frequency distribution plot. This plot displays the averaged percentage of the repository area subject to a particular percolation rate. Note that the normalized flux rates are determined by normalizing an infiltration value with respect to the averaged infiltration rate for the scenario. For example, "1" stands for the normalized flux rate corresponds to 3.03, 6.74, 11.03, and 16.89 mm/yr (Tables 6.1-2 and 6.1-3), respectively, for the four 10th percentile infiltration scenarios. The information, as shown in Figures 6.6-9, 6.6-10, 6.6-11, and 6.6-12 (see Appendix E for calculation details), is important to drift-scale modeling studies of flow and transport at drifts and flow-redistributing phenomena through the TSw. Figures 6.6-9 to 6.6-12 show the frequency distribution of normalized percolation flux within the repository horizon for the four 10th percentile infiltration rates of the four climates.

Figures 6.6-9 to 6.6-12 indicate that the highest flux frequencies, occurring at 14% to 24%, have normalized fluxes of about 1.2 to 1.5, except for the case of the glacial transition 10th percentile infiltration (gt_10), which has the highest frequency flux at the lowest range of normalized fluxes. In general, the areas with normalized percolation fluxes greater than 3 are very small, taking up less than 1% of the total repository area.

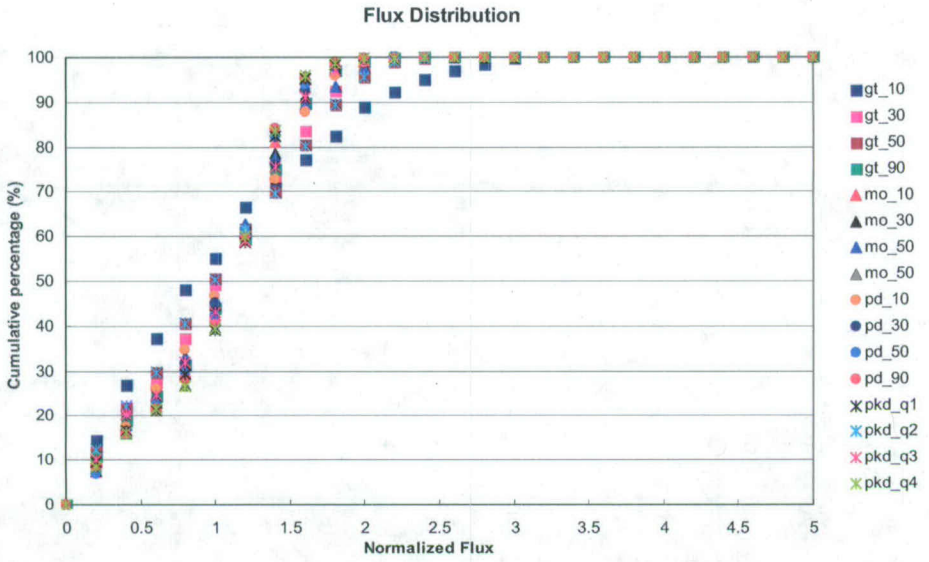

Output DTNs: LB06123DPDUZFF.001; LB07013DMOUZFF.001; LB07013DGTUZFF.001; LB0702UZP10KFF.002.

Figure 6.6-13. Cumulative Flux Distribution and Range as Functions of Normalized Percolation Flux within the Repository from the 16 Flow Fields of Four Climates

6.7 TRACER TRANSPORT TIMES

This section summarizes simulated tracer transport using the 16 UZ flow fields. The results present an evaluation of tracer or radionuclide transport processes from the repository to the water table (saturated zone) within the mountain, including the effects of different infiltration scenarios, advection, diffusion, and adsorption. Tracer-transport studies described in this section provide insight into UZ flow patterns, groundwater travel times, and tracer transport processes.

6.7.1 Methodology and Transport Parameters

Simulation results and analyses in this section are based on transport studies of conservative and reactive tracers, using the T2R3D V1.4 code (1999 [DIRS 146654]). The dual-permeability modeling approach with the three-dimensional TSPA-LA grid (Figure 6.1-1), as discussed in Section 6.1.1, is used in the transport simulations. In the tracer transport modeling, the 16 steady-state, three-dimensional flow fields of Section 6.6 are directly used as input to the T2R3D code for modeling transport from the repository to the water table.

To assess tracer transport times from the repository to the water table, tracers are treated as conservative (nonadsorbing) and reactive (adsorbing) components transported through the unsaturated zone. In both cases, hydrodynamic/mechanical dispersion through the fracture–matrix system is ignored, because sensitivity studies indicate that mechanical dispersion has an insignificant effect on the cumulative breakthrough curves of tracers at the water table (Wu et al. 2002 [DIRS 160195]). A constant molecular diffusion coefficient of 3.2×10^{-11} m^2/s is used for matrix diffusion of the conservative component, and 1.6×10^{-10} m^2/s is used for the

reactive component. Note that the non-reactive component is used to represent a radionuclide, which typically has a small diffusion coefficient due to heavy molecular weight and large size. The range of matrix diffusion coefficients is close to the values of typical diffusion coefficients for ions, anions and cations. For example, the diffusion coefficients of ions typically range from 3.0×10^{-10} to 20.0×10^{-10} m^2/s (Langmuir 1997 [DIRS 100051], p. 65), which summarizes that those of anions ($4.14 \times 10^{-10} - 52.7 \times 10^{-10}$ m^2/s) and cations ($1.53 \times 10^{-10} - 93.1 \times 10^{-10}$ m^2/s) (Lerman 1979 [DIRS 182304], Section 3.2, Table 3.1).

The two diffusion coefficients are multiplied by porosity and tortuosity in the simulation to account for various units. In the case of a reactive or adsorbing tracer, several K_d values are used, as given in Table 6.7-1, for different units. These values were selected to approximate those for neptunium (^{237}Np) transport (DTNs: LA0010JC831341.001 [DIRS 162476]; LA0010JC831341.002 [DIRS 153321]; LA0010JC831341.003 [DIRS 153322]; LA0010JC831341.004 [DIRS 153323]; LA0010JC831341.005 [DIRS 153320]; LA0010JC831341.006 [DIRS 153318]; LA0010JC831341.007 [DIRS 153319]). For a conservative tracer, K_d is set to zero. These molecular diffusion coefficients and K_d values are selected to represent technetium and neptunium. Model parameters such as porosity and rock grain density were taken from the matrix and thermal properties (DTNs: LB0207REVUZPRP.002 [DIRS 159672]; LB0210THRMLPRP.001 [DIRS 160799]).

Transport simulations were conducted for 1,000,000 years using 16 infiltration rates of four climates. At the start of each simulation, an initial, constant concentration source was instantaneously released from the fracture continuum gridblocks representing the repository.

Table 6.7-1. K_d Values Used for Reactive Tracer Transport in Different Hydrogeologic Units

Hydrogeologic Unit	K_d (cc/g)
Zeolitic matrix in CHn	4.0
Vitric matrix in CHn	1.0
Matrix in TSw	1.0
Fault matrix in CHn	1.0
Fractures and the matrix in the rest of units	0.0

Sources: DTNs:
LA0010JC831341.001 [DIRS 162476], LA0010JC831341.002 [DIRS 153321], LA0010JC831341.003 [DIRS 153322], LA0010JC831341.004 [DIRS 153323], LA0010JC831341.005 [DIRS 153320], LA0010JC831341.006 [DIRS 153318], and LA0010JC831341.007 [DIRS 153319].
CHn = Calico Hills nonwelded hydrogeologic unit; TSw = Topopah Spring welded hydrogeologic unit.

6.7.2 Simulation Scenarios

For each flow simulation, as listed in Table 6.2-6, there are two transport runs, one for conservative (tc_*) and one for reactive (np_*) tracer transport. Table 6.7-2 summarize a total of 16 × 2 tracer-fracture-release simulation scenarios, corresponding to the 16 UZ flow fields for the 16 infiltration maps of four climates, respectively.

transport times with different infiltration rates and types of tracers considered in the 32 simulations (listed in Table 6.7-2).

As indicated by Figures 6.7-1 and 6.7-2, the predominant factors in controlling tracer transport are (1) surface-infiltration rates or net water recharge and (2) adsorption effects (i.e., whether the tracer is conservative or reactive). Statistics of tracer transport times for 10% and 50% mass breakthrough at the water table for the 32 simulation scenarios are given in Table 6.7-3. Figure 6.7-3 correlates average infiltration rates and tracer transport times at 50% mass breakthrough for the 32 simulation scenarios. Figures 6.7-1, 6.7-2, 6.7-3, and the statistical data of Table 6.7-3 show the following:

- Tracer transport times vary inversely to the average surface infiltration (net water recharge) rate over the model domain (Figure 6.7-3). When the average infiltration rate increases from 3 to 70 mm/yr, average tracer transport (50% breakthrough) times decrease by more than two orders of magnitude for both adsorbing and nonadsorbing species.

- Nonadsorbing tracers migrate (from the repository to the water table) one to two orders of magnitude faster than an adsorbing tracer under the same infiltration condition (Figure 6.7-3).

6.8.3 Temperature and Chloride Data

In the Yucca Mountain unsaturated zone, the temperature profiles or geothermal gradients of the unsaturated zone system are controlled by several factors, such as formation thermal conductivity and net infiltration rates, in addition to the regional weather conditions or surface temperatures. Because of the small impact of uncertainties in measured thermal conductivities on simulated heat flow, the temperature profile can be used to constrain infiltration maps and determine weighting factors. There are total of five boreholes containing qualified temperature data: NRG-6, NRG-7a, SD-12, UZ#5, and UZ-7a. The borehole locations can be found in Figure 6.1-1. Simulated temperature distributions at these five boreholes were generated from the four infiltration maps, as described in Section 6.3 (Output DTN: LB0701UZMTHCAL.001). Near the ground surface in five of the boreholes, observed temperatures show significant seasonal variations. However, these seasonal changes in surface temperature have little impact on steady-state heat flow or temperature profiles in the deeper (more than 20 m) unsaturated zone . In this study, only measurements 40 m below ground surface were considered, resulting in a total of 50 temperature data points for comparison.

In addition to limited temperature measurements, natural chemical tracers can also be used to examine infiltration history. Chloride is considered a nearly ideal natural tracer for the study of water movement in the liquid phase in geological systems. Its measurements are available at two horizontal tunnels, the ECRB and ESF, and twelve vertical boreholes: G-2, NRG-6, NGR-7a, SD-12, SD-6, SD-7, SD-9, UZ-14, UZ-16, UZ-7a, UZ-N55, and WT-24. Again, a map showing the tunnel and borehole locations can be found in Figure 6.1-1. These measurements are compared with the chloride concentration outputs from the UZ chloride submodel. The simulations using the four infiltration maps are shown in Section 6.5, along with the simulated results (chloride concentrations) (Output DTN: LB0701UZMCLCAL.001). Because of the large spatial variations in chloride concentration, the comparison between the simulated and measured concentrations is done in log space. For simplicity, in this section, "the residual of chloride data" refers to the difference between the logarithm of the measured chloride concentration and the logarithm of the simulated chloride concentration.

For both data sets, because the numerical gridblock centers do not necessarily coincide with measurement points, linear interpolation is used to obtain the simulated temperatures at measurement locations.

6.8.4 UZ Flow Weighting Factors Definition/Description

The UZ flow scenarios correspond to selected present-day 10th, 30th, 50th, and 90th percentile infiltration scenarios generated by the infiltration model (DTN: SN0609T0502206.028 [DIRS 178753]). The UZ flow weighting factors (Output DTN: LB0701PAWFINFM.001, *factors.doc*) describe the probability of occurrence for each of the four infiltration scenarios, and therefore, the sum of the four weighting factors is one. The same weighting factors are expected to be used in all four climate states (present-day, monsoon, glacial transition, and post-10,000 years). The justification is given in Section 6.8.8.

2. Beven and Binley (1992 [DIRS 179079], Equation 5) provided a likelihood measure as follows:

$$L_i = \{\sum_{j=1}^{N_i} \frac{W_j}{(y_{ij} - O_j)^2}\}^N \quad \text{(Eq. 6.8-3)}$$

where W_j is the weight for observation j such that $\sum W_j = 1$. The same weight is used for all groups of observations. N is a parameter (called shape factor) chosen by the user. If $N=0$, all the infiltration maps will have the same weight, and if $N \to \infty$, the single best simulation will have a rescaled likelihood value of 1, and all others 0. In this study, likelihood values are calculated using $N=1$ and $N=0.5$, based on the following considerations: (1) $N = 1$ has been frequently used in the literature as reviewed by Beven et al. (2000 [DIRS 179825], Table 1), and (2) the use of $N = 0.5$ allows for evaluating the sensitivity of the likelihood-function value to changes in N within a certain range. Note that if $N=0$, all the infiltration maps will have the same weight. Similarly if $N \to \infty$, the best simulation will single out a rescaled likelihood value of 1, and all others 0. (As shown below, a smaller N value will result in a larger weighting factor value for an infiltration map with a higher average infiltration rate, which is conservative.)

3. The third category of likelihood measures is (Beven and Binley 1992 [DIRS 179079], Eq. 6):

$$L_i = 1/(\prod_{j=1}^{K_i} (y_{ij} - O_j)^2) \quad \text{(Eq. 6.8-4)}$$

This is a pseudo-maximum likelihood function, which is similar to maximum likelihood because in its formulation more observation data (either data points or data types) will accentuate the better simulations, leading to greater reduction of uncertainty. This function can be an alternative when measurement errors are not available.

4. The fourth category uses fuzzy measures as likelihood measures. Although there are different ways of choosing fuzzy membership functions (Beven 2006 [DIRS 179081]), Equation 6.8-5 expresses the most commonly used triangular membership function as (Franks and Beven 1997 [DIRS 179084], Eq. 8):

$$f_{ij} = 1 - \frac{|y_{ij} - O_j|}{\varepsilon} \quad \text{(Eq. 6.8-5)}$$

where ε is called acceptable error. In this case, a maximum absolute residual (the term "residual" refers to the difference between the observed (O) and simulated values (y)) from all observation locations out of the four infiltration maps is taken as ε. Then, membership values at different observation points are combined using an arithmetic mean (Zak et al. 1997 [DIRS 179088]).

For the above measures, the final likelihood values are normalized as shown in Equation 6.8-6, so that the sum of the likelihood values for the four infiltration maps is one:

$$L_{i\_normalized} = L_i \Big/ \sum_{i=1}^{4} L_i \qquad \text{(Eq. 6.8-6)}$$

Two types of data reflecting infiltration history are available: thermal data (temperature) and chloride concentration. The likelihood functions based on each type are calculated separately, and combined by multiplying the normalized likelihood value together, as shown in Equation 6.8-7:

$$L_i = L_i^t \bullet L_i^c \qquad \text{(Eq. 6.8-7)}$$

where L_i^c is the likelihood value calculated using chloride data, and L_i^t is the likelihood value calculated using temperature data. This treatment for different types of data ensures that the two kinds of data can be considered one at a time without affecting the final results (as shown below).

Measured chloride data are available for both boreholes (vertical) and tunnels (horizontal). The map indicating the locations of these boreholes and tunnels can be found in Figure 6.1-1. Note that the amount of information (i.e., infiltration history) contained in a certain number of observations from a tunnel is greater than the same number of observations from a borehole, due to greater horizontal area covered in a tunnel. To consider the effect, chloride data is placed into three groups, with two groups representing the two horizontal tunnels and one group representing all the area covered by boreholes. The average absolute residual (or residual squares) from each borehole is used (in the borehole group) to represent the contribution from the given borehole. Then, the further average of squared average-residuals (or average of residual squares) for all the individual boreholes within the borehole group is used for the likelihood value calculation. This treatment is to ensure that the likelihood calculation is not biased to boreholes with more data points, considering that each borehole represents roughly the same amount of horizontal area intercepting infiltration and should be treated equally in evaluating the infiltration maps. For the other two groups, the average of squared average-residual (or average of residual squares) is directly used for likelihood-value calculations. For likelihood measure Category 1, the average of residual squares is used. For likelihood-measure Categories 2 and 3, both the average of absolute residuals and average of residual squares are used to evaluate effects of different averaging schemes. For likelihood-measure Category 4, the average of fuzzy membership is used. To be consistent with the treatment of chloride data, the averaged residuals (or average of residual squares) for the individual borehole data are also used for temperature likelihood calculations.

As shown in Equation 6.8-7, the calculation of likelihood functions based on each type is calculated separately, and then combined by multiplying the normalized likelihood value together. An alternative way to consider the two types of data is to consider one at a time, for example:

1. Update the weights using likelihood values calculated by chloride data (L_i^c), then the posterior weights P_i^1 (after considering chloride data) is (Makowski et al. 2002 [DIRS 179044]):

$$P_i^1 = \frac{W_i L_i^c}{\sum W_i L_i^c} \quad \text{(Eq. 6.8-8)}$$

Table 6.8-1. Calculated Weighting Factors Using Both Chloride Data and Temperature Data

Summary of Final Weights From All The Methods				
Infiltration map	**10%**	**30%**	**50%**	**90%**
S1	100%	0%	0%	0%
s2_a1_N=1	59%	21%	17%	3%
s2_a1_N=0.5	40%	24%	26%	11%
s2_a2_N=1	47%	24%	25%	4%
s2_a2_N=0.5	34%	24%	30%	12%
s3_a1	97%	3%	0%	0%
s3_a2	94%	6%	1%	0%
s4_sum	26%	24%	32%	18%
Average weighting factors	62%	16%	16%	6%

Output DTN: LB0701PAWFINFM.001, *factors.doc*.

Not only are the likelihood values, L_i^t and L_i^c, measures of matches between simulated results and observed data in the unsaturated zone, but also the prior weightings W_i (given in 6.8.5.1 Step 1) determine P_i. As shown in Table 6.8-1, the weighting factors are sensitive to the choice of likelihood measures, and the final weighting factors passed to TSPA for the four selected infiltration maps are determined as the arithmetic mean of the weightings P_i using the previously discussed methods (Equation 6.8-1).

Figure 6.8-2 shows the final likelihood of each infiltration map. Four bars represent the four infiltration maps. The weights for each map using an individual likelihood value correspond to the y-axis value for that individual likelihood function times its prior weights. The mean infiltration rate for the 10th, 30th, 50th and 90th percentile infiltration map can be found in Table 6.1-2. Note that the weighting factors are subject to uncertainty because of the uncertainties in defining likelihood functions. The downstream users of the weighting factors should consider both the mean values and the uncertainties of these factors (Table 6.8-1). Specifically, TSPA calculations need to consider both the mean values for the weighting factors and the results of individual likelihood functions.

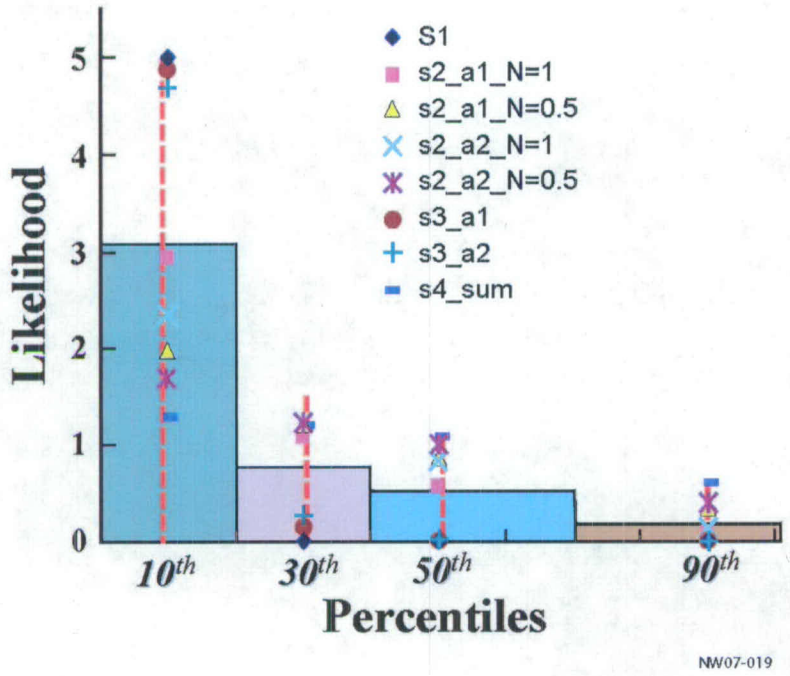

Output DTN: LB0701PAWFINFM.001.

NOTE: Shaded areas represent weighting factors and individual points represent likelihood values resulting from different calculation schemes.

Figure 6.8-2. Posterior Weighting Factors for Infiltration Map

6.8.6 Sensitivity Analysis for UZ Flow Weighting Factors

A number of sensitivity studies are performed to ensure that the results of likelihood value calculation are reasonable and robust.

6.8.6.1 Effects of Measurement Error for Temperature Data

The measurement errors (characterized by standard deviations) are used for evaluating the likelihood function given in Equation 6.8-2. For temperature measurement, the standard deviations representing measurement errors are on the order of 10^{-4}°C to ~ 10^{-3}°C (DTNs: GS031208312232.005 [DIRS 179284]; GS950208312232.003 [DIRS 105572]). A sensitivity analysis was performed for likelihood function 1 using a uniform standard deviation (0.1°C) for measurement errors to evaluate the effects of these deviations within a certain range for all the temperature observations. The resultant weighting factor values for the likelihood function are 1, 0, 0, and 0 for the 10th, 30th, 50th, and 90th percentile maps, respectively (Output DTN: LB0704UZWFINFM.001, file: *Cal_t1_sensitivity.xls*). That these are the same as those listed in Table 6.8-1 indicates that the variation of measurement errors within a reasonable range does not change the calculation results based on the first likelihood function.

7. VALIDATION

Validation activities for the UZ flow model and submodels were planned in *Technical Work Plan for: Unsaturated Zone Flow, Drift Seepage and Unsaturated Zone Transport Modeling, REV 04* (BSC 2006 [DIRS 177465], Section 2.2.1.1). The model validation approach for the UZ site-scale flow model is presented in *Technical Work Plan for Technical Work Plan for: Unsaturated Zone Flow, Drift Seepage and Unsaturated Zone Transport Modeling* (BSC 2006 [DIRS 177465], Section 2.2.1.1), which states that the UZ site-scale flow model requires Level I validation. The validation plan was developed under the BSC procedures in effect at the time. The BSC Level I validation is equivalent to Level I validation as described in SCI-PRO-002. The Level I validation includes the six steps of confidence building during model development as described in SCI-PRO-002 and at least one postdevelopment activities as described in SCI-PRO-006, Section 6.3.2. This model validation section deviates from the TWP (BSC 2006 [DIRS 177465], Section 2.2.1.1.2), in that temperature and chloride data are not used for validation. This is because the temperature and chloride data have been used to calibrate the flow weighting factors representing the effects of infiltration uncertainty discussed in Section 6.8. A second deviation includes the Alcove 8–Niche 3 flow and transport test data as one additional validation effort. The model validation efforts of this section include confidence building during model development and corroboration with experimental data. The additional validation activities presented in this section are corroboration with information published in refereed journals and literature, analysis of model uncertainties, and corroboration with natural analogues. The models will be accepted as valid for their purposes through confidence building during model development of Section 7.1, as well as through postdevelopment validation efforts of corroboration with experimental data in Sections 7.2 to 7.8, according to the following criteria (BSC 2006 [DIRS 177465], Section 2.2.1.1.2):

- The water-potential data measured from ECRB are used for validation by comparing with simulation results of the UZ flow model. The criterion for the validation is that simulated water-potential values are within the range of measurements along the ECRB tunnel. Demonstration that this criterion has been met is shown in Section 7.2.

- WT-24 perched water elevation data is used to validate the UZ flow model. The criterion for the validation is that simulated perched water elevation matches the observed value within 10 m). Demonstration that this criterion has been met is shown in Section 7.3.

- The gas-flow model was calibrated against the first 30 days of pneumatic data for borehole SD-12 (Section 6.4). Pneumatic data measured in SD-12 (for the second 30 days) and UZ-7a (for the second 30 days) are used for validation of the UZ flow model. The criterion for the validation is that simulated gas pressures and their patterns of variations consistently compare closely with the observed values. That is, the simulations will consistently reproduce increases and decreases resulting from changes in barometric pressure at the ground surface. Demonstration that this criterion has been met is shown in Section 7.4.

- Carbon-14 data from gas samples provide approximate C-14 residence times for pore water. The residence times can be interpreted as tracer transport time from the ground surface to where the gas samples were collected, based on the current conceptual model for UZ flow and transport. These data are used to validate the UZ flow model. The criterion for the validation is that simulated tracer transport times (i.e., the integral breakthrough curve at the sample-collection locations for a pulse input at the ground surface or the time for first moment of concentration) are within the range of times estimated from data in the TSw unit. Demonstration that this criterion has been met is shown in Section 7.5.

- Borehole and ECRB strontium concentrations are used to check the UZ flow model results using the strontium modeling analysis. The criterion for validation is qualitative agreement between the simulated strontium concentrations and the average of the observations at the same elevation, and agreement with the vertical trends. Demonstration that this criterion has been met is shown in Section 7.6.

- The calcite model is used to validate the UZ flow model with the abundance data of calcite. The calcite model is validated by comparing one-dimensional simulation results with measurements. The criterion is that the simulated volume fraction of calcite coating for each UZ model layer falls within the range of measurements for that layer. According to the TWP (BSC 2006 [DIRS 177465], Section 1, #1), the need of model validation runs are not expected for the calcite model results, because the uncertainty is already captured in the model runs. Demonstration that this criterion has been met is shown in Section 7.7. The current calcite model has not changed from the previous *UZ Flow Models and Submodels* (BSC 2004 [DIRS 169861], Section 7.9).

- A deviation from the work plan outlined in the TWP (BSC 2006 [DIRS 177465], Section 2.2.1.1) lies in the use of the Alcove 8–Niche 3 flow and transport test data. The original plan calls for the incorporation of the data to support the development of an enhancement factor to matrix diffusion in the unsaturated zone radionuclide transport model and the UZ transport abstraction model. This plan has not been implemented, and the resulting estimate of transport times through the unsaturated zone is conservative as explained in *Radionuclide Transport Models Under Ambient Conditions* (SNL 2007 [DIRS 177396], Section 6). Therefore, the information from the Alcove 8–Niche 3 fault test is used below to support the post-development validation of the site-scale UZ flow model. The same model validation criteria as described in the previous report (BSC 2004 [DIRS 169861], Section 7) are used for this model validation exercise (i.e., the criterion for validation is that the predicted results for the time to reach a given concentration of a conservative tracer are within a factor of 5 of the observed times, or that explanations can be found for why the observed and simulated results deviate significantly). Demonstration that this criterion was met is shown in Section 7.8. This validation exercise has not changed from the previous report (BSC 2004 [DIRS 169861], Section 7.6).

For the validation activities of this section, none of the corroborative data sets selected for use in model validation case used in model calibration and development of Section 6. In addition, there were no other similar data sets available for model validation activities. Note that model validation efforts, presented in this section, are carried out mostly by using the present-day, 10th and/or 30th percentile infiltration rates. This is because the present-day 10th and 30th percentiles are considered more realistic representations of the present-day conditions (Section 6.2).

Confidence Buidling with Information Published in Refereed Journals and Literature. In addition to the model validation activities described in the TWP, journal publications are used to provide confidence for model validation. Some methods listed here, including temperature and chloride modeling, are no longer conducted for validation (corroboration), but rather are part of the calibration or model development process. Three-dimensional unsaturated zone numerical models have been developed to simulate flow and distribution of moisture, gas, and heat at Yucca Mountain (Wu et al. 1999 [DIRS 117161]; Wu et al. 2004 [DIRS 173953]). Flow and transport processes within the unsaturated zone were characterized under current and future climates (Wu et al. 2002 [DIRS 160195]). Studies of capillary barriers in the unsaturated rock of Yucca Mountain have also been published (Wu et al. 2002 [DIRS 161058]). The perched water phenomena in the Yucca Mountain unsaturated zone have been investigated (Wu et al. 1999 [DIRS 117167]). Subsurface gas pressure variations have been used to determine the pneumatic diffusivity of important geological features (Ahlers et al. 1999 [DIRS 109715]; Wu et al. 2006 [DIRS 180289]). Subsurface borehole temperature data were used to estimate percolation flux (Bodvarsson et al. 2003 [DIRS 162477]). Chloride measurements were used to calculate infiltration rates along the ESF (Fabryka-Martin et al. 1998 [DIRS 146355]). Chloride data, in conjunction with hydrostructural and hydrogeological features, were also used to constrain infiltration rates (Liu et al. 2003 [DIRS 162478]). In addition, chloride and strontium geochemistry were investigated using three-dimensional modeling for insights into the hydrology of the unsaturated zone (Sonnenthal and Bodvarsson 1999 [DIRS 117127]). In particular, these published journal papers presented examples of using hydrologic, temperature, pneumatic and geochemical isotopic data to calibrate and validate the UZ flow model.

Analysis of Model Uncertainty. As discussed in Section 6.10, there are a number of uncertainties associated with the UZ flow model, including data, model, and climate uncertainties. The existence of these uncertainties stems from uncertainties in parameter and field data measurements, estimates of present-day and future climates, hydrogeological conceptual models and modeling approaches, and scale-dependent heterogeneity, and model input parameters. These data- and model- related uncertainties have been discussed, investigated or evaluated in this report using field observation data, modeling sensitivity analyses, model calibration, natural analogue information, and other arguments in Sections 6.2 through 6.9 and this section. These uncertainties are reasonably captured by simulation results using four different parameter sets and 16 infiltration maps, as discussed in Section 6.10. The effects of parameter and data uncertainties on UZ flow model results are generally encompassed by the model results for the 16 three-dimensional flow fields. Systematic sensitivity analyses of the UZ flow model results (to model input parameters) were carried out to assess uncertainties associated with parameters and models (BSC 2005 [DIRS 174116]; Zhang et al. 2006 [DIRS 180287]). In addition, the uncertainty of flow and radionuclide transport in the Yucca Mountain unsaturated zone was investigated using a Monte Carlo method with matrix

permeability, porosity, and sorption coefficient treated as random variables (Ye et al. 2006 [DIRS 180272]).

Corroboration with Natural Analogues. In addition, the key flow and transport processes pertaining to the unsaturated zone at Yucca Mountain have been investigated through natural analogues (BSC 2004 [DIRS 169218]). These natural analogue investigations contained both literature studies and analyses. One of the important case studies was the unsaturated zone flow and tracer tests at the Idaho National Engineering and Environmental Laboratory's Radioactive Waste Management Complex (BSC 2004 [DIRS 169218], Section 9.3). The field tests at the site provided calibrations of numerical models with needed in situ measured data. A consistent set of parameters was obtained from calibrating the model using the dual-permeability approach to multiple hydrographs (water potential as a function of time) from transient ponded infiltration tests. The studies demonstrated that conceptual models and large-scale, volume-averaged numerical modeling approaches used for the UZ flow model at Yucca Mountain can be applied with confidence (BSC 2004 [DIRS 169218], Section 9.3.7). The model validation effort of this section is intended to further build confidence in the UZ flow model and submodels with regard to their ability to predict flow and transport processes in the Yucca Mountain unsaturated zone system. In particular, these model validation efforts further confirm that using uniform hydrogeologic parameter values across the lateral extent of most hydrostratigraphic units in the UZ flow model provides reasonable approximations and simulation results, because of the model's capability for matching different types of data from boreholes that are a considerable distance apart.

7.1 CONFIDENCE BUILDING DURING MODEL DEVELOPMENT

To establish the scientific basis and the accuracy of intended use, SCI-PRO-006 and SCI-PRO-002 require documentation of decisions or activities that are implemented to generate confidence in the model during model development, including the following:

(1) Evaluate and select input parameters and/or data that are adequate for the model's intended use [SCI-PRO-002, Attachment 3, Level I (1)].

The selection of input parameters and/or input data for the UZ flow model and its submodels is discussed and presented in Sections 4.1, 6.1–6.5, and Appendix B. Model calibration results in Section 6 show that these selected input parameter values or input data are reasonable for simulating flow and transport processes in the Yucca Mountain unsaturated zone.

(2) Formulate defensible assumptions and simplifications that are adequate for the model's intended use [SCI-PRO-002, Attachment 3, Level I (2)].

As discussed in Sections 5 and 6.1.2, the development of the UZ flow model and its submodels is based on assumptions and simplifications that are accepted in the scientific community, which are supported by many scientific journal publications, as discussed above.

(3) Ensure consistency with physical principles, such as conservation of mass, energy, and momentum, to an appropriate degree commensurate with the model's intended use [SCI-PRO-002 Attachment 3, Level I (3)].

host rock are listed in Table 6.4-1. The criterion for the validation is that simulated gas pressures and their pattern variations are consistent with the observed values. That is, the simulations will consistently reproduce increases and decreases resulting from changes in barometric pressure at the ground surface.

7.4.1 Validation of the UZ Model for the Scenario of the 10th-Percentile Infiltration Map

Simulated results are compared with field-measured values of the 30-day validation period for the 10th percentile infiltration scenario (Figures 7.4-1 and 7.4-2) and the 30th percentile infiltration scenario (Figures 7.4-3 and 7.4-4), respectively. Overall, good agreement between the predicted gas pressures and observed data were found in both scenarios. The good match builds confidence that the calibrated properties are appropriate for gas flow simulations in either case. Comparisons between simulated and observed gas pressures at different locations of the two boreholes, shown in the two figures, prove that simulated gas pressures and their patterns of variations are consistent with observed values. In particular, the simulations consistently reproduce increases and decreases resulting from changes in barometric pressure at the ground surface. This satisfies the validation criterion for this case.

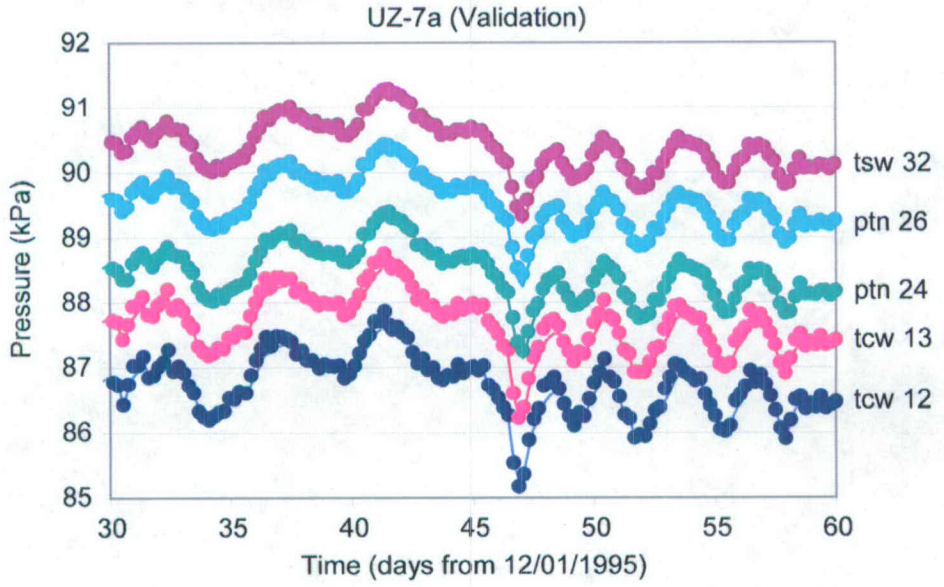

Source: DTN: LB0612MTSCHPFT.001 [DIRS 180296].

Output DTN: LB07043DGASCAL.001.

NOTE: The hydrogeologic units shown on the figure (e.g., tcw12) are determined from a comparison of the borehole location and measurement depth with the spatial data for the hydrogeolgic units available from the UZ model grid. Both observations and simulations have been vertically offset for clear display.

Figure 7.4-1. Comparison of Predicted (solid line) and Observed (solid dots) Gas Pressures at Borehole UZ-7a During the Second 30-day Period for the 10th Percentile Infiltration Scenario

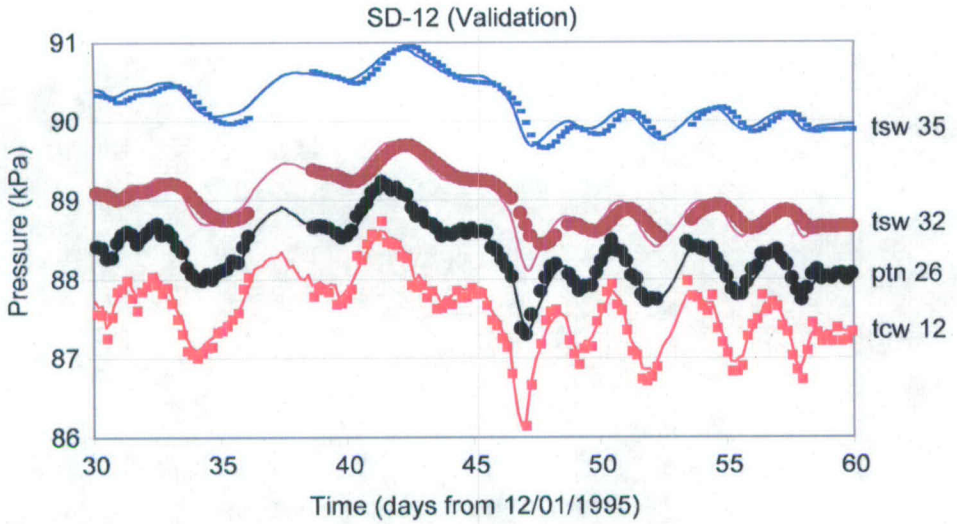

Source: DTN: LB0612MTSCHPFT.001 [DIRS 180296].

Output DTN: LB07043DGASCAL.001.

NOTE: The hydrogeologic units shown on the figure (e.g., tcw12) are determined from a comparison of the borehole location and measurement depth with the spatial data for the hydrogeolgic units available from the UZ model grid. Both observations and simulations have been vertically offset for clear display.

Figure 7.4-2. Comparison of Predicted (solid line) and Observed (solid dots) Gas Pressures at Borehole SD-12 During the Second 30-day Period for the 10th Percentile Infiltration Scenario

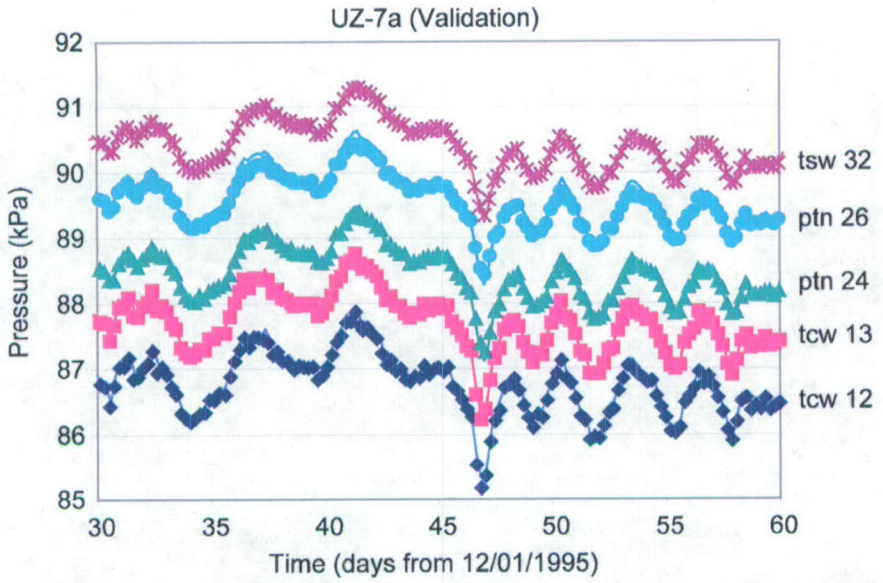

Source: DTN: LB0612MTSCHPFT.001 [DIRS 180296].

Output DTN: LB07043DGASCAL.001.

NOTE: The hydrogeologic units shown on the figure (e.g., tcw12) are determined from a comparison of the borehole location and measurement depth with the spatial data for the hydrogeolgic units available from the UZ model grid. Both observations and simulations have been vertically offset for clear display.

Figure 7.4-3. Comparison of Predicted (solid line) and Observed (solid dots or symbols) Gas Pressures at Borehole UZ-7a During the Second 30-day Period for the 30th Percentile Infiltration Scenario

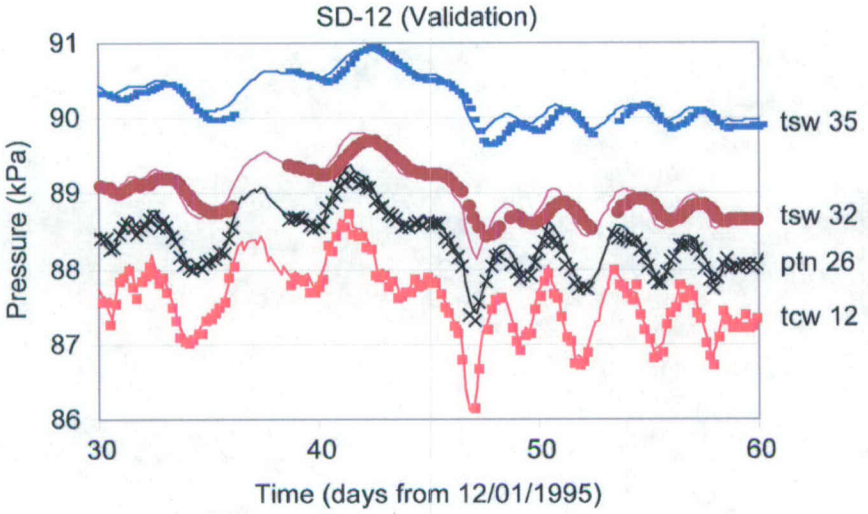

Source: DTN: LB0612MTSCHPFT.001 [DIRS 180296].

Output DTN: LB07043DGASCAL.001.

NOTE: The hydrogeologic units shown on the figure (e.g., tcw12) are determined from a comparison of the borehole location and measurement depth with the spatial data for the hydrogeolgic units available from the UZ model grid. Both observations and simulations have been vertically offset for clear display.

Figure 7.4-4. Comparison of Predicted (solid line) and Observed (solid dots or symbols) Gas Pressures at Borehole SD-12 During the Second 30-day Period for the 30th Percentile Infiltration Scenario

7.5 MODEL VALIDATION WITH ^{14}C DATA

This section describes the simulation of the solute travel times using the calibrated UZ flow models, and the comparison of the simulated travel times to the measured ^{14}C ages for borehole UZ-1 and SD-12, for validation of the UZ flow models. The criterion for the validation is that the simulated travel times for TSw units fall within the range of the measured ^{14}C ages for the TSw units.

7.5.1 Methodology

In a flow system, at a given location and time, the solute residence time (travel time) is determined within the whole system by the applicable transport processes, such as advection, diffusion and hydrodynamic dispersion. The actual residence time can be determined using a number of methods, including measuring a radioactive isotope activity and then calculating the residence time based on the decay rate. Residence time can also be simulated using a flow and conservative tracer transport model of the system (Goode 1996 [DIRS 162573]). The degree to which the model-simulated residence times fall within the range of the measured residence times can be used for validating the flow and transport model. The Yucca Mountain unsaturated zone is considered to be a quasi-steady-state flow system (Section 5). An appropriate solute residence time to use is the mean transport time required for the solute to move from the ground surface to the sample location in the subsurface system. The mean solute residence time can be considered to be constant at each location in this quasi-steady-state flow system, but spatially variable. When a tracer pulse is injected into the system through the ground surface, the tracer

to its half-life duration, which is on the same order of magnitude as the travel times in the unsaturated zone, and its detectable abundance. Gas samples were collected from different kinds of boreholes, including open and instrumented surface-based boreholes. Data from the latter boreholes (USW SD-12 and USW UZ-1) are regarded as more reliable indicators of solute travel time for the in situ matrix pore water (BSC 2004 [DIRS 169734], Section 5.2.2.5.4). Thus, the measured ^{14}C ages (BSC 2004 [DIRS 169734], Section 5.2.2.5.4) data from these two boreholes are used for validating the UZ flow model.

Gas-phase ^{14}C ages (Output DTN: LB0704C14FFVAL.001 for the conversion of ^{14}C activity into ages, and DTNs: GS961108312271.002 [DIRS 121708] for the ^{14}C activity of borehole USW SD-12, and MO0012CARB1314.000 [DIRS 153398] for the ^{14}C activity of borehole USW UZ-1) are interpreted to be representative of solute travel times for the *in-situ* matrix pore water. The rationale for this interpretation is provided by Yang (2002 [DIRS 160839], Section 4.1.2). The interpretation is based on the rapid exchange of gas-phase CO_2 (reaching equilibrium in hours to days) with dissolved CO_2 and HCO_3^- in pore water. Furthermore, the amount of carbon in an aqueous-phase reservoir is greater by orders of magnitude than carbon in the CO_2 gas-phase reservoir. Consequently, the aqueous phase will dominate the gaseous phase when exchange occurs, indicating the reasonableness of the interpretation (Yang 2002 [DIRS 160839], Section 4.1.2). The continuous calcite precipitation in the unsaturated zone removes carbon from groundwater. Although ^{14}C behaves a little differently from total carbon, the effect on the carbon isotopic fraction is minor, and the calcite precipitation is considered to have an insignificant impact on the ^{14}C activity in the groundwater and gas (Codell and Murphy 1992 [DIRS 100719]). Therefore, the measured gas-phase ^{14}C age is considered as representative data for the solute travel times of the matrix pore water of the Yucca Mountain unsaturated zone in the following model validation effort. Obviously, one necessary condition of this interpretation must be satisfied (i.e., there is no significant vertical gas flow through the borehole). This interpretation becomes limited if there is significant vertical gas flow through the borehole, because such flow would disturb the ^{14}C abundance distribution throughout the borehole. In fact, because the boreholes (USW SD-12 and USW UZ-1) were closed, disturbation from the atmosphere can be neglected (unless leakage of atmospheric CO_2 into the borehole occurs), vertical gas flow in these two boreholes is not likely significant, and the ^{14}C abundance is not significantly disturbed.

7.5.3 Model Discussion

Two three-dimensional transport simulations were performed using T2R3D V1.4 (LBNL 1999 [DIRS 146654]). The three-dimensional flow fields of two infiltration scenarios, 10th percentile and 30th percentile, from UZ flow models (Output DTN: LB06123DPDUZFF.001) were respectively used to simulate the solute travel times in the entire model domain. The numerical grid used in this transport simulation is the same as that used in the flow simulation (Figure 6.1-1). As discussed in Section 6.7, hydrodynamic dispersion was ignored because of low water percolation fluxes. Thus, the ^{14}C transport is carried out primarily by advective and diffusive processes. An effective-diffusion-coefficient value of 1.97×10^{-10} m^2/s was used, equal to the average value of measured coefficients for tritiated water through Yucca Mountain tuffs (DTN: LA000000000034.002 [DIRS 148603]).

In this model, a tracer source was introduced as a pulse on the ground surface through fractures, and the tracer concentration in rock matrix was observed in the entire domain over the whole simulation period (10^6 years). The simulated solute travel time of the matrix pore water, at a specific location, was then calculated using Equation 7.5-1 for each representative gridblock of borehole UZ-1 and SD-12. Then, the simulated solute travel times were compared to the measured ^{14}C ages. The simulated solute travel times of the matrix pore water for boreholes UZ-1 and SD-12 were plotted and compared, respectively, to the available measured ^{14}C age data in Figures 7.5-1 for UZ-1 and 7.5-2 for SD-12.

Figure 7.5-1 shows that the simulated solute travel times for the matrix porewater of borehole UZ-1 with the three-dimensional UZ model and the 10th percentile infiltration map are much larger than the measured ^{14}C ages, while the simulated ages with the 30th percentile infiltration map are closer to the measurements and fall within the range of measurements for TSw units. There are larger uncertainties in the measured data of the shallow layers (i.e. PTn units), resulting from the disturbance caused by possible leakage of the atmospheric CO_2 into the borehole. Figure 7.5-2 shows that the simulated solute travel times for the matrix pore water of borehole SD-12 with the three-dimensional UZ model and the 30th percentile infiltration map falls within the range of the measured ^{14}C ages for TSw units, while the simulated solute travel times with the 10th percentile infiltration map are larger than the measurements. These results reflect the spatial uncertainties of the infiltration maps as discussed in *Simulation of Net Infiltration for Present-Day and Potential Future Climates* (SNL 2007 [DIRS 174294], Section 6.6.1.1) and are consistent with the study results that more weight should be given to the infiltration maps with percentiles lower than 50th (Section 6.8).

Table 7.5-1. Infiltration Rates of the Representative Gridblock of Borehole UZ-1 and SD-12

	Local infiltration rates(mm/yr)		Domain-average infiltration rates (mm/yr)	
Boreholes	10%	30%	10%	30%
UZ-1	0.0	0.38	3.03	7.96
SD-12	0.8	2.17	3.03	7.96

Source: Output DTN: LB06123DPDUZFF.001, *PD_10.dat* and *PD_30.dat* (domain average infiltration rates in mm/yr and location infiltration rates in kg/s), also see Table 6.1-2.

Output DTN: LB0704C14FFVAL.001 (*infiltration.xls*, converted local infiltration rates in mm/yr).

* "Local infiltration" is the infiltration at the representative gridblock in the infiltration map. The "Domain-average infiltration" is the average infiltration rate of the whole model domain of the corresponding percentile.

As mentioned in Table 7.5-1, the infiltration map shows that the local infiltration rate of the representative gridblock for borehole UZ-1 is 0.0 mm/yr (10th percentile), compared to the domain average of 3.03 mm/yr. The fact that the calculated solute travel times of this borehole with the 10th percentile infiltration map are much larger than the measured ^{14}C ages (Figure 7.5-1) may primarily be a result of the too-low local infiltration rate (compared to the actual infiltration rate). The second possible reason of this deviation is the horizontal heterogeneity in the rock hydraulic properties (permeability and porosity), which is not considered in the model. The other possible reason is the scale-dependency of the effective matrix diffusion coefficient (BSC 2004 [DIRS 170035], Section 6.2.2), which is not considered

in the model. A larger effective matrix diffusion coefficient is expected to give a smaller travel time in the rock matrix.

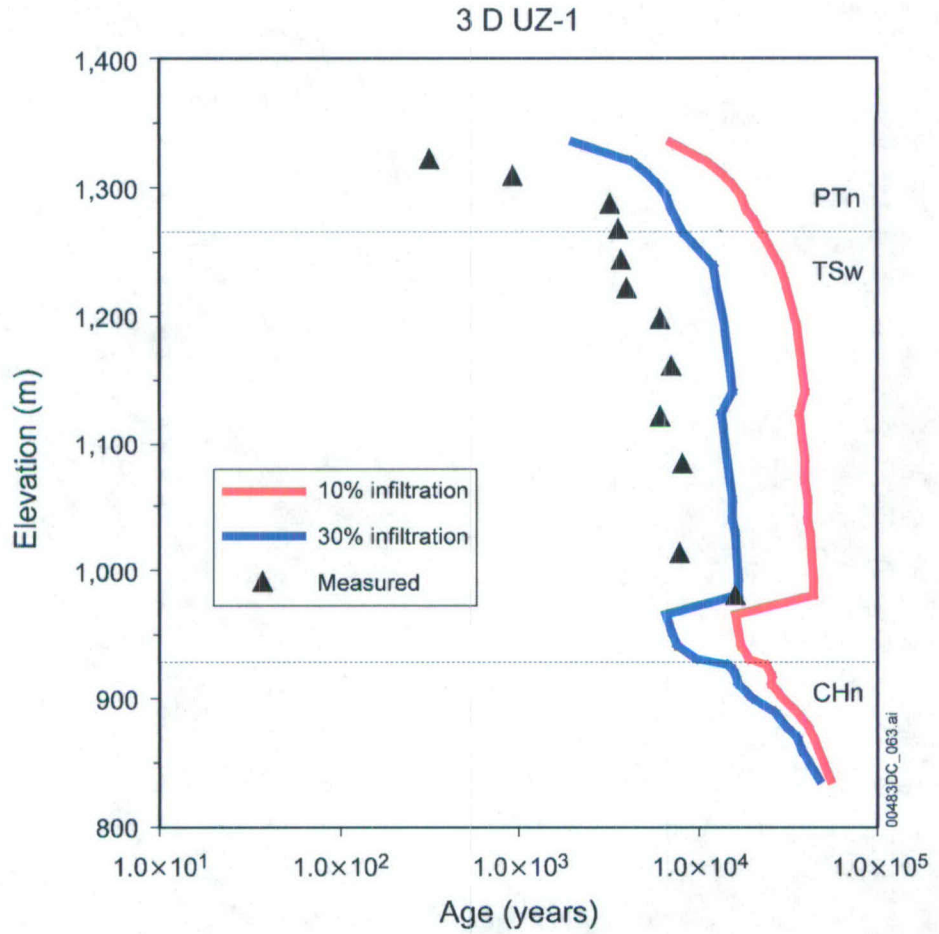

Sources: DTNs: MO0012CARB1314.000 [DIRS 153398] (Measured ^{14}C activities); MO0012MWDGFM02.002 [DIRS 153777] (borehole collar elevation and lithological layer interface elevation); LB06123DPDUZFF.001 (flow fields of 10% and 30% infiltration rate).

Output DTN: LB0704C14FFVAL.001, LB0707C14FFVAL.001, *Ages.xls* (simulated matrix porewater age, and measured ^{14}C ages converted from the measured ^{14}C activities).

Figure 7.5-1. Simulated Solute Travel Time of the Matrix Pore Water with Three-dimensional Simulation for Borehole UZ-1 Compared to the Measured ^{14}C Age

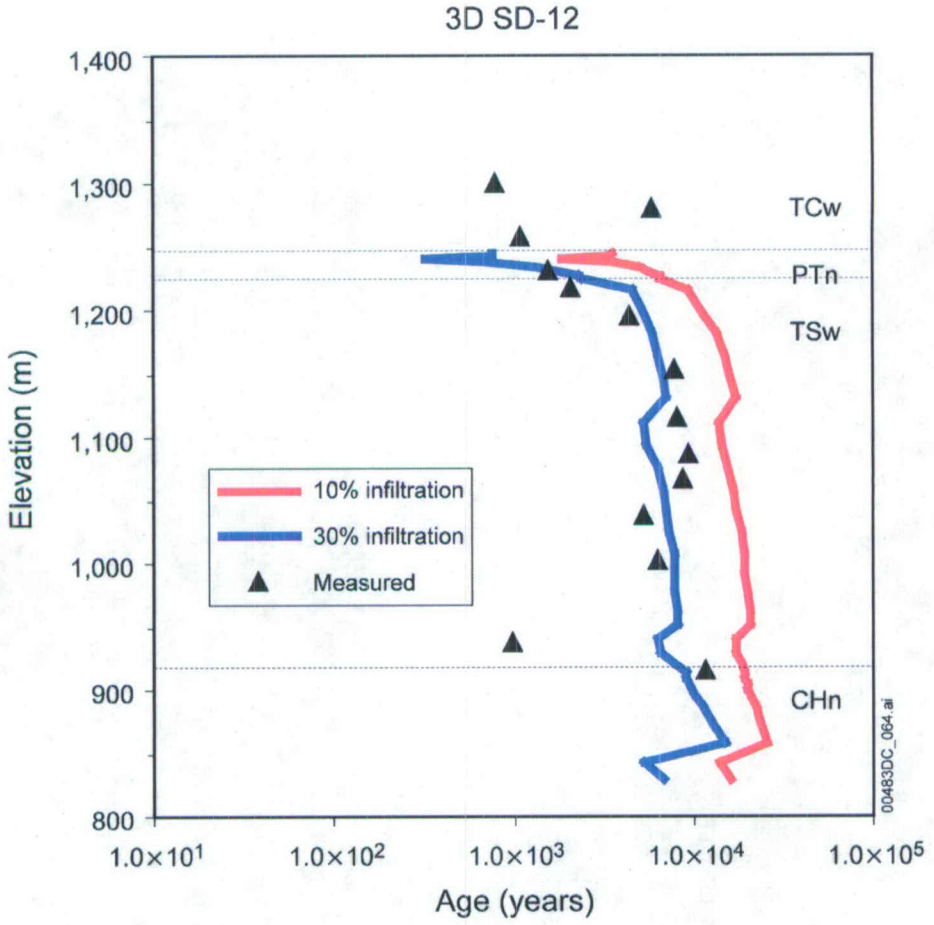

Sources: DTNs: GS961108312271.002 [DIRS 121708] (measured ^{14}C activities); MO0012MWDGFM02.002 [DIRS 153777] (borehole collar elevation and lithological layer interface elevation); Output DTN: LB06123DPDUZFF.001 (flow fields of 10% and 30% infiltration rate).

Output DTNs: LB0704C14FFVAL.001, LB0707C14FFVAL.001, *Ages.xls* (simulated matrix porewater age, and measured ^{14}C ages converted from the measured ^{14}C activities).

NOTE: Only one sample is plotted for each depth if there are multiple samples for one location.

Figure 7.5-2. Simulated Solute Travel Time of the Matrix Pore Water with Three-dimensional Simulation for Borehole SD-12 Compared to the Measured ^{14}C Age

To investigate how uncertainty in the infiltration maps affects the simulated solute travel times, a one-dimensional model was constructed for these two boreholes using the domain-average infiltration rate (10th and 30th percentile, respectively, Table 7.5-1) as an order of magnitude analysis. In comparison, the one-dimensional model reduces the uncertainties associated with spatial variation of surface infiltration rates and lateral flow with a three-dimensional model. Therefore, the one-dimensional model results are considered to be appropriate to examine the sensitivity of model simulated mean travel time to infiltration rates. The domain-average infiltration rates are higher than the respective local infiltration rate given in the 10th and 30th percentile infiltration map. The same tracer simulations described above were repeated using one-dimensional columns extracted from the three-dimensional model at locations representing SD-12 and UZ-1, and the domain-average infiltration rate (Table 7.5-1). A grid mesh of the one-dimensional simulations was made from the extracted representative gridblocks and the

connections of borehole UZ-1 and SD-12, from the three-dimensional grid mesh. Steady-state flow fields for UZ-1 and SD-12 with the domain-average infiltration rate of the 10th and 30th percentile were respectively performed using the EOS9 module of TOUGH2 V1.6 (2003 [DIRS 161491]). These steady-state flow fields (*flow9.dat* files) were then used to simulate the tracer transport processes through the representative one-dimensional columns of UZ-1 and SD-12, using T2R3D V1.4 (1999 [DIRS 146654]). The same methodology was used for tracer transport simulations and the conversion of the solute travel times of the matrix pore water from the simulated tracer concentration breakthrough, as described earlier for the three-dimensional simulations in this section. The simulated solute travel times of the pore water are plotted and compared to the measured ^{14}C age on Figure 7.5-3 (UZ-1) and Figure 7.5-4 (SD-12).

Figure 7.5-3 shows that the simulated solute travel times of borehole UZ-1 with the 30th percentile domain-average infiltration match better than that from the three-dimensional simulation (with the very low local infiltration rates), and the simulated solute travel times with the 10th percentile infiltration are also close to the measurements, but not as good as that for the 30th percentile infiltration. This finding implies that an infiltration rate between the 10th and 30th percentile domain-average infiltration will make a better fit to the measured ^{14}C ages for this borehole. Figure 7.5-4 shows that the simulated solute travel times of borehole SD-12 with the 30th percentile domain-average infiltration match the measurements well, and the results with the 10th percentile domain-average infiltration fall out of range of the measurements for TSw units. These results indicate that the simulated solute travel time is sensitive to the infiltration rate, and subject to the spatial uncertainties in the infiltration maps.

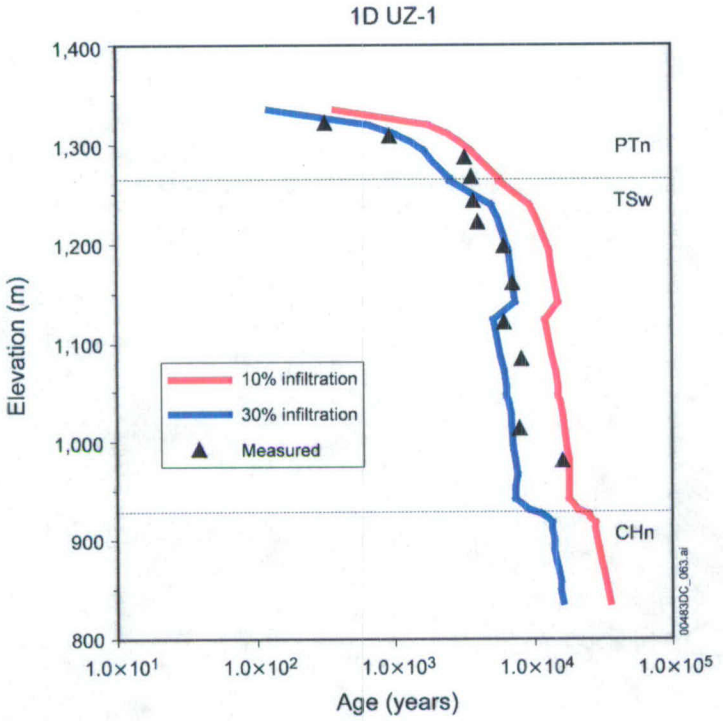

Sources: DTNs: MO0012CARB1314.000 [DIRS 153398] (Measured ^{14}C activity); MO0012MWDGFM02.002 [DIRS 153777] (borehole collar elevation and lithological layer interface elevation); Output DTN LB06123DPDUZFF.001 (flow fields of 10% and 30% infiltration rate).

Output DTN: LB0704C14FFVAL.001, LB0707C14FFVAL.001, *Ages.xls* (simulated matrix porewater age, and measured ^{14}C ages converted from the measured ^{14}C activities).

Figure 7.5-3. Simulated Solute Travel Time of the Matrix Pore Water with One-dimensional Simulation for Borehole UZ-1 Compared to the Measured ^{14}C Age

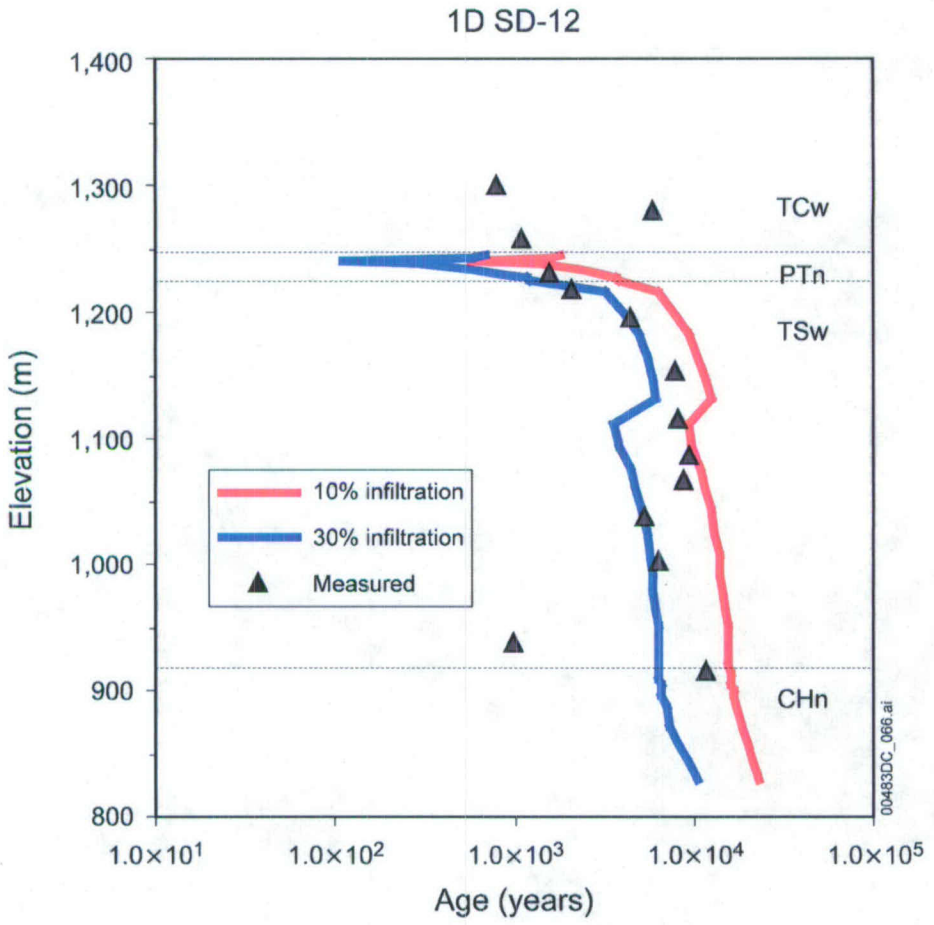

Sources: DTNs: GS961108312271.002 [DIRS 121708] (measured ^{14}C activities); MO0012MWDGFM02.002 [DIRS 153777] (borehole collar elevation and lithological layer interface elevation); Output DTN LB06123DPDUZFF.001 (flow fields of 10% and 30% infiltration rate).

Output DTN: LB0704C14FFVAL.001, LB0707C14FFVAL.001, *Ages.xls* (simulated matrix porewater age, and measured ^{14}C ages converted from the measured ^{14}C activities).

NOTE: Only one sample is plotted for each depth if there are multiple samples for one location.

Figure 7.5-4. Simulated Solute Travel Time of the Matrix Pore Water with One-dimensional Simulation for Borehole SD-12 Compared to the Measured ^{14}C Age

7.5.4 Summary

The solute travel times were simulated using a transport model based on the calibrated groundwater flow fields for the unsaturated zone, and using the 10th and the 30th percentile infiltration maps. The measured gas-phase ^{14}C ages from two instrumented boreholes (UZ-1 and SD-12) have been justified to be representative of the solute travel time for the matrix pore water. Data uncertainties were also discussed. Good matches between the calculated solute travel times and the measured ^{14}C ages was attained for borehole SD-12 with the three-dimensional UZ model and using the 30th percentile infiltration map, and an acceptable match was obtained for borehole UZ-1 using the 30th percentile infiltration map. These results reflect the spatial uncertainties in the infiltration maps as discussed in *Simulation of Net Infiltration for Present-Day and Potential Future Climates* (SNL 2007 [DIRS 174294], Section 6.6.1.1) and are

3. sr_high3_pd_30: High $C_{Sr,eff}$ (14.8 µg/liter) for present-day (pd) 30th percentile infiltration and precipitation rates. $K_{d,Sr}$ = 1.0 m^3/kg.

4. sr_high3_pd_30: High $C_{Sr,eff}$ (14.8 µg/liter) for present-day (pd) 30th percentile infiltration and precipitation rates. $K_{d,Sr}$ = 2.0 m^3/kg.

5. sr_mid2_pd_10: Lower $C_{Sr,eff}$ (5.8 µg/liter) for present-day (pd) 10th percentile infiltration and precipitation rates. $K_{d,Sr}$ = 1.0 m^3/kg.

6. sr_mid2_pd_30: Lower $C_{Sr,eff}$ (5.8 µg/liter) for present-day (pd) 30th percentile infiltration and precipitation rates. $K_{d,Sr}$ = 1.0 m^3/kg.

Inputs and outputs for the three-dimensional model simulations have been submitted to the TDMS under DTN: LB0705UZSRTRAN.001.

Modeled strontium concentrations are compared to measured values for pore salts extracted (by leaching) from two surface-based boreholes (SD-9 and SD-12; DTN: GS990308315215.004 [DIRS 145711]), perched waters, and pore waters obtained by ultracentrifugation of core samples from the ECRB and for SD-9 (DTN: GS020408312272.003 [DIRS 160899]). Comparison of concentrations determined by ultracentrifuge and by water leaches on the same samples have shown that the ultracentrifuge concentrations are higher and probably closer to the true pore water concentrations (see Figure 7.6-1a for SD-9 samples).

Comparisons of measured and modeled strontium concentrations as a function of elevation for the surface-based boreholes (SD-9 and SD-12) are shown in Figure 7.6-1(a and b). Measured concentrations in the unsaturated zone above the perched water show a range of concentrations from about 0.1 to 3 mg/L in nonzeolitic and down to about 0.005 mg/L in zeolitic. Moderately large variations exist in the measured strontium concentrations as a function of depth in the unsaturated zone above the zeolitic horizons. The high concentration, 30th percentile precipitation/infiltration and the lower (mid2) 10th percentile simulation results are closest to the measured data in boreholes SD-9 and SD-12. Looking more closely at the profiles, the near-surface data is closer to the 10th percentile precipitation/infiltration, and the deeper data (above the perched water) is closer the 30th percentile simulations at the lower effective concentration. This may be a result of climate changes where deeper waters reflect a higher proportion of older potential Pleistocene-age water (Sonnenthal and Bodvarsson 1999 [DIRS 117127]).

The sharp reduction in strontium concentrations in the perched water bodies, and in the zeolitic units below, is consistent with ion exchange in zeolitic rocks, since the decrease is much greater than the equivalent drop in chloride concentrations. Where perched water samples were collected in SD-9, the model results show a strong decrease, but not as small a value as those measured in zeolitic rocks. An increase in $K_{d,Sr}$ of a factor of 2 does not make a significant difference in the results. Owing to the initialization of the pore water in the zeolitic rocks to the saturated zone value, which is higher than those measured in the perched water in SD-9, the concentrations never drop below this value, and therefore do not match the perched water or zeolitic pore waters in SD-12. Changing the initialization to a much lower value would result in a much better match,

but could not be independently supported by any measured data. In SD-12, the measured and modeled

7.7 CALCITE MODEL

7.7.1 Introduction

According to the TWP (BSC 2006 [DIRS 177465], Section 1), the model validation runs do not need updating from the previous work, because the infiltration rates used in calcite modeling still bound the new base-case infiltration rates. As shown in Table 6.1-2, the average rate over the model domain for the present-day 10th percentile infiltration with the UZ model grid is 3.03 mm/yr (the base-case infiltration scenario). For the WT-24 location that was used for calcite analysis, the new base-case infiltration rate is 9.25 mm/yr. These infiltration rates in the current flow model fall into the range from 2 to 20 mm/yr used in the previous calcite modeling. Therefore, Section 7.7 is basically a reproduction of Section 7.9 of the previous report (BSC 2004 [DIRS 169861]). The current content has some revisions: (1) inclusion of a commentary by Dublyansky and Smirnov (2005 [DIRS 180650]) on the journal publication of this calcite model by Xu et al. (2003 [DIRS 162124]), and the reply to the commentary paper by Sonnenthal et al. (2005 [DIRS 180639]) (see the end of this section, and Section 7.7.5.1), and (2) some clarifications for technical reviews. The conclusions of the current report have not changed from the previous report (BSC 2004 [DIRS 169861]).

The percolation flux in the unsaturated zone is an important parameter because it controls seepage into drifts that may contact waste packages. As shown in Section 6.6, it depends strongly on the infiltration flux, which is a boundary condition of the UZ flow model. Observations of precipitated calcite in the unsaturated zone constrain the infiltration flux. Therefore, comparing observed hydrogenic calcite deposits to simulations increased confidence in the model's ability to capture this boundary condition. Because direct measurements of infiltration flux are not possible, this confirmation of the boundary condition generally builds confidence in the UZ flow model. Hydrogenic calcite deposits in fractures and lithophysal cavities at Yucca Mountain have been studied to estimate past percolation fluxes (Carlos et al. 1995 [DIRS 162118]; Marshall et al. 1998 [DIRS 107415]; BSC 2004 [DIRS 169734], Section 7.7.1).

One objective of these previous studies was to investigate the relationship between percolation flux and measured calcite abundances. The U.S. Geological Survey (USGS) determined calcite abundances from a deep surface-based borehole (WT-24) (DTN: GS021008315215.007 [DIRS 162127]). Geochronology work performed by the USGS (Neymark et al. 2001 [DIRS 156889]) indicates that this calcite formed over approximately 10 million years. Hydrogenic mineral coatings in the unsaturated zone are nonuniformly distributed and located almost entirely on fracture footwalls and cavity floors—in contrast to saturated environments, in which vein and cavity deposits usually coat all surfaces.

A one-dimensional model column corresponding to the location of a deep borehole (WT-24) was chosen for modeling calcite deposition because measured calcite abundances (DTN: GS021008315215.007 [DIRS 162127]) were available for comparison. Here, the results of a reactive transport numerical model for calcite deposition under different infiltration conditions are presented. The setup and results of the problem are cited from the report by Xu et al. (2003 [DIRS 162124]). The reactive transport model used here considers the following essential factors affecting calcite precipitation: (1) infiltration, (2) the ambient geothermal

gradient, (3) gaseous CO_2 diffusive transport and partitioning in liquid and gas phases, (4) fracture–matrix interaction for water flow and chemical constituents (dual permeability), and (5) water–rock interaction. Any water–rock interaction effects (e.g., pH modification) also affect the calcite solubility, hence, its abundance in each rock unit. The dual permeability model allows us to address not only the abundances of calcite with depth, but also its relative abundance in fractures and in the rock matrix as a function of the hydrological/geochemical processes in each medium, as well as the interaction of water flowing between fractures and matrix.

Dublyansky and Smirnov (2005 [DIRS 180650]) wrote a comment paper on the journal article by Xu et al. (2003 [DIRS 162124]), which questioned inappropriate thermal boundary conditions for simulations used. The comment paper contended that the calcite was formed by upwelling hydrothermal waters and that the original journal article considered a constant ambient geothermal gradient for the approximately 10 million-year period, rather than a higher gradient which has been inferred from fluid inclusions. In reply to the commentary paper, Sonnenthal et al. (2005 [DIRS 162127]) performed a simulation with variable bottom boundary temperatures approximating those measured in fluid inclusions. The results of this simulation is discussed later in Section 7.7.5.1.

It should be pointed out that the one-dimensional calcite data modeling and analysis do not have to do with the direct validation of the three-dimensional flow model, but this model may provide some additional evidence for the validation at a location. A steady-state one-dimensional flow field was used for the analysis, because here the primary interest is long-term calcite deposition within the TSw unit, in which flow is primarily one-dimensional vertical gravity-driven.

7.7.2 Calcite Precipitation Mechanisms

Along with wind-blown dust, precipitation carries much of the calcium to the surface (Vaniman et al. 2001 [DIRS 157427]). In the soil zone, strong evapotranspiration, along with some water–rock interaction and root-zone biological processes, leads to saturation with respect to calcite. The depth to reach calcite equilibrium depends on climate and infiltration variations over time, episodic water flow, and near-surface biogeochemical conditions. During more typical smaller infiltration events, calcite may reach equilibrium close to the surface. However, large infiltration pulses of calcite-undersaturated water can dissolve near-surface calcite and reach equilibrium at a greater depth. This model validation activity concerns calcite deposition in a deep geological unit, the TSw, where the repository is located. Uncertainty in the infiltrating water composition near the surface is, thus, insignificant because calcite reaches saturation well above this unit. In addition, the constant infiltration rate and steady-state water flow conditions over geological time used in the simulations are also justified by evidence that the rate of calcite growth in the unsaturated zone has remained approximately constant over at least the past 8 million years (Paces et al. 1998 [DIRS 107408]).

The primary driving force for calcite precipitation from percolating waters in the unsaturated zone is its decreasing solubility with increasing temperature; calcite precipitates as water flows downward because of the geothermal gradient. Therefore, consideration of the ambient geothermal gradient is very important for calcite precipitation. The temperature distribution is a function of the crustal heat flow and the effect of infiltration. The modeled temperature

distributions in borehole WT-24 are discussed later in Section 7.7.5.2. Pore waters extracted from Yucca Mountain rock matrix collected from deep locations are close to equilibrium with respect to calcite (BSC 2004 [DIRS 169734], Section 7.7.1), and no measurements of aqueous concentrations are available from fractures because they generally have low liquid saturations.

The calcium concentration and CO_2 partial pressure in percolating water is a major factor controlling the abundances of calcite and its stability. This is a result of the decreasing solubility of CO_2 gas in water with increasing temperature, which in turn causes the following degassing process: $HCO_3^- + H^+ \rightarrow CO_2$ (g) + H_2O. Gaseous CO_2 is also redistributed by gas-phase diffusive transport. Degassing increases the pH, and then contributes to calcite precipitation: $Ca^{2+} + HCO_3^- \rightarrow CaCO_3$ (calcite) + H^+. Water and gas flow between fractures and the adjacent matrix governs the resulting calcite distribution within each medium. Calcite precipitation is also affected by other factors, such as the dissolution and precipitation of aluminosilicate minerals (mainly through modifying the pH and the CO_2 partial pressure).

7.7.3 Reactive-Transport Model

Modeling of calcite deposition in the Yucca Mountain unsaturated zone was performed using the reactive transport computer code TOUGHREACT (Xu and Pruess 1998 [DIRS 117170]; 2001 [DIRS 156280]). (This version of the code has not been qualified under LP-SI.11Q-BSC, *Software* Management, but its use for corroboration is appropriate). The code uses a sequential iteration approach similar to the report by Yeh and Tripathi (1991 [DIRS 162125]), Walter et al. (1994 [DIRS 162122]), and Xu et al. (1999 [DIRS 162123]), which solves the transport and reaction equations separately. Flow and transport are based on space discretization by means of integral finite differences. An implicit time-weighting scheme is used for individual components of the model: flow, transport, and kinetic geochemical reaction. The chemical transport equations are solved independently for each component, whereas the reaction equations are solved on a gridblock basis using Newton-Raphson iteration. Full details of the code are given in reports by Xu and Pruess (1998 [DIRS 117170]; 2001 [DIRS 156280]).

In the model, advective and diffusive transport of aqueous chemical species is considered in the liquid phase. Molecular diffusive transport of gaseous species (CO_2) is considered in the gas phase. Aqueous chemical complexation and gas dissolution/exsolution are accounted for under local equilibrium, whereas mineral dissolution/precipitation can proceed at equilibrium and/or can be kinetically controlled. Gas species in the chemical computations are assumed to behave as ideal gases (i.e., fugacity equals partial pressure). Temperature effects are considered for geochemical reaction calculations, because equilibrium and kinetic data are functions of temperature.

Changes in porosity and permeability from mineral dissolution and precipitation on water flow are not considered for the present modeling. In fact, these changes are very small. Figure 7.7-3 shows that observed calcite precipitation in TSw unit is less than 1%. These effects have not appeared to close up any fracture in the deep system. By neglecting porosity and permeability change, modelers obtain quasi-steady flow conditions. This makes it possible to consider geochemistry in great detail for a simulation period of 10 million years.

A dual permeability approach, in which fractures and matrix are treated as two separate continua, was employed for water flow and chemical transport in the unsaturated fractured tuff. In this approach, interflow (water and chemicals) is allowed between fractures and the adjacent matrix, and global flow occurs within both fracture and matrix continua. The AFM developed by Liu et al. (1998 [DIRS 105729]) was used to describe fracture–matrix interaction and preferential liquid flow in fractures.

7.7.4 Hydrogeological and Geochemical Conditions

7.7.4.1 Hydrogeological Conditions

As discussed in the geological model of Section 6.1, the Yucca Mountain unsaturated zone consists of layers of welded and nonwelded volcanic tuffs. The welded and nonwelded tuffs have vastly different hydrological properties. Welded units are characterized by relatively low porosity, low matrix permeability, and high fracture density, whereas the nonwelded tuffs have higher matrix porosity and permeability, and lower fracture density (Liu et al. 1998 [DIRS 105729]). Montazer and Wilson (1984 [DIRS 100161]) developed a conceptual model for the Yucca Mountain unsaturated zone that identified five main hydrogeological units based on the degree of welding and on the associated relationships to fracture intensity. This model has formed the basis for modeling flow in the Yucca Mountain UZ. Table 7.7-1 describes three of the five units, each of which is further divided into a number of model layers with different hydrogeological and geochemical properties (SNL 2007 [DIRS 179545]; SNL 2007 [DIRS 177404]). The CHn unit is comprised of zeolitic and vitric nonwelded tuffs underlying the basal vitrophyre of the Topopah Spring Tuff. Below the CHn are the Crater Flat undifferentiated units, consisting of the lower Bullfrog and Tram Tuffs of the Crater Flat Group. The hydrogeological units below the TSw were not considered in geochemical transport simulations, so details regarding these units are not given in Table 7.7-1. The primary interest is in calcite deposition within the TSw unit, where the repository is located (tsw4 and tsw5 model layers in Table 7.7-1). The exclusion of the underlying hydrogeological units does not affect the results in the TSw unit because flow is predominantly gravity driven, and upward chemical diffusion is subordinate to downward advective transport. Note also that the previous set of porosity and permeability values (Table 7.7-1) used in calcite modeling are different from the current flow model. As mentioned before, a one-dimensional steady-state flow field was used for the calcite modeling—the amount of calcite precipitation mainly depends on infiltration rate and then the percolation flux. Therefore, effects of different porosity and permeability on calcite precipitation in TSw should be small.

Table 7.7-1. Hydrogeologic Units, Model Layers, and Hydrogeological Properties for the Yucca Mountain UZ Flow and Transport Model, as Given by the Calibrated Properties Model

Hydrogeologic Unit	Description	Model Layer	Fracture		Matrix	
			Permeability (m^2)	Porosity	Permeability (m^2)	Porosity
TCw: Tiva Canyon Welded unit	Moderately to densely welded portions of the Tiva Canyon Tuff of the Paintbrush Group	tcw1	2.41×10^{-12}	3.7×10^{-2}	3.86×10^{-15}	0.253
		tcw2	1.00×10^{-10}	2.6×10^{-2}	2.74×10^{-19}	0.082
		tcw3	5.42×10^{-12}	1.9×10^{-2}	9.23×10^{-17}	0.203

Table 7.7-1. Hydrogeologic Units, Model Layers, and Hydrogeological Properties for the Yucca Mountain UZ Flow and Transport Model, as Given by the Calibrated Properties Model (Continued)

Hydrogeologic Unit	Description	Model Layer	Fracture		Matrix	
			Permeability (m^2)	Porosity	Permeability (m^2)	Porosity
PTn: Paintbrush Nonwelded unit	Variably welded Paintbrush Tuff and its associated bedded tuffs, including those located at the bottom of the Tiva Canyon and top of the Topopah Spring Tuffs	ptn1	1.86×10^{-12}	1.4×10^{-2}	9.90×10^{-13}	0.387
		ptn2	2.00×10^{-11}	1.5×10^{-2}	2.65×10^{-12}	0.439
		ptn3	2.60×10^{-13}	3.2×10^{-3}	1.23×10^{-13}	0.254
		ptn4	4.67×10^{-13}	1.5×10^{-2}	7.86×10^{-14}	0.411
		ptn5	7.03×10^{-13}	7.9×10^{-3}	7.00×10^{-14}	0.499
		ptn6	4.44×10^{-13}	4.6×10^{-3}	2.21×10^{-13}	0.492

7.7.6 Concluding Remarks

Modeling calcite deposition provides additional evidence for validation of the UZ model. For the mean infiltration rate (2–5.92 mm/yr), simulations in Figure 7.7-3 are within the range of data for each unit (except at the PTn-TSw contact) for the more realistic extended-case geochemical system. The contact between the two units is where lateral flow may occur, which is not included in the one-dimensional model. The comparison in Figure 7.7-3 indicates that the validation criterion is met. This is because the acceptance criterion is applied only to the mean infiltration rate, which s the expected rate, and the other rates, representing extremes, would not be expected to simulate actual mean behavior. In addition, the validation is focused on the extended-case geochemical system. The excursion in the model results at the PTn-TSw contact is not important because it is an artifact of the lack of lateral flow in the one-dimensional model and would not occur in the three-dimensional UZ flow model.

Over a range of 2 to 20 mm/yr infiltration rates, the simulated calcite abundances generally fall within the range of calcite observed in the field, which satisfies the validation criterion. The simulated calcite distributions capture the USGS–measured data from the WT-24 well cuttings (DTN: GS021008315215.007 [DIRS 162127]). The 20-mm/yr infiltration rate may be the upper bound for WT-24 location, whereas the infiltration rate (2 to 5.92 mm/yr) used for the flow model gives the closest match to the data. The observed calcite precipitation for the top of TSw occurs mostly in the fractures, which is also captured. The modeling results can provide useful insight into process mechanisms such as fracture–matrix interaction, as well as conditions and parameters controlling calcite deposition. The modeled calcite abundances generally increase with increasing infiltration rate, but become less sensitive to infiltration at higher rates as a result of changes to the geothermal gradient. Therefore, between a 5.92 and 20 mm/yr infiltration rate, the amount of calcite increases only slightly in the TSw.

The calcite measurements may provide insight into the long-term average infiltration over the lifetime of Yucca Mountain. The findings imply that perhaps lower rates are more consistent with calcite data. That is, glacial transition values in the 2 to 6 mm/yr range, with correspondingly lower present-day values, are consistent with these data. This information suggests lower long-term average rates for the site.

One-dimensional simulation is appropriate because both flow and geothermal gradient are primarily vertical. The current observed calcite is formed cumulatively over about 10 million years. A number of uncertainties are involved in the numerical simulation results, the most influential of which are variations in geothermal gradient and infiltration over time. Differences between one-dimensional and three-dimensional flow are much less than the differences in geothermal gradient and infiltration over 10 million years. Agreement between simulated and measured calcite abundance could work to establish the validity of the flow field and infiltration rates used in the UZ flow model. No significant lateral flow (above TSw and within the TSw unit) was predicted in both the previous flow model and current flow model at the WT-24 location. Therefore, the calcite analysis conclusion based on the previous flow model is still valid for the current flow model.

Finally, in reply to a commentary paper by Dublyansky and Smirnov (2005 [DIRS 180650]), Sonnenthal et al. (2005 [DIRS 180639]) preformed a simulation with variable bottom boundary temperatures approximating those measured in fluid inclusions. The results of this simulation show slightly greater abundances of calcite compared to the ambient temperature simulation, yet show similar trends with depth. The new results are within the spread of the measured calcite abundances, and therefore the variable geothermal gradient did not change the conclusions of the first paper. Thus, the results with variable temperature boundary do not change the conclusions made above.

7.8 MODELING ANALYSIS OF ALCOVE 8/NICHE 3 FAULT TESTS

This section simulates in situ field tests of artificial infiltration along a fault at Alcove 8/Niche 3. The fault tests caused localized saturated conditions below the test spot in an otherwise UZ. Under this field condition, test data are compared to results of simulations using the same conceptual model, methodology, and modeling approach as those used in the UZ flow model. This modeling activity presents a different case of validation for the UZ flow model. The results will build confidence in the UZ flow model from a different perspective (in terms of different-scale model results and field conditions).

This modeling analysis uses both model calibration and prediction. Comparisons between simulated and observed data are useful for evaluating the validity of the methodology used in the UZ flow model for capturing UZ flow and transport processes. The criterion for validation is that the predicted results for the time required for a conservative tracer to reach a given concentration (e.g., peak concentration) are within a factor of five of the observed time. As demonstrated in Section 7.8.3.2 below (the discussion of modeling results), the criterion is met. This modeling activity is adopted from the previous version of *UZ Flow Models and Submodels* (BSC 2004 [DIRS 169861], Section 7.6).

7.8.1 Field Observations

Infiltration rate, seepage rate, and tracer concentration data from the fault test are used to corroborate model simulations. The fault test used water and two liquid tracers. The test was carried out in the upper lithophysal and middle nonlithophysal subunits in the Yucca Mountain UZ. These geological subunits correspond to model layers tsw33 and tsw34, respectively, in the UZ model. The tsw33 has some lithophysal cavities that may intersect fractures. Liquid water, first without and then with tracers, was released at the floor of an alcove along the fault (about 5 m long (DTN: GS020508312242.001 [DIRS 162129]) within tsw33. Seepage from the fault into a niche and tracer concentrations of seeping liquid were monitored as functions of time. The niche is located within tsw34, about 20 m below the floor of the alcove; the interface between tsw33 and tsw34 is about 15 m below the floor of the alcove (DTN: LB0301N3SURDAT.001 [DIRS 162130]).

A pressure head of 2 cm was maintained at the infiltration plot along the fault at the alcove. The plot consists of four trenches that have different infiltration rates as a result of subsurface heterogeneity along the fault. Figure 7.8-1 shows the total infiltration rate as a function of time (DTNs: GS020508312242.001 [DIRS 162129] and GS020908312242.002 [DIRS 162141]). For simplicity, this model considers the uniformly distributed infiltration rate along the infiltration

plot to be consistent with the uniform property distribution in the UZ model. One consideration in the modeling study is to evaluate approaches used in the site-scale model. Considerable

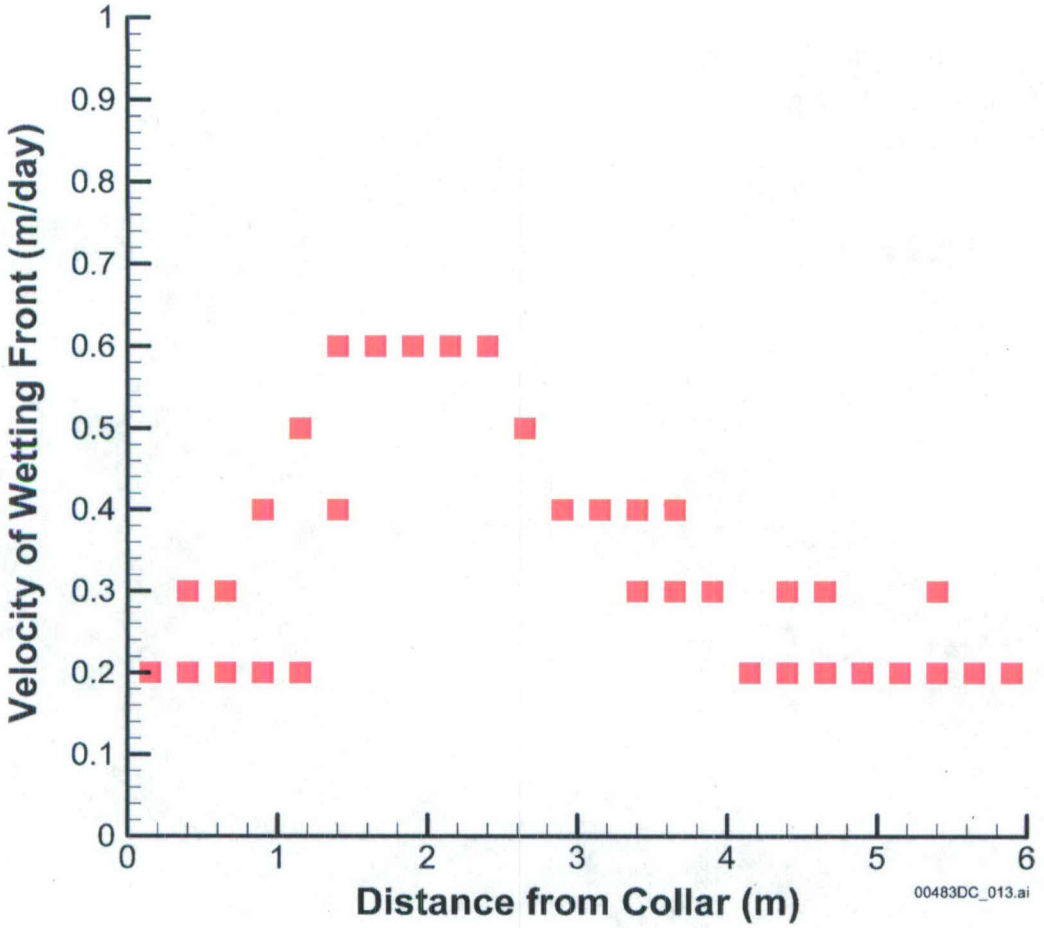

Source: DTN: LB0303A8N3LIQR.001 [DIRS 162570].

NOTE: Observation boreholes are approximately perpendicular to the fault. The distance from a borehole collar to the fault is about 2 m.

Figure 7.8-3. Water Travel Velocity Data for Boreholes 9 and 10

After 209 days, two tracers with different molecular diffusion coefficients, bromine and pentafluorobenzoic acid, were introduced into infiltrating water at the infiltration plot. Tracer concentrations in three of the trays (at the niche) capturing seeping water from the fault were measured (DTN: LB0303A8N3LIQR.001 [DIRS 162570]). Seepage rates corresponding to these three trays were not measured during the period of tracer concentration measurement. In this study, a flux-averaged breakthrough curve (concentration as a function of time) from these trays was used to represent the average breakthrough curve for all trays at the niche where seepage was captured. A constant flux value for each of the three trays was used for calculating the flux-averaged breakthrough curve shown in Figure 7.8-4. The constant flux values for the three trays were determined as the averaged value over 56 days before tracers were introduced. This flux-averaged breakthrough curve was compared with simulation results.

(1980 [DIRS 100610]) parameters (for matrix, fractures, and the fault), and the parameter of the AFM, γ, for fractures (DTNs: LB997141233129.001 [DIRS 104055]; LB980901233124.101 [DIRS 136593]; LB990861233129.001 [DIRS 110226]; and LB990501233129.001 [DIRS 106787]). Because fracture van Genuchten parameters for tsw33 and tsw34 are similar (Table 7.8.1), a simple average of these parameters was used as the corresponding parameters for the fault. The averaged k/ϕ (where k is fracture permeability and ϕ is the corresponding fracture porosity) was calculated as fault permeability. Note that because there is no matrix in the fault in the model (or $\phi = 1$), the weighted k/ϕ (rather than weighted k) is employed for estimating fault permeability. The aperture of the fault was estimated as the average of fracture apertures of the two subunits. Note that the AFM was developed for fracture networks rather than for a single fracture. Consequently, the AFM does not apply to the fault here. In fact, most of the parameter values mentioned above and given in Table 7.8-1 are not site specific for the fault test site. These values were used as initial guesses for model calibration against the seepage rate and water-travel-velocity data observed from the fault test. Note that not all site-specific parameters are available and the initial guess of some values were necessary. This is because the initial guess does not significantly affect the final calibrated values. To reduce the number of variables in model calibration (or inverse modeling), parameters expected to significantly affect simulated tracer transport time and seepage rate were varied in the calibration, while other parameters were kept unchanged. The varied parameters were fracture and fault permeabilities, fracture porosity, fault aperture, and fracture and fault van Genuchten α values.

Table 7.8-1. Uncalibrated Rock Properties

Rock property	Fault[e]	tsw33		tsw34	
		Fracture	Matrix	Fracture	Matrix
Permeability (m^2)	4.34×10^{-11}	5.5×10^{-13}[c]	3.08×10^{-17}[a]	0.35×10^{-13}	4.07×10^{-18}[a]
Porosity	1.00	6.6×10^{-3}[d]	0.154[a]	10^{-2}[d]	0.11[a]
Fracture frequency (m^{-1})		1.03[e]		1.5[e]	
Fracture aperture (m)	1.12×10^{-3}	1.49×10^{-3}[e]		1.14×10^{-3}[e]	
Active fracture model parameter γ	0.0	0.41[a]		0.41[a]	
van Genuchten α (Pa^{-1})	1.0×10^{-3}	11.46×10^{-3}[a]	2.13×10^{-5}[a]	5.16×10^{-4}[a]	3.86×10^{-6}[a]
van Genuchten m	0.608	0.608[a]	0.298[a]	0.608[a]	0.291[a]

Sources: [a]DTN: LB997141233129.001 [DIRS 104055].
[b]DTN: LB980901233124.101 [DIRS 136593].
[c]DTN: LB990861233129.001 [DIRS 110226].
[d]DTN: LB990501233129.001 [DIRS 106787].
[e]BSC 2004 [DIRS 169861], Table 7.6-1.

Infiltration-seepage processes in the fault and the surrounding fractured rock were determined by several mechanisms. Liquid water applied at the alcove floor (Figure 7.8-5) flowed first into the fault and then into fractured networks connected to the fault. Matrix imbibition occurred at interfaces between fractures and the matrix, and between the fault and the matrix. When water arrived at the intersection between the fault and the niche, it might not have immediately seeped into the niche until the capillary pressure became zero because of capillary barrier effects (Philip et al. 1989 [DIRS 105743]; Birkholzer et al. 1999 [DIRS 105170]). Such effects can divert flow away from the opening, resulting in only a portion of the water arriving at the niche ceiling actually seeping into the niche. Tracer transport time was determined by fracture porosity, fault aperture, and the matrix imbibition process.

fracture porosity of tsw33 (Table 7.8-3). While the actual width of the fault zone is unknown, the estimated equivalent fault aperture (3 cm) is used. The estimated fracture porosity is consistent with those estimated from water release tests performed in the same geological unit (BSC 2004 [DIRS 170004], Section 6.11.3.2).

Table 7.8-3. Rock Properties Calibrated from Both Seepage Rate and Water Travel Velocity Data (Run #2)

Rock property	Fault	tsw33	tsw34
Fracture Permeability (m^2)	1.12×10^{-10}	1.23×10^{-12}	5.01×10^{-13}
Fracture Porosity		0.066	
Fracture aperture (m)	0.03		
Fracture van Genuchten α (Pa^{-1})	1.24×10^{-3}	2.19×10^{-3}	1.09×10^{-3}

Source: Output DTN: LB0303A8N3MDLG.001 [DIRS 162773], file *Irun4Ni.par*.

NOTE: All other rock properties are the same as those in Table 7.8.1. Rock names "tswF3", "NetF3," and "NetF4" in file *Irun1i.par* correspond to "Fault", "tsw33," and "tsw34", respectively, in this table.

Figure 7.8-7 shows a comparison among calculated water travel velocities from two calibration runs and the velocity data observed from the fault test. The simulated water travel velocities from Run #2 are much closer to the observed data than those from Run #1 (especially near the fault). However, the water travel velocities away from the fault are still overestimated. One possible explanation is that matrix imbibition from fractures above the niche were underestimated because the dual-continuum approach considerably underestimates the pressure gradient near a fracture matrix interface during transient flow conditions (Pruess and Narasimhan 1985 [DIRS 101707]). While this problem can be resolved with the MINC model of the report by Pruess and Narasimhan (1985 [DIRS 101707]), the computational intensity of the inverse model problem under consideration would be significantly increased. Note that a model calibration involves a great number of forward simulation runs. Considering (1) that the transient flow effects would be considerably reduced later in the test, and (2) that the focus here is on flow and transport within and near faults, simulated flow field and calibrated rock properties from Run #2 were used for simulating tracer transport at the test site. Figure 7.8-8 also shows a comparison between simulated seepage rates as a function of time (Run #2) and field observations. The match is reasonable. Figure 7.8-8 matches both wetting-front velocity and seepage-rate, and it is, therefore, considered a better calibration than Figure 7.8-6, which only matches the seepage rate data. Note that to give a reasonable prediction of solute transport, the water flow must be correctly modeled.

8.7 TRACER TRANSPORT TIMES

A total of 32 tracer transport simulations were carried out to obtain insight into the impacts of infiltration rates, UZ flow model conceptual models, and retardation effects on tracer migration from the repository to the water table (Section 6.7). The 16 UZ flow fields were incorporated into these 32 transport runs. For each flow field, there were two tracer transport runs, one for conservative (or nonadsorbing) and the other for reactive (or adsorbing) tracer transport, with tracer release from repository fracture blocks. These tracer-transport studies indicate that there exists a wide range of tracer transport times associated with different infiltration rates and the type of tracers. The most important factors for tracer-transport times are found to be: (1) surface net infiltration rates, and (2) adsorption effects.

Statistics of tracer transport times at 10% and 50% mass breakthrough at the water table from the 32 simulations show that tracer-transport times vary inversely to the average surface infiltration (net water recharge) rate over the model domain. When the average infiltration rate increases from 3 to 70 mm/yr, average tracer transport (50% mass breakthrough) times decrease by more than two orders of magnitude for adsorbing and nonadsorbing species. Nonadsorbing tracers migrate (from the repository to the water table) one to two orders of magnitude faster than an adsorbing tracer under the same infiltration condition.

8.8 UZ FLOW WEIGHTING FACTORS

A generalized likelihood uncertainty estimation (GLUE) methodology was used to determine the weighting factors (Section 6.8). The generation of the UZ flow weighting factors accounts for prior information available from the infiltration model for the probability of infiltration maps, as well as matches between UZ flow model results (distributions of temperature and chloride concentration) and corresponding field data. Such weighting factors were derived from infiltration and UZ flow model results for present-day conditions.

8.9 ANALYZING TRANSIENT-PULSE INFILTRATION

How episodic surface infiltration affects deep percolation was investigated by examining variations in percolation fluxes at the bottom of the PTn versus time, using two one-dimensional column models (Section 6.9). Results from the two column models show that surface infiltration pulses can be effectively smoothed temporally once traveling to the bottom of the PTn unit. In general, after rapid changes during the first several hundred years of pulse infiltration, the percolation fluxes at the bottom of the PTn gradually approach the average value of net infiltration.

8.10 MODEL VALIDATION

Model validation efforts have been documented in this report (Section 7). Validation activities for the UZ flow model mainly include corroboration with experimental data and modeling studies, using the following corroboration with experimental data: (1) ECRB observation data; (2) WT-24 perched water data; (3) gas flow data from boreholes SD-12 and UZ-7a; and (4) borehole-measured ^{14}C data and Alcove 8—Niche 3 flow and transport data. In addition, validation efforts are also made for the strontium model and calcite model, using field-observed data from surface-based boreholes or from the ESF.

In these validation examples, the simulation results of the UZ flow model and submodels are shown to be able to match different types of available observation data, such as water potentials, perched water locations, tracer and geochemical concentrations, and pneumatic pressures. The criteria of the model validation of the TWP (BSC 2006 [DIRS 177465]) are, in general, satisfied. These efforts have provided validation of the UZ flow model and its submodels for their accuracy and reliability in describing hydrological, thermal, and chemical conditions, and predicting flow and transport processes in the unsaturated zone system of Yucca Mountain.

8.11 LIMITATIONS

The UZ flow model and submodels are appropriate tools for characterizing flow and transport processes in the Yucca Mountain unsaturated zone. The accuracy and reliability of the UZ flow model predictions are dependent on the accuracy of estimated model properties, other types of input data, and hydrogeological conceptual models. These models are limited mainly by the current understanding of Yucca Mountain system, including the geological and conceptual models, the volume-average modeling approach, and the available field and laboratory data.

Past site investigations have shown that large variabilities exists in the flow and transport parameters over the spatial and temporal scales of the mountain. Even though considerable progress has been made in this area, uncertainty associated with the UZ flow model input parameters exists. The major uncertainties in the UZ model parameters are: (1) the accuracy of estimated current, past, and future net infiltration rates over the mountain; (2) quantitative descriptions of the heterogeneity of welded and nonwelded tuffs, their flow properties, and detailed spatial distributions within Yucca Mountain, especially below the repository; (3) fracture properties in zeolitic units and faults from field studies; (4) evidence of lateral diversion caused by zeolites in the CHn units and within the PTn units; and (5) transport properties (e.g., adsorption or K_d coefficients in different rock types, matrix molecular diffusion coefficients in different units for different radionuclides, dispersivities in fracture and matrix systems). These uncertainties exist, but they have been addressed with the modeling studies in this report. In particular, most uncertainties are captured within the range of flow fields generated.

8.12 HOW ACCEPTANCE CRITERIA ARE ADDRESSED

The following information describes how this analysis addresses the acceptance criteria in *Yucca Mountain Review Plan, Final Report* (NRC 2003 [DIRS 163274], Section 2.2.1.3.6.3). Only those acceptance criteria that are applicable to this report (Section 4.2) are discussed. In most cases, the applicable acceptance criteria are not addressed solely by this report; rather, the acceptance criteria are fully addressed when this report is considered in conjunction with other analysis and model reports that describe flow in the unsaturated zone. Where a subcriterion includes several components, only some of those components may be addressed. How these components are addressed is summarized below.

To examine these relationships more closely, cumulative distributions from the previous and current models, for percolation in the host rock within the repository footprint, are compared in Figures H-1 through H-3 for the present-day, monsoon, and glacial transition climate states. Percolation flux in the host rock is a result from the UZ flow model and is selected for comparison here (rather than net infiltration at the ground surface) because it is used directly as a boundary condition for drift-scale coupled process models (e.g., multiscale model) and for the drift seepage abstraction in TSPA. In addition, percolation flux at the repository horizon is an important determinant of radionuclide mobility in the UZ transport abstraction.

These percolation data were developed by sorting the percolation flux values at the repository horizon in the 560 columns of the UZ flow model grid for both the previous (INFIL based; BSC 2004 [DIRS 170007]) and current (MASSIF based; SNL 2007 [DIRS 174294]) versions of the model. The 560 columns include the contingency area (SNL 2007 [DIRS 181383], Section 6.2.12[a]) that was not included in previous representations of the repository footprint. The distributions (Figures H-1 through H-3) preserve the full uncertainty and variability of the UZ flow model, and represent the same spatial domain.

Statistical approaches are used to compare the previous and current percolation fields (Tables H-2 and H-3): (1) compare mean values for the previous model, for the three climate states, with mean values for the current 10th, 30th, and 50th percentile fields (Table H-2); and (2) compare the ranges of spatial variation for the previous model with the same ranges for the current model (Table H-3). As noted above, the 90th percentile field from the current model is exceptional, but this field is assigned a relatively low weight in TSPA. A set of composite-weighted flux values is used for each climate state (Table H-2) that combines the averages of 10th, 30th, 50th, and 90th percentile fields from the current model, using the same sampling weights used in TSPA. These weights are combined in Table H-2 with flux values from different sources (as indicated) to develop composite-weighted values for the present-day, monsoon, and glacial transition climate states that can be readily compared to supplement the impact evaluation for Group 3 products. These modal values reasonably represent flux conditions likely to be assigned in TSPA to particular waste package locations in the repository. They are useful for evaluating the sensitivity of near-field behaviors such as thermally driven coupled processes, that do not depend on the far-field distribution of percolation flux.

For the previous model (BSC 2004, [DIRS 170007]), the overall spatial variation of percolation flux at the repository horizon within the repository footprint ranged from zero (discounting small negative values) to 294 mm/yr, whereas the current model (SNL 2007 [DIRS 174294]) ranges from 0.15 to 136 mm/yr (Table H-3). Current data for the 10th, 30th, and 50th percentile fields are mostly encompassed by the previous data for the "low" and "high" uncertainty states. Extreme values from the previous data (>95th percentile for the Mean and High uncertainty states) bracket all the current data (including the 90th percentile field). While these comparisons are only statistical, they show that application of the current values in TSPA falls mostly within the range of uncertainty and variability that existed when the Group 2 and Group 3 products were developed.

An important aspect of Figures H-1 through H-3 is that the differences between previous and current model results, for the comparisons described above, are typically smaller than the differences between the uncertainty states for either the previous or current data (Table H-3).

Table H-2. Average Flux Values for Comparison of Previous and Current Model Results

All fluxes in mm/yr	Present- Day	Monsoonal	Glacial-Transition	Weights	
Current Models for Infiltration and UZ Flow, Percolation Flux at PTn-TSw Interface					
Quantile	**Avg. Flux in Footprint [a]**				
0.1	4.1	7.8	12.2	0.6191	Weights: Table 6.8-1 of Section 6 (average values) Fluxes: SNL 2007 [DIRS 181383], Table 6.2-5[a].
0.3	10.2	16.1	26.3	0.1568	
0.5	14.6	19.5	36.2	0.1645	
0.9	34.1	92.4	69.7	0.0596	
Weighted	**8.6**	**16.1**	**21.8**	1.0000	
Previous Models for Infiltration and UZ Flow, Infiltration Flux at Ground Surface					
Case	**Avg. Flux in Footprint [a]**				
Lower	0.25	4.20	1.92	0.24	Fluxes and weights: BSC 2003 [DIRS 165991], Tables 6-4 and 6-7 (not including contingency area).
Mean	4.20	11.86	18.57	0.41	
Upper	10.80	19.53	35.23	0.35	
Weighted	**5.6**	**12.7**	**20.4**	1.00	
Previous Models for Infiltration and UZ Flow, Percolation Flux at PTn-TSw Interface					
Case	**Avg. Flux in Repository Footprint [a]**				
Lower	0.40	4.30	1.90	0.24	Fluxes: SNL 2007 [DIRS 181244], Table 6.6-11 Weights: BSC 2003 [DIRS 165991], Table 6-7
Mean	3.80	11.70	17.90	0.41	
Upper	11.10	20.30	35.10	0.35	
Weighted	**5.5**	**12.9**	**20.1**	1.00	
Drift-Scale Coupled Processes (DST and TH Seepage) Models (MDL-NBS-HS-000015 Rev. 02, Section 4.1.1.4)					
Values Used	6.0	16.0	25.0		Base values shown; model also includes sensitivity runs that multiply these values by factors of up to 100 (BSC 2005 [DIRS 172232], Section 6.2.1.4).
Drift-Scale THM Model (MDL-NBS-HS-000017 Rev. 01; Section 4.1.1.2)					
Values Used	6.0	16.0	25.0		
Mountain-Scale Coupled Processes (TH/THC/THM) Models (MDL-NBS-HS-000007 Rev. 03)					
Values Used	3.6	10.4	16.1	Average over three-dimensional TH model domain (Table 6.1-2)	
Values Used	5.8	17	28.8	Average over two-dimensional TH and THM model profiles (Section 6.1.4 and Table 6.5.6-1)	
Values Used	8.7	32.3	101.6	Average over segment of two-dimensional TH profile used for THC (Section 6.4.2.3)	
Ventilation Model and Analysis Report (ANL-EBS-MD-000030 Rev. 04, Section 6.9.1)					
Value Used	15.71	From mean flux field at location selected for sensitivity analysis.			

NOTE: [a] Refers to the 560-column footprint including the contingency area, for the previous and current data.